

Investigating the Air Stability of As-Grown and Intercalated 2D Materials for Future Electronics

Jimmy C. Kotsakidis

BSc, BEng (hons), Monash University

SUPERVISED BY:

Prof. Michael S. Fuhrer
Dr. D. Kurt Gaskill



MONASH
University

A thesis submitted for the degree of
Doctor of Philosophy,
Department of Physics and Astronomy,
Faculty of Science, Monash University.

August 2020

Copyright notices

Investigating the Air Stability of As-Grown and Intercalated 2D Materials for Future Electronics

© Jimmy C. Kotsakidis, 2020

Notice 1

Under the Copyright Act 1968, this thesis must be used only under the normal conditions of scholarly fair dealing. In particular no results or conclusions should be extracted from it, nor should it be copied or closely paraphrased in whole or in part without the written consent from the author. Proper written acknowledgement should be made for any assistance obtained from this thesis.

Notice 2

I certify that I have made all reasonable efforts to secure copyright permissions for third-party content included in this thesis and have not knowingly added copyright content to my work without the owner's permission.

This research was supported by an Australian Government Research Training Program (RTP) scholarship (formerly Australian Postgraduate Award, APA), and in part, funding from the Monash Centre for Atomically Thin Materials (MCATM).

Abstract

The two-dimensional (2D) materials graphene and monolayer WS₂ have demonstrated exciting physics that may lead to new electronic and optical devices. Furthermore, the modification of materials such as graphene *via* intercalation (insertion of atoms between graphene sheets, or between graphene and supporting substrate), have offered significant insight into basic physical phenomena such as superconductivity in calcium intercalated graphene. Yet the details surrounding their reaction with ambient atmosphere – which is critical for their technological implementation – is largely lacking. Thus, in this thesis, I seek to elucidate the ambient air reaction of monolayer WS₂ and alkaline earth (Mg/Ca) intercalated epitaxial graphene on silicon carbide.

In the first portion of this thesis, I present and discuss results regarding the ambient air oxidation of as-grown chemical vapor deposition (CVD) monolayers of WS₂ using optical microscopy, laser scanning confocal microscopy (LSCM), photoluminescence (PL) spectroscopy, and atomic force microscopy (AFM). I find that monolayer WS₂ exposed to ambient conditions in the presence of light that can excite a bandgap transition exhibits oxidation which can be detected with the LSCM and AFM. In contrast, samples kept in ambient air and darkness show no signs of oxidation for up to ten months. Low-irradiance/fluence light exposure experiments demonstrate that monolayer WS₂ can oxidise in as little as 7 days in above-bandgap light, even for irradiances and fluences eight and four orders of magnitude lower, respectively, than previously reported. No significant oxidation is observed for light with a photon energy below the threshold for optical excitations in WS₂. The strong wavelength dependence and lack of irradiance dependence implies that ambient oxidation of WS₂ is initiated by photon-mediated electronic band transitions, that is, photo-oxidation.

In the remaining parts of this thesis, I present and discuss recent results on the alkaline-earth (Ca and Mg) intercalation of epitaxial graphene on 6H-SiC(0001). While Ca-intercalation has been studied extensively, precisely where the Ca resides remains elusive. Furthermore, the intercalation of Mg underneath epitaxial graphene on 6H-SiC(0001) has not been reported. Here, I use low energy electron diffraction, X-ray photoelectron spectroscopy, secondary electron cut-off photoemission and scanning tunneling microscopy to elucidate the physical and electronic structure of both Ca- and Mg-intercalated epitaxial graphene on 6H-SiC(0001). I find that Ca intercalates underneath the buffer layer and bonds to the Si-terminated SiC surface, breaking the C-Si bonds of the buffer layer *i.e.* ‘freestanding’ the buffer layer to form Ca-intercalated quasi-freestanding bilayer graphene (Ca-QFSBLG). The situation is similar for the Mg-intercalation of epitaxial graphene on 6H-SiC(0001), where an ordered Mg-terminated reconstruction at the SiC surface is formed and Mg bonds to the Si-terminated SiC surface

are found, resulting in Mg-intercalated quasi-freestanding bilayer graphene (Mg-QFSBLG). Ca-intercalation underneath the buffer layer has not been considered in previous studies of Ca-intercalated epitaxial graphene. Furthermore, I find no evidence that either Ca or Mg intercalates between graphene layers. However, I do find that both Ca-QFSBLG and Mg-QFSBLG exhibit very low work functions, indicating high n-type doping. Upon exposure to ambient conditions, I find Ca-QFSBLG degrades rapidly, whereas Mg-QFSBLG remains remarkably stable.

Declaration

This thesis is an original work of my research and contains no material which has been accepted for the award of any other degree or diploma at any university or equivalent institution and that, to the best of my knowledge and belief, this thesis contains no material previously published or written by another person, except where due reference is made in the text of the thesis.

Signature:

Print Name: Jimmy C. Kotsakidis

Date: 28th of April, 2020

Publications During Enrolment

Kotsakidis, J. C., Grubišić-Čabo, A., Yin, Y., Tadich, A., Myers-Ward, R. L., DeJarlid, M., Pavunny, S. P., Currie, M., Daniels, K. M., Liu, C., Edmonds, M. T., Medhekar, N. V., Gaskill, D. K., de Parga, A. L. V., Fuhrer, M. S. (2020). Freestanding n-Doped Graphene via Intercalation of Calcium and Magnesium Into the Buffer Layer - SiC(0001) Interface. *Chemistry of Materials*, 32 (15), 6464-6482.

Grubišić-Čabo, A., Kotsakidis, J. C., Yin, Y., Tadich, A., Haldon, M., Solari, S., di Bernardo, I., Daniels, K.M., Riley, J., Huwald, E., Edmonds, M. T., Myers-Ward, R. L., Medhekar, N. V., Gaskill, D. K., Fuhrer, M. S. (2020). Magnesium-Intercalated Graphene on SiC: Highly n-Doped Air-Stable Bilayer Graphene at Extreme Displacement Fields. [arXiv:2005.02670](https://arxiv.org/abs/2005.02670)

Kotsakidis, J. C., Zhang, Q., de Parga, A. L. V., Currie, M., Helmerson, K., Gaskill, D. K., Fuhrer, M. S. (2019). Oxidation of Monolayer WS₂ in Ambient Is a Photoinduced Process. *Nano letters*, 19 (8), 5205-5215.

Clark, R. M., Kotsakidis, J. C., Weber, B., Berean, K. J., Carey, B. J., Field, M. R., Khan, H., Zhen, J., Ahmed, T., Harrison C. J., Cole, I. S., Latham, K., Kalantar-Zadeh, K., Daeneke, T. (2016). Exfoliation of Quasi-Stratified Bi₂S₃ Crystals into Micron-Scale Ultrathin Corrugated Nanosheets. *Chemistry of Materials*, 28 (24), 8942-8950.

Walia, S., Balendhran, S., Ahmed, T., Singh, M., El-Badawi, C., Brennan, M. D., Weerathunge, P., Karim, M. D., Rahman, F., Rassell, A., Duckworth, J., Ramanathan, R., Collis, G. E., Lobo, C. J., Toth, M., Kotsakidis, J. C., Weber, B., Fuhrer, M. S., Dominguez-Vera, J. M., Spencer, J. S., Aharonovich, I., Sriram, S., Bhaskaran, M., Bansal, V. (2017). Ambient Protection of Few-Layer Black Phosphorus via Sequestration of Reactive Oxygen Species. *Advanced Materials*, 29 (27), 1700152.

Acknowledgements

Out of all the words in this text, I have found the following most important (and difficult) to write.

The past 4 years of my PhD candidature have been filled with unique experiences and fantastic colleagues, for which I am very grateful. No experimental physics PhD is done completely ‘in a vacuum’, it is a collaborative effort and I am thankful to all those who have helped me along the way. Although initially there was some doubt if I was to be even *allowed* into the PhD program, since I had not completed an honours or masters in physics prior. I believe the decision came down to a few people. I had a meeting with the postgraduate coordinator at the time, Dr. Alexis Bishop, who (I believe) determined my suitability for candidature largely from my tenacity and attention to detail in the undergraduate laboratory!

First, I would like to extend gratitude to Prof. Michael Fuhrer for giving me the opportunity to begin my PhD in his laboratory at Monash University. Michael has been a wealth of knowledge on all topics, and has constantly challenged me over the years, while simultaneously allowing me to independently investigate new ideas. Personally, I like this style, and it has helped shape me into the independent scientist I am today. I feel lucky to have worked at Monash University, as there is so much science going on in the immediate area – the Australian Synchrotron, Melbourne Centre for Nanofabrication and CSIRO, are all within walking distance, and I have used all these facilities during my PhD.

In the first year (2016) of my PhD, I met Dr. D. Kurt Gaskill who was working in our laboratory at Monash University while on sabbatical from the U.S. Naval Research Laboratory (NRL). It was at this point that I decided to pursue his wild idea of the calcium intercalation of graphene. Initially, we analysed hydrogen intercalated samples with the STM (which were very insightful, and led to some new findings which were later presented in Graphene Week of 2017), and tried some preliminary calcium intercalation experiments at the Australian Synchrotron. At this point, the intercalation work was becoming quite interesting, and I wanted to pursue it further. I subsequently asked Kurt to become a secondary supervisor on this thesis, the rest as they say, is history. Absolutely none of the intercalation work would have been possible without our collaboration with Kurt and the Advanced Silicon Carbide Epitaxial Research group at the Electronics Science and Technology Division at NRL. I am very grateful for our interactions in the laboratory, but also outside. Barbecues and birding trips to Virginia, Bendigo and the Mornington Peninsula have provided necessary and joyful distraction from the laboratory.

On that note, I am extremely grateful for the visitors we have had in the laboratory over the years. Dr. Felix Bischoff from the Technical University of

Munich who taught me a few tricks with the STM, and Dr. Michael Lodge from the University of Central Florida who was a constant source of positivity and knowledge around the laboratory.

In mid-2017, I was able to spend 5 weeks at NRL working with NRL engineers to fabricate a 4-contact graphene device and I simultaneously investigated WS₂ crystals I had grown in Melbourne (the WS₂ project was still something I was pursuing as a side project, even though graphene and the intercalation experiments were taking up most of my time). I think the volume of ideas and work conducted in these 5 weeks were some of the most productive in my entire PhD. Many thanks must be extended to Dr. Anindya Nath, Dr. Matthew DeJarld, Dr. Marc Currie, Dr. Byoung-Don ('B.D.') Kong, Dr. Kevin Daniels, Dr. Shojan P. Pavunny, Dr. Karthik Sridhara, Dr. Anthony Boyd, Dr. Glenn Jernigan and Dr. Rachael L. Myers-Ward. The enthusiasm I experienced at NRL has been unparalleled in all my other interactions, and I have tried to apply this same enthusiasm in other aspects of my work. Furthermore, the comradery at NRL was quite infectious, and for this I must give a special mention to Dr. Virginia Anderson and Dr. Nicholas Sharac. In this 5-week period, a two-day collaboration between Dr. Marc Currie and I produced the necessary initial data that began my investigation into WS₂ oxidation (and has set the tone for this entire thesis). In fact, I had come to Dr. Marc Currie with a completely different idea – I wanted to understand what was happening at the edges of the WS₂ crystals. So, I devised an experiment that would make use of the small vacuum cell in the laboratory (which could be heated and cooled to LN₂ temperatures). The competing ideas then (and now it seems) was that either the edge was chemically heterogeneous, or that water was intercalated at the edges of the WS₂ crystallites. The plan then was to heat the crystals to try and drive off the water that may be there, and take before and after PL measurements of the same edge. Although the experiments were inconclusive, Marc's comment on 'odd' features with some WS₂ samples he had worked with previously (possibly linked to degradation) prompted further examination of the samples I had grown under the laser scanning confocal microscope at NRL. Low and behold, the samples exhibited these odd features as well, to the point where the crystal looked of very poor quality, covered in triangular defects. I took out some other samples (that I had stored for a year or more in a draw back in Melbourne) to see how they had fared – to our astonishment there were no defects. I took this knowledge back with me to Melbourne, and over the next few months performed the crucial experiments which found that the true mechanism causing this degradation was a photo-oxidation reaction, likely involving moisture (it was *very* humid in D.C. in the summer of 2017). The fact that those crystals I had grown a year prior were stored in a dark draw were fundamental in solving the mystery, as was Marc's experimental insight. A short discussion with Dr. Glenn Jernigan really got me thinking about the XPS data and how to set up the experiment at the synchrotron. Another short meeting between Anindya, Marc, Kurt and I set in motion the idea for laser patterning voids in the graphene samples (using

the laser patterning technique that was developed by Marc) that were eventually used in the XPS experiments in the Australian Synchrotron. These samples ended up being quite important in verifying certain components in the spectra, and in finding the possible mechanism of magnesium intercalation. I was also able to obtain some hBN samples from Dr. Karthik Sridhara, which ended up being used in some separate experiments. I am extremely thankful for all these interactions.

At the beginning of 2018, Prof. Amadeo L. Vázquez de Parga from the Autonomous University of Madrid visited our laboratory on a 1-year sabbatical. Amadeo's prior expertise in STM, graphene intercalation, UHV and surface science were of immense help in the completion of this thesis. We worked closely on both the intercalation project and the WS₂ project, and it is safe to say that the quality of this thesis has been enhanced as a result.

On this note, I must thank my PhD comrades in the Fuhrer laboratory. Firstly Dr. Qianhui (Sherry) Zhang – thank you for all the support in the CVD lab, and with the WS₂ oxidation investigation. You have always been there to lend a hand, and I couldn't imagine the CVD lab functioning as smoothly without your presence. To Mr. James Collins, thank you for always being willing to help. As the main user of the other STM in the laboratory, we shared a lot of the struggles of upkeep such a complex machine. Our travels to the U.S. were both fun, and an amazing learning experience. To Mr. Chang Liu for helping about the laboratory and at the synchrotron. Thank you to Mr. Dhaneesh Gopalakrishnan and Ms. Marina Castelli – the 'other' STM team. There was always great benefit from interactions between our groups, something that I hope continues in the next generation of PhD students.

I also want to thank the past and present post-docs at Monash University. In particular, Dr. Semonti Bhattacharyya who assisted with use of the glove box, Dr. Changxi Zheng who helped setup the CVD furnace, Dr. Bent Weber for initially imparting STM and nanofabrication knowledge onto me, A/Prof Mark Edmonds for suggesting the XPS experiments at the synchrotron, Dr. Cornelius Krull for much needed expertise in all things STM and Dr. Antonija Grubišić-Čabo for help with synchrotron data collection. Many late nights and long days were had, but these efforts have made a clear impact on this thesis.

Since I am on the subject of synchrotrons, I'd like to extend a massive thank you to all the staff at the soft X-ray beamline at the Australian Synchrotron. Much credit must be given to Dr. Anton Tadich, who helped immensely on the synchrotron proposals and data collection at the beamtime. Anton's passion for surface science and wealth of knowledge inspired me to be more interested in synchrotron science.

Also, I would like to thank Dr. Anthony Chesman at the Commonwealth Scientific and Industrial Research Organisation (CSIRO) for assistance with

all the absorption/transmittance and reflection measurements on WS₂. A special thank you to Mr. Findley Shanks in the Department of Chemistry for assistance and training on the Raman spectrometer. Thank you Prof. Kris Helmerson for being an amazing postgraduate coordinator throughout the years (Duncan has some big shoes to fill, but I am happy to report, through my brief interactions, that I am sure he will make a similarly fantastic postgraduate coordinator), and for allowing me to use the optical table for my odd WS₂ experiments. In fact, I am grateful for the amazing BEC group at Monash, (the late) Dr. Shaun P. Johnstone, Dr. Sebastian Tempone-Wiltshire and Dr. Philip T. Starkey for all the help in and around the laboratory throughout the years. We always sought to help each other whenever possible, and made it an extremely collaborative environment around the experimental laboratories at Monash University.

Thank you to our collaborators at Monash University, A/Prof. Nikhil Medhekar and Dr. Yuefeng Yin, who conducted theoretical calculations on the structure of calcium and magnesium intercalated graphene. The quality of the experimental work was enhanced greatly by your contributions. Of course, no acknowledgement would be complete without thanks to the amazing administration staff, Jean and Karen in the School of Physics and Astronomy.

This thesis before you truly would not have been possible without the constant support from my wife, family, and friends. It was my parents who first got me interested in science (from my earliest memory of observing the night sky with a telescope), and they have supported me since my undergraduate studies both financially and emotionally. They have always been there for me, and I am eternally grateful. After my mother was diagnosed with cancer just prior to beginning my PhD, I questioned whether pursuing such a gruelling and intense program was really something I wanted to do. My father provided the necessary guidance, “If you think you will discover something new, go for it”. This has stayed with me since I began (my mother has since made a full recovery). I am sure they are more than relieved to see me finish this chapter in my life.

I am also grateful for the support and advice of my friends in Australia and abroad – I hope we can catch up properly after I hand this in.

And last but surely not least, thank you to my wife Michelle for your never-ending love, support, and patience. Writing during the COVID-19 pandemic and current global uncertainty has not been easy, but it is finally done!

To my amazing wife, Michelle

CONTENTS

CONTENTS	12
LIST OF FIGURES.....	16
LIST OF TABLES.....	28
1 INTRODUCTION	33
1.1 THESIS OBJECTIVE AND SCOPE	35
2 TWO-DIMENSIONAL MATERIALS.....	39
2.1 OVERVIEW.....	39
2.2 GRAPHENE.....	40
2.2.1 <i>Atomic and Electronic Band Structure</i>	40
2.2.2 <i>Epitaxial Graphene Synthesised on Silicon Carbide</i>	47
2.3 MONOLAYER TUNGSTEN DISULPHIDE.....	53
2.3.1 <i>Atomic and Electronic Band Structure</i>	53
2.3.2 <i>Optical Properties</i>	56
3 EXPERIMENTAL TECHNIQUES.....	58
3.1 INTRODUCTION.....	58
3.2 SCANNING TUNNELLING MICROSCOPY	59
3.2.1 <i>Theoretical Basis for the Scanning Tunnelling Microscope</i>	60
3.2.2 <i>Practical Basis for the Scanning Tunnelling Microscope</i>	62
3.2.3 <i>The Scanning Tunnelling Microscope in the Fuhrer Laboratory</i>	64
3.3 ATOMIC FORCE MICROSCOPY	66
3.3.1 <i>Working Principle of a Modern Atomic Force Microscope</i>	68
3.3.2 <i>Scanning Modes of an Atomic Force Microscope</i>	69
3.4 X-RAY PHOTOELECTRON SPECTROSCOPY	71
3.4.1 <i>Overview of the X-ray Photoemission Process</i>	72
3.4.2 <i>Secondary Electron Cut off Photoemission Spectroscopy</i>	77
3.4.3 <i>Spectral Interpretation</i>	79
3.4.4 <i>The Advantages of Synchrotron Radiation</i>	88
3.5 LOW ENERGY ELECTRON DIFFRACTION	93
3.5.1 <i>Experimental Setup</i>	95
3.5.2 <i>Interpreting Low Energy Electron Diffraction Spectrograms</i>	97
3.6 CHEMICAL VAPOUR DEPOSITION	99
3.6.1 <i>Chemical Vapour Deposition Growth of Tungsten Disulphide</i>	100
3.7 RAMAN AND PHOTOLUMINESCENCE SPECTROSCOPY.....	101

3.7.1	<i>Raman Spectroscopy</i>	102
3.7.2	<i>Photoluminescence Spectroscopy</i>	106
3.8	LASER SCANNING CONFOCAL MICROSCOPY	109
4	OXIDATION OF MONOLAYER WS₂ IS A PHOTOINDUCED PROCESS.....	112
4.1	OVERVIEW.....	112
4.2	INTRODUCTION.....	113
4.3	METHODS.....	115
4.3.1	<i>Chemical Vapour Deposition</i>	115
4.3.2	<i>Photoluminescence Mapping Spectroscopy</i>	116
4.3.3	<i>Reflectance, Transmission and Absorptance Spectroscopy</i>	117
4.3.4	<i>Laser Scanning Confocal Microscopy</i>	117
4.3.5	<i>Atomic Force Microscopy</i>	119
4.3.6	<i>Low Irradiance Light Exposure Experiments</i>	119
4.3.7	<i>Glove Box Experiments</i>	121
4.4	RESULTS	122
4.4.1	<i>Initial Laser Scanning Confocal Microscope Investigations</i>	122
4.4.2	<i>Photoluminescence Mapping and Atomic Force Microscopy</i>	126
4.4.3	<i>Low-Irradiance Light Experiments</i>	131
4.4.4	<i>Effects of Light Exposure in a Nitrogen Environment</i>	134
4.4.5	<i>Effects of Light and Heating in Ambient</i>	135
4.5	DISCUSSION.....	136
4.6	CONCLUSION.....	140
5	CALCIUM INTERCALATION OF GRAPHENE ON SILICON CARBIDE.....	142
5.1	OVERVIEW.....	142
5.2	INTRODUCTION.....	143
5.3	METHODS.....	146
5.3.1	<i>Low Energy Electron Diffraction</i>	146
5.3.2	<i>X-ray Photoelectron Spectroscopy</i>	147
5.3.3	<i>Scanning Tunnelling Microscopy</i>	150
5.3.4	<i>Ca-Intercalation Procedure</i>	151
5.3.5	<i>Secondary Electron Cut-Off Photoemission Spectroscopy</i>	152
5.4	RESULTS AND DISCUSSION.....	153
5.4.1	<i>Low Energy Electron Diffraction</i>	153
5.4.2	<i>X-ray Photoelectron Spectroscopy of Ca-QFSBLG</i>	156
5.4.3	<i>Low Temperature Scanning Tunnelling Microscopy of Ca-QFSBLG</i>	169
5.4.4	<i>Density Function Theory Calculations of Ca-QFSBLG Structure</i>	175
5.4.5	<i>Carrier Type and Concentration in Ca-QFSBLG</i>	177

5.5	CONCLUSION.....	183
6	MAGNESIUM INTERCALATION OF GRAPHENE ON SILICON CARBIDE.....	185
6.1	OVERVIEW.....	185
6.2	INTRODUCTION.....	186
6.3	METHODS AND EXPERIMENTAL TECHNIQUES.....	188
6.3.1	<i>Mg-Intercalation Procedure</i>	188
6.3.2	<i>Low Energy Electron Diffraction</i>	189
6.3.3	<i>X-ray Photoelectron Spectroscopy (XPS)</i>	190
6.3.4	<i>Scanning Tunnelling Microscopy (STM)</i>	191
6.3.5	<i>Secondary Electron Cut-Off (SECO) Photoemission</i>	192
6.3.6	<i>Angle Resolved Photoemission Spectroscopy (ARPES)</i>	193
6.4	RESULTS AND DISCUSSION.....	194
6.4.1	<i>Low Energy Electron Diffraction (LEED)</i>	194
6.4.2	<i>X-ray Photoelectron Spectroscopy (XPS)</i>	197
6.4.3	<i>Low Temperature Scanning Tunnelling Microscopy (STM)</i>	208
6.4.4	<i>Carrier Type and Concentration in Mg-QFSBLG</i>	209
6.4.5	<i>Angle Resolved Photoemission Spectroscopy (ARPES)</i>	213
6.5	CONCLUSION.....	217
7	AMBIENT AIR STABILITY OF CA- AND MG-INTERCALATED QUASI-FREESTANDING BILAYER GRAPHENE	218
7.1	OVERVIEW.....	218
7.2	INTRODUCTION.....	219
7.3	METHODS.....	222
7.3.1	<i>Sample Intercalation and Ambient Air Exposure</i>	222
7.3.2	<i>X-ray Photoelectron Spectroscopy Using a Lab-Based Source</i>	224
7.3.3	<i>Raman Mapping Spectroscopy</i>	224
7.4	RESULTS AND DISCUSSION.....	225
7.4.1	<i>Ambient Air Exposure of Calcium-Intercalated Quasi-Freestanding Bilayer Graphene on SiC(0001) (Ca-QFSBLG)</i>	225
7.4.2	<i>Ambient Air Exposure of Magnesium-Intercalated Quasi-Freestanding Bilayer Graphene on SiC(0001) (Mg-QFSBLG)</i>	238
7.5	CONCLUSION.....	245
8	OUTLOOK AND CONCLUDING REMARKS	246
8.1	INTRODUCTION.....	246
8.2	OXIDATION OF MONOLAYER WS ₂ IS A PHOTOINDUCED PROCESS.....	247
8.2.1	<i>Proposed Photo-Oxidation Mechanism and Reaction Pathway</i>	247
8.2.2	<i>Finding the Threshold Temperature of Oxidation for WS₂</i>	251

8.3	CA-INTERCALATED QUASI FREESTANDING BILAYER GRAPHENE (CA-QFSBLG) ...	255
8.3.1	<i>Surface Deposition of Calcium on Epitaxial Graphene on 6H-SiC(0001)</i>	255
8.3.2	<i>Is Ca-QFSBLG a Superconductor?</i>	258
8.4	MG-INTERCALATED QUASI FREESTANDING BILAYER GRAPHENE (MG-QFSBLG) ..	259
8.4.1	<i>Density Functional Theory Calculations of the Mg-QFSBLG Structure</i>	259
8.4.2	<i>Using the Relative Reactivity of Intercalants for Device Fabrication</i>	261
8.4.3	<i>Intercalation Mechanism and Increasing Intercalation Efficiency</i>	261
8.5	OXIDATION OF CA-QFSBLG AND MG-QFSBLG	266
8.5.1	<i>Long-term Ambient Air Stability of Mg-QFSBLG</i>	266
8.5.2	<i>Gas Sensors: Utilising Ambient Air Reacted Intercalated Compounds</i>	273
8.6	CONCLUDING REMARKS	274
	BIBLIOGRAPHY.....	278
	APPENDIX A TUNGSTEN DISULPHIDE	324
A1.	MATLAB CODE FOR WS ₂ PL PEAK MAPPING	324
A2.	PHOTOLUMINESCENCE QUENCHING OF WS ₂ AFTER OXIDATION.....	327
	APPENDIX B CALCIUM INTERCALATION	328
B1.	FUNCTIONS USED FOR THE FITTING OF XPS COMPONENTS	328
B2.	COMPLETE C 1S AND SI 2P TABLE OF VALUES FOR CA-INTERCALATION EXPERIMENTS	329
B3.	COMPLETE C 1S AND SI 2P XPS SPECTRA FOR CA-QFSBLG FABRICATED FROM PRISTINE EMLG.....	341
B4.	FABRICATION OF CA-QFSBLG FROM H-QFSBLG	349
B5.	STM SURFACE CLEANING PROCEDURE FOR CA-QFSBLG	361
	APPENDIX C MAGNESIUM INTERCALATION	363
C1.	TABLES OF VALUES FOR MG-INTERCALATION EXPERIMENTS	363
C2.	COMPLETE C 1S AND SI 2P XPS SPECTRA FOR MG-QFSBLG	374
C3.	THE MG-INTERCALATION OF H-QFSBLG	380
C4.	STEP-WISE MG-INTERCALATION OF EPITAXIAL MONOLAYER GRAPHENE ON 6H-SiC(0001).....	386
C5.	RAMAN SPECTROSCOPY MAP OF BUFFER LAYER / EMLG SISTER SAMPLE USED IN ARPES STUDY.....	390
	APPENDIX D PUBLICATIONS ARISING FROM THESIS.....	392

List of Figures

FIGURE 1.1 – THE METAL-OXIDE-SEMICONDUCTOR FIELD EFFECT TRANSISTOR (MOSFET).....	35
FIGURE 2.1: ATOMIC STRUCTURE OF GRAPHENE.	41
FIGURE 2.2: THE BANDSTRUCTURE AND DENSITY OF STATES OF GRAPHENE.	43
FIGURE 2.3: ATOMIC STRUCTURE AND ELECTRONIC BANDSTRUCTURE OF BILAYER GRAPHENE.....	46
FIGURE 2.4: STRUCTURE OF 6H-SiC(0001) AND GRAPHENE SAMPLES USED.....	47
FIGURE 2.5: SIMPLIFIED PROCESS FOR EPITAXIAL MONOLAYER GRAPHENE (EMLG) AND QUASI-FREESTANDING BILAYER GRAPHENE (QFSBLG) ON SILICON CARBIDE.	51
FIGURE 2.6: EFFECTS OF INTERCALATING EPITAXIAL GRAPHENE WITH HYDROGEN..	52
FIGURE 2.7: ATOMIC AND ELECTRONIC BANDSTRUCTURE OF BULK, BILAYER AND MONOLAYER TUNGSTEN DISULPHIDE.....	55
FIGURE 2.8: OPTICAL SPECTRA OF WS ₂ AT ROOM TEMPERATURE.....	57
FIGURE 3.1: THE FIRST SCANNING TUNNELLING MICROSCOPE (STM).	60
FIGURE 3.2: SIMPLE SCHEMATIC OVERVIEW AND IMAGING CAPABILITY OF THE SCANNING TUNNELLING MICROSCOPE (STM).	64
FIGURE 3.3: OVERVIEW OF THE LOW TEMPERATURE SCANNING TUNNELLING MICROSCOPE IN THE FUHRER LABORATORY.....	65
FIGURE 3.4: SAMPLE HOLDER AND EFFUSION CELL SETUP.	66
FIGURE 3.5: THE FIRST ATOMIC FORCE MICROSCOPE (AFM); COMPARISON OF THE FIRST AND MODERN DAY CANTILEVERS.	67

FIGURE 3.6: LENNARD-JONES POTENTIAL MODEL FOR THE ATOMIC FORCE MICROSCOPE TIP-SAMPLE INTERACTION.	68
FIGURE 3.7: SCHEMATIC OF THE BRUKER DIMENSION ICON ATOMIC FORCE MICROSCOPE (AFM) SCAN HEAD.	69
FIGURE 3.8: DIFFERENT OPERATING MODES OF THE ATOMIC FORCE MICROSCOPE.	70
FIGURE 3.9: SIMPLIFIED SCHEMATIC OF A MODERN X-RAY PHOTOELECTRON SPECTROMETER AT A SYNCHROTRON.	72
FIGURE 3.10: OVERVIEW OF THE PHOTOEMISSION PROCESS IN X-RAY PHOTOEMISSION SPECTROSCOPY.....	74
FIGURE 3.11: INELASTIC MEAN FREE PATH (IMFP) AND PHOTOIONIZATION CROSS SECTIONS FOR SILICON AND CARBON.	76
FIGURE 3.12: OVERVIEW OF THE SECONDARY ELECTRON CUT-OFF PHOTOEMISSION PROCESS.....	78
FIGURE 3.13: X-RAY PHOTOEMISSION SPECTROGRAM OF THE Au 4f CORE LEVEL OF SPUTTER ANNEALED GOLD SHOWING SPIN-ORBIT SPLITTING OF $J = 7/2$ (GREEN) AND $J = 5/2$ (BLUE) LEVELS.....	80
FIGURE 3.14: X-RAY PHOTOEMISSION SPECTRUM SHOWING THE Si 2p CORE LEVEL OF A SiC SAMPLE WITH SURFACE OXIDATION, AT A PHOTON ENERGY OF $E_{hv} = 150$ eV.	81
FIGURE 3.15: VISUALISATION OF THE FINAL STATE EFFECTS ON THE X-RAY PHOTOEMISSION SPECTRUM.....	84
FIGURE 3.16: SUMMARY OF THE COMMON BACKGROUND SUBTRACTION TECHNIQUES.	85
FIGURE 3.17: DONIACH-ŠUNJIĆ LINESHAPE WITH $\Gamma = 0.25$ eV.....	87

FIGURE 3.18: COMPARISON OF A DONIACH-ŠUNJIĆ (DS) AND BREIT-WIGNER-FANO (BWF) FIT TO THE C 1S CORE LEVEL OF HYDROGEN INTERCALATED GRAPHENE ON SILICON CARBIDE (H-QFSBLG) AT AN X-RAY ENERGY OF $E_{hv} = 330$ eV....	88
FIGURE 3.19: BEAM ENERGY TUNEABILITY USING A SYNCHROTRON RESULTS IN DEPTH DEPENDENT MEASUREMENTS.	90
FIGURE 3.20: THE NECESSITY FOR SYNCHROTRON RADIATION IN 2D MATERIALS EXPERIMENTS CONCERNING INTERCALATION.	92
FIGURE 3.21: EWALD SPHERE CONSTRUCTION AND CORRESPONDING LEED DIFFRACTION SPOTS.	95
FIGURE 3.22: SCHEMATIC OF A LOW ENERGY ELECTRON DIFFRACTION SET-UP.....	96
FIGURE 3.23: REAL SPACE HEXAGONAL LATTICE STRUCTURES AND THEIR RECIPROCAL SPACE TRANSFORMATIONS DESCRIBED USING WOOD'S NOTATION.....	97
FIGURE 3.24: SKETCH OF THE LEED DIFFRACTION PATTERN OF PRISTINE GRAPHENE ON 4H-SiC(0001).....	98
FIGURE 3.25: GENERAL SCHEMATIC OVERVIEW OF THE CHEMICAL VAPOUR DEPOSITION (CVD) PROCESS.....	100
FIGURE 3.26: THE LINDBURG/BLUE HTF55122A SINGLE-ZONE TUBE FURNACE IN THE FUHRER LABORATORY.....	101
FIGURE 3.27: SCHEMATIC OF A CONFOCAL MICRO-RAMAN/MICRO-PHOTOLUMINESCENCE (MAPPING) SPECTROMETER.....	102
FIGURE 3.28: THE RAMAN PROCESS AND ACTIVE RAMAN MODES IN GRAPHENE.	104
FIGURE 3.29: A TYPICAL RAMAN SPECTRUM AND OVERVIEW OF SOME OF THE RAMAN PROCESSES OF GRAPHENE.....	105
FIGURE 3.30: THE PHOTOLUMINESCENCE (PL) PROCESS.	106

FIGURE 3.31: EXCITON STRUCTURE AND CORRESPONDING PHOTOLUMINESCENCE SPECTROSCOPY IN WS ₂	108
FIGURE 3.32: SCHEMATIC OF A LASER SCANNING CONFOCAL MICROSCOPE (LSCM).	110
FIGURE 3.33: LASER SCANNING CONFOCAL MICROSCOPE (LSCM) MICROGRAPH OF MONOLAYER WS ₂ SHOWING CONTRAST ENHANCEMENT.	111
FIGURE 4.1: SETUP OF THE CHEMICAL VAPOUR DEPOSITION FURNACE.....	116
FIGURE 4.2: TRANSMITTANCE, REFLECTANCE AND ABSORPTANCE OF WS ₂	117
FIGURE 4.3: LASER SCANNING CONFOCAL MICROSCOPE (LSCM) LIGHT SOURCES FOR THE OLS4100 LSCM.	118
FIGURE 4.4: LASER SPECTRA OF LASERS USED IN LOW-IRRADIANCE EXPERIMENTS.	120
FIGURE 4.5: LOW IRRADIANCE EXPERIMENTAL SETUP.	120
FIGURE 4.6: LIGHT BOX SETUP FOR LOW-IRRADIANCE EXPERIMENTS IN GLOVE BOX.	121
FIGURE 4.7: GREEN LED SPECTRUM.	122
FIGURE 4.8: LASER SCANNING CONFOCAL MICROGRAPHS OF MONOLAYER WS ₂ . ..	124
FIGURE 4.9: EFFECTS OF LSCM.....	125
FIGURE 4.10: μ -PL AND AFM OF CVD-GROWN MONOLAYER WS ₂	127
FIGURE 4.11: THE EDGE OF A WS ₂ CRYSTAL ANALYSED WITH AFM AND LSCM. ...	128
FIGURE 4.12: HEIGHT ANALYSIS OF OXIDISED REGIONS ON THE SURFACE OF WS ₂	130
FIGURE 4.13: ABSORPTANCE SPECTRUM OF MONOLAYER WS ₂ AND LOW-IRRADIANCE EXPERIMENTS.	132
FIGURE 4.14: EFFECTS OF BRIEF AMBIENT AND STRAY LIGHT EXPOSURE ON WS ₂	133
FIGURE 4.15: LOW-IRRADIANCE LIGHT EXPOSURES IN A GLOVE BOX.	134

FIGURE 4.16: HEATING MONOLAYER WS ₂ IN AMBIENT AND DARKNESS.....	135
FIGURE 5.1: SOFT X-RAY BEAMLINE SETUP AT THE AUSTRALIAN SYNCHROTRON... ..	149
FIGURE 5.2: CREATEC LOW TEMPERATURE SCANNING TUNNELLING MICROSCOPE (STM).....	150
FIGURE 5.3: LOW ENERGY ELECTRON DIFFRACTION (LEED) OF PRISTINE AND CA- INTERCALATED GRAPHENE ON 6H-SiC(0001) AT AN ELECTRON ENERGY OF 100 eV.	155
FIGURE 5.4: X-RAY PHOTOEMISSION SPECTRA OF THE Si 2p CORE LEVEL OF PRISTINE EPITAXIAL MONOLAYER GRAPHENE (EMLG) AND CALCIUM INTERCALATED QUASI-FREESTANDING BILAYER GRAPHENE ON SILICON CARBIDE (Ca-QFSBLG) AT TWO INCIDENT X-RAY ENERGIES, E _{hv} = 150 eV (LEFT, SURFACE SENSITIVE) AND 600 eV (RIGHT, BULK SENSITIVE).	158
FIGURE 5.5: X-RAY PHOTOEMISSION SPECTRA OF THE C 1s CORE-LEVEL OF PRISTINE EPITAXIAL MONOLAYER GRAPHENE (EMLG) AND Ca-INTERCALATED GRAPHENE ON SILICON CARBIDE (Ca-QFSBLG) AT TWO X-RAY ENERGIES, E _{hv} = 330 eV (LEFT, SURFACE SENSITIVE) AND E _{hv} = 600 eV (RIGHT, BULK SENSITIVE).	162
FIGURE 5.6: X-RAY PHOTOEMISSION SPECTRA OF THE O 1s CORE LEVEL AFTER EACH Ca-INTERCALATION STEP OF EPITAXIAL MONOLAYER GRAPHENE (EMLG) TAKEN AT AN X-RAY ENERGY OF E _{hv} = 900 eV.	164
FIGURE 5.7: Ca 2p CORE LEVEL OF PURE CALCIUM DEPOSITED ON EPITAXIAL MONOLAYER GRAPHENE (EMLG) AT AN X-RAY ENERGY OF E _{hv} = 500 eV.....	165
FIGURE 5.8: X-RAY PHOTOEMISSION SPECTRA SHOWING THE Ca 2p CORE LEVEL OF Ca-INTERCALATED EPITAXIAL MONOLAYER GRAPHENE (Ca-QFSBLG) AT AN X- RAY ENERGY OF E _{hv} = 500 eV.	166

FIGURE 5.9: SCANNING TUNNELLING MICROSCOPE (STM) MICROGRAPHS OF PRISTINE EPITAXIAL MONOLAYER GRAPHENE (EMLG) BEFORE AND AFTER Ca-INTERCALATION.	173
FIGURE 5.10: SCANNING TUNNELLING MICROSCOPE (STM) MICROGRAPHS OF Ca-QFSBLG AT 4.6 K SHOWING MAGNIFIED VIEW OF BRIGHT AND DARK SPOTS AT VARIOUS TIP BIASING CONDITIONS.	174
FIGURE 5.11: ATOMIC MODELS (DARK BLUE = Si, BROWN = C, LIGHT BLUE = Ca) OF Ca-INTERCALATED MONOLAYER GRAPHENE ON SiC(0001) SHOWING THE TWO POSSIBLE INTERCALATION REGIMES.	176
FIGURE 5.12: THEORETICALLY CALCULATED VALUES (FROM REF. [25]) OF THE C 1s CORE LEVEL OF HIGHLY DOPED BILAYER (AND MONOLAYER) GRAPHENE COMPARED WITH Ca-QFSBLG (2 nd Ca-INTERCALATION, $E_{hv} = 600$ eV, FIGURE 5.5d).	180
FIGURE 5.13: SECONDARY ELECTRON CUT-OFF (SECO) PHOTOEMISSION MEASUREMENTS OF Ca-QFSBLG.....	182
FIGURE 5.14: SECO MEASUREMENTS SHOWING THE WORKFUNCTION (W_f) OF Ca-QFSBLG (SAMPLE FROM FIGURE 5.13) AFTER DEPOSITION OF 0.6 nm OF CALCIUM ON THE SURFACE (DASH DOT, BLUE LINE) COMPARED TO PRISTINE EMLG (DOTTED, BLACK LINE).	183
FIGURE 6.1: ETCHING A TUNGSTEN TIP FOR THE SCANNING TUNNELLING MICROSCOPE.	192
FIGURE 6.2: TOROIDAL ANALYSER AT THE AUSTRALIAN SYNCHROTRON.	193

FIGURE 6.3: LOW ENERGY ELECTRON DIFFRACTION (LEED) OF PRISTINE AND Mg-INTERCALATED EPITAXIAL MONOLAYER GRAPHENE ON 6H-SiC(0001) (Mg-QFSBLG) AT AN ELECTRON ENERGY OF 100 eV.....196

FIGURE 6.4: X-RAY PHOTOEMISSION SPECTRA OF THE Si 2p CORE LEVEL OF PRISTINE EPITAXIAL MONOLAYER GRAPHENE (EMLG) AND Mg-INTERCALATED QUASI-FREESTANDING BILAYER GRAPHENE (Mg-QFSBLG) ON SiC(0001) AT X-RAY ENERGIES OF $E_{hv} = 150$ eV (LEFT, SURFACE SENSITIVE) AND $E_{hv} = 600$ eV (RIGHT, BULK SENSITIVE).....199

FIGURE 6.5: X-RAY PHOTOEMISSION SPECTRA FOR THE C 1s CORE LEVEL OF PRISTINE EPITAXIAL MONOLAYER GRAPHENE ON 6H-SiC(0001) (EMLG) AND Mg-INTERCALATED EMLG (Mg-QFSBLG) AT X-RAY ENERGIES OF $E_{hv} = 330$ eV (LEFT, SURFACE SENSITIVE) AND $E_{hv} = 600$ eV (RIGHT, BULK SENSITIVE).203

FIGURE 6.6: X-RAY PHOTOEMISSION SPECTRA OF THE O 1s CORE LEVEL OF Mg-QFSBLG AT AN X-RAY ENERGY OF $E_{hv} = 900$ eV.....205

FIGURE 6.7: X-RAY PHOTOEMISSION SPECTRA OF THE Mg 2p CORE LEVEL OF Mg-QFSBLG AT AN X-RAY ENERGY OF $E_{hv} = 100$ eV.....207

FIGURE 6.8: SCANNING TUNNELLING MICROSCOPE (STM) MICROGRAPH OF MAGNESIUM INTERCALATED EPITAXIAL MONOLAYER GRAPHENE, TO FORM MAGNESIUM-INTERCALATED QUASI-FREESTANDING BILAYER GRAPHENE (Mg-QFSBLG).208

FIGURE 6.9: THEORETICALLY CALCULATED VALUES (FROM REF. [25]) OF THE C 1s CORE LEVEL OF HIGHLY DOPED FREESTANDING BILAYER (AND MONOLAYER) GRAPHENE COMPARED WITH EXPERIMENTAL VALUES OF THE C 1s CORE LEVEL OF Mg-QFSBLG (2nd Mg-INTERCALATION, $E_{hv} = 600$ eV, FIGURE 6.5d).....211

FIGURE 6.10: SECONDARY ELECTRON CUT-OFF (SECO) PHOTOEMISSION MEASUREMENTS TO DETERMINE THE WORKFUNCTION OF EMLG AND Mg-QFSBLG	213
FIGURE 6.11: ANGLE RESOLVED PHOTOEMISSION SPECTRA OF PRISTINE EPITAXIAL MONOLAYER GRAPHENE ON 6H-SiC(0001) (EMLG) AND Mg-INTERCALATED EMLG (Mg-QFSBLG) [26]	216
FIGURE 7.1: X-RAY PHOTOEMISSION SPECTRA SHOWING THE C 1s CORE LEVEL OF SHORT-TERM AMBIENT AIR EXPOSED Ca-QFSBLG AT AN X-RAY ENERGY OF $E_{hv} = 600$ eV	226
FIGURE 7.2: X-RAY PHOTOEMISSION SPECTRA SHOWING THE Si 2p CORE LEVEL OF SHORT-TERM AMBIENT AIR EXPOSED Ca-QFSBLG AT AN X-RAY ENERGY OF $E_{hv} = 150$ eV	228
FIGURE 7.3: X-RAY PHOTOEMISSION SPECTRA SHOWING THE O 1s CORE LEVEL OF SHORT-TERM AMBIENT AIR EXPOSED Ca-QFSBLG AT AN X-RAY ENERGY OF $E_{hv} = 900$ eV	231
FIGURE 7.4: SECONDARY ELECTRON CUT-OFF (SECO) PHOTOEMISSION MEASUREMENTS SHOWING THE WORKFUNCTION OF Ca-QFSBLG EXPOSED TO AMBIENT AIR FOR 30 MINUTES.....	232
FIGURE 7.5: X-RAY PHOTOEMISSION SPECTRA SHOWING THE C 1s CORE LEVEL OF Ca-QFSBLG EXPOSED TO AMBIENT AIR FOR 1 YEAR.....	234
FIGURE 7.6: RAMAN MAPPING SPECTROSCOPY OF Ca-QFSBLG EXPOSED TO AMBIENT AIR FOR 1 YEAR.....	237

FIGURE 7.7: X-RAY PHOTOEMISSION SPECTRA SHOWING THE Si 2p AND C 1s CORE LEVELS OF Mg-QFSBLG AFTER SHORT-TERM (6-HOUR) EXPOSURES TO AMBIENT AIR, AT X-RAY ENERGIES OF $E_{hv} = 150$ eV AND 600 eV, RESPECTIVELY.....	239
FIGURE 7.8: X-RAY PHOTOEMISSION SPECTRA SHOWING THE O 1s CORE LEVEL OF Mg-QFSBLG EXPOSED AFTER SHORT-TERM (6-HOUR) EXPOSURES TO AMBIENT AIR, AT AN X-RAY ENERGY OF $E_{hv} = 900$ eV.....	240
FIGURE 7.9: RAMAN MAPPING SPECTROSCOPY OF $30.3 \times 30.3 \mu\text{m}$ AREA USING A 9.6 mW 532 nm LASER, 16 AVERAGES, 0.25 s EXPOSURE AND $0.3 \mu\text{m}$ PIXEL SIZE.	243
FIGURE 7.10: RAMAN MAPPING SPECTROSCOPY OF $20.1 \times 20.1 \mu\text{m}^2$ AREA USING A 9.6 mW 532 nm LASER, 8 AVERAGES, 0.25 s EXPOSURE AND $0.3 \mu\text{m}$ PIXEL SIZE.	244
FIGURE 8.1: FINDING THE THRESHOLD TEMPERATURE OF OXIDATION: HEATING WS ₂ IN THE ABSENCE OF LIGHT.....	253
FIGURE 8.2: ROOM TEMPERATURE CALCIUM DEPOSITION (≈ 1 MONOLAYER) ON THE SURFACE OF EPITAXIAL GRAPHENE ON 6H-SiC(0001).	257
FIGURE 8.3: DENSITY FUNCTIONAL THEORY CALCULATIONS OF THE Mg-QFSBLG STRUCTURE.....	260
FIGURE 8.4: SCHEMATIC OF LASER PATTERNED EPITAXIAL MONOLAYER GRAPHENE ‘DEFECTED’ SAMPLE.	263
FIGURE 8.5: X-RAY PHOTOEMISSION SPECTRA SHOWING THE C 1s CORE LEVELS OF STEPWISE Mg-INTERCALATED PRISTINE AND LASER PATTERNED EPITAXIAL MONOLAYER GRAPHENE (EMLG) SAMPLES AT AN X-RAY ENERGY OF $E_{hv} = 600$ eV.	265

FIGURE 8.6: X-RAY PHOTOEMISSION SPECTRA SHOWING THE C 1S AND Si 2P CORE LEVELS OF LONG-TERM (8 MONTHS) AMBIENT AIR EXPOSED Mg-QFSBLG AT AN X-RAY ENERGY OF $E_{hv} = 1486.6$ eV 268

FIGURE 8.7: X-RAY PHOTOEMISSION SPECTRA AT AN X-RAY ENERGY OF $E_{hv} = 1486.6$ eV OF THE O 1S CORE LEVEL OF PRISTINE EMLG AND LONG-TERM (8-MONTH) AMBIENT AIR EXPOSED Mg-QFSBLG. 272

FIGURE A.2-1: PHOTOLUMINESCENCE (PL) MAPPING SPECTROSCOPY MEASUREMENT OF MONOLAYER WS₂ AFTER OXIDATION SHOWING PL INTENSITY. 327

FIGURE B.3-1: X-RAY PHOTOEMISSION SPECTRA SHOWING THE C 1S CORE LEVEL OF PRISTINE EMLG AND Ca-QFSBLG AT TWO X-RAY ENERGIES, $E_{hv} = 330$ eV (LEFT, SURFACE SENSITIVE) AND $E_{hv} = 600$ eV (RIGHT, BULK SENSITIVE) SHOWING ALL Ca-INTERCALATION STEPS AND PHENOMENOLOGICAL FITS FOR THE G' PEAK. 342

FIGURE B.3-2: X-RAY PHOTOEMISSION SPECTRA OF THE C 1S AND Si 2P CORE LEVELS OF Ca-QFSBLG (SAMPLES EMLG#2 AND EMLG#3) AT AN X-RAY ENERGY OF $E_{hv} = 330$ eV AND 150 eV, RESPECTIVELY. 344

FIGURE B.3-3: SECONDARY ELECTRON CUT-OFF PHOTOEMISSION (SECO) MEASUREMENTS SHOWING THE WORKFUNCTION (W_f) OF THE OMITTED 1st Ca-INTERCALATION STEP AND EMLG#2 AND EMLG#3 COMPARED TO THEIR PROSPECTIVE PRISTINE EMLG STARTING SAMPLES. 345

FIGURE B.3-4: X-RAY PHOTOEMISSION SPECTRA OF THE Si 2P CORE LEVEL OF PRISTINE EMLG AND Ca-QFSBLG AT TWO X-RAY ENERGIES, $E_{hv} = 150$ eV (LEFT, SURFACE SENSITIVE) AND $E_{hv} = 600$ eV (RIGHT, BULK SENSITIVE) SHOWING THE 1st Ca-

INTERCALATION STEP THAT WAS OMITTED FROM FIGURE 5.4 OF THE
MANUSCRIPT 348

FIGURE B.4-1: X-RAY PHOTOEMISSION SPECTRA SHOWING THE C 1s CORE LEVELS OF
PRISTINE H-QFSBLG AND Ca-QFSBLG AT BEAM ENERGIES OF $E_{hv} = 330$ eV
(LEFT, SURFACE SENSITIVE) AND $E_{hv} = 600$ eV (RIGHT, BULK SENSITIVE). 351

FIGURE B.4-2: X-RAY PHOTOEMISSION SPECTRA SHOWING THE Si 2p CORE LEVELS OF
PRISTINE H-QFSBLG AND Ca-INTERCALATED H-QFSBLG (Ca-QFSBLG) AT
BEAM ENERGIES OF $E_{hv} = 150$ eV (SURFACE SENSITIVE) AND $E_{hv} = 600$ eV (BULK
SENSITIVE). 354

FIGURE B.4-3: X-RAY PHOTOELECTRON SPECTRA SHOWING Si 2p CORE LEVELS AT AN
X-RAY ENERGY OF $E_{hv} = 150$ eV OF TWO SEPARATE (SISTER) PRISTINE H-QFSBLG
SAMPLES USED FOR CA-INTERCALATION EXPERIMENTS 355

FIGURE B.4-4: X-RAY PHOTOEMISSION SPECTRA SHOWING THE O 1s CORE LEVEL OF
Ca-QFSBLG COMPARED TO PRISTINE EMLG AT AN X-RAY ENERGY OF $E_{hv} = 900$
eV. 356

FIGURE B.4-5: X-RAY PHOTOEMISSION SPECTRA SHOWING THE Ca 2p CORE LEVEL OF
Ca-INTERCALATED H-QFSBLG (Ca-QFSBLG) AT AN X-RAY ENERGY OF $E_{hv} =$
500 eV. 357

FIGURE B.4-6: SECONDARY ELECTRON CUT-OFF (SECO) PHOTOEMISSION
MEASUREMENTS SHOWING THE WORKFUNCTION (W_f) OF PRISTINE AND Ca-
INTERCALATED H-QFSBLG (Ca-QFSBLG). 359

FIGURE B.4-7: SECO MEASUREMENTS SHOWING THE WORKFUNCTION (W_f) OF Ca-
QFSBLG (SAMPLE FROM FIGURE B.4-6) AFTER DEPOSITION OF 0.6 nm OF
CALCIUM ON THE SURFACE (DASH DOT, BLUE LINE) COMPARED TO PRISTINE

EMLG (DOTTED, BLACK LINE). DASHED BLACK LINES SHOW W_f MEASUREMENT.

.....359

FIGURE B.5-1: CLEANING THE SURFACE OF Ca-QFSBLG FROM CALCIUM DEBRIS. .362

FIGURE C.2-1: X-RAY PHOTOEMISSION SPECTRA OF C 1s CORE LEVEL OF PRISTINE EPITAXIAL MONOLAYER GRAPHENE (EMLG) AND Mg-INTERCALATED QUASI-FREESTANDING GRAPHENE (Mg-QFSBLG) AT X-RAY ENERGIES OF 330 eV (SURFACE SENSITIVE) AND 600 eV (BULK SENSITIVE), SHOWING ALSO THE PLASMON LOSS PEAKS AND THE 1st Mg-INTERCALATION STEP THAT WERE OMITTED IN THE MAIN DISCUSSION.377

FIGURE C.2-2: X-RAY PHOTOEMISSION SPECTRA OF Si 2p CORE LEVEL OF PRISTINE EPITAXIAL MONOLAYER GRAPHENE (EMLG) AND Mg-INTERCALATED QUASI-FREESTANDING (Mg-QFSBLG) GRAPHENE AT X-RAY ENERGIES OF 150 eV (SURFACE SENSITIVE) AND 600 eV (BULK SENSITIVE), SHOWING ALSO THE 1ST Mg-INTERCALATION STEP THAT WAS OMITTED IN THE MAIN DISCUSSION.378

FIGURE C.3-1: LOW ENERGY ELECTRON DIFFRACTION PATTERN OF H-QFSBLG AT AN ELECTRON ENERGY OF 100 eV.380

FIGURE C.3-2: X-RAY PHOTOEMISSION SPECTRA OF THE Si 2p AND C 1s CORE LEVELS OF THE ATTEMPTED Mg-INTERCALATION OF H-QFSBLG AFTER MULTIPLE INTERCALATION ATTEMPTS AT AN X-RAY ENERGY OF $E_{hv} = 150$ AND 600 eV, RESPECTIVELY.....381

FIGURE C.3-3: X-RAY PHOTOEMISSION SPECTRA OF THE Mg 2p CORE LEVEL SHOWING BOTH ATTEMPTS OF THE Mg-INTERCALATION OF H-QFSBLG.383

FIGURE C.3-4: X-RAY PHOTOEMISSION SPECTRA OF THE O 1s CORE LEVEL OF H-QFSBLG AFTER ATTEMPTED Mg-INTERCALATIONS AND SUBSEQUENT 6-HOUR AIR EXPOSURE AND ANNEAL AT 623 K FOR 1.5 HOURS.....	385
FIGURE C.4-1: LOW ENERGY ELECTRON DIFFRACTION AT AN ELECTRON ENERGY OF 100 eV OF PRISTINE AND Mg-INTERCALATED EPITAXIAL MONOLAYER GRAPHENE ON 6H-SiC(0001) (EMLG).....	387
FIGURE C.4-2: LOW ENERGY ELECTRON DIFFRACTION AT AN ELECTRON ENERGY OF 100 eV OF PRISTINE AND Mg-INTERCALATED ‘PATTERNEDE’ EPITAXIAL MONOLAYER GRAPHENE ON 6H-SiC(0001) (EMLG-p).....	388
FIGURE C.4-3: X-RAY PHOTOEMISSION SPECTRA SHOWING THE Si 2p CORE LEVEL OF STEP-WISE Mg-INTERCALATED EMLG AT AN X-RAY ENERGY OF $E_{hv} = 150$ eV AND 600 eV, SEE FIGURE 6.10 AND FIGURE 8.5.....	389
FIGURE C.5-1: RAMAN MAP OF EMLG/BUFFER LAYER SISTER SAMPLE SHOWN IN FIGURE 6.8 AND FIGURE 6.11.....	390
FIGURE C.5-2: CALCULATING THE APPROXIMATE AREA OF BUFFER LAYER ON THE SAMPLE USING IMAGEJ.....	391

List of Tables

TABLE 3-1: SPIN-ORBIT SPLITTING FACTORS FOR EACH ORBITAL. REPRODUCED WITH PERMISSION FROM REF. [135] © 2012 JOHN WILEY & SONS.....	80
TABLE 4-1: SUMMARY OF WS ₂ LIGHT EXPOSURE EXPERIMENTS.....	123
TABLE 5-1: SUMMARY OF THE FIT PARAMETERS FOR THE MAJOR COMPONENTS IN FIGURE 5.4.....	159

TABLE 5-2: SUMMARY OF THE FIT PARAMETERS FOR THE MAJOR COMPONENTS IN FIGURE 5.5	163
TABLE 5-3: Ca 2P CORE LEVEL FIT PARAMETERS FOR Ca-INTERCALATED EMLG (Ca-QFSBLG).....	167
TABLE 6-1: SUMMARY OF THE FIT PARAMETERS FOR THE MAJOR Si 2P COMPONENTS IN FIGURE 6.4	200
TABLE 6-2: SUMMARY OF THE FIT PARAMETERS FOR THE MAJOR C 1S COMPONENTS IN FIGURE 6.5	204
TABLE 7-1: FIT PARAMETERS FOR THE O 1S CORE LEVEL OF AMBIENT AIR EXPOSED Ca-QFSBLG AT AN X-RAY ENERGY OF $E_{hv} = 900$ eV.	231
TABLE 8-1: Si 2p CORE LEVEL FIT PARAMETERS FOR ALL COMPONENTS IN FIGURE 8.6	269
TABLE 8-2: C 1s CORE LEVEL FIT PARAMETERS FOR ALL COMPONENTS IN FIGURE 8.6	269
TABLE 8-3: O 1s CORE LEVEL FIT PARAMETERS FOR ALL COMPONENTS IN FIGURE 8.10	272
TABLE B.2-1: Si 2p CORE LEVEL FIT PARAMETERS FOR COMPONENTS IN FIGURE 5.4 AND FIGURE B.3-4	330
TABLE B.2-2: Si 2p CORE LEVEL FIT PARAMETERS FOR COMPONENTS SHOWN IN FIGURE 5.4 AND FIGURE B.3-4	331
TABLE B.2-3: C 1s CORE LEVEL FIT PARAMETERS FOR PRISTINE AND Ca-INTERCALATED EMLG COMPONENTS SHOWN IN FIGURE 5.5 AND FIGURE B.3-1	332

TABLE B.2-4: Si 2p CORE LEVEL FIT PARAMETERS FOR PRISTINE AND Ca-INTERCALATED H-QFSBLG COMPONENTS SHOWN IN FIGURE B.4-2.....	333
TABLE B.2-5: C 1s CORE LEVEL FIT PARAMETERS FOR PRISTINE AND Ca-INTERCALATED H-QFSBLG SHOWN IN FIGURE B.4-1.....	334
TABLE B.2-6: C 1s CORE LEVEL FIT PARAMETERS FOR SAMPLE EMLG#2 USED IN AMBIENT AIR EXPOSURE EXPERIMENTS SHOWN IN FIGURE 7.1a-c.....	335
TABLE B.2-7: Si 2p CORE LEVEL FIT PARAMETERS FOR PRISTINE Ca-QFSBLG AND 30-MINUTE AMBIENT AIR EXPOSED Ca-QFSBLG, FABRICATED FROM SAMPLE EMLG#2 (FIGURE 7.2a, c).....	336
TABLE B.2-8: C 1s CORE LEVEL FIT PARAMETERS FOR Ca-INTERCALATED SAMPLE EMLG#3 (Ca-QFSBLG) USED IN AMBIENT AIR EXPOSURE EXPERIMENTS SHOWN IN FIGURE 7.1d.....	337
TABLE B.2-9: Si 2p CORE LEVEL FIT PARAMETERS FOR PRISTINE Ca-QFSBLG AND 30-MINUTE AMBIENT AIR EXPOSED Ca-QFSBLG, FABRICATED FROM SAMPLE EMLG#2 (FIGURE 7.2b, d).....	338
TABLE B.2-10: C 1s CORE LEVEL FIT PARAMETERS FOR PHENOMENOLOGICAL PLASMON COMPONENTS IN FIGURE 7.1b-d.....	339
TABLE B.2-11: C 1s CORE LEVEL FIT PARAMETERS FOR PRISTINE EMLG AND SEPARATE Ca-QFSBLG SAMPLE (SAME SAMPLE FROM TABLE B.2-1/TABLE B.2-3) AFTER EXPOSURE TO THE AMBIENT AIR FOR 1 YEAR (FIGURE 7.5).....	340
TABLE B.3-1: PHENOMENOLOGICAL PLASMON LOSS FIT PARAMETERS FOR Ca-QFSBLG IN FIGURE B.3-1.....	341
TABLE B.4-1: PHENOMENOLOGICAL FIT PARAMETERS FOR Ca-QFSBLG IN FIGURE B.4-1.....	352

TABLE B.4-2: Ca 2p CORE LEVEL FIT PARAMETERS FOR Ca-INTERCALATED H-QFSBLG (FIGURE B.4-5)	358
TABLE C.1-1: Si 2p CORE LEVEL FIT PARAMETERS FOR ALL COMPONENTS IN FIGURE 6.4 AND FIGURE C.2-2.....	364
TABLE C.1-2: FIT PARAMETERS FOR Si 2p CORE LEVEL OF ADATOM COMPONENTS IN PRISTINE EMLG IN FIGURE 6.4a-b AND FIGURE C.2-2a-b.....	365
TABLE C.1-3: C 1s CORE LEVEL FIT PARAMETERS FOR ALL COMPONENTS IN FIGURE 6.5 AND FIGURE C.2-1.	366
TABLE C.1-4: Si 2p CORE LEVEL FIT PARAMETERS OF ALL COMPONENT FOR Mg-QFSBLG AFTER SHORT-TERM AIR EXPOSURE IN FIGURE 7.7.	367
TABLE C.1-5: C 1s CORE LEVEL FIT PARAMETERS OF ALL COMPONENTS FOR Mg-QFSBLG AFTER SHORT-TERM AIR EXPOSURE IN FIGURE 7.7.	368
TABLE C.1-6: Mg 2p CORE LEVEL FITTING PARAMETERS FOR Mg-QFSBLG (Mg-INTERCALATED EMLG) COMPONENTS SHOWN IN FIGURE 6.7.	369
TABLE C.1-7: C 1s CORE LEVEL FIT PARAMETERS FOR ALL COMPONENTS IN FIGURE 8.8a, c, e, g (STEP-WISE Mg-INTERCALATION OF EMLG).	370
TABLE C.1-8: C 1s CORE LEVEL FIT PARAMETERS FOR ALL COMPONENTS IN FIGURE 8.8b, d, f, h (STEP-WISE INTERCALATED PATTERNED EMLG).	371
TABLE C.1-9: Si 2p CORE LEVEL FIT PARAMETERS FOR ALL COMPONENTS IN FIGURE C.4-3.....	372
TABLE C.1-10: FIT PARAMETERS FOR Si 2p CORE LEVEL OF ADATOM COMPONENTS IN FIGURE C.4-3.....	373

TABLE C.2-1: PARAMETERS USED FOR THE VOIGT FITS OF THE PLASMON LOSS PEAKS

FOR Mg-QFSBLG IN [FIGURE C.2-1](#) SHOWING BINDING ENERGY (E_B), RELATIVE INTENSITY (RI) AND FULL WIDTH AT HALF MAXIMUM (FWHM). PARAMETERS FOR G_o ARE SHOWN IN [TABLE C.1-3](#) AS G''379

TABLE C.3-1: COMPONENT PARAMETERS FOR THE C 1s CORE LEVEL PHOTOEMISSION

SPECTRA IN [FIGURE C.3-2b](#) AND [FIGURE C.3-2d](#) SHOWING BINDING ENERGY (E_B), ASYMMETRY/LORENTZIAN WIDTH (Q/W_L) OF THE BWF FIT OR GAUSSIAN WIDTH/LORENTZIAN WIDTH (W_G/W_L) OF THE VOIGT FIT.....382

TABLE C.3-2: COMPONENT PARAMETERS FOR THE Si 2p CORE LEVEL PHOTOEMISSION

SPECTRA IN [FIGURE C.3-2a](#) AND [FIGURE C.3-2c](#) SHOWING BINDING ENERGY (E_B), AND GAUSSIAN WIDTH/LORENTZIAN WIDTH (W_G/W_L) OF THE VOIGT FIT. .382

TABLE C.3-3: FITTING PARAMETERS FOR THE Mg 2p CORE LEVEL (AT AN X-RAY

ENERGY OF 100 eV) OF Mg-INTERCALATED H-QFSBLG IN [FIGURE C.3-3](#) SHOWING BINDING ENERGY (E_B), RELATIVE INTENSITY (RI) AND THE GAUSSIAN WIDTH (W_G)/LORENTZIAN WIDTH (W_L) FOR ALL PEAKS. Mg_M WAS FIT WITH A DONIACH-ŠUNJIĆ PROFILE, $W_L = 0.2$ eV, ASYMMETRY = -0.2.384

1

Introduction

Chapter

*“Those who do not stop asking
silly questions become scientists”*

- LEON M. LEDERMAN

Most modern electronics still use the semiconductor material silicon to construct the transistors, which form the crucial components in computers and amplifiers. Transistors, such as the one shown in [Figure 1.1a-b](#), can control (*via* the ‘gate’) the flow of electrical current (from ‘source’ to ‘drain’) to produce two states – on (conducting) and off (not conducting). This means that the transistor can not only amplify electrical signals, but also act as a switch in which the off and on states can be translated into bit logic, performing useful calculations. In fact, silicon transistors have become so ubiquitous in our society, that it is difficult to comprehend our modern world without them – telecommunications, power generation and transmission, space exploration, control systems, metrology, navigation, information storage and automation – are all but a few examples of how silicon transistors are used in our everyday lives. Yet not many appreciate that silicon’s rise to dominance in the electronics industry was not only due to its inherent material properties (such as a relatively large band gap), but crucially, of the material properties of *its oxide*. Silicon is able to form a stable, protective oxide, and by doing so, almost completely neutralises silicon surface states [\[1-2\]](#). Furthermore, silicon oxide is a dielectric, thus, coupled with the neutralisation of surface states, an electric field can penetrate the silicon bulk. By the deposition of an electrode (gate) on top of the dielectric and application of a suitable voltage, the conductivity of the underlying silicon can be modulated. Hence, the study of silicon oxidation ultimately heralded a new type of transistor design – the metal-oxide-semiconductor field effect transistor, or MOSFET; shown in [Figure 1.1a-b](#), a design which continues to dominate the underlying architecture of every computer to this day. Studying the air stability of silicon, and specifically its reaction with oxygen, allowed the advancement of one of the most important discoveries of the modern era – the silicon transistor.

Around the year 2004, graphene (a single atomic layer of graphite) [3] and monolayer MoS₂ (a semiconducting transition metal dichalcogenide, S-TMD) [4] were isolated *and* electrically characterised for the first time (this is important, since these materials were isolated much before this time – see refs. [5-6]). Graphene was found to be highly conductive, yet could be gated like a semiconductor [3]. On the other hand, monolayer MoS₂ was found to be semiconducting [4], with a sizeable bandgap [7-8]. Prior to this point in time, it was thought theoretically impossible for 2D materials (*i.e.* a monolayer of material) to be isolated in ambient atmosphere without spontaneously becoming three-dimensional or reacting with ambient atmosphere (although previous reports claiming the isolation of 2D materials were in existence, the wider research community was largely unaware) [5, 9]. For the determination of the electrical properties of graphene, the Nobel Prize was subsequently awarded to Geim and Novoselov in 2010 [5]. These initial findings have now led to the discovery of a multitude of other 2D materials [10], and an explosion of research interest in the field of 2D materials over the last 2 decades [10-12]. This research has resulted in improvements in crystal quality, the characterisation of new physical phenomena, improvement in fabrication processes and the ultimate utilisation of these materials in a multitude of applications. For example, graphene has been investigated for device applications such as gas sensors, field effect transistors, transparent electrodes and flexible electronics to name a few [13-15]. Many potential applications have also been proposed for the 2D S-TMDs, which have been implemented in photonic and opto-electronic applications such as light emitting diodes, lasers and photodetectors [16], as well as electronics such as field effect transistors [10].

In much the same way as bulk semiconductors have defined the modern electronics industry, recent developments in 2D materials are poised to further revolutionise the electronics industry. There is, however, a problem: the 2D materials field seems to be at a crucial point in history – as in the story of silicon – where the fundamental oxidation properties of 2D materials (especially in ambient conditions) are less understood in the literature. For example, until the work described in this thesis, it was not known that monolayer WS₂ oxidises *via* a photo-induced oxidation mechanism in ambient atmosphere [17]. Furthermore, intercalated graphene (the 2D analogue of intercalated graphite), where alkalis or alkaline earths such as Li, K or Ca are inserted in-between or underneath the graphene, represent one of the most highly n-type doped graphene systems. These systems are being investigated for a variety of applications, including superconducting electronics [18-19] and transparent and highly conducting electrodes [20]. Yet, a detailed account of their reactivity in ambient has scarcely been reported in literature. Moreover, highly n-type doped and air stable intercalants for graphene are largely lacking from the literature. As will become clear in this thesis, the analysis of the air stability of as-grown (WS₂) and intercalated (graphene) 2D materials is of fundamental importance to further development of these materials for incorporation into electronics of

the future; in much the same way as the air stability and oxidation of silicon was fundamental to silicon's utilisation in what we now call 'modern' electronics.

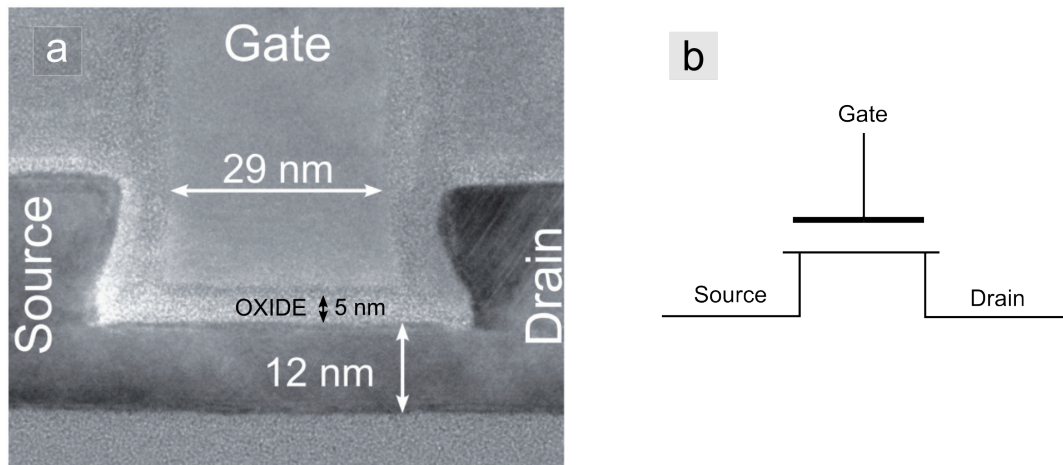


FIGURE 1.1 – THE METAL-OXIDE-SEMICONDUCTOR FIELD EFFECT TRANSISTOR (MOSFET).

(a) Scanning electron micrograph of a MOSFET-type device showing the gate, source, drain and gate oxide. Modified and reproduced with permission from ref. [21] © 2012 American Institute of Physics. *(b)* Schematic of (a) showing simplified circuit diagram of a MOSFET. Electrons can flow from source to drain electrodes when a suitable voltage is applied to the gate electrode.

1.1 Thesis Objective and Scope

In this thesis, I will present recent experimental (and theoretical) results – using a variety of optical and surface science techniques – to investigate the structural, optical and electronic properties of monolayer tungsten disulphide (WS_2), calcium intercalated epitaxial monolayer graphene on silicon carbide and magnesium intercalated epitaxial monolayer graphene on silicon carbide, before and after reaction in ambient atmosphere. In order to assess the effects of ambient air exposure, the as-grown and modified materials must be first analysed prior to ambient exposure (or as in the case of WS_2 , prior to significant oxidation) and this is conducted in [Chapters 4, 5](#)

and 6 for WS₂, calcium intercalated graphene and magnesium intercalated graphene, respectively.

In order to understand the pristine material systems presented in this thesis, a short summary of the physical, optical, and electronic properties of WS₂ and graphene/graphene on silicon carbide is discussed in [Chapter 2](#). In [Chapter 3](#), I overview the major experimental techniques and tools employed in each experimental chapter. These chapters form the necessary background information required for interpretation of this thesis.

In [Chapter 4](#), I present a series of experiments that show WS₂ oxidation is initiated only with exposure to light that can excite an optical bandgap transition in the material, *i.e.* oxidation is a photoinduced process. In fact, I find that the minimum energy required to begin this oxidation (1.88 eV) is associated with excitation of the trion, rather than the exciton. I show that there is likely no optical fluence or irradiation threshold which begins the oxidation of WS₂, a finding which is in support of photoinduced oxidation, and contrasts with a recent study which did suggest a threshold [22]. I demonstrate that the oxidation manifests in specific locations that are thought to harbour a greater concentration of sulphur vacancies; implying oxidation may begin at sulphur vacancies on the surface of the WS₂. The possible reaction pathway and implications of a photoinduced oxidation pathway for a material that has applications in future opto-electronic devices are briefly discussed.

In [Chapter 5](#), I present results which characterise the structural, chemical, and electrical structure of calcium intercalated graphene, using (nominally) monolayer epitaxial graphene synthesised on silicon carbide (EMLG) as the starting material. Using low energy electron diffraction (LEED) and X-ray photoelectron spectroscopy (XPS), I find that calcium preferentially intercalates between the silicon surface of the silicon carbide and buffer layer, chemically interacting form a Ca-silicide layer at the surface. This structurally transforms the nominally monolayer graphene sample to bilayer graphene by releasing and ‘quasi-freestanding’ the buffer layer to form calcium-intercalated quasi-freestanding bilayer graphene (Ca-QFSBLG). The stoichiometry of Ca : Si on the surface is estimated using the experimental data to find that the concentration of Si > Ca on the surface of the SiC. Moreover, I show that low temperature scanning tunnelling microscopy (STM) micrographs and density functional theory calculations (DFT, performed by collaborators) agree with LEED and XPS results. No evidence of intercalation between graphene layers, or between the buffer layer and the top graphene layer are found, which is contradictory to previous calcium intercalation studies using graphene on silicon carbide [18-19, 23-24].

Finally, the charge carrier sign and concentration (constituting part of the electronic structure) are determined to be n-type (electrons) with a concentration of $\approx 10^{14}$ cm⁻² via secondary electron workfunction

measurements (to find the change in workfunction) and comparisons with theoretical calculations for a highly doped freestanding bilayer [25]. The results presented in [Chapter 5](#) are also supported by experiments conducted on hydrogen intercalated bilayer graphene on silicon carbide (H-QFSBLG), which show calcium displacing hydrogen to form Ca-QFSBLG; shown in [Appendix B4](#).

In [Chapter 6](#), I present results which characterise the structural, chemical and electrical structure of magnesium intercalated graphene, using again EMLG as the starting material. Using the same surface science techniques as in [Chapter 5](#), I find that magnesium similarly intercalates the silicon carbide – buffer layer interface to form a magnesium silicide layer that decouples the buffer layer, forming another graphene layer. This results in the structural transformation of EMLG into magnesium intercalated quasi-freestanding bilayer graphene (Mg-QFSBLG), and is supported by LEED, XPS and STM measurements. As with Ca-QFSBLG, no evidence of intercalation between the graphene layers is found from any of the techniques implemented, suggesting that as with Ca, Mg preferentially intercalates the buffer layer-SiC interface. The charge carrier sign and concentration are again determined *via* secondary electron cut-off photoemission spectroscopy (SECO) and comparisons to freestanding highly doped bilayer graphene [25]. These techniques find that in Mg-QFSBLG, the charge carriers are electrons (n-type) with a carrier concentration of $\approx 10^{14} \text{ cm}^{-2}$. These results are further supported with recent angle resolved photoemission spectra [26], which determine the carrier concentration of Mg-QFSBLG (from fits to the tight-binding model) to be a highly n-type doped graphene with charge carrier concentration of $\approx 2 \times 10^{14} \text{ cm}^{-2}$, in agreement with SECO and comparisons with theory for highly doped bilayer graphene. Furthermore, it is shown that the Mg-QFSBLG forms a bandgap of $\approx 0.36 \text{ eV}$, which is thought to be a direct consequence of the Mg-silicide layer.

With the pristine Ca-QFSBLG and Mg-QFSBLG samples characterised, [Chapter 7](#) then investigates how these samples react with ambient atmosphere. In the case of Ca-QFSBLG, I show that almost all the Ca-silicide is reacted after 30 minutes of ambient air exposure. After 9 hours of ambient air exposure, no silicide remains, and the sample is no longer significantly n-type doped. Raman spectroscopy measurements show that after long-term air exposures of 1 year, the Ca-QFSBLG sample remains quasi-freestanding, but that the surface is significantly defected (which is also supported by XPS). The chemical reactions occurring underneath the graphene are elucidated using XPS, and I show that Ca-QFSBLG oxidises in a predictable way, first forming calcium oxide/calcium hydroxide, then after long-term exposure, forming calcium carbonate/bicarbonate.

On the other hand, I show that Mg-QFSBLG is remarkably stable in air after 6 hours of ambient air exposure, with most of the Mg-silicide layer remaining intact. After long-term ambient air exposures of ≈ 8 months, Raman

spectroscopy measurements show that Mg-QFSBLG is still bilayer, and in contrast to Ca-QFSBLG, has no observable defects. Although the Mg-QFSBLG is found to eventually oxidise ([Chapter 8](#)), it suggests that Mg-QFSBLG is an incremental step forward in realising an air-stable, yet highly n-type doped freestanding graphene.

In [Chapter 8](#), I further explore the ideas presented in [Chapters 4, 5, 6 and 7](#). In [Section 8.2](#), I further discuss the proposed photo oxidation mechanism presented in [Chapter 4](#), as well as present preliminary results exploring the thermal oxidation of monolayer WS₂ in ambient atmosphere. In [Section 8.3](#), STM results of the surface deposition of calcium on epitaxial graphene are presented, along with a discussion of the possible repercussions regarding the origin of superconductivity in calcium intercalated graphenes on silicon carbide, given the findings presented in [Chapter 5](#). In [Section 8.4](#), density functional theory calculations for the structure of Mg-QFSBLG are given, and a possible experiment is outlined to experimentally determine the Mg:Si stoichiometric ratio (as was done in the case of Ca-QFSBLG in [Chapter 5](#)). The relative reactivity of intercalants are discussed in the context of magnesium (which could not displace hydrogen in H-QFSBLG samples, see [Appendix C](#)). The inability of intercalants such as magnesium (n-type dopant) to displace hydrogen (p-type dopant) is explored as a potential pathway for the creation of atomically sharp n-p graphene junction devices. Furthermore, the intercalation mechanism of magnesium is shown to likely occur from voids in the graphene, supported by intercalation experiments on laser ablated EMLG samples. Finally, [Section 8.5](#) explores preliminary data on the long-term (8-month) ambient air exposure of Mg-QFSBLG, where it is found that the underlying Mg-silicide likely oxidises to MgO and Mg(OH)₂. Finally, use of Mg-QFSBLG and Ca-QFSBLG as novel gas sensors, with the intercalant used as the gas sensing medium, are discussed. This constitutes the Outlook section. The chapter is then summarised, and concluding remarks on the field of 2D materials are given.

2

Chapter

Two-Dimensional Materials

Keywords: Transition metal dichalcogenide, WS₂, graphene, properties.

“Only fullness leads to clarity, and truth lies in the abyss”
- FRIEDRICH SCHILLER

2.1 Overview

In this chapter, I will review the atomic structure and necessary theory behind the electronic and optical properties of the 2D materials used in this thesis – monolayer WS₂ and (monolayer and bilayer) graphene. The general properties of these materials are quite well understood, and thus, only a brief overview with focus on the aspects which are important for this thesis will be given.

In [Section 2.2](#), I will review the atomic structure and subsequent electronic band structure of graphene, the first truly 2D material to be isolated and electrically measured. Due to its unique atomic structure, graphene does not possess a band gap like a semiconductor, but is also not considered a metal due to its special band structure. In the case of bilayer graphene, a bandgap can develop in the presence of a potential difference between the graphene layers. In this thesis, I use graphene grown on silicon carbide, which has structural and electronic differences to ‘freestanding’ graphene usually considered in theoretical calculations, as I discuss in this section.

In [Section 2.3](#), I will review the atomic and ensuing electronic band structure of monolayer tungsten disulphide (WS₂). Monolayer WS₂ is a semiconductor that has distinct optical properties that differ from its bulk semiconductor form. The optical properties of monolayer WS₂ dictate its photochemistry, as will be further elucidated in [Chapter 4](#).

2.2 Graphene

Graphene represents the first ‘truly’ 2D material that was isolated and electrically characterised in 2004 by Novoselov and Geim [3]. The discovery and electrical measurement of graphene led to Novoselov and Geim receiving the Nobel Prize in physics in 2010 [5]. But the story of graphene begins much before this time (see ref. [5] for a brief historical overview). For instance, the theory behind graphene’s electronic structure was largely described many decades prior by Wallace in 1947 [27].

This section will overview some of the properties of graphene that are most pertinent to this thesis, namely, the atomic and electronic structure of monolayer and bilayer graphene. In both these considerations, a freestanding structure is assumed. But in practice this is rarely the case, as graphene is typically grown on a substrate (such as copper, iridium, or silicon carbide) which imparts structural and electrical perturbations on the overlaying graphene. These effects, as well as the growth process, will be briefly overviewed in the context of epitaxial graphene synthesised on silicon carbide, which is used extensively throughout this thesis.

2.2.1 Atomic and Electronic Band Structure

The atomic structure of graphene is shown in Figure 2.1a. Graphene is an allotrope of carbon, consisting of a single sheet of hexagonally bonded carbon atoms. Figure 2.1a shows the unit cell of the graphene and primitive lattice vectors which are labelled $\mathbf{a} = a(1,0)$ and $\mathbf{b} = a(-1/2, \sqrt{3}/2)$, where the lattice parameter a , is ≈ 0.246 nm [28]. The entire graphene structure can be constructed from the basis atoms labelled ‘A’ and ‘B’, and thus, comprise the primitive unit cell of graphene. The distance between the A and B carbon atoms is 0.142 nm [28]. Figure 2.1b shows the reciprocal transformation of the primitive unit cell shown in Figure 2.1a (i.e. the Brillouin Zone). The reciprocal lattice vectors are $\mathbf{a}^* = (2\pi/a)(1, 1/\sqrt{3})$ and $\mathbf{b}^* = (2\pi/a)(0, 2/\sqrt{3})$. The reciprocal space representation of graphene will become more important in Chapter 6, in which recent angle resolved photoemission spectroscopy (ARPES) results will be presented. The ARPES technique is able to directly image the bandstructure of graphene in reciprocal space, and is further explained in Chapter 6, Section 6.3.6.

The electronic band structure of graphene is well known, and is given by the following dispersion (ϵ - k) relationship (i.e. bandstructure) calculated from the tight binding model (considering only interactions from the nearest neighbour) [27-28]:

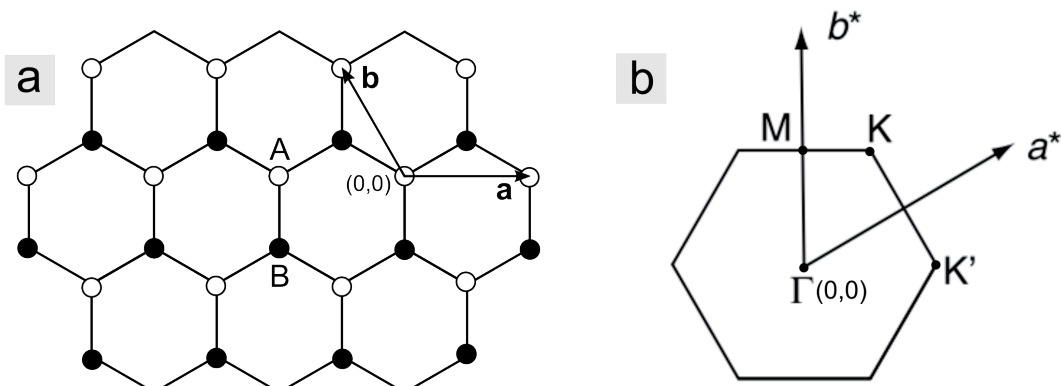


FIGURE 2.1: ATOMIC STRUCTURE OF GRAPHENE.

(a) Real-space crystal structure of graphene. The graphene unit cell consists of the two-atom basis A and B. The primitive lattice vectors are given by \mathbf{a} and \mathbf{b} . (b) The reciprocal space transformation of the primitive unit cell given by \mathbf{a} and \mathbf{b} showing the Brillouin zone and reciprocal lattice vectors \mathbf{a}^* and \mathbf{b}^* . Reproduced with permission from ref. [28] © 2014 Springer International Publishing.

$$\varepsilon(k'_x, k'_y) = \pm \gamma_0 \sqrt{1 + 4 \cos \frac{ak'_x}{2} \cos \frac{\sqrt{3}ak'_y}{2} + 4 \cos^2 \frac{ak'_x}{2}}. \quad \dots 2-1$$

Where γ_0 is the nearest neighbour hopping energy (also called the ‘hopping parameter’ $\approx 2.8 - 3$ eV [28-29]) and k'_x and k'_y are the wavevectors in the x and y directions (with units of inverse length), originating at the point (0, 0). The resulting bandstructure is shown in Figure 2.2a. At the K and K' points where the bands intersect through zero energy (charge neutrality point, i.e., the Fermi level for charge neutral graphene), and for small deviations around these points, the ε - \mathbf{k} relationship becomes linear [28-29]:

$$\varepsilon(\mathbf{k}) = \pm \hbar v_F |\mathbf{k}|, \quad \dots 2-2$$

$$\varepsilon(k_x, k_y) = \pm \hbar v_F \sqrt{\delta k_x^2 + \delta k_y^2}. \quad \dots 2-3$$

Where v_F is the Fermi velocity (m s^{-1}), \hbar is reduced Planck’s constant and k' is the relative wavevector measured from K or K' to some final location in which $|\mathbf{k}| \ll |\mathbf{K}|$ [29], defined by $\mathbf{k} = \mathbf{k}' - \mathbf{K}$. The Fermi velocity is given by [28]:

$$v_F = \frac{\sqrt{3}}{2} \frac{a\gamma_0}{\hbar}. \quad \dots 2-4$$

For $\gamma_0 = 2.8$ eV and $a \approx 0.246$ nm, $v_F \approx 0.9 \times 10^6$ m s⁻¹. The bandstructure for monolayer graphene (at small deviations from K/K', i.e. low energy) is shown in Figure 2.2b, and demonstrates the typical ‘conical/linear’ bandstructure of graphene. Equation 2-2 describes particles moving at constant velocity independent of energy, and is similar to the expression expected for ultra-relativistic particles described by the Dirac equation [30], but with the speed of light, c , replaced with the Fermi velocity v_F . Consequently, at the K and K' points where the bands intersect through zero energy lies a singularity often called the Dirac point (E_D , where $\epsilon=0$). This is due to the experimental observation of massless charge carriers, and affirmation that the Dirac equation describes charge carriers in graphene. This is why the bandstructure of graphene results in many unusual physical properties, such as graphene’s extremely high carrier velocity (v_F) [30].

Another physical quantity that is relevant in this thesis is the carrier concentration. In Chapter 5 and Chapter 6, I explore how intercalation of the alkaline earth elements calcium and magnesium alter the carrier concentration of graphene. Calcium and magnesium are known to be electron donors, and thus, it is expected that intercalation of graphene with the alkaline earths (which have a valency of 2) should donate electrons to the graphene making it more ‘n-type’; effectively increasing the graphene carrier concentration. The physical repercussions of this on the bandstructure of graphene are a shift of the Fermi level (E_F) with respect to E_D , as shown in Figure 2.2b. The following discussion applies to the low energy region near the Dirac point of graphene, where the linear dispersion relation found in Equation 2-2 is valid (i.e. $\epsilon < 1$ eV [31]). The carrier concentration (in m⁻²) of graphene can then be found via integration of the graphene density of states with respect to the energy, ϵ [28]:

$$D(\epsilon) = \frac{g_s g_v \epsilon}{2\pi \hbar^2 v_F^2} , \quad ...2-5$$

and is given by [28]:

$$n = \frac{g_s g_v \epsilon^2}{4\pi \hbar^2 v_F^2} . \quad ...2-6$$

Where g_s is the spin degeneracy (2), g_v is the valley degeneracy (2) [28] (this is a direct consequence of the identical two-atom basis) and the carrier sign is determined by the location of the E_F with respect to the E_D (see Figure 2.2b). It is important to note that the energy, ϵ , represents the *energy difference* between the Dirac point and the Fermi level (since at the charge neutrality point, there are no excess carriers). Thus, Equation 2-6 simplifies to:

$$n = \frac{(E_F - E_D)^2}{\pi \hbar^2 v_F^2} . \quad ...2-7$$

Since v_F , E_D (for n-type samples) and E_F are directly probed in ARPES experiments (where E_F is set to zero), the carrier density can be estimated using Equation 2-7.

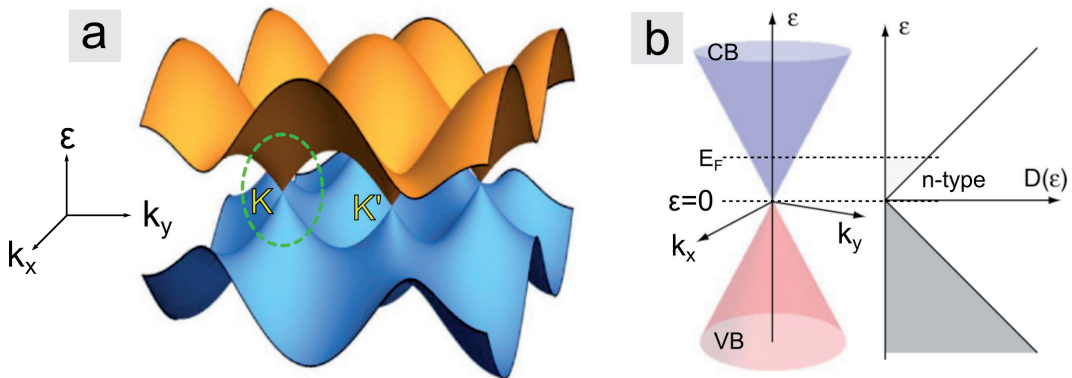


FIGURE 2.2: THE BANDSTRUCTURE AND DENSITY OF STATES OF GRAPHENE.

(a) A plot of the complete ϵ - k dispersion relationship (bandstructure) for graphene from the tight binding (nearest neighbour) model. Reproduced with permission from ref. [31] © 2019 American Physical Society. **(b)** Magnified view from dotted region in (a) of the low energy bandstructure of graphene near the K (Dirac) point, E_D (left) and corresponding density of states (right). At equilibrium (charge neutrality) where $\epsilon = 0$, the Fermi level (E_F) is at the Dirac point (E_D). Adding electrons to the graphene shifts E_F into the conduction band (CB) away from the Dirac point. If instead holes are added, E_F shifts into the valence band (VB) away from the Dirac point. Modified and reproduced with permission from ref. [28] © 2014 Springer International Publishing.

2.2.1.1 Bilayer Graphene

The structure of bilayer graphene consists of one layer of graphene oriented above another, separated by $d \approx 0.334$ nm [28] as shown in Figure 2.3a. The basis atoms are now labelled A₁/B₁ in the bottom layer, and A₂/B₂ in the top layer. There are different ways that this additional layer can be stacked – AA, AB or turbostratic [28]. In AA stacking, the A₁ and A₂ atoms in the layers are stacked on top of each other, so that the top down view looks like monolayer graphene (see Figure 2.1a). AB stacking is shown in Figure 2.3b, and shows the B₂ atom on top of the A₁ atom. Turbostratic stacking induces a rotation of one layer with respect to the other [28]. AB stacking in graphene is often called Bernal stacking [32], and is the most stable stacking for bilayer graphene [28, 33]. It is also commonly found to be the stacking order for bilayer graphene grown on silicon carbide [34-35], which will be discussed in Section 2.2.2. As such, the following theoretical discussion will be based around solutions to the tight binding model of AB stacked bilayer graphene using the Slonczewski-Weiss-McClure parameterisation [28].

The consequences of two layers of AB stacked graphene manifest in the band structure as two sets of quadratic bands due to the four atom basis of the

bilayer structure (A_1, B_1, A_2, B_2), as shown in [Figure 2.3c](#). The nearest neighbour hopping energy for in-plane transitions ($A_1 \leftrightarrow B_1, A_2 \leftrightarrow B_2$), γ_0 , remains the same as in [Equation 2-1](#) for monolayer graphene. Three additional parameters called the interlayer nearest neighbour coupling energy are required to parameterise bilayer graphene, and are labelled γ_1 (for $B_1 \leftrightarrow A_2$ transitions), γ_3 (for $A_1 \leftrightarrow B_2$ transitions), and γ_4 (for $A_1 \leftrightarrow A_2$ or $B_1 \leftrightarrow B_2$ transitions) [[28, 36-37](#)]. In the following discussion I will consider only the lower energy (in magnitude) band ($\varepsilon_{\pm}^{(1)}$, see [Figure 2.3c](#)), and the interlayer coupling transition energy γ_1 , since γ_3 and γ_4 only introduce a small perturbation [[28](#)]. In the absence of an interlayer potential (Δ), the solutions of the bilayer graphene Hamiltonian near the K point ($0 < \varepsilon < \gamma_1$) are [[38](#)]:

$$\varepsilon_{\pm}^{(1)}(p) = \pm \frac{1}{2} \gamma_1 \left[\sqrt{1 + \frac{4v_F^2 p^2}{\gamma_1^2}} - 1 \right]. \quad \dots 2-8$$

Where the momentum, p , is related to the wavenumber by:

$$p = \hbar k. \quad \dots 2-9$$

At large momentum (since v_F is also a large number), [Equation 2-8](#) becomes [[38](#)]:

$$\varepsilon_{\pm}^{(1)}(k) \approx v_F \hbar k. \quad \dots 2-10$$

But for small values of momentum near the K point at the limit of the linear regime where $k = \gamma_1/2\hbar v_F$ (or $n \approx 3 \times 10^{12} \text{ cm}^{-2}$, when $\gamma_1 = 0.4 \text{ eV}$ – see below), and making use of the binomial approximation where $(1+x)^a \approx 1 + ax$, and $ax \ll 1$, the bands become quadratic [[38](#)]:

$$\varepsilon_{\pm}^{(1)}(k) = \frac{\hbar^2 k^2}{2m^*}. \quad \dots 2-11$$

Where $m^* = \gamma_1/2v_F^2$ is the effective mass. For $v_F = 0.9 \times 10^6 \text{ m s}^{-1}$ and $\gamma_1 = 0.4 \text{ eV}$, then $m^* \approx 0.043m_e$ (where m_e is the mass of the electron), which is close to experimentally obtained values for exfoliated graphene on SiO_2 [[39](#)]. Thus, the electron mass in bilayer graphene is *massive*, as opposed to monolayer graphene [[30](#)]. (I will note here that the value for v_F of monolayer graphene on silicon carbide has been experimentally determined, and is approximately $1.11 \pm 0.04 \times 10^6 \text{ m s}^{-1}$; where here, I have obtained this value by averaging the values in the following refs.: [[40-43](#)]. Bilayer graphene typically has a slightly smaller v_F value [[40, 43](#)]. Thus, it is often ‘convenient’ to approximate $v_F \approx 1 \times 10^6 \text{ m s}^{-1}$).

Furthermore, the concentric bands are separated by an energy of $\varepsilon \approx \gamma_1$ [[44](#)]. Experimental values for γ_1 have been determined as $0.43 \pm 0.03 \text{ eV}$ for

epitaxial bilayer graphene [34] and 0.404 ± 0.010 eV for mechanically exfoliated bilayer graphene on SiO_2 [45]. The quadratic shape of the bands is clearly illustrated in Figure 2.3c.

Without an interlayer potential difference, Δ , the parabolic bands $\varepsilon_{\pm}^{(1)}$ and $\varepsilon_{\pm}^{(2)}$ touch at $\varepsilon = 0$, as shown in Figure 2.3c (neglecting the effects of trigonal warping [38]). But something interesting happens when the layers gain a potential difference, which can be achieved through the application of an external potential [36]. The result of this potential is to modify the Hamiltonian, the solutions of which are [36]:

$$\varepsilon^{(a)2}(p) = \frac{\gamma_1^2}{2} + \frac{\Delta^2}{4} + v_F^2 p^2 + (-1)^a \sqrt{\frac{\gamma_1^4}{4} + v_F^2 p^2 (\gamma_1^2 + \Delta^2)}, \quad \dots 2-12$$

where a is a constant (1 or 2, describing the lower/higher energy bands – see Figure 2.3d) and p is the magnitude of the momentum near the K point. At the K point ($p = 0$), the energies are [36]:

$$\varepsilon_{\pm}^{(1)}(0) = \frac{|\Delta|}{2}, \quad \dots 2-13$$

for the lowest-lying energy bands and [36]:

$$\varepsilon_{\pm}^{(2)}(0) = \sqrt{\gamma_1^2 + \frac{\Delta^2}{4}}, \quad \dots 2-14$$

for the higher energy bands. The effects can be observed in Figure 2.3d, which shows that the lower energy bands have been separated by Δ (i.e. a bandgap has formed!), while the higher energy bands have shifted linearly to a higher (in magnitude) energy. Another feature of the applied potential is the so called ‘Mexican hat’ shape, in which another parameter, $\tilde{\Delta}$, which represents the smallest energy between the (conduction and valence) bands is required to describe the bandgap [36]:

$$\tilde{\Delta} = \frac{|\Delta|\gamma_1}{\sqrt{\gamma_1^2 + \Delta^2}}. \quad \dots 2-15$$

Equation 2-15 is applicable for large $|\Delta|$, otherwise for $|\Delta| \ll \gamma_1$, $\tilde{\Delta} \approx \Delta$ [36]. Thus, a bandgap will develop by application of a potential between the graphene layers of bilayer graphene. This phenomenon is especially pertinent in magnesium intercalated graphene [26], as will be shown in Chapter 6.

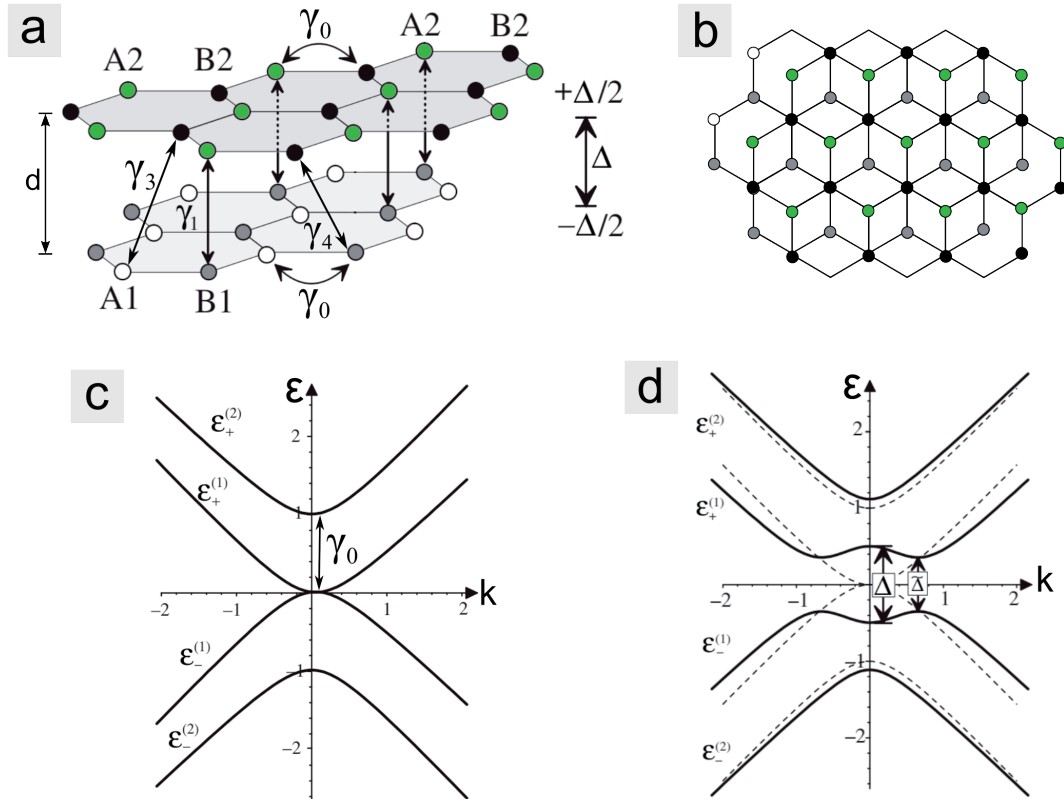


FIGURE 2.3: ATOMIC STRUCTURE AND ELECTRONIC BANDSTRUCTURE OF BILAYER GRAPHENE.

(a) *Atomic structure of bilayer graphene.* Atom basis for bilayer graphene is now A_1 (white)/ B_1 (grey) for the bottom layer and A_2 (green)/ B_2 (black) for the top layer. The nearest neighbour hopping energy (γ_0) now has extra terms corresponding to hopping between the layers – γ_1 (B_1 to A_2 transitions), γ_3 (A_1 to B_2) and γ_4 (B_1 to B_2) – called the nearest layer hopping potentials. A typical value for γ_1 is ≈ 0.4 eV [34]. The quantity ‘ d ’ represents the physical separation between graphene layers (≈ 0.334 nm [28]), whereas Δ represents the potential difference between the layers. Modified and reproduced with permission from ref. [37] © 2007 EDP Sciences, Springer-Verlag. **(b)** Top down view of AB stacked graphene. **(c)** Bandstructure as a function of reduced energy and reduced wavenumber for bilayer graphene. Due to the four-atom basis, there are four bands close to the K -point. Bilayer graphene has parabolic bands, separated by the interlayer hopping potential γ_0 . Modified and reproduced with permission from ref. [37] © 2007 EDP Sciences, Springer-Verlag. **(d)** A nonzero potential applied between the layers of bilayer graphene gives rise to an interlayer potential (Δ) causing a bandgap to open and form the ‘Mexican hat’ bandstructure. Reproduced with permission from ref. [36] © 2006 American Physical Society.

2.2.2 Epitaxial Graphene Synthesised on Silicon Carbide

In this thesis, I use nominally monolayer graphene samples synthesised on semi-insulating silicon carbide. Although stoichiometrically simple, SiC can exist in a variety of polymorphs, including cubic, hexagonal or rhombohedral [46-47], and has been found to exhibit as many as 250 different polytypes [47]. Throughout this thesis, the 6H polytype is used, where the ‘6’ represents the number of atomic planes in the primitive cell (see Figure 2.4a) and the ‘H’ represents the crystal symmetry (hexagonal) [47]. The distance between atomic planes is $d = 2.52 \text{ \AA}$, which gives the value for the lattice parameter in the c-axis direction as $c_{6\text{H}} \approx 15.12 \text{ \AA}$ [46, 48]. The lattice parameter in the a-axis plane is $\approx 3.08 \text{ \AA}$ [46, 48].

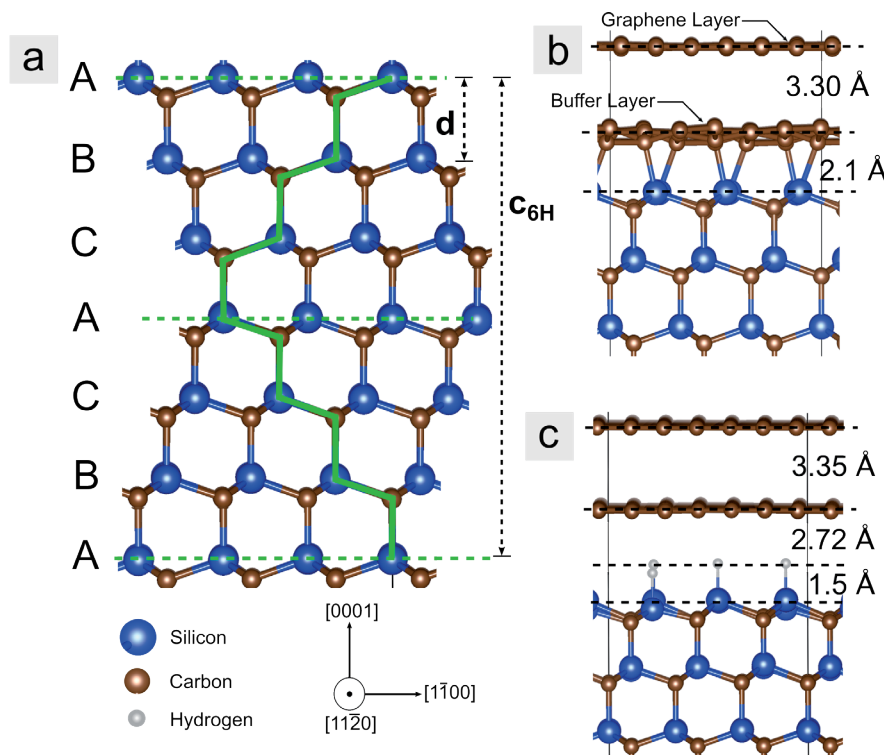


FIGURE 2.4: STRUCTURE OF 6H-SiC(0001) AND GRAPHENE SAMPLES USED.

(a) 6H-SiC(0001) showing the unit cell (green) and stacking order (ABCACB...) for 6H-SiC(0001). Si-termination (Si-face) exists in the (0001) direction, whereas the (000-1) direction is C-terminated (C-face). The inter-layer distance, $d \approx 2.52 \text{ \AA}$, and the unit cell length is given by $c_{6\text{H}} \approx 15.12 \text{ \AA}$. (b) Monolayer graphene synthesised on 6H-SiC(0001) showing relevant distances. The underlying carbon layer is often called the zero layer or buffer layer (see text for details). (c) Intercalating the epitaxial monolayer graphene sample in (b) results in a quasi-freestanding hydrogen intercalated bilayer graphene on silicon carbide (H-QFSBLG). Distances taken from ref. [49].

The two types of graphene on silicon carbide samples used in this thesis are epitaxial monolayer graphene (EMLG) and hydrogen intercalated ‘quasi-freestanding’ bilayer graphene on silicon carbide (H-QFSBLG), shown in [Figure 2.4b](#) and [Figure 2.4c](#), respectively. How these samples are fabricated will be further explained in the following sections.

2.2.2.1 Epitaxial Graphene on SiC Synthesis Method

The process for graphene synthesis on SiC can be segmented into a few procedural steps – (1) preparation of the SiC substrate, (2) epitaxial growth of the graphene on SiC, and in the case of H-QFSBLG, (3) hydrogen intercalation upon cool-down. These steps are illustrated in the cartoon of [Figure 2.5](#). In the following sections, I will provide some historical background information and briefly outline the typical steps that are undertaken by collaborators at the U.S. Naval Research Laboratory to grow both EMLG and QFSBLG samples.

It is likely that the first graphene growths using SiC were not recognised as monolayers of carbon. For instance, around 1975, Van Bommel, Crombeen and Van Tooren [50] observed that 6H-SiC(0001) developed a layer of graphite that was monocrystalline on the Si-face. The surface of the 6H-SiC(0001) sample was monitored with low energy electron diffraction (LEED, see [Chapter 3, Section 3.5](#)) as a function of temperature, and it was observed that at 1273 K, that the characteristic $(6\sqrt{3}\times 6\sqrt{3})R30^\circ$ pattern signifying formation of the buffer layer, evolved prior to the graphite layers [50]. Thus, it is likely that graphene was controllably grown at this time. Nonetheless, in 2002, Charrier *et al.* [51] recognised that graphene could be grown on 6H-SiC(0001). Shortly afterwards in 2004, Berger *et al.* [52] showed that the ultrathin graphite films (what we would now call bilayer or trilayer graphene) grown on 6H-SiC(0001) could be gated with a field effect, and furthermore, showed quantum effects such as Shubnikov-de Haas oscillations. Additional confirmation of the growth of monolayer and bilayer graphene on silicon carbide came from ARPES measurements in circa 2006, which have since shown the typical linear/conical ([Figure 2.2](#)) and parabolic bandstructure ([Figure 2.3](#)), respectively [34, 40, 53].

There are two growth environments which are commonly used to synthesise graphene on silicon carbide – growth in a (1) vacuum or (2) Ar environment [54-55]. Initially, graphene was grown on SiC using the vacuum method, but more recently, it has been demonstrated that graphene samples grown in an Ar environment show decreased roughness and increased layer uniformity [54-55]. Moreover, graphene is typically grown on the (0001) Si-face rather

than the $(000\bar{1})$ C-face because of better layer uniformity, even though growth on the Si-face yields formation of an unwanted (non-graphene) carbon ‘buffer’ layer (see below) [54].

Nonetheless, in both vacuum and Ar synthesis routes, the temperature of the SiC is increased to a point where the SiC begins to decompose. In a vacuum of 1×10^{-10} mbar, this temperature is approximately 1353 – 1423 K [56] (the buffer layer, see below, has also been observed to form as low as 1073 – 1273 K in similar vacuum conditions [50]). Since the vapour pressure of Si is much higher than that of C, after SiC decomposition the Si sublimes leaving behind solid C [57], which restructures into a (buckled [58-59] – see Figure 2.4b) hexagonal carbon rich structure [60-61]; often called the interfacial layer [54], zero layer, or buffer layer [60] (the precise structure of the buffer layer may be more complicated – and is still under investigation see refs. [62-63]).

Moreover, approximately every third carbon atom in the buffer layer is covalently bonded to a Si atom on the Si-face [53, 64-66]. Consequently, in contrast to graphene, the buffer layer does not have the typical graphene bandstructure which was discussed in Section 2.2.1, and instead has a large bandgap [53, 61, 67-68] making it a poor electrical conductor [53, 60, 64-65]. To obtain graphene, the substrate must be further heated to 1523 – 1623 K [54-55]. This causes the SiC layers beneath the existing buffer layer to decompose (breaking the Si-C covalent bonds), creating a new buffer layer underneath the initial buffer layer which subsequently becomes graphene (as illustrated in Figure 2.4b). To form one layer of graphene, three bilayers of SiC (*i.e.* all layers comprising the stacking sequence ABCACB in Figure 2.4a) are required to decompose [60]. Thus, by repeating this process, more layers of graphene can be epitaxially synthesised, eventually becoming graphite *via* the continuous decomposition of the SiC underneath each subsequent buffer layer. Furthermore, the graphene that is grown on SiC is not completely freestanding (as was theoretically considered in Section 2.2.1), and the underlying buffer layer causes electronic effects such as charge transfer to the graphene layer [64, 69]. This ultimately n-type dopes epitaxial monolayer graphene on SiC, shifting the Fermi level ≈ 0.4 eV above the Dirac point [34, 40, 70-72]. In addition to causing secondary electronic transport effects such as decreased mobility from the localised positive charges in the buffer layer after charge transfer [73], the buffer layer is thought to play a direct role in the significant dependence of carrier mobility on temperature that is observed for epitaxial graphene, but not freestanding graphene [74]. This is thought to occur *via* electron-phonon scattering from the buffer layer [75].

In this thesis, all graphene samples are grown by collaborators at the U.S. Naval Research Laboratory using the Ar blanket gas synthesis method [54], which was initially implemented by Virojanadara *et al.* [76] and Emtsev *et al.* [77]. The SiC substrates used for growth throughout this thesis are semi-

insulating, nominally on-axis (0.1° offcut) 6H-SiC substrates from II-VI Incorporated.

A typical process for epitaxial monolayer graphene synthesis begins with cleaning and removal of polishing scratches off the SiC surface [54]. This is achieved by first cleaning the wafer in acetone and isopropanol solvents (to remove organic matter), followed by a series of acid/base cleaning steps, ending with a HF cleaning process to remove the surface oxide [76, 78]. After HF treatment, the SiC substrate is etched in a furnace (Aixtron/Epigress VP508 horizontal hot wall reactor) at a temperature between 1773 – 1873 K in a partial hydrogen atmosphere (100 – 200 mbar, flow rate 50 – 80 slm / 50,000 – 80,000 sccm) with \approx 2 – 10 sccm of C₃H₈ [54, 78-80]. The time held at this temperature is \approx 5 – 25 minutes [78-79]. These parameters result in a substrate that has steps 2.5 – 5.0 Å high (1 – 2 SiC atomic steps – see Figure 2.4a) and terraces that are \approx 3 μm wide [54]. The SiC is cooled, and then, Ar gas is introduced into the growth chamber to a pressure of 10 – 1000 mbar [76-77, 81]. The sample is heated between 1743 – 1843 K for \approx 15 – 60 minutes [77, 81] which results in the formation of monolayer graphene on the terraces of the 6H-SiC(0001) sample that are \approx 3 × 100 μm² [55].

The Ar synthesis method has the effect of decreasing the rate of Si evaporation from the surface (at a given temperature) due to the increased pressure in the growth chamber. This results in a decreased graphene growth rate in comparison to vacuum synthesis methods at the same temperatures. The decreased growth rate enables SiC surface reconstruction to occur prior to graphene growth, which increases SiC surface uniformity [54]. Furthermore, higher temperatures are required to appreciably evaporate the Si from the surfaces. The higher temperatures increase the mobility of the remaining carbon, leading to improved graphene layer uniformity [55]. Thus, the Ar synthesis method produces higher quality SiC surfaces *and* graphene. But the structural and electronic quality of the graphene can be further enhanced through a process of *hydrogen intercalation*.

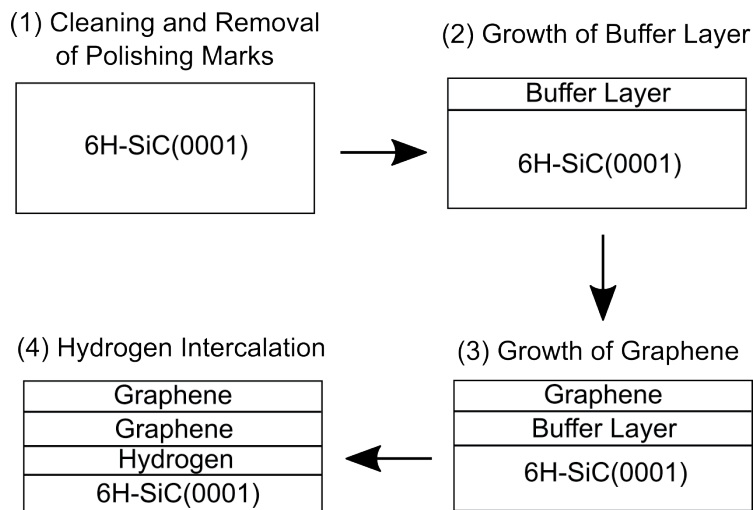


FIGURE 2.5: SIMPLIFIED PROCESS FOR EPITAXIAL MONOLAYER GRAPHENE (EMLG) AND QUASI-FREESTANDING BILAYER GRAPHENE (QFSBLG) ON SILICON CARBIDE.

(1) Solvent and acid/base cleaning of 6H-SiC(0001) to remove organic/inorganic matter. (2) Upon heating to ≈ 1353 K, the buffer layer forms. (3) Heating to ≈ 1523 K forms graphene. The temperatures and annealing times vary from process to process (see text for details). (4) Upon cooling down to ≈ 1273 K, hydrogen is introduced at atmospheric pressure and the Si-face is passivated with hydrogen, releasing the buffer layer-Si covalent bonds to create another graphene layer from the buffer layer.

2.2.2.2 Hydrogen Intercalation of Epitaxial Graphene on Silicon Carbide

The first hydrogen intercalation of epitaxial graphene was undertaken by Riedl *et al.* [82] in 2009. Epitaxial graphene samples were annealed between 873 – 1273 K in molecular hydrogen at atmospheric pressure [82], resulting in the passivation of the Si-face of SiC with hydrogen, *i.e.* hydrogen intercalation underneath the buffer layer, as shown in Figure 2.4c. When the hydrogen intercalation process is undertaken on buffer layer only samples, the monolayer graphene bandstructure (and bilayer structure for epitaxial monolayer graphene samples) is observed, as judged by ARPES measurements [82] (see Figure 2.6a). Hydrogen intercalation was subsequently demonstrated and corroborated by other groups [75, 83].

Hydrogen intercalated graphene has benefits over epitaxial monolayer graphene. For instance, the electronic effects of the buffer layer which were discussed briefly in the preceding section can be almost eliminated by hydrogen intercalation, leading to a weak temperature dependence of the carrier mobility [75]. Coupled with the observation that the linear dispersion (ϵ - k) curve of monolayer graphene (see Equation 2-2 and Figure 2.2/

2.6) is obtained after hydrogen intercalation of buffer layer-only samples; have led these samples to be called ‘quasi-freestanding’ graphene.

Furthermore, hydrogen intercalated graphene demonstrates increased layer uniformity in comparison to epitaxial graphene [84–85]. It is now well-known that graphene growth on the Si-face of 6H-SiC is not uniform at step edges, and that if nominally monolayer graphene is grown on the terraces, that on the step edges bilayer and trilayer graphene is observed. The step edges of 6H-SiC(0001) are in the $(1\bar{1}\bar{2}0)$ direction, which does not grow a buffer layer [84], and so grows graphene at a faster rate than the (0001) terraces. Upon hydrogen intercalation of epitaxial monolayer graphene, the monolayer terraces become bilayer graphene, while the step edges are unaffected [85]. The situation is demonstrated in Figure 2.6b using Raman spectroscopy (see Chapter 3, Section 3.7). Moreover, the ‘flattening’ of epitaxial graphene has been shown to increase the carrier mobility [86], and could partly explain the increased carrier mobility of hydrogen intercalated graphene *via* decreased scattering from step edges.

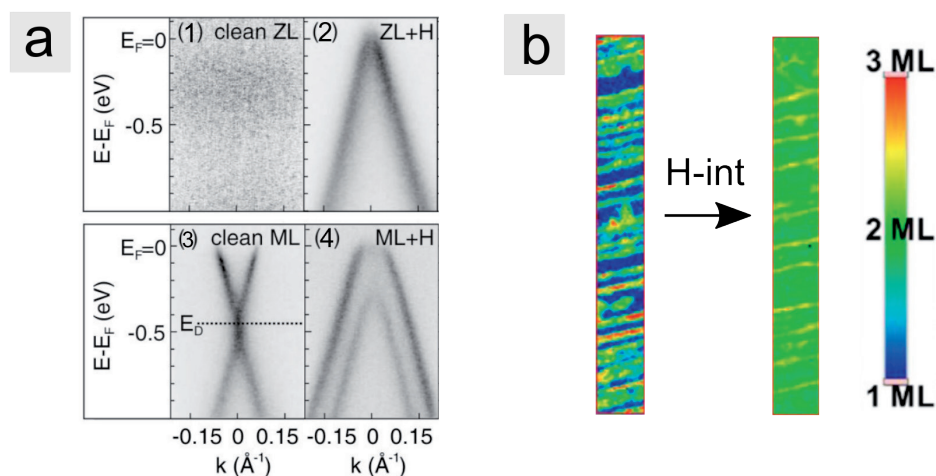


FIGURE 2.6: EFFECTS OF INTERCALATING EPITAXIAL GRAPHENE WITH HYDROGEN.

(a) Angle resolved photoemission spectra showing the bandstructure of (1) pristine buffer layer on 4H/6H-SiC(0001). (2) Buffer layer after hydrogen intercalation. Linear bands typical of monolayer graphene form, implying the buffer layer has now become monolayer graphene. (3) Pristine epitaxial monolayer graphene. (4) Hydrogen intercalated epitaxial monolayer graphene now showing two bands typical of bilayer graphene, implying the buffer layer has become another graphene layer after intercalation. Reproduced with permission from ref. [82] © 2009 The American Physical Society. **(b)** Raman spectroscopic map of the ‘2D’ peak width (see Section 3.7.1). (left) Epitaxial monolayer graphene on 6H-SiC(0001) showing monolayer graphene (blue) areas and bilayer/trilayer graphene (green/red) areas. (right) After hydrogen intercalation (H-int), the terraces become bilayer, while the layer number at the edges is not altered, increasing the layer uniformity of the sample. Reproduced with permission from ref. [85] © 2017 IOP Publishing.

2.3 Monolayer Tungsten Disulphide

Tungsten disulphide, WS_2 , is a compound in the family of materials called the transition metal dichalcogenides (TMDs). TMDs comprise of a transition metal (Mo, W, Te, V, Re, Hf, Pt etc.) and two chalcogen atoms (S, Se, Te), and can be layered – as in the case of WS_2 and MoS_2 – or not layered, as in the case of FeS_2 (pyrite) [87]. The TMD family of materials comprises of approximately 60 species, with two-thirds being layered structures [88]. Monolayers of these materials can be easily isolated because of their layered structure, which is bound by weak van der Waals bonds – as in the case of graphene. Thus, like graphene, TMDs were first exfoliated to obtain thin layers of material and the first demonstration of a monolayer TMD was in 1986, in which monolayer MoS_2 was isolated [6]. But at that time, the electrical and optical properties were not investigated. Around 2004, graphene and monolayer MoS_2 were again isolated and electrically measured [3-4], and garnered more interest in their unique properties from the research community. It wasn't until 2010 when the optical properties of monolayer WS_2 were found to be significantly different to its bulk counterpart [7-8].

Since this time, there has been an explosion of interest in monolayer TMDs across a wide range of disciplines [88]. Even so, there are still properties and phenomena related to these materials that are unexplained or not well known, as will be shown in Chapter 4. In the following sections, I will overview the basic atomic structure, electronic band structure and optical properties of bulk and monolayer WS_2 which are pertinent to this thesis.

2.3.1 Atomic and Electronic Band Structure

The atomic structure of WS_2 is shown in Figure 2.7a, and consists of chalcogen-metal-chalcogen (X-M-X) layers which are bound by van der Waals forces. In each layer, a tungsten atom is covalently bonded to six sulphur atoms. Since the intralayer bonding is covalent, this enables WS_2 to be exfoliated, much like graphene. As can be seen in Figure 2.7a, WS_2 can manifest as different polytypes in which the stacking order varies only in the c-axis, similar to the case of SiC. For WS_2 there exist 3 major polytypes – 2H (hexagonal), 3R (rhombohedral) and 1T (tetragonal). The most stable of these is the 2H polytype, and has a trigonal prismatic coordination [88-89].

The corresponding bulk electronic bandstructure of 2H- WS_2 (determined by density functional theory, DFT) is shown in Figure 2.7b, and shows WS_2 to be an indirect bandgap semiconductor with optical bandgap of ≈ 1 eV, in approximate agreement with previous experimental literature values of ≈ 1.30

- 1.35 eV [90-91] (theoretically calculated values for the optical bandgap vary quite considerably depending on the approximations employed, see refs. [92-93]). Since WS₂ is a semiconductor TMD, I often refer to it as an ‘S-TMD’ in this thesis, to distinguish it from metallic TMDs. Figure 2.7c shows the electronic bandstructure of bilayer WS₂ (2L-WS₂) from DFT calculations (here the energy is referenced to the conduction band minimum) and demonstrates that bilayer WS₂ is still an indirect bandgap semiconductor with an optical bandgap of ≈ 1.2 eV [94], close to the bulk value.

But for monolayer WS₂ the situation changes drastically; the bandstructure changes from indirect to direct at the K/K' points of the Brillouin zone, as is shown in Figure 2.7d. The reason for this is not straightforward, and cannot be explained by simply considering quantum confinement of a semiconductor with isotropic bandstructure [89, 95]. For instance, quantum confinement of a semiconductor with isotropic bandstructure predicts that the energy of the bandgap of a S-TMD will change according to [96]:

$$\Delta E_G = \pi^2 \hbar^2 / 2\mu L_z^2, \quad \dots 2-16$$

where, L_z is the thickness of the S-TMD layer and μ is the reduced exciton (see below) mass given by [96]:

$$\frac{1}{\mu} = \frac{1}{m_e^*} + \frac{1}{m_h^*}. \quad \dots 2-17$$

But for thicknesses less than ≈ 4 nm, the predicted E_G value from Equation 2-16 deviates significantly from measured values (see ref. [96] for brief review).

The unexpected behaviour of the change in bandstructure for S-TMDs can be partly understood by considering the orbital contributions at the Λ , Γ and K points shown in Figure 2.7b-d. It has been found that wavefunction contributions from the Γ_v and Λ_c -points have interlayer contributions from chalcogen p_z-orbitals forming bands with relatively isotropic three-dimensional character. In contrast, the K_c and K_v -points have wavefunction contributions from mostly intralayer metal d-orbitals [95, 97], and form bands with highly two-dimensional character. Upon thinning WS₂ to the monolayer, contributions from the p_z-orbitals will be affected by confinement more than the d-orbitals, thus explaining why the Λ_c and Γ_v points change more rapidly than the K_c/K_v points.

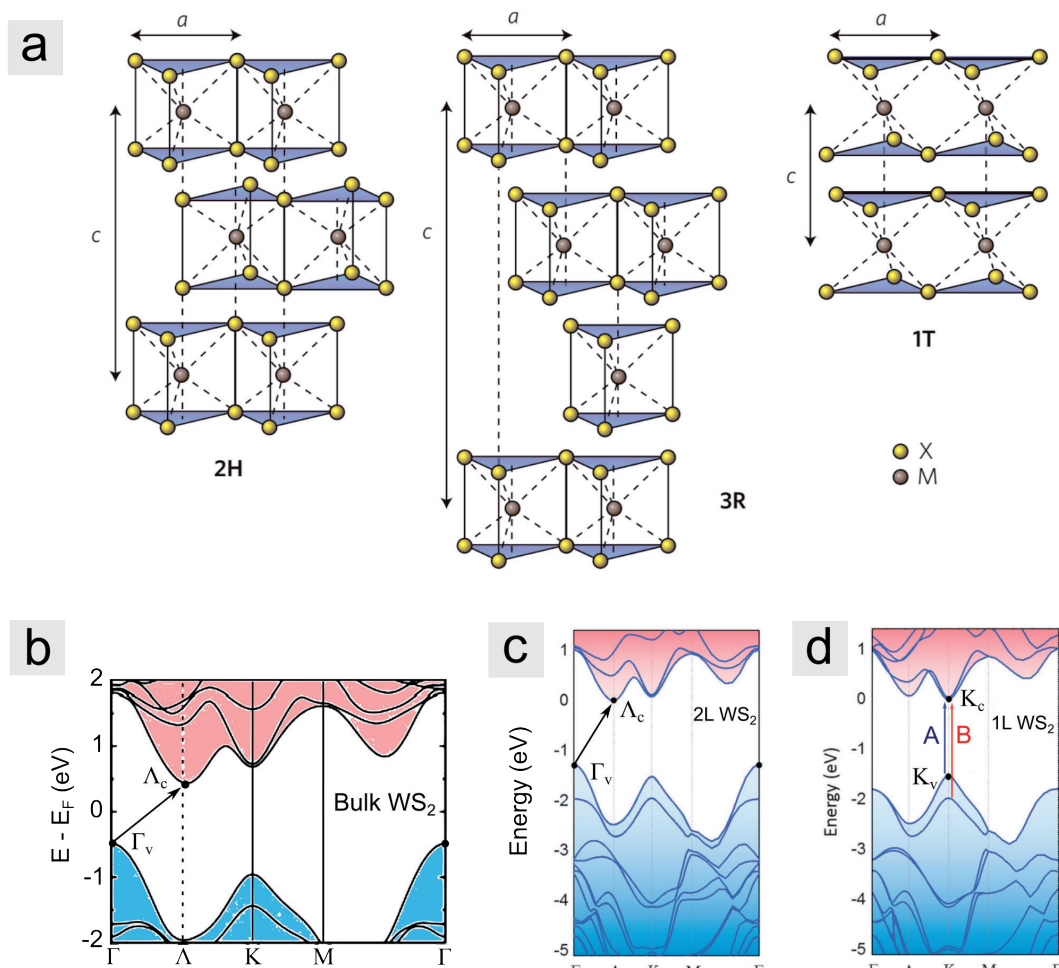


FIGURE 2.7: ATOMIC AND ELECTRONIC BANDSTRUCTURE OF BULK, BILAYER AND MONOLAYER TUNGSTEN DISULPHIDE.

(a) Atomic structure of the different polytypes of WS₂ – 2H-WS₂ (hexagonal), 3R-WS₂ (rhombohedral) and 1T-WS₂ (tetragonal). Intralayer bonding is covalent, whereas interlayer bonding is van der Waals. This allows the layers to slide easily against each other, and be exfoliated much the same way as graphene. Lattice parameters $a \approx 3.154$ [87], $c \approx 12.323$ [98] (2H). X = Sulphur, M = Tungsten. Reproduced with permission from ref. [99] © 2012 Macmillan Publishers Limited. **(b)** Electronic bandstructure of bulk 2H-WS₂ showing energy (referenced to the Fermi level E_F) versus reciprocal lattice space for the 1st Brillouin zone. 2H-WS₂ is an indirect bandgap semiconductor with an optical bandgap of ≈ 1.35 eV (see text), with transition from the valence band at the Γ -point (Γ_v) to the Λ -point in the conduction band (Λ_c). Modified and reproduced with permission from ref. [93] © 2014 Wiley-VCH Verlag GmbH & Co. **(c)** Electronic bandstructure of bilayer WS₂ (2L-WS₂). 2L-WS₂ is still an indirect bandgap material, with transition from Γ_v to Λ_c . **(d)** Electronic bandstructure of monolayer WS₂ (1L-WS₂). At the monolayer limit, WS₂ becomes a direct bandgap semiconductor with an optical bandgap of ≈ 2 eV (see text). In (b-d) the effects of spin-orbit coupling have been included in calculations. For 1L-WS₂ the bands at the K -point are split, and allows for two optical transitions, given by A and B. (c-d) Modified and reproduced with permission from ref. [100] © 2015 The Royal Society of Chemistry.

2.3.2 Optical Properties

The optical properties of monolayer S-TMDs (MoS_2) were first (experimentally) investigated by Splendiani *et al.* [8] and Mak *et al.* [7], which both found that monolayer MoS_2 (isotypic and with similar bandstructure to monolayer WS_2) exhibited a relatively bright photoluminescence response in comparison to bilayer or few layer MoS_2 . This effect was then quickly confirmed to also occur for monolayer WS_2 , which exhibited bright photoluminescence, but negligible photoluminescence when the layer number was greater than one [101].

Photoluminescence (PL) spectroscopy is further explained in [Chapter 3 Section 3.7.2](#), but briefly, light of an energy greater than the band gap of the material allows excitation of an electron from the valence band to the conduction band, leaving behind a hole. Upon recombination, a photon is emitted (radiative recombination) that roughly corresponds in energy to the bandgap of the material. In materials with a strong Coulomb interaction, it is important to consider that the electron and hole can bind to form a quasiparticle bound by Coulombic forces, called an exciton. This reduces the energy needed to create the excitation, and consequently, the emitted photon when the exciton radiatively recombines. An example of the photoluminescence spectrum of monolayer WS_2 (at room temperature) is shown in [Figure 2.8a](#), and shows a PL peak at ≈ 2 eV, which is characteristic of the optical band gap of WS_2 at room temperature [101]. Compared to bilayer and few-layer WS_2 , the PL response of monolayer WS_2 is orders of magnitude greater. The reason for this is that monolayer WS_2 is a direct bandgap semiconductor ([Figure 2.7d](#)), whereas bilayer and few-layer WS_2 is an indirect bandgap semiconductor ([Figure 2.7b-c](#)). Radiative recombination is much more probable in direct bandgap materials than indirect materials, since a phonon is not required for radiative recombination [95].

A feature of the bandstructure that is noticeable in the DFT calculated bandstructures in [Figure 2.7c-d](#) is the ‘splitting’ of the bands at the K/K’ point. This splitting is caused by the spin-orbit coupling effect, and arises from the d orbitals of the metal atoms for S-TMDs [88], resulting in the observation of distinct spectral features in optical absorbance, transmission or reflectance measurements, as shown in [Figure 2.8b](#). The ‘A’ and ‘B’ peaks [102] arise from direct excitonic transitions between the spin split bands at the K/K’ point, as shown in [Figure 2.7d](#) [88-89]. Thus, the spin-orbit coupling energy (Δ_{SO}) can be calculated as the energy difference between the A and B peaks (often called the A- and B-excitons). For WS_2 , $\Delta_{\text{SO}} \approx 0.4$ eV [88, 103]. On the other hand, the C peak (C-exciton) is thought to arise from band nesting – an effect which ultimately causes optical resonances at certain energies corresponding to points of equivalent energy band transitions [104]. Excitons and the exciton

binding energy for WS_2 is further explained in [Chapter 3, Section 3.7.2](#) in the context of photoluminescence spectroscopy.

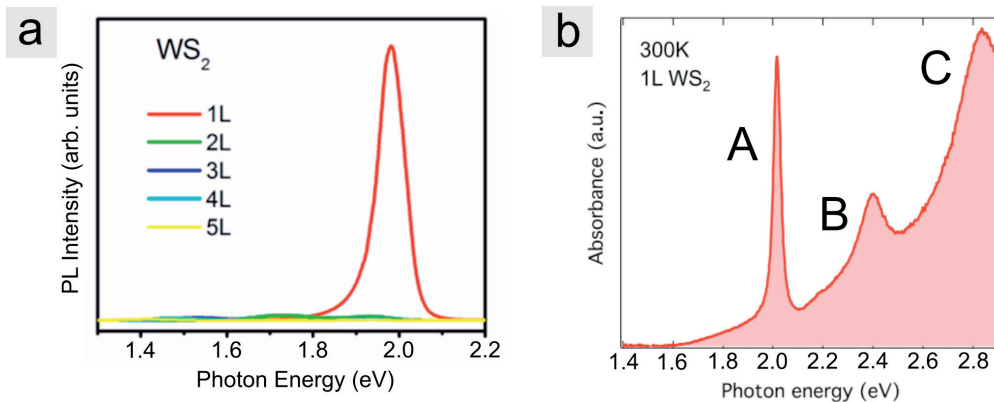


FIGURE 2.8: OPTICAL SPECTRA OF WS_2 AT ROOM TEMPERATURE.

(a) Photoluminescence (PL) spectrum of monolayer (1L) WS_2 (red), bilayer (2L) (green), 3-layer (3L), 4-layer (4L) and 5-layer (5L) WS_2 . The PL intensity of monolayer WS_2 is orders of magnitude greater, due to its direct bandgap. Reproduced with permission from ref. [95] © 2014 American Chemical Society.

(b) Absorbance spectrum of monolayer (1L) WS_2 showing A (≈ 2 eV), B (≈ 2.4 eV) and C-exciton (≈ 2.8 eV) features. The A- and B-exciton are from transitions at the spin-split bands at the K/K'-point. Modified and reproduced with permission from ref. [89] © 2017 Springer Japan KK.

3

Chapter

Experimental Techniques

Keywords: Surface Science, AFM, CVD LEED, PL, Raman, STM, XPS

*"It doesn't make a difference
how beautiful your guess is. If
it disagrees with experiment, it's
wrong"*

- RICHARD FEYNMAN

3.1 Introduction

In this chapter, I will review the necessary theory behind the experimental techniques used throughout this thesis. Most of the techniques in this thesis can be brought under one broad heading – *surface science*. Surface science began in the 1960’s when the technology for creating an ultra-high vacuum ‘UHV’ environment became possible [105]. UHV is typically defined as a pressure below 10^{-9} torr / 10^{-9} mbar [105-106], and these low pressures are required for the analysis of surfaces, since higher pressures result in the speedy contamination of the surface, and spectroscopies requiring electrons becomes impossible due to scattering effects. For instance, at a temperature of 293 K, a monolayer of contamination (assuming density of 10^{15} cm⁻²) can cover a surface at a pressure of 10^{-6} torr in 2 seconds, and a surface at ambient pressure (760 torr) in 3 nanoseconds [106]! With further development of vacuum technology, pressures in the 10^{-10} torr range are now routinely achieved, and surfaces can remain relatively contamination free for hours (at 10^{-10} torr, a monolayer accumulates over the course of a day). This is especially important in the study of ambient air reactions and oxidation, since it is useful to start with a baseline that does not have ambient air effects.

Furthermore, in this thesis, I explore 2D materials which do not have a ‘bulk’, and so their properties are almost completely governed by their surface

structure and interactions with surface or sub-surface structures. In this context, surface science techniques represent an extremely important toolkit for investigating the properties of 2D materials, and are used extensively in this thesis. The experimental techniques discussed in this chapter will include scanning tunnelling microscopy (STM), atomic force microscopy (AFM), X-ray photoelectron microscopy (XPS), secondary electron cut-off photoemission (SECO), low energy electron diffraction (LEED), chemical vapour deposition (CVD), Raman and photoluminescence (PL) spectroscopy and laser scanning confocal microscopy (LSCM).

3.2 Scanning Tunnelling Microscopy

The scanning tunnelling microscope (STM) had its beginnings with the invention of the ‘Topografiner’ at what is now the National Institute of Standards and Technology (NIST) in 1971 [107-108]. The Topografiner worked using the principle of (Fowler-Nordheim) field emission, in which a relatively high voltage of 50 – 100 V was applied to a (tungsten) metallic tip placed \approx 20 nm away from the surface [108]. The tip was scanned over the surface in the x, y and z directions using piezoelectric motors to obtain an image of the surface. Unfortunately, the Topografiner project was stopped prematurely, but who knows how history would have changed if the project kept going [109]!

It was not until a decade after the initial experiments with the Topografiner when Binnig, Rohrer, Weibel and Gerber invented the STM in 1981 [110]. The STM is in principle very similar to the Topografiner, and is comprised of a few main elements: the metallic tip (which is often tungsten or platinum-iridium), piezoelectric scanning motors, feedback control electronics and crucially, the vibration dampening system. A replica of the first STM and its schematic is shown in [Figure 3.1a-c](#) and outlines the simplistic setup of an STM. What set the STM and the Topografiner apart was the fact that the STM operated in the quantum or ‘direct’ tunnelling regime (lower voltages, smaller tip-sample distance – the so called ‘metal-insulator-metal’ tunnelling current described in Young’s 1971 paper [107]), whereas the Topografiner operated in the Fowler-Nordheim tunnelling regime (large voltages, larger tip-sample distance, ‘field emission’ current). Thus, lower voltages (and closer tip-sample distances) enabled the STM to image at the atomic scale. This work resulted in Binnig and Rohrer sharing the 1986 Nobel Prize in physics for their efforts [111].

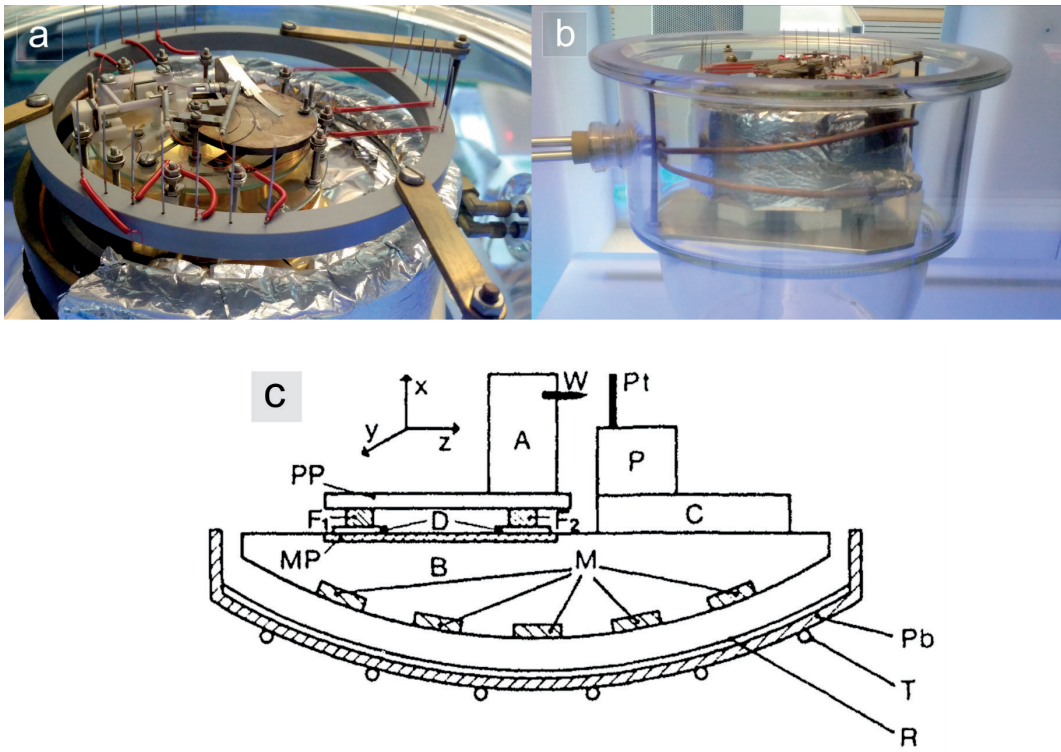


FIGURE 3.1: THE FIRST SCANNING TUNNELLING MICROSCOPE (STM).

(a), (b) Top and side view of a replica of the first STM made by Binnig, Rohrer, Weibel and Gerber in 1981 (photo taken at Deutsches Museum von Meisterwerken der Naturwissenschaft und Technik by Jimmy C. Kotsakidis) (c) Schematic of the first STM describing instrument parts in (a) and (b). W = tungsten tip, A = support, B = bench, PP = piezoplate, F₁, F₂ = metal feet, D = dielectric material, MP = metal plate, P = piezodrive, R = conducting sheet (eddy current dampening), M = permanent magnets, T = Helium cooling tubes, Pb = lead bowl (for superconducting magnetic levitation vibration dampening). Reproduced with permission from ref. [110] © 1982 American Institute of Physics.

3.2.1 Theoretical Basis for the Scanning Tunnelling Microscope

The STM works on the principle of quantum mechanical tunnelling, and more specifically, *direct tunnelling* (as opposed to Fowler-Nordheim/cold emission). An atomically sharp metallic tip is brought so close to a conducting surface (sample) that electrons can tunnel between the sample and the tip (experiments have shown that this distance is approximately 4-7 Å [112]), overcoming the vacuum potential barrier (*i.e.* the workfunction, W_f). When a voltage is applied from tip to sample (smaller in magnitude than the workfunction), a net tunnelling current can flow between the metallic tip and sample.

If one considers classical mechanics, this should not be possible – the electrons from the sample or tip should not be able to overcome the energy barrier if their energy is below it. But the situation changes when one considers the physics of quantum mechanics; the electrons *can* penetrate the barrier due to the electrons possessing ‘wave-like’ properties, and a non-zero probability of these ‘waves’ existing in the classically forbidden region [113]. The physical scenario of sample–vacuum–tip can be analysed by considering solutions of Schrödinger’s equation for an electron impinging on one dimensional square potential barrier. The solution to the one-dimensional potential barrier problem for an electron moving in the +z direction has the form [112]:

$$\psi(z) = \psi(0)e^{-\kappa z}, \quad \dots 3-1$$

where

$$\kappa = \frac{\sqrt{2m(W_f - E)}}{\hbar}, \quad \dots 3-2$$

is the decay constant, m is the mass of the electron, \hbar is reduced Planck’s constant, W_f is the workfunction of the metal (defined as the energy required to move an electron at the Fermi level, E_F , to the vacuum), and E is the energy of the electron. The probability density is thus [112]:

$$\psi(z)^2 = |\psi(0)|^2 e^{-2\kappa z}. \quad \dots 3-3$$

If the energy supplied to the electron is << than the energy barrier, then the decay constant in [Equation 3-3](#) simplifies to [112]:

$$\kappa = \frac{\sqrt{2m(W_f)}}{\hbar}, \quad \dots 3-4$$

for an electron at the Fermi level of the sample. One can then substitute in values to evaluate the decay constant [112]:

$$\kappa = 0.51 \text{ \AA}^{-1} \sqrt{W_f(eV)}. \quad \dots 3-5$$

If one assumes a small applied bias voltage, low temperature and an ideal point probe, then the tunnelling current given by Bardeen’s tunnelling formula [114] yields [115]:

$$I \propto \sum_n |\psi_n(z)|^2 \delta(E_n - E_F) . \quad \dots 3-6$$

For a sample state ψ_n at position X on the surface and energy E_n , where E_F is the Fermi level (here δ is the Dirac delta). The right-hand side of [Equation 3-6](#) is the local density of states (LDOS) which represents the number of electrons in a given volume per unit energy, consequently describing the number of electronic states of a system. The Tersoff-Hamann model [115] showed that if one assumes a spherical wavefunction (s-wave) and spherical potential well for the tip, then the LDOS is equivalent to the expression in [Equation 3-6](#). Thus, the tunnelling current can then be expressed as [112]:

$$I \propto V \rho_s(0, E_F) e^{-1.025 \text{ \AA}^{-1} \sqrt{W_f(\text{eV})} z} , \quad \dots 3-7$$

for electrons coming from the tip surface at a distance z . Here, V is the voltage applied between the tip and sample, and $\rho_s(0, E_F)$ is the local density of electron states at the Fermi level in the sample. [Equation 3-7](#) states that if the sample has a constant density of electron states, the tunnelling current will be proportional to the applied bias voltage and the LDOS of the sample, and will decay exponentially as a function of distance and workfunction. In terms of monolayer epitaxial graphene on silicon carbide, the W_f is approximately 4 eV [116], which gives a decay constant of $\approx 1 \text{ \AA}^{-1}$ (see [Equation 3-5](#)). Such sensitivity to tunnelling current on the ångström-scale is what enables atomic resolution.

Although a simplistic model, the 1D model barrier potential (and the Tersoff-Hamann assumptions) gives physical insight to the basic working principle of the STM. Here I have shown that the STM works based on the principle of quantum mechanical tunnelling, and the resultant tunnelling current is proportional to the LDOS at the Fermi level of the sample, which is sensitive to changes on the scale of the atom. Thus, when conducting STM, one observes directly the LDOS topology (*i.e. conductivity*) of the sample, enabling the real-space structure determination of periodic and non-periodic surface structures on the atomic scale.

3.2.2 Practical Basis for the Scanning Tunnelling Microscope.

[Section 3.2.1](#) outlined the theoretical basis of how the STM is able to use an atomically sharp tip to image conductivity changes on the surface in the atomic resolution limit. But to fabricate a functioning STM, there are a few

more critical components which must be considered (as was demonstrated by Binnig *et al.* [10] in [Figure 3.1!](#)), and these are illustrated in [Figure 3.2a](#).

First, one needs a system to precisely scan the surface and control the position of the metallic tip. In the first STM ([Figure 3.1](#)) this was achieved by using piezoelectric actuators. This method of tip positioning and scanning is still used in modern STMs, and while there now exist a few different STM designs [117], all still use *piezoelectric actuators* for scanning and positioning. Piezoelectric actuators work based on the principle of the piezoelectric effect, or more accurately, the converse piezoelectric effect [117]. When a suitable non-centrosymmetric (*i.e.* inversion asymmetric) crystal is deformed, a net voltage is produced – this is the basis of the piezoelectric effect. But the converse also holds true: if a sufficiently large voltage is applied to the crystal, it can deform in the x , y or z direction, dependent upon the direction of the electric field. Thus, the *converse piezoelectric effect* is used to control the deformation of piezoelectric elements, enabling sub-ångström precision control in all three spatial coordinates [117].

Secondly, in order to keep the tip with respect to the sample stable to within sub-ångström distances requires extremely low vibrational perturbations of less than a factor of ten lower (*i.e.* 1 pm). This level of vibration minimisation must consider vibration sources such as nearby trains, vehicles etc., and so STMs are typically located in basements, or on ground floors of buildings; in fact, the whole apparatus can be mounted on specialised floating tables [117].

Furthermore, to keep the tip from crashing into the surface of the sample upon scanning, a suitable feedback loop needs to be implemented so that the tip can follow the topography of the sample. There are two STM operating modes: constant height and constant current. In constant height mode, the feedback controller is not needed, and the STM records the current as a function of position for a given tip-sample distance. In many cases, imaging in this manner is risky, as debris on the surface (from say un-intercalated calcium atoms!) or temperature fluctuations (causing tip-surface distance to decrease) can cause a tip crash event (defined as the tip making mechanical contact with the surface, typically detrimentally altering the state of the tip so that atomic resolution is lost). In this thesis, constant current mode is exclusively used in which the feedback controller is turned on, and a set point current is maintained by the system moving the tip closer or further away from the surface to maintain this setpoint. Subsequently, constant current mode follows the topography of the sample. In an STM, a proportional-integral (PI) controller is typically used [117-118]. The feedback controller is nowadays implemented digitally using a digital signal processor (DSP), and allows for quick parameter changes [117].

When all systems are performing in unison, atomically resolved images can be obtained, such as that of graphene on silicon carbide shown in [Figure 3.2b](#).

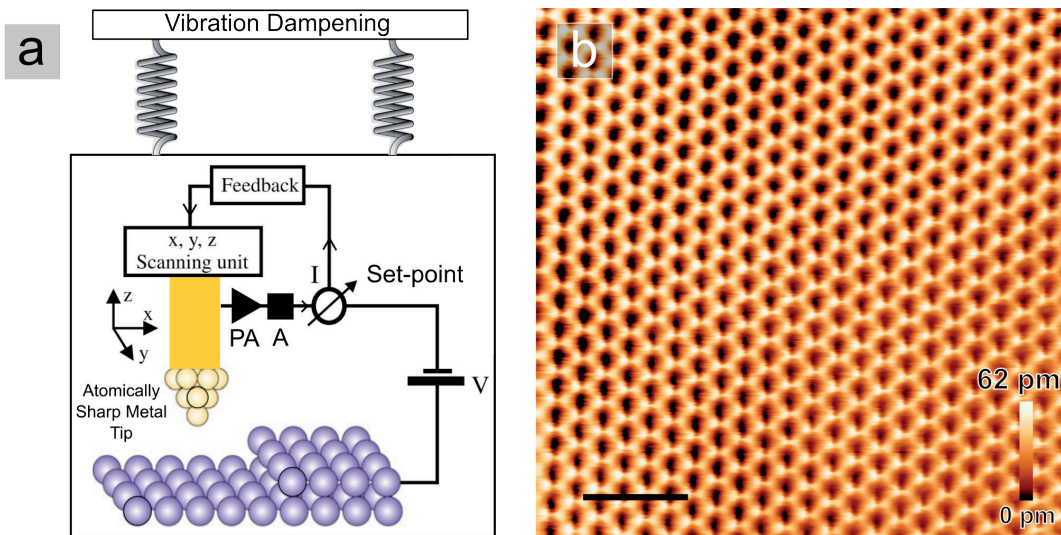


FIGURE 3.2: SIMPLE SCHEMATIC OVERVIEW AND IMAGING CAPABILITY OF THE SCANNING TUNNELLING MICROSCOPE (STM).

(a) Major components of a STM – atomically sharp metallic tip, scanning unit (piezoelectric actuators), vibration dampening and feedback control. PA = pre-amplifier and A = amplifier. A PI controller (feedback loop) tries to maintain the current set-point by moving the tip up or down. Modified and reproduced with permission from ref. [117] © Springer-Verlag Berlin Heidelberg. **(b)** Image of epitaxial graphene on silicon carbide obtained with a platinum-iridium metallic tip at 4.6K (0.2 V, 100 pA). Scale bar = 1 nm.

3.2.3 The Scanning Tunnelling Microscope in the Fuhrer Laboratory

The STM in the Fuhrer laboratory is an ultra-high vacuum low temperature STM (CT-104 610) from CreaTec Fischer & Co. The STM can be operated at liquid helium (LHe) temperatures of ≈ 4.6 K, liquid nitrogen (LN₂) temperatures of ≈ 77 K or at room temperature ≈ 293 K. The system is comprised of 3 main chambers: the load lock, the preparation chamber and the analysis chamber (which houses the STM), shown in Figure 3.3. The load lock is used to introduce samples (which are mounted on 'Omicron' type sample holders – see Figure 3.4a) from ambient atmosphere into the UHV environment of the preparation chamber, and can achieve a base pressure of $\approx 1 \times 10^{-8}$ mbar. Samples are transferred from the load lock to the preparation chamber. The base pressure of the preparation chamber is $\approx 5 \times 10^{-11}$ mbar, but typically operates at around 1×10^{-10} mbar. The manipulator in the preparation chamber is attached to a differentially pumped rotary motion feedthrough, which can rotate the manipulator without breaking vacuum (this is essential for rotating samples to face the effusions cells). The preparation chamber is also connected to the analysis chamber which is

typically at a vacuum of $\leq 1 \times 10^{-10}$ mbar. The preparation chamber also has an ion gun and argon gas leak valve for argon sputtering (a standard technique for cleaning surfaces in vacuum since 1955 [109]). This technique is used to clean the Au(111) standard, which is in turn used to condition the tip *in-situ* so as to obtain an atomically sharp tip for surface imaging (or a tip suitable for spectroscopy).

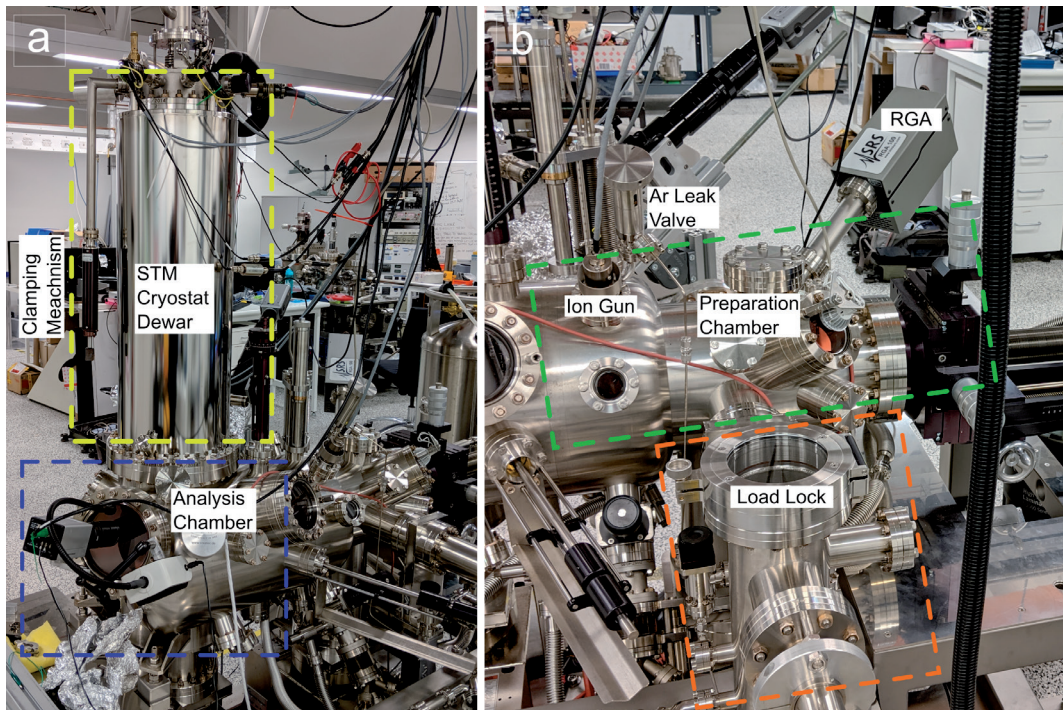


FIGURE 3.3: OVERVIEW OF THE LOW TEMPERATURE SCANNING TUNNELLING MICROSCOPE IN THE FUHRER LABORATORY.

(a) *Analysis chamber showing the prominent STM cryostat Dewar which can maintain temperatures of 4.6 K for ≈ 2 days, or 77 K for ≈ 5 days.* **(b)** *The load lock is used to transfer samples to and from ambient atmosphere to UHV. The preparation chamber is used for calcium deposition and sample annealing/cleaning using Ar sputtering and is equipped with a residual gas analyser (RGA).*

For the Ca-intercalation experiments, an effusion cell was purchased from CreaTec Fischer & Co. and mounted onto the preparation chamber. The effusion cell is also connected to the load lock for initial vacuum pumping. The setup is shown in [Figure 3.4b-c](#).

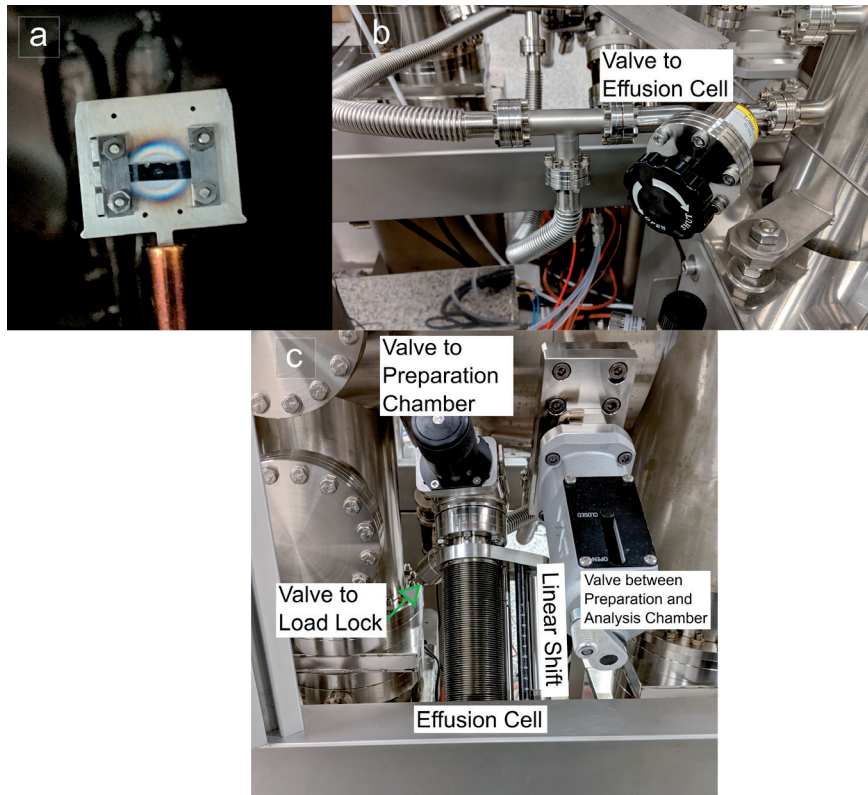


FIGURE 3.4: SAMPLE HOLDER AND EFFUSION CELL SETUP.

(a) *Sample holder for STM measurements.* (b) *Valve which connects the calcium effusion cell to the load lock for vacuum pumping prior to preparation chamber insertion.* (c) *Effusion cell setup. The effusion cell is mounted on a linear shift which allows insertion into the preparation chamber.*

Coarse adjustment of the STM head is achieved with use of a Pan slider type piezoelectric motor. The Pan slider was designed in 1993 by S. H. Pan, and is a piezoelectric motor for coarse movement of the STM tip [120]. For fine adjustment of the STM tip (*i.e.* for surface approach and sample scanning) a tube piezo element is used [117]. Two types of STM tips are used in this thesis. The first is a Pt-Ir wire of $0.3\text{ }\mu\text{m}$ diameter that is cut roughly using wire cutters. The second is a W wire of $0.1\text{ }\mu\text{m}$ diameter that is electrochemically etched in a solution of NaOH (4 g) and H_2O (50 ml).

3.3 Atomic Force Microscopy

The atomic force microscope (AFM) was developed in 1985 – not long after the realisation of the STM – by Binnig, Quate and Gerber (the same Binnig and Gerber that were involved in the first STM) [121]. The atomic force

microscope can measure extremely small forces on the order of nano Newtons (or less) and translate these forces into three-dimensional images of the material surface on the micron to sub-nano scale (not long after the AFM's inception, atomic resolution of graphite was achieved) [122]. The AFM achieves this by measuring the deflection of a sharp probe (cantilever/tip) as it scans over the surface. Because the AFM and STM both use a probe to scan over the surface, the AFM and STM are often called 'scanning probe' techniques. Although, unlike the STM which requires a conductive substrate to measure tunnelling currents, the AFM instead relies on interatomic forces between the sample and the cantilever, and so can image non-conductive samples.

The first AFM design in fact used an STM as a feedback controller to measure deflection of the cantilever [121-122], as shown in Figure 3.5a. The cantilever was composed of a piece of diamond glued to gold foil! Modern AFMs such as the Bruker Dimension Icon AFM, which is used throughout this thesis, use the 'optical lever' method [123] (see description below) to detect the deflection of the cantilever (which are now nanofabricated from silicon nitride to strict tolerances – see Figure 3.5b), but the working principle is no different from the first AFM made by Binnig *et al.* [121].

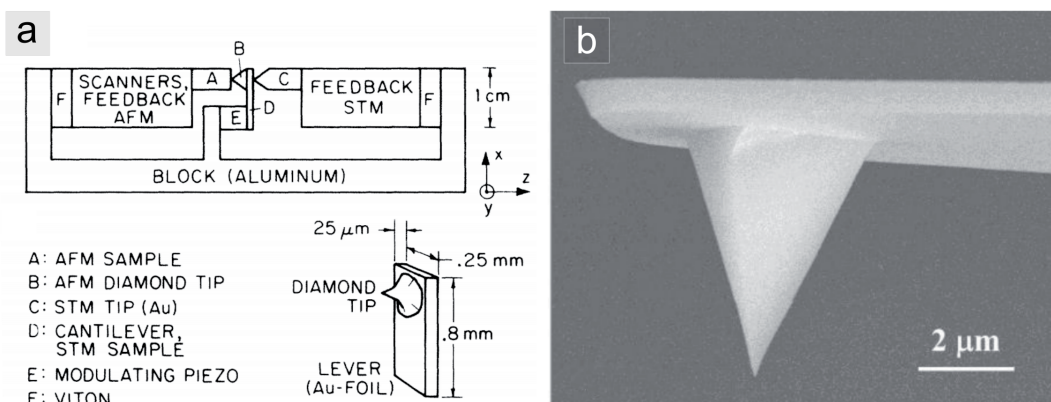


FIGURE 3.5: THE FIRST ATOMIC FORCE MICROSCOPE (AFM); COMPARISON OF THE FIRST AND MODERN DAY CANTILEVERS.

(a) *The first AFM built by Binnig, Quate and Gerber showing schematic overview. Two feedback mechanisms were implemented, one of which included an STM to measure and control the force on the cantilever. The cantilever is shown on the bottom right, and consists of a diamond tip attached to a gold foil. Reproduced with permission from ref. [121] © 1986 American Physical Society. (b) A modern-day probe used in the Bruker Dimension Icon (scansyst-air) composed of silicon nitride. Reproduced with permission from ref. [124] © 2015 IEEE.*

3.3.1 Working Principle of a Modern Atomic Force Microscope

In AFM, we are interested in measuring the interatomic forces between the tip and sample. The total force on the AFM cantilever is composed of van der Waals forces (more specifically, London forces) which act as a long range attractive force on the cantilever, and short-range repulsive forces which arise from the Pauli exclusion principle [117]. This is a simple description, but a more complete description of the forces on the cantilever are much more complex [117]. Thus, to approximate these tip-sample forces, the Lennard-Jones potential [125] is often implemented, which gives the potential energy between neutral atoms [117]:

$$U_{LJ}(r) = 4U_0 \left[\left(\frac{R_a}{r} \right)^{12} - \left(\frac{R_a}{r} \right)^6 \right]. \quad \dots 3-8$$

Where U_0 is the depth of the potential well, r is the distance between atoms (*i.e.* tip-sample distance) and R_a is the distance at which $U_{LJ}(r)$ is zero. [Equation 3-8](#) describes a long-range attractive force proportional to $-1/r^6$ and a short-range repulsive force proportional to $+1/r^{12}$, where the force can be found by differentiating [Equation 3-8](#): $F = -\partial U / \partial r$. [Equation 3-8](#) and the resulting force is shown in [Figure 3.6a](#) and [Figure 3.6b](#), respectively. As will be discussed below, different scanning modes operate in different parts of this force curve.

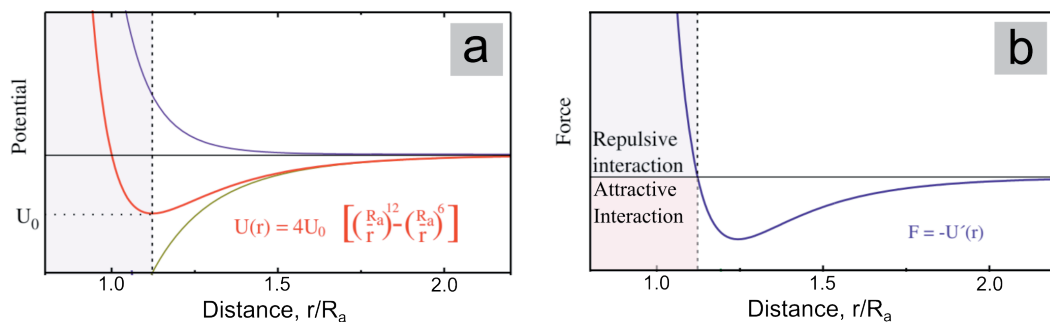


FIGURE 3.6: LENNARD-JONES POTENTIAL MODEL FOR THE ATOMIC FORCE MICROSCOPE TIP-SAMPLE INTERACTION.

(a) The green (bottom line) line shows the attractive component ($-1/r^6$) and the blue (top line of top panel) shows the repulsive component ($+1/r^{12}$) of the Lennard-Jones potential. The red (middle) line shows the total potential as a function of distance. **(b)** The derivative of the curve in (a), showing total force as a function of distance. (a-b) Modified and Reproduced with permission from ref. [117] © Springer-Verlag Berlin Heidelberg.

One way in which to measure these forces is by correlating the deflection of the AFM cantilever as it interacts with the sample. In the Bruker AFM, this is achieved by use of the optical lever technique. A detailed and simplified schematic of the Bruker Dimension Icon AFM scan head is shown in [Figure 3.7a](#) and [Figure 3.7b](#), respectively. In the optical lever technique, light from a laser diode is passed through several beam shaping optics and is focused onto the reflective backside of the cantilever. Small motions in the cantilever deflect the light at different angles, and this light is brought to the photodetector *via* mirrors and lenses. The photodetector is comprised of 4 photodiode quadrants and converts the deflection of the light from the cantilever into an electrical signal, which is then deconvoluted into a three-dimensional image *via* digital electronics. Consequently, AFMs which implement the optical lever technique of measuring the cantilever deflection are called ‘beam deflection’ type AFMs [[117](#)].

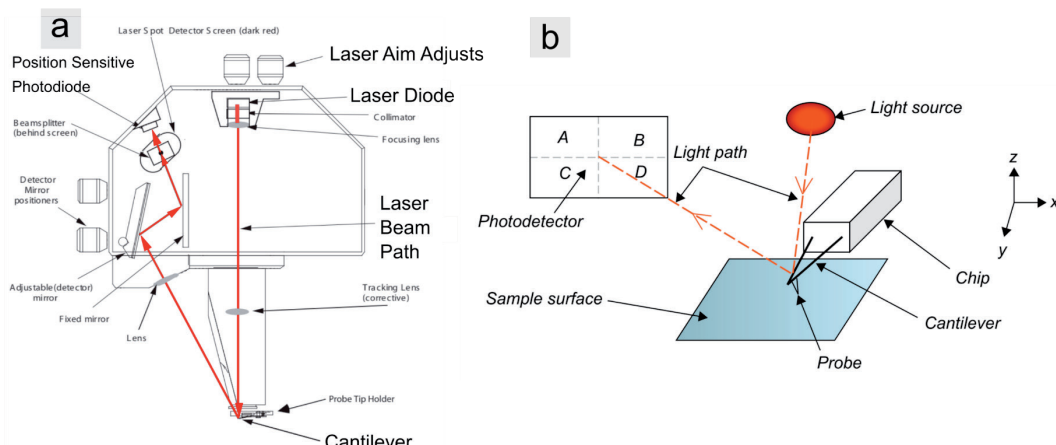


FIGURE 3.7: SCHEMATIC OF THE BRUKER DIMENSION ICON ATOMIC FORCE MICROSCOPE (AFM) SCAN HEAD.

(a) *The Bruker Dimension Icon AFM scan head showing the optical lever setup. A laser diode is directed at the reflective backing of the cantilever through beam shaping optics. The beam is reflected through collecting optics to the four-quadrant photodiode which can measure the amount of deflection in the beam. Image courtesy of Bruker Corporation.* **(b)** *A simplified schematic of the schematic in (a). Reproduced with permission from ref. [[123](#)] © 2009 Elsevier Ltd.*

3.3.2 Scanning Modes of an Atomic Force Microscope

The AFM can operate in distinct modes that are characterised by the probe’s distance to the sample. The main operation modes are contact, intermittent (or tapping) and non-contact mode, and are shown on the force-distance

graph of [Figure 3.8](#). In contact mode, the probe is scanned over the sample while in close contact. In intermittent contact, the probe periodically touches then retracts from the sample surface. In non-contact mode, the probe does not touch the sample surface.

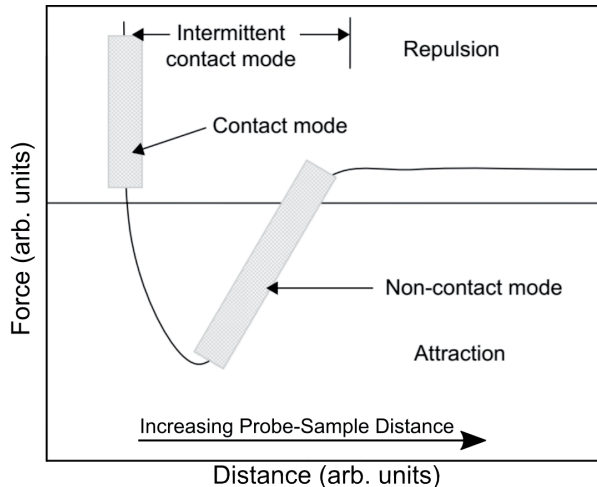


FIGURE 3.8: DIFFERENT OPERATING MODES OF THE ATOMIC FORCE MICROSCOPE.
The intermittent contact (tapping) mode operates in both the repulsive and attractive regimes of the Lennard-Jones potential. Modified and reproduced with permission from ref. [123] © 2009 Elsevier Ltd.

3.3.2.1 Intermittent Contact Mode

In this thesis, the Bruker AFM is operated in intermittent contact (tapping) mode. In tapping mode, the probe is oscillated at a frequency close to (but below) its resonant frequency, and will periodically touch and disengage from the sample surface [[117](#), [123](#)]. When the probe approaches the surface of the sample, it interacts with the sample and dampens the oscillation of the probe, causing frequency and amplitude to lower, pushing the oscillation frequency even further from resonance. The system then seeks to restore the original amplitude by moving away from the surface using feedback control, hence restoring the original amplitude and frequency and tracing out the topography of the sample [[123](#)].

As was mentioned, upon interaction of the probe and surface, the resonant frequency of the cantilever can differ from the set frequency. This frequency difference is detected upon comparison to the set frequency. Thus, images of the surface can be constructed from these frequency changes, and are called phase contrast images [[123](#)]. Since the phase is measuring the energy

dissipation between tip and sample, material properties which can induce these changes are for instance heterogeneous viscoelasticity and adhesion/friction forces across the surface of the sample [126]. Although it should be noted that quantitative analysis with phase contrast images is difficult, since their composition is a mixture of complex parameters [123] (see ref. [127] for review). Nonetheless, phase contrast images are useful for qualitatively determining heterogenous regions in the sample which have different composition, mechanical or adhesion properties [127], and will be used in [Chapter 4](#).

3.4 X-ray Photoelectron Spectroscopy

X-ray photoelectron spectroscopy (XPS) is based on the physical principle of the photoelectric effect, which was first observed by Hertz in 1887 [128], further characterised by Lenard [129] and then finally explained by Einstein in 1905 [130] (for which he won the 1921 Nobel prize in physics [131]) using Planck's 'quantum theory' formed only 5 years prior [132]. The photoelectric effect describes the emission of electrons from a material (typically metal) surface after excitation with photons – *i.e.* discrete quanta of light. Importantly, the energy of the photons must exceed a certain energy threshold of the material, which we now term the 'workfunction'. In early experiments, ultra-violet (UV) light was used to remove electrons from metals. In modern XPS, X-ray wavelengths are used, but the physical principle remains the same – photons are used to eject electrons from the (typically solid and conductive) material.

The first X-ray photoelectron spectrometer was developed by Siegbahn and co-workers [133], and was initially called electron spectroscopy for chemical analysis, or ESCA for short. For this discovery, Siegbahn was awarded the Nobel Prize in 1981 [134]. A modern X-ray photoelectron spectrometer schematic (similar to what would be found at the Australian Synchrotron), is shown in [Figure 3.9](#) below. Here, a concentric hemispherical analyser (CHA) is implemented, as is also implemented at the Australian Synchrotron which uses a PHOIBOS 150 (*i.e.* hemisphere with 150 mm mean radius). The CHA can differentiate the kinetic energies of the electrons collected from a surface undergoing photoemission. The CHA achieves this by applying different voltages on the two concentric hemispheres, which sets up an electric field, deflecting the electrons a distance which is proportional to their kinetic energy [135].

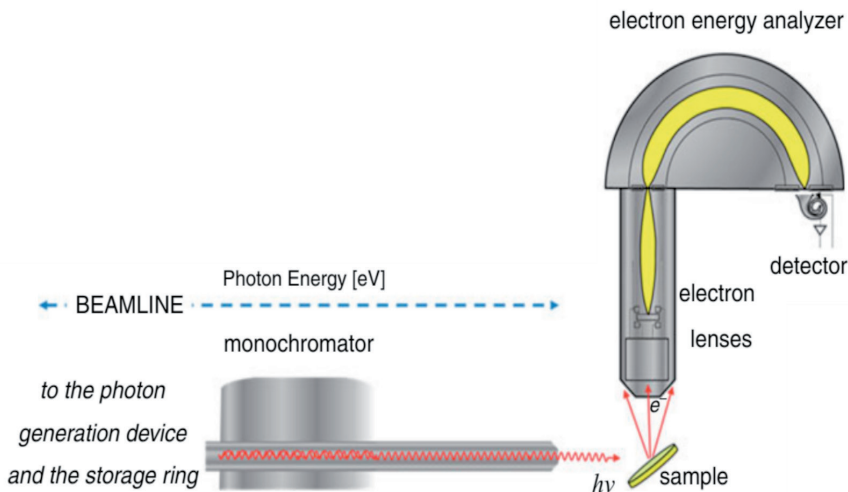


FIGURE 3.9: SIMPLIFIED SCHEMATIC OF A MODERN X-RAY PHOTOELECTRON SPECTROMETER AT A SYNCHROTRON.

X-rays from the synchrotron storage ring pass through a monochromator before hitting the sample, causing photoemission of electrons, photoelectrons. The photoelectrons then pass through lenses and the concentric hemispherical analyser (CHA) to determine their kinetic energy. The photoelectrons are then counted by a suitable detector – the Australian Synchrotron implements a 9-channeltron (channel electron multiplier, CEM) detector. Reproduced with permission from ref. [136] © 2015 Springer-Verlag Berlin Heidelberg.

3.4.1 Overview of the X-ray Photoemission Process

The basic physical process of photoemission is shown in more detail in Figure 3.10. Initially, a photon in the X-ray energy range impinges on a conductive sample. The X-rays can cause photoemission of the core-level electrons in the sample such that their kinetic energy is given by [135]:

$$E_{k,s} = E_{hv} - E_B - W_{f,s} , \quad \dots 3-9$$

where E_{hv} is the energy of the X-ray, E_B is the binding energy of the electron in the specific core level defined as the difference in energy between the core level and Fermi level (see Figure 3.10a), and $W_{f,s}$ is the workfunction of the sample under investigation, defined as the difference in energy between the Fermi level of the sample and vacuum level (see Figure 3.10a). As the electron makes its way to the spectrometer for detection, the spectrometer workfunction also needs to be considered, since two dissimilar workfunctions set up a contact potential difference (CPD), defined by [137]:

$$\Delta W_f = W_{f,a} - W_{f,s}. \quad \dots 3-10$$

Where $W_{f,a}$ is the workfunction of the spectrometer defined as the difference in energy between the Fermi level of the spectrometer and vacuum level. The resulting kinetic energy of the electron after detection by the spectrometer ($E_{k,a}$) is then lesser by an amount equal to the CPD:

$$E_{k,a} = E_{hv} - E_B - W_{f,s} - (W_{f,a} - W_{f,s}), \quad \dots 3-11$$

$$E_{k,a} = E_{hv} - E_B - W_{f,a}. \quad \dots 3-12$$

Where E_{hv} is the energy of the X-ray, E_B is the binding energy, and $W_{f,a}$ is the workfunction of the spectrometer. The result in [Equation 3-12](#) is quite fortuitous, since only the workfunction of the spectrometer needs to be considered, and this is a parameter that is well known (*i.e.* can be designed, and thus, a known value). This expression is valid since we assumed the material was conductive, and the Fermi level of the sample and spectrometer aligned precisely. A typical XPS spectrum is shown in [Figure 3.10b](#), and demonstrates that each core level corresponds to a unique kinetic energy for a certain photon energy. [Equation 3-12](#) can be re-arranged in terms of the binding energy of the electron:

$$E_B = E_{hv} - E_{k,a} - W_{f,a}. \quad \dots 3-13$$

Since the electron binding energy is constant for a change in photon energy, XPS spectra are typically shown in terms of binding energy. Furthermore, the workfunction of the spectrometer is well-known, so a suitable voltage can be applied to cancel its effect [138], in which case [Equation 3-13](#) becomes [136, 138]:

$$E_B = E_{hv} - E_{k,a}. \quad \dots 3-14$$

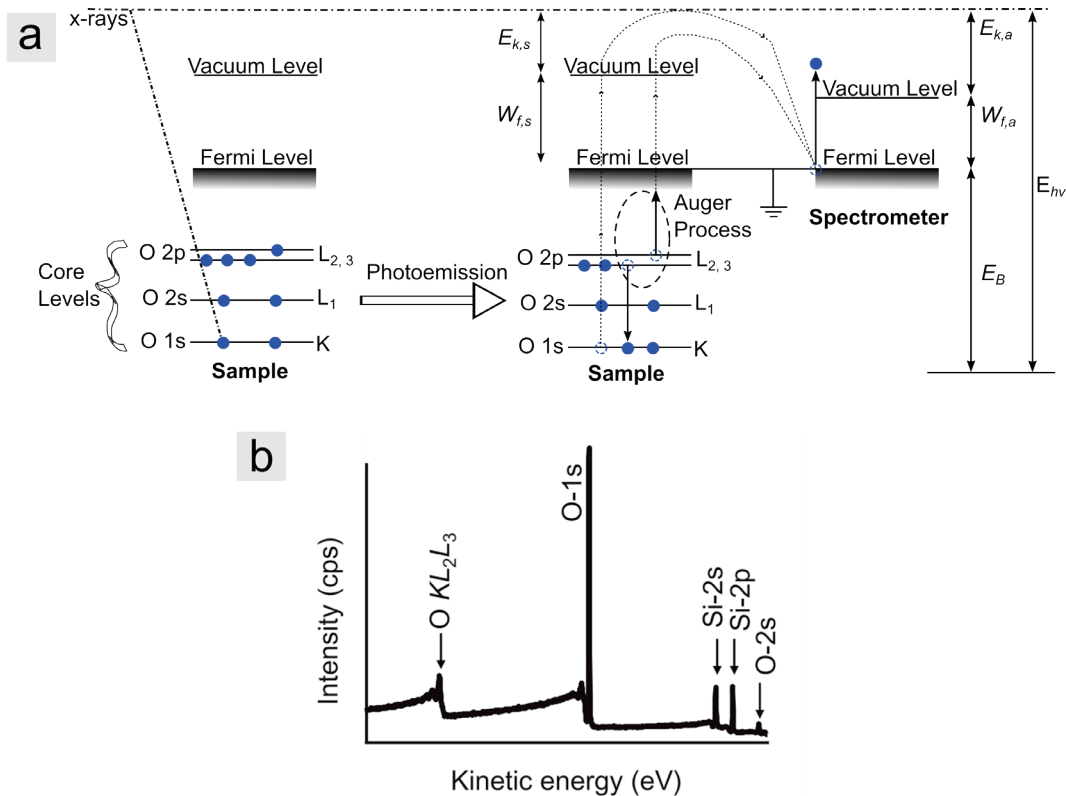


FIGURE 3.10: OVERVIEW OF THE PHOTOEMISSION PROCESS IN X-RAY PHOTOEMISSION SPECTROSCOPY.

(a) The process of photoemission from the sample to the detector. Using an oxygen atom in silicon dioxide as an example, an X-ray with sufficient energy is able to excite an electron (blue circle) to the vacuum level by overcoming the binding energy of the core level (E_B) and the workfunction of the sample ($W_{f,s}$), hence causing photoemission and forming a core-hole. The photoemitted electron with kinetic energy $E_{k,s}$ is then measured by the spectrometer, which must overcome the spectrometers own workfunction ($W_{f,a}$). The resulting measured kinetic energy ($E_{k,a}$) is thus diminished by the spectrometer workfunction which must be taken into account. Since the sample and spectrometer are in electrical contact, their Fermi levels are aligned, and thus, enables calculation of the binding energy, E_B . **(b)** Typical X-ray photoemission spectrum of silicon dioxide showing the oxygen core levels (O-1s, O-2s), as well as Auger electron features (O KL_2L_3). Reproduced with permission from ref. [135] © 2012 John Wiley and Sons.

Using the ‘common’ formalism for XPS [139] and for photons incident at the ‘magic angle’ ($\approx 54.74^\circ$) [140], the photoemission intensity of any given peak in an XPS experiment can be expressed as [139, 141]:

$$I(E_k) = nf\sigma\Delta\Omega yA\lambda(E_k)t(E_k), \quad \dots 3-15$$

where n represents the number of atoms per cm^3 of the particular element, f the flux of X-ray photons on the sample in $\text{cm}^{-2} \text{ s}^{-1}$, σ the photoionization cross-section in cm^{-2} per atom, $\Delta\Omega$ is the acceptance solid angle of the analyser, y is a numeric factor assigned to the efficiency of photoelectric process to yield photoelectrons, A is the probed area of the sample, $\lambda(E_k)$ is the inelastic mean free path, and $t(E_k)$ is the spectrometer transmission function (which are functions of the kinetic energy of the electron, E_k). Two terms which are essential to understanding XPS are the inelastic mean free path and the photoionization cross section.

The inelastic mean free path (IMFP) is defined as the mean distance over which an electron travels before experiencing an energy loss *via* an (inelastic) collision [138]. In fact, for all elements, the IMFP versus the kinetic energy of the photoelectron is closely approximated by a universal curve, shown in [Figure 3.11a](#), with only slight variation between different elements. The IMFP ignores elastic scattering, and typically the electron attenuation length (EAL) – which takes into account elastic scattering – is considered nowadays; adding a small correction factor to the IMFP [138] (elastic scattering *increases* the apparent depth from which the photoelectron emanates).

On the other hand, the photoionization cross section represents the probability of creating a photoemitted electron. The photoionization cross section can vary greatly across atomic species and core level, and is dependent upon the photon energy. A typical graph of the photoionization cross section versus photon energy for the core levels of silicon and carbon is shown in [Figure 3.11b-c](#).

In addition to the core-level peaks, the XPS spectrum will consist of secondary electrons and Auger peaks. These phenomena add intensity to the XPS spectrum. For instance, secondary electrons are created by collisions of the photoelectron with other electrons, and contribute to the background signal of the photoemission spectrum. This signal must be subtracted to correctly fit spectra for qualitative and quantitative analysis. Auger peaks are due to the Auger process, outlined in [Figure 3.10](#). The process in [Figure 3.10](#) is as follows. A core level electron is initially ejected by a suitable energy X-ray, creating a core-hole (in the oxygen ‘K’ shell in this example). This core hole is then filled by an electron from a lower binding energy level (the ‘ $L_{2,3}$ ’ level), bringing the atom into an excited state. Upon de-excitation, a photon (X-ray) can be emitted or, another electron from a lower binding energy (the $L_{2,3}$ level) can be emitted, becoming an Auger electron [135, 138]. Since the Auger process is photon-energy independent (energy is only governed by the difference in shell energies), one needs to take care when tuning the photon energy to ensure core levels and peaks from the Auger process do not overlap.

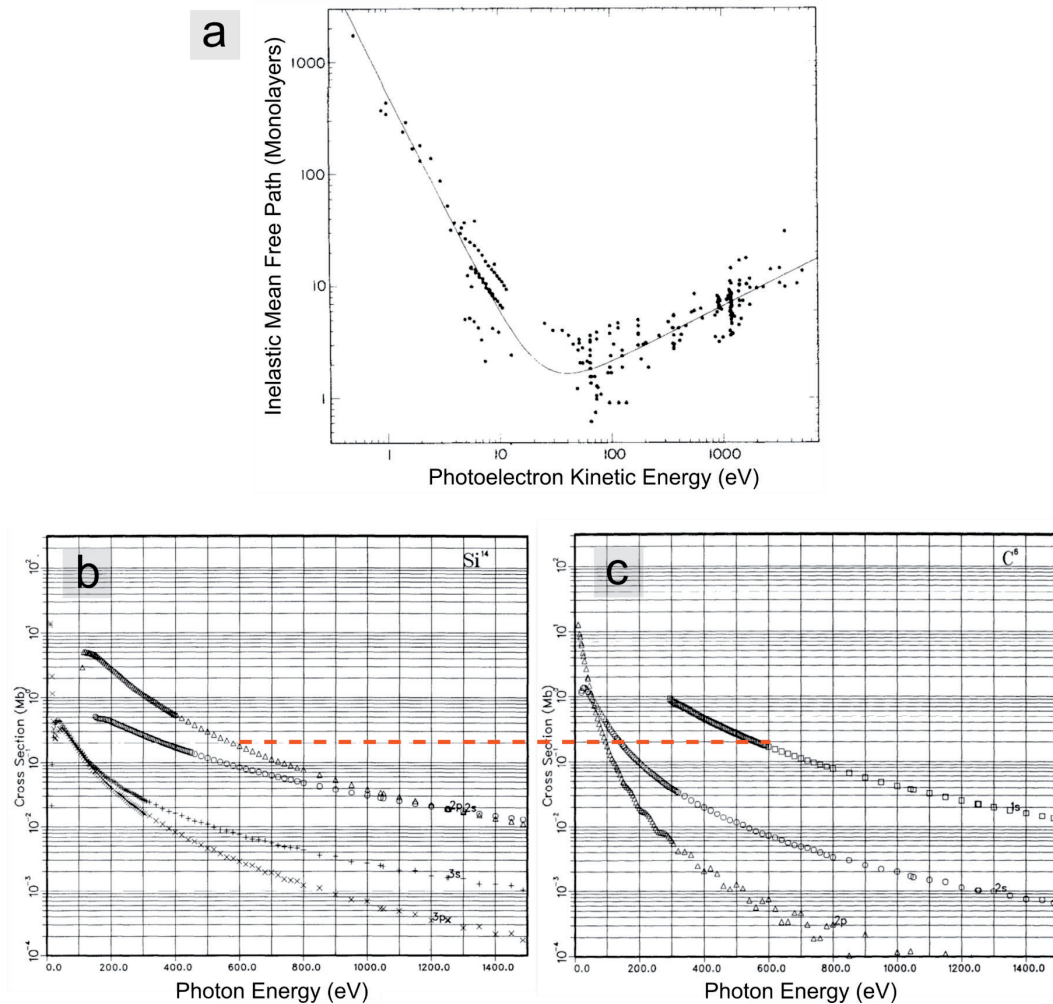


FIGURE 3.11: INELASTIC MEAN FREE PATH (IMFP) AND PHOTOIONIZATION CROSS SECTIONS FOR SILICON AND CARBON.

(a) The IMFP (in units of monolayers) plotted against the kinetic energy of the photoelectrons from various elements. There is a slight variation of the IMFP between different elements, but all follow a universal curve. Reproduced with permission from ref. [142] © 1979 Heyden & Son Ltd. (b) Photoionization cross section of silicon. As the photon energy changes, the photoionization cross section (measured in megabarn on the logarithmic scale) drastically changes. (c) Photoionization cross section of carbon. Red dotted line shows at a photon energy of 600 eV, the photoionization cross section of the C 1s and Si 2p core levels are approximately equivalent. (b-c) Modified and reproduced with permission from ref. [143] © 1985 Elsevier Inc.

3.4.2 Secondary Electron Cut off Photoemission Spectroscopy

In the previous section, it was shown that measurement of the kinetic energy of the photoemitted electron was independent of the sample workfunction. However, it is possible to measure the sample workfunction using photoemission spectroscopy [137, 144]. To make this possible, a bias voltage must be applied to the sample, as shown in Figure 3.12a-b. The reason for this is that electrons that emanate from the sample Fermi level which have just enough energy to overcome the vacuum level (*i.e.* electrons with energy corresponding to the sample workfunction), have zero kinetic energy. These photoelectrons consist of secondary electrons. To accelerate these electrons to the spectrometer, the electrons are given energy *via* the application of a negative voltage to the sample. This overcomes the spectrometer workfunction, and accelerates these electrons to the spectrometer for detection. Thus, the workfunction of the sample can be found at the onset of photoemission (and hence the name secondary electron cut-off), as shown in Figure 3.12c. The sample workfunction can then be calculated as:

$$W_{f,s} = E_{k,min} - |V_b|. \quad \dots 3-16$$

Where $E_{k,min}$ is the minimum energy of detected electrons, called the secondary electron cut-off energy, and V_b is the applied bias voltage. A negative bias voltage applied to the sample shifts $E_{k,min}$ to higher kinetic energies, so as to ensure measurement is possible. The bias voltage used throughout this thesis is $V_b = -9\text{V}$, applied to the sample. $E_{k,min}$ is typically determined *via* the intersection between a linear fit to the steep edge of the cut-off and the background [144]. The workfunction of the detector is typically compensated for (see Equation 3-14), and thus does not need to be subtracted from Equation 3-16. Secondary electron cut-off (SECO) photoemission is typically conducted using photon energies of $\leq 50\text{ eV}$. Since lower photon energies are used, this technique is often called ultraviolet photoemission spectroscopy (UPS). However, synchrotron radiation is tuneable over a range of photon energies and thus, the distinction between XPS and UPS in synchrotron experiments is more blurred as both experiments can be conducted simultaneously [145].

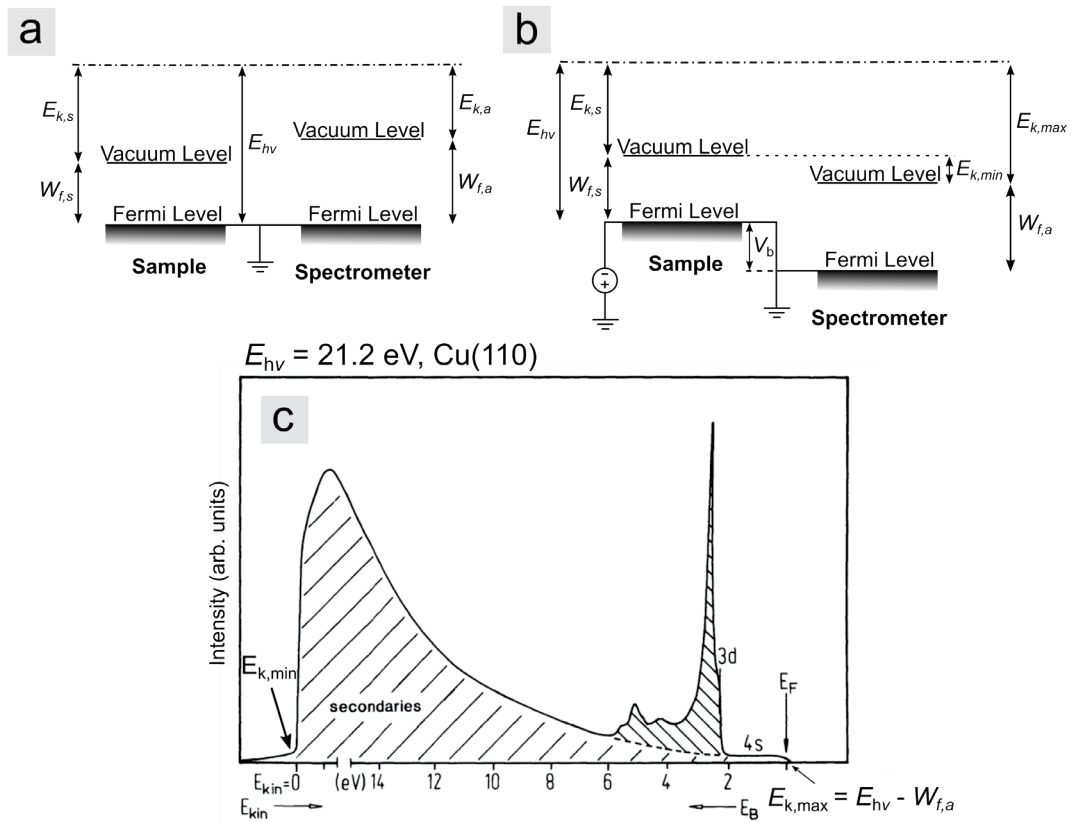


FIGURE 3.12: OVERVIEW OF THE SECONDARY ELECTRON CUT-OFF PHOTOEMISSION PROCESS.

(a) When the sample and the spectrometer Fermi level are kept at the same level, electrons with an energy equal to the workfunction of the sample ($W_{f,s}$) are ejected with a kinetic energy ($E_{k,s}$) of zero, and thus, cannot overcome the spectrometer workfunction ($W_{f,a}$). **(b)** By the application of a suitable negative bias voltage (V_b) to the sample, the zero kinetic energy electrons gain enough energy to overcome the spectrometer workfunction for detection by the spectrometer. Thus, as the kinetic energy of the photoemitted electrons goes to zero, V_b must be increased proportionally in magnitude to overcome the spectrometer workfunction. **(c)** An example of a secondary electron cut-off photoemission spectrum of $\text{Cu}(110)$ using an excitation energy of 21.2 eV. The photoelectrons corresponding to the sample workfunction are at the 'cut-off' (minimum photoelectron kinetic energy) of the photoemission spectrum given by $E_{k,min}$. Typically, this point is below or close to zero, and thus, a negative bias voltage is applied to the sample to shift the spectrum to higher kinetic energies. Modified and reproduced with permission from ref. [146] © 2003 Springer-Verlag Berlin Heidelberg.

3.4.3 Spectral Interpretation

In this section, I will briefly discuss the spectral features that are observed in this thesis. Spectral features for XPS can be split into two broad categories: Initial state effects and final state effects. Furthermore, the background subtraction technique for removal of the signal background (from secondary i.e. inelastically scattered electrons) used in this thesis is elucidated. Finally, the XPS peak fitting methods used in this thesis are outlined.

3.4.3.1 *Initial State Effects*

Initial state effects include spin-orbit splitting and coulombic effects. In the case of spin-orbit splitting, photoelectrons from orbitals with a non-zero angular momentum quantum number (l) and spin ($m_s = \pm 1/2$ for spin ‘up’ and spin ‘down’ electrons) split the photoelectron signal into two distinct peaks, the area ratio of which is defined by the total angular momentum of the electron (J). The situation is illustrated in [Table 3-1](#). [Figure 3.13](#) shows the effects of spin-orbit splitting for the 4f level of gold.

The binding energy of the measured photoelectron is a result of the sum of the attractive forces from the atomic nucleus and the repulsive forces from surrounding electrons [[135](#)]. Each material will have a unique electron bonding environment, and thus, a photoelectron ejected from any core level will have a specific binding energy associated with it. This effect on the photoemitted electron is thus a consequence of a ‘coulombic effect’. The fact that each photoemitted electron will experience a slightly different coulombic environment dependent on its bonding environment is what allows XPS to differentiate unique chemical species. This is clearly demonstrated in [Figure 3.14](#), which shows the Si 2p core level of a silicon carbide sample with surface oxidation. Here, speciation is directly observable since each silicon containing compound is separated by a binding energy which is larger than the uncertainty of the measurement. This distinction is not always possible with a single core level (for example, oxygen containing compounds are difficult to differentiate in the O 1s core level, even at 0.1 eV resolution), and thus it is often the case that all relevant core levels are scanned so as to gain enough information on the chemical composition of a sample.

TABLE 3-1: SPIN-ORBIT SPLITTING FACTORS FOR EACH ORBITAL. REPRODUCED WITH PERMISSION FROM REF. [135] © 2012 JOHN WILEY & SONS.

Orbital	l	m_s	$J (l + m_s)$	Area ratio ($2J + 1$)
p	1	-1/2, +1/2	1/2, 3/2	1:2
d	2	-1/2, +1/2	3/2, 5/2	2:3
f	3	-1/2, +1/2	5/2, 7/2	3:4

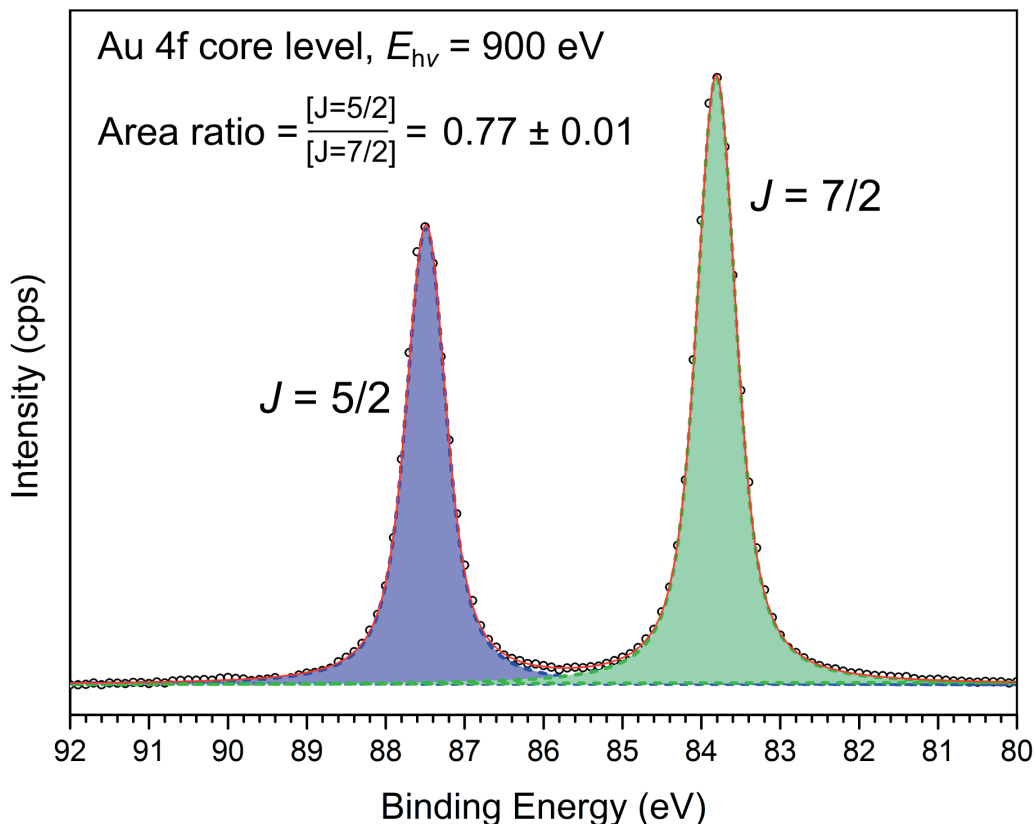


FIGURE 3.13: X-RAY PHOTOEMISSION SPECTROGRAM OF THE Au 4f CORE LEVEL OF SPUTTER ANNEALED GOLD SHOWING SPIN-ORBIT SPLITTING OF $J = 7/2$ (GREEN) AND $J = 5/2$ (BLUE) LEVELS.

A Voigt fit to the data (see [Section 3.4.3.4](#)) shows that the peaks are in an approximate 3:4 ratio, in close agreement with theory (total fit shown by red line).

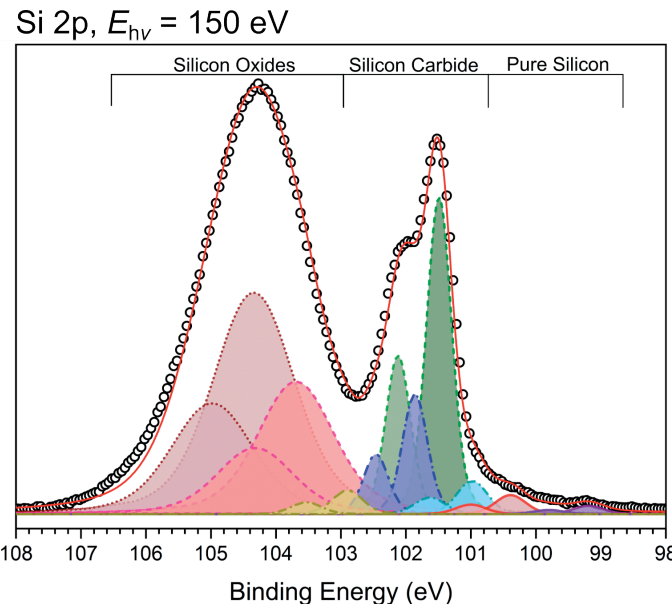


FIGURE 3.14: X-RAY PHOTOEMISSION SPECTRUM SHOWING THE Si 2p CORE LEVEL OF A SiC SAMPLE WITH SURFACE OXIDATION, AT A PHOTON ENERGY OF $E_{hv} = 150$ eV.

The chemical shift between the silicon in the silicon carbide (coloured green and blue) is easily observed from the silicon in the silicon oxide (coloured pink, wine and yellow). Pure silicon on the surface of the SiC appears at lower binding energy. The Si 2p level has spin orbit splitting ($l=1$), so 2 peaks (of the same colour) are fit for each component, separated by ≈ 0.62 eV.

3.4.3.2 Final State Effects

In the following discussion I will ignore multiplet splitting and the Auger parameter, which do not feature in this thesis. Nonetheless, all final state effects are the result of *rearrangement* of electrons due to the formation of a core-hole. These rearrangement processes can be grouped into the following distinct processes [135]:

- (1) Shake-up processes (excitation of valence band electrons).
- (2) Shake-off processes (removal of valence band electrons).
- (3) Plasmon generation (excitation of conduction band electrons).
- (4) Peak asymmetry (formation of electron-hole pairs)

Processes (1) – (3) are often called ‘satellites’ in the literature, and thus, can confuse readers as to which physical phenomenon is taking place. Broadly, ‘satellite’ can refer to any feature in the XPS spectrum that cannot be explained by the simple (i.e. single particle core-hole production) photoemission process [146]. Furthermore, satellite features can also arise from the use of polychromatic light as an excitation source. Although

nowadays, most XPS instruments have monochromators, so that this source of satellite features is not commonly encountered.

(1) Shake-up Processes.

These features occur when the outgoing photoelectron interacts with an outer shell valence electron, imparting some of its energy and exciting a valence band electron in the process. This produces a satellite peak at higher binding energy to the main photoelectron peak, as shown in [Figure 3.13a](#).

(2) Shake-off Processes.

Shake-off processes are related to shake-up processes, but instead of the valence electron being in an excited state, it is ejected and contributes to the background signal intensity. The generic shape of this background is shown in [Figure 3.13b](#).

(3) Plasmon Peaks.

Plasmon peaks can result in XPS spectra when a system is metallic (or has a high density of electron states around the Fermi level). Photoelectron production causes a charge imbalance, either *via* production of the core-hole directly, or indirectly *via* outgoing photoelectrons caused by inelastic collisions [\[146\]](#). Plasmons produced by the core-hole are called intrinsic plasmons, whereas when produced by outgoing photoelectrons are called extrinsic plasmons [\[138, 146\]](#). Nonetheless, in both cases these excitations cause a local change in charge density, and the ensuing physical process can be understood in the following way. In metallic systems, there are enough electrons about the Fermi level that they can move to screen any excess charge caused by the core-hole or inelastically scattering photoelectron. But while electrons in the conduction band move to screen the excess charge, they overshoot their target, forcing them to oscillate about a setpoint (analogous to a mass on a spring) [\[135\]](#). This oscillation frequency is termed the ‘free electron plasmon frequency’ (ω_{pl}) and will occur at specific energy intervals defined as the free electron plasmon energy given by [\[147\]](#):

$$E_{pl} = \hbar\omega_{pl} = \hbar \sqrt{\frac{ne^2}{m_e \epsilon_0}} \quad ...3^{-17}$$

Where n is the number of valence electrons per atom, e is the charge of the electron, m_e is the mass of the electron and ϵ_0 is the permittivity of free space.

[Equation 3-17](#) defines ‘bulk’ plasmons, but for surface plasmons, [Equation 3-17](#) is divided by $\sqrt{2}$ [135, 138]. Surface plasmons are thus closer in binding energy to the main photoelectron peak. An example of plasmon formation in the Mg 2s core level is shown in [Figure 3.15c](#), and shows that plasmon peaks are at higher binding energy to the core level (characteristic of all satellite features, as they have decreased kinetic energy from the main line photoelectron peak), and decrease in intensity for higher harmonics (oscillation modes). The distinction between surface and bulk plasmons is also evident in [Figure 3.15c](#).

(4) Peak Asymmetry

As I have outlined above, production of a core-hole has significant physical implications for electrons surrounding the core-hole. When conduction band electrons move to screen the core-hole, these electrons can form electron-hole pairs [148]. The effect, which is prominent in metallic systems, was first explained by *Mahan* [149], and underwent slight modification by *Andersson* [150]. An exact solution to the problem was then provided by *Nozières* and *De Dominicis* [151]. This subtlety manifests as an asymmetry towards higher binding energy in the XPS intensity for metals, as shown for the Mg 2p core level in [Figure 3.15d](#), and is governed by a power law of the form [148]:

$$I(E_B) \propto \frac{1}{E_B^{1-\alpha}} \quad \dots 3-18$$

Where E_B is the binding energy and α is an asymmetry factor $0 < \alpha < 1$. [Equation 3-18](#) is valid for binding energies greater than the peak maximum, as demonstrated in [Figure 3.15](#). In [Section 3.4.3.4](#), I will show how this peak asymmetry can be incorporated into a function (Donaich-Šunjić) that has been quite successful in predicting the line shape of metals which possess an asymmetric line shape.

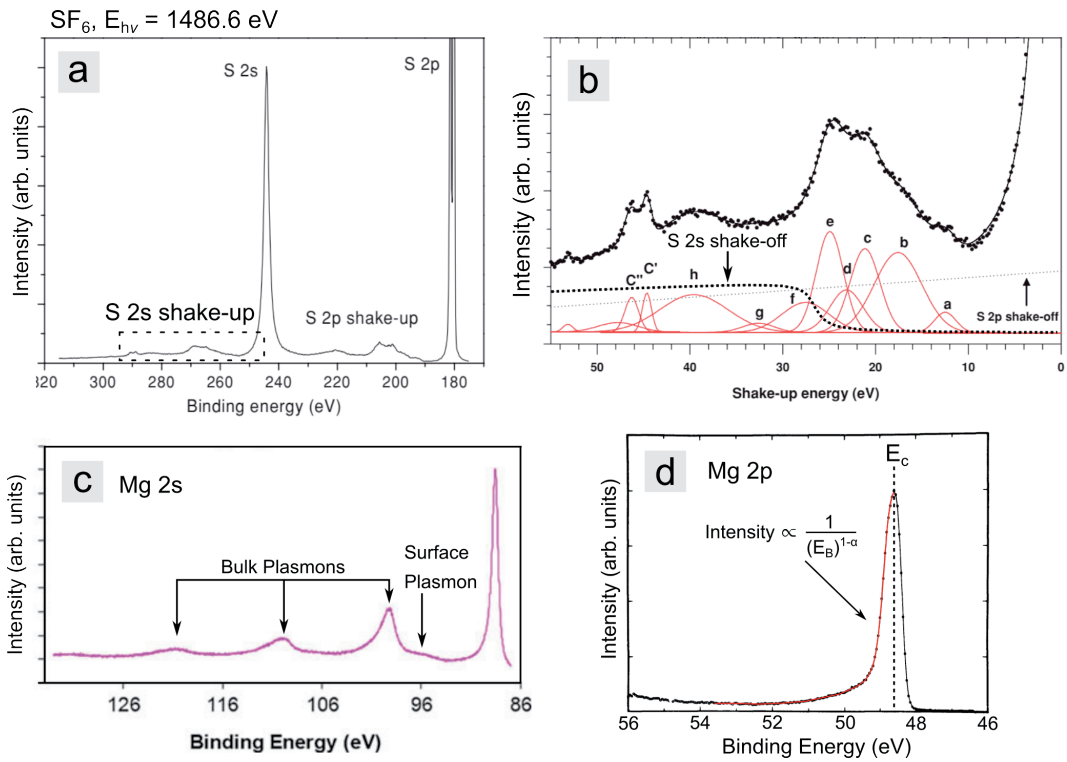


FIGURE 3.15: VISUALISATION OF THE FINAL STATE EFFECTS ON THE X-RAY PHOTOEMISSION SPECTRUM.

(a) The shake-up structure of the S 2s and S 2p core levels of an SF_6 molecule. (b) Magnified view of dotted box in panel a showing shake-off contribution to background. See ref. [152] for symbol meanings. (a-b) Modified and reproduced with permission from ref. [152] © 2009 IOP Publishing (c) Mg 2s core level of metallic magnesium showing surface and bulk plasmons. Surface plasmons are a factor of $\sqrt{2}$ closer to the main photoelectron peak. Reproduced with permission from ref. [138] © 2013 Springer-Verlag Berlin Heidelberg (d) Mg 2p core level of metallic magnesium showing asymmetric peak with $\alpha = 0.13$. The intensity to higher binding energy past the centre of the peak (E_c) is proportional to $1/E_B^{1-\alpha}$. Modified and reproduced with permission from ref. [146] © 2003 Springer-Verlag Berlin Heidelberg.

3.4.3.3 Background Subtraction

Every XPS spectrum will have a significant background signal from inelastically scattered electrons and (to a lesser extent) shake-off photoelectrons (such as the features observed in Figure 3.15b). The most commonly used methods for removing these inelastic contributions are the linear, Shirley [153] and Tougaard background subtraction techniques [138]. The three techniques are summarised in Figure 3.16. In this thesis, I use the Shirley background subtraction method for all spectra (except Ca 2p core levels, which had a significant inelastic contribution, see Chapter 5 Section

5.4.2.3). The Shirley background method is the most commonly used method in the literature [135], likely because of its high accuracy and easy implementation [138]. The Shirley background subtraction process is iterative, and care needs to be taken as to the start and finish energy locations (see ref. [154] for updated and comprehensive review on the Shirley background subtraction method and ref. [138] for general overview of all three techniques).

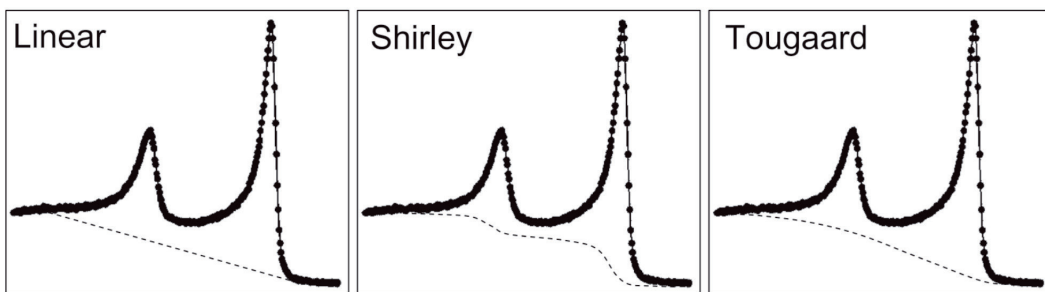


FIGURE 3.16: SUMMARY OF THE COMMON BACKGROUND SUBTRACTION TECHNIQUES. (left to right) The linear subtraction approximates the background using a linear line. The Shirley background subtraction uses an iterative method. The Tougaard subtraction method attempts to calculate the background using a universal loss function. In the above, the background subtraction is given by the dashed line. Reproduced with permission from ref. [135] © 2012 John Wiley & Sons.

3.4.3.4 Peak Fitting

After background subtraction, the XPS spectrum can be fit with a suitable curve. The underlying curve shape of the photoemission process is given by the Lorentzian function, and has a width that is determined by the core-hole lifetime. The so-called natural linewidth energy is then given by [138]:

$$\Delta E_0(eV) = \frac{h}{\tau}, \quad \dots 3-19$$

Where h is Planck's constant and τ is the core-hole lifetime. The natural linewidth is dependent on the core level and atomic number, and increases for inner orbitals and higher atomic number elements [155]. The Lorentzian profile is never observed in practice because many secondary effects broaden the detected photoelectron peak. For instance, the radiation source itself has a small energy spread, and at finite temperatures, vibrations in the material

will cause a broadening of the Lorentzian function. Since the electron analyser also has finite resolution, this will lead to further broadening effects. These effects will contribute to the total energy broadening observed in the experiment, (there are other sources not considered here, see ref. [155]) [135].

These broadening effects can be physically captured *via* convolution of the natural linewidth Lorentzian function with a Gaussian function (Voigt function). All the stated formula in the proceeding discussion describe the peak intensity (y or $f(E_B)$) as a function of binding energy (x or E_B). Most peaks in this thesis are fit using the following Voigt function:

$$y = y_0 + A \frac{2\ln 2}{\pi^{\frac{3}{2}}} \frac{W_L}{W_G^2} \int_{-\infty}^{\infty} \frac{e^{-t^2}}{(\sqrt{\ln 2}) \frac{W_L}{W_G})^2 + ((\sqrt{4\ln 2}) \frac{x - x_c}{W_G} - t)^2} dt \quad ...3-20$$

Where y_0 is the baseline, x_c is the peak centre, A is the area, W_G is the Gaussian full width at half maximum (FWHM, in eV) and W_L is the Lorentzian FWHM (in eV). The Voigt FWHM is calculated as:

$$FWHM = 0.5346W_L + \sqrt{0.2166W_L^2 + W_G^2} \quad ...3-21$$

Generally, fitted Voigt peaks in XPS have approximately a 70 – 90 % Gaussian contribution, and 30 – 10 % Lorentzian contribution (dependent on source, analyser, material and core level, as described above) [135, 155-156].

As was eluded to in [Section 3.4.3.2](#), metallic peaks can have a degree of asymmetry to them, caused by interaction of the core-hole with conduction band electrons. Using the *Mahan, Nozières and De Dominicis* [149, 151] theory, Doniach and Šunjić devised an equation that combined the power law dependence in [Equation 3-18](#) on the high-binding energy side of asymmetric metallic peaks with the inherent Lorentzian function of the core-hole lifetime [148, 157]. The resulting function takes the form [157]:

$$f(E_B) = \frac{\Gamma(1 - \alpha)\cos[\frac{\pi\alpha}{2} + (1 - \alpha)\arctan(\frac{E_B}{\gamma})]}{(E_B^2 - \gamma^2)^{(1-\alpha)/2}} \quad ...3-22$$

Where Γ is the gamma function, α is an asymmetry factor, E_B is the binding energy and γ is the core-hole lifetime width (*i.e.* Lorentzian width). An example of the Donaich-Šunjić (DS) lineshape is shown in [Figure 3.17](#). An interesting consequence of the function is that the DS lineshape diverges, and so it is not integrable. Subsequently, the DS lineshape is often characterised by its asymmetry factor rather than its area [158].

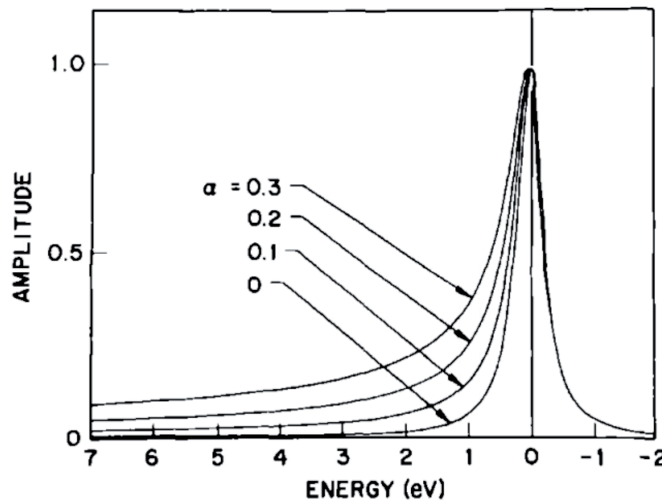


FIGURE 3.17: DONIACH-ŠUNJIĆ LINESHAPE WITH $\gamma = 0.25$ eV.

Increasing the value of α results in a more asymmetric line (hence it is often called the asymmetry parameter). Setting $\alpha = 0$ retrieves the Lorentzian lineshape. Reproduced with permission from ref. [148] © 1978 Springer-Verlag.

In this thesis, I characterise graphene using XPS. Graphene is not quite a semiconductor, yet not a metal either, due to its unique bandstructure (see Chapter 2, Section 2.2). The DS function is a ‘phenomenological’ fit to simple metallic systems, and does not fully capture the lineshape of graphene (since graphene is not a metal). The situation is illustrated in Figure 3.18a, and shows a DS fit of hydrogen intercalated quasi-freestanding graphene on silicon carbide (H-QFSBLG). H-QFSBLG is an instructive sample, as the graphene is almost ‘freestanding’, and has decreased contributions from the buffer layer (see Chapter 2, Section 2.2.2.2 for further information). It was found that the pristine H-QFSBLG graphene peak could not be satisfactorily fit with the DS lineshape at higher binding energy, and so another type of asymmetric lineshape was implemented, which was phenomenologically found to describe the experimental lineshape well. The lineshape is shown in Figure 3.18b, and takes the form of the Breit-Wigner-Fano (BWF) lineshape:

$$y = y_0 + \frac{H \left(1 + \frac{x - x_c}{QW_L}\right)^2}{1 + \left(\frac{x - x_c}{W_L}\right)^2}, \quad \dots 3-23$$

where y_0 is the baseline, x_c is the peak centre, H is the height (counts per second, cps), W_L is the width (in eV) of the Lorentzian contribution and Q is the Asymmetry parameter. As $Q \rightarrow \infty$, the BWF lineshape becomes Lorentzian. This function thus represents an asymmetric transformation of the Lorentzian profile, much like the DS lineshape. The BWF fit yields a much closer fit to the data at higher binding energy, quantified by the regular

residual shown in [Figure 3.18c](#) and [Figure 3.18d](#), respectively. Thus, I use the BWF fit to fit all graphene peaks.

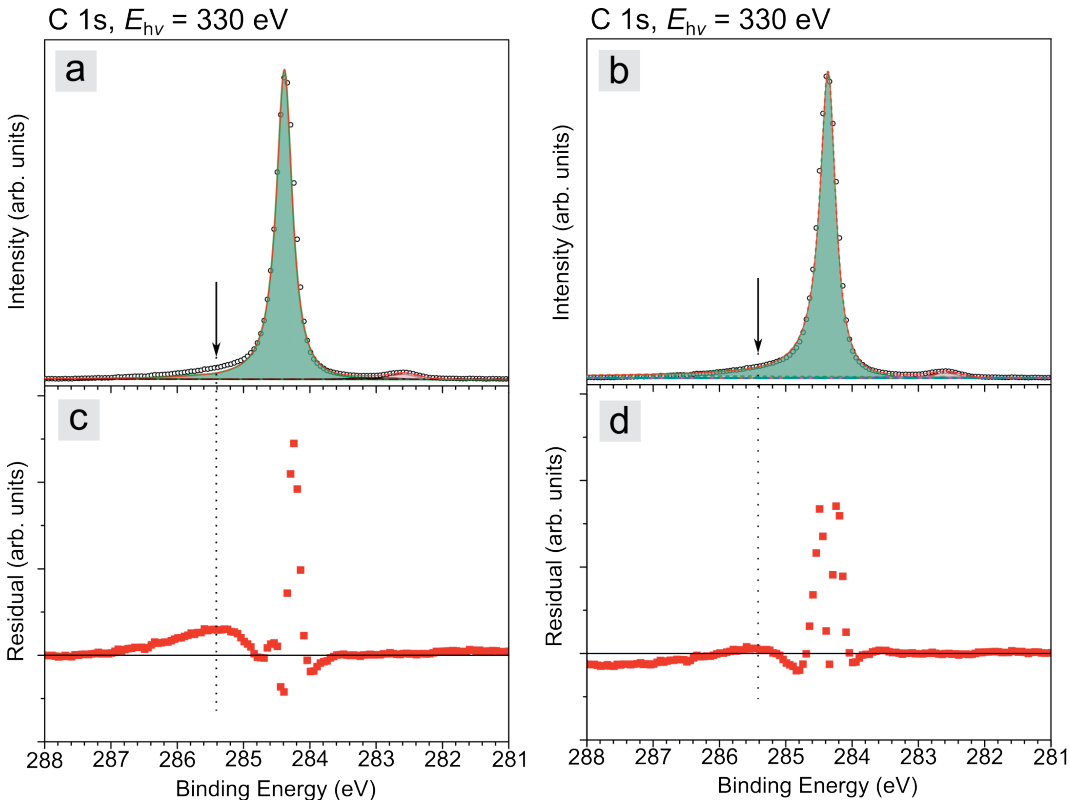


FIGURE 3.18: COMPARISON OF A DONIACH-ŠUNJIĆ (DS) AND BREIT-WIGNER-FANO (BWF) FIT TO THE C 1s CORE LEVEL OF HYDROGEN INTERCALATED GRAPHENE ON SILICON CARBIDE (H-QFSBLG) AT AN X-RAY ENERGY OF $E_{hv} = 330$ eV.

(a) DS fit to C 1s core level of H-QFSBLG. **(b)** BWF fit to C 1s core level of H-QFSBLG. **(c)** Residual between experimental data and DS fit. **(d)** Residual between experimental data and BWF fit. The BWF fit explains more of the high binding energy data, while the DS fit is unable to obtain a good fit at higher binding energy. Residual scales in (c) and (d) have been equalised enabling comparison.

3.4.4 The Advantages of Synchrotron Radiation

In this thesis, I mostly use synchrotron radiation to perform XPS, and the technique features heavily in [Chapter 5](#) and [Chapter 6](#). The Australian Synchrotron soft X-ray beamline has an energy range of $\approx 90 - 2500$ eV [[159](#)], and beam size of $\approx 0.15 \times 0.05$ mm². The main advantages of synchrotron radiation are [[136](#)]:

- (1) Intense Radiation.
- (2) High Energy Resolution.
- (3) Energy Tuneability.

I will discuss each briefly below.

(1) Intense Radiation

The integrated photon flux of the soft X-ray beamline at the Australian Synchrotron is $> 1 \times 10^{11}$ photons s⁻¹ when the storage ring beam current is 200 mA [159]. The increased photon number allows for a higher signal to noise ratio relative to most lab-based systems.

(2) High Energy Resolution

The width of the photoelectron peak is determined by the natural linewidth (given by a Lorentzian curve), electron analyser and the linewidth of the X-rays [136]. Synchrotron sources typically have a smaller X-ray linewidth than laboratory sources, and so can achieve better energy resolution of the photoelectron peak (*i.e.* decreased full width at half maximum). This results in the ability of synchrotron based XPS to monitor small changes in binding energy of approximately $\pm 0.05 - 0.10$ eV, aiding also in peak deconvolution.

(3) Energy Tuneability

The main advantage of synchrotron radiation, especially for 2D materials, lies in its ability to tune the photon energy over a wide range. Being able to change the photon energy, E_{hv} , directly results in altering the kinetic energy of the photoelectrons emitted (see [Equation 3-14](#)). Thus, the depth at which the photoelectron emanates can be altered since the inelastic mean free path (which describes how far the photoelectron can travel before losing its energy – see [Section 3.4](#)) is dependent upon the kinetic energy of the photoelectron. In other words, changing the photon energy changes the depth at which the photoelectron emerges from the sample. This is captured in what is often called the ‘sampling depth’ or ‘information depth’ (ID) of XPS, and is given by [136]:

$$\text{ID} = 3\lambda(E_k) \cos \theta. \quad \dots 3-24$$

Where $\lambda(E_k)$ is the IMFP and θ is the angle between the sample and the analyser (typically set to 0°). The ID is defined as the depth in the sample from where 95 % of the photoelectrons emanate from. The situation is illustrated in [Figure 3.19](#).

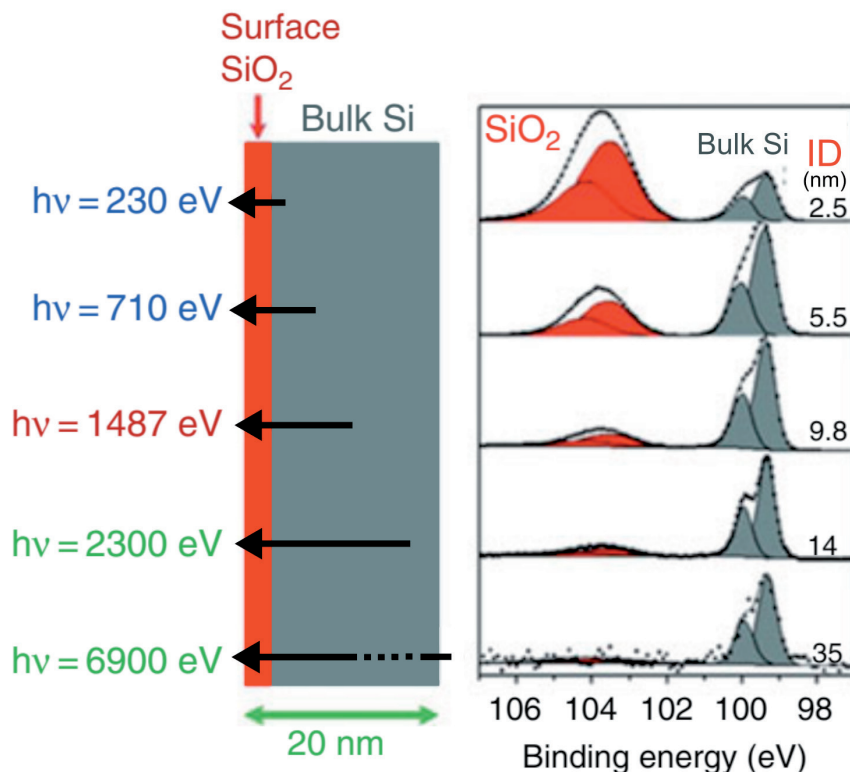


FIGURE 3.19: BEAM ENERGY TUNEABILITY USING A SYNCHROTRON RESULTS IN DEPTH DEPENDENT MEASUREMENTS.

In the above, the beam energy (here given as $h\nu$) is altered for a silicon sample with a thin oxide ($< 2 \text{ nm}$). The information depth (ID, for silicon dioxide) is given on the right in nanometres. As the beam energy is increased, the bulk signal increases with respect to the surface oxide signal. In this way, lower energy photons (hence producing lower kinetic energy photoelectrons with a smaller inelastic mean free path) are more ‘surface sensitive’; whereas higher energy photons (producing higher kinetic energy photoelectrons with a longer inelastic mean free path) are more bulk sensitive. Modified and reproduced with permission from ref. [160] © 2012 American Chemical Society.

In addition to photoelectron kinetic energy changes, the change in photon energy can directly affect the value for the photoionization cross section (see Figure 3.11b-c) since photoionization cross section is dependent on photon energy. This allows one to tune the photon energy to maximise the cross section, thus maximising the signal to noise ratio.

In lab-based sources, surface sensitivity is typically achieved by changing the angle of the sample with respect to the analyser (since only a single X-ray source is usually available), and is thus termed ‘angle resolved XPS’. This causes photoelectrons in the bulk to travel a longer distance to escape the solid, and increases the probability that electrons are scattered in the bulk rather than collected at the analyser, increasing surface sensitivity. Although

this technique is also possible in the setup at the Australian Synchrotron, changing the angle has a detrimental effect on the signal to noise ratio. A more general equation for the photoelectron intensity (I) which considers the angle between the sample normal and analyser is [139]:

$$I \propto \exp\left(-\frac{t}{\lambda_{IMFP} \cos(\theta)}\right). \quad ...3-25$$

Where λ_{IMFP} is the IMFP, t is the thickness of the material layer and θ is the angle between the sample normal and the analyser. Thus, if one changes the angle from $\theta = 0$, there will be a decrease in intensity of the signal, and this is demonstrated in [Figure 3.20](#) for a calcium intercalated epitaxial graphene sample. In the alkaline earth intercalation experiments in [Chapter 5](#) and [Chapter 6](#), the intercalated layer is on the order of a monolayer thick, buried under a bilayer of graphene. This represents an extremely difficult experiment for a lab-based instrument, and the situation is illustrated in [Figure 3.20](#), which shows the same Ca 2p core level from the same Ca-intercalated sample scanned at different angles and photon energies. It is quite apparent that changing the angle to obtain surface sensitive measurements while using a high photon energy (E_{hv}) typical of a lab-based instrument is impossible for such an experiment, as the signal intensity goes to the noise level for $E_{hv} = 1486.6$ eV (a commonly used photon energy for lab-based systems) already at $\theta = 0$.

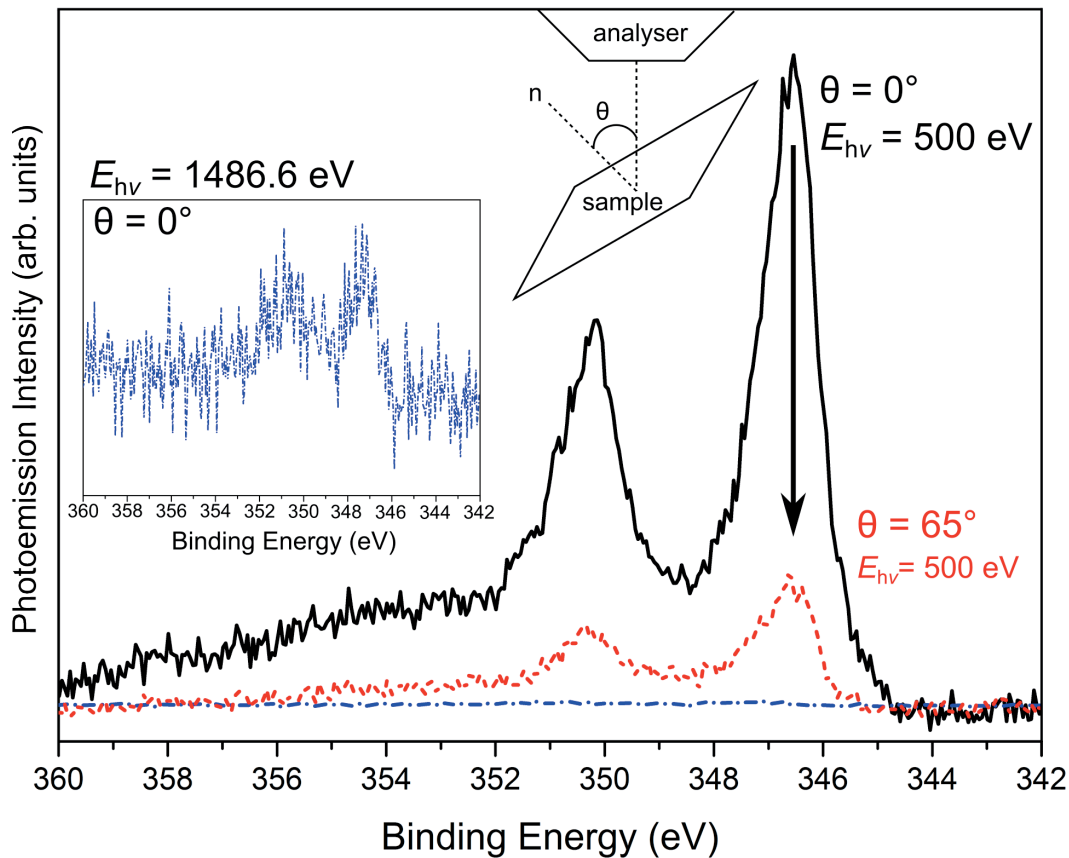


FIGURE 3.20: THE NECESSITY FOR SYNCHROTRON RADIATION IN 2D MATERIALS EXPERIMENTS CONCERNING INTERCALATION.

The above shows the Ca 2p core level of a calcium intercalated epitaxial graphene sample (details to be found in [Chapter 5](#)). Here a calcium silicide layer has been formed that is on the order of a monolayer thickness. The black line (top) shows the results of the sample normal (n) at 0° with respect to the analyser (θ). Upon changing this angle to 65° , the intensity attenuated significantly (middle, red dotted line). The blue dash-dot curve at the bottom (magnified in the inset) is the sample at an angle of 0° , but this time the photon energy (E_{hv}) has been tuned to $E_{hv} = 1486.6$ eV (a similar value to Al K α X-rays used in lab-based instruments). As is visible in the inset, the signal is close to the noise level, and changing θ to increase surface sensitivity would decrease the signal-to-noise even further.

3.5 Low Energy Electron Diffraction

Low energy electron diffraction (LEED) is based on the physics of diffraction and the wave-like nature of the electron, and was pioneered by the experimentalists Davisson, Germer [161], Thomson and Reid [162], and aided by the wave-particle duality theory of de-Broglie [163]. For their efforts, Davisson and Thomson were awarded the 1937 Nobel prize in physics [164], while de-Broglie received the 1929 Nobel prize in physics [165]. The de Broglie wavelength of an electron is given by [166]:

$$\lambda [\text{\AA}] = \sqrt{\frac{150}{E (\text{eV})}} \quad \dots 3.26$$

Where E is the energy of the electron. LEED uses a range of energies from $\approx 30 - 200$ eV in which the electron wavelength is then $\approx 0.9 - 2$ Å. Since the electrons have low energy, their mean free path is on the order a few atomic layers. This makes LEED a surface sensitive technique, providing useful structural information of the surface.

Thus, it is often useful to consider the concept of a 2D lattice to understand the patterns observed by LEED. A 2D crystal needs only 2 lattice vectors to describe its structure (as opposed to 3 lattice vectors for a 3D crystal), and is defined such that at any point \mathbf{r} , the 2D crystal looks the same when viewed at the translated point \mathbf{r}' given by [106]:

$$\mathbf{r}' = \mathbf{r} + n\mathbf{a}_1 + m\mathbf{a}_2 \quad \dots 3.27a$$

Where n, m are integers and \mathbf{a}_1 and \mathbf{a}_2 are the lattice vectors in the real space 2D plane. The surface structure of a crystal can significantly differ from its bulk crystal structure. This is especially the case with adsorbed atoms and molecules on the surface, which form a superstructure that can be described with respect to the base 2D lattice, as will be shown in the following sections.

Nonetheless, LEED diffraction patterns represent the surface structure of a crystal in *reciprocal space*. Any point in 2D real space represented by Equation 3.27a, can be transformed into reciprocal space by [106]:

$$\mathbf{G}_{hk} = h\mathbf{a}_1^* + k\mathbf{a}_2^* . \quad \dots 3.27b$$

Where h, k are integers, and \mathbf{a}_1^* and \mathbf{a}_2^* are now the reciprocal lattice vectors related to the real space lattice vectors \mathbf{a}_1 and \mathbf{a}_2 via [164]:

$$\mathbf{a}_1^* = 2\pi \frac{\mathbf{a}_2 \times \mathbf{n}}{\mathbf{a}_1 \cdot |\mathbf{a}_2 \times \mathbf{n}|}; \quad \mathbf{a}_2^* = 2\pi \frac{\mathbf{n} \times \mathbf{a}_1}{\mathbf{a}_2 \cdot |\mathbf{n} \times \mathbf{a}_1|}. \quad \dots 3.27c$$

Where \mathbf{n} is a unit vector normal to the surface. In transforming from real space to reciprocal space, the underlying symmetry is not altered – *i.e.* a hexagonal lattice will remain hexagonal. Furthermore, [Equation 3.27c](#) requires that the dot product of the vectors $\mathbf{a}_1 \cdot \mathbf{a}_2^* = \mathbf{a}_2 \cdot \mathbf{a}_1^* = 0$, and $\mathbf{a}_1 \cdot \mathbf{a}_1^* = \mathbf{a}_2 \cdot \mathbf{a}_2^* = 2\pi$ [164]. The resultant diffraction pattern observed in LEED is then directly related to the 2D reciprocal lattice *via* the 2D diffraction condition [106]:

$$\mathbf{k}^{\parallel} - \mathbf{k}_0^{\parallel} = \mathbf{G}_{hk} \quad \dots 3.27d$$

Where \mathbf{k}_0^{\parallel} is the incident wavevector parallel to the surface, \mathbf{k}^{\parallel} is the scattered wavevector parallel to the surface and \mathbf{G}_{hk} is the reciprocal lattice vector (since scattering is elastic, $|\mathbf{k}_0| = |\mathbf{k}|$). When this condition is met, then diffraction will be observed. This can be visualised using the Ewald sphere construction, which follows the following rules [166]:

- 1) Each point in the reciprocal lattice is represented by a reciprocal lattice rod, defined by the integers (h, k) .
- 2) The incident wavevector (\mathbf{k}_0) is orientated at the (0,0) origin point defined by the integers (h, k) , and its length is $1/\lambda$, where λ is defined by the wavelength of the incident electron.
- 3) A sphere of radius $\mathbf{k}_0 = 1/\lambda$ is drawn centred on the origin point.
- 4) The diffraction spots are given by the intersection of the Ewald sphere and the reciprocal lattice rods (or similarly the condition in [Equation 3.27d](#)).

The situation is illustrated in [Figure 3.21](#), where it can be seen that the Ewald sphere (bottom) outlines the diffraction spots observed on the LEED screen (top). It should be noted that the Ewald sphere in [Figure 3.21](#) is shown in only one direction on the plane (*i.e.* with only values of $k = 0$), so appears as a 2D circle; but when considering all directions in the plane of the sample, nonzero ' k ' indices would also be intersected by the Ewald sphere. Furthermore, as the energy is increased (wavelength decreased), the Ewald sphere increases in radius, and thus, higher diffraction orders become visible.

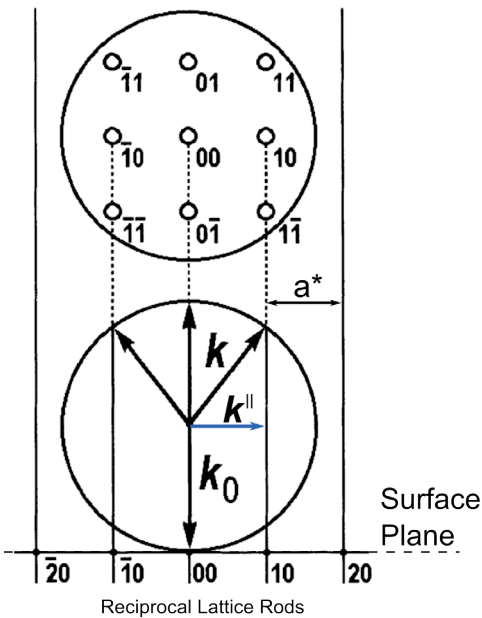


FIGURE 3.21: EWALD SPHERE CONSTRUCTION AND CORRESPONDING LEED DIFFRACTION SPOTS.

(bottom) *Ewald sphere construction for diffraction of a 2D crystal showing incident (\mathbf{k}_0) and scattered (\mathbf{k}) wavevectors. Here, \mathbf{k}_0 is aligned with the (0,0) lattice rod, and thus, has no parallel component to the surface so that $\mathbf{k}^{\parallel} = \mathbf{G}_{hk}$. The lattice rods are spaced according to the reciprocal space vectors.*

(top) *The diffraction spots observed in LEED are defined by the intersection of the reciprocal lattice rods and the Ewald sphere. Since the sphere extends in two dimensions (only one dimension is shown above), the sphere will intersect also at non-zero 'k' indices (i.e. (1,1), (0,1) etc.). Modified and reproduced with permission from ref. [106] © 2003 Springer-Verlag Berlin Heidelberg*

3.5.1 Experimental Setup

A schematic of a basic LEED spectrometer setup is shown in Figure 3.22, and consists of the following major components [106, 166].

- (1) Electron gun. In Figure 3.22, the design is of the Wehnelt-type [167-168], which describes a voltage-biased metallic cap encasing a V-shaped filament (typically W [164]). The Wehnelt can create a virtual source spot which is then further focused by subsequent lenses. The electron gun assembly produces the focused beam of low energy electrons (30 – 200 eV) required in the LEED experiment.
- (2) Sample holder/goniometer. This is a sophisticated sample holder that can rotate the sample 360° in the x-y plane, and can also tilt to orientate the sample surface normal with the electron gun [164].

- (3) Detector. This is typically a hemispherical fluorescent screen which directly translates the diffracted electrons into observable bright spots on the screen. This is achieved by accelerating voltages on a series of grids (dotted lines in Figure 3.22).
- (4) Ultra-high vacuum. UHV is required so that the surface stays clean from surface contamination, since it would take seconds at a moderate vacuum (10^{-6} torr) for the surface to become completely covered with a contamination layer [166]. Furthermore, UHV is necessitated by the fact that the electron gun operates at high temperatures, which would be detrimental for W filaments operating at poorer vacuum. Furthermore, UHV is required to increase the mean free path of the electron in the chamber [166].

The LEED spectrometer at the Australian Synchrotron is from OCI Vacuum Engineering. The displays for these systems consist of silica glass coated with indium tin oxide and P31 phosphor ($ZnS:Ag:Cu$, phosphorescence at 525 nm). The setup is in the *reverse view* arrangement [106], which means that the display/viewport is behind the fluorescent screen (left side of Figure 3.22). The image is acquired with a CCD camera.

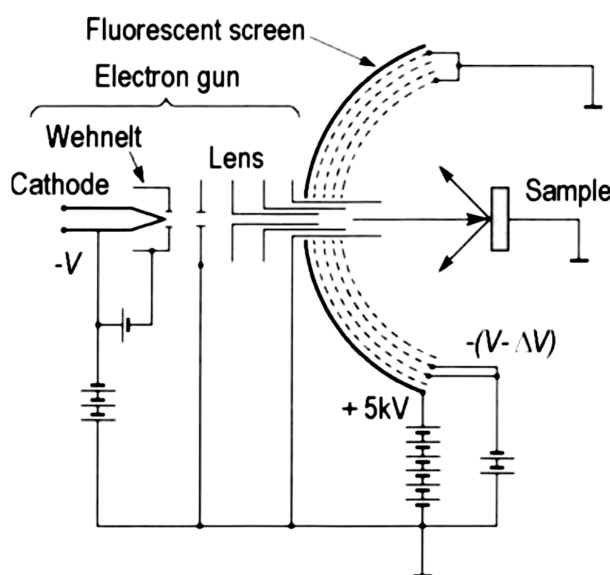


FIGURE 3.22: SCHEMATIC OF A LOW ENERGY ELECTRON DIFFRACTION SET-UP.

The cathode produces low energy electrons which are focussed by the Wehnelt cap (see text) and sent to the sample, mounted perpendicular to the beam with the help of a goniometer. The diffracted electrons are accelerated via 4 grids so that electron impacts on the fluorescent screen light up. Thus, diffraction spots are directly visualised on the fluorescent screen as bright spots. Reproduced with permission from ref. [106] © 2003 Springer-Verlag Berlin Heidelberg.

3.5.2 Interpreting Low Energy Electron Diffraction Spectrograms

The surface structure of the LEED diffraction pattern is often described with respect to the bulk structure using Wood's notation [169]. An example of this notation is shown in Figure 3.23. Figure 3.23a shows a bulk sample with an underlying real space hexagonal lattice symmetry (left). Lattice vectors are shown as \mathbf{a}_1 and \mathbf{a}_2 . The reciprocal space transformation of the real space lattice is shown on the right-hand side. Figure 3.23b shows the effect of an adatom that has re-arranged on the surface of the sample with underlying hexagonal symmetry from Figure 3.23a. In this example, the real space lattice vectors of the adatoms ($\mathbf{b}_1/\mathbf{b}_2$) are $\sqrt{3}$ times larger than the underlying bulk lattice vectors ($\mathbf{a}_1/\mathbf{a}_2$ from Figure 3.23a). Thus, Wood's notation for this structure is $(\sqrt{3} \times \sqrt{3})R30^\circ$, since the adatoms have a 30° rotation with respect to the underlying hexagonal symmetry of the substrate.

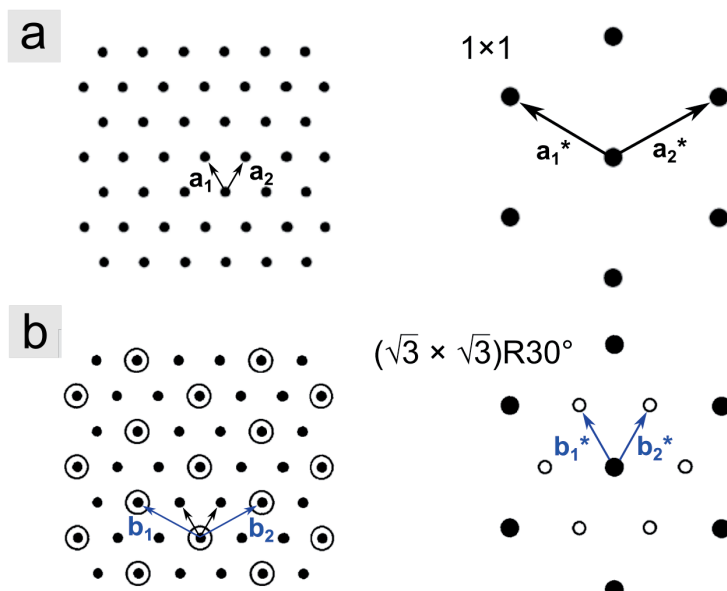


FIGURE 3.23: REAL SPACE HEXAGONAL LATTICE STRUCTURES AND THEIR RECIPROCAL SPACE TRANSFORMATIONS DESCRIBED USING WOOD'S NOTATION.

(a) (left) Real space hexagonal lattice structure showing primitive lattice vectors \mathbf{a}_1 and \mathbf{a}_2 ; (right) the reciprocal space pattern that would be observed using LEED, showing reciprocal lattice vectors \mathbf{a}_1^* and \mathbf{a}_2^* . Wood's notation is 1×1 . **(b)** (left) Real space hexagonal structure (solid) decorated with an adatom (circled). (right) The reciprocal space structure that would be observed using LEED. Wood's notation is $(\sqrt{3} \times \sqrt{3})R30^\circ$, since the unit vector of the adatom structure is symmetrically $\sqrt{3}$ larger and rotated 30° with respect to the bulk unit structure. Modified and reproduced with permission from ref. [106] © 2003 Springer-Verlag Berlin Heidelberg.

In this thesis, I use low energy electron diffraction (LEED) to qualitatively determine the surface structure of pristine and alkaline (calcium and magnesium) intercalated graphene on silicon carbide. LEED spectra complement characterisations by STM, as both can determine surface structure symmetries. A sketch of the generally observed LEED structure of graphene on 4H-SiC(0001) (analogous to the 6H-SiC(0001) surface, as 6H and 4H crystals have the same surface structure, yet different unit cells in the c-axis - see [Chapter 2, Section 2.2.2](#)) is summarised in [Figure 3.24](#). The $(\sqrt{3}\times\sqrt{3})R30^\circ$ spots ($\sqrt{3}$ grid in [Figure 3.24](#)) arise during the heating phase of epitaxial graphene synthesis, which leaves behind a $1/3$ monolayer of silicon adatoms on top of the SiC [170]. The $(6\sqrt{3}\times6\sqrt{3})R30^\circ$ spots ($6\sqrt{3}$ grid in [Figure 3.24](#)) result after formation of the buffer layer, and arises from the different lattice constants of this carbon layer and the SiC [50, 171-172]. The $(6\sqrt{3}\times6\sqrt{3})R30^\circ$ and (6×6) periodicity has also been observed using STM, although the (6×6) periodicity was found to be ‘quasi-periodic’ [172]. Lastly, the (5×5) spots have been observed in LEED and STM [172], although its formation has been shown to be affected by the specific SiC surface preparation procedure employed [172].

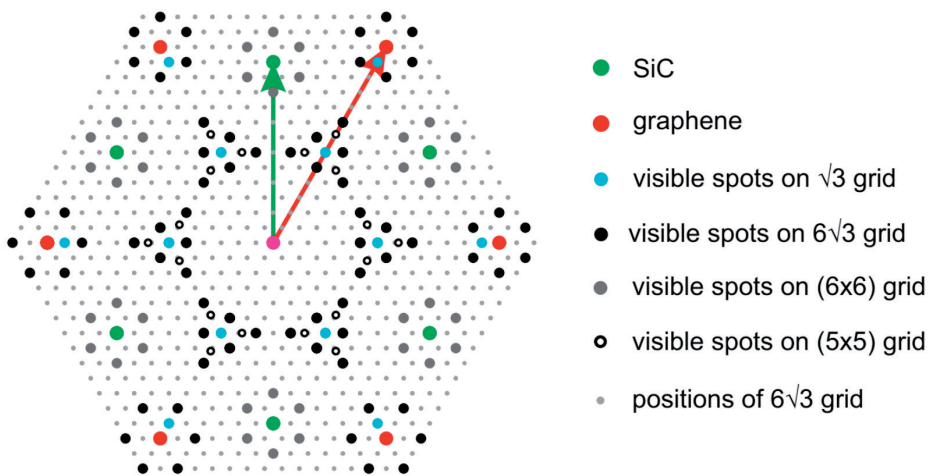


FIGURE 3.24: SKETCH OF THE LEED DIFFRACTION PATTERN OF PRISTINE GRAPHENE ON 4H-SiC(0001).

Shows the various symmetries expected for pristine graphene on 4H-SiC(0001), which is analogous to the diffraction pattern expected for graphene on 6H-SiC(0001) used throughout this thesis. The graphene spots (red) are shown by the reciprocal space vector, which is larger than that of the SiC lattice vector by a factor of 1.25. See text and ref. [60] for explanation of other diffraction spots. Reproduced with permission from ref. [60] © 2010 IOP Publishing Ltd.

3.6 Chemical Vapour Deposition

Chemical vapour deposition (CVD) involves the chemical reaction (in the gas flow and on the substrate) of vapour-phase precursors to form a crystalline thin film on a substrate. In CVD, the key parameters that affect crystalline film growth are the carrier gas type and flow rate, reactant chemistry/concentration/purity, chamber pressure and substrate temperature. Substrate temperature and pressure play a critical role in controlling reaction rate, reaction processes and adsorption/desorption of reactants from the substrate [173]. The basic process can be split up into the following steps [174], shown in [Figure 3.25](#). Here, I will discuss these basic steps in terms of the CVD of WS_2 . For the CVD of WS_2 , the pressure of the tube is assumed to be at ambient pressure (though in reality, it is likely slightly above since carrier gas flow is slightly impeded). Moreover, for the purposes of discussing the basic mechanics of CVD, the carrier gas flow is assumed to be in the laminar regime (though for the simple furnace setup in [Figure 3.26](#) this assumption is incorrect).

- (1) *Transport of the reactants from their source to the substrate.* The reactants for the growth of WS_2 are sulphur and tungsten oxide, and these are heated in the CVD reaction tube to produce S and WO_3 vapour, respectively. Hydrogen gas is introduced into the flow to help reduce the WO_3 , speeding up reaction of W and S. In addition to these gases, argon is used to transport these gases to the substrate (sapphire for WS_2 growths) and, to displace most of the oxygen from the reaction tube (as this would react with the S, WO_x and H_2).
- (2) *Reactions occurring in the gas form prior to deposition on the substrate.* In the case of CVD of WS_2 , the possible reactions are outlined below in [Equation 3.28](#) and [Equation 3.29](#).
- (3) *Diffusion of the reactants through a boundary layer (δ).* For the WS_2 growths, this boundary layer gas is argon. For a non-laminar (turbulent) flow, this boundary layer would likely possess random eddies, vortices, and flow fluctuations; further complicating the diffusion of reactants across this barrier [175].
- (4) *Adsorption of the gas-phase reactants onto the surface of the substrate.* At this point, the reactants might include S, WO_x ($0 < x < 3$) species and WS_2 .
- (5) *Further reaction at the substrate surface.* The S and WO_x reacts further to produce WS_2 .

- (6) *Desorption of reactants.* This process is pressure and temperature dependent, and desorption increases with increasing temperature. The goal of CVD is to have adsorption significantly outweigh desorption of reactants, so that solid material grows on the surface.
- (7) *Exit of reactants.* Once reactants are desorbed, they are carried away by the carrier gas, which in this case is Ar.

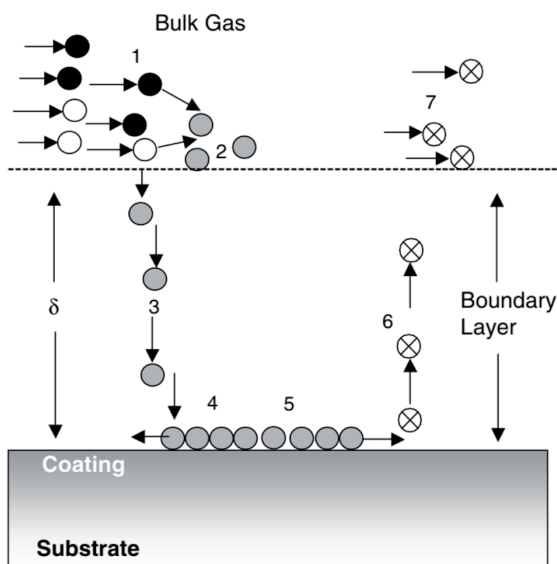


FIGURE 3.25: GENERAL SCHEMATIC OVERVIEW OF THE CHEMICAL VAPOUR DEPOSITION (CVD) PROCESS.

Steps 1-7 are outlined in the main text. Reproduced with permission from ref. [174] © 2001 ASM International.

3.6.1 Chemical Vapour Deposition Growth of Tungsten Disulphide

In this thesis, I use a Lindburg/Blue HTF55122A single zone tube furnace (see Figure 3.26) to grow monolayers of WS₂ on one-side polished c-sapphire (i.e. C-axis, Al₂O₃(0001) [176]) substrates via CVD. Hydrogen (99.999 %) and argon (99.9995 %) gas are flowed between 5-10 standard cubic centimetres per minute, (sccm, mass flow rate) and 200 sccm, respectively, and sulphur (\geq 99.5 %) and tungsten oxide (\geq 99.9 %) powder are heated (200 °C and \approx 900 °C, respectively) so that there is appreciable sublimation. The sulphur is heated via external heating coils, and not in the furnace itself (see Chapter 4, Section 4.3.1). The chemical reactions occurring in the WS₂ CVD process can be summarised as follows [177]:



[Equation 3.28](#) describes the reduction of WO_3 with S, whereas [Equation 3.29](#) describes the reduction of WO_3 with H_2 . Both of these reactions are thought to occur during the synthesis of WS_2 [177].



FIGURE 3.26: THE LINDBURG/BLUE HTF55122A SINGLE-ZONE TUBE FURNACE IN THE FUHRER LABORATORY.

3.7 Raman and Photoluminescence Spectroscopy

When light impinges on matter it can be absorbed, scattered, and/or transmitted. When the energy of the light corresponds to the difference in energy levels between the ground state and excited state of a molecule or atom, an electron can be shifted to this excited state. Upon de-excitation of the electron, the molecule may emit a photon. This process is called photoluminescence (PL). The energy and intensity of this emitted photon can

be measured using photoluminescence spectroscopy. On the other hand, inelastically scattered light results in relatively much smaller energy shifts of the interacting photon. The measurement of the intensity and energy location of these photon shifts is called Raman spectroscopy. Both processes will be described in more detail below.

The experimental setup of a PL or Raman spectrometer is very similar, and is shown in the schematic of Figure 3.27 (micro-Raman/PL systems simply incorporate focusing optics). Generally, PL processes are at higher energy than Raman processes, and so different optical elements (filters, gratings) and lasers may be necessary to conduct both types of measurements for any given sample. In the case of graphene and WS₂, both Raman and PL measurements (respectively) can be carried out on the same tool. When a piezo scanner is incorporated, the system can build up a Raman or PL map (2D picture) of the surface. In this case, the technique is called micro-Raman/PL mapping. In the following sections, I will review both Raman and PL spectroscopy, focusing on how it is applied to graphene and WS₂ systems, respectively.

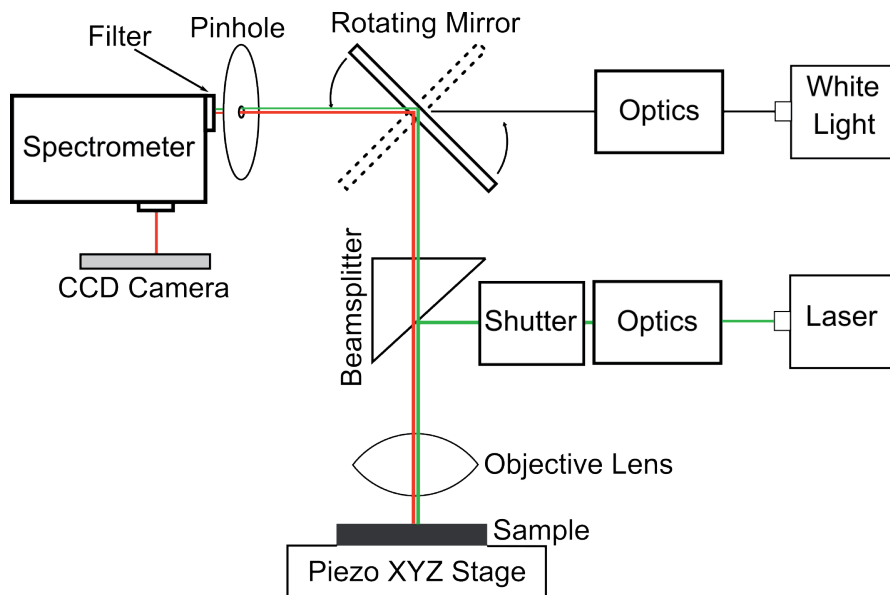


FIGURE 3.27: SCHEMATIC OF A CONFOCAL MICRO-RAMAN/MICRO-PHOTOLUMINESCENCE (MAPPING) SPECTROMETER.

3.7.1 Raman Spectroscopy

The inelastic scattering of light (*i.e.* photon energy is not conserved, as opposed to Rayleigh/elastic scattering) by molecular vibrations was first observed experimentally by Raman and Krishnan in 1928 [178], and led to

Raman receiving 1930 Nobel Prize in physics [179]. The inelastic scattering of photons by phonons is thus called Raman scattering, and the process of detecting the intensity of these scattered photons as a function of energy is called Raman spectroscopy.

In the Raman scattering process, incoming photons interact with the electron cloud of the material while the nucleus is simultaneously in motion (the requirement for this motion is why Raman spectroscopy is often called ‘vibrational’ spectroscopy). In comparison to Rayleigh scattering, this process occurs every 1 in 10^6 to 10^8 photons [180]. The combined effect is that the vibrational modes (phonons) of the nucleus/atom/molecule can impart a net increase (anti-Stokes) or net decrease (Stokes) in energy to the scattered photon [180]. More specifically, there are three general processes that occur for Raman scattering, the interaction of which is mediated by electrons (since they remain unchanged after the process) [179]:

- 1) The photon excites an electron-hole pair to a ‘virtual’ state.
- 2) The electron-hole pair is scattered to another (allowed) state by absorbing or emitting a phonon *via* the electron-phonon interaction.
- 3) The electron-hole pair recombines radiatively, emitting a photon with energy changed relative to the interaction with the phonon.

If the system is in the ground state and is excited to a higher energy vibrational state, the electron-hole energy will be decreased equal to the phonon energy, causing subsequent emission of a lower energy photon. This is the Stokes process. Conversely, if the system is already in an excited vibrational state, the electron-hole can interact with the vibrational state so as to de-excite back to the ground state, causing the electron-hole pair to gain energy by an amount equal to the phonon energy and subsequently emit a photon with higher energy. This is the anti-Stokes process. The situation is illustrated in [Figure 3.28a](#), and compares the Stokes and anti-Stokes regimes with Rayleigh scattering. The Stokes process is more probable [179], and thus, most Raman spectroscopy results in literature (and this thesis) are presented in the Stokes regime, and the energy shifts of the photons are typically given in *wavenumbers* (cm^{-1}).

3.7.1.1 Raman Spectroscopy of Graphene

There is another Raman process that is important for graphene, due to its special bandstructure. In [Chapter 2, Section 2.2.1](#) I showed that the bandstructure of monolayer graphene does not possess a bandgap, thus, when light of *any* wavelength is incident upon graphene, it can cause inter-band transitions to occur to well defined excited states (*i.e.* the virtual state in [Figure 3.28a](#) is no longer involved). This has the effect of greatly increasing the Raman intensity, and is called *resonant* Raman spectroscopy [179, 181].

This is illustrated in the cartoon of Figure 3.28a. For monolayer graphene, the only active Raman mode is the E_{2g} mode. The A_{1g} mode is called the ‘breathing mode’ and is activated when there is a structural defect [182]. The various Raman modes of graphene are shown in Figure 3.28b-c.

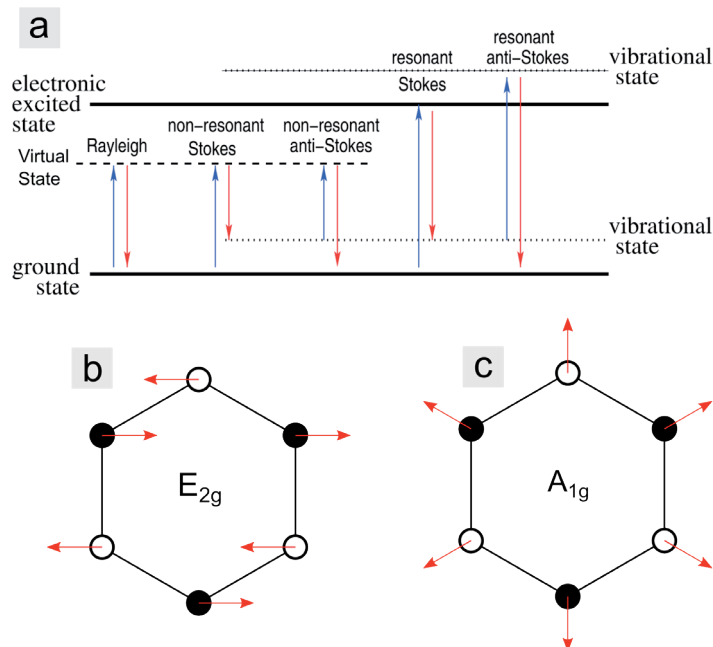


FIGURE 3.28: THE RAMAN PROCESS AND ACTIVE RAMAN MODES IN GRAPHENE.

(a) Overview of all photon scattering processes that can occur for monolayer graphene (see text for details). Blue (up arrow) = excitation, Red (down arrow) = de-excitation Modified and reproduced with permission from ref. [181] © 2013 Macmillan Publishers Ltd. (b) The E_{2g} Raman mode, (c) the A_{1g} ‘breathing’ Raman mode.

A typical Raman spectrum for pristine and defected graphene is shown in Figure 3.29a-b, and shows various peaks associated with the Raman modes discussed thus far. For instance, the G peak is associated with the E_{2g} mode, whereas the D peak is associated with the A_{1g} mode [181-183]. Figure 3.29c shows the steps of the Raman processes corresponding to the G, D and 2D peaks shown in Figure 3.29c. The G peak (located at $\approx 1582 \text{ cm}^{-1}$ for graphene [184-185]) corresponds to a one-phonon mode (1st order scattering), and can be resonant or non-resonant (the non-resonant transition is shown in Figure 3.29c) [181, 184]. The condition for 1st order scattering processes is that the phonon wavevector, $\mathbf{q} \approx 0$ near the Γ -point [179]. On the other hand, the D ($\approx 1350 \text{ cm}^{-1}$ at 2.41 eV excitation [185]) and 2D peak ($\approx 2700 \text{ cm}^{-1}$ at 2.41 eV [185]) peaks result from 2nd order processes, and involve 2 phonons. The fundamental Raman selection rule ($\mathbf{q} = 0$) can be satisfied for equal and opposite phonon wavevectors, $\mathbf{q}_1 = -\mathbf{q}_2$ [179]. In this case, a phonon can be

emitted by the electron and hole, as is shown in [Figure 3.29c](#), or by the electron or hole itself [181]. It should be noted here that the 2D and D processes are *dispersive*, and their Raman shift changes depending on the laser excitation energy [185].

Raman spectroscopy is utilised in this thesis to determine whether defects are present (D peak in [Figure 3.29a](#)) and how many graphene layers are present (full width half maximum of the ‘2D’ peak in [Figure 3.29b](#)). More specifically, this is conducted over large (10’s of μm^2) areas of the graphene sample using a Thermo Scientific DXRxi Raman confocal imaging microscope with laser wavelength of 532 nm and resolution of ≈ 500 nm.

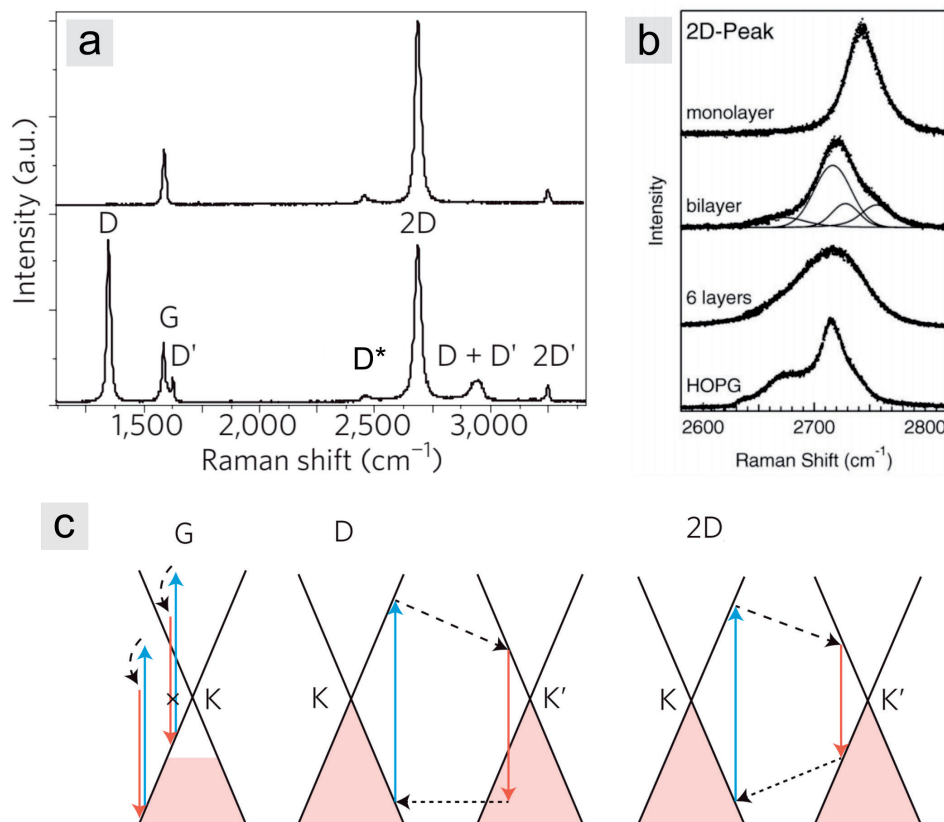


FIGURE 3.29: A TYPICAL RAMAN SPECTRUM AND OVERVIEW OF SOME OF THE RAMAN PROCESSES OF GRAPHENE.

(a) (Top panel) Raman spectrum of pristine monolayer graphene. (Bottom panel) Defected monolayer graphene. Raman spectroscopy can quickly determine if (and by how much) graphene is defected. Reprinted with permission from ref. [181] © 2013 Macmillan Publishers Limited. **(b)** The ‘2D’ peak of monolayer, bilayer, 6-layer (graphene on SiC) and highly orientated pyrolytic graphite (HOPG). As layer number increases, the full width at half maximum of the 2D peak increases. Reprinted with permission from ref. [186] © 2008 American Institute of Physics. **(c)** Some of the major Raman processes of graphene, (see text for details). Reprinted with permission from ref. [181] © 2013 Macmillan Publishers Limited.

3.7.2 Photoluminescence Spectroscopy

In contrast to Raman spectroscopy, the photons in a PL process are absorbed and later *emitted* (at lower energy), as opposed to scattered. The difference in energy between absorbed and emitted photons is called the *Stokes shift* (as in Raman). The PL process consists of 3 main stages [179, 187], which are summarised in Figure 3.30:

- (1) **Absorption/Excitation:** The material absorbs a photon with energy higher than the bandgap of the material causing electrons in the ground state (valence band, VB) to be excited to the conduction band (CB). Excited electrons leave behind a hole.
- (2) **Relaxation/Thermalisation:** The excited electron non-radiatively de-excites to the lowest excited state (bottom of conduction band) and interacts with a hole forming an exciton, bound by coulombic forces.
- (3) **Radiative Recombination:** The electron de-excites by emission of a photon, approximately equal to the band gap (minus the binding energy of the exciton [179]) and recombines with the hole.

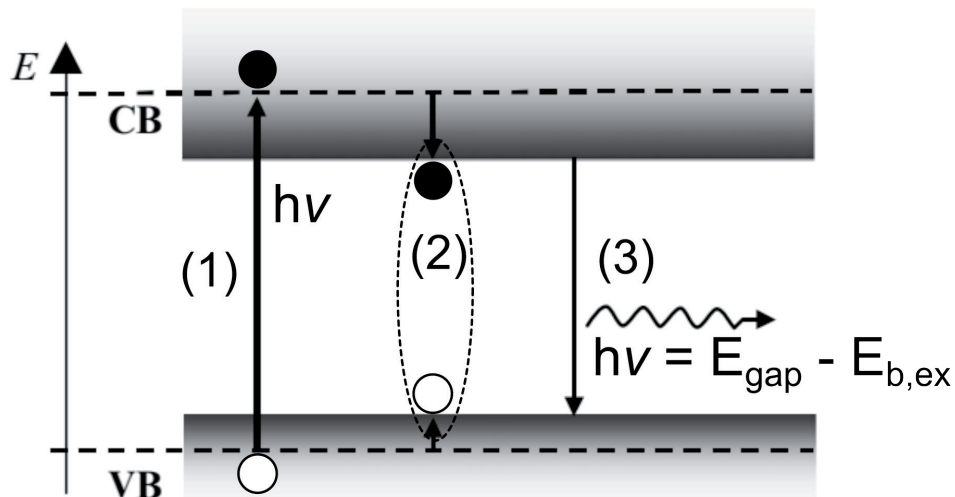


FIGURE 3.30: THE PHOTOLUMINESCENCE (PL) PROCESS.

(1) Absorption/excitation. A photon with energy $E = h\nu$ is absorbed creating electrons (black) and holes (white) in the conduction band (CB) and valence band (VB), respectively. **(2) Relaxation.** Electron and hole interact via coulombic forces to form a bound exciton. **(3) Radiative recombination.** A photon ($h\nu$) is emitted with an energy equal to the band gap energy (E_{gap}) minus the energy of the exciton binding energy ($E_{b,\text{ex}}$). Modified and reproduced with permission from ref. [187] © 2012 Springer-Verlag Berlin Heidelberg.

3.7.2.1 Photoluminescent Spectroscopy of WS₂

The motion of the exciton has similarities to the dynamics of the hydrogen model for an electron and proton. Thus, the excitons exist in bound states given by the principle quantum number $n = 1, 2, 3$ etc. [179] and can be visualised for WS₂ as in Figure 3.31 (showing only $n = 1$). For strong electron-hole interactions with binding energies of 0.1 – 1 eV [88], the excitons are called Frenkel excitons [179]. Whereas excitons with smaller binding energies on the order of 0.01 eV [88] are called Wannier-Mott excitons [179]. For a 2D material, the hydrogenic model predicts an exciton binding energy of [188]:

$$E_{b,ex}(n) = \frac{\mu e^4}{2\hbar^2 \varepsilon^2 (n - \frac{1}{2})^2} \quad \dots 3-30$$

Where $\mu = 1/(m_e^{-1} + m_h^{-1})$ is the reduced exciton mass, m_e is the electron mass, m_h is the hole mass, e is the elementary charge, ε is the dielectric constant of the WS₂ and n is the principle quantum number. Upon analysis of Equation 3-30, for monolayer WS₂ and 2D materials in general, the dimensionality increases the binding energy by a factor of 4 over 3D materials. Furthermore, the dielectric screening is reduced as a direct consequence of the 2D nature of the material (field lines extend outside the material), and thus, results in a large binding energy. Experiments have shown that the exciton binding energy for WS₂ is 0.32 ± 0.04 eV [188], which is much larger than conventional semiconductor materials such as GaAs, which has an exciton binding energy of ≈ 0.010 eV [88]. The small dielectric constant and effective mass yields a relatively large Bohr radius (Bohr radius is $\propto \varepsilon/\mu$), and so excitons in WS₂ have both Wannier and Frenkel exciton properties [88]. Furthermore, the binding energy of WS₂ trions (charged exciton, consisting of two electrons and a hole bound by coulombic forces) is an order of magnitude smaller than the exciton binding energy, which is typically around 0.030 eV for S-TMDs [189-190]. The binding energy of trions in S-TMDs is higher than the thermal energy, $k_B T$ at 300 K (0.0257 eV), and so both excitons and trions are stable at room temperature, which is not the case with II-VI and III-V semiconductor wells [191-192]. Thus, one expects to find both excitons and trions in the PL spectrum of WS₂ at room temperature (indeed this is the case – see below).

A typical PL spectrum of WS₂ across a range of temperatures is shown below in Figure 3.31b. As can be seen, at low temperatures, there exist a variety of emission processes. The L₁, L₂ and L₃ have been extensively reported on in the literature (see ref. [193] for review), and have been attributed to the recombination of localised excitons complexes from crystal defects or impurities, but could also be due to normally ‘dark’ transitions [193].

Nonetheless, since all PL measurements are conducted at room temperature in this thesis, only the spectrum at 280 K is relevant to the discussion here. Thus, the most important excitations at room temperature are the neutral exciton, X_A (electron-hole system shown in the schematic of Figure 3.29) and the charged exciton, or ‘trion’, T^S+T^T (here, T^S refers to the singlet trion, and T^T refers to the triplet trion). In WS_2 , the trion is negative due to an excess of electrons in a concentration of approximately $\approx 5 \times 10^{12} \text{ cm}^{-2}$ [194] (typical of CVD-grown WS_2 due to sulphur vacancies [195-196]). Thus, the singlet state refers to a spin up and down electron in the same valley (K-point in the Brillouin zone), whereas the triplet state refers to a spin up electron in one valley (K) and spin up electron in another (K'). Trions were first observed in II-VI and III-V quantum wells [191-192], and have been confirmed to occur in S-TMDs [189, 197-200], as shown in Figure 3.30b. Thus, it is expected that PL measurements on the CVD grown WS_2 investigated in this thesis will yield both quasiparticles.

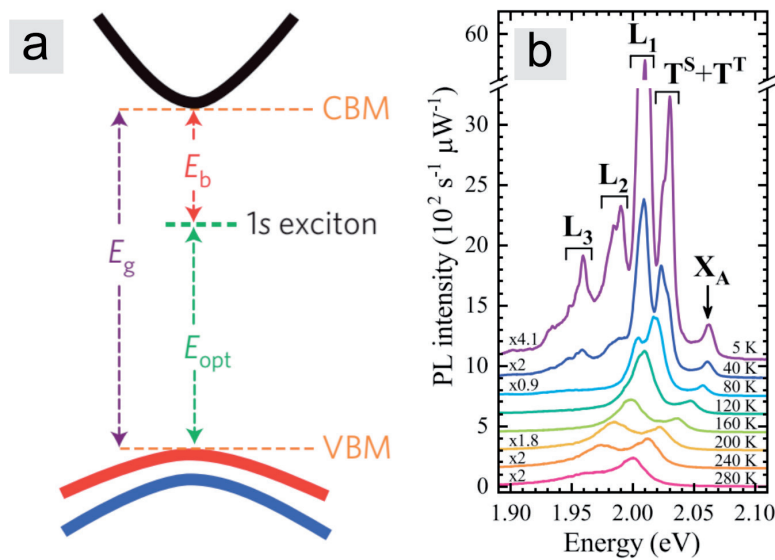


FIGURE 3.31: EXCITON STRUCTURE AND CORRESPONDING PHOTOLUMINESCENCE SPECTROSCOPY IN WS_2 .

(a) Hydrogen model for WS_2 showing $1s$ exciton level which corresponds to the exciton measured in this thesis. Reproduced with permission from ref. [201] © 2014 Macmillan Publishers. **(b)** Exciton structure of WS_2 at low temperatures mapped to ambient temperatures showing the evolution of the neutral exciton (X_A) and trions ($T^S + T^T$). See text and ref. [202] for component descriptions. Reproduced with permission from ref. [202] © 2018 IOP Publishing.

3.8 Laser Scanning Confocal Microscopy

The scanning confocal microscope was invented by Minsky circa 1955 [203]. After invention of the laser in 1960 [204], lasers were eventually incorporated into scanning confocal microscopes, and hence called laser scanning confocal microscopes (LSCM). The basic working principle of the LSCM is that a laser raster scans the imaging field point-by-point, and collates these points together *via* a pinhole aperture to form an image [205]. In this thesis, I use an OLS4100 and Keyence VK-X200 LSCM. Although slightly different, both share the same major components and functionalities. The unique components of the LSCM which sets it apart from a traditional light microscope include a solid state laser (405 nm in the OLS4100, 408 nm in the VK-X200), controllable mirrors to scan in the x-y direction (in the case of the OLS4100, this is a galvanic mirror and microelectronic mechanical MEM mirror), and confocal optics (a pinhole). A schematic of a typical LSCM is shown in [Figure 3.32](#).

The LSCM has a much greater resolution and contrast than traditional white light microscopes. The lateral (XY) resolution in traditional light microscopes is usually given by the Rayleigh criterion [205]:

$$XY_{min} \cong 0.6 \frac{\lambda}{NA_{obj}} \quad ...3-31$$

Where NA_{obj} is the numerical aperture of the objective lens (typically 0.95) and λ is the wavelength of light. However, the situation with a confocal microscope is different – the Rayleigh criterion can be minimised if the *field of view* is decreased (which results in a faster decaying Bessel function) [206]. The resolution limit of the LSCM is then [205]:

$$XY_{min} \cong 0.4 \frac{\lambda}{NA_{obj}} \quad ...3-32$$

The wavelength of the OLS4100 and VK-X200 is ≈ 400 nm, giving a lateral resolution of ≈ 170 nm using [Equation 3-32](#). The lateral resolution from the manufacturer is given as ≈ 120 nm for the OLS4100, whereas it is ≈ 130 nm for the VK-X200, and thus, [Equation 3-32](#) gives an estimate of the lateral resolution for these instruments.

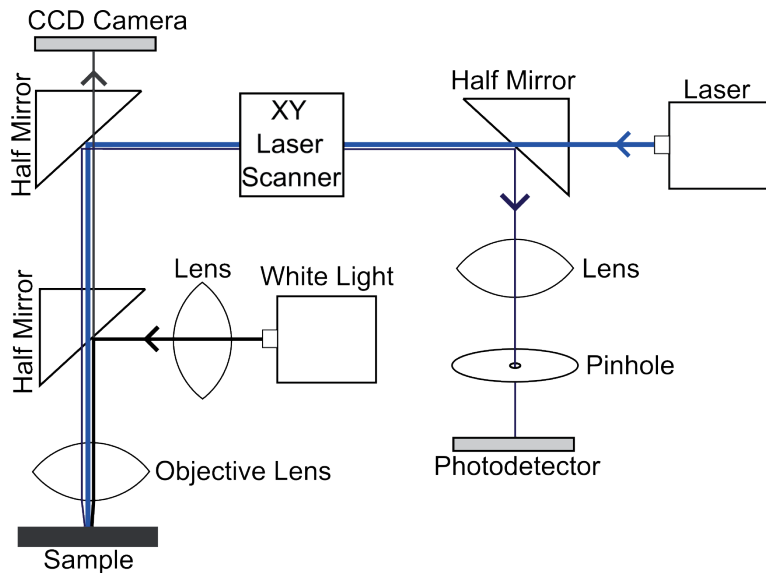


FIGURE 3.32: SCHEMATIC OF A LASER SCANNING CONFOCAL MICROSCOPE (LSCM).

Simplified setup of an LSCM showing the major internal components. The blue laser is raster scanned over the sample by the XY laser scanners. The reflected laser light from the sample is directed to a pinhole which can reject light not in the focal plane of the objective lens. LSCM's also generally incorporate a standard white light microscope, which can be turned off when the laser is in operation.

But there is another consideration apart from the spatial resolution. The images from the LSCM may also be enhanced in comparison to those from a conventional light microscope because of their superior contrast. The pinhole of a LSCM system reduces the amount of scattered light, and thus improves optical visibility of the scanned object. This can aid greatly in the case of defect detection. This is especially the case for materials such as WS₂ in which the optical absorption/transmission properties of the oxide are very different to the optical absorption and transmission properties of the pristine material. Figure 3.33a shows an example oxidised WS₂, where the oxidised regions (black) can easily be distinguished from pristine WS₂ (grey) regions (the sapphire substrate is also black). The contrast arises from the differences in transparency of the materials; tungsten oxide and aluminium oxide are more transparent to 405 nm light than WS₂. Figure 3.33b shows a magnified region of Figure 3.33a, where oxidation spots at the resolution limit of the LSCM are observed (circled in red).

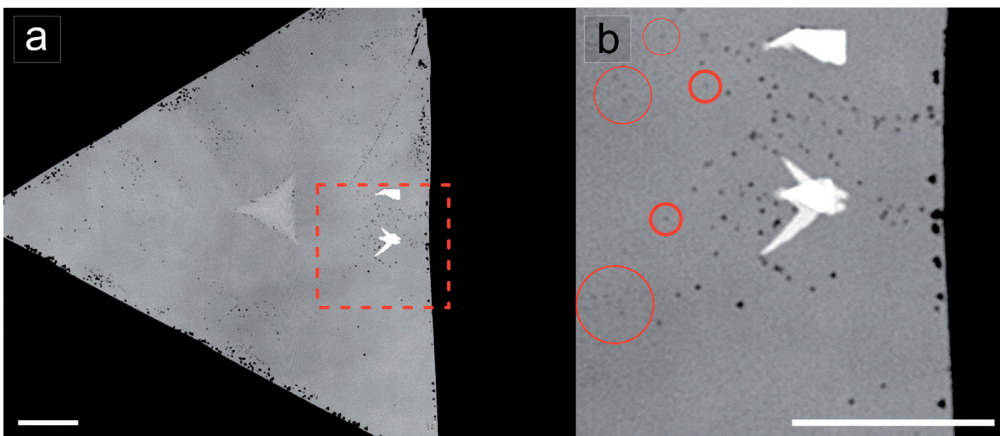


FIGURE 3.33: LASER SCANNING CONFOCAL MICROSCOPE (LSCM) MICROGRAPH OF MONOLAYER WS₂ SHOWING CONTRAST ENHANCEMENT.

(a) Oxidised WS₂ shown as small black spots (some large enough to be resolved as triangular oxidation islands). (b) Magnified region in (a) showing oxidised regions that are at the resolution limit of the microscope (small red circles), and some features which seem to be beyond the resolution capabilities of the microscope (larger red circles). These features are visible (yet not very well resolved) due to their enhanced contrast. Scale bars = 10 µm. Image taken with a 100×/0.95 objective on the Keyence VK-X200.

4

Chapter

Oxidation of Monolayer WS₂ Is a Photoinduced Process

Keywords: Photo-oxidation, Semiconductor Transition Metal Dichalcogenides, Tungsten Disulphide

"The truth is always destined to have only one brief victory parade between two long time spans in which it is first condemned as paradoxical, and then, belittled as trivial"

- ARTHUR SCHOPENHAUER

4.1 Overview

In this chapter, I will investigate the ambient air oxidation of chemical vapor deposition (CVD) grown monolayers of the semiconducting transition metal dichalcogenide (S-TMD) WS₂ using optical microscopy, laser scanning confocal microscopy (LSCM), photoluminescence (PL) spectroscopy, and atomic force microscopy (AFM). While the ambient air oxidation of S-TMDs such as monolayer WS₂ is quite well-known [207-208], the attribution of the ambient-air oxidation solely to absorbed wavelengths of light i.e. a photoinduced oxidation mechanism – has not been considered in the literature to date until recently [17]. Monolayer WS₂ exposed to ambient conditions in the presence of light (typical laboratory ambient light for weeks, or typical PL spectroscopy map), exhibits damage due to oxidation which can be detected with the LSCM and AFM; although may not be evident in conventional optical microscopy due to poorer contrast and resolution. Additionally, this oxidation was not random, and correlated with ‘high-symmetry’ and red-shifted areas in the PL spectroscopy map – areas thought to contain a higher concentration of sulphur vacancies. In contrast, samples kept in ambient and darkness showed no signs of oxidation for up to 10 months. Low-irradiance/fluence experiments showed that samples subjected

to excitation energies at or above the trion excitation energy (532 nm/2.33 eV and 660 nm/1.88 eV) oxidized in as little as 7 days, even for irradiances and fluences eight and four orders of magnitude lower (respectively) than previously reported [22]. No significant oxidation was observed for 760 nm/1.63 eV light exposure, which lies below the trion excitation energy in WS₂. The strong wavelength dependence and apparent lack of irradiance dependence strongly implies that the ambient oxidation of WS₂ is initiated by photon-mediated electronic band transitions, that is, photo-oxidation. These findings have important implications for prior, present and future studies concerning S-TMDs measured, stored or manipulated in ambient conditions.

4.2 Introduction

Since the discovery of two-dimensional (2D) van der Waals materials such as graphene [3] and the semiconducting transition metal dichalcogenides (S-TMDs) [4], 2D physics has become more accessible to laboratories around the world, leading to an exponential increase of published papers year upon year [11-12]. S-TMDs (and similarly graphene) possess radically different and useful properties in their 2D, monolayer form (as was discussed in Chapter 2). Properties shared among some of the monolayer S-TMDs of family (Mo, W)(S, Se)₂ include a large direct bandgap [7, 101, 209], exceptional optical characteristics [210] and strong spin-orbit coupling along with broken inversion symmetry [211]. This has lead various groups to demonstrate the usefulness of S-TMDs in potential applications ranging from ultra-low power electronics [14], valley-tronics [212-213], photonics [214] and qubits [215] to gas sensors [216].

Understanding S-TMDs stability in ambient conditions and under light illumination – crucial for measurements and manipulations undertaken in those conditions – is essential for their development into potential applications. It is now well-known that monolayer and multilayer S-TMDs oxidize upon exposure to extreme conditions such as ultra-violet (UV) light irradiation in moisture-rich conditions [217-218] or elevated temperatures in ambient atmosphere [219-222]. More recently however, monolayer S-TMD oxidation has been reported in ambient conditions. For example, Gao *et al.* [207] were among the first to report that WS₂ and MoS₂ had poor long-term stability in ambient conditions and observe that H₂O greatly sped up the oxidation process. Gao suggested the oxidation began with oxygen substitution at sulphur vacancy sites and progressed via O or OH radicals, with H₂O acting as a ‘catalyst’ lowering the energy barrier for reaction. In a subsequent report, Kang *et al.* [208] showed that oxidation was greatly suppressed, though not eliminated, when the S-TMD (in this case WS₂) was

epitaxially grown on graphene compared to an oxide substrate. It was proposed that electric fields were necessary for WS₂ oxidation, although the detailed mechanism was unclear. Recently, Atkin *et al.* [22] determined that the oxidation reaction could be initiated by laser light (440 nm), and proposed a fluence threshold ($>1.5 \times 10^{10} \text{ J m}^{-2}$) necessary for oxidation. Atkin also found that H₂O was necessary for the oxidation reaction to proceed at any measurable rate (in agreement with Gao) [207], and in addition, found that sulphate was a likely reaction product [22]. Although these studies have identified important factors in the oxidation process *i.e.* ambient conditions, humidity, substrate, reaction products and radiant exposure levels – a complete and fundamental understanding of the conditions under which oxidation takes place, and more critically the conditions that completely avoid oxidation, is lacking.

In this chapter, I investigate ambient-exposed monolayers of the S-TMD WS₂ using standard characterization tools – optical microscopy, photoluminescence (PL) spectroscopy and atomic force microscopy (AFM). Moreover, we also employ laser scanning confocal microscopy (LSCM), which serves as an integral tool in this work. By correlating AFM images with LSCM images, oxidized regions of monolayer WS₂ can be rapidly determined, which may not be evident from optical microscopy or PL spectroscopy. Oxidation is evident in samples kept in ambient conditions and exposed to light characteristic of laboratory conditions (typical room light for weeks), or moderate laser powers in PL mapping spectroscopy, but is not seen in as-grown samples or those stored in ambient conditions and darkness for up to 10 months. I further explore the role of light by irradiating monolayer WS₂ samples with low-irradiance, visible light at 532 (2.33 eV), 660 (1.88 eV), and 760 nm (1.63 eV). For WS₂ samples exposed to 532 and 660 nm light (above the threshold necessary for electronic excitation), oxidation was observed, whereas samples exposed to 760 nm light did not show appreciable oxidation (similar to those left in darkness). These results indicate that oxidation of WS₂ in ambient conditions requires photo-excitation, *i.e.*, oxidation is a wavelength dependent, photo-induced process – at odds with recent interpretations in literature [22, 207-208]. Furthermore, photo-induced oxidation occurs at irradiances and fluences of eight and four orders of magnitude lower, respectively, than the irradiance and fluence thresholds proposed in Ref. [22]; suggesting that the threshold for oxidation is extraordinarily low or absent. To our knowledge, a photo-oxidation mechanism in ambient conditions has not been previously described in detail for any member of the 2D S-TMD family of materials. The details of the oxidation reaction – likely Förster resonance energy transfer (FRET) and/or photo-catalysis involving redox reactions with H₂O and O₂ – requires further study (see Chapter 8, Section 8.2.1 for details). However, it is expected that the ambient air photo-oxidation of other direct bandgap S-TMDs (such as MoS₂) should occur similarly. These findings are important for future S-TMD based optoelectronic and electronic applications, since these findings

establish important protocols for all researchers seeking to avoid damaging S-TMDs *via* oxidation.

4.3 Methods

WS₂ was grown on c-sapphire substrates (single side polished, Shinkosha) which were initially cleaned in acetone, and then in ethanol, using ultrasonication in both instances for approximately 2 minutes. The substrates were then dried using nitrogen (99.9 %) and transported to the atmospheric-pressure CVD furnace (single-zone) for further cleaning via oxygen annealing. The process was as follows: high purity (99.995 %) oxygen was flowed at 50 sccm for approximately 5 minutes to purge the furnace (see [Figure 4.1](#)) after which the furnace was ramped to 1050 °C in 30 minutes and held at this temperature for 1 hour and then allowed to cool down naturally. This process took approximately 2.5 hours (the oxygen was flowed continuously until the substrates were taken out of the furnace).

4.3.1 Chemical Vapour Deposition

The same atmospheric-pressure CVD used for cleaning the c-sapphire substrates was used to grow monolayer WS₂ on the cleaned c-sapphire substrates (though different tubes were used to avoid contamination). The furnace is shown in [Figure 4.1](#).

After oxygen annealing, approximately 1.1 ± 0.1 g of sulphur powder (≥ 99.5 %, Sigma-Aldrich) and 2 ± 0.1 g of WO₃ powder (≥ 99.9 %, Sigma-Aldrich) was loaded in separate quartz boats. The sulphur was placed upstream and away from the central part of the furnace heating coils and under external heating coils (controlled by a separate temperature controller), while the WO₃ was loaded in the central part of the furnace along with the oxygen annealed sapphire substrates. A quartz test tube (approximately 22 mm in diameter) was placed against the substrate quartz boat (with the open-end facing outwards) so as to restrict the flow of reactants. This is thought to help increase the partial pressure of reactants over the substrates, thus promoting growth of WS₂.

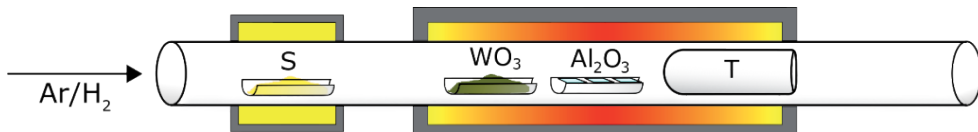


FIGURE 4.1: SETUP OF THE CHEMICAL VAPOUR DEPOSITION FURNACE.

The CVD furnace consists of a 1-inch quartz tube furnace (single-zone) loaded with reactants for growth of monolayer WS₂. Sulphur powder (S) is heated via external heating coils which are separate from the furnace, and are also controlled separately. The WO₃ powder and c-sapphire substrates (Al₂O₃) are loaded into the central part of the furnace, followed by a quartz test tube (labelled 'T') with a diameter of ≈ 22 mm – used to disrupt the flow of reactants downstream, and thought to increase the local partial pressure of reactants near the substrates via eddy currents or vortices causing recirculation.

Argon (99.9995 %) and molecular hydrogen (99.999 %) were used as the carrier gases and flowed at 200 sccm, and 8 sccm, respectively (H₂ was only flowed after purging the furnace with argon for 10 minutes). The furnace and external heating coils were then heated to approximately 900 °C and 200 °C from 30 °C in 30 minutes, respectively and held for approximately 5 minutes at these temperatures. After cooling to 800 °C, the furnace lid was opened slightly to rapidly cool the furnace. Between 600 °C and 500 °C, the furnace was fully opened, and the H₂ gas turned off. The sulphur was allowed to naturally cool from 200 °C to room temperature. After growth, the monolayer WS₂ samples were removed and immediately stored in plastic containers wrapped with aluminium foil and stored in a light-tight box.

4.3.2 Photoluminescence Mapping Spectroscopy

Crystals were analysed using a WITec 300R spectrometer equipped with a 532 nm laser and power set at approximately 140 µW (as judged by an optical power meter after the 100x objective). 2D confocal PL maps (μ -PL) were taken using the 100x/0.9 (Olympus MPLFLN) objective lens. A Gaussian beam profile was assumed, and the maximum irradiance estimated as $I = 8P/(\pi D^2)$, where P is the laser power and D is the diameter of the beam, estimated as $D = 1.22\lambda/NA \approx 721$ nm, where λ is the wavelength in nanometres and NA is the numerical aperture of the lens. The μ -PL map shown in Figure 4.10 took ≈ 25 minutes to complete (75×75 pixels, ≈ 0.27 seconds integration time per pixel). All PL measurements were undertaken at 20 °C ambient temperature and rel. humidity of 40 – 60%. In Figure 4.10b, the map was created using the MATLAB® code shown in Appendix A.

4.3.3 Reflectance, Transmission and Absorptance Spectroscopy

Figure 4.2 shows the reflectance, transmission and absorptance spectra of the WS₂ monolayer crystals over the wavelength range of 350 – 800 nm using a PerkinElmer Lambda 1050, equipped with an integrating sphere. **Figure 4.2a** shows measurements of samples grown on c-sapphire (Shinkosha) which were mounted on clear glass microscope slides (Sail). **Figure 4.2b** shows measurements of blank sapphire substrates (Shinkosha) mounted on clear glass microscope slides from the same batch. This allowed the absorptance from only the WS₂ to be determined in the following way. The absorptance of the substrates, $A_s = 1 - T_s - R_s$ (shown in **Figure 4.2b**), was subtracted from the absorptance of the WS₂ and substrate, given as $A_{WS_2+S} = 1 - T_{WS_2+S} - R_{WS_2+S}$ (shown in **Figure 4.2a**), to yield the absorptance from only the WS₂ (see **Figure 4.13a**) using the formula $A_{WS_2} = A_{WS_2+S} - A_s = (T_s - T_{WS_2+S}) + (R_s - R_{WS_2+S})$, where T_i and R_i are the measured transmittance and reflectance, respectively, of the substrate ($i = S$) and WS₂ plus substrate ($i = WS_2+S$).

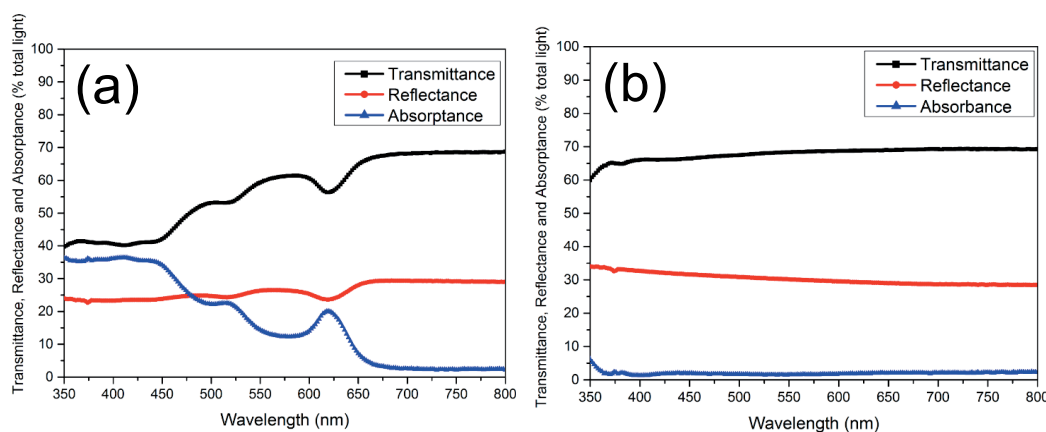


FIGURE 4.2: TRANSMITTANCE, REFLECTANCE AND ABSORPTANCE OF WS₂.

(a) WS₂ on c-sapphire on glass slide and **(b)** blank c-sapphire on glass slide.

4.3.4 Laser Scanning Confocal Microscopy

Two different LSCM's were used. In **Figure 4.8b**, a Keyence VK-X200 system was employed, and for all other LSCM figures, an Olympus OLS4100 system was used. These microscopes are also able to take standard optical images, as shown juxtaposed in **Figure 4.8b-c** in the **Results, Section 4.4.1**, by use of a

white LED. The white LED irradiance was calculated for the OLS4100 by first measuring the spectrum of the white LED, whose output was confined to the range 420 – 650 nm. A power meter was then used to measure the optical power exiting the 100x/0.95 objective lens. The responsivity of the power meter's silicon photodetector varies monotonically over this range of wavelengths; hence I was able to place bounds on the power measurement by calibrating the responsivity at two extrema of the spectrum, 420 nm and 650 nm – as judged *via* the spectrogram shown in Figure 4.3a, taken using a Thorlabs CCS200 spectrometer. The power was found to be bounded by $\approx 0.210 \pm 0.070$ mW. The field of view of the 100x/0.95 is 128 μm , and the irradiance was then calculated using $I = 4P/(\pi D^2)$. For the blue laser, the spectrogram shown in Figure 4.3b was measured using the same spectrometer, and the peak determined to lie at 405 nm. A power meter measured the maximum output at this wavelength as ≈ 14 μW after the 100x/0.95 objective. The irradiance was then calculated assuming a Gaussian beam, similar to the photoluminescence setup. The time taken per scan varied depending on the magnification used, though the longest time of approximately 50 seconds (corresponding to un-zoomed 100x magnification) was used to calculate the fluence, H , in which case the irradiance was multiplied by the total exposure time for each pixel, t : $H = 2Pt/(\pi r^2)$. The exposure time was calculated by dividing the total time for the scan (50 seconds) by the total number of pixels (1024×1024). The laser beam diameter is much larger than a pixel, and so would result in the laser 'spilling over' to multiple pixels. To estimate this effect, the area of the laser beam was divided by the area of a pixel to give ≈ 14 . Thus, the calculated time was multiplied by 14 to estimate an upper limit to the true exposure time, yielding $\approx 8.8 \times 10^4$ J m^{-2} . A similar estimate is obtained by dividing the total energy delivered during the complete scan by the total area imaged.

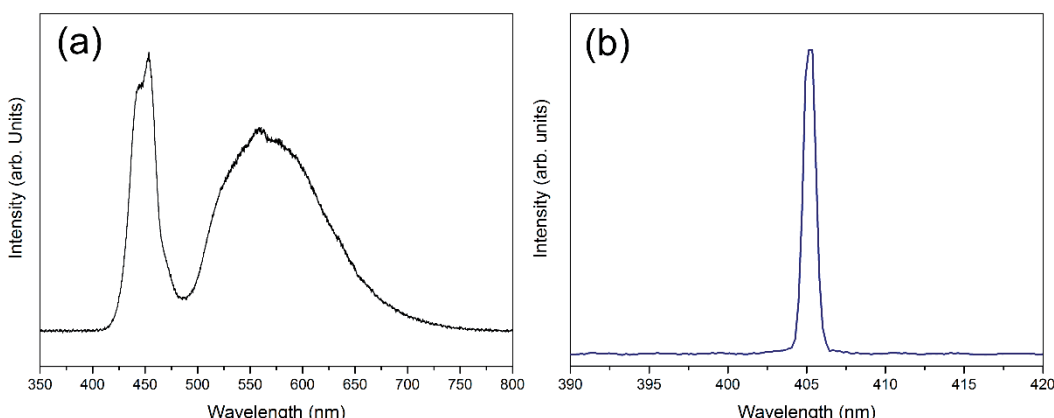


FIGURE 4.3: LASER SCANNING CONFOCAL MICROSCOPE (LSCM) LIGHT SOURCES FOR THE OLS4100 LSCM.

(a) Spectrum of the white light LED used for standard viewing in the LSCM. **(b)** Spectrum of the blue laser diode from the LSCM with central peak at ≈ 405 nm, used for high resolution scanning.

4.3.5 Atomic Force Microscopy

A Bruker Dimension Icon AFM in tapping mode (in ambient and at ≈ 20 °C) was used to obtain the atomic force micrographs. RTESPA-300 tips were used, and analysis was conducted using WSXM v4.0 [223]. In Figure 4.10f-h, the image was flattened, and the contrast enhanced. Bruker's own software was also used to analyse the height of the oxidized triangular islands (using the step height analysis function, see Figure 4.12). In this case, the measured heights were averaged.

4.3.6 Low Irradiance Light Exposure Experiments

The laser light sources used were a 532 nm and 650 nm laser diode (measured to be 660 nm, and thus referred to as the 660 nm laser) and halogen light source (XGY-II) with appropriate bandpass filter at 760 nm ± 10 nm (Thorlabs FB760-10, OD 6+ for 200 nm to 719 nm). The optical spectra of the laser sources are shown in Figure 4.4., and the filter setup is shown in Figure 4.5c. All light sources were measured using a Thorlabs PM100D optical power meter. A custom-built enclosure was used to shroud the experiment in darkness. In the enclosure, the optics used were an iris (Thorlabs ID25), beam steering mirrors, a circular linear variable neutral density filter (NDF) and a simple convex lens to expand the beam to an appropriate size. The setup is shown in Figure 4.5a. Samples were mounted onto a glass slide using double sided sticky tape (Figure 4.5c). Standard samples (typically sister samples from the same growth run) were kept in darkness for the entirety of the light exposure experiments. The irradiance and fluence for the sources were calculated similarly to the LSCM and PL sections above with the exception that the 760 nm light was assumed to be non-Gaussian (as in the white LED case with the LSCM), *i.e.* $I = 4P/(\pi D^2)$. The diameters were measured as ≈ 20 mm, ≈ 12 mm and ≈ 30 mm. Values for the irradiance were calculated as 3.8 W m⁻², 14.2 W m⁻² and 2.2 W m⁻² for the 532 nm, 660 nm and 760 nm light, respectively. Fluence values were then found by multiplying the irradiance by 604800 seconds (seconds in 7 days) to give 2.3×10^6 , 8.6×10^6 and 1.3×10^6 J m⁻² for the 532, 660 and 760 nm light, respectively.

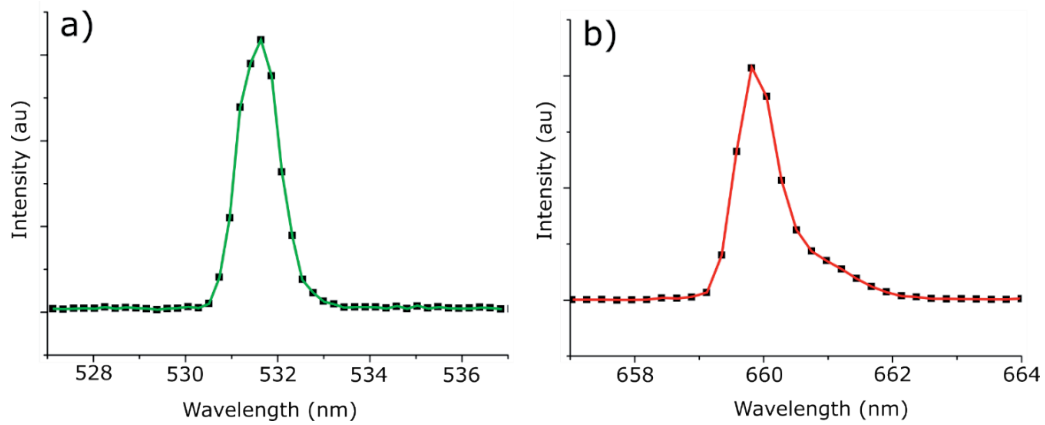


FIGURE 4.4: LASER SPECTRA OF LASERS USED IN LOW-IRRADIANCE EXPERIMENTS.
(a) 532 nm green laser showing measured spectrum centred at 531.6 nm. **(b)** 650 nm red laser showing spectrum centred around 660 nm.

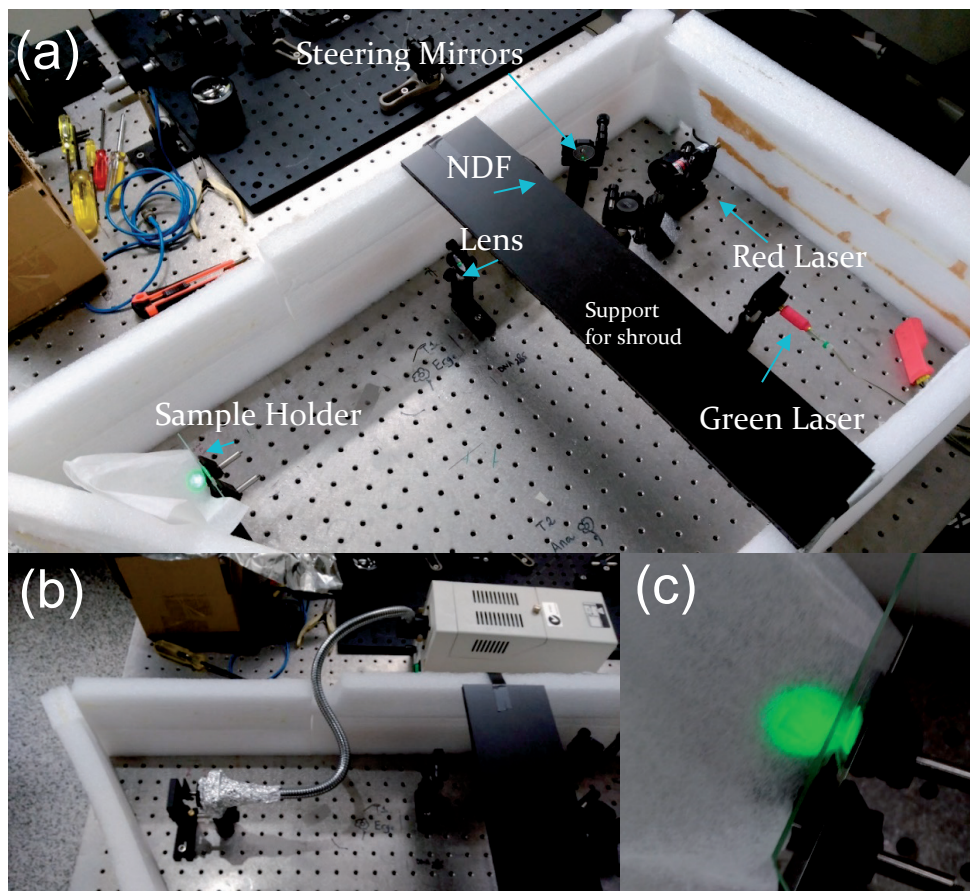


FIGURE 4.5: LOW IRRADIANCE EXPERIMENTAL SETUP.
(a) Overview of low irradiance experimental setup showing all optical components used for steering and shaping the lasers. The setup was covered with a light-blocking fabric (shroud) to prevent ambient light from entering the enclosure while the experiment was running. **(b)** Halogen light and 760 nm filter setup. **(c)** The sample mounting system showing the green laser covering the whole substrate.

4.3.7 Glove Box Experiments

The same low-irradiance light exposure experiments were conducted in a low humidity and low oxygen ($O_2 < 0.1$ ppm, $H_2O < 0.1$ ppm) nitrogen filled glovebox. Two identical light boxes (shown in [Figure 4.6](#)) were custom fabricated in which green light from an LED source ($\approx 3\text{ W m}^{-2}$ at 515 nm, see [Figure 4.7](#)) was shone continuously onto monolayer WS₂ (sister) samples for 7 days in ambient and in a nitrogen glovebox.

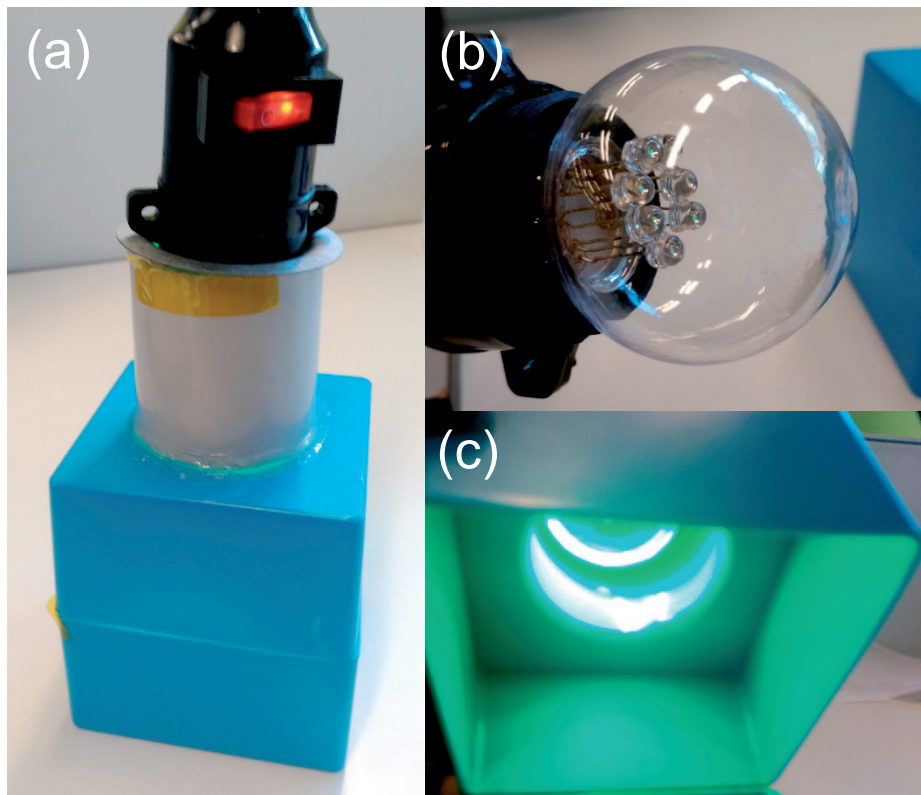


FIGURE 4.6: LIGHT BOX SETUP FOR LOW-IRRADIANCE EXPERIMENTS IN GLOVE BOX.

(a) *Constructed light box. WS₂ samples sit on the inside of the bottom part of the container, in the middle of the light source.* (b) *The green light was produced from 6 identical green LEDs.* (c) *View from inside the light box, showing that the entirety of the box is flooded with green light.*

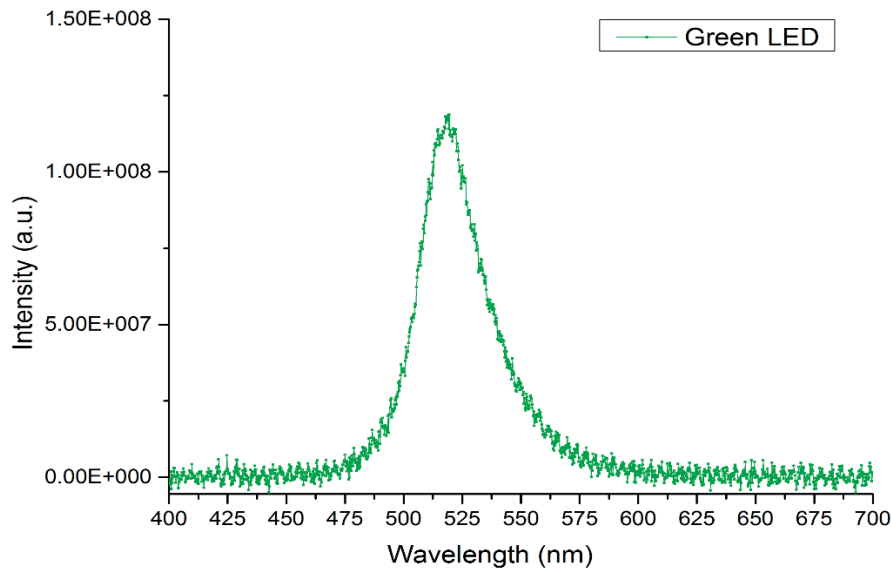


FIGURE 4.7: GREEN LED SPECTRUM.

Spectrum from the Green LEDs shown in Figure 4.6.

4.4 Results

Monolayer WS₂ is grown on c-sapphire (single side polished) in an atmospheric-pressure chemical vapor deposition (CVD) process described previously [224], using mixtures of argon/hydrogen with WO₃ and sulphur powder precursors (see preceding [Methods](#) section for details).

4.4.1 Initial Laser Scanning Confocal Microscope Investigations

[Figure 4.8a](#) shows an LSCM micrograph of an as-grown monolayer WS₂ crystal, stored in darkness after growth for approximately one month, and exposed to laboratory and LSCM light for short durations before being stored again in darkness. [Figure 4.8b](#) shows LSCM and optical micrographs taken on a similarly grown sample after approximately 19 days of exposure to ambient atmosphere and typical laboratory room lighting. The LSCM image (left side of [Figure 4.8b](#)) shows dark spots within the WS₂ crystal in [Figure 4.8b](#), although these are not apparent in [Figure 4.8a](#). These dark spots are difficult or impossible to observe in the optical micrograph of the same crystal, shown on the right side of [Figure 4.8b](#) (and similarly in [Figure 4.8c](#)).

As discussed in more detail below, the dark spots correspond to the complete or partial oxidation of small ($< 0.5 \mu\text{m}$) regions of WS₂ (i.e. WO_x, where $x \leq 3$). This observation is consistent with recent reports on the ambient air oxidation of monolayer S-TMDs, which have recorded samples in laboratory conditions oxidising in months [207] to as little as weeks [208]. After the observation of dark spots/oxidation in [Figure 4.8b](#), care was taken to not expose freshly grown samples to ambient UV light in the room, as this was thought to contribute to the oxidation of the WS₂ [217-218]. Thus, freshly grown crystals were stored in darkness.

To understand the optical properties of CVD grown WS₂ and investigate whether this could provide clues as to the causes of the observed oxidation in [Figure 4.8b](#), samples were mapped using confocal PL spectroscopy (μ -PL). [Figure 4.8c](#) shows LSCM and optical micrographs of a monolayer WS₂ crystal after performing μ -PL of the sample, but otherwise the sample was protected from light, while [Figure 4.8d](#) shows a sister sample imaged with the LSCM after storage in darkness for 10 months. The conditions of the μ -PL imaging (excitation wavelength 532 nm, power 140 μW , irradiance $\approx 6.9 \times 10^8 \text{ W m}^{-2}$, with total fluence of $\approx 1.8 \times 10^8 \text{ J m}^{-2}$, see [Methods](#) for details) are similar to those routinely used for optical characterization of S-TMD crystals [225]. [Table 4-1](#) shows all the irradiances and fluences used in this chapter.

TABLE 4-1: SUMMARY OF WS₂ LIGHT EXPOSURE EXPERIMENTS.

Wavelengths, irradiances and corresponding fluences, as well as if oxidation was visible with the LSCM for all experiments and analyses. LOW refers to low-irradiance experiments.

Wavelength (nm)	Experiment /Analysis	Irradiance (W m^{-2})	Fluence (J m^{-2})	Oxidation Visible?
415–700 (white light from LSCM)	LSCM	1.6×10^4	1.6×10^5	No
405 (blue)	LSCM	1.3×10^8	8.8×10^4	No
515 (green)	LED*	3	1.8×10^6	Yes
532 (green)	LOW	3.8	2.3×10^6	Yes
532 (green)	μ -PL	6.9×10^8	1.8×10^8	Yes
660 (red)	LOW	14.2	8.6×10^6	Yes
760 (far red)	LOW	2.2	1.3×10^6	No**

*See [Methods Section 4.3.6](#) for details.

**Some crystals had signs of small amounts of oxidation. See [Figure 4.14](#)

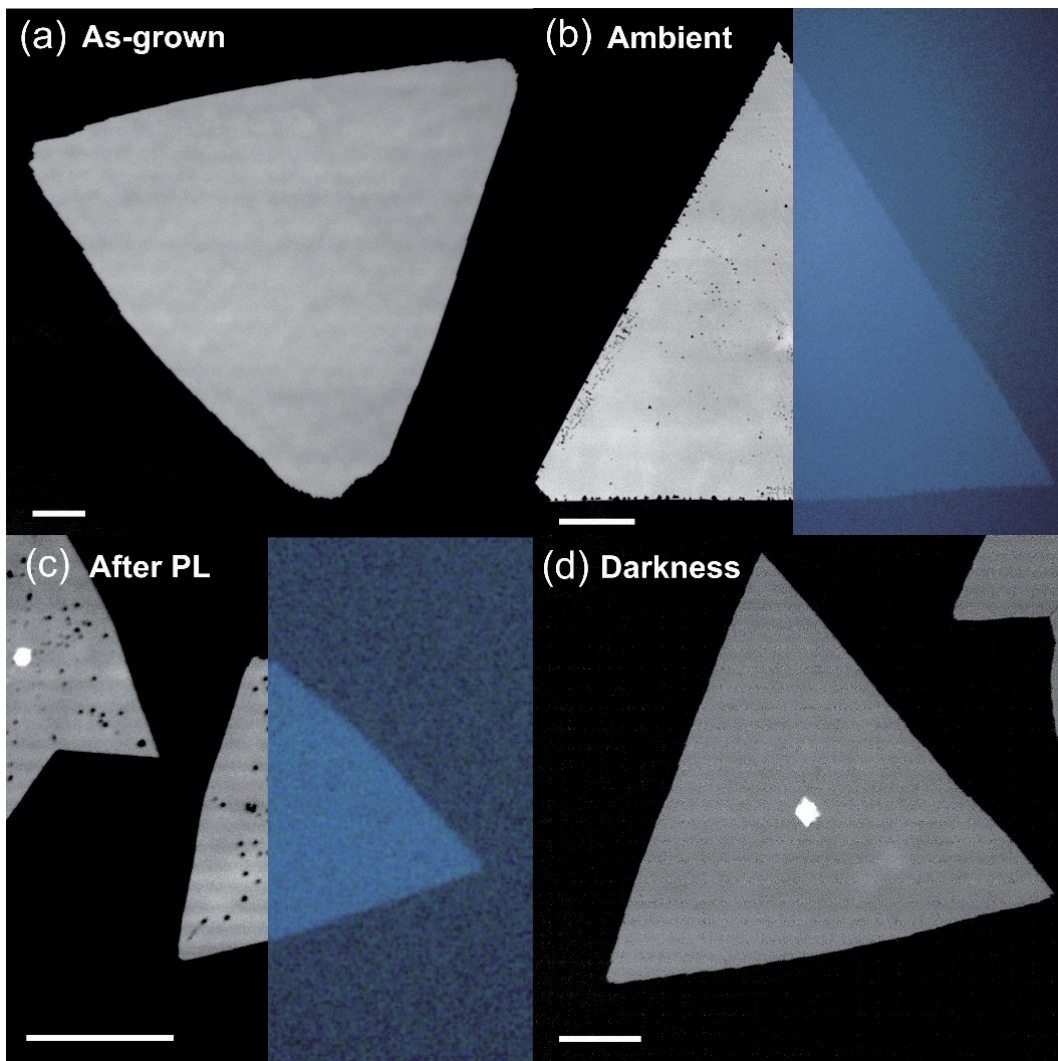


FIGURE 4.8: LASER SCANNING CONFOCAL MICROGRAPHS OF MONOLAYER WS_2 .

(a) CVD grown monolayer WS_2 exposed to minimal amounts of light before imaging with the LSCM approximately 1 month after growth. (b) WS_2 after approximately 19 days in ambient conditions, juxtaposed with an optical image of the same crystal. (c) WS_2 after routine photoluminescence spectroscopy, juxtaposed with an optical image of the same crystal and (d) WS_2 crystals kept in darkness for approximately 10 months, with brief exposure to ambient light. In the middle of this crystal is a crystal seed centre, which was common throughout growths. Scale bars in all images are $10 \mu\text{m}$.

For the PL-exposed sample in Figure 4.8c, similar dark spots as in Figure 4.8b are evident with the LSCM micrographs, though are not obvious in the conventional optical micrograph shown on the right side of Figure 4.8c. The standard sample shown in Figure 4.8d, which remained in darkness, appears pristine (in Figure 4.8d, a bright spot in the middle of the WS_2 is evident; I identify this feature as a crystal seed centre or multi-layer WS_2 , and not associated with oxidation). The results imply that light is responsible for the

ambient air oxidation of monolayer WS₂. Considering there are many reports using PL excitation conditions of S-TMDs on the same order of magnitude as that used in this chapter, the observation of oxidation after μ -PL was unexpected. Moreover, since the LSCM uses light to image the samples, it also carries a probability of oxidising the WS₂. Thus, care was taken to ensure that the final step in the analysis was light exposure from the LSCM, and that sister samples (such as the one in Figure 4.8d) were used as standards to compare with the effects of any analysis/light exposure experiments that were undertaken. Yet even after two subsequent LSCM exposures, no oxidation is observed, as is evident in Figure 4.9.

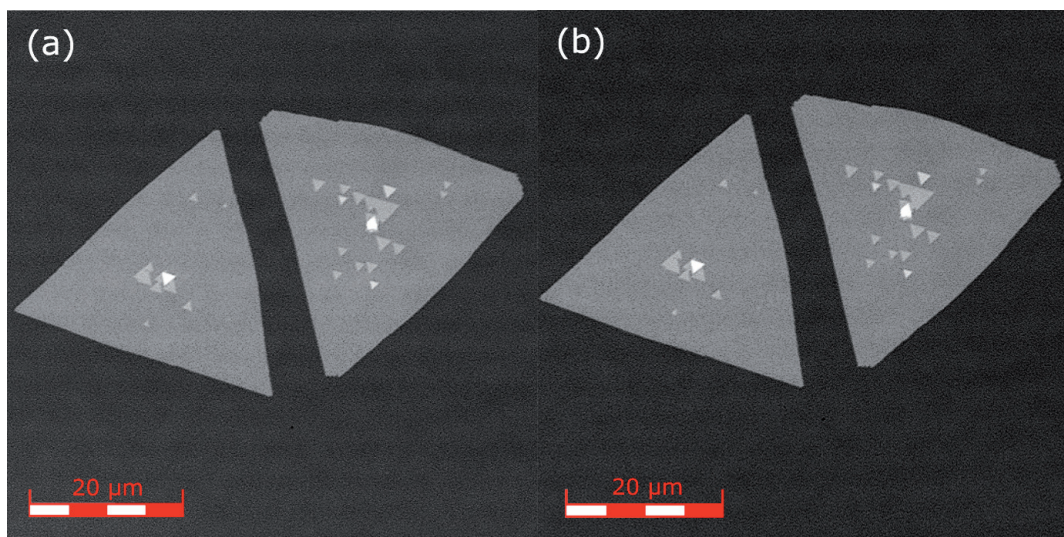


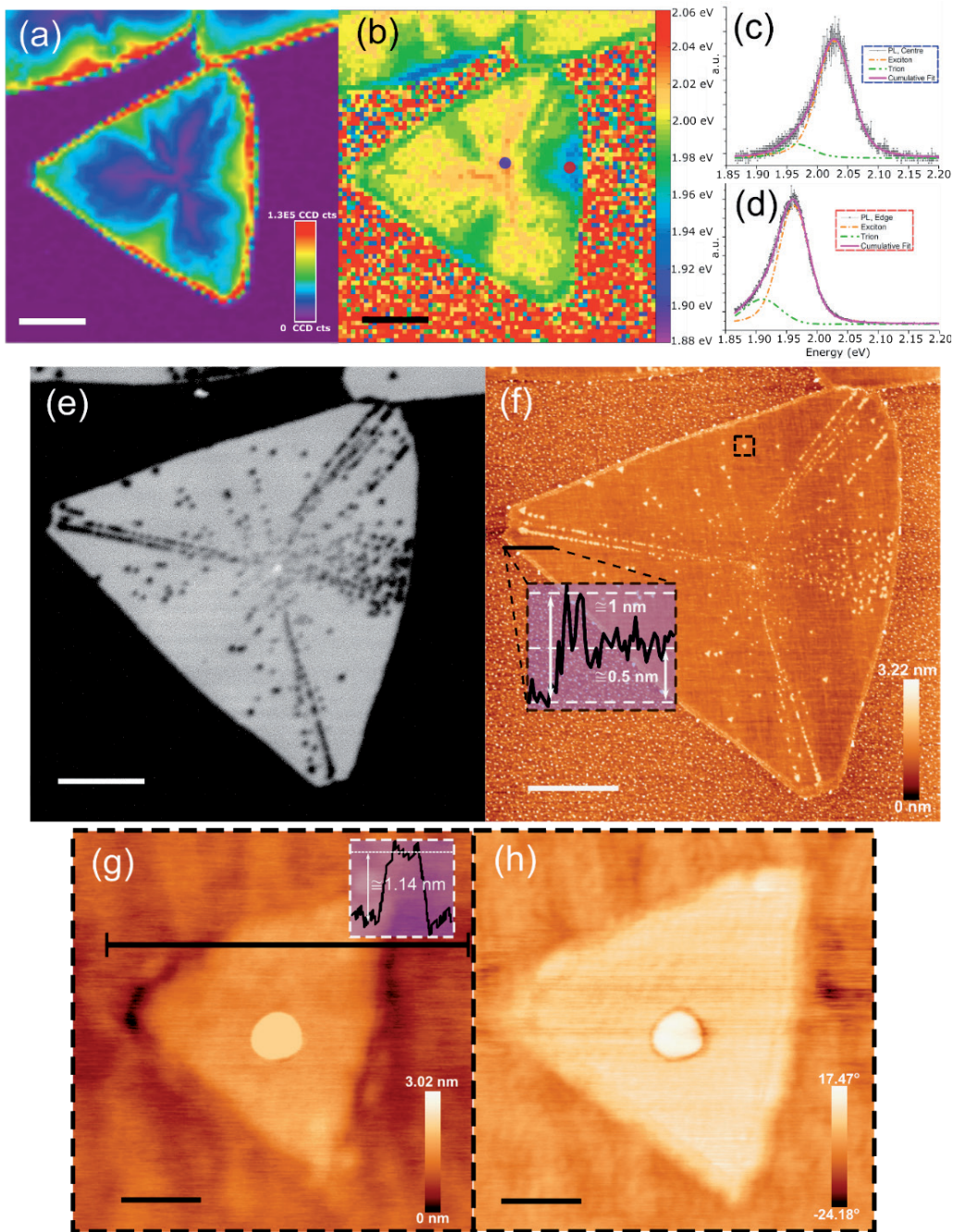
FIGURE 4.9: EFFECTS OF LSCM.

(a) LSCM micrograph of pristine monolayer WS₂ and **(b)** the same crystals analysed again with the LSCM after 2 days stored in darkness. As can be seen, these crystals have multilayer regions on the basal plane of the WS₂, represented in the LSCM image by brighter triangles in these regions, which is common during CVD growth.

As will become clear, the advantages of LSCM characterisation stem not only from its superior contrast and resolution, but also from its inherent operation at low incident fluence – much lower than those found in PL experiments, or under low-light illumination for days. The LSCM can operate in two modes, the first uses white light from an LED (standard optical micrographs in Figure 4.8b-c) and the second uses 405 nm light in a confocal laser scanning setup. In the case of the white light, the WS₂ is subjected to an irradiance of $\approx 1.6 \times 10^4$ W m⁻² and fluence of $\approx 1.6 \times 10^5$ J m⁻² (for 10 second exposures at 100 \times magnification). In the case of the 405 nm light, the irradiance and fluence were $\approx 1.3 \times 10^8$ W m⁻², and $\approx 8.8 \times 10^4$ J m⁻², respectively (see Methods, Section 4.3.4 for calculation details).

4.4.2	Photoluminescence Mapping and Atomic Force Microscopy
-------	---

Figure 4.10a-d shows the results of a photoluminescence map (μ -PL) taken at standard laboratory conditions on a different crystal on the same sample as in **Figure 4.8c**. **Figure 4.10a** shows the μ -PL intensity distribution of the WS₂ monolayer. It can be seen that the PL intensity on the edges is much brighter than that of the centre, as is observed in many other reports [22, 101, 177, 225-229]. Also, the μ -PL shows a three-fold rotationally symmetric pattern, not only in the intensity map, but also mirrored in the map of the peak photon energy (related to the location of the exciton, see **Appendix A1** for code which generated the image) shown in **Figure 4.10b**, *i.e.*, the two correlate with each other [177]. **Figure 4.10c** shows a representative spectrum from the central region of the crystal, deconvolved as two Voigt [230] spectra identified as the exciton peak at approximately 2.03 ± 0.01 eV and smaller trion peak at 1.97 ± 0.01 eV. A representative spectrum from the edge of the crystal is shown in **Figure 4.10d**, and is similarly deconvolved, showing a red-shifted exciton peak at approximately 1.96 ± 0.01 eV and trion peak at 1.91 ± 0.01 eV. These values for the neutral exciton (1.95 – 2.04 eV) and trion (1.90 – 1.98 eV) of WS₂ are in agreement with previously measured literature values for WS₂ on sapphire [227, 229, 231]. Furthermore, the separation of the trion and exciton of 0.055 ± 0.02 eV is also in agreement with previous literature values [232]. The deviation of the exciton/trion values between the two locations of the crystal shown in **Figure 4.10c-d** is likely due to (tensile) strain, which can red-shift the photoluminescence emission peak at least 0.013 eV/% of strain in WS₂ [233] (0.045 eV/% in MoS₂ [234-235], 0.027 eV/% in MoSe₂ [236]). The difference in the exciton peak of 0.06 ± 0.02 eV in **Figure 4.10c-d** thus, corresponds to a tensile strain of $3.5 - 7.1\%$. **Figure 4.10c** and **Figure 4.10d** show the heterogeneity of the optical characteristics of CVD grown monolayer WS₂ on sapphire; similar optical heterogeneity was found in all other samples. After μ -PL analysis, the sample was stored in darkness and then imaged with the LSCM and is shown in **Figure 4.10e**. **Figure 4.10e** shows that the WS₂ was oxidised after standard PL spectroscopy, as evidenced by the small (< 0.5 μ m) dark spots (see-through to substrate), as observed in **Figure 4.8c** and similar to those observed in previous reports using conventional light microscopy or atomic force microscopy [207-208, 218, 221-222, 225]. The μ -PL results *after* oxidation are shown in **Appendix A2**, **Figure A.2-1.**, and show a significant decrease in the intensity of the PL response after oxidation, in agreement with previous reports [207].

FIGURE 4.10: μ -PL AND AFM OF CVD-GROWN MONOLAYER WS₂.

(a-d) μ -PL of monolayer WS₂. **(a)** Map showing the intensity in charged coupled device (CCD) counts (cts) (scale bar = 5 μ m) and **(b)** shows the location of the peak in intensity from **(a)** (scale bar = 5 μ m). **(c)** shows the PL spectrum obtained from the central spot (blue) in **(b)** with exciton and trion peak energies at 2.03 ± 0.01 and 1.97 ± 0.01 eV, respectively. **(d)** shows the PL spectrum from the edge region (red spot) with exciton and trion peak energies of 1.96 ± 0.01 and 1.91 ± 0.01 eV, respectively. **(e), (f)** LSCM and AFM images showing oxidation of the same monolayer WS₂ crystal in **(a-d)**, after analysis with μ -PL (scale bars = 4 μ m). In **(e)**, an LSCM micrograph shows the oxidation as dark spots due to their altered transmittance. The morphology of these oxidation triangles was further investigated using AFM. In **(f)**, the tapping mode AFM height micrograph shows unambiguously that these oxidation zones are raised,

triangular and located along the 3-fold symmetric lines and red-shifted zones of the crystal. Inset shows the height of the crystal. (g), (h) Show a zoom in of the boxed area (scale bars = 65 nm) in (f) of a triangular oxidation island. The AFM height image in (g) shows the height of this island is ≈ 1.14 nm (inset) and the AFM phase image in (h), shows that the island is different in composition from the surrounding WS_2 .

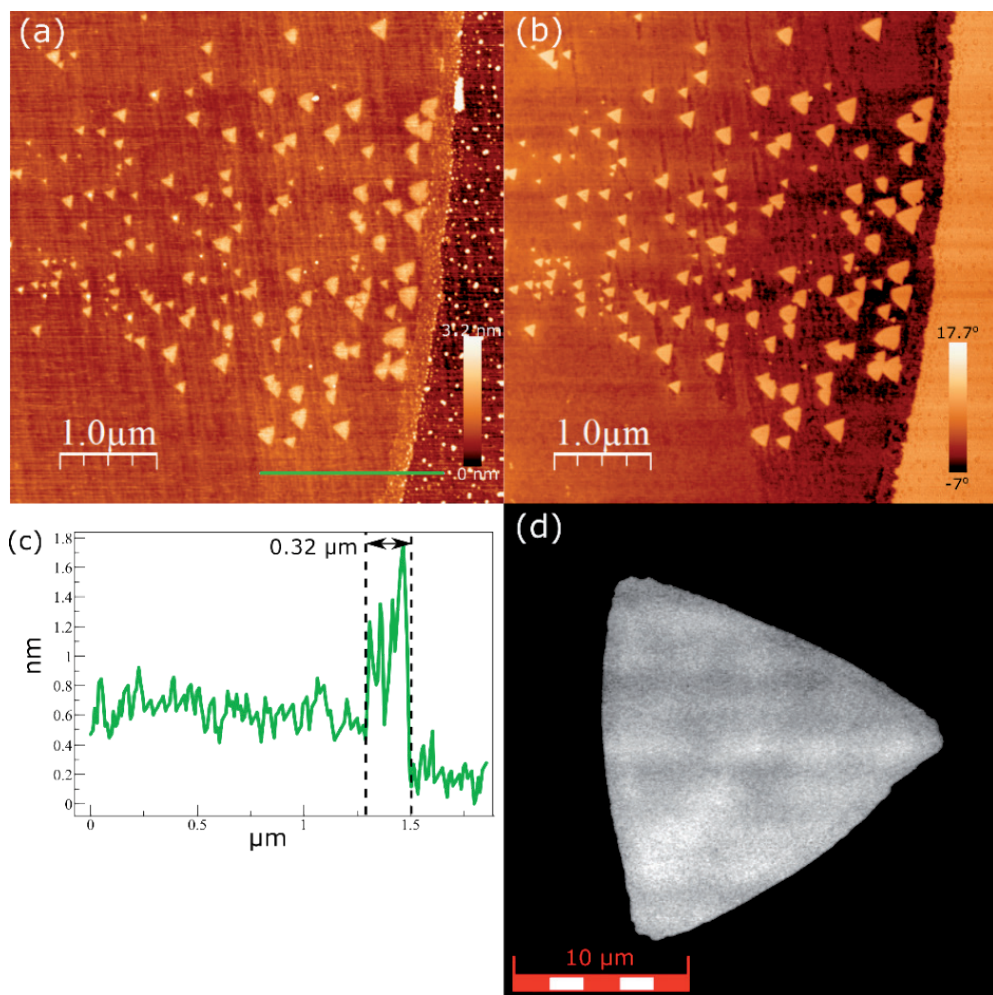


FIGURE 4.11: THE EDGE OF A WS_2 CRYSTAL ANALYSED WITH AFM AND LSCM.

(a-c) Shows a zoom up of the edge of the crystal in Figure 4.10. (a) Height AFM micrograph, (b) phase AFM micrograph showing that the edge is raised, though not oxidised, and oxidation is only present at the very edges of the crystal. (c) Shows the trace from the green line in (a). Width of the edge region is ≈ 0.32 nm. (d) LSCM micrograph of a different, yet similarly grown monolayer WS_2 crystal showing edges with a dissimilar contrast to the central part of the crystal. This edge feature correlates to the brighter PL intensity on the edge regions.

To better understand the oxidised regions seen with the LSCM, the same sample was then imaged with AFM in intermittent-contact mode, shown in [Figure 4.10f-h](#). [Figure 4.10f](#) shows an overview of the sample, and the extent of the oxidation. AFM resolves more clearly the dark spots seen in LSCM as raised triangular islands. These triangular islands in S-TMDs have been observed before and identified as tungsten oxide in various oxidation states, WO_x ($x \leq 3$) [[22](#), [208](#), [218](#), [225](#)]. Upon comparison of the μ -PL maps shown in [Figure 4.10a-b](#) and the after effects of oxidation seen in the LSCM and AFM micrographs of [Figure 4.10e-f](#), respectively, it is observed that oxidation occurs more prevalently in the three-fold symmetric pattern of lines extending from the centre towards the vertices of the triangular crystal. Also, significant oxidation can be seen outside these areas, for example in the region with red-shifted PL corresponding to the spectrum in [Figure 4.10d](#).

The inset of [Figure 4.10f](#) shows the height of the central part of the crystal as ≈ 0.5 nm, with the very edge of the crystal higher than that of the central part by ≈ 0.5 nm, and edge width of ≈ 0.32 nm (see [Figure 4.11a-c](#)). As can be seen in the inset of [Figure 4.10f](#) and even more clearly in [Figure 4.11a](#), the edge is rough, and contains local increases in height some of which are above or below 0.5 nm. These small raised ‘particles’ that coalesce on the WS₂ crystalline edge and just outside (*i.e.* on the substrate) the edges of the WS₂ crystal and substrate have also been observed in previous reports [[237-239](#)], and have been attributed to precursors or partially converted tungsten oxide particulates which have not been desorbed during growth. The maximum variation measured for these particulates was ≈ 1.3 nm higher than the WS₂ basal plane.

In some samples (from different growth runs), the crystalline WS₂ edge was also discernible under the LSCM (see [Figure 4.11d](#)). This higher edge region correlates well to the increased edge PL intensity of the μ -PL map ([Figure 4.10a](#)), and thus I tentatively ascribe the bright edge in the PL spectrum to this physical feature observed with the AFM (and LSCM). Increased PL brightness around the edges of monolayer S-TMDs has also been reported on by others [[22](#), [101](#), [177](#), [225-229](#), [240](#)], and the effect is attributed to either differences in chemical composition on the edges of the crystal [[101](#), [177](#), [225-228](#), [240](#)] or to water intercalation at the edges of the S-TMDs [[22](#), [229](#), [241](#)].

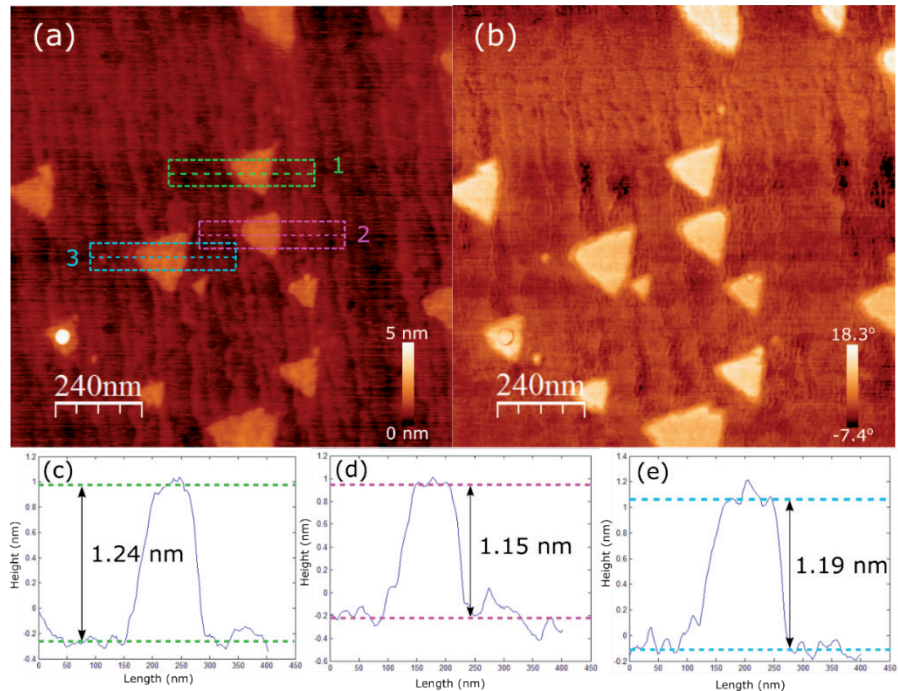


FIGURE 4.12: HEIGHT ANALYSIS OF OXIDISED REGIONS ON THE SURFACE OF WS₂.

The oxidation islands are from the same crystal shown in Figure 4.10. (a) Height AFM micrograph showing the oxidized islands analysed (numbered regions from 1 to 3). (b) Corresponding phase AFM micrograph. (c), (d), (e) AFM height analysis from (a) showing the height traces of regions 1, 2 and 3, respectively.

Figure 4.10g-h show higher-resolution AFM topography and phase images, respectively, of the triangular oxidation island feature outlined by the dotted black box in Figure 4.10f. The AFM topography image in Figure 4.10g shows that these triangular oxidation islands are not holes (as suggested by the LSCM in Figure 4.10e) but raised in topography by ≈ 1.14 nm above the surrounding WS₂; this is consistent with thicker WO_x remaining as the reaction product and Figure 4.12, which shows the analysis of 3 separate triangular oxidation islands on the surface of the same crystal in Figure 4.10. The average value obtained for the height of the oxidation islands analysed in Figure 4.12 is 1.19 ± 0.05 nm above the surrounding WS₂, which is in agreement with the value obtained in Figure 4.10g, and is in approximate agreement with previously published work which found that oxidised regions (on multilayer WSe₂) ranged from 1.2 to 3.0 nm [218]. The phase contrast between the oxidation island and WS₂ (Figure 4.10h) also indicates that the oxidised area is a different material. Thin films of WO_x have higher transmittance than WS₂ at visible wavelengths (see Methods Section 4.3.3 for transmittance, reflectance and absorptance spectra of monolayer WS₂) explaining the dark (see-through to substrate) appearance of these regions under the LSCM [242]. It was observed that for some oxidation islands, there was a small (<60 nm), round, raised region in the middle of the oxidation

island. This spot, seen more clearly with the enhanced contrast of the phase image in [Figure 4.10h](#) (also visible in [Figure 4.12b](#)), suggests this feature is a liquid drop, and could result from hygroscopic sulphur oxides (see [Discussion](#) and [Chapter 8, Section 8.2.1](#) details) [22].

4.4.3 Low-Irradiance Light Experiments

The experiments thus far imply that visible light with wavelengths as long as 532 nm can cause oxidation of WS₂ in ambient, at irradiances typically used for PL spectroscopy. To determine the physical mechanism of WS₂ oxidation, controlled, low-irradiance light exposure experiments were conducted with monolayer WS₂ samples at three specific wavelengths. The low irradiances used allow for me to completely eliminate heating as a source of oxidation, and instead, focus on any possible wavelength dependence of the oxidation. The experiments used two lasers at 532 nm (2.33 eV) and 660 nm (1.88 eV) (see [Methods Section 4.3.6](#) for details, and [Figure 4.4](#) for laser spectra) and a halogen light (XGY-II) filtered at 760 nm (1.63 eV), with irradiances of approximately 3.8, 14.2, and 2.2 W m⁻², respectively. Previous experiments observed heating only at irradiances approximately nine orders of magnitude higher (in MoS₂) [243]. [Figure 4.13a](#) shows the absorptance spectrum of the WS₂ monolayers at \approx 293 K, determined *via* subtracting the measured transmission and reflectance spectra from the total light impinging on the sample (additional details in [Methods](#), see [Figure 4.2](#)). The absorptance spectrum is consistent with previous observations for monolayer WS₂ [103, 199, 244], and shows features characteristic of the ‘A’ exciton at 619 ± 2 nm (2.003 ± 0.006 eV) and ‘B’ exciton at 516 ± 2 nm (2.403 ± 0.009 eV), which arise from excitonic transitions in the spin-orbit split bands at K/K' points in the Brillouin zone. The observed spin-orbit splitting, Δ_{SO} , of 0.400 ± 0.015 eV is close to previously measured values for monolayer WS₂ [88, 103].

The corresponding wavelengths used in the controlled low-irradiance light exposure experiments are highlighted and superimposed on [Figure 4.13a](#). The 532 nm light was chosen to mimic the conditions found in the PL experiment, the 660 nm light was chosen as it is at the edge of the absorption of WS₂ (excites mainly the trion) and 760 nm light which is not significantly absorbed by the WS₂ (*i.e.* photon induced electronic transitions are improbable). Light was shone constantly on the samples for 7 days in ambient atmosphere (ranging from \approx 40 to \approx 60 % humidity) and they were subsequently imaged using the LSCM, giving a total fluence (un-corrected for absorptance) of 2.3×10^6 , 8.6×10^6 and 1.3×10^6 J m⁻² for the 532, 660 and 760 nm light, respectively. Note that these fluences are at least an order of magnitude larger than that of the LSCM.

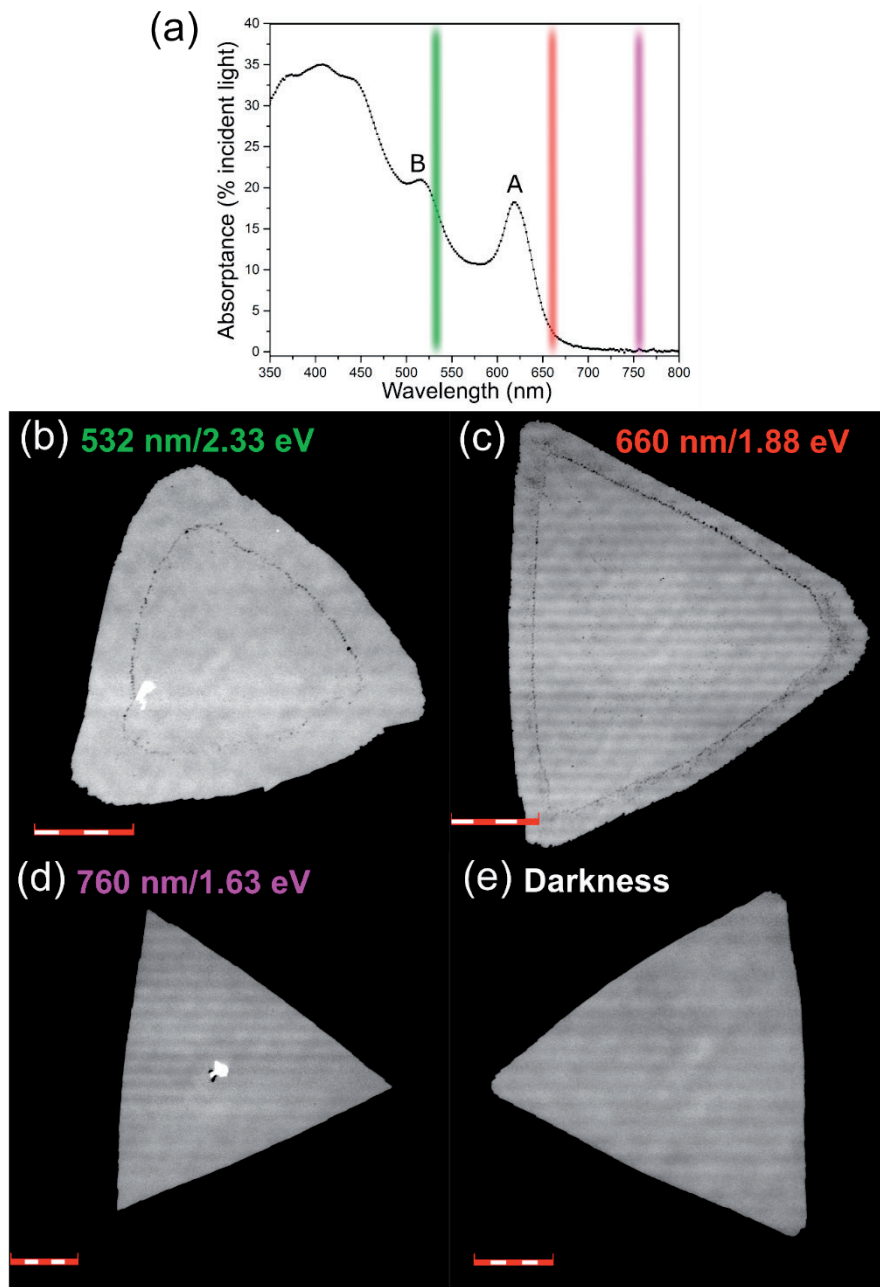


FIGURE 4.13: ABSORPTANCE SPECTRUM OF MONOLAYER WS₂ AND LOW-IRRADIANCE EXPERIMENTS.

(a) Shows the absorptance spectrum of monolayer WS₂ taken at ≈ 293 K. Labels denote the 'A' exciton at 619 ± 2 nm (2.003 ± 0.006 eV) and 'B' exciton at 516 ± 2 nm (2.403 ± 0.009 eV). Color bands correspond to the wavelengths used for the low light exposure experiments, from left to right these are 532 nm (green), 660 nm (red) and 760 nm (purple). (b), (c), (d) Low-irradiance light exposure experiments. Laser scanning confocal micrographs of monolayer WS₂ after (b) 7 days exposure to green laser (532 nm/2.33 eV, 4.2 W m⁻²) scale bar = 20 μ m, (c) 7 days of exposure to red light (660 nm/1.91 eV, 14 W m⁻²) scale bar = 20 μ m, (d) 7 days of exposure to far-red light (760 nm/1.63 eV, 2.2 W m⁻²) scale bar = 10 μ m. (e) A standard sample kept in darkness for 2 weeks to compare against light exposed samples, scale bar = 10 μ m.

[Figure 4.13b-e](#) show the results of the low-irradiance experiments after 7 days of exposure to the different wavelengths ([Figure 4.13b-d](#)) or kept in darkness for two weeks ([Figure 4.13e](#)) as imaged with the LSCM. In [Figure 4.13b-c](#), small triangular islands on the edges and the interior of the WS₂ indicate that the 532 nm ([Figure 4.13b](#)), and 660 nm ([Figure 4.13c](#)) light caused significant oxidation of these samples. [Figure 4.13d](#) shows the results of 760 nm light exposure; no significant amount of oxidation could be detected, though on some crystals, minute traces of oxidation were observed (see [Figure 4.14](#)). All samples (including those in [Figure 4.13b-d](#)) were exposed to small amounts of ambient light while mounting/removing the samples from the optical setup (and CVD furnace) and loading/measuring the samples for analysis with the LSCM. Additionally, the 760 nm exposure used a filter (see Methods) instead of a pure wavelength source such as a laser, which may have further contributed to stray light exposure. As can be seen in [Figure 4.13d](#), these brief ambient light exposures do not cause extensive oxidation (as observed with the LSCM) compared to [Figure 4.13b-c](#) which are severely oxidized. [Figure 4.13e](#) shows an LSCM image of a control sample kept in darkness for two weeks after growth; no oxidation in any samples kept in darkness was observed.

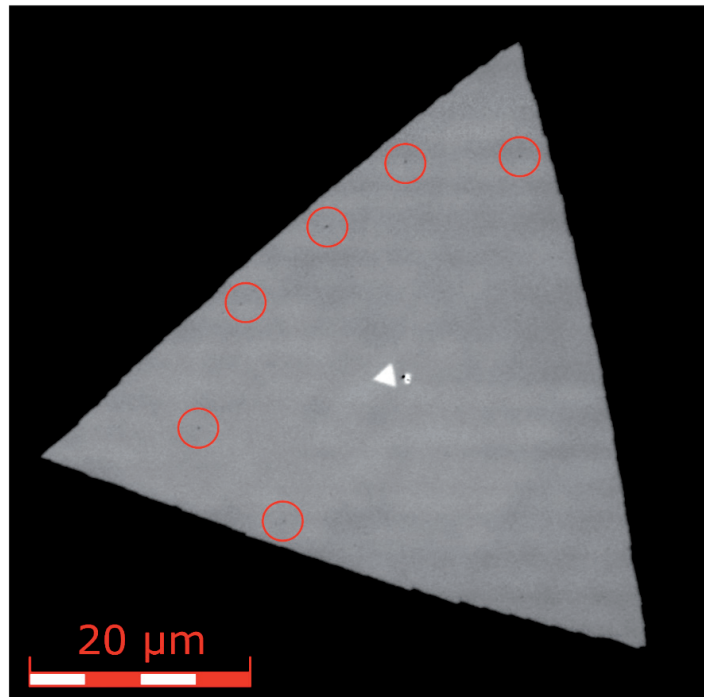


FIGURE 4.14: EFFECTS OF BRIEF AMBIENT AND STRAY LIGHT EXPOSURE ON WS₂.

An LSCM image showing that some of the WS₂ crystals in the 760 nm exposed sample started to oxidise even with brief exposures to ambient/stray light, evident via the dark spots (oxidation) highlighted here with red circles.

4.4.4 Effects of Light Exposure in a Nitrogen Environment

In order to explore the effects of H_2O and O_2 , WS_2 monolayers were exposed to similar low-irradiance ($\approx 3 \text{ W m}^{-2}$) green ($\approx 515 \text{ nm}$ – see Methods section) light in a nitrogen filled glove box environment with ultra-low levels of O_2 and H_2O for 7 days. To compare with the effects in ambient conditions, a standard was exposed using an identical setup, shown in [Figure 4.15a](#). The results of the glove box exposure are shown in [Figure 4.15b](#). It is immediately apparent that in contrast to the ultra-low irradiance experiments in ambient conditions, the same lighting conditions in a glovebox environment (that excludes water and oxygen) shows no damage or adverse effects due to oxidation (as judged by the LSCM). This indicates that light-induced oxidation does not proceed at any measurable rate in the absence of O_2 and H_2O , and that these molecules may play an essential role in the oxidation of WS_2 and similar S-TMDs. It also shows that processing S-TMDs in environments that exclude H_2O and O_2 is beneficial for S-TMD manipulations, for example in device processing, to ensure pristine S-TMD surfaces.

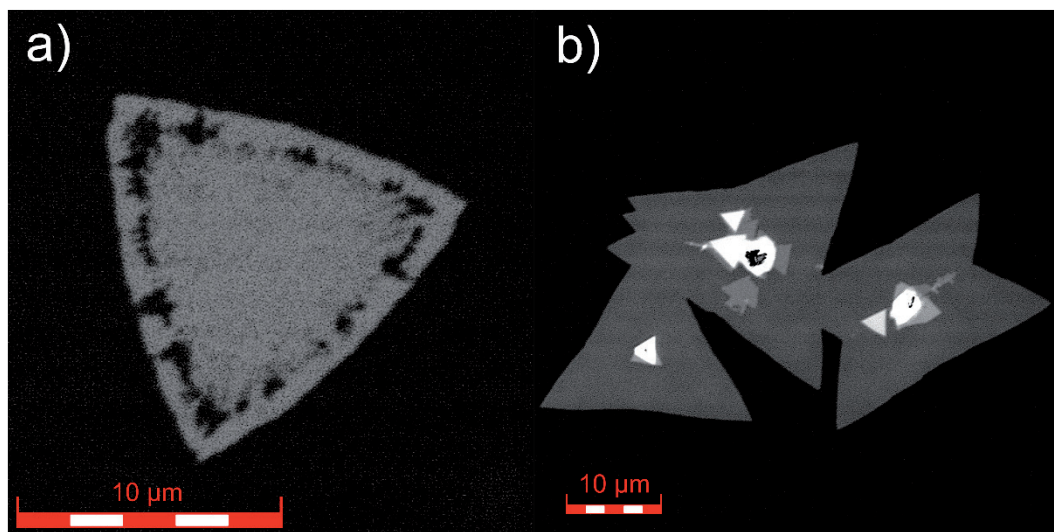


FIGURE 4.15: LOW-IRRADIANCE LIGHT EXPOSURES IN A GLOVE BOX.

WS_2 monolayers exposed for 7 days with low-irradiance green light from the light box setup in [Figure 4.6](#) in (a) ambient conditions, and (b) nitrogen filled glovebox (concentration of H_2O and $\text{O}_2 < 0.1 \text{ ppm}$).

4.4.5 Effects of Light and Heating in Ambient

Heating in ambient is known to cause significant oxidation [207, 219-222], though the effects of illuminating WS₂ while heating in ambient has not been investigated in the literature. To investigate whether ambient light influences the oxidation of monolayer WS₂ crystals while heated, monolayer WS₂ samples were heated to 80 °C for 2 hours in darkness. The results were imaged with the LSCM and are shown in Figure 4.16a-b. This temperature was selected, as it was shown by Gao *et al.* [207] that heating at only 80 °C for 20 minutes was sufficient to induce oxidation of monolayer WS₂ samples (light was not controlled for in this experiment). As can be seen, no oxidation is visible on any of the crystals, especially on grain boundaries from twinning crystals (Figure 4.16a) which have been shown to be especially susceptible to oxidation [219-220]. Although, as can be seen in Figure 4.16c-d, when monolayer S-TMD samples were heated to 350 °C for 3.5 hours, high temperatures were able to cause significant oxidation.

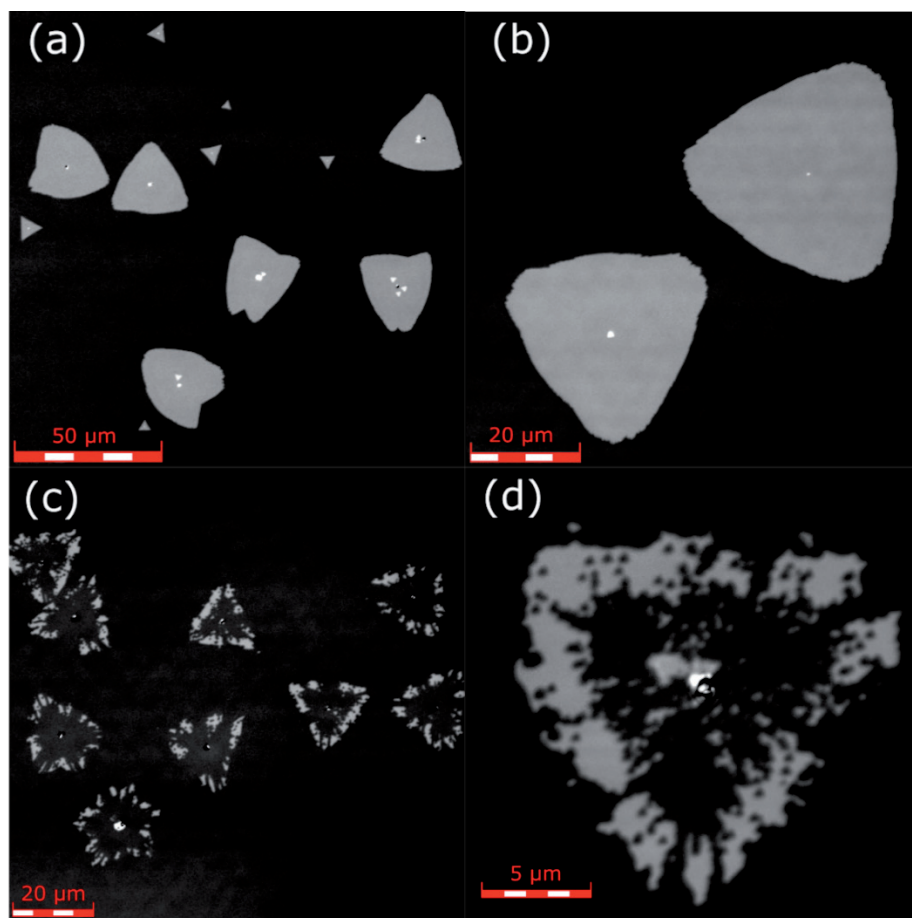


FIGURE 4.16: HEATING MONOLAYER WS₂ IN AMBIENT AND DARKNESS.
 (a), (b) At 80 °C for 2 hours. (c), (d) At 350 °C for 3.5 hours.

4.5 Discussion

I have identified for the first time that the previously observed [22, 207-208] ambient oxidation of a monolayer S-TMD requires exposure to light that is able to excite electronic transitions within the WS₂, *i.e.*, the physical mechanism of oxidation in ambient is photo-oxidation. While heating of S-TMDs in ambient has been shown to cause oxidation [207, 219-222], I can rule out heating as the cause of oxidation in the μ -PL experiments performed (Figure 4.10), as I observe similar oxidation for long-time exposures at low-irradiance in Figure 4.13b-c. These low-irradiances are approximately eight orders of magnitude lower than the high-irradiance μ -PL exposure (Figure 4.8c and Figure 4.10a-d) and are much below any levels that would cause measurable heating [243]. In fact, I completely rule out heating given the results in Figure 4.16 which show that monolayer WS₂ is stable up to at least 80 °C in ambient conditions (and darkness). This temperature far exceeds any temperature increase from the light sources used, and thus, heating can be ruled out as the cause of oxidation in the low-irradiance experiments.

Furthermore, the LSCM uses higher irradiance than the green or red low-irradiance experiments, yet results in no significant observable oxidation for short time exposures. This implies that irradiance is not an important factor for oxidation. In contrast, fluence does appear to be an essential metric for oxidation. Light exposure at 440 nm (2.82 eV) at high fluence ($>1.5 \times 10^{10} \text{ J m}^{-2}$) has been previously observed to cause oxidation of monolayer S-TMDs [22]. Here, I find that lower photon energy light (down to the threshold for electronic excitation, 1.88 eV or 660 nm in WS₂) is sufficient for oxidation, using a fluence approximately 4 orders of magnitude lower ($\approx 2.3 \times 10^6 \text{ J m}^{-2}$ in Figure 4.13b) than previously reported. It should be noted, that by taking into account the absorptance of WS₂ (from Figure 4.13a), the actual amount of absorbed light (*i.e.* light that can excite electronic transitions) is lower by an order of magnitude for the 532 and 660 nm light and approximately zero for the 760 nm light (the uncorrected values of irradiance and fluence are quoted here for direct comparison with literature). In comparison, the LSCM images, which show no obvious signs of oxidation, were obtained using fluences of $\approx 8.8 \times 10^4 \text{ J m}^{-2}$. A summary of the irradiances, fluences and whether oxidation was visible in each light exposure experiment is presented in Table 4-1. These observations suggest that a fluence threshold for oxidation is either non-existent or extraordinarily low, and that oxidation will simply proceed at a rate that is proportional to the fluence and the efficacy in which the material generates excited carriers from optical excitation. Thus, depending on the resolution of the probe used, oxidation may not be observed, yet still be present even with brief exposures at low fluence.

The strong wavelength dependence of oxidation indicates a photo-excitation mechanism involving the WS₂ itself. We can rule out direct excitation of

oxygen to create singlet oxygen (excited, reactive form of oxygen – see [Chapter 8, Section 8.2.1](#)), which would occur at 760 ± 10 nm wavelength excitation [[245-246](#)], as we observe no oxidation in the low-irradiance 760 nm/1.63 eV experiment. The fact that the threshold photon energy (wavelength) corresponds well to the energy (wavelength) threshold for electronic excitation (excitation of the trion), strongly suggests that oxidation instead occurs through a photo-excitation process, *i.e.* photo-oxidation. The detailed mechanism — likely Förster resonance energy transfer (FRET) and/or photo-catalysis reactions involving excited H₂O and/or O₂ species — requires further study (see [Chapter 8, Section 8.2.1](#) for more details). However, I also expect the ambient air photo-oxidation of other direct bandgap S-TMDs (such as MoS₂) to occur similarly due to very similar chemistry. For instance, Ding *et al.* [[247](#)] have recently discovered singlet oxygen present in photo-excited solutions of MoS₂ quantum dots, and have suggested FRET as the mechanism of oxidation. The necessity of photo-excited carriers for oxidation also explains the protection from oxidation of monolayer S-TMDs placed on graphene [[208](#)]: semi-metallic graphene efficiently quenches the photoexcited carriers through non-radiative recombination, thus greatly reducing the available excited carriers for chemical reaction *via* FRET and/or photo-catalysis [[248](#)].

I note at this point that the photo-oxidation of semiconductors (especially direct bandgap) is not a new observation, and has been reported on since at least 1977 in materials such as GaAs [[249-251](#)] (see reference [[250](#)] and references therein) and with other direct bandgap semiconductors such as InP [[251](#)] and TiO₂ [[252](#)]. Other 2D materials such as black phosphorous and the recently discovered 2D ferromagnet, CrI₃, have also been found to photo-oxidize (more rapidly compared to WS₂) when exposed to ambient conditions and light [[253-254](#)]. In the ambient air photo-oxidation of black phosphorous and CrI₃, H₂O has been identified as a crucial component for oxidation. In the case of black phosphorous, oxidation required the presence of both adsorbed water and oxygen – oxidation did not occur unless both molecules were present, even though the oxidation rate was found to only depend on the concentration of O₂ [[253](#)]. This was also found with GaAs, in which H₂O was found to have a ‘catalytic’ effect on oxidation [[255](#)]. S-TMDs are no exception, and have also been found to only oxidize substantially in ambient with H₂O present [[22, 207, 256-258](#)], suggesting a similar mechanism may be responsible. The photo-oxidation of semiconductors is not limited to direct bandgap materials, and has also been reported for silicon (note that CrI₃ also has an indirect bandgap [[259](#)]), although the effect was found to be less pronounced than for direct bandgap materials [[251](#)]. Thus, it is expected that even multilayers of S-TMDs will undergo ambient air photo-oxidation, and indeed this has been reported by Budania *et al.* [[257](#)] which observed oxidation for exfoliated multilayer MoS₂ samples left in ambient conditions (though the role of light was not investigated). The photo-induced oxidation of semiconductors in ambient atmosphere seems to be a universal effect, yet not much attention has been paid to the mechanism in the 2D community,

especially regarding S-TMDs. Thus, it is expected that past experiments may have been affected by photo-oxidation since the results I have presented thus far show that even for ultra-low light exposures (see [Table 4-1](#)), that it only takes on the order of days for there to be significant oxidation present. For example, oxidation may have affected past S-TMD electrical devices by increasing contact resistivity (WO_x has a larger bandgap), explaining at least in-part the large variation in measurements and lack of reproducibility from group to group and device to device [[260](#)]. This may have also occurred in the case of heating S-TMDs in ambient, where it was shown in [Figure 4.16a-b](#) that heating at $80\text{ }^\circ\text{C}$ in darkness for 2 hours caused no visible oxidation effects, whereas in reference [[207](#)], it was shown that heating at $80\text{ }^\circ\text{C}$ in ambient light for 20 minutes did cause visible oxidation. This suggests that the observed oxidation was in fact due to photo-oxidation, rather than heating, which does not appear to cause oxidation at $80\text{ }^\circ\text{C}$ when light is omitted (see [Chapter 8, Section 8.2.2](#) for further details).

Furthermore, I observe that oxidation does not occur randomly across individual monolayer WS_2 crystals, but rather, shows a preference for regions running roughly from the centres to the vertices of triangular crystals, *i.e.* arranged with threefold rotational symmetry around the crystal centres ([Figure 4.10e-f](#)), as well as the edges and red-shifted PL regions of the crystals ([Figure 4.8b](#), [Figure 4.13b-c](#) and [Figure 4.10d](#), respectively). The same threefold rotationally symmetric pattern is seen in the μ -PL ([Figure 4.10a-b](#)) and has been observed in our group previously [[229](#)], and by other groups [[177](#), [225-228](#)]. Recent work counting individual defects using conductive AFM has demonstrated that this three-fold symmetric region has a higher defect density than surrounding areas of the single crystal [[261](#)]. Additionally, this three-fold symmetric region has previously been shown to be preferentially oxidized under high-power laser irradiation and suggests that it contains a higher density of defects [[225](#)]. The observation of increased defect density has not been limited to the three-fold symmetric areas. Carozo *et al.* [[195](#)] measured defect densities in CVD grown WS_2 using scanning transmission electron microscopy and found that the edges of single crystals typically have higher sulphur vacancies than the interior of the crystal. More recently, Hu *et al.* [[240](#)] analysed CVD-grown WS_2 using PL and has found that the bright edges observed in PL are most likely due to oxygen chemically bonded to the edges. This was found when artificially created edges (scratched single crystal WS_2) were brightened in their PL response after heating at $200\text{ }^\circ\text{C}$ in an oxygen rich atmosphere. Though as with Gutiérrez *et al.* [[101](#)], no enhancement of the edge was observed after artificial edge creation in ambient, casting doubt as to whether the modification of the edge with oxygen is the culprit of increased edge PL response in freshly grown crystals [[240](#)]. In regards to the red-shifted PL regions, it has been demonstrated that short duration plasma treatments can increase defect density in WS_2 , creating a neutral exciton peak that is red-shifted in energy $\approx 0.1\text{ eV}$ below the ‘defect free’ neutral exciton peak at $\approx 2.03\text{ eV}$ (see [Figure 4.10c](#)) [[230](#)]. In that study, high resolution transmission electron microscopy

was performed and in conjunction with simulations, suggested that the red-shifted neutral exciton peak was due to single sulphur vacancies. These prior results suggest that the oxidation I observed in my experiments may have begun at three-fold symmetric regions, edge sites and red-shifted regions due to the increased defect densities contained there.

There is now overwhelming evidence that the most common structural defects present in S-TMDs are in the form of sulphur vacancies, and this is true (with the exception of atomic layer deposition grown samples) [262] whether the samples are exfoliated [262-264], grown via chemical vapor transport (CVD) [265] or, as in my case, CVD [195, 228, 261-262]. When sulphur vacancies are present on the surface of WS₂, oxygen dissociative chemisorption at these sites has been experimentally[266] and theoretically[267] shown to be favourable. Thus, by forming the initial seed centre, it is likely that sulphur vacancies chemisorbed with oxygen nucleate the oxidative growth of WO_x species.

In addition to the small (< 250 nm) triangular oxide islands formed (Figure 4.10e-f), we observed with the AFM small (< 65 nm) droplets in the centres of some of the triangular oxidation islands. The contents of these droplets are most likely aqueous H₂SO₄ (H₂SO₄ is hygroscopic) which forms one of the products in the oxidation of S-TMDs [22, 256, 258, 268-269]. Studies on the oxidation of MoS₂ have found traces of molybdic acid (MoO₃·H₂O and MoO_{2.4}·xH₂O, x = 0.7 - 1) [256, 269], although due to the low to negligible solubility of tungstic and molybdic oxides in water (or H₂SO₄) [269], it is unlikely that these droplets contain any significant quantities of tungstic acid. Not all triangular oxidation islands were observed to have a droplet in the middle of them, and this could be due to tungsten oxide forming in the absence of excess water.

However, the physical reasons behind the changes in PL intensity [177, 225-229] and peak position [177] observed in the PL of WS₂ (Figure 4.10a-d) remain unclear. In particular, some groups have considered strain from lattice mismatch between crystal and substrate to explain changes in PL, but have subsequently ruled out this strain due to the persistence of the threefold symmetric pattern upon transfer of the crystal to another substrate, which is thought to relieve strain in as-grown crystals [225, 227]. Since oxidation was also observed in a region in which the exciton (and trion) emission peak was red-shifted (see Figure 4.10a-d), it may be that the measured red-shifted peak has contributions from both the trion and a defected neutral exciton (due to sulphur vacancies); further studies are required for confirmation. What is clear, is that the results I have presented in this chapter indicate that the process of obtaining PL spectra in ambient conditions will necessarily form small oxide regions and hence, the analysis of the spectra could be affected by several associated mechanisms, for example, strain imparted to surrounding WS₂ developed during oxide formation [234]. Furthermore, the

direct consequence of oxidation on the PL response of WS₂ is to decrease significantly, *i.e.* quench the PL intensity, as shown in [Appendix A2](#).

Nonetheless, there is reason to believe most of these issues can be mitigated, as I have shown (see [Figure 4.15](#)) that illumination by light in a nitrogen atmosphere results in no measurable oxidation. Thus, performing PL in an inert environment is likely to be useful. Further work is needed, for example by growing crystals and performing PL in an inert environment or vacuum, and then exposing these crystals to ambient and light in order to determine the effect of defected regions on PL (see [Appendix A2](#)). Additional work is also needed to confirm the nature of the oxidation mechanism (FRET or photocatalysis) and whether defects are necessary to initiate the oxidation, or whether it can proceed in a defect-free basal-plane of WS₂ in ambient with light exposure. Further elucidation of the oxidation mechanism would enable accurate prediction of the oxidation rate, which would be valuable in other aspects of S-TMD research, and not limited to future oxidation studies.

4.6 Conclusion

The results I have presented in this chapter show that the physical mechanism that causes the oxidation of WS₂ in ambient conditions is a photoinduced, *i.e.*, photo-oxidation mechanism. Oxidation is observed to occur not randomly, but in three-fold symmetric areas extending from the centre of the triangular crystallites to the vertices (as shown by μ -PL/AFM), edges and areas in which there is an observed red-shift in exciton emission – as judged by μ -PL measurements. It is thought that all these areas contain more defects in the form of sulphur vacancies, where oxygen atoms can attach (chemisorb), and so provide a starting point from which oxidation can proceed. The fluence threshold that begins this photo-oxidation is at least four orders of magnitude lower than previously thought [22], $< 2.3 \times 10^6 \text{ J m}^{-2}$. Photo-oxidation does not occur when the samples are left in darkness, nor is significant oxidation visible when the WS₂ is exposed to wavelengths that are not absorbed appreciably – as found in the low-irradiance 760 nm experiment. Taking into consideration that oxidation is only observed upon excitation of an electronic transition, it is likely that no fluence threshold exists, and that oxidation occurs on a probabilistic basis. That is, lower light levels progress the reaction at much slower rates that are difficult to observe using the LSCM or AFM. Still, the results I have presented in this chapter already places severe constraints on the processing and analysis of S-TMD films in ambient conditions, since exposure to typical room light for extended periods (days), or exposure to a single typical scanning PL or Raman spectroscopy measurement (minutes) may cause significant oxidative damage. Furthermore, I expect that these findings will guide the

development of new nanofabrication techniques that completely avoid significant oxidation of S-TMDs, as the storage of S-TMDs in darkness or exposure to light that cannot excite electronic transitions should completely prevent progression of the oxidation reaction.

5

Chapter

Calcium Intercalation of Graphene on Silicon Carbide

Keywords: Epitaxial Graphene, Calcium, Intercalation, STM, LEED, XPS.

"Nothing has such power to broaden the mind as the ability to investigate systematically and truly all that comes under thy observation in life"
- MARCUS AURELIUS

5.1 Overview

The graphite intercalation compounds have long been studied as a way of increasing functionality in graphite – typically through increasing conductance. Recently, it has been shown that the Ca-intercalation of graphite has resulted in the highest temperature superconductor ever recorded in this class of materials [270-271]. Even more recently, these Ca-intercalation experiments have been repeated for graphene on SiC(0001) [18-19]. The Ca-intercalation of epitaxial graphene on SiC(0001) has been explored extensively, yet precisely where the Ca resides remains elusive, with conflicting reports existing [18-19, 23-24, 272].

Therefore, in this chapter I will first investigate the structure of Ca-intercalated epitaxial monolayer graphene on SiC(0001), ‘EMLG’, using low energy electron diffraction (LEED), synchrotron-based X-ray photoelectron spectroscopy (XPS) and scanning tunnelling microscopy (STM), and compare my experimental results with density functional theory calculations performed by my collaborators. I find that there is overwhelming evidence indicating Ca intercalates underneath the buffer layer and bonds to the Si-terminated SiC surface (forming a Ca-silicide type compound), breaking the C-Si bonds and ‘freestanding’ the buffer layer to form Ca-intercalated quasi-freestanding bilayer graphene (Ca-QFSBLG). Density functional theory calculations find that the lowest energy configuration is indeed Ca

intercalated underneath the buffer layer, in agreement with the experimental techniques employed in this chapter. This is further supported *via* the Ca-intercalation of hydrogen intercalated quasi-freestanding graphene on 6H-SiC(0001), in which the Ca is shown to replace the hydrogen bonded to the surface of the SiC (the results of which are shown and discussed in [Appendix B4](#)). The intercalation of Ca underneath the buffer layer is in stark contrast to previous reports [[18-19](#), [24](#)].

Finally, I investigate the electronic properties of Ca-QFSBLG using secondary electron cut-off photoemission spectroscopy (SECO) to find the workfunction; and compare the theoretical C 1s core level lineshape of highly doped graphene to the experimentally obtained C 1s core level lineshape of Ca-QFSBLG to estimate the carrier concentration. From these measurements, I find that Ca-QFSBLG is a low workfunction (3.71 ± 0.05 eV) and highly n-type doped ($\approx 10^{14}$ carriers cm^{-2}) graphene, in agreement with previous reports on the electronic structure of Ca-intercalated graphene on SiC.

Thus, this chapter forms the crucial groundwork needed to study the ambient-air stability of Ca-QFSBLG (see [Chapter 7](#)), by elucidating the structure and electronic properties of pristine Ca-QFSBLG, which until now has not been completely forthcoming.

5.2 Introduction

Graphene, the two dimensional (2D) allotrope of carbon consisting of a network of hexagonally bonded C atoms [[3](#)], possesses radically different properties than that of its bulk material (graphite), owing to its Dirac cone band structure at low energy (see [Chapter 2, Section 2.2](#) for details) [[273](#)]. In addition, considerable research has been conducted on the modification of graphene's properties *via* doping using techniques such as electrostatic gating [[274](#)], surface decoration [[275-276](#)], structure modification [[277](#)] and intercalation [[82](#)]. Of these methods, intercalation (*i.e.*, insertion of atomic or molecular species under or in-between graphene layers) has proven a powerful method for achieving the highest doping levels in graphene [[23, 278-279](#)]. Intercalation has enabled various investigations into the fundamental physics of superconductivity [[19, 23, 280](#)] and many-body interactions [[23, 278-279](#)] as well as potential applications such as highly conductive and transparent electrodes [[281](#)] and energy storage [[282](#)].

Historically, the study of the superconductivity of carbon-based material systems had its beginnings with the study of the graphite intercalation compounds (GICs), which can exhibit a range of diverse physical phenomena

dependent on the intercalant atom or molecule used [283]. In 1965, Hannay *et al.* [284] made some of the first observations of superconductivity in GICs using alkali intercalants (K, Rb and Cs) – although these GICs yielded a low superconducting transition temperature, $T_c \ll 1\text{ K}$.

More recently, interest in GICs was again re-ignited with the experiments of Emery *et al.* [271] and Weller *et al.* [270] in 2005 which, for the first time, used Ca as the intercalant to achieve the highest T_c of $\approx 11.5\text{ K}$ in this class of materials. With the discovery of graphene less than a year old [3], interest turned to performing the same intercalation experiments in low dimensional systems. Though for this to become an experimental reality, the exfoliated graphene originally obtained in ref. [3] could not be used, owing to the typically small ($< 100\text{ }\mu\text{m}^2$) size of the exfoliated graphene flakes. Standard surface science techniques such as scanning tunnelling microscopy (STM), low energy electron diffraction (LEED) or X-ray photoelectron spectroscopy (XPS) and angle resolved photoemission spectroscopy (ARPES), typically require large ($> 100\text{ }\mu\text{m}^2$) areas of uniform material. Thus, this type of experiment could only be realized with large area and uniform graphene, such as graphene grown on silicon carbide [52].

Graphene on SiC can be synthesised by heating 6H-SiC(0001) substrates at temperatures of $1250 - 1450\text{ }^\circ\text{C}$ for $1 - 20$ minutes in UHV [50-52]. The process decomposes the top layers of the SiC to elemental Si and C, and since the vapor pressure of silicon is higher than that of carbon, the silicon sublimates while the remaining (solid) carbon atoms form a hexagonal carbon network. More precisely, six layers of SiC are required to decompose for the synthesis of a single carbon layer (see [Chapter 2, Section 2.2.2](#)). The first layer of carbon is often termed the zero layer or buffer layer [60], and is bonded to the Si dangling bonds on the surface of the SiC(0001) [53, 64-65]. If the process of sublimation continues, then another buffer layer forms beneath, breaking the C-Si bonds of the original buffer layer, which then becomes monolayer graphene. Although this graphene growth method is relatively simple, there exist drawbacks such as poor layer control (due to rapid Si sublimation) and small crystal grain sizes [285]. The growth of graphene in argon overpressures (on the order of 10 to 1000 mbar) can overcome these inherent growth drawbacks observed in UHV synthesis [77]. This is due to the fact that argon over-pressures are able to decrease the sublimation rate of Si (yielding more control over the layer uniformity), and the higher temperatures ($> 1500\text{ }^\circ\text{C}$) increase the speed at which the SiC surface and carbon reconstructs prior to graphene formation (increasing surface quality) [77] – see [Chapter 2, Section 2.2.2](#) for details.

Initial experiments investigating Ca-intercalated graphene superconductivity (with ARPES) used graphene on SiC(0001) [23]. McChesney *et al.* [23] found that by Ca-intercalating islanded, *i.e.* partially grown monolayer graphene on SiC and decorating the surface with Ca (and K) atoms, the Fermi level (E_F) could be shifted high into the graphene conduction band, reaching the van

Hove singularity (VHS). Superconductivity with a high- T_c via conventional electron-phonon coupling [286], or unconventional electron-electron coupling [287-288], has been predicted in highly n-type doped graphene if the E_F is shifted high into the conduction band near the VHS. This scenario has analogies to the high- T_c cuprates, in which superconductivity is associated with the interaction between E_F and the VHS [289]. Thus, it was suggested that Ca-intercalated graphene could be a superconductor [23], as was the case with Ca-intercalated graphite [270-271]. Kanetani *et al.* [18] also suggested that Ca-intercalated bilayer graphene on SiC(0001) could be a superconductor, and based on STM measurements, implied that the calcium intercalated between the graphene layers. This was similar to the assumptions made by McChesney *et al.* [23], which assumed that the Ca intercalated only between the graphene sheets or between the buffer layer and 1st graphene layer (*i.e.* the buffer layer bonding to the Si was not disrupted by the intercalation).

Ichinokura *et al.* [19] used a similar method of intercalation to that of Kanetani *et al.* [18] in order to measure the electrical properties of Ca-intercalated bilayer graphene on silicon carbide. A superconducting transition of $T_c \approx 2$ K was measured, significantly lower than the previously measured T_c of Ca-intercalated graphite (≈ 11.5 K) [270-271] or multilayer graphene on SiC (3.4 – 7 K) [280]. Up until recently [24], the position of the Ca intercalant was assumed to lie between the graphene layers [18-19]. Using a similar method of Ca-intercalation to Kanetani *et al.* [18] and Ichinokura *et al.* [19], Endo *et al.* [24] determined that the Ca-intercalant position for bilayer graphene on SiC was between the buffer layer and 1st graphene layer, in contrast to these previous reports [18-19]. As is evident from the literature, the structure of Ca-intercalated graphene on SiC(0001) is conflicting, with recent reports in disagreement on the structure of Ca-intercalated graphene.

In this chapter, I present new findings on the structure of Ca-intercalated graphene on silicon carbide *via* the Ca-intercalation of epitaxial monolayer graphene (EMLG) (and hydrogen intercalated ‘quasi-freestanding’ bilayer graphene, ‘H-QFSBLG’ – see [Appendix B4](#)) on 6H-SiC(0001). I show that Ca intercalates underneath the buffer layer of EMLG, bonding with the Si-terminated surface of the SiC(0001) to form a Ca-silicide – ‘quasi-freestanding’ the buffer layer to create another graphene layer – *i.e.*, forming quasi-freestanding bilayer graphene (QFSBLG) above the Ca-silicide layer, which I term Ca-QFSBLG. As judged by LEED, the intercalated Ca forms a new ordered $(\sqrt{3} \times \sqrt{3})R30^\circ$ interface reconstruction with respect to the graphene. The observations are supported by density functional theory (DFT) calculations (performed by my collaborators), which show Ca under the buffer layer as the lowest energy configuration and in agreement with experimental structural data from the STM regarding height changes after Ca-intercalation. This finding is in contrast to all previous published data to-date regarding the structure of Ca-intercalated epitaxial graphene, which has assumed that the buffer layer remained intact [18-19, 23-24, 290].

Nonetheless, it is found that Ca-QFSBLG has a C 1s lineshape and exceptionally low workfunction (3.71 ± 0.05 eV) characteristic of a highly n-type doped graphene. This is in agreement with previous findings [19, 23] that have assumed Ca-intercalation taking place between carbon layers rather than the SiC – buffer layer interface.

5.3 Methods

The results were obtained *via* experiments at the Australian Synchrotron on the soft X-ray beamline end station (XPS, SECO, LEED – see [Figure 5.1](#)) and, at Monash University in Prof. Michael S. Fuhrer's laboratory (low temperature STM – see [Figure 5.2](#)) under UHV ($\approx 1 \times 10^{-10}$ mbar). All graphene samples were prepared by the U.S. Naval Research Laboratory using semi-insulating 6H-SiC(0001), nominally on-axis ($\approx 0.1^\circ$ deg offcut) from II-VI Incorporated. The EMLG samples were prepared using a previously described method [29].

In addition to the experiments on the Ca-intercalation of EMLG, I have studied the Ca-intercalation of H-QFSBLG, prepared using a previously described method [85]. I found that H-QFSBLG could also be Ca-intercalated and converted to Ca-QFSBLG, with almost identical result to Ca-QFSBLG formed from EMLG. I briefly discuss some of the results in this chapter, but leave most of the results and discussion for the interested reader in [Appendix B4](#).

5.3.1 Low Energy Electron Diffraction

LEED measurements were conducted at the Australian Synchrotron on the soft X-ray beamline using an 8-inch LEED spectrometer (OCI Vacuum Microengineering Inc.). Initial measurement coordinates on pristine samples were recorded, and for each subsequent intercalation / deposition, the same measurement positions were recorded. All measurements were taken at an electron energy of 100 eV. The location of the LEED optics is shown in [Figure 5.1a](#), and the sample holders used at the Australian Synchrotron are shown in [Figure 5.1b](#). It should be noted that all synchrotron experiments used sister samples (*i.e.* synthesised in the same run, from the same or similar SiC wafer), and thus the pristine samples in [Figure 5.3a](#) and [Figure 5.3c](#) are the sister samples of those in [Figure 5.3b](#) and [Figure 5.3d](#), respectively. The rotation of the LEED patterns observed in [Figure 5.3](#) is a direct result of these samples being mounted slightly differently (*i.e.* rotated) with respect to each other.

5.3.2 X-ray Photoelectron Spectroscopy

XPS data was taken at the soft X-ray beamline at the Australian Synchrotron ([Figure 5.1a](#)), with a PHOIBOS 150 (9 channeltrons) hemispherical analyser, shown more clearly in [Figure 5.1c](#). The setup at the Australian synchrotron is such that the angle between the incoming X-rays and the analyser is fixed at 55°, close to the ‘magic angle’ of $\approx 54.74^\circ$ [[140](#)]. Each recorded spectrum was energy calibrated using the Au 4f_{7/2} line at 84.0 eV from an Au foil in electrical contact with the sample. All core levels were taken with a pass energy of 5 eV.

I analysed the XPS data as follows. Inelastic contributions were removed from each XPS spectrum in by subtraction of a Shirley line shape (see [Chapter 3, Section 3.4.3.3](#)), except for the Ca 2p spectra ([Figure 5.7](#) and [Figure 5.8](#)) in which I used a spline-type subtraction due to the large inelastic background which could not be removed effectively with the Shirley or Tougaard background subtraction methods.

Furthermore, the Ca-intercalation experiments were conducted in two steps, named 1st Ca-intercalation and 2nd Ca-intercalation with both types of samples (EMLG/H-QFSBLG) being present at the same time (more details in [Section 5.3.4](#)). The results presented for the Si 2p and C 1s spectra in this chapter show pristine EMLG and the 2nd Ca-intercalation spectra (the omitted 1st Ca-intercalation step can be found in [Appendix B3](#) and [Appendix B4](#)).

The Si 2p spectra were obtained at $E_{hv} = 600$ eV (bulk sensitive) and 150 eV (surface sensitive) – and were fit with Voigt functions with a Lorentzian full width at half maximum (FWHM) of 0.1 eV and Gaussian FWHM of 0.4 or 0.5 eV. The Lorentzian FWHM of the EMLG samples, which was kept constant, was determined from the narrower Si 2p linewidths of pristine H-QFSBLG samples (see [Appendix B4](#)). The narrower linewidths were a consequence of the lack of higher binding energy components associated with silicon oxides, and thus, acted as standards in the experiment. Additionally, the area ratio of the Si 2p spin-orbit split peaks (and Mg 2p/Ca 2p core levels) was strictly kept as 2p_{1/2}:2p_{3/2} = 1:2 [[292](#)], and the spin-orbit splitting of the Si 2p core level was measured as $\approx 0.61 \pm 0.02$ eV (after allowing this parameter to vary in the fitting), in excellent agreement with previously measured values [[292-293](#)].

The C 1s ‘graphene’ peak (un-intercalated) was fit with a Briet-Wigner-Fano (BWF) asymmetric lineshape [[294](#)] (a type of asymmetric Lorentzian, see [Appendix B1](#) for further details); as this lineshape was found to fit component G more accurately than the often used Doniach-Šunjić lineshape [[295](#)]. Upon intercalation, the n-type doped graphene peak component G' was phenomenologically fit using a model that incorporated a BWF lineshape

along with the addition of 3 Voigt functions (the details of which can be found in [Appendix B3](#)), as this was an approximation of the plasmon effects on lineshape recently described [[25](#), [296](#)]. The width and asymmetry of the BWF lineshape were kept relatively consistent, with only small changes in the asymmetry parameter (Q) being allowed in order to optimise the fit (for the pristine samples only). All C 1s core level SiC-related components were fit with Voigt lineshapes using a Gaussian width of 0.4 eV and Lorentzian width of 0.2 eV [[297](#)] (resulting in a FWHM = 0.52 eV, all parameters are outlined in [Table 5-2](#) and [Table B.2-1](#)). Care was taken to keep the Gaussian and Lorentzian contributions constant, *i.e.* the width of the Voigt functions did not change for the same components. Additionally, stringent conditions were placed on the binding energy location of the fitted peaks, which typically did not vary more than the uncertainty of the measurement, taken as ± 0.05 eV. The position of each component was calculated by averaging the available measurements of the same component (in the same sample) across the various X-ray energies (E_{hv}). If the standard deviation was higher than the instrumental uncertainty (*i.e.* > 0.05 eV), then the standard deviation was taken as the uncertainty in the measurement.

To semi-quantitatively assess the surface sensitivity of the fitted components, the relative intensity (RI) was calculated by using the bulk SiC components of EMLG – B_{Si}/B_C as the intensity reference (*i.e.* the RI of B_{Si} and $B_C = 1$). The RI ratio (RI_R) was then used to calculate a semi-quantitative measure of the surface sensitivity of a particular component by division of the lower E_{hv} RI with the RI of the same component at higher E_{hv} . In this regime, an $RI_R > 1$ signifies a more surface-like component, and an $RI_R \leq 1$ signifies a more bulk-like component – see [Appendix B1](#) for details.

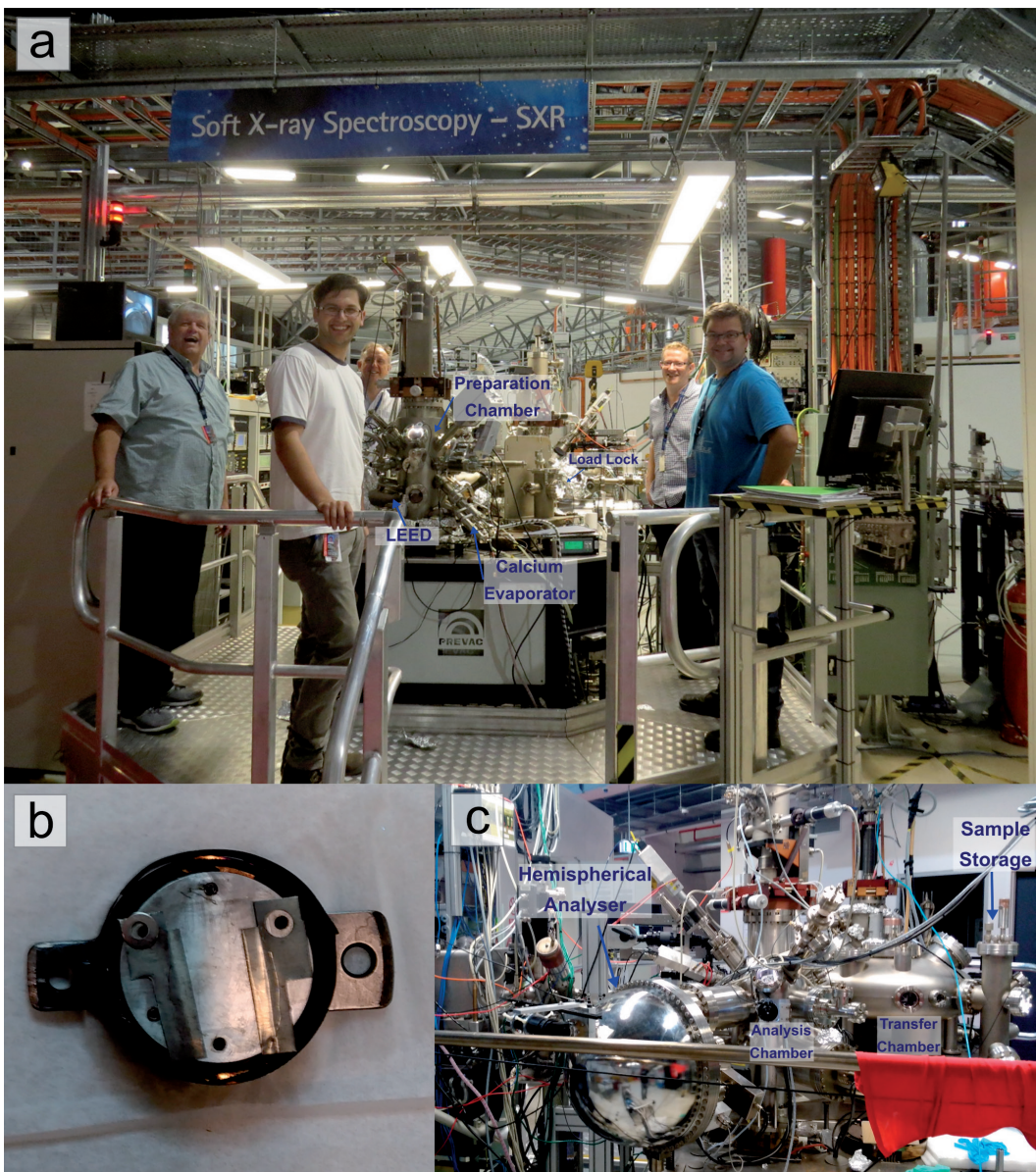


FIGURE 5.1: SOFT X-RAY BEAMLINE SETUP AT THE AUSTRALIAN SYNCHROTRON.

(a) Beamline experimental setup showing position of low energy electron diffraction (LEED) optics and Ca evaporator attached to the preparation chamber, as well as load lock where samples are introduced. (b) Typical sample holder used. These sample holders have a thermocouple attached to them (wire in top hole) and in-built heating element from which the samples were annealed. (c) Backside of the experimental setup showing the PHOIBOS 150 hemispherical analyser, analysis chamber, transfer chamber and sample storage area.

5.3.3 Scanning Tunnelling Microscopy

All STM images were taken with a Createc low temperature STM, shown in [Figure 5.2](#). Micrographs shown in [Figure 5.9a-b](#) were taken at 77 K, whereas [Figure 5.9c](#) was taken at 4.6 K. In [Figure 5.9](#), a cut 0.3 μm diameter Pt-Ir tip was used. STM Micrographs were analysed using WSxM [223].

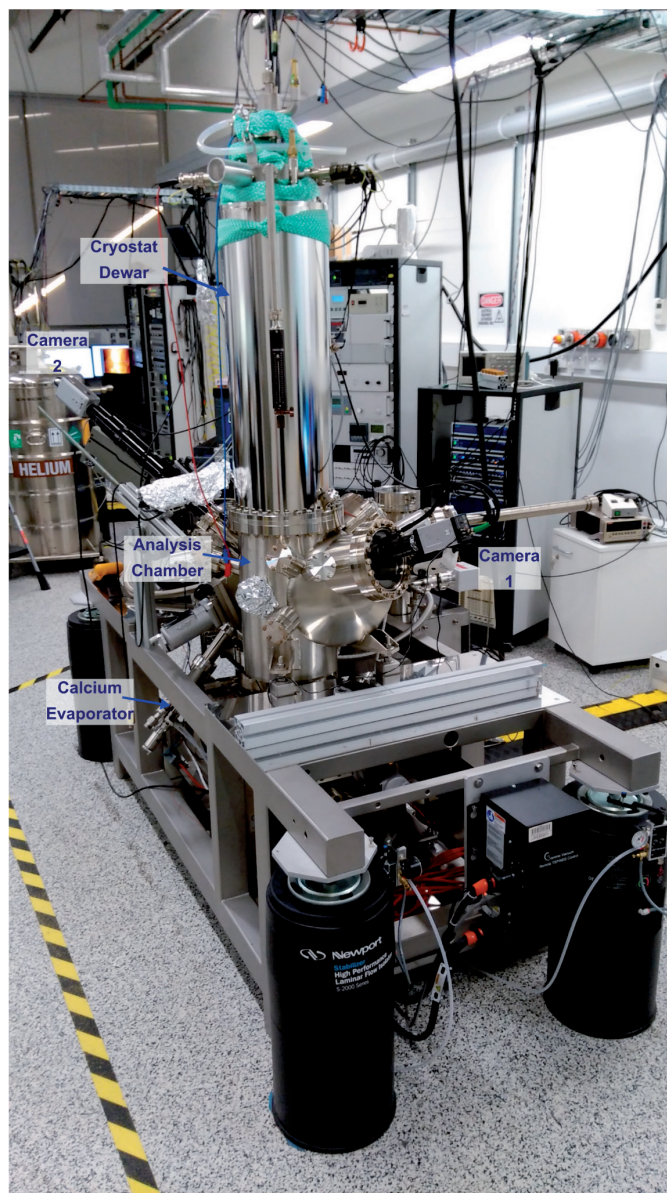


FIGURE 5.2: CREATEC LOW TEMPERATURE SCANNING TUNNELLING MICROSCOPE (STM).

The low temperature STM in Prof. Fuhrer's Laboratory at Monash University showing important features. Camera 1 is used for coarse adjustment, whereas camera 2 is used for fine adjustment of the tip position.

5.3.4 Ca-Intercalation Procedure

Two types of graphene samples were used in the synchrotron experiments – epitaxial monolayer graphene synthesized on semi-insulating 6H-SiC(0001) (EMLG) [291] and hydrogen intercalated bilayer graphene synthesized on semi-insulating 6H-SiC(0001) (H-QFSBLG) [85]. H-QFSBLG results are discussed in [Appendix B4](#). The synthesis details of the EMLG and H-QFSBLG samples can be found in [Chapter 2, Section 2.2.2](#).

In the experiment, these samples were mounted side-by-side (on the sample holder shown in [Figure 5.1b](#)) so that the amount of deposited calcium and annealing procedure was equal in both cases. It is well known that high temperature annealing can cause removal *i.e.* de-intercalation of the hydrogen in H-QFSBLG (at $\approx 973\text{K}$, hydrogen intercalated graphene has been shown to undergo band structure changes, as observed using angle resolved photoemission spectroscopy [82]). It has also recently been shown by Khademi *et al.* [298] that higher annealing temperatures ($\approx 900\text{ K}$) facilitates higher doping concentrations when lithium is deposited onto epitaxial graphene surfaces; attributed to increased surface cleanliness. Since both EMLG and H-QFSBLG samples were mounted together, a trade-off was made. To ensure no de-intercalation and clean surfaces, all samples were annealed in UHV ($\approx 1 \times 10^{-10}\text{ mbar}$) between 673 and 773 K (determined with a single-colour pyrometer – LumaSense Technologies, IMPAC 8 Pro series – *and* thermocouple) for approximately 8 hours prior to measurement (XPS/LEED/SECO) and Ca-intercalation. All alkaline earth metal depositions were then undertaken while the samples were at room temperature.

The intercalation procedure at the Australian Synchrotron (in which the LEED, XPS and SECO measurements were taken) is as follows. For Ca-intercalation, samples ($\approx 4 \times 4\text{ mm}^2$) were mounted on the same sample holder ([Figure 5.1b](#)), consisting of 2 EMLG and 2 H-QFSBLG samples. Approximately 6 nm of Ca was deposited (as judged by a quartz crystal monitor, QCM) using a WEZ effusion cell (MBE Komponenten) loaded with Ca metal (dendritic pieces, 99.99%, Sigma-Aldrich) in a pyrolytic boron nitride (PBN) crucible. The deposition required heating of the crucible to $\approx 698\text{ K}$ and exposure of 15 minutes to the Ca flux. After deposition, the sample was heated at $\approx 753\text{ K}$ for 1.5 hours to intercalate and clean the sample surface. This procedure constituted the 1st Ca-intercalation step. This intercalation procedure was then repeated for the 2nd Ca-intercalation step, except the anneal temperature was $\approx 736\text{ K}$. All intercalation step data is shown in [Appendix B](#), whereas in this Chapter, I focus on results for only the pristine EMLG samples and final Ca-intercalation step.

The Ca-intercalated graphene sample studied by STM ([Figure 5.9](#)) was prepared as follows. An EMLG sample was cleaned in the STM UHV ($\approx 1 \times 10^{-10}\text{ mbar}$)

10 mbar) chamber by annealing at ≈ 743 K for 1.2 hours (all temperatures were determined with a 2-color pyrometer). The depositions were carried out with a Createc effusion cell using a PBN crucible loaded with Ca (dendritic pieces, 99.99 %, Sigma-Aldrich) that was baked at 473 K overnight prior to depositions. In the 1st intercalation (Figure 5.9b), ≈ 1 nm of Ca was deposited while the sample was held at room temperature (all thicknesses were determined with a QCM). After deposition, the sample was heated to a temperature of 653 K, held for 10 minutes, after which the sample was ramped to ≈ 743 K and held at this temperature for 1.5 hours to facilitate intercalation and remove excess surface Ca. For the 2nd Ca-intercalation, another 1 nm of Ca was deposited after re-calibration with the QCM. After deposition, the sample was heated to ≈ 653 K and held for 30 minutes, then ramped to ≈ 743 K and held for 1 hour before allowing the sample to cool naturally.

5.3.5 Secondary Electron Cut-Off Photoemission Spectroscopy

Secondary electron cut-off photoemission spectrograms (SECO) (Figure 5.13) were taken at $E_{hv} = 100$ eV (at a pass energy of 2 eV) to find the workfunction (W_f) of the clean and Ca-intercalated graphene samples. A bias of -9 V was applied to the sample in order to effectively measure the low energy cut-off, and all samples were measured with the surface normal perpendicular to the entrance plane of the analyser – as this is known to increase the accuracy of W_f measurement [137]. The W_f was then determined by the intersection of 2 linear fits to the steep edge and background, as is common with SECO determinations of the W_f [144, 299].

5.4 Results and Discussion

The results and discussion are organised according to characterisation techniques in the order of LEED, XPS, STM, density functional theory (DFT) calculations (see ref. [300] for details), comparison of the C 1s lineshape to highly doped graphene and SECO (workfunction) measurements. I first analyse the LEED spectra of *both* Ca-intercalated EMLG and Ca-intercalated H-QFSBLG and demonstrate that both result in identical LEED diffraction patterns after Ca-intercalation, from which I infer that the resulting intercalated structure is similar.

Then, in the interest of brevity, I will present only the XPS/STM/DFT/C 1s lineshape/SECO data from the Ca-intercalated EMLG samples, and leave the discussion of the Ca-intercalated H-QFSBLG results (which are almost identical to the Ca-intercalated EMLG case) to [Appendix B4](#) for interested readers.

5.4.1 Low Energy Electron Diffraction

[Figure 5.3](#) shows the LEED images taken at an electron energy of 100 eV for both pristine EMLG/H-QFSBLG and Ca-intercalated EMLG/H-QFSBLG. [Figure 5.3a](#) shows a typical pristine EMLG sample with graphene (G(1x1)) and SiC (SiC(1x1)) spots, as well as the expected $(6\sqrt{3}\times 6\sqrt{3})R30^\circ$ and (6x6) spots (relative to the SiC) which originate from the buffer layer – SiC interaction [[172](#)].

The Ca-intercalated EMLG sample is shown in [Figure 5.3b](#). It is observed that the relative intensity of the SiC(1x1) to the G(1x1) spots after Ca-intercalation is greatly reduced. This is in contrast to the similar intensity of the G(1x1) and SiC(1x1) spots in pristine EMLG prior to intercalation ([Figure 5.3a](#)). Secondly, the $(6\sqrt{3}\times 6\sqrt{3})R30^\circ$ spots are strongly suppressed in the Ca-intercalated sample, when compared to pristine EMLG ([Figure 5.3a](#)). These observations are similar to the case of pristine H-QFSBLG after H-intercalation of EMLG shown in [Figure 5.3c](#), which is known to decouple the buffer layer [[60](#)], and thus, suggests that the buffer layer of the EMLG is similarly decoupled after Ca-intercalation and transformed to QFSBLG (*i.e.* Ca-QFSBLG). Consequently, our LEED results present the first evidence that intercalation of Ca occurs between the SiC(0001) surface and the buffer layer, for *both* EMLG/H-QFSBLG starting samples, in disagreement with previous reports. I note that the weak $(6\sqrt{3}\times 6\sqrt{3})R30^\circ$ spots after Ca-intercalation (shown in [Figure 5.3b](#) and [Figure 5.3d](#)), are also observed after H-intercalation (see

[Figure 5.3c](#)) [82], and likely result from incomplete (*i.e.* partial) intercalation [301].

Furthermore, [Figure 5.3b](#) and [Figure 5.3d](#) show the emergence of $(\sqrt{3} \times \sqrt{3})R30^\circ$ spots with respect to the $G(1 \times 1)$ spots after Ca-intercalation (which are labeled ‘ $G(\sqrt{3} \times \sqrt{3})R30^\circ$ ’, and do not fall onto the $6\sqrt{3} \times 6\sqrt{3}$ grid). Previous Ca-intercalation studies [18] also reported $G(\sqrt{3} \times \sqrt{3})R30^\circ$ spots and interpreted these as due to Ca atoms intercalating between the graphene layers. Yet the $G(\sqrt{3} \times \sqrt{3})R30^\circ$ spots are not definitive evidence for intercalation between the graphene layers, as their emergence has been observed after the intercalation of Yb in buffer-layer-only samples to form ‘quasi-freestanding’ monolayer graphene on SiC [279]. Thus, it is plausible that the $G(\sqrt{3} \times \sqrt{3})R30^\circ$ spots instead describe a Ca-QFSBLG structure. As discussed further in the proceeding sections of this chapter, the prior interpretation is incorrect, and the Ca indeed lies between the SiC(0001) surface and the buffer layer.

The LEED spot patterns have elucidated the overlaying symmetries resulting from Ca-intercalation of EMLG *and* H-QFSBLG and suggest that Ca intercalates underneath the buffer layer (in the case of EMLG) or the 1st graphene layer (in the case of the H-QFSBLG) to form Ca-QFSBLG in both cases. We can begin to form an atomic model of the situation. In the case of the EMLG sample, it is likely that Ca intercalates and breaks the C-Si bonds of the buffer layer – SiC surface, whereas in the H-QFSBLG case, hydrogen is displaced by the calcium. Nonetheless, LEED alone cannot determine the chemistry occurring underneath the graphene, and so a technique such as XPS must be employed to investigate the chemical changes occurring underneath the graphene. Below, I first discuss the Si 2p, C 1s, O 1s and Ca 2p core level XPS spectra of Ca-QFSBLG resulting from the Ca-intercalation of EMLG (further discussion of Ca-intercalated H-QFSBLG is relegated to [Appendix B4](#), as the results are almost identical to Ca-intercalated EMLG), before discussing the surface morphology as imaged by STM and density functional theory calculations concerning the calculated structure of Ca-QFSBLG.

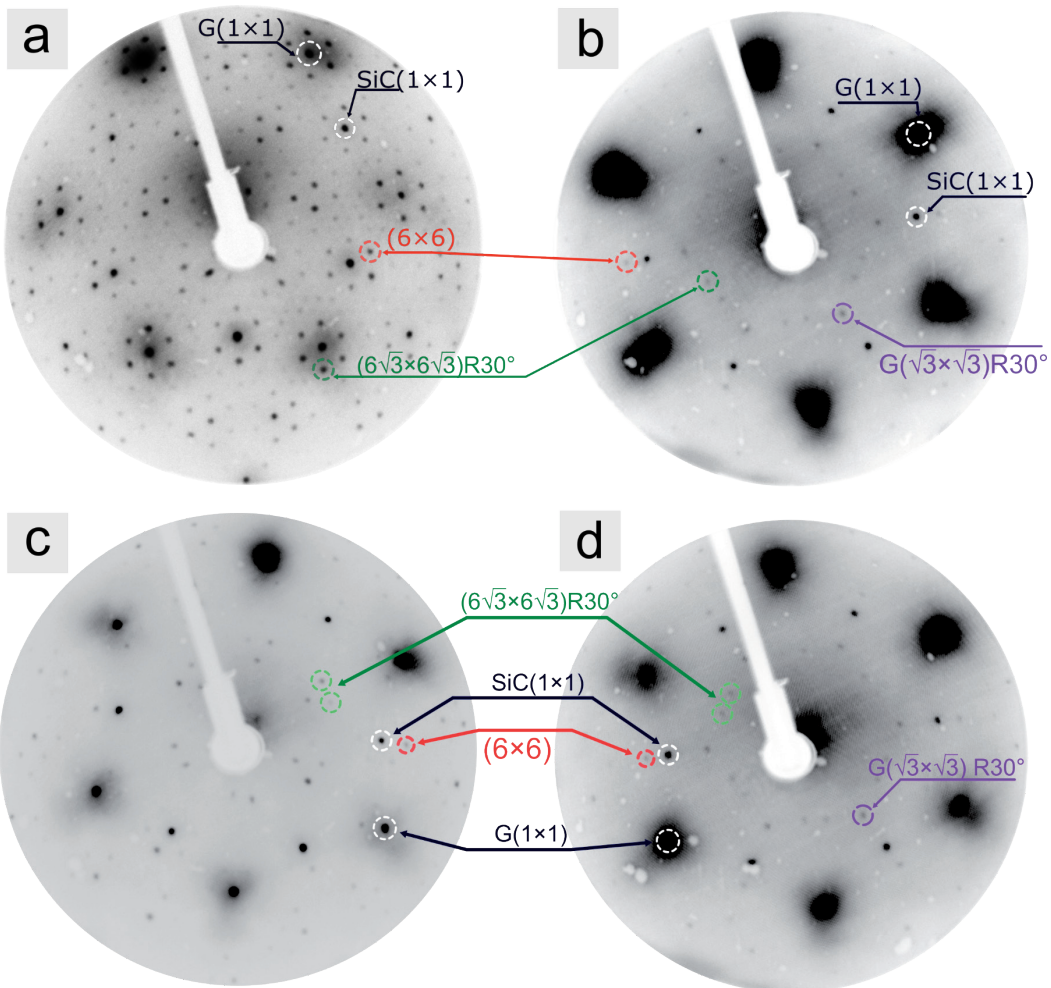


FIGURE 5.3: LOW ENERGY ELECTRON DIFFRACTION (LEED) OF PRISTINE AND Ca-INTERCALATED GRAPHENE ON 6H-SiC(0001) AT AN ELECTRON ENERGY OF 100 eV.

(a) Pristine epitaxial monolayer graphene on 6H-SiC(0001) (EMLG) prior to Ca-intercalation showing graphene ($G(1\times 1)$) and SiC ($SiC(1\times 1)$) spots, as well as $(6\sqrt{3}\times 6\sqrt{3})R30^\circ$ and (6×6) spots arising from the buffer layer. **(b)** Ca-QFSBLG after Ca-intercalation of EMLG from (a) showing the emergence of $(\sqrt{3}\times\sqrt{3})R30^\circ$ spots with respect to the $G(1\times 1)$ spots ($G(\sqrt{3}\times\sqrt{3})R30^\circ$). **(c)** Pristine hydrogen intercalated quasi-freestanding bilayer graphene on 6H-SiC(0001) (H-QFSBLG) showing $G(1\times 1)$ and $SiC(1\times 1)$ spots as well as contributions $((6\sqrt{3}\times 6\sqrt{3})R30^\circ$ and (6×6) spots) from incomplete H-intercalation. **(d)** Ca-QFSBLG after Ca-intercalation of H-QFSBLG from (c).

5.4.2 X-ray Photoelectron Spectroscopy of Ca-QFSBLG

Here I present and discuss the XPS results for the C 1s, Si 2p, O 1s and Ca 2p core levels for the same EMLG sample, the LEED of which is shown in [Figure 5.3b](#). H-QFSBLG samples were also Ca-intercalated using the same method as for the EMLG samples, and showed almost identical XPS spectral features – see [Appendix B4](#) for details.

5.4.2.1 Si 2p Core Level Spectra

[Figure 5.4](#) shows the Si 2p core level XPS spectrum – photoemission intensity as a function of binding energy, E_B – before and after Ca-intercalation. For all XPS plots, experimental data points are shown as open black circles, and the final fit is overlaid as a red line. Each Si 2p component is comprised of $2p_{3/2}$ and $2p_{1/2}$ peaks coloured identically for the same compound to avoid confusion, and I quote only (averaged – see [Section 5.3.2](#)) E_B values corresponding to the $2p_{3/2}$ peak. Fit parameters of the major components are given in [Table 5-1](#); the full set of fit parameters (which includes the omitted 1st Ca-intercalation step) can be found in [Appendix B4](#).

[Figure 5.4a-b](#) shows the Si 2p core level spectra of pristine EMLG. The tunability of the synchrotron source allowed for different X-ray energies ($E_{hv} = 150$ eV, 600 eV) to be used in order to determine the surface and bulk nature of the various components, aiding greatly in spectrum deconvolution. Pristine EMLG shows two major components: B_{Si} ($E_B = 101.47 \pm 0.05$ eV) corresponds to “bulk” SiC [82, 302-303], and Z_{Si} ($E_B = 101.83 \pm 0.05$ eV) to surface Si bonded to the C in the buffer layer/zero layer [82, 297, 304]. (The components corresponding to compounds present in both the Si 2p and C 1s XPS spectra are designated using the same label, with different subscript labels, in order to distinguish the specific core level, *i.e.*, B_{Si} and B_C are the bulk SiC signals in the Si 2p and C 1s spectra, respectively). The corresponding atomic positions are shown schematically in the insets of [Figure 5.4a-b](#). These positions are determined by a calculation of the relative intensity ratio, RI_R , discussed in more detail in [Section 5.3.2](#) and [Appendix B1](#). The RI_R is a semi-quantitative measure of surface sensitivity, with an $RI_R > 1$ indicating that the component is more towards the surface. For instance, the RI_R of component Z_{Si} is 1.25 [$RI(150\text{ eV})/RI(600\text{ eV}) = 0.4/0.32 = 1.25$], and implies a more surface origin for this component. Additional components – Ox_o , A_o , A_1 and A_2 are seen with intensities <8% relative to component B_{Si} , and likely result from oxygen contamination (Ox_o) and silicon adatoms (A_o , A_1 , A_2). These components, along with components Ox_1 and Ox_2 (which are thought to arise from differing Ca-Si stoichiometry), are in small concentration, and thus, are

not significant for the determination of the general Ca-intercalated structure. I refer the reader to [Appendix B3](#) for further discussion of these features.

[Figure 5.4c-d](#) shows the Si 2p XPS spectra of Ca-QFSBLG formed by Ca-intercalation of the sample in [Figure 5.4a-b](#). Only the 2nd Ca-intercalation step is shown, and the results of the intermediate intercalation step – which do not affect the conclusions presented here – can be found in [Appendix B3](#). Upon comparison with pristine EMLG, it is observed that most of the bulk component, B_{Si}, has disappeared, and has been replaced by several components at lower binding energy.

Component C_{Si} is highly surface-like, with an $RI_R = 4$. It is substantially shifted relative to component B_{Si} (and Z_{Si}) of pristine EMLG by $\Delta E_B = 2.18 \pm 0.11$ eV, suggesting a significant chemical change at the Si surface. Its binding energy of $E_B = 99.29 \pm 0.06$ eV, is similar to that of a Ca-silicide [305-306]. This is strong evidence for a Ca-Si bonding environment at the SiC surface underneath the graphene and buffer layer, and is in contrast with previous reports that Ca intercalates between the graphene layers [18-19], or between the buffer layer and the 1st graphene layer [23-24].

In fact, many reports have been made on the intercalation of alkalis [70, 307-308], transition metals [72, 309-310], rare earths [278-279, 311] and various elements [71, 297, 312-315] underneath the buffer layer (see ref. [316] for a brief review of intercalation of graphene on SiC). Furthermore, many prior reports on the intercalation of graphene on SiC have specifically reported the formation of silicide-like compounds [72, 310, 313, 315, 317-319], and thus, it is not surprising that a surface Si component matching closely in binding energy with that of a Ca-silicide is observed. The observation of a Ca-Si chemical interaction implies disruption of the Si-C bonds on the SiC(0001) surface with the C-rich buffer layer, and is supported by the LEED intensity suppression of the (6 $\sqrt{3}$ ×6 $\sqrt{3}$)R30° spots (which arise from the buffer layer), and an increase in the intensity of the G(1x1) spots relative to the SiC(1x1) spots which indicates decoupling of the buffer layer to form another layer of graphene (see [Figure 5.3](#)). Hence, both XPS and LEED observations are consistent with the formation of a Ca-Si compound and a new graphene layer.

Two other major peak components in [Figure 5.4c-d](#) include components B'__{Si} and Z'__{Si} located at binding energies of $E_B = 100.07 \pm 0.05$ eV and $E_B = 100.48 \pm 0.07$ eV, respectively. These new components are shifted equally in binding energy relative to B_{Si} and Z_{Si} by 1.4 ± 0.1 eV (B_{Si}→B'__{Si}) and 1.35 ± 0.12 eV (Z_{Si}→Z'__{Si}), and are separated equally in binding energy – 0.36 ± 0.1 eV (Z_{Si}→B'__{Si}) and 0.41 ± 0.12 eV (Z'__{Si}→B'__{Si}) to within error. The RI_R of these components suggests that B'__{Si} ($RI_R = 0.35$) is in the bulk, while Z'__{Si} ($RI_R = 1.1$) is closer to the surface. This situation is illustrated with the atomic model inset in [Figure 5.4d](#), and further supports that components B_{Si} (Z_{Si}) and B'__{Si} (Z'__{Si}) are simply binding energy-shifted equivalents of each other. The shift to

lower binding energy of SiC components is typically observed in the intercalation of graphene on silicon carbide systems and is caused by significant band bending upon intercalant insertion beneath the buffer layer [71-72, 82, 297, 312, 320-322].

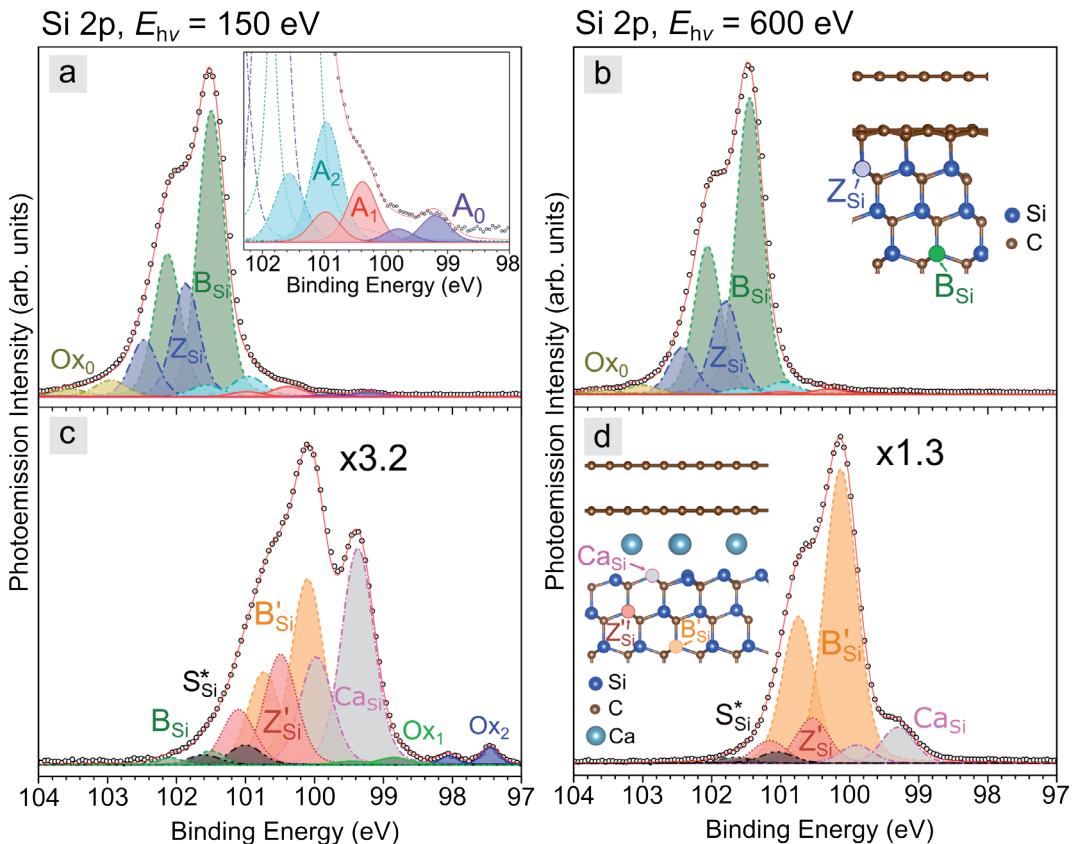


FIGURE 5.4: X-RAY PHOTOEMISSION SPECTRA OF THE Si 2P CORE LEVEL OF PRISTINE EPITAXIAL MONOLAYER GRAPHENE (EMLG) AND CALCIUM INTERCALATED QUASI-FREESTANDING BILAYER GRAPHENE ON SILICON CARBIDE (Ca-QFSBLG) AT TWO INCIDENT X-RAY ENERGIES, $E_{hv} = 150$ eV (LEFT, SURFACE SENSITIVE) AND 600 eV (RIGHT, BULK SENSITIVE).

(a), (b) Pristine EMLG before intercalation showing all components. Component B_{Si} is the bulk component of SiC, whereas component Z_{Si} is a more surface SiC component. The approximate atom locations of components B_{Si} and Z_{Si} are shown in the inset of (b). (c), (d) Shows EMLG after Ca-intercalation (Ca-QFSBLG) and new components Ca_{Si} , B'_{Si} , Z'_{Si} and S^{*}_{Si} . Components Z_{Si} and B_{Si} have been shifted to lower binding energy and are now labelled Z'_{Si} and B'_{Si} , respectively. Figure 5.4c has its y-scale magnified $\times 3.2$ from Figure 5.4a, and Figure 5.4d has its y-scale magnified $\times 1.3$ from Figure 5.4b. The approximate atom positions of the major components are shown in the inset of Figure 5.4d; see text for further explanation of the components.

TABLE 5-1: SUMMARY OF THE FIT PARAMETERS FOR THE MAJOR COMPONENTS IN FIGURE 5.4.

Both Si $2p_{3/2}$ and $2p_{1/2}$ peak locations are given, as well as the relative intensity (RI) of the $2p_{3/2}$ peaks as referenced to the bulk SiC peak ‘ B_{Si} ’ corresponding to pristine SiC prior to Ca intercalation. G_w refers to the Gaussian FWHM for the Voigt fit (which was fixed to one of two values, except for component Ox_2), whereas the Lorentzian FWHM (W_L) was kept constant at 0.1 eV in all fits. Dash line corresponds to no observation.

EMLG, Si 2p		(a), (b), Pristine EMLG				(c), (d) 2 nd Ca Intercalation			
Component	E_{hv} (eV)	E_B (eV) $2p_{3/2}$	E_B (eV) $2p_{1/2}$	RI	G_w (eV)	E_B (eV) $2p_{3/2}$	E_B (eV) $2p_{1/2}$	RI	G_w (eV)
B_{Si}	150	101.50	102.13	1	0.4	101.45	102.05	0.016	0.4
	600	101.45	102.06	1	0.4	-	-	-	-
Z_{Si}	150	101.86	102.47	0.40	0.4				
	600	101.80	102.43	0.32	0.4				
Ox_o	150	102.95	103.55	0.06	0.5				
	600	102.95	103.55	0.03	0.5				
B'_{Si}	150					100.11	100.74	0.24	0.5
	600					100.13	100.74	0.68	0.5
Z'_{Si}	150					100.51	101.13	0.12	0.5
	600					100.54	101.16	0.10	0.5
S^*_{Si}	150					101	101.63	0.02	0.5
	600					101.05	101.65	0.026	0.5
Ca_{Si}	150					99.37	99.97	0.24	0.5
	600					99.30	99.90	0.08	0.5
Ox_1	150					98.85	99.45	0.008	0.5
	600					-	-	-	-
Ox_2	150					97.45	98.05	0.02	0.25
	600					-	-	-	-

5.4.2.2 C 1s Core Level Spectra

[Figure 5.5](#) (component fit parameters shown in [Table 5-2](#)) shows the C 1s core level spectra before and after Ca-intercalation of the same EMLG sample as in [Figure 5.3b](#) and [Figure 5.4](#). An E_{hv} of 330 eV and 600 eV was used to characterize surface and bulk components, respectively. [Figure 5.5a-b](#) shows the pristine EMLG sample prior to intercalation, consisting of 5 components. Component G located at $E_B = 284.83 \pm 0.05$ eV, corresponds to graphene, in agreement with prior reports [53].

Components S₁ ($RI_R = 10.48$) and S₂ ($RI_R = 11.73$) are due to Si-C bonds from the buffer layer to the underlying SiC and C-C bonds in the buffer layer, respectively [53, 82], and have an intensity ratio of $S_2:S_1 \approx 2:1$, in agreement with previous findings [53]. Additionally, two components at lower binding energy are resolved – components Z_C and B_C. These components are related to the carbon in the SiC surface and bulk, respectively. Component B_C at $E_B = 283.73 \pm 0.05$ eV ($RI_R = 1$, used as the RI reference) represents the well-known EMLG bulk component of SiC, and agrees well in binding energy with prior measurements [53, 302]. There is also evidence of a surface-like component, Z_C, related to the carbon in SiC at $E_B = 284.05 \pm 0.05$ eV ($RI_R = 1.74$) – particularly evident from the asymmetry of the SiC peak in [Figure 5.5b](#). Component Z_C has been fitted in previous reports in order to explain the different bonding environment of carbon towards the surface of the SiC [297, 304] (see [Appendix B3](#) for further discussion of component Z_{Si}/Z_C). The shift of Z_C relative to B_C of $\Delta E_B = 0.32 \pm 0.1$ eV, agrees with the shift observed in the Si 2p spectra (Z_{Si}→B_{Si}) and suggests a similar chemical environment for these components. The inset in [Figure 5.5a](#) shows components Z_C and B_C more clearly at $E_{hv} = 150$ eV, and the inset of [Figure 5.5b](#) shows the approximate location of all components in an atomic model.

[Figure 5.5c-d](#) shows the C 1s XPS spectra for the same sample after Ca-intercalation. It is immediately apparent from the lineshape of the C 1s that components S₁ and S₂ are either no longer present, or significantly reduced in amplitude, implying the absence (or near elimination of) bonding between the SiC and buffer layer. Moreover, although significantly suppressed in intensity, components B_C and Z_C are still present in the Ca-intercalated spectra. This agrees with the Si 2p core level spectra in [Figure 5.4c-d](#) (which showed the presence of component B_{Si}) and LEED ([Figure 5.3b](#)) suggesting partial intercalation, similar to that observed with hydrogen intercalation [301].

The graphene peak, now labelled G' located at $E_B = 284.88 \pm 0.05$ eV, is not shifted significantly (within measurement error) with respect to the original EMLG graphene component G ($E_B = 284.83 \pm 0.05$ eV), although from prior Ca-intercalation experiments [19, 23], significant n-type doping of the

graphene is expected. On the other hand, I do observe changes in the lineshape of the graphene component, which is significantly broadened and more asymmetric. This increase in asymmetry of the G' peak is predicted to arise in highly doped graphene due to 2D plasmon losses [25, 296] (see [Appendix B3](#) and [Section 5.4.5.1](#) for details), and suggests that the doping level of the graphene has increased significantly. The sign of these excess carriers is most certainly n-type, as will be discussed in [Section 5.4.5](#).

Nonetheless, it is observed that the bulk component B_C and the associated surface component of the bulk, Z_C , have been shifted to lower binding energy – labelled as components B'_C ($E_B = 282.33 \pm 0.05$ eV) and Z'_C ($E_B = 282.70 \pm 0.05$ eV). The respective shifts in E_B are -1.40 ± 0.1 eV ($B_C \rightarrow B'_C$), -1.35 ± 0.1 eV ($Z_C \rightarrow Z'_C$), with a separation between components of 0.32 ± 0.1 eV ($Z_C \rightarrow B'_C$) and 0.37 ± 0.1 eV ($Z'_C \rightarrow B'_C$). These shifts are in good agreement with the shifts in E_B for the analogous Si 2p components in [Section 5.4.2.1](#), and thus gives confidence in the assignment of components B'_C/B_{Si} and Z'_C/Z_{Si} as the shifted components B_C/B_{Si} and Z_C/Z_{Si} , brought about by band bending effects induced by the creation of Ca-Si on the SiC(0001) surface.

An additional component, which I label S'_C , is evident in the Ca-intercalated spectra, located at $E_B = 283.26 \pm 0.05$ eV, shifted from component B_C by 0.47 ± 0.1 eV. An analogous component was observed in the Si 2p core level spectrum ([Figure 5.4c-d](#)), S'_{Si} at $E_B = 101.01 \pm 0.05$ eV, shifted to higher binding energy from component B_{Si} by 0.47 ± 0.1 eV. This equivalence in binding energy shift across both core levels suggests that these components are from the same SiC compound. The E_B value of component S'_C agrees well with sub-stoichiometric values of SiC [323]. Indeed, judging from [Figure 5.5c-d](#), it can be seen that S'_C ($RI_R = 8.25$) is a surface component (hence the “S” assignment), and thus could be a result of SiC unreacted with Ca, yielding a C-rich SiC compound residing at the surface (and thus, explaining the relatively smaller $RI_R \approx 1$ in the Si 2p core level).

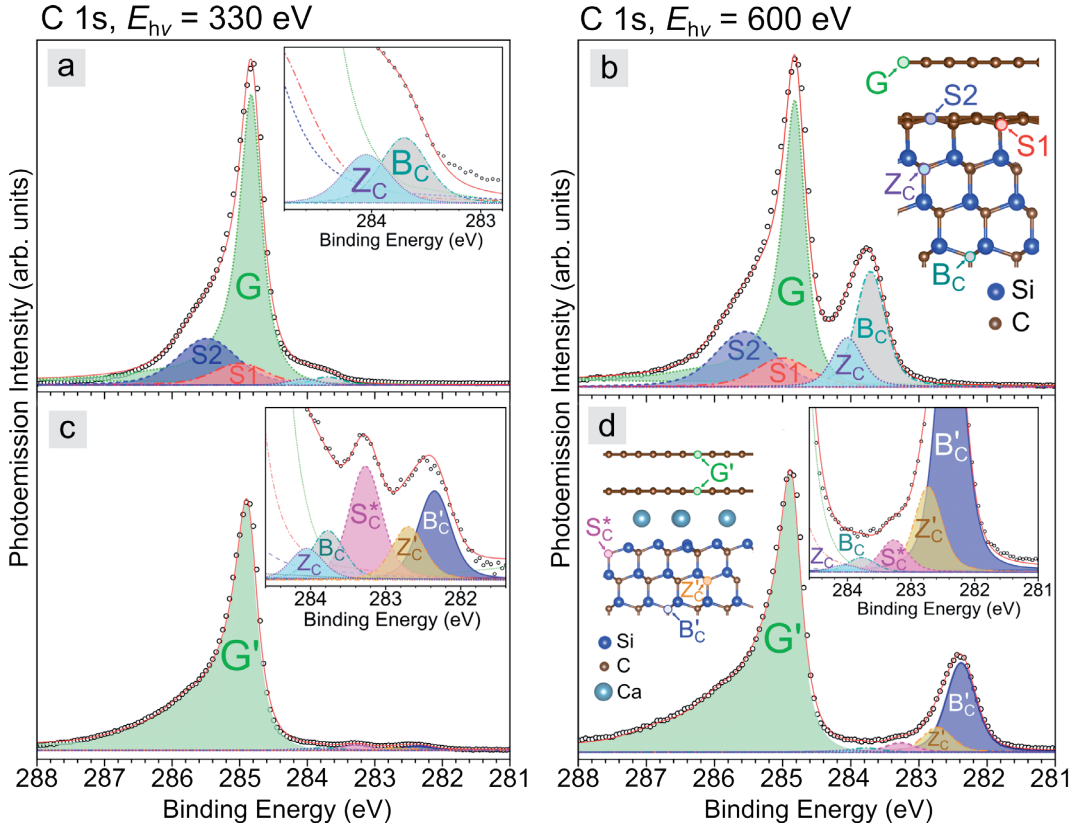


FIGURE 5.5: X-RAY PHOTOEMISSION SPECTRA OF THE C 1s CORE-LEVEL OF PRISTINE EPITAXIAL MONOLAYER GRAPHENE (EMLG) AND Ca-INTERCALATED GRAPHENE ON SILICON CARBIDE (Ca-QFSBLG) AT TWO X-RAY ENERGIES, $E_{hv} = 330$ eV (LEFT, SURFACE SENSITIVE) AND $E_{hv} = 600$ eV (RIGHT, BULK SENSITIVE).

(a), (b) Pristine EMLG before Ca-intercalation showing deconvoluted components G (graphene), S_1/S_2 (carbon in the buffer layer) and Z_C/B_C (surface/bulk SiC). The SiC components at lower binding energy are more clearly seen in the magnified view of the inset of (a). The approximate atomic location of these components is shown in the inset of (b) (see text for details). (c), (d) Ca-QFSBLG showing component G' . Three additional SiC components have emerged – S_C^* , Z'_C and B'_C , related to the changed SiC conditions due to formation of a Ca-Si compound between the SiC and buffer layer. The SiC components at lower binding energy are magnified in the right insets. The approximate atom locations for the new components are shown in the left inset of (d).

TABLE 5-2: SUMMARY OF THE FIT PARAMETERS FOR THE MAJOR COMPONENTS IN FIGURE 5.5

The binding energy location (E_B) is stated, as well as the relative intensity (RI) of the $1s$ peaks as referenced to the bulk SiC peak ‘ B_C ’ corresponding to pristine SiC prior to Ca intercalation. ‘Q’ refers to the asymmetry parameter of the graphene (which was fit using a BWF function). ‘ W_G ’ refers to the gaussian FWHM for the Voigt fit, whereas the Lorentzian FWHM (W_L) was kept constant at 0.2 eV in all fits except for the buffer layer components S_1 and S_2 .

EMLG, C $1s$		(a), (b), Pristine EMLG			(c), (d) 2 nd Ca-Intercalation		
Component	E_{hv} (eV)	E_B (eV)	RI	Q/W_L or W_G/W_L (eV)	E_B (eV)	RI	Q/W_L or W_G/W_L (eV)
S_2	330	285.48	5.63	0.8/0.4			
	600	285.55	0.48	0.8/0.4			
S_1	330	285.00	2.62	0.7/0.4			
	600	285.00	0.25	0.7/0.4			
G	330	284.83	35.0	12/0.2			
	600	284.82	2.47	9/0.2			
G'	330				284.89	26.75	9/0.2
	600				284.88	2.09	9/0.2
Z_C	330	284.05	0.75	0.4/0.2	284.05	0.18	0.4/0.2
	600	284.05	0.43	0.4/0.2	284.05	0.02	0.4/0.2
Z'_C	330				282.70	0.31	0.4/0.2
	600				282.73	0.22	0.4/0.2
B_C	330	283.7	1	0.4/0.2	283.77	0.29	0.4/0.2
	600	283.71	1	0.4/0.2	283.78	0.04	0.4/0.2
B'_C	330				282.35	0.52	0.4/0.2
	600				282.38	0.77	0.4/0.2
S_C^*	330				283.27	0.66	0.4/0.2
	600				283.27	0.08	0.4/0.2

5.4.2.3 O 1s and Ca 2p Core Level Spectra

[Figure 5.6](#) shows the O 1s core level for pristine EMLG prior to, and after Ca-intercalation. Shown here is the 1st Ca-intercalation step (which was omitted in the Si 2p and C 1s core level spectra – see [Appendix B3](#)) to illustrate that oxygen contamination was present even after the 1st Ca-intercalation step. Small amounts of oxygen were present during the course of the experiment, evident by the fact that the peak is barely above the noise level, shown as the dash-dot black line (representing vacuum annealed pristine EMLG sample prior to Ca-intercalation). Furthermore, the oxidation peak grew in intensity after each intercalation.

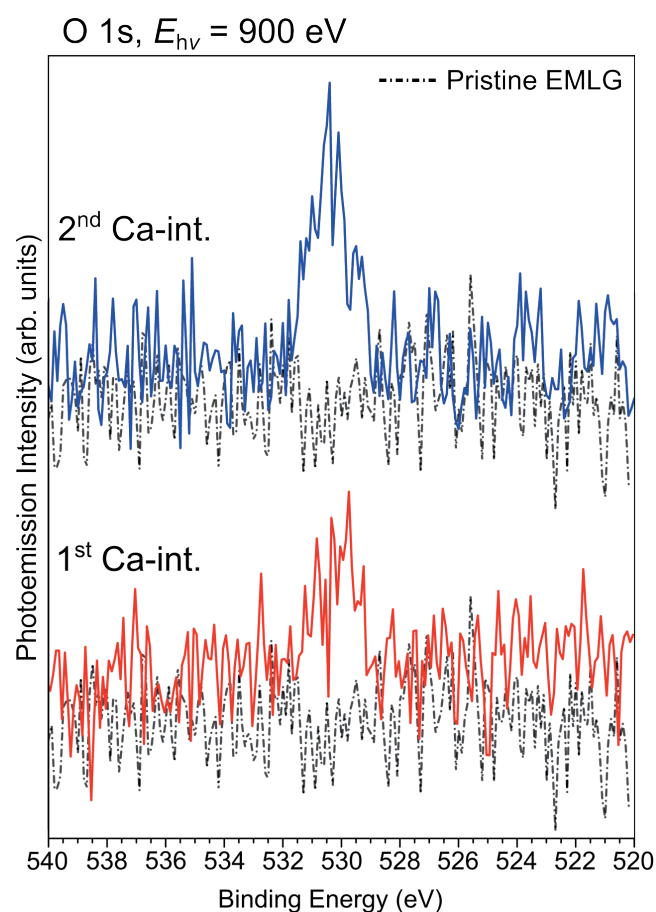


FIGURE 5.6: X-RAY PHOTOEMISSION SPECTRA OF THE O 1S CORE LEVEL AFTER EACH Ca-INTERCALATION STEP OF EPITAXIAL MONOLAYER GRAPHENE (EMLG) TAKEN AT AN X-RAY ENERGY OF $E_{hv} = 900$ eV.

The solid red line (bottom) shows data from the 1st Ca-intercalation, while the solid blue line (top) shows data from the 2nd Ca-intercalation. Spectra are offset vertically for clarity. For comparison, a spectrum from pristine EMLG prior to intercalation is shown as a black dash-dot line.

Thus, it is likely that most of the initial oxygen contamination is from oxidation of the excess Ca on the surface of the graphene (which did not intercalate – see [Appendix B5](#)). Although difficult to determine from the data in [Figure 5.6](#), the peak is approximately in the range of values expected from CaO [324] and it is likely these CaO surfaces reacted quickly (even in UHV) with trace amounts of water to form a partial hydroxide ($\text{Ca}(\text{OH})_2$) [325], and thus, the spectra may comprise of more than one oxide component.

To further determine the nature of the calcium contamination components, analysis of the Ca 2p spectra are necessary. [Figure 5.7](#) shows the Ca 2p core level taken at $E_{\text{hv}} = 500$ eV for pure Ca deposited on top of EMLG and shows the $2p_{3/2}$ peak of metallic Ca to lie at $E_B = 346.58 \pm 0.05$ eV, in agreement with past measurements [326-328]. The pure Ca metal component core level was fit with a Doniach-Šunjić lineshape. This experiment served as the ‘standard’ to which the resultant Ca-intercalated spectra presented in [Figure 5.8](#) (for H-QFSBLG samples, see [Appendix B4](#)) were compared. In all cases, the Ca 2p core levels were flattened using a spline background subtraction in order to remove the prominent inelastic scattering features of the Ca 2p core level background, which could not be easily removed using either the Shirley or Tougaard background subtraction methods.

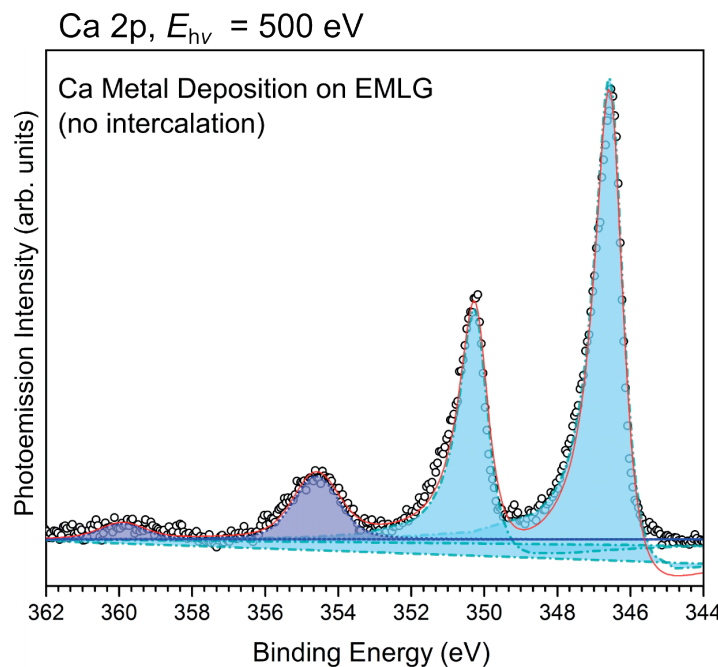


FIGURE 5.7: Ca 2p CORE LEVEL OF PURE CALCIUM DEPOSITED ON EPITAXIAL MONOLAYER GRAPHENE (EMLG) AT AN X-RAY ENERGY OF $E_{\text{hv}} = 500$ eV.

An asymmetric Doniach-Šunjić (DS) lineshape was used to fit the metallic Ca peaks, and the satellite features were fit using a Voigt profile. The asymmetry of the DS linshape caused the fitted line to dip below the baseline. The metallic Ca peaks (dash-dot light blue) are located at 346.58 ± 0.05 eV ($2p_{3/2}$) and 350.28 ± 0.05 eV ($2p_{1/2}$), whereas the satellite features (dotted, dark blue) are located at 354.60 ± 0.05 eV and 359.91 ± 0.05 eV.

After background subtraction, 3 components were fit to the Ca-intercalated data and shown in Figure 5.8: these are components Ca_{Si} at $E_{\text{B}} = 346.32 \pm 0.05$ eV, Ca_{O} at $E_{\text{B}} = 347.07 \pm 0.05$ eV and Ca_{OH} at $E_{\text{B}} = 348.03 \pm 0.05$ eV, as referenced to the $2\text{p}_{3/2}$ line (all values were calculated by averaging also the Ca-intercalated H-QFSBLG values which can be found in Appendix B4). The spin-splitting of the Ca $2\text{p}_{3/2}$ and Ca $2\text{p}_{1/2}$ lines was kept as 3.5 ± 0.2 eV [329], and the $2\text{p}_{3/2}$ to $2\text{p}_{1/2}$ area ratio was kept as 2:1. Component Ca_{Si} agrees well in binding energy with that of a Ca-silicide [305]. Component Ca_{O} is most likely a Ca-oxide or a Ca-O containing compound [326, 328]. Component Ca_{OH} likely represents $\text{Ca}(\text{OH})_2$ [330]. Typically, the Ca 2p spectrum is difficult to deconvolve, although in this case, we can rule out CaCO_3 , as there was no evidence of carbonates in the C 1s spectrum during the in-situ experiment. Furthermore, there was no trace of the original Ca metal ($E_{\text{B}} = 346.58 \pm 0.05$ eV), suggesting that any surface lying Ca was oxidised (see Section 5.4.3). The complete peak fitting details can be found in Table 5-3.

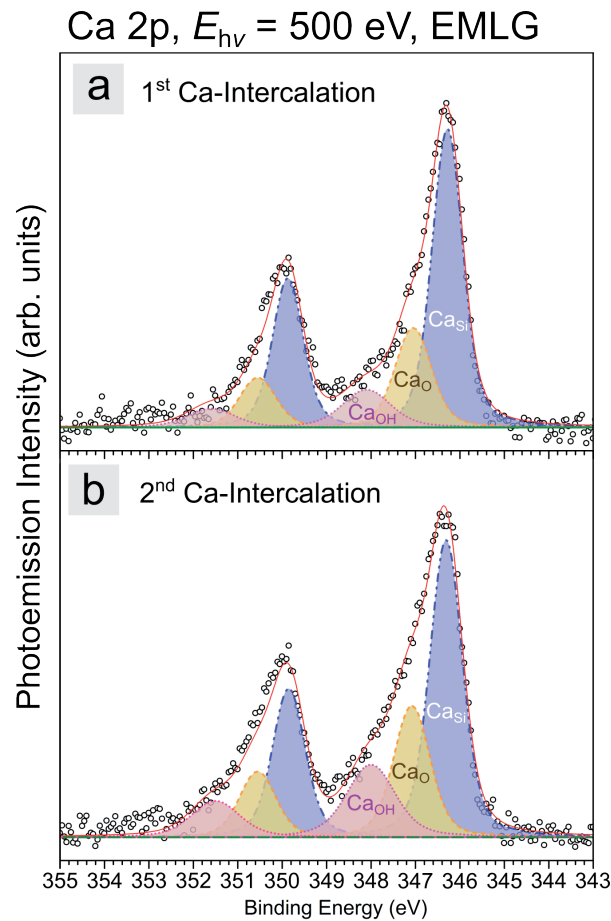


FIGURE 5.8: X-RAY PHOTOEMISSION SPECTRA SHOWING THE Ca 2p CORE LEVEL OF Ca-INTERCALATED EPITAXIAL MONOLAYER GRAPHENE (Ca-QFSBLG) AT AN X-RAY ENERGY OF $E_{\text{hv}} = 500$ eV.

Ca-intercalated EMLG (Ca-QFSBLG) showing 3 components. Ca_{Si} (blue) = Ca-Si compound, Ca_{O} (yellow) = Calcium oxide containing compound, Ca_{OH} (Red) = Ca-hydroxide compound. (a) 1st Ca-intercalation. (b) 2nd Ca-intercalation.

TABLE 5-3: Ca 2p CORE LEVEL FIT PARAMETERS FOR Ca-INTERCALATED EMLG (Ca-QFSBLG).

This table shows the binding energy (E_B) of $2p_{3/2}$ and $2p_{1/2}$ peaks, binding energy separation of spin-orbit split peaks ($2p_{3/2} - 2p_{1/2}$) and the Lorentzian (W_L)/Gaussian (W_G) full width at half maximum (FWHM) contributions of the Voigt functions used to fit components Ca_Si (Ca-silicide), Ca_O (Ca-oxide) and Ca_OH (Ca-hydroxide).

EMLG, Ca 2p		(a), EMLG, 1 st Ca-Intercalation				(b), EMLG, 2 nd Ca-Intercalation			
Component	E_{hv} (eV)	E_B (eV) $2p_{3/2}$	E_B (eV) $2p_{1/2}$	$2p_{1/2}$ -	W_L/W_G (eV)	E_B (eV) $2p_{3/2}$	E_B (eV) $2p_{1/2}$	$2p_{1/2}$ -	W_L/W_G (eV)
Ca_Si	500	346.28	349.87	3.59	0.3/0.65	346.31	349.85	3.54	0.3/0.65
Ca_O	500	347.05	350.55	3.50	0.3/0.8	347.08	350.55	3.47	0.3/0.8
Ca_OH	500	348.10	351.60	3.50	0.5/1.0	348.00	351.50	3.50	0.5/1.0

5.4.2.4 Calculation of Experimental Calcium Silicide Stoichiometric Ratio

The stoichiometric ratio of the Ca-silicide formed after intercalation can be estimated by comparing the relative intensities of the respective core level components, scaled by the photoelectron cross-section of the element at a given X-ray energy. A short derivation is given below.

Using the ‘common’ formalism for XPS [139] and for angles at the ‘magic angle’ ($\approx 54.74^\circ$) [140], the photoemission intensity of any given peak as a function of kinetic energy in an XPS experiment can be expressed as [139, 141]:

$$I(E_k) = nf\sigma\Delta\Omega yA\lambda(E_k)t(E_k), \quad \dots 5-1$$

where n represents the number of atoms per cm^3 of the particular element, f the flux of X-ray photons on the sample in $\text{cm}^{-2} \text{ s}^{-1}$, σ the photoionization cross-section in cm^{-2} per atom, $\Delta\Omega$ is the acceptance solid angle of the analyser, y is a numeric factor assigned to the efficiency of photoelectric process to yield photoelectrons, A is the probed area of the sample, $\lambda(E_k)$ is the inelastic mean free path, and $t(E_k)$ is the analyser transmission function

(which are functions of the kinetic energy of the electron, E_k). [Equation 5-1](#) can be simplified [[331-332](#)]:

$$I(E_k) = Bn\sigma\lambda(E_k)t(E_k), \quad \dots 5-2$$

so that B now represents the constant instrumentation factors in [Equation 5-1](#). The transmission function can be approximated by [[331, 333-335](#)]:

$$t(E_k) \propto \frac{1}{\sqrt{E_k[eV]}}, \quad \dots 5-3$$

It should be noted at this point that [Equation 5-3](#) represents an over-simplification of the transmission function, which also relies on the pass energy (E_a). In all core level measurements in this thesis, $E_a = 5$ eV. For these pass energies, Jiříček measured experimentally $t(E_k) \propto E_k^{-0.69}$ [[336](#)]. For different analysers, this value can vary, thus, having $t(E_k) \propto E_k^{-0.5}$ is a good approximation for the purposes of this calculation [[333, 336](#)].

The inelastic mean free path for inorganic compounds (such as calcium silicide) is given by [[142](#)]:

$$\lambda(E_k) = \frac{2170}{(E_k[eV])^2} + 0.72\sqrt{a[nm]E_k[eV]}, \quad \dots 5-4$$

where a is the so-called ‘monolayer thickness’ (measured in nm), given by [[142](#)]:

$$a [nm] = \sqrt[3]{\frac{m_a}{\rho n_m N}} \times 10^{24}. \quad \dots 5-5$$

Here m_a is the atomic or molecular weight, ρ is the bulk density in kg m⁻³, n_m is the number of atoms in the molecule and N is Avogadro’s number. For $E_k > 150$ eV, [Equation 5-4](#) becomes:

$$\lambda(E_k) \cong \sqrt{a[nm]E_k[eV]}. \quad \dots 5-6$$

Now, the $\lambda(E_k)$ and $t(E_k)$ terms in [Equation 5-2](#) cancel, since a will be similar for both Ca and Si then [[331](#)]:

$$I \cong Bn\sigma. \quad \dots 5-7$$

Thus, it is found that the number of atoms comprising the peak can be estimated by the area of the peak divided by the photoionization cross section, following ref. [[331](#)].

Using the combined ($2p_{1/2}$ and $2p_{3/2}$) area of the Ca_{Si} peaks for Si 2p at $E_{\text{hv}} = 600$ eV, the Ca_{Si} peaks for the Ca 2p core level at $E_{\text{hv}} = 500$ eV and the respective photoelectron cross sections [143], the stoichiometric ratio of Ca : Si is calculated to be 1 : 1.96 (for the 1st Ca-intercalation, see Appendix B3) and 1 : 1.74 for the 2nd Ca-intercalation (see Figure 5.4 and Figure 5.8). The results obtained in either case suggest that there is stoichiometrically more silicon than calcium, as is expected. In both the EMLG and H-QFSBLG case (see Appendix B4), the 2nd Ca-intercalation yielded stoichiometries with lower Si content.

Of course, it is likely that this value has additional error. As was discussed above, the transmission function also a function of pass energy [333, 336]. Moreover, Equation 5-1 neglects elastic scattering, the effects of which would modify Equation 5-1 by multiplication of the photoionization cross section by a factor, effectively decreasing the measured intensity [139]. Furthermore, Equation 5-1 makes the assumption that the solid is uniform to a depth of 10 – 20 nm [141] (dependent on the information depth [139]), which is not the case here since the Ca-Si layer is likely a monolayer or two thick.

5.4.2.5 Summary of X-ray Photoelectron Spectroscopy Results

In summary, the Si 2p and C 1s core level spectra have yielded strong evidence for: (1) Ca-Si bonding, *i.e.* formation of a Ca-silicide at the surface of the $\text{SiC}(0001)$, and (2) elimination of buffer layer-SiC bonds, *i.e.* formation of another graphene layer, respectively. The formation of a Ca-Si compound closely matching a Ca-silicide was also supported by the Ca 2p core level spectra (Figure 5.7 and Figure 5.8), which showed a component in binding energy agreement with a Ca-silicide after intercalation. Furthermore, a quantitative analysis using the area of component Ca_{Si} from the Ca 2p and Si 2p core level spectra showed that the atomic ratio of Ca : Si, had more silicon present than calcium. While approximate, the Ca : Si ratio further supports the faithfulness of the fits to the experimental data, as will be demonstrated using DFT calculations in Section 5.4.4. Along with the LEED results of Figure 5.3, there is strong evidence in support of Ca intercalating between the buffer layer and $\text{SiC}(0001)$, bonding with the silicon at the $\text{SiC}(0001)$ surface to form a Ca-silicide, eliminating the bonds between the buffer layer-SiC and converting the buffer layer into a new graphene layer.

5.4.3 Low Temperature Scanning Tunnelling Microscopy of Ca-QFSBLG

In this section I use the low temperature STM to explore the morphology of Ca-intercalated EMLG (using the same method of intercalation as in the

synchrotron experiments – see [Section 5.3.4](#)). After Ca-intercalation, the surface of the epitaxial monolayer graphene is radically altered – the long-range Moiré periodicity is eliminated and simultaneously, bright and dark ‘defects’ are observed – both strongly implying Ca-intercalation at the SiC-buffer layer interface. No $(\sqrt{3}\times\sqrt{3})R30^\circ$ spots around the G(1x1) spots (which are related to Ca intercalated between graphene layers) are observed in the fast Fourier transform of the STM micrographs. Furthermore, the height displacement of the graphene is measured as ≈ 0.26 nm, and later compared with density functional theory calculations.

5.4.3.1 Calcium Intercalation of Epitaxial Graphene on 6H-SiC: Ca-QFSBLG

[Figure 5.9a](#) shows an STM micrograph of pristine EMLG prior to Ca-intercalation. Apparent is the atomic resolution and Moiré pattern of the underlying buffer layer showing the $(6\sqrt{3}\times 6\sqrt{3})R30^\circ$ and associated (6×6) periodicity as expected [58, 61, 172]. The inset in [Figure 5.9a](#) shows the fast Fourier transform (FFT) of the STM micrograph in [Figure 5.9a](#). The graphene spots, labelled G(1x1), yield a lattice parameter of 0.253 ± 0.005 nm, in reasonable agreement with the lattice parameter of graphene (0.246 nm). In addition, we observe the $(6\sqrt{3}\times 6\sqrt{3})R30^\circ$ spots around the G(1x1) spots, in agreement with the pristine LEED images in [Figure 5.3](#). Another feature in [Figure 5.9a](#) are the bright spots (circled in [Figure 5.9a](#)) scattered randomly on the surface of the EMLG. These bright spots have been previously observed, and have been attributed to silicon adatoms on the surface of the SiC [337]. This is further strengthened by our interpretation that the spectral components A₀, A₁ and A₂, observed in the Si 2p photoemission spectra of pristine EMLG ([Figure 5.4a-b](#)), as corresponding to Si adatoms.

[Figure 5.9b](#) shows the same sample (from [Figure 5.9a](#)) after partial Ca intercalation as imaged with the STM at 0.12 V, 300 pA. What is immediately apparent is that the surface is now covered by a network of raised ‘islanded’ areas which no longer show the long-wavelength $(6\sqrt{3}\times 6\sqrt{3})R30^\circ/(6\times 6)$ modulation associated with the buffer layer. This is consistent with previous alkali [307-308, 338] and hydrogen [339] intercalation STM studies of graphene on SiC, and indicates the formation of a freestanding structure. This observation is also consistent with the LEED data in [Figure 5.3b](#) and with the XPS data in [Figure 5.4](#) and [Figure 5.5](#) which imply that the Si-C bonds that define the buffer layer are largely eliminated via the suppression of the $(6\sqrt{3}\times 6\sqrt{3})R30^\circ/(6\times 6)$ spots and formation of a Ca-silicide compound (component Ca_{Si})/elimination of components S₁ and S₂, respectively. The height of the newly formed feature is $\approx 0.26 \pm 0.01$ nm as judged by a histogram of heights from the STM micrograph shown in the inset of [Figure 5.9b](#). This is in agreement with recent density functional theory calculations of the theoretical height increase for Ca-QFSBLG [300] (see [Section 5.4.4](#)),

and similar to the displacements measured by Fiori *et al.* [308] and Omidian *et al.* [338] after the intercalation of Li atoms underneath the buffer layer.

Figure 5.9c shows an STM micrograph of the same sample after another intercalation step, imaged at 0.1 V and 400 pA. Imaging the sample became increasingly challenging after each intercalation step due to the difficulty of removing excess Ca, which formed clusters on the graphene surface. A method for the removal of excess Ca on the surface using the STM tip was developed, and resulted in atomically clean surfaces (see [Appendix B5](#) for details). Nonetheless, **Figure 5.9c** shows that after the 2nd Ca-intercalation, entire terraces now lack the $(6\sqrt{3}\times 6\sqrt{3})R30^\circ/(6\times 6)$ modulation; again the interpretation is that these are Ca-intercalated (*i.e.* Ca-QFSBLG) regions.

Figure 5.9d shows the FFT of the surface in **Figure 5.9c** and elucidates the underlying symmetry of the surface. Here we can see graphene spots ($G(1\times 1)$), SiC spots ($SiC(1\times 1)$) and the $(6\sqrt{3}\times 6\sqrt{3})R30^\circ$ symmetry that still exists, in agreement with the LEED from Fig. 1. Notably however, unlike the LEED results which showed $(\sqrt{3}\times \sqrt{3})R30^\circ$ spots with respect to the $G(1\times 1)$ spots (*i.e.* the $G(\sqrt{3}\times \sqrt{3})R30^\circ$ spots in **Figure 5.3b**), **Figure 5.9d** shows no evidence of the $G(\sqrt{3}\times \sqrt{3})R30^\circ$ symmetry. This provides strong evidence that the graphene bilayer created by Ca-intercalation is not itself intercalated with Ca to form CaC_6/C_6CaC_6 [18], which has a unit cell that is $(\sqrt{3}\times \sqrt{3})R30^\circ$ with respect to the graphene and should be visible using the bias conditions applied to the STM tip in **Figure 5.9c**. Thus, we conclude that Ca intercalation has formed quasi-freestanding bilayer graphene (*i.e.* Ca-QFSBLG), separated from the SiC surface by a Ca layer which has interacted strongly with the Si on the $SiC(0001)$ surface. The $(\sqrt{3}\times \sqrt{3})R30^\circ$ spots observed in LEED (**Figure 5.3b**) indicate that the Ca is indeed in registry with the graphene, however the STM measurements show that the perturbation of the $(\sqrt{3}\times \sqrt{3})R30^\circ$ Ca layer on the resultant bilayer graphene is small.

The Ca-intercalated graphene areas observed in **Figure 5.9b** and **Figure 5.9c** encompass ‘dark’ and ‘bright’ spots on the surface (spots are particularly evident on the uniform terrace in **Figure 5.9c**, but can also be seen in the partially intercalated ‘island’ areas in **Figure 5.9b**), and are visibly distinct in appearance compared to the pristine EMLG starting sample in **Figure 5.9a**. Since pristine EMLG also possessed bright spots, we tentatively label these post-intercalation bright spots. **Figure 5.10a-b** shows a magnified view of the dark and post-intercalation bright spots in **Figure 5.9c**, and shows that the graphene is continuous over these features. The dark spots have a height variation of < 40 pm (see **Figure 5.9c** inset), whereas the bright spots have a height of < 30 pm (see **Figure 5.10b** inset) and thus, are likely not due to the buffer layer corrugation which is ≈ 60 pm [61]. **Figure 5.10c** and **Figure 5.10d** show an STM micrograph of the same Ca-QFSBLG sample in **Figure 5.9b-c**, imaged at 0.1 V, 400 pA and -0.1 V and 400 pA, respectively. Here, it is shown that altering the sign of the bias does not invert the contrast of the dark (turning them bright) or bright (turning them dark) spot features, which

would be expected from a charged defect, as was observed after Intercalation by Kim *et al.* [304]. This may be due to screening by the graphene and thus, the height measurement of the bright and dark spot features are likely reliable [301].

The dark spots are in agreement with the height variation of similar features measured with STM after H-intercalation of graphene on SiC [301]. In fact, similar ‘dark’ features have been observed using STM after alkali [307-308], indium [304] and hydrogen [301] intercalation of graphene on silicon carbide. The observation of these features is thus, intercalant *independent*, and points to a universal underlying mechanism involving the SiC surface. In the case of H-intercalation, Murata *et al.* [301] attributed these features to hydrogen vacancies, with a measured density ranging from $\approx 10^{11}$ to 10^{13} cm^{-2} depending on the intercalation temperature used. Here, I find that the dark spot density of $\approx 9 \times 10^{12} \text{ cm}^{-2}$ is within this range, and agrees favourably to the dark spot density reported after hydrogen intercalation [301]. The density of silicon adatoms (bright spots in Figure 5.9a) are on the order of 10^{13} cm^{-2} in the measured data, whereas Rutter *et al.* [337] observed Si adatom densities on the order of 10^{14} cm^{-2} , in rough agreement with the numbers obtained from Figure 5.9a (the adatom density may have large variations on the surface, and could be higher or lower from preparation to preparation and area to area). Thus, I propose that the dark spots are Ca vacancies that are tied to Si adatom locations on the surface of the SiC.

As for the post-intercalation bright spots (arrow in Figure 5.9c), the height does not exceed $\approx 30 \text{ pm}$ and the density is $\approx 1 \times 10^{12} \text{ cm}^{-2}$, in approximate agreement with prior measurements on H-intercalated graphene on SiC [301]. Previous reports have attributed these bright spots to defects [301] or protrusions from intercalants bonded to the underlying graphene, rather than the SiC surface [340]. Since we do not observe electron scattering standing waves from the post-intercalation bright spots [341-342] (see Figure 5.10a-b) our observations suggest the latter. Thus, we tentatively attribute these bright spots to excess metallic Ca that may be present on top of the underlying Ca-silicide. We mention here briefly that the STM of Ca-intercalated graphene has been previously conducted [18, 272, 290], but the bright and dark spot features shown in Figure 5.9 and Figure 5.10 have not (to the best of my knowledge) been reported.

The STM has elucidated the surface structure of Ca-intercalated EMLG on 6H-SiC(0001). In summation, we have found that Ca-QFSBLG has formed upon intercalation of Ca via elimination of EMLG’s Moiré pattern, and the appearance of bright and dark spot defects which are likely associated with the SiC surface. Furthermore, no Ca-intercalation between the graphene layers occurred, as no $(\sqrt{3} \times \sqrt{3})R30^\circ$ spots with respect to the G(1x1) spots were observed from the FFT of the Ca-intercalated areas – consistent with the LEED (Figure 5.3) and XPS (Figure 5.4, Figure 5.5 and Figure 5.8) results.

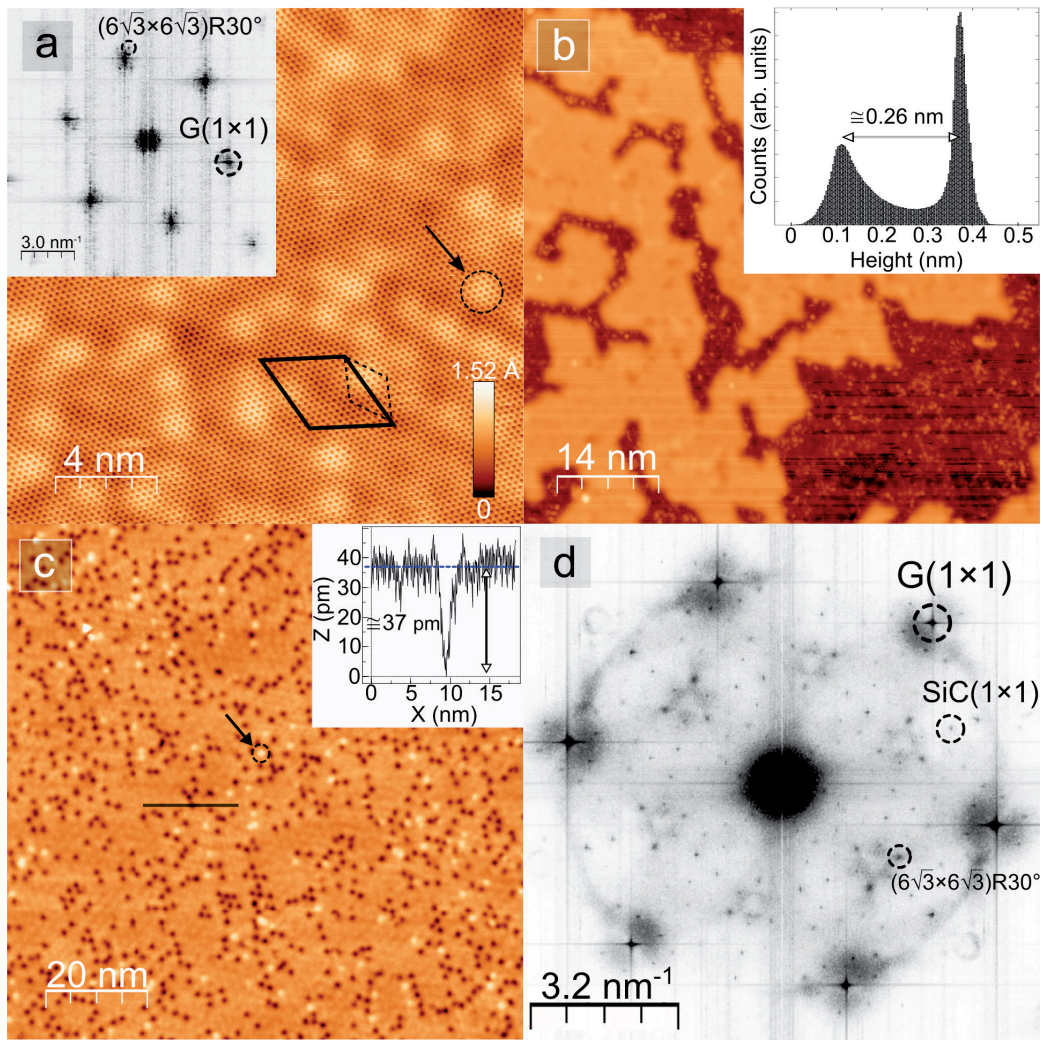


FIGURE 5.9: SCANNING TUNNELLING MICROSCOPE (STM) MICROGRAPHS OF PRISTINE EPITAXIAL MONOLAYER GRAPHENE (EMLG) BEFORE AND AFTER Ca-INTERCALATION.

(a) *Pristine EMLG (1 V, 200 pA, 77 K) showing atomic resolution, along with real space $(6\sqrt{3}\times 6\sqrt{3})R30^\circ$ (solid line) and (6×6) (dashed line) quasi-periodicities (Moiré). The bright spots correspond to silicon adatom features (dotted circle, arrow). Inset shows the fast Fourier transform (FFT) of same image showing $G(1\times 1)$ graphene spots with measured lattice parameter of ≈ 0.25 nm, and $(6\sqrt{3}\times 6\sqrt{3})R30^\circ$ spots around $G(1\times 1)$ spots.*

(b) *1^{st} Ca-intercalation step (0.12 V, 300 pA, 4.6 K) showing formation raised areas (Ca-QFSBLG). The height difference between these raised areas and the un-intercalated graphene is 0.26 ± 0.01 nm (see inset).*

(c) *After the 2^{nd} Ca-intercalation, Ca-QFSBLG formed on entire terraces (0.1 V, 400 pA, 4.6 K). Arrow and dotted circle shows post-intercalation bright spot feature (different from bright spot in (a)). Inset shows a topographic line scan across one of the dark spots in the image, denoted by the solid black line.*

(d) *FFT of (c) showing underlying symmetry of Ca-QFSBLG surface and graphene ($G(1\times 1)$), SiC ($SiC(1\times 1)$) and $(6\sqrt{3}\times 6\sqrt{3})R30^\circ$ spots.*

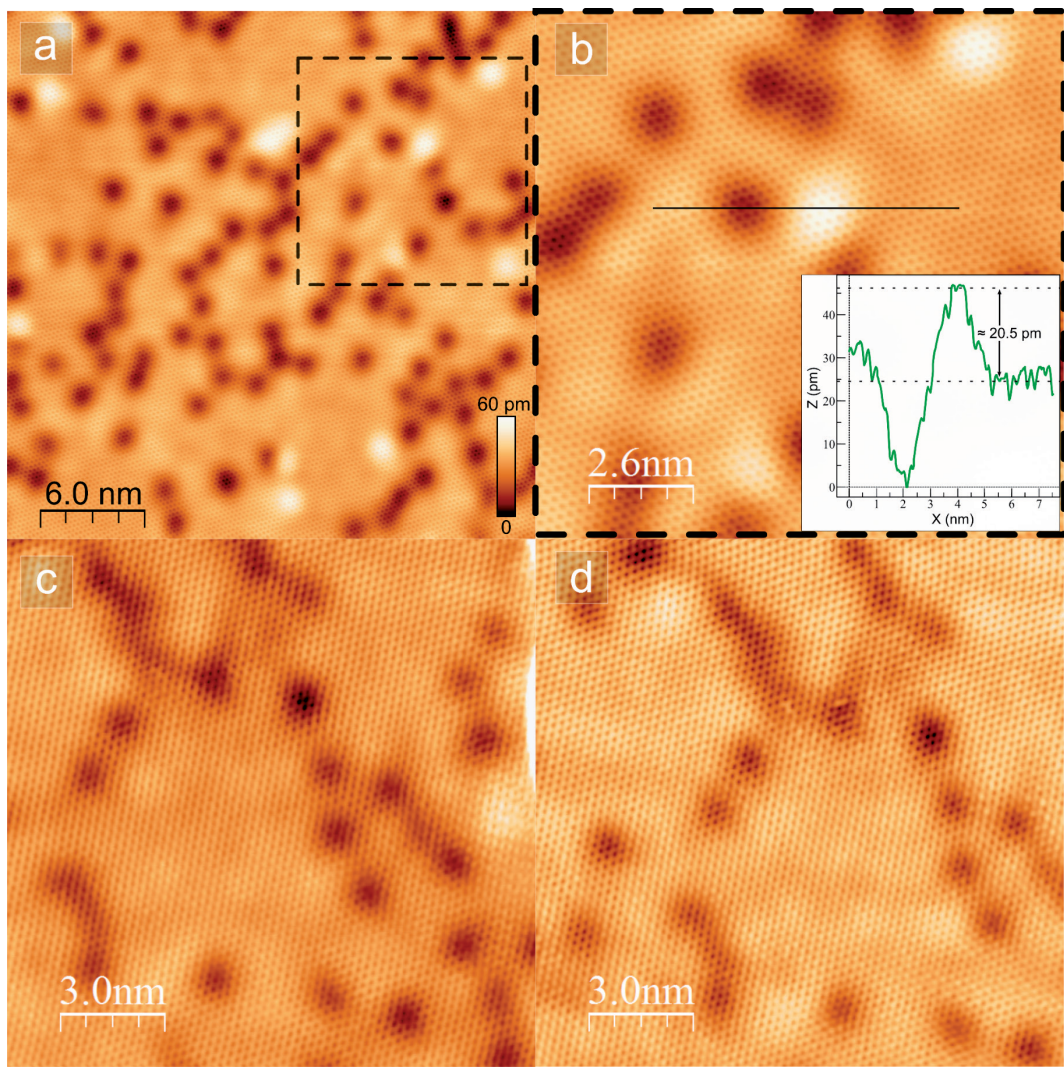


FIGURE 5.10: SCANNING TUNNELLING MICROSCOPE (STM) MICROGRAPHS OF Ca-QFSBLG AT 4.6 K SHOWING MAGNIFIED VIEW OF BRIGHT AND DARK SPOTS AT VARIOUS TIP BIASING CONDITIONS.

(a) Overview of the intercalated area showing atomic resolution (1 V, 300 pA). (b) Magnified area in dashed square from (a) showing that the dark and bright spots are not holes or defects, as the graphene is continuous and we observe no electron scattering, respectively. Inset shows topographic line scan across one of the bright spots (1 V, 300 pA). (c) Different area on the sample at positive voltage (0.1 V, 400 pA) (d) Same area in (c) (slightly shifted) at negative voltage (-0.1 V, 400 pA) showing no contrast inversion of bright or dark spots.

5.4.4	Density Function Theory Calculations of Ca-QFSBLG Structure
-------	---

The results presented thus far strongly imply that Ca-intercalation of EMLG occurs between the buffer layer and SiC(0001) surface to form Ca-QFSBLG, and not between the buffer layer and graphene (or between graphene layers). These conclusions match exactly those of Ca-intercalated H-QFSBLG, and the reader is referred to [Appendix B4](#) for further information. To better understand this, we utilize DFT to investigate the energetics of Ca-intercalation, the methods of which can be found in ref. [300].

[Figure 5.11](#) shows schematics of the two structures modelled using DFT. [Figure 5.11a-b](#) show side and top views of the first modelled structure, corresponding to Ca-QFSBLG, i.e., Ca intercalated between the buffer layer – SiC interface to produce bilayer graphene from EMLG (SiC/Ca/Graphene/Graphene). The former buffer layer is raised to lie 0.467 nm above the surface Si atoms, a change in height (Δh), compared to pristine EMLG, of approximately 0.26 nm (using the known value for buffer layer – Si distance of 0.21 nm [49]), in excellent agreement with my experimentally measured value of $\Delta h = 0.26 \pm 0.01$ nm from STM. [Figure 5.11c-d](#) show a second modelled structure, corresponding to Ca instead intercalated between the 1st graphene layer and buffer layer (SiC/Buffer Layer/Ca/Graphene), a model that has been, up until now, thought to describe Ca-intercalation [24]. Using this model, the insertion of Ca gives a $\Delta h = 0.153$ nm when compared with pristine EMLG, which is not in agreement with our STM measurements (see [Figure 5.9b](#) inset). The energy, E_I , required to intercalate Ca was calculated using [300]:

$$E_I = E(\text{SiC}/\text{graphene} + \text{Ca}) - E(\text{SiC}/\text{graphene}) - E(\text{Ca}) \quad ...5-8,$$

where $E(\text{SiC}/\text{graphene})$, $E(\text{Ca})$ and $E(\text{SiC}/\text{graphene}+\text{Ca})$ are the energy of SiC/graphene heterostructure, atomic energy of Ca in its bulk state, and the energy of SiC/graphene system upon Ca intercalation, respectively. This yields $E_I = -2.5$ and +1.57 eV/atom for Ca intercalated underneath the buffer layer and Ca intercalated between the 1st graphene layer and buffer layer, respectively. Here, a negative value indicates the process is energetically favourable. Thus, DFT supports our experimental finding that the favoured intercalation site for the Ca is between the SiC and the buffer layer.

It should be noted that our DFT results closely match the conclusions of Sandin *et al.* [307] (which used Na as the intercalant), but disagrees with a recent publication by Zhang *et al.* [290] concerning Ca-intercalation. Sandin *et al.* [307] concluded that a (SiC/Na/Graphene/Graphene) structure accurately describes Na-intercalation by comparing experimentally

measured and theoretically calculated work function shifts. Zhang *et al.* [290] used STM and DFT calculations to find that low concentrations of Ca could intercalate in a ‘meta-stable’ configuration underneath the buffer layer, although (SiC/buffer layer/Ca/Graphene) and (SiC/buffer layer/Graphene/Ca/Graphene) structures were found to be more energetically favourable – in stark disagreement with our findings which suggest that the (SiC/Ca/Graphene/Graphene) structure is most stable. Furthermore, the change in height after intercalation in ref. [290] was experimentally measured as 0.283 nm (theoretically calculated as 0.29 nm), and this disagrees with both of our experimental and theoretical results presented here.

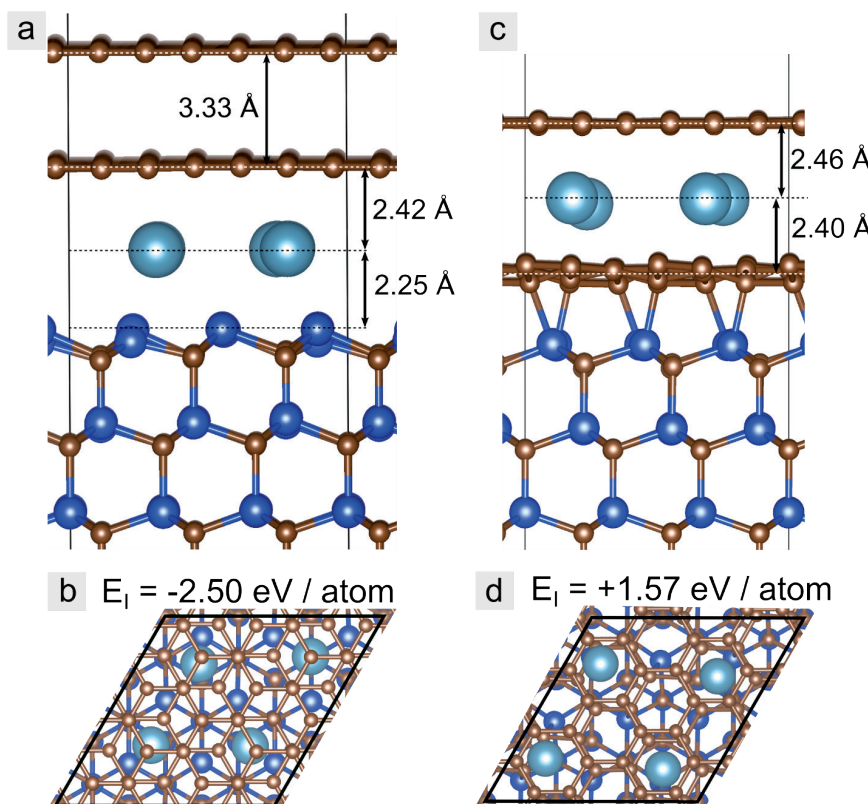


FIGURE 5.11: ATOMIC MODELS (DARK BLUE = Si, BROWN = C, LIGHT BLUE = Ca) OF Ca-INTERCALATED MONOLAYER GRAPHENE ON SiC(0001) SHOWING THE TWO POSSIBLE INTERCALATION REGIMES.

(a) Side view of Ca-QFSBLG showing vertical distances and, (b) top down view of Ca-QFSBLG showing the unit cell and approximate $(\sqrt{3} \times \sqrt{3})R30^\circ$ coordination of the Ca with respect to the graphene. The energy required for intercalation, $E_I = -2.50 \text{ eV / atom}$ (energetically favourable). (c) Side view of Ca intercalated between the 1st graphene layer and buffer layer (SiC/Buffer/Ca/Graphene) showing distances and, (d) top down view of Ca intercalated between the 1st graphene layer and buffer layer showing unit cell. In the case of (SiC/Buffer/Ca/Graphene) the coordination of the Ca was slightly larger than $(\sqrt{3} \times \sqrt{3})R30^\circ$. The energy required for intercalation, $E_I = +1.57 \text{ eV / atom}$ (not energetically favourable).

Finally, I find that the stoichiometric ratio of Ca : Si given by the model in [Figure 5.11a-b](#) of 1 : 2.25, yields a silicon rich ratio – in agreement with the experimental value found from the calculation in [Section 5.4.2.4](#).

5.4.5 Carrier Type and Concentration in Ca-QFSBLG

In this section I will investigate the effect that Ca-intercalation has on the carrier concentration of the graphene layers. First, I will compare the lineshape of the graphene C 1s core level photoemission with the theoretical calculations of the photoemission lineshape of highly doped graphene, in order to obtain an estimate of the magnitude of the carrier density. Secondly, I will discuss SECO measurements to measure the workfunction of Ca-QFSBLG, and hence infer the carrier type of Ca-QFSBLG.

5.4.5.1 Ca-QFSBLG C 1s Lineshape Comparison to Theoretical Calculations

In [Section 5.4.2.2](#), it was stated that the Ca-intercalated graphene peaks (G') were fit using a combination of an asymmetric BWF lineshape (to fit the graphene peak), in addition to several Voigt functions which were used to fit the prominent tail in Ca-QFSBLG (see [Appendix B3](#)). This asymmetry region at higher binding energy to the main photoelectron line is often observed in the core level spectra of metals – attributed to the energy spectrum of electron-hole pairs that form upon movement of conduction band electrons to screen the core-hole formed by photoemission (see [Chapter 3, Section 3.4.3.2](#)) [148, 158]. The DS lineshape was initially used to explain the asymmetry observed in the X-ray spectra of simple metals [157], but has since been used to fit the photoemission spectra of a range of metals [148], and more recently, the asymmetric tail region observed in C 1s measurements of graphene [295, 343], and graphene on silicon carbide [60, 297, 312].

However, application of the DS lineshape to graphene poses problems due to the fact that (undoped) graphene is not a ‘true’ metal, and also because of its 2D nature [25, 296]. Even so, the DS lineshape *has* been applied to epitaxial graphene on silicon carbide with success, although in these cases, the graphene was relatively undoped, or slightly p- or n-type doped [60, 297, 312]. In the case of H-QFSBLG, H-intercalation induces p-type doping corresponding to a carrier concentration of $\approx 5 \times 10^{12} \text{ cm}^{-2}$ [75] to $\approx 1 \times 10^{13} \text{ cm}^{-2}$ [85, 344], whereas EMLG is n-type with a carrier concentration of $\approx 1 \times 10^{13} \text{ cm}^{-2}$ [345]. This is not the case with Ca-intercalated graphene which is relatively highly n-type doped [23] (and other highly n-type doped intercalated graphenes [278]).

Unlike low p- or n-type doped graphene on silicon carbide systems, Ca-intercalated graphene has a pronounced asymmetry region at higher binding

energy, clearly seen in [Figure 5.5c-d](#), making fitting of the high-binding energy asymmetry of the C 1s core level difficult only using one asymmetric lineshape. The reason for this difference is connected intimately to the band structure of graphene itself. For undoped graphene, the Fermi level is located at the Dirac point at K and K' (see [Chapter 2](#)), whereas the introduction of doping (p- or n-type) shifts the Fermi level up or down to intersect the bands making it more metallic in nature, effectively increasing the density of election states about the Fermi level. In traditional '3D' metals (where the Fermi level already intersects a band), the core-hole is responsible for the distinct plasmon loss features which are separated (typically a few eV's) from the core level peaks. These are brought about by oscillations of the electrons in the conduction band, and thus, are associated with a plasmon frequency (see [Chapter 3, Section 3.4.3](#)) which determines the energy separation of the plasmon features from the main photoelectron line. For plasmons confined in 2D, the dispersion relation is no longer constant, and the plasmon frequency has a square root dependency on the wave vector [346]. Unlike a traditional ('3D') metal which has some energy separation between the plasmon loss peaks and the core level component, the 2D condition causes the plasmon loss peaks to appear closer to the core level component, and thus, 2D plasmon loss peaks contribute to the high binding energy peak asymmetry in the C 1s lineshape [25, 296]. Thus, this suggests that the lineshape of the C 1s graphene peak can estimate the doping, since the concentration of carriers around the Fermi level should yield a greater plasmon loss effect (i.e. a higher doping should yield a more pronounced asymmetry).

Recently, the C 1s core level for quasi-freestanding highly doped monolayer [296] and bilayer [25] graphene considering both shake-up processes and plasmon loss features was calculated for various doping levels. The results for some of the doping levels are reproduced in [Figure 5.12](#), and are compared with the experimental C 1s values for Ca-QFSBLG taken at $E_{hv} = 600$ eV ([Figure 5.5d](#)). Since ref. [25] corrected the background with a linear correction, the same correction was applied to the raw C 1s core level data so a direct comparison could be made. It was found that the linewidth of the synchrotron data obtained was narrower than the theoretically calculated data in [Figure 5.12](#) (also true for Mg-QFSBLG data, see [Chapter 6, Section 6.4.4.1](#)), and thus the experimental data was convoluted with a gaussian function of the form:

$$f(x) = \frac{1}{\sigma\sqrt{2\pi}} e^{-\frac{1}{2}\left(\frac{x-\mu}{\sigma}\right)^2} \quad ...5-9.$$

Where σ is the standard deviation and μ is the mean. For the convolution, $\mu = 0$ and $\sigma = 0.1$. Furthermore, the experimental data was normalised and aligned (shifted in binding energy) to the C 1s peak of the theoretical data. The resultant convoluted, normalised and aligned spectra are shown in [Figure 5.12](#) and are compared to the theoretical values of from ref. [25]. [Figure](#)

[Figure 5.12a](#) shows the experimental data compared with quasi-freestanding bilayer graphene (QFSBLG) with a carrier concentration of 10^{13} cm^{-2} on both layers, and 10^{13} cm^{-2} on one and 10^{14} cm^{-2} on the other. The nomenclature of the doping is as follows: $10^{14}:10^{14} \text{ cm}^{-2}$ signifies both graphene layers are doped at the same carrier concentration, whereas $10^{14}:10^{13} \text{ cm}^{-2}$ signifies the graphene layers are doped by different amounts. The first number represents the carrier concentration of the graphene layer in which the core-hole is created (*i.e.* the layer from which the signal is obtained) [25]. This does not imply that the layer in which the core-hole is not created has no effect, as this layer is coupled to the other [25].

[Figure 5.12b](#) shows the theoretically obtained curves for quasi-freestanding monolayer graphene (QFSMLG) at $10^{14} \text{ carriers cm}^{-2}$ and QFSBLG with both layers at $10^{14} \text{ carriers cm}^{-2}$ compared to the experimental data for Ca-QFSBLG. It is apparent that Ca-QFSBLG does not agree with the curves presented in either [Figure 5.12a](#) or [Figure 5.12b](#) for either monolayer or bilayer graphene doped at these carrier concentrations.

[Figure 5.12c](#) shows the theoretically obtained curves for QFSBLG with at least one of the layers (the one in which the core-hole is created) at $10^{14} \text{ carriers cm}^{-2}$, while the other is either at 10^{12} or $10^{13} \text{ carriers cm}^{-2}$ (the curves are almost identical in this case). Here, I observe good agreement between experiment and theory, and thus, this implies that Ca-QFSBLG is a quasi-freestanding bilayer graphene doped with at least one layer at a carrier density of 10^{14} cm^{-2} and the other at 10^{12} or 10^{13} cm^{-2} . This agrees with the ARPES observations by McChesney *et al.* [23], which found that Ca-intercalated monolayer graphene on SiC shifted the Fermi level with respect to the Dirac point by $\approx 1.2 \text{ eV}$, corresponding to a carrier concentration of $\approx 1.06 \times 10^{14} \text{ cm}^{-2}$ (assuming a Fermi velocity of $1 \times 10^6 \text{ m s}^{-1}$). This pronounced tailing in the C 1s core level has also recently been observed by Link *et al.* [278] after gadolinium intercalation of zero-layer graphene (to produce Gd-intercalated monolayer graphene on SiC). This resulted in a highly n-type graphene, with carrier concentration of $\approx 4.5 \times 10^{14} \text{ cm}^{-2}$ (though a comparison with the theory from ref. [25] was not made).

The results presented in this section are thus, supported by the predictions of Sernelius [25, 296] which proposed that the asymmetric tail in the C 1s spectrum is due to the effects of highly doped graphene. It is interesting to note that the results presented here differ slightly from the predictions of Sernelius regarding the shift of the C 1s peak due to doping, where a graphene bilayer doped with $10^{14}:10^{13}$ or $10^{14}:10^{12} \text{ carriers cm}^{-2}$ corresponds to a binding energy shift in the C 1s graphene peak of $\Delta E_B \approx 0.15 \text{ eV}$. The maximum uncertainty in the experimental measurement is 0.1 eV, so measurement of this shift should be within the capabilities of the instrument. But as can be seen in [Figure 5.5](#) (and [Appendix B3](#)), I find no measurable shift in the C 1s peak of the doped graphene compared to pristine EMLG (within uncertainty), even though the graphene exhibits characteristics of a high

carrier density. The possible reason as to why there is no observation of a shift in the C 1s lineshape is further discussed in [Chapter 6, Section 6.4.5](#).

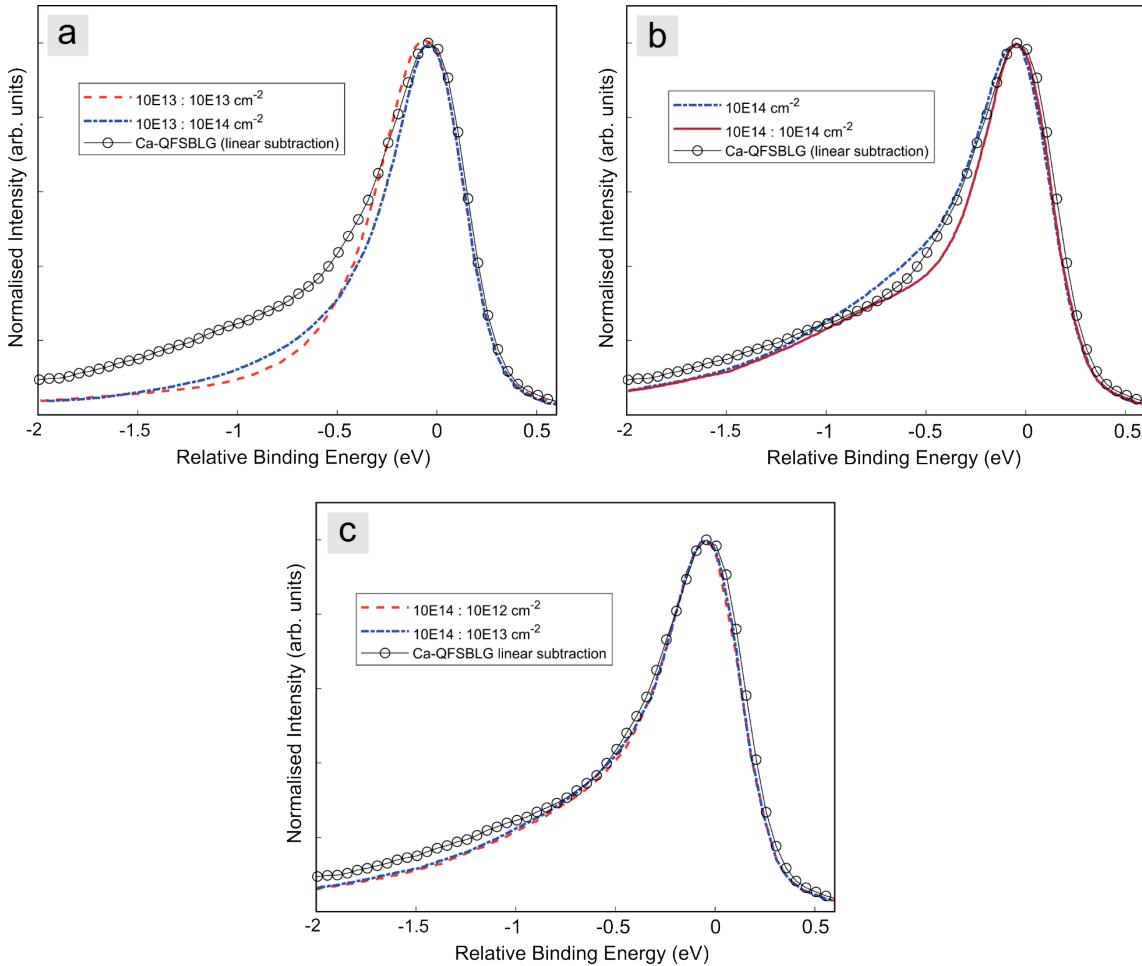


FIGURE 5.12: THEORETICALLY CALCULATED VALUES (FROM REF. [25]) OF THE C 1s CORE LEVEL OF HIGHLY DOPED BILAYER (AND MONOLAYER) GRAPHENE COMPARED WITH Ca-QFSBLG (2nd Ca-INTERCALATION, $E_{hv} = 600 \text{ eV}$, [FIGURE 5.5d](#)).

The doping levels of the graphene layers are indicated in the legends, with the first doping level representing the doping in the layer in which the core-hole (excitation) is created (see text for explanation). (a) Experimental spectrum of Ca-QFSBLG (open circles) and theoretically calculated spectra from ref. [25] corresponding to a doping level of $10^{13}:10^{13} \text{ cm}^{-2}$ (red dash) and $10^{13}:10^{14} \text{ cm}^{-2}$ (blue dash dot) in quasi-freestanding bilayer graphene (QFSBLG). (b) Experimental spectrum of Ca-QFSBLG (open circles) and theoretically calculated spectra from ref. [25] corresponding to a doping level of 10^{14} cm^{-2} (blue dash dot) and $10^{14}:10^{14} \text{ cm}^{-2}$ (red solid line) in quasi-freestanding monolayer graphene and QFSBLG, respectively. (c) Experimental spectrum of Ca-QFSBLG (open circles) and theoretically calculated spectra from ref. [25] corresponding to a doping level of $10^{14}:10^{12} \text{ cm}^{-2}$ (red dash) and $10^{14}:10^{13} \text{ cm}^{-2}$ (blue dash dot) in QFSBLG.

5.4.5.2 Secondary Electron Cut-Off Photoemission Spectroscopy

To gain experimental insight into whether the carriers in Ca-QFSBLG are n- or p-type, SECO measurements were performed. The workfunction (W_f) of graphene on silicon carbide is predictably tied to the carrier type. In previous W_f measurements, it has been shown that p-type graphene on SiC has a higher W_f value than that of n-type graphene on SiC [116, 347]. Thus, we can use the measurement of W_f as a test to find whether the charge carriers are more n- or p-type.

Figure 5.13 shows the results of SECO measurements on pristine and Ca-intercalated graphene (Ca-QFSBLG) for both the 1st Ca-intercalation (the core levels of which are shown in [Appendix B](#)), and the 2nd Ca-intercalation (the results of which are shown in [Figure 5.4c-d](#) and [Figure 5.5c-d](#)). **Figure 5.13a** shows the photoemission intensity as a function of kinetic energy for pristine EMLG (prior to Ca-intercalation) and Ca-QFSBLG after the 1st Ca-intercalation (a bias of -9V was applied to the sample in order to ensure effective measurement – see [Methods, Section 5.3.5](#)). The measurement of $W_f = 3.96 \pm 0.05$ eV for pristine EMLG agrees with measurements by Gugel *et al.* [116] (4.05 ± 0.04 eV), though is in disagreement with values measured by Mammadov *et al.* [347] (4.16 ± 0.05 eV – this result might have been due to mixed monolayer/bilayer samples in this case causing an increase in W_f). After the 1st Ca-intercalation, the workfunction of the graphene decreases to $W_f = 3.74 \pm 0.05$ eV, giving a change in workfunction, $\Delta W_f = -0.22 \pm 0.1$ eV. This implies that the graphene has become more n-type, since the workfunction of graphene on SiC changes in a predictable way based on the carrier type – where a lower workfunction implies n-type carriers [116, 347].

Figure 5.13b shows that after the 2nd Ca-intercalation, the $W_f = 3.68 \pm 0.05$ eV ($\Delta W_f = -0.28 \pm 0.1$ eV), and does not significantly change (within error) from the 1st Ca-intercalation. However, we do observe a small signal (arrow in [Figure 5.13b](#)) that arises, corresponding to a workfunction of $W_f = 2.30 \pm 0.05$ eV, significantly lower than the accepted value of the workfunction of bulk calcium of 2.8 eV [348]. Gaudart and Rivoira [349] found that thin (5.5 nm) calcium films had a workfunction of $W_f \approx 2.5$ eV, significantly lower than bulk values (≥ 10 nm) which had a workfunction of 2.87 ± 0.06 eV. Thus, we attribute this lower workfunction to unconnected or extremely thin films of calcium on the surface of the graphene [350], in agreement with the decreased LEED intensity and attenuation of the C 1s and Si 2p spectra after Ca-intercalation, in which it was thought that some Ca persisted on the surface (see [Sections 5.4.1](#) and [5.4.2](#)). It is clear that this small amount of excess calcium did not affect the measurement of the workfunction, as the decrease in workfunction did not deviate beyond the uncertainty in the measurement.

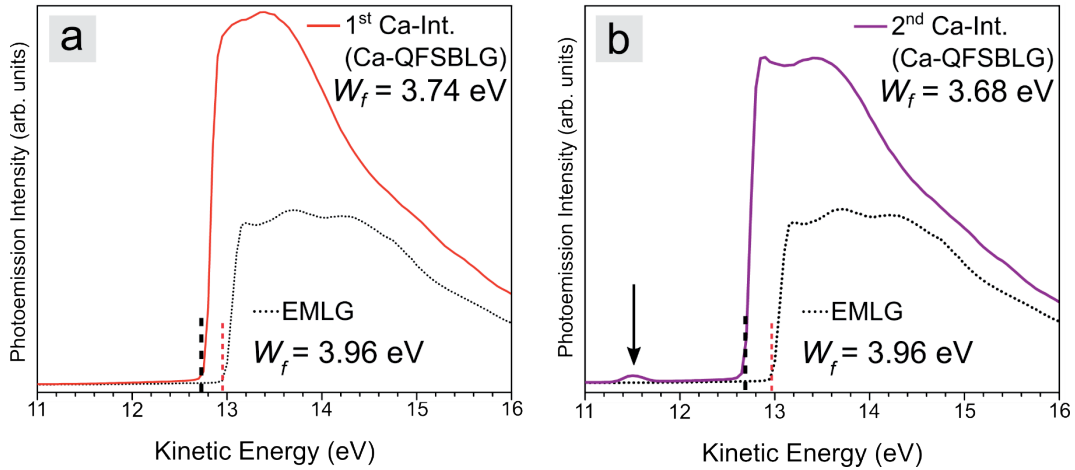


FIGURE 5.13: SECONDARY ELECTRON CUT-OFF (SECO) PHOTOEMISSION MEASUREMENTS OF Ca-QFSBLG.

Pristine EMLG (dotted line) at 3.96 eV and (a) Ca-QFSBLG (solid red line, 1st Ca-intercalation) showing a workfunction (W_f) of 3.74 eV. (b) Ca-QFSBLG (solid purple line, 2nd Ca-intercalation) showing a W_f of 3.68 eV.

Although it is the case that a small amount of surface calcium is not able to shift the workfunction of the underlying Ca-QFSBLG appreciably, I also explored the effect of depositing larger amounts of Ca on the surface. Figure 5.14 shows the result of depositing ≈ 0.6 nm of Ca on the surface of Ca-QFSBLG, on the same sample as in Figure 5.13 (performed after the Ca-intercalation experiments). The peak I have associated with metallic calcium is now more obvious, and still corresponds to the same workfunction of $W_f = 2.30 \pm 0.05$ eV, as in Figure 5.14b. The major onset of intensity, which I associate with the Ca-QFSBLG itself, now shows a lower workfunction of $W_f = 3.09 \pm 0.05$ eV (this value was the same in the Ca-intercalated and Ca-decorated H-QFSBLG samples – see Appendix B4, Figure B.4-7). This further indicates that the SECO measurement reliably probes the workfunction of Ca-QFSBLG, and not Ca overlayers, although the deposition of additional surface Ca may further lower the workfunction of Ca-QFSBLG.

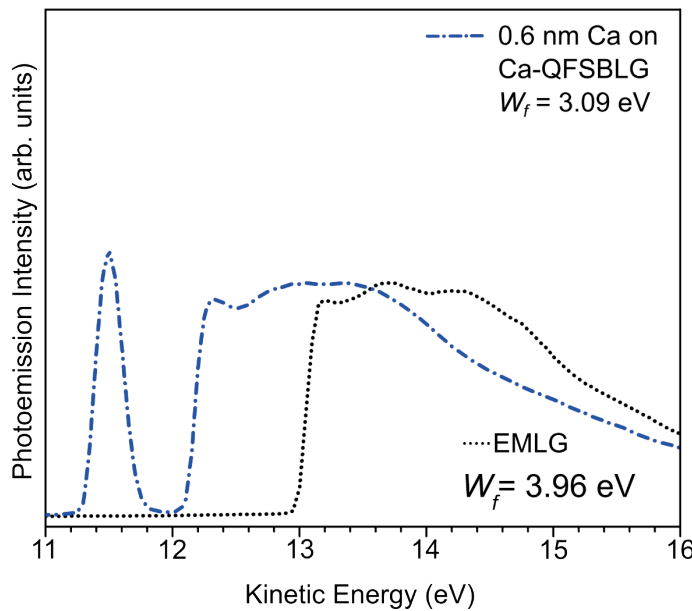


FIGURE 5.14: SECO MEASUREMENTS SHOWING THE WORKFUNCTION (W_f) OF Ca-QFSBLG (SAMPLE FROM FIGURE 5.13) AFTER DEPOSITION OF 0.6 nm OF CALCIUM ON THE SURFACE (DASH DOT, BLUE LINE) COMPARED TO PRISTINE EMLG (DOTTED, BLACK LINE).

SECO measurements have shown that there is a measurable shift in the workfunction of EMLG after formation of Ca-QFSBLG amounting to a workfunction change of $\Delta W_f = -0.25 \pm 0.10 \text{ eV}$, shifting to a final value of $W_f = 3.71 \pm 0.05 \text{ eV}$ (average of 1st and 2nd Ca-intercalation). Although traces of un-intercalated calcium were present on the surface of the graphene, it was determined that this did not significantly affect the measurement of the Ca-QFSBLG workfunction, to within uncertainty of the measurement. Thus, the lower workfunction in Ca-QFSBLG is a strong indication that the formation of Ca-QFSBLG corresponds to an increase in n-type carrier concentration.

5.5 Conclusion

In this chapter the effects of Ca-intercalation on the physical and electronic structure of epitaxial monolayer graphene on 6H-SiC(0001) have been elucidated. By combining LEED, XPS and STM with DFT modelling, I have demonstrated that the favoured route for Ca-intercalation is insertion at the buffer layer – SiC(0001) interface to form an ordered $(\sqrt{3} \times \sqrt{3})R30^\circ$ reconstruction relative to the graphene. The intercalated Ca breaks the buffer

layer-SiC covalent bonding, and the Ca and Si interact chemically resulting in XPS signatures resembling a Ca-silicide compound (closely matching CaSi_2 from the literature), while simultaneously ‘freestanding’ the buffer layer to form Ca-QFSBLG. An approximate calculation from the Si 2p and Ca 2p data finds that it is likely that the Ca-silicide formed contains, stoichiometrically, more silicon than calcium. This is supported by the DFT model, and lends further credibility to the component fits and reason for the similarity of the Si 2p core level binding energy with that of CaSi_2 . Together, these investigations have helped elucidate the structure of Ca-QFSBLG.

Moreover, I sought to investigate the electronic properties of Ca-QFSBLG. In this regard, I found good agreement between experimental values for the C 1s core level lineshape of Ca-QFSBLG with theoretical calculations of highly doped quasi-freestanding bilayer graphene. The comparison suggested that the layers were heterogeneously doped after Ca-intercalation, with one at a carrier concentration of $\approx 1 \times 10^{14} \text{ cm}^{-2}$ and the other at $\approx 10^{12} - 10^{13} \text{ cm}^{-2}$. Using SECO measurements, I found that the workfunction of Ca-QFSBLG decreased to $W_f = 3.71 \pm 0.05 \text{ eV}$, implying that the carriers in Ca-QFSBLG are n-type, and have increased in carrier concentration from their original values in EMLG (*i.e.* the system is more n-type).

Furthermore, I observe no evidence of Ca intercalation between the graphene layers under the conditions for intercalation used here, consistent with the predictions of our DFT modelling. While I cannot rule out that further processing could result in additional intercalation between graphene layers, or whether intercalation could proceed with graphene grown on the C-face of SiC – the results presented here indicate conclusively that the first intercalation step is at the SiC-buffer layer interface, which was previously unknown. This result already prompts a re-examination of previous studies where it was assumed that Ca intercalated *only* between graphene layers and *not* at the buffer layer – SiC interface [18-19, 23-24, 272].

6

Chapter

Magnesium Intercalation of Graphene on Silicon Carbide

Keywords: Graphene, Magnesium, Intercalation, XPS, STM, LEED, ARPES.

“You see things ; and you say “Why?” But I dream things that never were ; and I say “Why not?”
- GEORGE BERNARD SHAW

6.1 Overview

This chapter investigates the structural and electronic properties of magnesium intercalated epitaxial monolayer graphene on 6H-SiC(0001) using low energy electron diffraction, X-ray photoelectron spectroscopy, scanning tunnelling microscopy, secondary electron cut-off photoemission and angle resolved photoemission spectroscopy. The intercalation of graphene on silicon carbide with magnesium has not been reported in the literature prior to the work discussed in this chapter [26, 300]. Mg was likely overlooked as an intercalant in graphene research due to the fact that Mg (unlike chemically similar Ca) is known to not intercalate graphite. However, it is already known that some atomic species will readily intercalate the graphene-SiC interface which do not readily intercalate graphite (for example, Na, see refs. [351-353]). This, and my observation of the facile intercalation of Ca at the buffer layer-SiC interface (as demonstrated in [Chapter 5](#)), caused me to postulate that Mg might behave similarly upon interacting with epitaxial monolayer graphene on SiC (EMLG). Indeed, I find that the Mg-intercalation of EMLG shares many similarities with Ca-QFSBLG, whereby the magnesium intercalates underneath the buffer layer to form, in this case, a Mg-silicide layer, resulting in a highly n-type doped Mg-intercalated quasi freestanding bilayer graphene ‘Mg-QFSBLG’. The workfunction and carrier type is evaluated using secondary electron cut-off photoemission, in which I find a workfunction of 3.78 ± 0.05 eV, implying the carriers are electrons that after Mg-intercalation, i.e. Mg-QFSBLG is n-type

(and more n-type than EMLG). The carrier concentration is estimated by a comparison to theoretically calculated C 1s values of highly doped quasi-freestanding bilayer graphene, in which it is found that Mg-QFSBLG closely matches that of a graphene bilayer with a carrier concentration of at least 10^{14} cm⁻². These conclusions are supported by recent angle resolved photoemission (ARPES) which I devised and carried out at the Australian Synchrotron (and were subsequently analysed by my collaborators), are reviewed in this chapter. ARPES measurements show that Mg-intercalated epitaxial monolayer graphene transforms into a highly n-type doped bilayer graphene with carrier concentration of $\approx 2.10 \times 10^{14}$ cm⁻² (in agreement with the comparisons to the C 1s lineshape) and bandgap of ≈ 0.36 eV.

This chapter forms the crucial groundwork needed to study the ambient-air stability of Mg-QFSBLG (see [Chapter 7](#)), by elucidating the structure and electronic properties of pristine Mg-QFSBLG, since Mg-QFSBLG has never before been reported in the literature.

6.2 Introduction

After discovery of the electrical properties of graphene in 2004 [3], and the synthesis of uniform and large area graphene on substrates such as silicon carbide [52], intercalation experiments using graphene became experimentally accessible to common surface science techniques such as scanning tunnelling microscopy (STM) and angle resolved photoemission spectroscopy (ARPES). Since then, many elements have been successfully intercalated underneath graphene on SiC including H [82], Li [318], Ca [23], O [321], F [340, 354], Al [71], Si [297, 355-356], Ag [357], Au [319], Pt [72] and many others (see ref. [316] for a brief review). Currently more than 20 elements have been intercalated underneath graphene on SiC. Typically, these elements are intercalated underneath the buffer layer (as was the case for calcium – see [Chapter 5](#)) and form chemical bonds with the underlying silicon (some forming silicide-like compounds [72, 310, 313, 315, 317-319]), breaking the buffer layer – SiC bonds and quasi-freestanding the buffer layer to form another layer of graphene [71, 278, 304, 314, 358]. In some cases, no evidence of chemical bonding of the intercalant and surface is recorded, but even in these cases, evidence supports that the buffer layer – SiC bonds are broken to form quasi-freestanding graphene [279, 307-308, 314, 322].

The calcium intercalation of graphite [270-271] and graphene [18-19, 23-24, 272, 290, 359] has been well documented, and can highly n-type dope these systems [23]. On the other hand, the alkaline earth magnesium has not been investigated as an intercalant in graphene on silicon carbide systems. Since Mg shares the same valency as Ca and is much easier to obtain in pure form

than Ca, the Mg-intercalation of graphene on SiC would be beneficial, although the experiment has not been attempted in literature (until the work discussed in this chapter [300]). Some reasons for this may be due to the well-known experimental knowledge that metallic magnesium does not intercalate graphite [283], and also may be exacerbated by magnesium's well-known high vapour pressure [360]. More recent theoretical considerations have substantiated the difficulty of magnesium intercalation for a range of different materials (including graphite), and have implied that the difficulty of Mg intercalation is a result of its weak binding forces to the material which one wishes to intercalate (such as graphite) [351]. Thus, it is likely that for these reasons that the intercalation of graphene on SiC with magnesium was *not* considered.

Despite these challenges, magnesium has been intercalated underneath graphene on Ni(111) [361], and between layers of a 'graphite-like' material composed of boron carbon and nitrogen [362]. Furthermore, magnesium intercalation for energy storage applications has long been sought after to replace lithium [363]. But in this case, magnesium forms part of an electrolyte or organic molecule [364-365].

As a rule, it has generally been understood that Mg-intercalation of pure carbon systems is not possible, but the fact that intercalation of graphene on SiC(0001) systems can occur at the buffer layer – SiC(0001) interface (as was found with calcium in [Chapter 5](#)) implies that the 'traditional' notion of intercalation from experiments with graphite in which the intercalant is inserted between graphite layers, may not apply (as was also the case with other substrates and modified materials [361-362]). Indeed this holds true, and in this chapter I show how magnesium *is* able to intercalate graphene on silicon carbide by bonding with the Si surface of SiC(0001) to form a Mg-Si compound (closely resembling a Mg-silicide), as was the case in [Chapter 5](#) with calcium.

This chapter initially elucidates the structure of Mg-intercalated epitaxial monolayer graphene, which is found to form Mg-intercalated quasi-freestanding bilayer graphene on SiC(0001) – 'Mg-QFSBLG'; supported *via* low energy electron diffraction (LEED), X-ray photoelectron spectroscopy (XPS) and scanning tunnelling microscopy (STM) results.

Secondly, the electronic properties of Mg-QFSBLG are investigated using a comparison of the experimentally measured C 1s lineshape to theoretically calculated values of highly doped quasi-freestanding bilayer graphene (QFSBLG) (to estimate the carrier concentration); and secondary electron cut-off photoemission spectroscopy (SECO) (to determine the workfunction and hence carrier type).

Finally, the above techniques are reinforced by a review of recent direct measurements of the Mg-QFSBLG bandstructure using angle resolved

photoemission spectroscopy (ARPES), which are able to corroborate the carrier concentration ($2.10 \pm 0.2 \times 10^{14} \text{ cm}^{-2}$) and type (n-type), as well as the structural conversion of monolayer graphene to bilayer graphene [26]. The ARPES measurements also show that the formation of Mg-Si bonds result in a large electric field being applied to the bilayer graphene, and thus, observation of a sizeable bandgap of $0.36 \pm 0.01 \text{ eV}$. Ultimately, the ARPES measurements corroborate the findings laid out in this chapter, that Mg-QFSBLG is a highly n-type doped and freestanding bilayer graphene.

6.3 Methods and Experimental Techniques

The results were obtained *via* experiments at the Australian Synchrotron on the soft X-ray beamline and toroidal analyser end station (LEED, XPS, SECO – see [Figure 5.1](#) and ARPES – see [Figure 6.2](#)), and at Monash University in Prof. Michael S. Fuhrer’s laboratory (low temperature STM – see [Figure 5.2](#)) under UHV ($\approx 1 \times 10^{-10} \text{ mbar}$). All graphene samples were prepared by the U.S. Naval Research Laboratory using semi-insulating 6H-SiC(0001), nominally on-axis ($\approx 0.1 \text{ deg. offcut}$) from II-VI Incorporated. The EMLG samples were prepared using a previously described method [291].

In addition, I have studied the Mg-intercalation of hydrogen intercalated, quasi-freestanding bilayer graphene (H-QFSBLG). These samples were prepared using a previously described method [85]. It was found that Mg was not able to intercalate H-QFSBLG (see [Appendix C3](#)).

6.3.1 Mg-Intercalation Procedure

The samples used for Mg-intercalation were mounted similarly to the Ca-intercalation case (1 EMLG, 1 H-QFSBLG, see sample holder in [Figure 5.1b](#)), and an NTEZ effusion cell (MBE Komponenten) was used with a PBN crucible loaded with Mg (1/8-inch turnings, 99.95%, Sigma-Aldrich). All temperatures for the Australian Synchrotron experiments (XPS, LEED, SECO) were measured *via* a thermocouple attached to the sample holder ([Figure 5.1b](#)) and a single-colour pyrometer (LumaSense Technologies, IMPAC 8 Pro series). Magnesium metal deposition thicknesses were measured using a quartz crystal microbalance (QCM).

In the first Mg-intercalation step, $\approx 7.5 \text{ nm}$ of Mg metal was deposited onto the samples (cell temperature 673 K, 10 minutes of Mg flux exposure) which

were then heated to ≈ 773 K for 2 hours. Immediately afterwards, ≈ 3.8 nm (cell temperature 673 K, 5 minutes Mg flux exposure) of Mg was deposited before heating the sample to ≈ 773 K for 2.5 hours. These steps constituted the 1st Mg-intercalation step. In the 2nd Mg-intercalation step, the effusion cell was heated to 673 K, and the sample exposed to 10 minutes of Mg flux before annealing at 623 K for 1.5 hours.

The sister sample used for the collection of SECO data in [Figure 6.10](#) was intercalated in a step-wise fashion (the details of which are further discussed in [Chapter 8, Section 8.4.3](#) and [Appendix C4](#)) and consisted of 3 Mg-intercalations, with the 3rd Mg-intercalation yielding similar results to the final (*i.e.* 2nd) Mg-intercalation of the above sample (see [Figure 8.5](#) and [Figure C.4-3](#) for comparison). In the first Mg-intercalation step, ≈ 15 nm of Mg was deposited on the sample (cell temperature 673 K, 20 minutes of Mg flux exposure), which was then heated to 463 K for ≈ 1.5 hours. For the 2nd Mg-intercalation, ≈ 15 nm of Mg was deposited on the sample (cell temperature 673 K, 20 minutes of Mg flux exposure), which was then heated to 623 K for ≈ 1.5 hours. For the 3rd Mg-intercalation, ≈ 15 nm of Mg was deposited on the sample (cell temperature 673 K, 20 minutes of Mg flux exposure), which was then heated to 623 K for ≈ 1.5 hours.

The Mg-QFSBLG sample in [Figure 6.8](#) (STM) and [Figure 6.11](#) (ARPES) was fabricated *via* the Mg-intercalation of an EMLG sample (not a sister sample of the above, but grown *via* a similar technique, in the same furnace) with approximately 50 % monolayer, and 50 % buffer layer-only (see [Appendix C5](#) for Raman mapping spectroscopy of sister sample). The same evaporator (NTEZ, PBN cell) and Mg source were used in a different UHV chamber (the toroidal at the Australian Synchrotron – See [Figure 6.2](#)). For this sample, the cell was heated to a temperature of 673 K and the sample was exposed to the Mg flux for 25 minutes (≈ 18.8 nm) before heating to 623 K for 30 minutes. Intercalation was confirmed in-situ *via* analysis of the LEED spectrum. The sample was then taken from storage in the UHV chamber after ≈ 1 month and mounted onto an STM holder in ambient (≈ 45 minutes) before being loaded into the STM chamber. The sample was cleaned at ≈ 673 K for ≈ 2 hours before scanning.

6.3.2 Low Energy Electron Diffraction

LEED measurements were conducted at the Australian Synchrotron on the soft X-ray beamline using an 8-inch LEED spectrometer (OCI Vacuum Microengineering Inc.). Initial measurement coordinates on pristine samples were recorded, and for each subsequent intercalation / deposition, the same measurement positions were recorded. All measurements were taken at an electron energy of 100 eV so as to easily compare changes in the LEED

intensity. The location of the LEED optics is shown in [Figure 5.1a](#), and the sample holders used at the Australian Synchrotron are shown in [Figure 5.1b](#). It should be noted that all synchrotron experiments used sister samples and thus, the pristine sample in [Figure 6.3a](#) and the Mg-intercalated sample in [Figure 6.3b](#) are sister EMLG samples. The rotation of the LEED patterns in [Figure 6.3](#) is a direct result of this.

6.3.3 X-ray Photoelectron Spectroscopy (XPS)

XPS data was taken at the soft X-ray beamline at the Australian Synchrotron, with a PHOIBOS 150 (9 channeltrons) hemispherical analyser, shown in [Figure 5.1c](#). Each recorded spectrum was energy calibrated using the Au $4f_{7/2}$ line at 84.0 eV from an Au foil in electrical contact with the sample. The pass energy for all core levels was set at 5 eV. As in the Ca-intercalation experiment (see [Section 5.3.2](#)), the Mg-intercalation was conducted in 2 intercalation steps. In this chapter, I present only the 2nd (final) Mg-intercalation step. The omitted 1st Mg-intercalation step can be found in [Appendix C2](#).

The Si 2p spectra were obtained at $E_{hv} = 600$ eV (bulk sensitive) and 150 eV (surface sensitive) – and were fit with Voigt functions with a Lorentzian full width at half maximum (FWHM) of 0.1 eV and Gaussian FWHM of 0.4 eV (0.5 eV was used only for oxide components). The Lorentzian FWHM of the EMLG samples, which was kept constant, was determined from the narrower Si 2p linewidths of pristine H-QFSBLG samples (see [Appendix B4/C3](#)). The narrower linewidths were a consequence of the lack of higher binding energy components associated with silicon oxides, and thus, acted as standards in the experiment. Additionally, the area ratio of the Si 2p spin-orbit split peaks (and Mg 2p/Ca 2p core levels) was strictly kept as $2p_{1/2}:2p_{3/2} = 1:2$ [292], and the spin-orbit splitting of the Si 2p core level was 0.61 ± 0.02 eV in the fits (averaged, standard deviation), in excellent agreement with previously measured values [292-293]. The analysis was performed identically to the Ca-intercalation case in [Chapter 5](#). All values for the fit parameters of the Voigt functions can be found in [Appendix C1](#).

The pristine (and intercalated) C 1s ‘graphene’ peak was fit with a Briet-Wigner-Fano (BWF) asymmetric lineshape [294] (a type of asymmetric Lorentzian, see [Appendix B1](#) for further details); as this lineshape was found to fit component G more accurately than the often used Doniach-Šunjić lineshape [295]. Upon intercalation, the n-type doped graphene peak component G' was phenomenologically fit using a model that incorporated a BWF lineshape convoluted with 3 Voigt functions (the details of which can be found in [Appendix C2](#)), as this was an approximation of the plasmon effects on lineshape recently described [25, 296]. The width and asymmetry

of the BWF lineshape were kept relatively consistent, with only small changes in the asymmetry parameter (Q) being allowed in order to optimise the fit (for the pristine samples only). All C 1s core level SiC-related components were fit with Voigt lineshapes using a Gaussian width of 0.4 eV and Lorentzian width of 0.2 eV [297] (resulting in a FWHM = 0.52 eV, all parameters are outlined in [Table 6-2](#) and [Table C.1-3](#)). Care was taken to keep the Gaussian and Lorentzian contributions constant, *i.e.* the width of the Voigt functions did not change for the same components. Additionally, stringent conditions were placed on the binding energy location of the fitted peaks, which typically did not vary more than the uncertainty of the measurement, taken as ± 0.05 eV. The position of each component was calculated by averaging the available measurements of the same component (in the same sample) across the various X-ray energies (E_{hv}). If the standard deviation was higher than the uncertainty in the tool (*i.e.* $> \pm 0.05$ eV), then the standard deviation was taken as the uncertainty in the measurement.

To semi-quantitatively assess the surface sensitivity of the fitted components, the relative intensity (RI) was calculated by using the bulk SiC components of EMLG – B_{Si} (for the Si 2p core level) and B_C (for the C 1s core level) as the intensity reference (*i.e.* the RI of B_{Si} and $B_C = 1$). The RI ratio (RI_R) was then used to calculate a semi-quantitative measure of the surface sensitivity of a particular component by division of the lower E_{hv} RI with the RI of the same component at higher E_{hv} . In this regime, an $RI_R > 1$ signifies a more surface-like component, and an $RI_R \leq 1$ signifies a more bulk-like component – see [Appendix B1](#) for details.

6.3.4 Scanning Tunnelling Microscopy (STM)

The STM micrograph of [Figure 6.8](#) was taken with a Createc low temperature STM operating in UHV. For this micrograph, the temperature was 77 K, and the image was acquired with an (electrochemically) etched tungsten tip. The etching solution used 4 g of NaOH in 50 ml of milli-Q water. The tip (≈ 100 μm in diameter, 99.95% W – see [Figure 6.1a](#)) was submerged in the solution, and a ± 50 nA current was applied. In these conditions, the tip was etched within 10 seconds ([Figure 6.1b](#)). After etching, the tip was dipped in milli-Q water for 30 seconds, then isopropyl alcohol (IPA) for 30 seconds ([Figure 6.1c](#)). The etching and cleaning procedure is shown in [Figure 6.1](#).

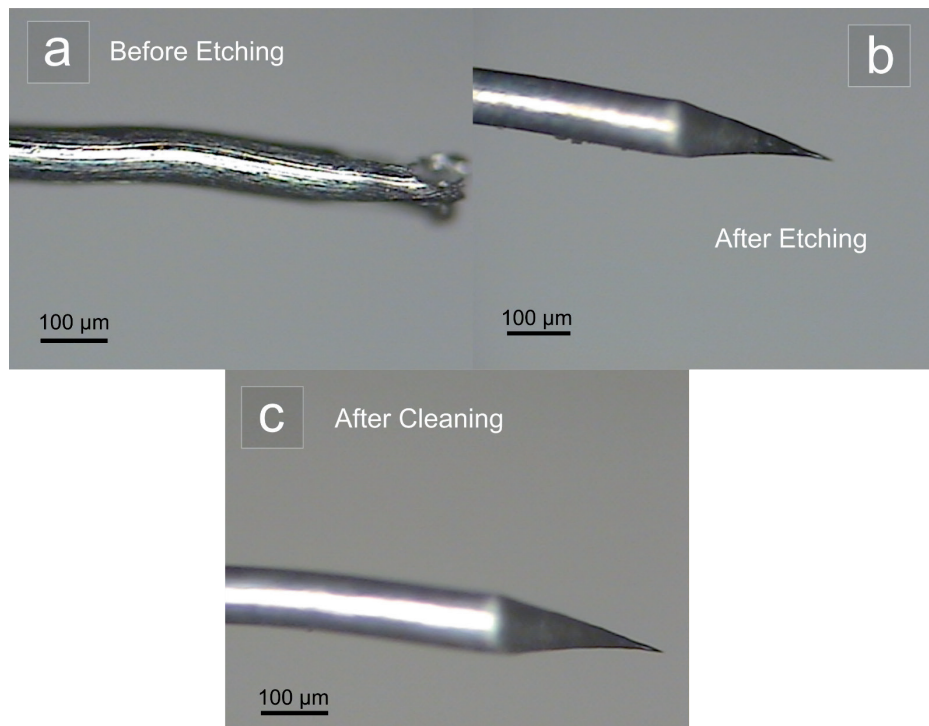


FIGURE 6.1: ETCHING A TUNGSTEN TIP FOR THE SCANNING TUNNELLING MICROSCOPE.

All images acquired with an optical light microscope. (a) The 100 μm tungsten wire was coarsely cut with wire cutters prior to etching. This creates an extremely blunt tip, as can be seen under the optical microscope. (b) After the etching procedure, a sharp tip is formed, but this still has some visible particulates. (c) After cleaning in milli-Q water and IPA, the tip is largely free of these particulates.

6.3.5 Secondary Electron Cut-Off (SECO) Photoemission

SECO data (Figure 6.10) was taken at $E_{hv} = 100$ eV (pass energy set to 2 eV) to find the workfunction (W_f) of the clean and Mg-intercalated EMLG. A bias of -9 V was applied to the sample in order to effectively measure the low energy cut-off, and all samples were measured while perpendicular to the analyser – as this is known to increase the accuracy of W_f measurement [137]. The W_f was then determined by the intersection of 2 linear fits to the steep edge and background, as is common with SECO determinations of the W_f [144, 299]. Further details on the SECO technique can be found in Chapter 3 Section 3.4.2.

6.3.6 Angle Resolved Photoemission Spectroscopy (ARPES)

ARPES data was obtained at an X-ray energy of $E_{hv} = 100$ eV at room temperature. The X-rays were linearly polarised with a spot size of $100 \mu\text{m} \times 60 \mu\text{m}$, incident normal to the sample. All binding energies (E_B) were referenced to the Fermi level (E_F), which was obtained using the Fermi edge of a reference Au foil in electrical contact with the sample, which acted as the standard. The energy and wavevector (k) resolution was estimated to be 100 meV and 0.2 \AA^{-1} , respectively.

The toroidal analyser setup [366] is shown in Figure 6.2, and differs from a ‘standard’ ARPES setup as it permits all polar emission angles ($\theta = -90^\circ$ to $+90^\circ$) to be measured along the high symmetry azimuth (φ). Figure 6.11 was obtained by measurement of the Dirac cone perpendicular to the $\overline{K} - \overline{\Gamma} - \overline{K}$ direction, see ref. [26] for further details.

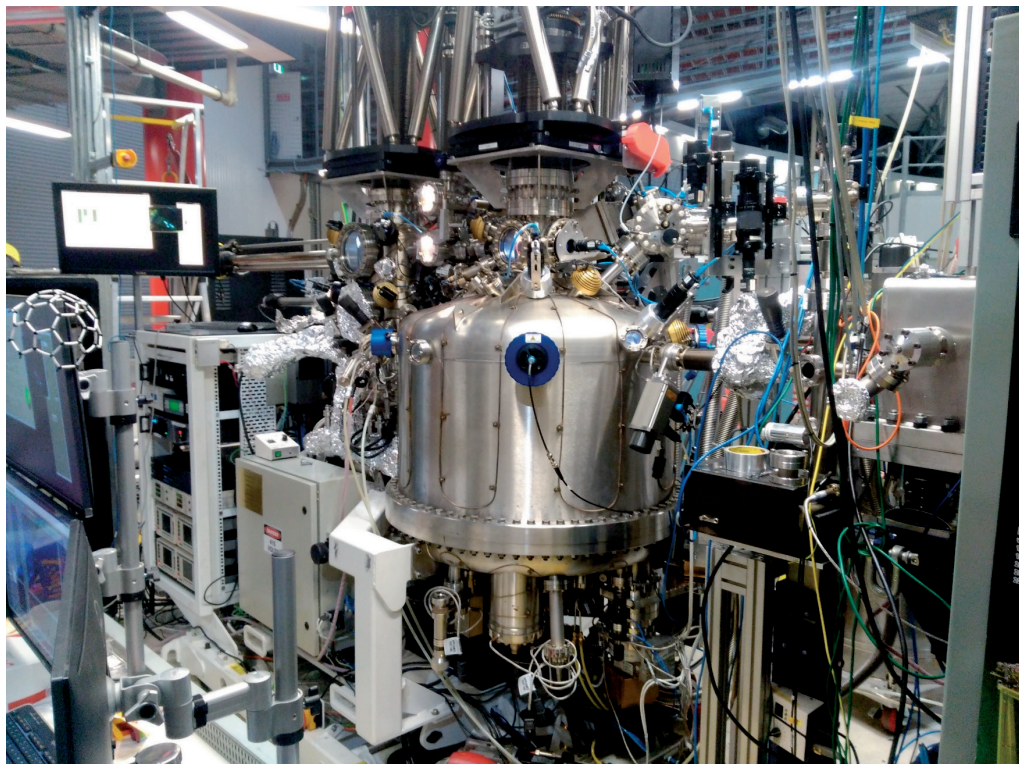


FIGURE 6.2: TOROIDAL ANALYSER AT THE AUSTRALIAN SYNCHROTRON.

6.4 Results and Discussion

The results and discussion will be segmented according to the respective characterisation techniques in the order of LEED, XPS and STM which will serve to overview the structural and chemical consequences of Mg-intercalation on EMLG. Then, the electrical properties of Mg-QFSBLG will be investigated with SECO (workfunction) measurements and comparisons to the C 1s lineshape of highly doped graphene. Finally, recent ARPES measurements [26]; and compared to theoretical models for Mg-QFSBLG. Unlike Ca-QFSBLG, I only show here the analysis of Mg-intercalated EMLG, as it was found that H-QFSBLG could not be intercalated with Mg (See [Appendix C3](#)). Nonetheless, I show that the Mg-intercalation of EMLG results in similar physical/chemical and electronic changes to Ca-intercalated EMLG, and forms highly n-type doped Mg-intercalated quasi-freestanding bilayer graphene, *i.e.* Mg-QFSBLG.

6.4.1 Low Energy Electron Diffraction (LEED)

[Figure 6.3](#) shows LEED images of pristine and Mg-intercalated EMLG taken at an electron energy of 100 eV. LEED images were also taken of pristine and Mg-intercalated H-QFSBLG (and can be found in [Appendix C3](#)), although in this case, magnesium was found to **not** intercalate H-QFSBLG. Thus, in this section we show only the results for EMLG, and leave discussion of H-QFSBLG to [Appendix C3](#).

[Figure 6.3a](#) shows a pristine EMLG sample with graphene (G(1x1)) and SiC (SiC(1x1)) spots, as well as the expected $(6\sqrt{3}\times 6\sqrt{3})R30^\circ$ and (6x6) spots which originate from the buffer layer – SiC interaction [172]. The Mg-intercalated sample is shown in [Figure 6.3b](#), and shares some features with Ca-QFSBLG (see [Chapter 5, Section 5.4.1](#)) and H-QFSBLG. Firstly, in [Figure 6.3b](#), it can be seen that the relative intensity of the SiC(1x1) to the G(1x1) spots is greatly reduced upon Mg-intercalation. This is in contrast to the similar intensity of the G(1x1) and SiC(1x1) spots in pristine EMLG prior to intercalation ([Figure 6.3a](#)). Secondly, the $(6\sqrt{3}\times 6\sqrt{3})R30^\circ$ spots are strongly suppressed in the Mg-intercalated samples ([Figure 6.3b](#)), when compared to pristine EMLG ([Figure 6.3a](#)). These observations are similar to the case of H-QFSBLG after H-intercalation of EMLG, which is known to decouple the buffer layer [60], and thus, suggests that the buffer layer of the EMLG is similarly decoupled after Mg-intercalation and transformed to QFSBLG (*i.e.* Mg-QFSBLG). Consequently, our LEED results present the first evidence that intercalation of Mg occurs between the SiC(0001) surface and the buffer layer. It should be noted that the weak $(6\sqrt{3}\times 6\sqrt{3})R30^\circ$ spots after Mg-intercalation (seen in

[Figure 6.3b](#)), are also observed after H-intercalation [82] (and Ca-intercalation, see [Chapter 5, Section 5.4.1](#)), and likely results from incomplete (*i.e.* partial) intercalation [301].

In contrast to Ca-QFSBLG, the Mg-QFSBLG in [Figure 6.3b](#) shows the emergence of $(\sqrt{3}\times\sqrt{3})R30^\circ$ spots with respect to the SiC(1x1) spots (*i.e.* SiC($\sqrt{3}\times\sqrt{3})R30^\circ$), not the G(1x1) spots as was observed in the case of Ca-QFSBLG (see [Figure 5.3](#)). The presence of SiC($\sqrt{3}\times\sqrt{3})R30^\circ$ spots indicates reconstruction of the SiC surface, tripling the unit cell. Such spots were observed by Stöhr *et al.* [358] and Kim *et al.* [304] after intercalation of buffer layer-only on SiC with Bi and In, respectively, and by Xia *et al.* [355] after Si-intercalation of EMLG. The SiC($\sqrt{3}\times\sqrt{3})R30^\circ$ spots have also been observed in the past with Si adatoms bonded via the dangling bonds of the Si surface of SiC [170]. Thus, the observation of these SiC($\sqrt{3}\times\sqrt{3})R30^\circ$ spots strongly indicates that Mg has intercalated beneath the buffer layer, releasing the buffer layer – SiC bonds to create Mg-QFSBLG; in agreement with the disappearance of the $(6\sqrt{3}\times6\sqrt{3})R30^\circ$ / (6x6) and brightness increase in G(1x1) spots relative to the SiC(1x1) spots.

Also visible in [Figure 6.3b](#) are extra spots concentric around both the G(1x1) and SiC(1x1) spots. These spots are shown more clearly in the magnified and enhanced views in the right inset of [Figure 6.3b](#). In regards to the G(1x1) spots, the new concentric spots correspond to an (18x18) reconstruction, rotated 30° with respect to the $(6\sqrt{3}\times6\sqrt{3})R30^\circ$ spots. Observation of the (18x18) spots is consistent with the expected expansion of the Moiré pattern from the interaction of graphene with SiC(0001) from $(6\sqrt{3}\times6\sqrt{3})R30^\circ$ to (18x18) upon the $(\sqrt{3}\times\sqrt{3})R30^\circ$ reconstruction of the surface (*i.e.* $(\sqrt{3}\times\sqrt{3})R30^\circ \times (6\sqrt{3}\times6\sqrt{3})R30^\circ = (18\times18)$). These LEED spots have been observed previously after the intercalation of Pt underneath graphene on SiC(0001), and their appearance was attributed to the concurrent formation of a Pt-silicide [72]. Similarly, I observe the appearance of $(6\sqrt{3}\times6\sqrt{3})R30^\circ$ spots around the SiC(1x1) spots, corresponding to the expansion of the (6x6) Moiré by the $(\sqrt{3}\times\sqrt{3})R30^\circ$ reconstruction.

[Figure 6.3b](#) also shows (5x5) spots but these were not found to have significance regarding the Mg-intercalation structure since these spots are known to appear after synthesis of the buffer layer [172]. But in [Figure 6.3b](#), a (5x5) spot pattern was observed only *after* Mg-intercalation, and not in the pristine EMLG sample of [Figure 6.3a](#). The visibility of the (5x5) spots has been previously found to depend on the preparation of the SiC substrate [172]. Although here, it is clearly observed that this spot pattern is visible only after Mg-intercalation, which suggests that high temperatures are not necessary for the formation of the (5x5) symmetry, and that intercalation by itself can enhance this spot pattern. Interestingly, this spot pattern was not observed for Ca-QFSBLG. As discussed further below, the Mg-QFSBLG sample was not as ‘completely’ intercalated as the Ca-QFSBLG sample due to the difficulty of Mg-intercalation, and thus, the (5x5) spot pattern may arise due to stresses

imposed which cause spontaneous re-orientation of the remaining buffer layer.

However, there also exists an alternate interpretation of the aforementioned (18×18) and (5×5) spot patterns. The (18×18) spots coincide with the spots expected on the $6\sqrt{3}$ grid (see Figure 3.24), whereas in pristine EMLG (Figure 6.3a), these spots are not visible due to kinematic suppression via the buffer layer [172]. Upon Mg-intercalation (Figure 6.3b), the buffer layer is transformed into graphene, lifting the kinematic suppression condition and resulting in the observation of the additional $6\sqrt{3}$ spots (*i.e.* the previously referred to (18×18) spots). Thus, the (5×5) spot patterns may instead also lie on the $6\sqrt{3}$ grid – as these spots are close to each other (see Figure 3.24) – and is difficult to determine from the resolution in Figure 6.3b.

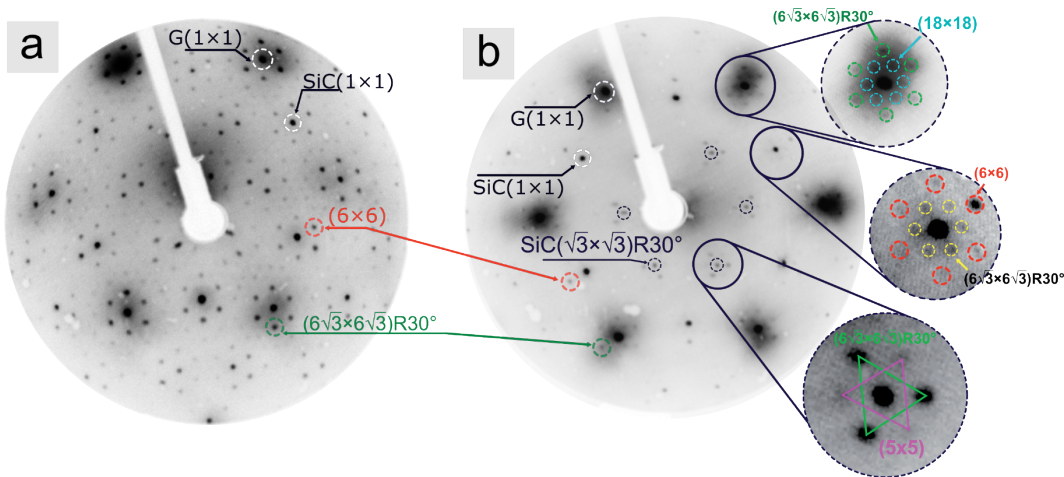


FIGURE 6.3: LOW ENERGY ELECTRON DIFFRACTION (LEED) OF PRISTINE AND Mg-INTERCALATED EPITAXIAL MONOLAYER GRAPHENE ON 6H-SiC(0001) (Mg-QFSBLG) AT AN ELECTRON ENERGY OF 100 eV.

(a) Pristine epitaxial monolayer graphene on 6H-SiC(0001) (EMLG) showing graphene ($G(1 \times 1)$) and SiC ($SiC(1 \times 1)$) spots, as well as $(6\sqrt{3} \times 6\sqrt{3})R30^\circ$ and (6×6) spots arising from the buffer layer. **(b)** Mg-QFSBLG with spots corresponding to a $(\sqrt{3} \times \sqrt{3})R30^\circ$ reconstruction relative to the $SiC(1 \times 1)$ spots ($SiC(\sqrt{3} \times \sqrt{3})R30^\circ$), along with (5×5) , (18×18) (around the $G(1 \times 1)$), and $(6\sqrt{3} \times 6\sqrt{3})R30^\circ$ (around the $SiC(1 \times 1)$) spots. The suppression of $(6\sqrt{3} \times 6\sqrt{3})R30^\circ/(6 \times 6)$ spots related to the buffer layer and increase in brightness of the $G(1 \times 1)$ with respect to the $SiC(1 \times 1)$ spots, as compared to pristine EMLG in (a) is apparent.

6.4.2 X-ray Photoelectron Spectroscopy (XPS)

Here I present and discuss the XPS results for the C 1s, Si 2p, O 1s and Mg 2p core levels for the Mg-intercalated EMLG sample, the LEED of which is shown in [Figure 6.3b](#). For the Si 2p and C 1s spectra, only the pristine and 2nd Mg-intercalation step are shown for brevity. The omitted 1st Mg-intercalation step is shown in [Appendix C2](#), but does not alter the conclusions found in this section. XPS results for the H-QFSBLG samples can be found in [Appendix C3](#), but in this case, it was found magnesium could not intercalate H-QFSBLG significantly (at detection limit). Further discussion on the technological implications of this finding can be found in [Chapter 8, Section 8.4.2](#).

6.4.2.1 Si 2p Core Level Spectra

[Figure 6.4](#) shows the Si 2p core level spectra before ([Figure 6.4a-b](#)) and after Mg-intercalation ([Figure 6.4c-d](#)). As I detail below, the Si 2p core level spectrum after Mg-intercalation is similar to the Si 2p core level spectrum after Ca-intercalation. Further investigation will show that the changes we observe in the XPS spectra correspond to the creation of Mg-QFSBLG, and the XPS spectra are in fact similar to the Ca-QFSBLG sample (with the exception that Mg could not displace the hydrogen in H-QFSBLG, see [Appendix C3](#)).

The pristine EMLG spectra shown in [Figure 6.4a-b](#) are almost identical to those presented in [Figure 5.4a-b](#) for a sister EMLG sample prior to Ca-intercalation. As such, I refer the reader to [Chapter 5 Section 5.4.2.1](#) for further details regarding the specific components. Again, the RI's (and thus RI_R 's) are referenced to the bulk of the SiC, components B_{Si}/B_C , and I retain the same nomenclature as in [Figure 5.4a-b](#). The relevant fit parameters can be found in [Table 6-1](#).

[Figure 6.4c-d](#) shows the sample after the 2nd Mg-intercalation and the emergence of several new spectral components. Component Mg_{Si} located at $E_B = 99.94 \pm 0.05$ eV ($RI_R \approx 2.9$) matches closely in binding energy to an Mg-silicide compound [306, 367-368].

Additionally, component Ox_3 at $E_B = 99.53 \pm 0.05$ eV is also a surface ($RI_R \approx 2.73$) sensitive component, and this may suggest that it is either a Mg-silicate (*i.e.* the Mg has reacted with the available surface oxygen that was present as contamination in the sample, component Ox_o , to produce an Mg-Si-O compound) or another form of Mg-silicide. An Mg-silicate component can be ruled out, as prior studies have determined the binding energy of an Mg-

silicate is much higher than what is observed ($E_B = 102 - 103$ eV) [369-370]. It is well known that magnesium silicide is only able to form in the stoichiometry Mg_2Si , but the extreme conditions under which this Mg-silicide is formed could facilitate the formation (underneath graphene), of a stable stoichiometry differing from that of Mg_2Si (varying stoichiometries for Mg-Si have recently been investigated in the context of high-density anode materials [371]). For instance, Pi *et al.* [306] found that upon Mg deposition on Si(001), a sub-stoichiometric interfacial ‘transition layer’ Mg-silicide formed in addition to Mg_2Si ; the components separated by $\Delta E_B \approx 0.42$ eV with the interfacial layer lying at higher binding energy. The binding energy separation between components Mg_{Si} and Ox_3 is $\Delta E_B = 0.41 \pm 0.1$ eV, in agreement with Pi *et al.* [306]. Since component Mg_{Si} is at higher binding energy than component Ox_3 , it may be the case that component Mg_{Si} is a transition layer (sub-stoichiometric Mg-silicide), and that component Ox_3 is an Mg-silicide with stoichiometry closer to Mg_2Si [306]. It should be noted here that component Ox_3 remarkably resembles component Ox_1 in the Ca-intercalated XPS spectra (Figure 5.4), in which it was also implied that the component consisted of a sub-stoichiometric Ca-silicide, in agreement with Pi *et al.* [306] (see Appendix B3 for discussion).

Components B''_{Si} ($E_B = 100.32 \pm 0.05$ eV) and Z''_{Si} ($E_B = 100.69 \pm 0.05$ eV) are analogous to the bulk and sub-surface SiC components (B_{Si} and Z_{Si}), respectively, shifted in energy by surface band bending. These components are analogous to components B'_{Si} and Z'_{Si} , which were also observed to shift in binding energy after Ca-intercalation. Also observed in Figure 6.4c-d are the original bulk components B_{Si} and Z_{Si} , yet with reduced intensity. This again suggests that the Mg-intercalation is incomplete or partial in agreement with the LEED data in Figure 6.3b, which still showed the (albeit diminished) presence of a buffer layer (see Section 6.4.1 discussion).

I also observe the formation of component Mg_{2s} at $E_B = 103.94 \pm 0.05$ eV. A similar component has been observed in previous XPS studies of magnesium silicide formation on Si(111) and Si(100), though its origin is controversial [331, 367]. The observation of a higher binding energy component in the Si 2p core level spectrum after Mg_2Si formation on Si(100) was attributed to plasmon losses from Mg 2s electrons [331]. However, in the intercalation experiments here, there is no observable Mg metal on the surface after the 2nd Mg-intercalation (see the Mg 2p core level in Section 6.4.2.3, Figure 6.7), and thus, component Mg_{2s} cannot be caused by metallic plasmon losses. In the case of Mg_2Si on Si(111), the higher binding energy component in the Si 2p spectrum ($E_B \approx 104$ eV, in agreement with our measurements) was attributed to satellite peaks from Mg 2s emission [367]. Satellite features can also (in addition to plasmons) be caused by polychromatic light and shake-up features. Since the experiment uses monochromatic light, I tentatively attribute this peak to a shake-up feature. Furthermore, component Mg_{2s} disappears into the signal noise level when $E_{hv} = 600$ eV, strongly implying that this component resides near to the surface (*i.e.* is associated with the formation of the Mg-silicide).

Further work is needed to confirm the origin of this feature, but its association with magnesium silicide formation lends support to our conclusion that Mg has intercalated at the buffer layer-SiC interface to interact with Si.

Thus, the XPS results complement the LEED results in Figure 6.3b and imply that magnesium has intercalated Mg between the buffer layer – SiC interface of EMLG, producing an Mg-Si compound closely resembling an Mg-silicide and decoupling the buffer layer to form another graphene layer; identical to the Ca-intercalation case.

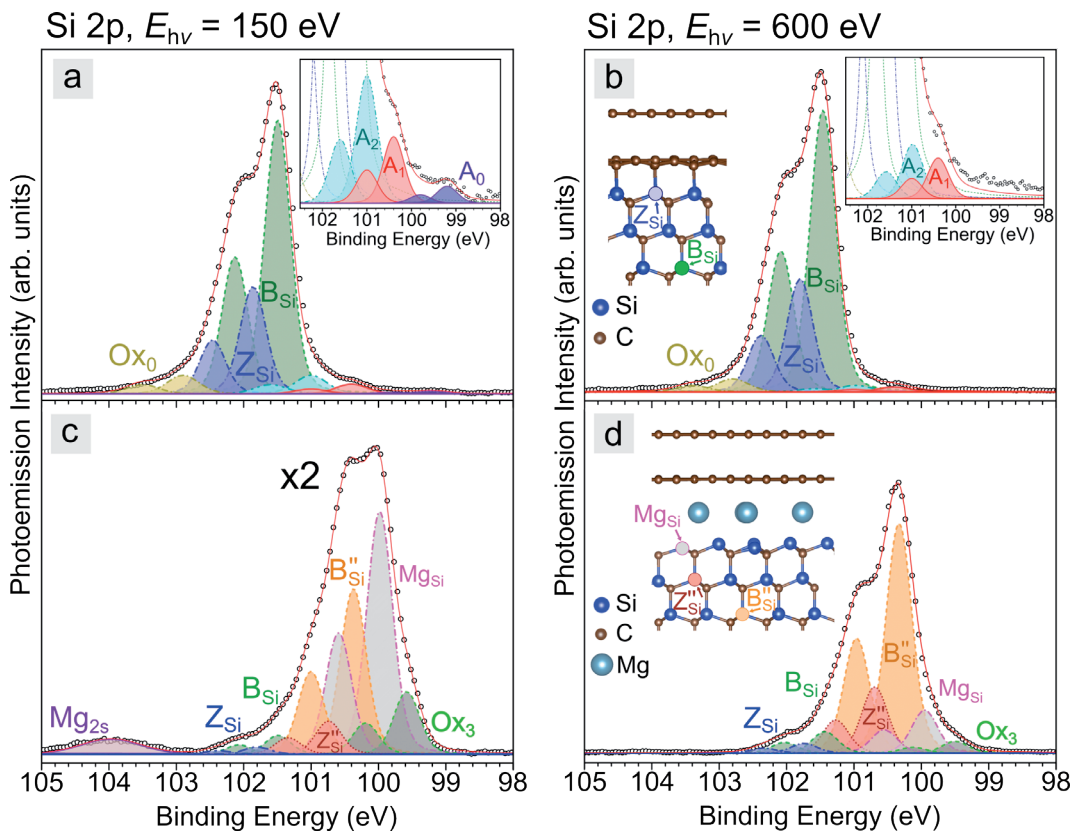


FIGURE 6.4: X-RAY PHOTOEMISSION SPECTRA OF THE Si 2P CORE LEVEL OF PRISTINE EPITAXIAL MONOLAYER GRAPHENE (EMLG) AND Mg-INTERCALATED QUASI-FREESTANDING BILAYER GRAPHENE (Mg-QFSBLG) ON SiC(0001) AT X-RAY ENERGIES OF $E_{hv} = 150$ eV (LEFT, SURFACE SENSITIVE) AND $E_{hv} = 600$ eV (RIGHT, BULK SENSITIVE).

(a), (b) Pristine EMLG showing deconvolution of spectra into components (see main text for details). Right hand side inset in (a), (b) shows magnified view of lower binding energy components, left hand side inset in (b) shows atomic model and approximate location of EMLG spectral components. **(c), (d)** After Mg-intercalation, Mg-QFSBLG was formed. Spectra are deconvolved into components (see main text for details). Left hand side inset in (d) shows atomic model and approximate location of Mg-QFSBLG spectral components. Scale of (c) is magnified $\times 2$ from (a).

TABLE 6-1: SUMMARY OF THE FIT PARAMETERS FOR THE MAJOR Si 2p COMPONENTS IN FIGURE 6.4.

Both $2p_{3/2}$ and $2p_{1/2}$ are stated, as well as the relative intensity (RI) of the $2p_{3/2}$ peaks as referenced to the bulk SiC peak ‘ B_{Si} ’ corresponding to pristine SiC prior to Mg intercalation. W_G refers to the gaussian FWHM for the Voigt fit (which was fixed to one of two values), whereas the Lorentzian FWHM (W_L) was kept constant at 0.1 eV in all fits. Component Mg_{2s} is not a 2p core level, and is thus coloured differently (see text). Dash line corresponds to no observation, n/a = not applicable.

EMLG, Si 2p		(a), (b), Pristine EMLG				(c), (d) 2 nd Mg Intercalation			
Component	E_{hv} (eV)	E_B (eV) $2p_{3/2}$	E_B (eV) $2p_{1/2}$	RI	W_G (eV)	E_B (eV) $2p_{3/2}$	E_B (eV) $2p_{1/2}$	RI	W_G (eV)
Ox_0	150	102.90	103.50	0.068	0.5				
	600	102.80	103.40	0.046	0.5				
Z_{Si}	150	101.86	102.46	0.392	0.4	101.80	102.38	0.014	0.4
	600	101.80	102.38	0.401	0.4	101.74	102.34	0.035	0.4
B_{Si}	150	101.50	102.13	1	0.4	101.49	102.07	0.034	0.4
	600	101.46	102.09	1	0.4	101.43	102.03	0.076	0.4
B''_{Si}	150					100.37	101.0	0.304	0.4
	600					100.33	100.96	0.817	0.4
Z''_{Si}	150					100.74	101.34	0.061	0.4
	600					100.69	101.27	0.235	0.4
Mg_{Si}	150					99.98	100.59	0.446	0.4
	600					99.95	100.55	0.152	0.4
Ox_3	150					99.58	100.19	0.115	0.4
	600					99.50	100.12	0.042	0.4
Mg_{2s}	150					103.97	n/a	n/a	1
	600					-	n/a	n/a	-

6.4.2.2 C 1s Core Level Spectra

Figure 6.5a-b shows the pristine EMLG C 1s core level spectra, and is almost identical to the Ca-intercalation case in **Figure 5.5a-b**. The components, elucidated in **Figure 6.5a-b**, comprise of S₁ and S₂ (related to the carbon atoms in the buffer layer) [53], graphene (G) and the surface and bulk SiC components ‘Z_C’ and ‘B_C’, respectively. The fit parameters for these components are summarised in **Table 6-2**. Since the spectrum in **Figure 6.5a-b** is almost identical to that of **Figure 5.5a-b**, the reader is encouraged to review the preceding discussion in **Chapter 5, Section 5.4.2.2** for further details. Again, there is no observation of a shift in the C 1s spectrum, as is commonly associated with doping in the graphite/graphene system (see ref. [372] for review of C 1s core level shifts in graphene). As will become obvious, the Mg-QFSBLG system is highly n-type doped (see **Section 6.4.4 – 6.4.4** for further details on doping of Mg-QFSBLG).

Figure 6.5c-d shows the C 1s core level after Mg-intercalation, and it can be observed that it shares many features with the change in the C 1s core level after Ca-intercalation shown in **Figure 5.5c-d**. Upon comparison, a similar change in shape and lack of peak shift of the graphene component G, now labelled G'', is observed (which is attributed to plasmonic effects due to high doping, and a reduction of the buffer layer contribution - see **Appendix C2**).

Furthermore, the emergence of 2 new components, labelled Z_C'' ($E_B = 282.93 \pm 0.05$ eV) and B_C'' ($E_B = 282.61 \pm 0.05$ eV) is apparent. These components are analogous to the shifted bulk (B_{Si}'/B_C') and sub-surface (Z_{Si}'/Z_C') SiC components in Ca-QFSBLG (see **Figure 5.4** and **Figure 5.5**), which arise from surface band bending caused by formation of, in this case, magnesium intercalation underneath the buffer layer. The shift of SiC components towards lower binding energy due to band bending at the SiC surface has been observed in many other graphene on SiC intercalation experiments [71-72, 82, 297, 312, 320-322].

The binding energy separation of these newly formed components and components B_C and Z_C are $\Delta E_B = 1.07 \pm 0.1$ eV (B_C->B_C '') and $\Delta E_B = 1.11 \pm 0.1$ eV (Z_C->Z_C ''), which is less shifted than what was found with Ca-intercalation. The binding energy difference, ΔE_B , between components B_C and Z_C is 0.36 ± 0.1 eV, and agrees well with the $\Delta E_B = 0.32 \pm 0.1$ eV of components B_C'' and Z_C''. These ΔE_B values agree with those of the Si 2p core level components (**Figure 6.4**) in which the binding energy separation is measured as $\Delta E_B = 1.14 \pm 0.1$ eV (B_{Si}->B_{Si} ''), 1.09 ± 0.1 eV (Z_{Si}->Z_{Si} ''), 0.37 ± 0.1 eV (Z_{Si}''->B_{Si} '') and 0.32 ± 0.1 eV (Z_{Si}->B_{Si}).

After analysis of the C 1s and Si 2p XPS spectra, it is found that there are remarkable similarities between Ca- and Mg-intercalated graphene. In the case of Mg-intercalation, it is found that: (1) an Mg-Si compound matching closely to a Mg-silicide is formed underneath the buffer layer at the SiC(0001) surface, as judged by the Si 2p spectra, and (2) the buffer layer contribution is diminished in the Mg-intercalated C 1s spectra. These conclusions are further strengthened by the LEED results in [Figure 6.3b](#), and thus, the conclusions drawn here are that Mg has intercalated between the buffer layer and SiC(0001), interacting strongly with the SiC surface and disrupting the buffer layer-SiC bonding to convert the buffer layer into a new graphene layer (Mg-QFSBLG).

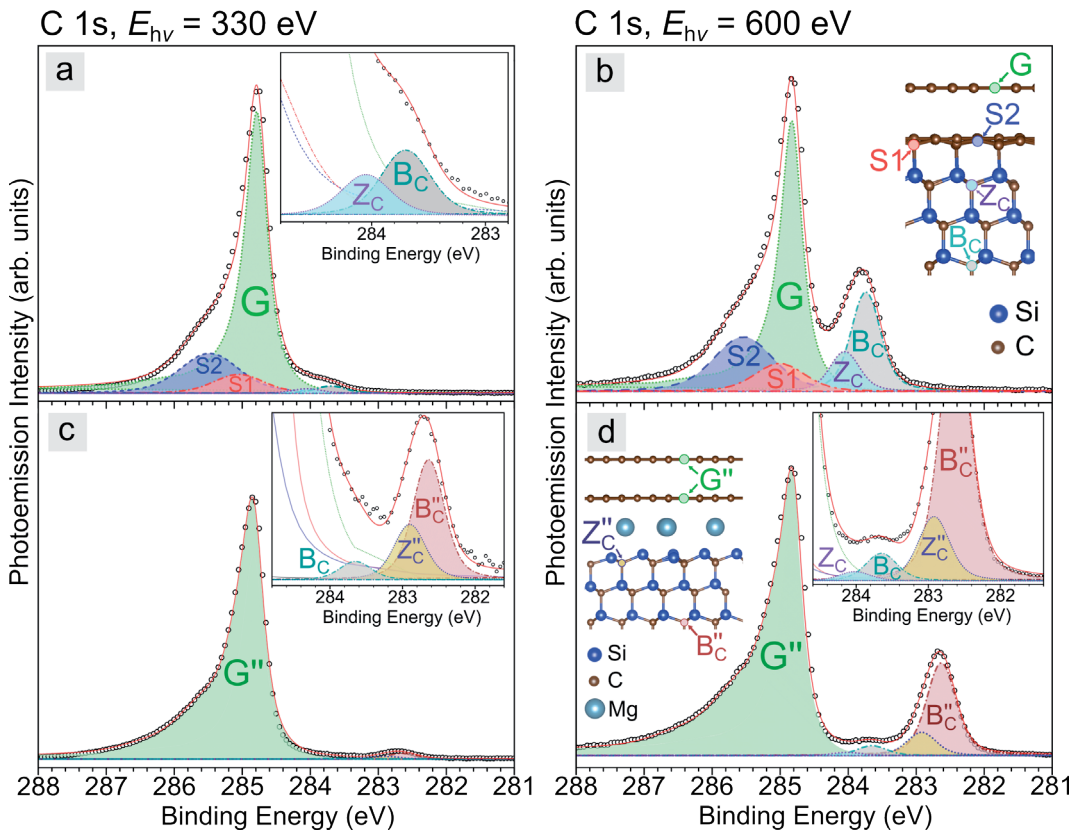


FIGURE 6.5: X-RAY PHOTOEMISSION SPECTRA FOR THE C 1s CORE LEVEL OF PRISTINE EPITAXIAL MONOLAYER GRAPHENE ON 6H-SiC(0001) (EMLG) AND Mg-INTERCALATED EMLG (Mg-QFSBLG) AT X-RAY ENERGIES OF $E_{hv} = 330$ eV (LEFT, SURFACE SENSITIVE) AND $E_{hv} = 600$ eV (RIGHT, BULK SENSITIVE).

(a), (b) Pristine EMLG prior to Mg-intercalation showing graphene (G), buffer layer (S_1, S_2) and SiC (Z_C, B_C) components. Inset in (a) shows magnified view of Z_C and B_C components. Inset in (b) shows the approximate location of all components with respect to an atomic model of EMLG. **(c), (d)** After Mg-intercalation and the formation of Mg-QFSBLG showing new components, G'' (doped graphene), B_C'' (shifted bulk SiC component) and Z_C'' (shifted 'surface' SiC component). Components Z_C and B_C are still present as the sample was only partially intercalated. Right hand side inset in (c) and (d) shows a magnified view of components B_C'' and Z_C'' . Left hand side inset in (d) shows the approximate location components B_C'' and Z_C'' .

TABLE 6-2: SUMMARY OF THE FIT PARAMETERS FOR THE MAJOR C 1S COMPONENTS IN FIGURE 6.5.

The binding energy location (E_B) is stated, as well as the relative intensity (RI) of the 1s peaks as referenced to the bulk SiC peak 'Bc' corresponding to pristine SiC prior to Ca intercalation. 'Q' refers to the asymmetry parameter of the graphene (which was fit using a BWF function). 'W_G' refers to the gaussian FWHM for the Voigt fit, whereas the Lorentzian FWHM (W_L) was kept constant at 0.2 eV in all fits except for buffer layer components S1 and S2. Dash line corresponds to no observation.

EMLG, C 1s		(a), (b), Pristine EMLG			(c), (d) 2 nd Mg Intercalation		
Component	E_{hv} (eV)	E_B (eV)	RI	Q/W _L or W _G /W _L (eV)	E_B	RI	Q/W _L or W _G /W _L (eV)
S ₂	330	285.48	5.563	0.8/0.4			
	600	285.54	0.550	0.8/0.4			
S ₁	330	285.05	2.636	0.7/0.3			
	600	285.005	0.281	0.7/0.3			
G	330	284.787	39.31	12/0.2			
	600	284.830	2.723	12/0.2			
G"	330				284.836	36.66	12/0.2
	600				284.822	2.898	9/0.2
Z _C	330	284.05	0.625	0.4/0.2	-	-	-
	600	284.05	0.400	0.4/0.2	284.02	0.033	0.4/0.2
Z _C "	330				282.90	0.375	0.4/0.2
	600				282.92	0.233	0.4/0.2
B _C	330	283.70	1	0.4/0.2	283.65	0.125	0.4/0.2
	600	283.74	1	0.4/0.2	283.65	0.100	0.4/0.2
B _C "	330				282.64	0.900	0.4/0.2
	600				282.63	0.933	0.4/0.2

6.4.2.3 O 1s and Mg 2p Core Level Spectra

Figure 6.6 shows the O 1s core level for *both* intercalation steps (the details of the 1st Mg-intercalation can be found in [Appendix C2](#)) at an X-ray energy of $E_{hv} = 900$ eV. For context, the spectrum of pristine EMLG is overlaid (dotted, black) with both intercalation steps shown as a solid red (1st Mg-intercalation, bottom) and blue (2nd Mg-intercalation, top) lines in [Figure 6.6](#). In contrast to the Ca-QFSBLG (which showed signs of oxidation after each intercalation, see [Figure 5.6](#)), no significant oxygen contamination is observed after Mg-intercalation, and this is likely due to Mg being less reactive than Ca. Also, it is likely that less Mg remained on the top surface of the graphene than in the case of Ca, which is visible from the fact that the Si 2p and C 1s spectra in [Figure 6.4](#) and [Figure 6.5](#) are less attenuated after Mg-intercalation than after Ca-intercalation. This may have contributed to more O 1s signal in the case of Ca, as metal remaining on the surface is more prone to oxidation.

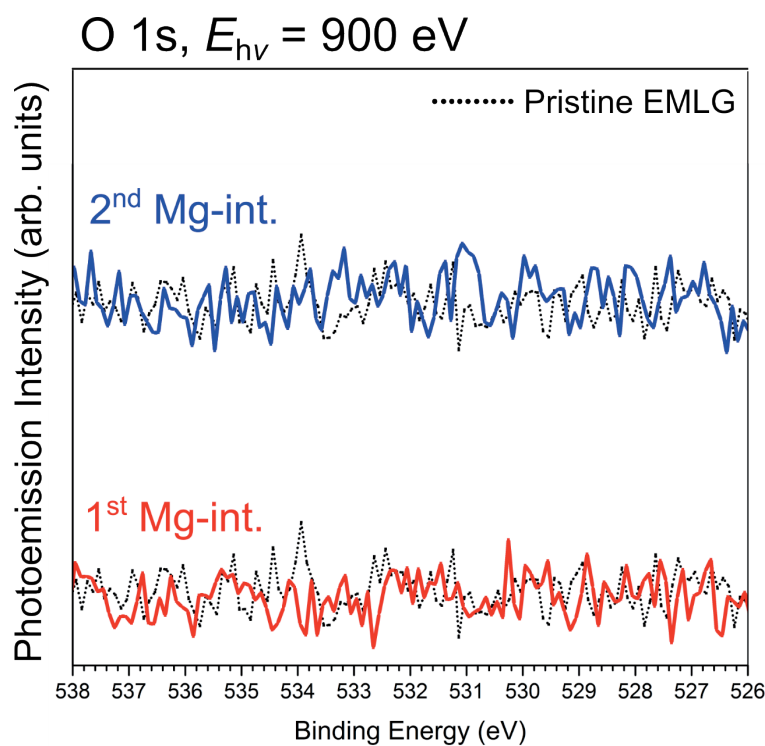


FIGURE 6.6: X-RAY PHOTOEMISSION SPECTRA OF THE O 1S CORE LEVEL OF Mg-QFSBLG AT AN X-RAY ENERGY OF $E_{hv} = 900$ eV.

Shows both Mg-intercalation steps – 1st Mg-intercalation (1st Mg-int.) and 2nd Mg-intercalation (2nd Mg-int.). Significant oxygen contamination was not detectable at either Mg-intercalation step using $E_{hv} = 900$ eV.

[Figure 6.7](#) shows the Mg 2p core level after each Mg-intercalation of EMLG to form Mg-QFSBLG. The spin-orbit splitting of the Mg 2p peaks was taken as ≈ 0.25 eV [373-374].

The 1st Mg-intercalation spectrum is shown in [Figure 6.7a](#), from which 4 components – Mg_M ($E_B = 49.71 \pm 0.05$ eV), Mg_{Si} ($E_B = 50.70 \pm 0.05$ eV), Mg_{Ox} ($E_B = 51.27 \pm 0.06$ eV) and Mg_{OH} ($E_B = 51.72 \pm 0.05$ eV) – can be elucidated, corresponding to Mg metal [375-376], a Mg-Si (Mg-silicide) compound [370, 376], a Mg-oxide compound (*i.e.* MgO)[370] and a Mg-hydroxide (*i.e.* Mg(OH)₂) [377] compound, respectively. Here, the metallic component Mg_M was fit using a Doniach-Šunjić lineshape, as is typical for this asymmetric component [378], whereas all other components employed a Voigt lineshape (see [Table C.1-6](#) for fit parameters). In contrast to the observations regarding the 1st and 2nd Mg-intercalation steps in the O 1s spectra of [Figure 6.6](#), the Mg 2p spectra suggest formation of oxides at higher binding energy, although these oxides are not in high concentration (from a comparison of the relative intensity, *RI* of Mg_{Si}). The reason oxide was observable in the Mg 2p core level spectra and not the O 1s core level spectra is likely due to the increased surface sensitivity at $E_{hv} = 100$ eV versus $E_{hv} = 900$ eV (also, the photoionization cross-section for the Mg 2p core level is ≈ 39 times greater than the O 1s at these X-ray energies [143]). Nonetheless, this oxidation likely originates from small amounts of Mg metal residing on the surface of the graphene which oxidised prior to annealing and thus, did not sublime after annealing.

After the 2nd Mg-intercalation ([Figure 6.7b](#)), component Mg_M vanishes, suggesting that the Mg metal that was initially remaining on the surface either sublimated or oxidized after the second anneal (within the detection limits of XPS), in agreement with the expectation that less magnesium metal was left on the surface to react and form oxides (O 1s) and attenuate the photoemission spectra (Si 2p/C 1s, in contrast to Ca-QFSBLG). All fit parameters for the Mg 2p components can be found in [Appendix C1, Table C.1-6](#).

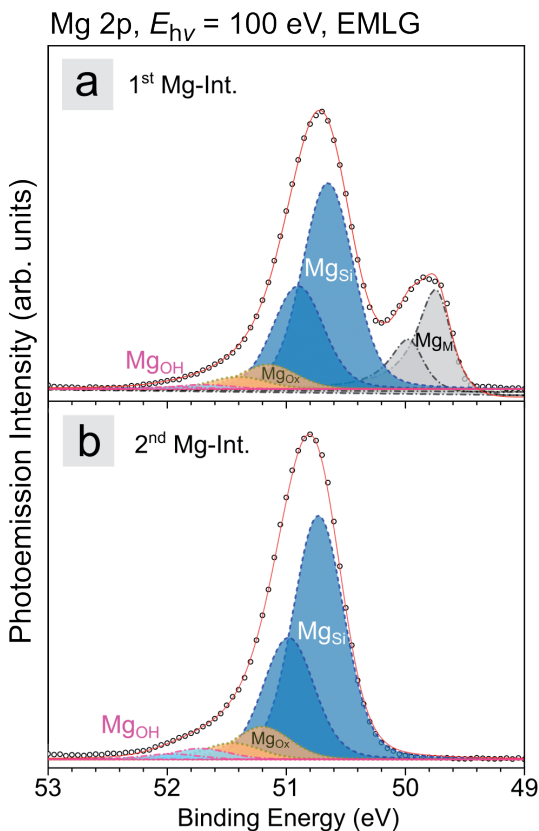


FIGURE 6.7: X-RAY PHOTOEMISSION SPECTRA OF THE Mg 2p CORE LEVEL OF Mg-QFSBLG AT AN X-RAY ENERGY OF $E_{hv} = 100$ eV.

(a) 1st Mg-intercalation showing excess metal (Mg_M , dashed grey), magnesium silicide (Mg_{Si} , dashed, blue), magnesium oxide component (Mg_{Ox} , dashed-dotted orange) and magnesium hydroxide component (Mg_{OH} , dashed-dotted, pink). **(b)** 2nd Mg-intercalation, no metallic magnesium remains on the surface, and we see only components Mg_{Si} , Mg_{Ox} and Mg_{OH} .

6.4.2.4 Summary of X-ray Photoelectron Spectroscopy Results

The Si 2p and Mg 2p core level spectra have shown that a component matching closely in binding energy to a Mg-silicide was formed after the Mg-intercalation of EMLG. The C 1s core level spectra also showed a diminishment of the buffer layer contributions, components S1 and S2. This strongly implies that upon formation of the Mg-silicide, the buffer layer-SiC bonds are broken, and a quasi-freestanding bilayer is created, *i.e.*, Mg-QFSBLG. The O 1s and Mg 2p core level spectra show that little oxidation was present during the intercalation experiments, in contrast to Ca-QFSBLG, in which oxidation was observed after the 1st intercalation. This was attributed to the decreased reactivity and the fact that there was no metallic magnesium present after the 2nd Mg-intercalation step. The oxidation that was present was likely in the form of a Mg-oxide, or Mg-hydroxide.

6.4.3	Low Temperature Scanning Tunnelling Microscopy (STM)
-------	--

A second EMLG sample was intercalated with magnesium in UHV to form Mg-QFSBLG, then exposed to ambient air for no more than approximately 45 minutes during transfer to the low temperature UHV STM (see [Chapter 7, Section 7.4.2](#) for further air stability discussion of Mg-QFSBLG). Prior to scanning, the sample was annealed in UHV (see [Methods and Experimental Techniques, Section 6.3.1](#)). [Figure 6.8](#) shows the STM topography map of the Mg-intercalated sample surface. The surface of the Mg-intercalation is almost identical to the Ca-intercalation sample in [Figure 5.9c/Figure 5.10](#), and does not show the $(6\sqrt{3}\times 6\sqrt{3})R30^\circ$ Moiré pattern characteristic of pristine EMLG ([Figure 5.9a](#)). The Mg-QFSBLG sample in [Figure 6.8](#) exhibits similar post-intercalation bright ($5\times 10^{13} \text{ cm}^{-2}$) and dark ($4\times 10^{14} \text{ cm}^{-2}$) spot densities, as seen in [Figure 5.9c](#), further supporting the claims in [Chapter 5](#) that the dark and post-intercalation bright spots are generic to graphenes intercalated at the SiC/buffer layer interface. The structure of Mg-QFSBLG is explored further in [Chapter 8, Section 8.4.1](#) using density functional theory calculations.

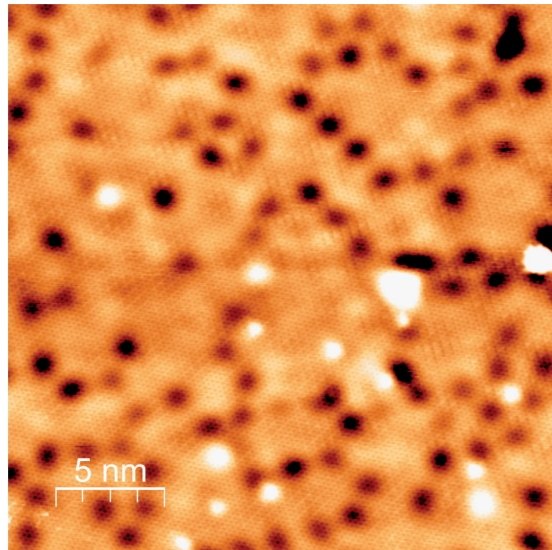


FIGURE 6.8: SCANNING TUNNELLING MICROSCOPE (STM) MICROGRAPH OF MAGNESIUM INTERCALATED EPITAXIAL MONOLAYER GRAPHENE, TO FORM MAGNESIUM-INTERCALATED QUASI-FREESTANDING BILAYER GRAPHENE (MG-QFSBLG).

The sample was exposed to air for ≈ 45 minutes before transferring to the STM (0.3 V, 200 pA, 77 K).

6.4.4 Carrier Type and Concentration in Mg-QFSBLG

In this section I will investigate the electronic effect that Mg-intercalation has on EMLG using a comparison of C 1s core level experimental measurements with theoretical calculations of the lineshape of highly doped graphene, and by analysing SECO measurements to find the workfunction, hence inferring the carrier type of Mg-QFSBLG. Finally, these methods will be compared against angle resolved photoemission measurements on Mg-QFSBLG, which has recently confirmed that Mg-QFSBLG is highly n-type doped [26].

6.4.4.1 Mg-QFSBLG C 1s Lineshape Comparison to Theory

Recently [25], the theoretical C 1s core level spectrum was calculated for highly doped freestanding bilayer graphene at carrier concentrations of up to 10^{14} cm^{-2} . The asymmetry of the C 1s spectrum generally increases with increasing carrier concentration. The reason for this is tied to the bandstructure of graphene and its 2D nature (see [Chapter 5, Section 5.4.5.1](#) for more details). Briefly, unlike a traditional ('3D') metal which has some separation between the plasmon loss peaks and the core level component, the 2D condition causes the plasmon loss peaks to appear closer to the core level component, and thus, 2D plasmon loss peaks contribute to the asymmetry and tail to higher binding energy in the C 1s lineshape [25, 296]. Thus, this suggests that the amount of asymmetry of the C 1s graphene peak can estimate the total carrier concentration, as a higher concentration of carriers around the Fermi level should yield a greater plasmon loss effect (*i.e.* a higher carrier concentration should yield a more pronounced tailing or asymmetry) which yields a unique tail shape at higher binding energy to the main photoelectron line.

As was observed for the C 1s lineshape of Ca-QFSBLG (see [Figure 5.12](#)), Mg-QFSBLG similarly exhibits an increased asymmetry at higher binding energy after Mg-intercalation. [Figure 6.9](#) shows experimental values for the C 1s core level of Mg-QFSBLG at $E_{hv} = 600 \text{ eV}$ compared to theoretically calculated C 1s core level values for quasi-freestanding monolayer (QFSMLG) and bilayer (QFSBLG) graphene at various doping levels. The same naming convention from [Chapter 5, Section 5.4.5.1](#) is carried over here. In addition, the experimental data was convoluted with a Gaussian (see [Equation 5-9](#)) with the same parameters as in [Chapter 5, Section 5.4.5.1](#), as it was found the experimental data was narrower than the theoretical data.

[Figure 6.9a](#) shows the experimental C 1s core level data for Mg-QFSBLG compared to the C 1s core level of QFSBLG with a carrier concentration of 10^{13} cm^{-2} on both layers, and 10^{13} cm^{-2} on one and 10^{14} cm^{-2} on the other.

[Figure 6.9b](#) shows the theoretically obtained curves comparing the C 1s core level of quasi-freestanding monolayer graphene (QFSMLG) at 10^{14} carriers cm^{-2} and QFSBLG with both layers at 10^{14} carriers cm^{-2} to the experimental data for Mg-QFSBLG. It is apparent that the C 1s lineshape of Mg-QFSBLG does not agree with the curves presented in either [Figure 6.9a](#) or [Figure 6.9b](#) for either monolayer or bilayer graphene doped at these carrier concentrations.

[Figure 6.9c](#) shows the theoretically obtained curves for QFSBLG with at least one of the layers (the one in which the core-hole is created) at 10^{14} carriers cm^{-2} , while the other is either at 10^{12} or 10^{13} carriers cm^{-2} (the curves are almost identical in this case). Here, I observe excellent agreement between experiment and theory, and thus, implies that Mg-QFSBLG is a quasi-freestanding bilayer graphene doped with at least one layer at a carrier density of 10^{14} cm^{-2} and the other at 10^{12} or 10^{13} cm^{-2} . As [Section 6.4.5](#) will reveal, this is extremely close to recently measured values using ARPES [26].

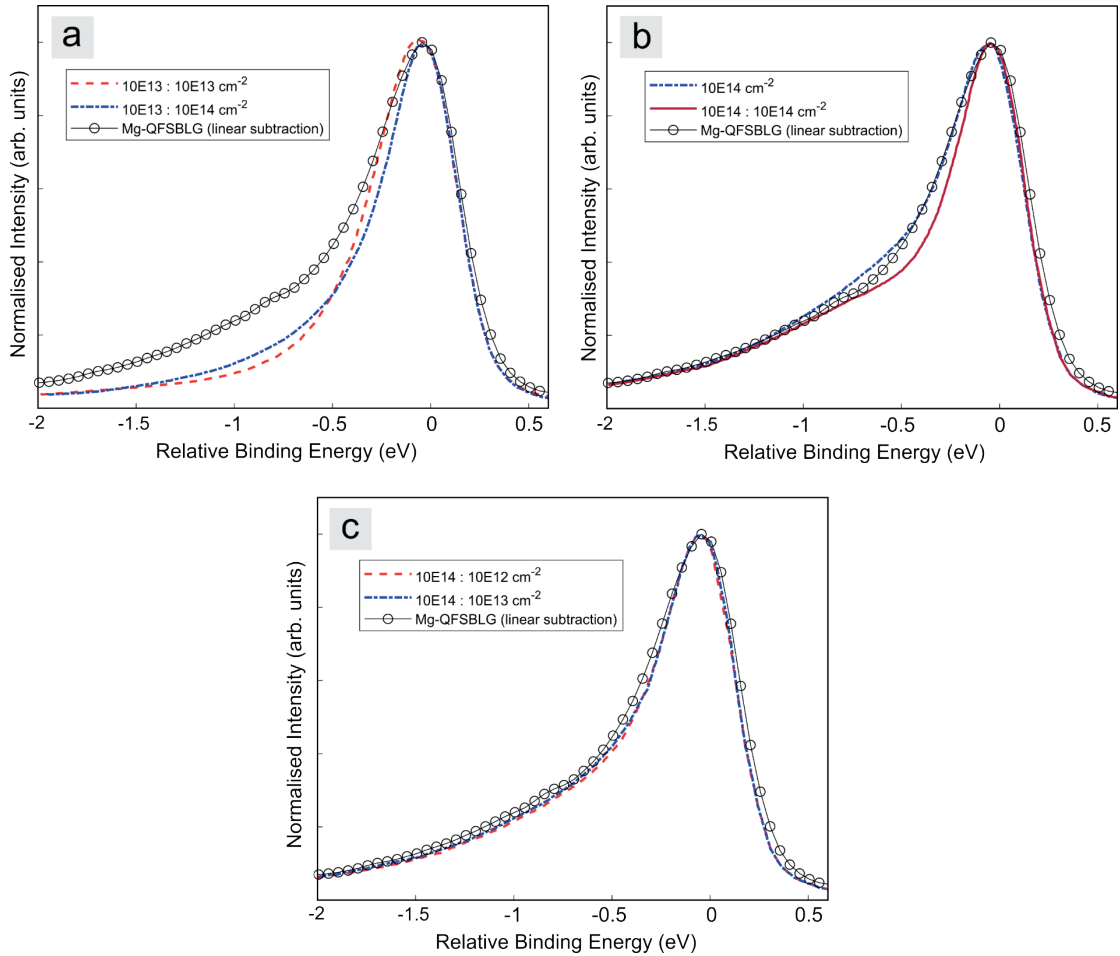


FIGURE 6.9: THEORETICALLY CALCULATED VALUES (FROM REF. [25]) OF THE C 1S CORE LEVEL OF HIGHLY DOPED FREESTANDING BILAYER (AND MONOLAYER) GRAPHENE COMPARED WITH EXPERIMENTAL VALUES OF THE C 1S CORE LEVEL OF Mg-QFSBLG (2nd Mg-INTERCALATION, $E_{hv} = 600$ eV, FIGURE 6.5d).

The doping levels of the graphene layers are indicated in the legends, with the first doping level representing the doping in the layer in which the core-hole (excitation) is created (see text for explanation). (a) Experimental spectrum of Mg-QFSBLG (open circles) and theoretically calculated spectra from ref. [25] corresponding to a doping level of $10^{13}:10^{13}$ cm⁻² (red dash) and $10^{13}:10^{14}$ cm⁻² (blue dash dot) in quasi-freestanding bilayer graphene (QFSBLG). (b) Experimental spectrum of Mg-QFSBLG (open circles) and theoretically calculated spectra from ref. [25] corresponding to a doping level of 10^{14} cm⁻² (blue dash dot) and $10^{14}:10^{14}$ cm⁻² (red solid line) in quasi-freestanding monolayer graphene and QFSBLG, respectively. (c) Experimental spectrum of Mg-QFSBLG (open circles) and theoretically calculated spectra from ref. [25] corresponding to a doping level of $10^{14}:10^{12}$ cm⁻² (red dash) and $10^{14}:10^{13}$ cm⁻² (blue dash dot) in QFSBLG.

6.4.4.2 Secondary Electron Cut-off Photoemission Spectroscopy (SECO)

The comparison of the C 1s lineshape to theoretically calculated C 1s lineshapes at high carrier concentrations is insightful in estimating the total carrier concentration after intercalation. But since no binding energy shift in the C 1s core level was observed, whether the Mg n-type or p-type doped the graphene could not be determined. To gain experimental insight into whether the carriers in Mg-QFSBLG are more n- or p-type than EMLG, secondary electron cut-off photoemission spectroscopy (SECO) measurements were performed. SECO measurements enable the experimental determination of the workfunction (W_f) of the graphene, and carrier type and concentration, since the W_f of graphene on silicon carbide is predictably tied to the carrier type *and* concentration. For instance, in previous W_f measurements, it has been shown that p-type graphene on SiC has a higher W_f value than that of n-type graphene on SiC [116, 347]. Thus, measurement of W_f can be used as a quick test to find whether the excess carrier type (*i.e.* the charge carriers in Mg-QFSBLG) are n- or p-type, and (roughly) whether the system is more n-type or p-type than EMLG.

[Figure 6.10](#) shows the SECO measurements of pristine EMLG prior to Mg-intercalation (dotted, black line), and Mg-QFSBLG after multiple Mg-intercalations (solid, blue line). The sample used here was a sister sample of the Mg-QFSBLG sample presented in [Figure 6.4](#) and [Figure 6.5](#) – see [Figure C.4-3](#), [Table C.1-9](#) and [Table C.1-10](#) in [Appendix C](#) for the Si 2p core level spectra of this sample (the C 1s core level spectra are shown for only $E_{hv} = 600$ eV in [Figure 8.8a, c, e, f](#)). For pristine EMLG, the $W_f = 3.96 \pm 0.05$ eV, which is in agreement with the value found in [Chapter 5, Section 5.4.5.2](#), and previously measured values [116]. After Mg-intercalation to form Mg-QFSBLG (see [Methods and Experimental Techniques, Section 6.3.1](#)), the workfunction decreases to $W_f = 3.78 \pm 0.05$ eV, a (significant) change in workfunction from pristine EMLG of $\Delta W_f = 0.18 \pm 0.1$ eV. This suggests that the carrier type in Mg-QFSBLG are electrons (*i.e.* n-type), and that Mg-QFSBLG is more n-type than EMLG since the workfunction of Mg-QFSBLG is lower in value than pristine EMLG [116, 347].

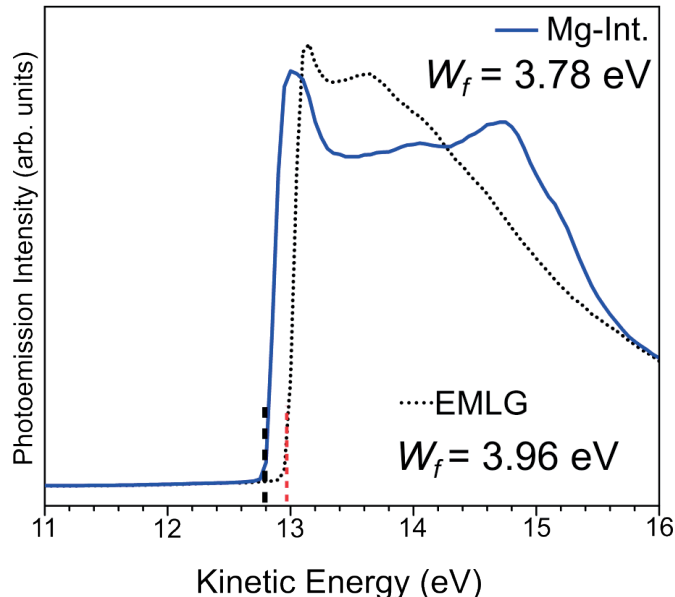


FIGURE 6.10: SECONDARY ELECTRON CUT-OFF (SECO) PHOTOEMISSION MEASUREMENTS TO DETERMINE THE WORKFUNCTION OF EMLG AND Mg-QFSBLG. The workfunction of EMLG and Mg-QFSBLG was found to be $W_f = 3.96$ eV and $W_f = 3.78$ eV, respectively. See [Figure C.4-3g-h](#) for corresponding Si 2p spectra of this Mg-QFSBLG sample.

6.4.5 Angle Resolved Photoemission Spectroscopy (ARPES)

I (along with some assistance from Dr. Anton Tadich) devised and set up (wrote synchrotron proposal, intercalation methods, liaised with collaborators for graphene samples, sourced and loaded crucibles with Ca/Mg starting materials) an ARPES experiment at the Australian Synchrotron to explore the electronic structure of Mg-QFSBLG, as part of my investigation into alkaline earth intercalated graphene. Data collection for this experiment was mainly undertaken by myself, Dr. Antonija Grubišić-Čabo and Dr. Anton Tadich. Dr. Antonija Grubišić-Čabo analysed the data and performed the comparisons to the theoretical tight-binding model. First-principles density functional theory modelling was carried out by A/Prof. Nikhil Medhekar and Dr. Yuefeng Yin. The results are found in ref. [26]; I only briefly review the main conclusions here.

[Figure 6.11](#) shows the ARPES results of pristine EMLG ([Figure 6.11a-b](#)) and Mg-QFSBLG ([Figure 6.11c-d](#)) [26]. For pristine EMLG in [Figure 6.11a](#) showing the $\bar{K} - \bar{\Gamma} - \bar{K}$ direction, a linear fit to the data was used to obtain a Fermi velocity of $v_F = 1.17 \pm 0.02 \times 10^6$ m s⁻¹, Dirac point of 0.35 ± 0.01 eV (with respect to the Fermi level) and carrier concentration of $n = 6.6 \pm 0.4 \times 10^{12}$ cm⁻². These agree

favourably with previously measured v_F [40-43, 379-382], Dirac point [34, 40, 70-72] (a small discrepancy is likely due to these 6H-SiC(0001) substrates being n-type doped rather than semi-insulating, which is known to increase slightly the n-type doping in the epitaxial graphene [69]) and carrier density [383-384] values for epitaxial monolayer graphene on silicon carbide. Figure 6.11b shows the momentum distribution curve (MDC) of the highlighted region from Figure 6.11a, and illustrates that the sample is monolayer graphene.

Figure 6.11c shows the result of Mg-intercalation. The bands in Figure 6.11c were fit using a tight binding model, the details of which are outlined in ref. [26]. The resultant fit shown in Figure 6.11c is overlaid in black. Apparent is the conversion of the 'V' shaped monolayer graphene bandstructure to the 'Mexican hat' [36] bandstructure of bilayer graphene under influence of an electric field (see Chapter 2, Section 2.2), in agreement with the LEED (Figure 6.3), XPS (Figure 6.4) and STM results (Figure 6.8) which implied conversion of EMLG to Mg-QFSBLG upon Mg-intercalation. This is made clearer by inspection of the MDC (highlighted section in Figure 6.11c) shown in Figure 6.11d. The MDC of Mg-intercalated EMLG clearly shows 2 bands (4 curves), which is characteristic of bilayer graphene.

Furthermore, since the experimental data is well explained by the tight binding model of Bernal stacked bilayer graphene, this leads to the following conclusions. Since there is no observable hybridization with Mg-bands, the graphene is well described by a freestanding bilayer. The fact that the model used is based on an interacting Bernal stacked bilayer also implies that the Mg is not intercalated between the layers, since this would complicate the fitting model.

Moreover, the Mg-QFSBLG is more n-type than EMLG (Dirac point now resides at -1.07 ± 0.07 eV), with a carrier concentration of $2.10 \pm 0.2 \times 10^{14}$ cm⁻² in agreement with the C 1s lineshape theory comparison (Figure 6.9) and SECO measurements (Figure 6.10) [26]. The asymptotic high energy velocity determined from fits to the tight binding model is $0.97 \pm 0.04 \times 10^6$ m s⁻¹. This validates that Mg-QFSBLG is highly doped, even though no observable binding energy shift in the C 1s lineshape (see Figure 6.5) is observed, and is typically associated with doping in graphite and graphene systems [372]. The theoretical C 1s core level shift for quasi-freestanding bilayer graphene on SiC has been calculated by Sernelius [25], and a bilayer with carrier concentration of $10^{14}:10^{13}$ cm⁻² should result in a binding energy shift of $\Delta E_B \approx 0.15$ eV to higher binding energy from neutral bilayer graphene. Since the system converts from monolayer to bilayer, the real shift is difficult to calculate from the values in ref. [25]. A shift of 0.15 eV is close to the experimental uncertainty of ≈ 0.1 eV in ΔE_B , so if the ΔE_B value was smaller (as it may be, see ref. [25]), then this would partly explain why there is no observed core level shift in the C 1s spectra. In addition, the C 1s core level shifts of graphene on Ir(111) was investigated by Schröder *et al.* [372] via intercalation of O, H,

Eu, and Li where it was found that the C 1s core level shift did not monotonically increase with the increase in carrier concentration. In this work, it was found that the difference in the graphene peak in the C 1s core level did not appreciably change at high carrier concentration, and rather 'levelled' out. This also would explain the difficulty in observing a shift in the C 1s core level, since differences in binding energy at high carrier concentration are close to each other.

Another feature apparent in the tight binding model fit is the formation of a bandgap with magnitude 0.36 ± 0.01 eV. The formation of such a large bandgap suggests that the intercalated Mg induces a large displacement field [36, 385-387] (see ref. [387] for brief review) of 2.6 ± 0.2 V nm⁻¹, approximately equal to the largest displacement fields that have been applied to gated bilayer graphene devices [388-390]. Thus, rather counter-intuitively (to what is observed with the traditional graphite intercalation compounds), Mg-intercalation causes a positive charge to accumulate at the SiC interface (formation of Mg-Si layer), in which an equal and opposite charge accumulates in the graphene layer. This implies that the Mg-Si layer is equally p-type doped, which may be due to a Mg deficiency in the stoichiometry of the Mg-Si layer.

Nonetheless, ARPES measurements of Mg-QFSBLG have supported the findings from LEED, XPS, SECO and the theoretical C 1s lineshape of highly doped bilayer graphene which have shown Mg-QFSBLG to be a highly n-type doped and freestanding bilayer graphene. Furthermore, tight binding model fits to the ARPES measurements of Mg-QFSBLG have shown that a sizeable bandgap forms, thought to be caused by the large electric field set up by the Mg-silicide layer.

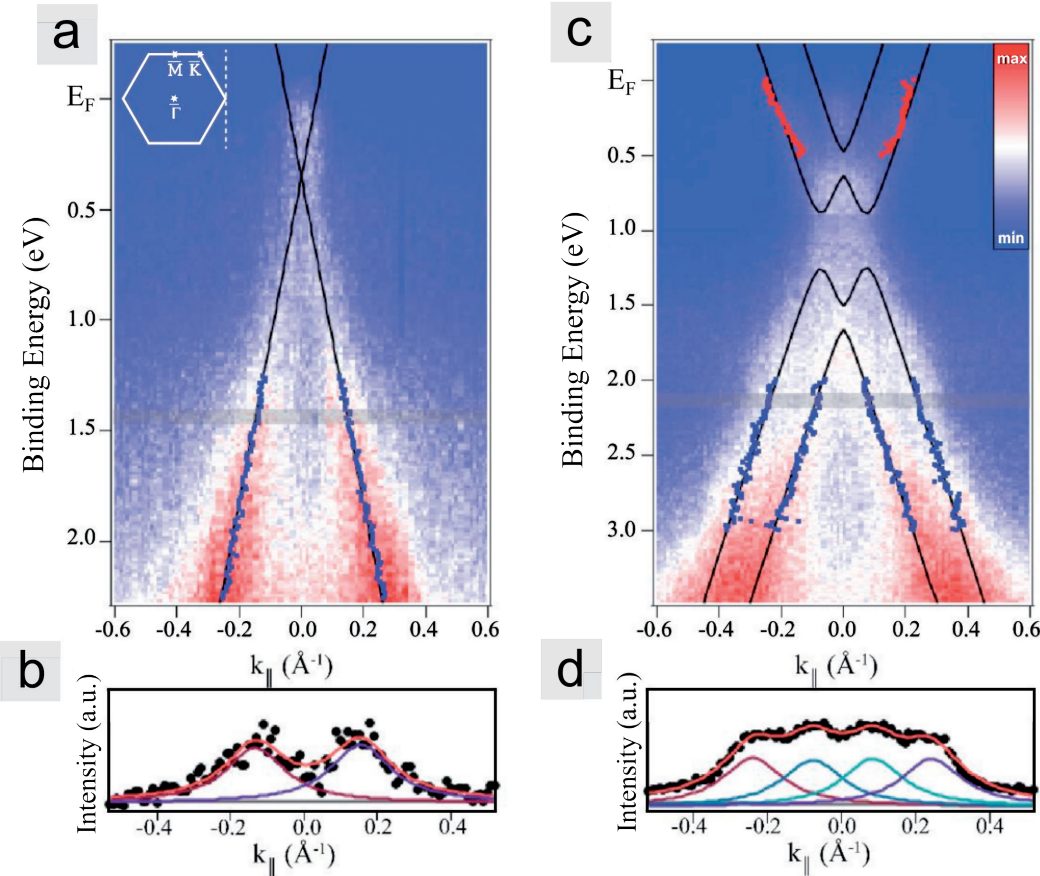


FIGURE 6.11: ANGLE RESOLVED PHOTOEMISSION SPECTRA OF PRISTINE EPITAXIAL MONOLAYER GRAPHENE ON 6H-SiC(0001) (EMLG) AND Mg-INTERCALATED EMLG (Mg-QFSBLG) [26].

(a) Energy-momentum dispersion measured perpendicular to the $\bar{K} - \bar{\Gamma} - \bar{K}$ direction centred on the \bar{K} point of EMLG. Dirac point is at 0.35 ± 0.01 eV. (b) Momentum distribution curve (MDC) across highlighted section (1.1 eV below Dirac point) in (a) showing 2 features corresponding to linear bands. (c) Energy-momentum dispersion measured perpendicular to the $\bar{K} - \bar{\Gamma} - \bar{K}$ direction centred on the \bar{K} point of Mg-QFSBLG. Dirac point now lies at 1.07 ± 0.07 eV, and a gap of 0.36 ± 0.01 eV has opened. (d) MDC of highlighted region in (c) (taken 1.1 eV below Dirac point) now has 4 prominent features which correspond to the 2 bands of bilayer graphene.

6.5 Conclusion

I have shown through LEED, XPS and STM measurements that the structural consequences concerning the Mg-intercalation of epitaxially synthesised monolayer graphene on silicon carbide results in the intercalation of Mg underneath the buffer layer. This breaks the buffer layer – SiC bonds, converting the buffer layer into another graphene layer, and thus, transforming the system into Mg-intercalated quasi-freestanding bilayer graphene (Mg-QFSBLG). Electrical characterisation of Mg-QFSBLG using SECO and comparisons with theoretical calculations of the C 1s lineshape of highly doped QFSBLG, imply that Mg-QFSBLG is highly n-type doped, with a carrier concentration of $\approx 1 \times 10^{14} \text{ cm}^{-2}$, and low workfunction ($W_f = 3.78 \text{ eV}$).

Moreover, recent ARPES results have found that Mg-intercalated EMLG transforms into a system well described as *freestanding* and *bilayer* graphene upon Mg-intercalation (in agreement with the structural characterisation techniques – LEED, XPS, and STM employed in this chapter). As with LEED, XPS and STM, no evidence of Mg-intercalation between the graphene layers was found. Additionally, the ARPES results were able to quantify the electrical characteristics of Mg-QFSBLG to find a highly n-type doped graphene, with a carrier density of $2.10 \pm 0.2 \times 10^{14} \text{ cm}^{-2}$; in agreement with SECO and theoretical comparisons to the C 1s lineshape.

Furthermore, the ARPES results determined that upon Mg-Si formation, that an extremely high displacement field of $2.6 \pm 0.2 \text{ V nm}^{-1}$ opened a band gap of $0.36 \pm 0.01 \text{ eV}$ in the bilayer graphene system of Mg-QFSBLG. This implies that the high carrier concentration in the graphene does not originate from Mg donating charges directly to the graphene itself (as in the case of the intercalated graphite compounds), rather the Mg-Si layer is positively charged which induces and equal and opposite charge in the graphene.

7

Chapter

Ambient Air Stability of Ca- and Mg-Intercalated Quasi-Freestanding Bilayer Graphene

Keywords: Oxidation, Magnesium, Calcium, Ambient Air Stability, XPS.

“Only a small part of scientific progress has resulted from planned search for specific objectives. A much more important part has been made possible by the freedom of the individual to follow his own curiosity.”

- IRVING LANGMUIR

7.1 Overview

The ambient air stable (*i.e.* at standard laboratory conditions) n-type doping of graphene *via* intercalation remains one of the unsolved problems in materials science. Typically, intercalants which induce high n-type doping in graphene are not air-stable, because their susceptibility to donate electrons also makes them highly reactive to atmospheric molecules. The problem is further exacerbated by the fact that the oxidation details of intercalated samples is not widely reported in literature, and so almost all the reported intercalated graphene compounds to date have an unknown reactivity in ambient. Thus, in this chapter I will explore the ambient air stability of Ca-intercalated quasi-freestanding bilayer graphene on 6H-SiC(0001) (Ca-QFSBLG), and Mg-intercalated quasi-freestanding bilayer graphene on 6H-SiC(0001) (Mg-QFSBLG) samples fabricated in [Chapter 5](#) and [Chapter 6](#) at short- and long-term time scales.

Using X-ray photoelectron spectroscopy (XPS), I find that the ambient air exposure of Ca-QFSBLG results in the rapid oxidation of the Ca-Si bonds (Ca-silicide layer). The oxidation of calcium silicide follows a predictable path, initially forming calcium hydroxide in short-term ambient air exposures (30

minutes – 9 hours), before finally forming calcium carbonate for long-term ambient air exposures. Calcium carbonate presents the final product in the oxidation of calcium in ambient atmosphere. The short-term oxidation of Ca-QFSBLG results in a decrease of n-type carriers in the graphene, as measured using secondary electron cut-off photoemission spectroscopy (SECO). After long-term oxidation, the graphene is significantly defected, and this is shown *via* XPS and Raman spectroscopy measurements. Although the graphene is defected by the oxidation reactions, Raman spectroscopy measurements show that the graphene is still quasi-freestanding, *i.e.* the buffer layer does not re-form, and the graphene remains bilayer.

On the other hand, using XPS I show that after short-term (6-hour) ambient air exposure, much of the Mg-Si bonds are still intact, and thus, oxidation of Mg-QFSBLG progresses at a much (at least an order of magnitude) slower rate than Ca-QFSBLG. After long-term ambient air exposures of 8 months, Raman spectroscopy measurements show that the graphene is not defected after exposure *and* that the graphene remains quasi-freestanding. Thus, Mg-QFSBLG is surprisingly air-stable in ambient air conditions, and forms a steppingstone towards the achievement of a fully air-stable and highly n-type doped graphene.

7.2 Introduction

The intercalation (*i.e.* insertion between layers) of graphite with various atoms and molecules in the production of graphite intercalation compounds (GICs) has been an ongoing area of research since 1840, when it was discovered that graphite would ‘swell’ when immersed in sulphuric and nitric acid [391]. Since then, >> 100 compounds have been intercalated into graphite, with previous reports investigating the resulting structural, chemical, and electrical properties [283]. For instance, alkali and alkaline earth GICs (which highly n-type dope the graphite) have led to insights regarding basic physical phenomena such as superconductivity [270-271, 284]. However, most highly doped GICs are not completely air stable, and require encapsulation or other such engineering measures to ensure protection from the ambient atmosphere [20, 283, 392]. For instance, Li-intercalated graphite begins oxidation upon exposure to air instantaneously [20, 393] (although, relatively stable alkali GICs have been recently demonstrated with Cs and K – see ref. [393]; these compounds generally become much less stable with decreasing graphite layer number [394]). On the other hand, FeCl₃-GICs (a highly p-type doped GIC [395]) have been found to be relatively stable in ambient atmosphere, but degrade after 4 months of exposure [395].

After the discovery of the electrical properties of graphene in 2004 [3], and the capability to synthesise uniform and large area graphene on substrates such as silicon carbide [52], intercalation experiments using large-area and layer controlled graphene became experimentally accessible. The intercalation of graphene allows high doping to be achieved [23, 278-279] without disrupting the surface of the graphene and thus, makes this method ideal for future device applications such as gas sensing, graphene interconnects [396-397] and transparent electrodes [281]. But in the case of graphene on 6H-SiC(0001), intercalation can occur exclusively underneath the buffer layer, with the intercalant reacting with the underlying silicon, releasing the buffer layer to form another graphene layer – as was observed with calcium and magnesium intercalation in Chapter 5 and Chapter 6. This makes intercalation of graphene on SiC distinct from graphite, in which the intercalant is inserted *only* between carbon layers. Thus, in the graphene on SiC scenario, the intercalant can be air-stabilised by bonding to the underlying silicon, as is the case with hydrogen [82], oxygen [321, 398] and fluorine [340, 354]. In these cases, intercalation results in significant p-type doping with hole densities on the order of $\approx 2 \times 10^{12}$ [399] and $\approx 5 \times 10^{12} - 6.5 \times 10^{12}$ [75], to $\approx 1 \times 10^{13} \text{ cm}^{-2}$ [85, 344] for hydrogen intercalated graphene, $\approx 8 \times 10^{12} \text{ cm}^{-2}$ [303] for oxygen intercalated graphene, and $\approx 4.5 \times 10^{13} \text{ cm}^{-2}$ [354] for fluorine intercalated graphene. Although air-stable graphene with high carrier densities can be achieved *via* p-type doping, this has the effect of also increasing the workfunction, W_f of the graphene ($W_f \approx 4.8 \text{ eV}$ for H-intercalated monolayer graphene on SiC) [347]. On the other hand, epitaxially synthesised monolayer graphene on SiC (EMLG) has been shown to possess a lower (by $\approx 0.6 \text{ eV}$) workfunction of $\approx 4.0 \text{ eV}$ (the workfunctions of O- and F-intercalated graphene have not, to the best of my knowledge, been measured) [347]. Low workfunction materials to contact n-type semiconductors that have excellent transparency properties are desired for applications in photovoltaics, LEDs, touch screen displays and photodetectors.

Hence, intercalants which induce a similarly high n-type carrier concentration (and low workfunction) that are stable in air, although desired, are unfortunately lacking in literature reports [316]. Previously investigated intercalants including Mn, Si, Fe and Co do induce n-type carriers in graphene, but at concentrations not above $\approx 3 \times 10^{13} \text{ cm}^{-2}$ [355]. The exception to this is Au-intercalated graphene, but this results in either n-type or p-type doping of $\approx 5 \times 10^{13}$ (electrons) or 7×10^{11} (holes), respectively [316, 319]. This effect was thought to be due to the degree of intercalation and the corresponding distance of the graphene from the gold, with a partial Au intercalation (Au-graphene distance smaller) forming n-type with high carrier concentration and a more complete Au intercalation (Au-graphene distance greater) forming p-type carriers with relatively low density [319, 400]. Although, more recent results [401] have suggested that the difference in carrier sign is the consequence of either a monolayer (n-type), or bilayer (p-type) of intercalated Au. In this same report, it was also stated that the

intercalated Au layers were stable in atmosphere (although no systematic study was presented). Nonetheless, having the number of intercalated layers affect the outcome of the sign and density of charge carriers is not ideal regarding device fabrication, in which processes must be finely tuned. On the other hand, the alkali's [70, 352] and rare-earths [278-279] have been intercalated to produce highly n-type doped graphene, but the air-stability of many of these intercalants has not been widely reported (see ref. [20] for Li-intercalation), nor systematically investigated; although much like their GIC counterparts, it is unlikely that these intercalants are air-stable given their high reactivity. (With some exception – see ref. [402] for preliminary report on the air-stability of Ga-intercalated graphene on SiC, nonetheless, Ga does not highly n-type dope the graphene). Furthermore, the air stability of the other n-type intercalated systems listed above have not been thoroughly investigated in the literature (except for Si, for which there exists some evidence to suggest that it may be somewhat air-stable, but as with Au [401], no systematic air-stability study has been conducted [403]).

In [Chapter 5](#) and [Chapter 6](#), it was found that the alkaline earth intercalants Ca and Mg were able to induce high n-type doping in graphene on silicon carbide on the order of 10^{14} carriers cm^{-2} . Again, the calcium intercalation of graphite and graphene has been extensively studied experimentally [18-19, 23-24, 272, 280, 290, 359] and theoretically [286-288], yet the air-stability of Ca-intercalated graphene on SiC(0001) systems has not been thoroughly investigated. Similarly, there are no past reports on the air-stability of Mg-intercalated graphene on SiC(0001), although this has only recently been synthesised [300]. Mirroring the developments in silicon, one would need a way of inducing both n-type and p-type carriers in the same graphene crystal, important for the fabrication of ohmic contacts (Shottky-Mott rule [404]) and p-n junctions [405]. Clearly, if intercalated graphene systems are to have technological significance, an intercalant that is air-stable, and results in a highly n-type doped graphene, is desired.

In this Chapter, I will investigate the short- (minutes/hours) and long-term (months) air stability of Ca- and Mg-intercalated graphene on SiC(0001) i.e. the Ca-QFSBLG and Mg-QFSBLG compounds that were synthesised in [Chapter 5](#) and [Chapter 6](#), respectively, using X-ray photoelectron spectroscopy (XPS), secondary electron cut-off photoemission spectroscopy (SECO) and Raman mapping spectroscopy. The findings indicate that as expected (due to calcium silicide's high reactivity) Ca-QFSBLG is unstable in air, and the underlying Ca-Si bonds almost completely oxidise between 30 minutes to 1 hour after ambient air exposure. Upon oxidation, the Ca-Si bonds initially present undergo a series of reactions resulting in the formation of calcium hydroxide, calcium oxide (from annealing, see [Section 7.4.1.1](#)), and finally, calcium carbonate. The oxidation of the original Ca-Si compound results in a *decrease* of the carrier concentration and *increase* in the workfunction. For long-term ambient air exposures of 1 year, Raman mapping spectroscopy shows that the graphene is significantly defected upon

ambient air reaction, but that the air-reacted Ca remains underneath the graphene preventing the buffer layer re-forming. Thus, I find that ambient air exposed Ca-QFSBLG remains quasi-freestanding.

On the other hand, Mg-QFSBLG shows remarkable short-term stability in ambient air. After 6 hours, it is shown that the original Mg-Si compound that was formed remains in high proportion, intercalated underneath the graphene. For long-term ambient air exposures (8 months) of Mg-QFSBLG, Raman mapping spectroscopy shows that as in the Ca-QFSBLG case, Mg-QFSBLG remains quasi-freestanding. But *unlike* Ca-QFSBLG, Mg-QFSBLG *does not show evidence of any defects after long-term ambient air exposures*. Thus, Mg-intercalation provides a steppingstone toward highly n-type doped, low workfunction and air-stable graphene, which is largely lacking in the literature up to date.

7.3 Methods

Below I will outline the method used for the ambient air exposure of Ca-QFSBLG and Mg-QFSBLG samples, as well as the lab-based methods used to analyse the samples after long-term ambient air exposure. Short-term ambient exposures were investigated using the soft X-ray beamline at the Australian Synchrotron, and more information can be found regarding the experimental methods in [Chapter 5](#) and [Chapter 6](#). The long-term air exposure samples were analysed using lab-based equipment.

Ambient air conditions are defined in this chapter as exposure to standard laboratory conditions, *i.e.* temperatures of ≈ 298 K, pressures of 100 kPa and a relative humidity of $\approx 50\%$.

7.3.1 Sample Intercalation and Ambient Air Exposure

All ambient air exposed samples were intercalated at the Australian Synchrotron using the same equipment and raw materials as the samples intercalated in [Chapter 5](#) and [Chapter 6](#). For further experimental details regarding XPS and SECO, I refer the reader to [Chapter 5](#) and [Chapter 6](#). All annealing temperatures were measured with a single-colour pyrometer (LumaSense Technologies, IMPAC 8 Pro series) and thermocouple.

7.3.1.1 Ca-Intercalation and Ambient Air Exposure

Two additional pristine epitaxial monolayer graphene on 6H-SiC(0001) sister samples (samples grown in the same growth run, from the same wafer) were Ca-intercalated at the Australian Synchrotron (in addition to the sister sample Ca-intercalated in [Chapter 5](#)), which I name EMLG#2 and EMLG#3. The pristine X-ray photoemission spectrum of the C 1s core level of EMLG#2 is shown in [Figure 7.1a](#), and shows no major differences from the pristine EMLG spectrum shown in [Figure 5.5a](#).

For EMLG#2, approximately 6 nm of calcium was deposited, and the sample was then annealed at ≈ 741 K for 2 hours in UHV. For EMLG#3, approximately 6 nm of calcium was deposited, and the sample annealed at ≈ 723 K for 2 hours in UHV. Both samples were first confirmed via LEED and XPS to be transformed into Ca-QFSBLG prior to ambient air exposure.

After Ca-intercalation, EMLG#2 was subsequently exposed to the ambient air environment at the Australian Synchrotron for approximately 30 minutes. After ambient air exposure, EMLG#2 was annealed at $\approx 723 - 773$ K in UHV for ≈ 1 hour to remove atmospheric contaminants, after which the SECO data was taken. EMLG#3 was exposed to the ambient air environment at the synchrotron for 9 hours. After ambient air exposure, EMLG#3 was annealed at $\approx 723 - 773$ K in UHV for ≈ 1 hour to remove atmospheric contaminants. These experiments constituted the short-term ambient air exposure experiments which tested the air-stability of Ca-QFSBLG.

For the long term air exposure experiment, the Ca-QFSBLG sample from [Chapter 5](#) was stored in a dark container in the laboratory until analysis approximately 1 year after the experiments at the Australian Synchrotron.

7.3.1.2 Mg-Intercalation and Ambient Air Exposure

Two EMLG samples were Mg-intercalated. The first was analysed in [Chapter 6](#) and was used for the short-term air exposures. The intercalation details are repeated here: in the first Mg-intercalation step, ≈ 7.5 nm was deposited onto the samples (cell temperature 673 K, 10 minutes of Mg flux exposure) which were then heated to ≈ 773 K for 2 hours. Immediately afterwards, ≈ 3.8 nm (cell temperature 673 K, 5 minutes Mg flux exposure) of Mg was deposited before heating the sample to ≈ 773 K for 2.5 hours. These steps constituted the 1st Mg-intercalation step. In the 2nd Mg-intercalation step, the effusion cell was heated to 673 K, and the sample exposed to 10 minutes of Mg flux before annealing at 623 K for 1.5 hours. This sample was then exposed to the

ambient air environment of the Australian Synchrotron for \approx 6 hours (Air Exposed) and then annealed at 623 K for 1.5 hours (Anneal). All annealing steps were conducted in UHV.

The second Mg-intercalated sample was the sister sample used in [Chapter 6](#) for the collection of SECO data (see [Figure 6.10](#)) and was intercalated in a step-wise fashion (the details of which are further discussed in [Chapter 8, Section 8.4.3](#)), comprising three Mg-intercalations, with the final Mg-intercalation yielding similar results to the final (*i.e.* 2nd) Mg-intercalation of the above sample (see [Chapter 6](#)). In the first Mg-intercalation step, \approx 15 nm of Mg was deposited on the sample (cell temperature 673 K, 20 minutes of Mg flux exposure), which was then heated to 463 K for \approx 1.5 hours. For the 2nd Mg-intercalation, \approx 15 nm of Mg was deposited on the sample (cell temperature 673 K, 20 minutes of Mg flux exposure), which was then heated to 623 K for \approx 1.5 hours. For the 3rd Mg-intercalation, \approx 15 nm of Mg was deposited on the sample (cell temperature 673 K, 20 minutes of Mg flux exposure), which was then heated to 623 K for \approx 1.5 hours. This sample was then stored in darkness and ambient air for approximately 8 months before analysis.

7.3.2 X-ray Photoelectron Spectroscopy Using a Lab-Based Source

For the analysis of short-term ambient air exposed samples, X-ray photoelectron spectroscopy (XPS) at the soft X-ray beamline at the Australian Synchrotron was used. The details of the experiments can be found in [Chapter 5, Section 5.3.2](#) (Ca-QFSBLG) and [Chapter 6, Section 6.3.3](#) (Mg-QFSBLG).

The analysis of the long-term exposed samples was conducted with a lab-based XPS (Thermo Scientific K-Alpha X-ray photoelectron spectrometer) using monochromatic Al K α X-rays (1486.6 eV, 400 μ m spot size) and operating at base pressures of $< 5 \times 10^{-8}$ mbar. The tool is calibrated once every 4 months using the Au 4f_{7/2}, Ag 3d_{5/2} and Cu 2p_{3/2} lines, in which the energy uncertainty is ± 0.1 eV. The incident X-rays are at the ‘magic’ angle of 57°, and photo-excited electrons are collected at 0° with respect to the sample surface normal. The energy uncertainty was taken as ± 0.1 eV in binding energy of the final fitted component.

7.3.3 Raman Mapping Spectroscopy

The Raman mapping and spectroscopy results were obtained using a Thermo Scientific DXRxi Raman imaging microscope. A laser wavelength of 532 nm was chosen, and all scans were taken at a laser power of 9.6 mW using a 100 \times

objective lens. The spatial resolution of the instrument is approximately 0.5 μm . All measurements were taken at ambient conditions. In [Figure 7.6a](#), 12 averages per pixel were taken, with each exposure set to 0.125 seconds. In [Figure 7.9a](#), 16 averages were taken, with each exposure set to 0.25 seconds. In [Figure 7.10a](#), 8 averages were taken, with each exposure set to 0.25 seconds. The pixel size for all scans was set to 0.3 μm .

7.4 Results and Discussion

The results and discussion are split into two main sections. The first concerns the ambient air exposure of Ca-QFSBLG and the second section concerns the ambient air exposure of Mg-QFSBLG. In both cases, the short- and long-term ambient air stability will be considered.

7.4.1 Ambient Air Exposure of Calcium-Intercalated Quasi-Freestanding Bilayer Graphene on SiC(0001) (Ca-QFSBLG)

In this section, I present and discuss recent results on the short- and long-term ambient air stability of Ca-QFSBLG using XPS, SECO and Raman mapping spectroscopy.

7.4.1.1 Short-Term Ambient Air Exposure

Two ambient air exposure experiments were performed at the Australian Synchrotron on two additional (sister) EMLG samples, EMLG#2 and EMLG#3 (see [Methods, Section 7.3.1.1](#)). The C 1s core levels at an X-ray energy of $E_{\text{hv}} = 600$ eV for these ambient air exposed samples are shown in [Figure 7.1](#). [Figure 7.1a](#) shows pristine sample EMLG#2 prior to Ca-intercalation, which is almost identical to the spectrum from [Figure 5.5b](#). [Figure 7.1b](#) shows EMLG#2 after Ca-intercalation, and again the C 1s results are almost identical to those obtained for Ca-QFSBLG in [Figure 5.5d](#). [Figure 7.1c](#) shows the C 1s core level for EMLG#2 (the same sample in [Figure 7.1b](#)) after a 30-minute ambient air exposure. Components B'_C and Z'_C have significantly decreased in amplitude (although are still present), and have mostly shifted to higher in binding energy, which I label components B'_{air} and Z'_{air} , located at $E_B = 282.93 \pm 0.05$ eV and 283.29 ± 0.05 eV, respectively (calculated by averaging the components in both [Figure 7.1c](#) and [Figure 7.1d](#)). The superscript ‘i’ signifies

the ‘initial’ oxidation product, whereas the subscript ‘air’ signifies that the sample was exposed to ambient air. The separation of these components is $\Delta E_B = 0.36 \pm 0.1$ eV, in agreement with the binding energy separation of components B'_C and Z'_C from Figure 5.5 ($\Delta E_B = 0.37 \pm 0.1$ eV). This suggests that these components are the same, simply shifted in energy due to the change in bonding conditions at the surface of the SiC, which I attribute to oxidation, as shall become clearer.

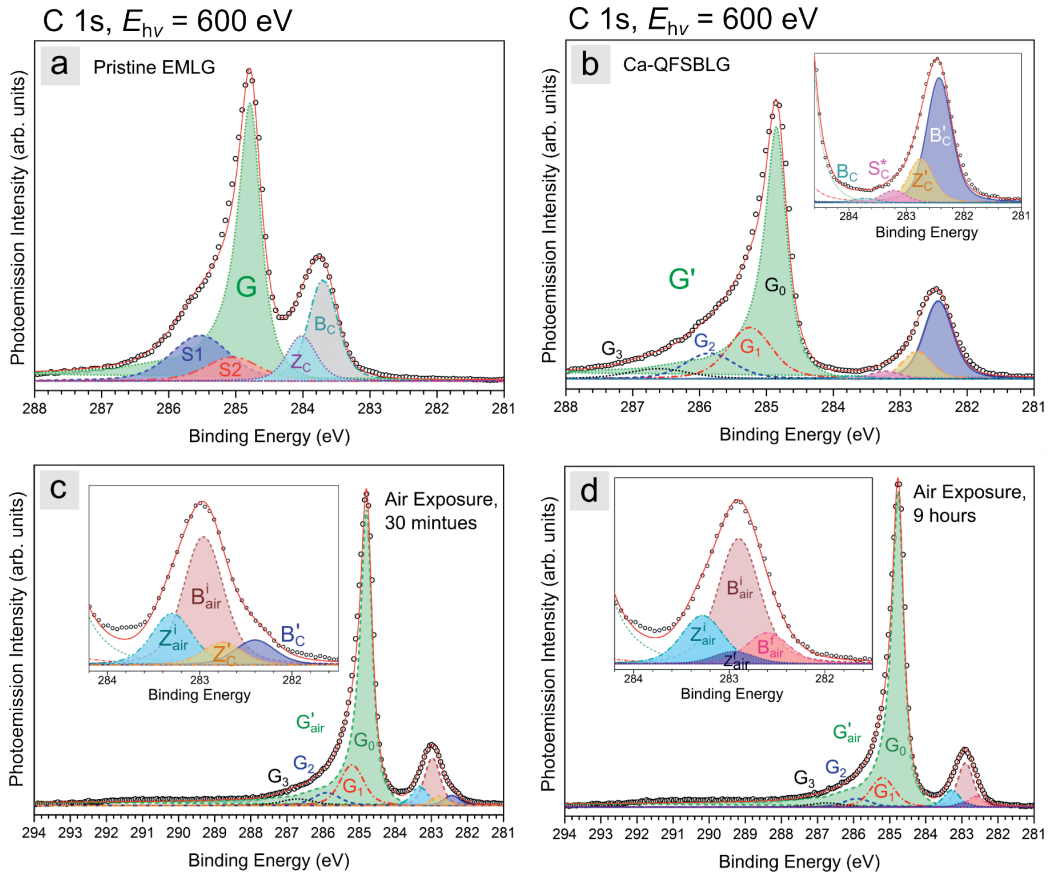


FIGURE 7.1: X-RAY PHOTOEMISSION SPECTRA SHOWING THE C 1s CORE LEVEL OF SHORT-TERM AMBIENT AIR EXPOSED Ca-QFSBLG AT AN X-RAY ENERGY OF $E_{hv} = 600$ eV.

(a) Pristine EMLG, sample EMLG#2. (b) Ca-intercalation of sample shown in (a) to create Ca-QFSBLG. Component G' is shown with the graphene (G_0) and plasmon (G_1 , G_2 and G_3) components – see Appendix B3 for details. (c) 30-minute ambient air exposure of sample in (b), showing emergence of two new components labelled B'_{air} and Z'_{air} . (d) 9-hour ambient air exposure of sample EMLG#3 (pristine/Ca-QFSBLG C 1s spectra not shown). Components B'_C and Z'_C have now disappeared, and components B'_{air} and Z'_{air} have arisen.

[Figure 7.1d](#) shows sample EMLG#3 exposed to ambient air for 9 hours, where it can be observed that components B_C and Z_C have completely disappeared. Instead, two new components, B_{air}^f and Z_{air}^f located at $E_B = 282.60 \pm 0.05$ eV and 282.95 ± 0.05 eV, respectively, can be fit. Again, $\Delta E_B = 0.35 \pm 0.1$ eV, in agreement with the original separation between bulk and surface SiC components (*i.e.* B_C and Z_C , see discussion in [Section 5.4.2](#)). Here the ‘f’ superscript label refers to the ‘final’ oxidation product, and ‘air’ in the subscript refers to the exposure to ambient air (it was observed that component B_{air}^f eventually dominated the C 1s spectrum at longer air exposure times, as will soon be shown).

[Figure 7.2](#) shows the Si 2p core levels of the pristine and air-exposed Ca-QFSBLG EMLG#2 and EMLG#3 samples. [Figure 7.2a](#) shows the pristine Ca-QFSBLG sample (sample EMLG#2 from [Figure 7.1b](#)) prior to air exposure. [Figure 7.2b](#) shows the sample after a 30-minute ambient air exposure. It is immediately apparent that component C_{Si} ($E_B = 99.30 \pm 0.05$ eV), the intensity of which is directly proportional to the amount of Ca-silicide on the SiC surface, has almost disappeared. This is in agreement with the decrease in amplitude of the C 1s components B_C and Z_C ([Figure 7.1c](#)), which are the result of Ca-silicide formation at the SiC interface (see discussion in [Section 5.4.2](#)).

Components B_{air}^i and Z_{air}^i are located at $E_B = 100.76 \pm 0.05$ and 101.1 ± 0.05 eV, respectively (values calculated as the average of those in [Figure 7.2b](#) and [Figure 7.2d](#)). The separation of these components is $\Delta E_B = 0.34 \pm 0.1$ eV, in agreement with the values calculated from the C 1s spectra. This strongly supports the assignment of components B_{air}^i and Z_{air}^i to SiC components representing the bulk and surface, respectively.

[Figure 7.2c](#) shows the pristine Ca-QFSBLG Si 2p core level for EMLG#3 shown in [Figure 7.1d](#). It was observed that the local concentration of silicide varied slightly from sample to sample and this is easily observable upon comparison of the peak area in [Figure 5.4b](#), [Figure 7.2a](#) and [Figure 7.2c](#). Nonetheless, this slight variation over the surface does not affect the interpretation of the results. [Figure 7.2d](#) shows the Si 2p core level of the sample in [Figure 7.2c](#) after a 9-hour air exposure. In this case, I observe the complete disappearance of components B_{Si} and Z_{Si} , in agreement with the C 1s core level measurements ([Figure 7.1d](#)). The disappearance of components B_{Si} and Z_{Si} is thus, also tied to the disappearance of component C_{Si} , further supporting the assessment of these components as being the result of Ca-silicide altering the chemical environment of the surface and bulk of the SiC, causing the binding energy shift to occur. The disappearance of components B_{Si} and Z_{Si} is also tied to the emergence of components B_{air}^f and Z_{air}^f at $E_B = 100.28 \pm 0.05$ and 100.55 ± 0.05 eV, with separation of $\Delta E_B = 0.37 \pm 0.1$ eV, in agreement with the C 1s core level components shown in [Figure 7.1d](#). This suggests that the

Ca-silicide is reacting with ambient air. All component fit parameters are tabulated and can be found in [Appendix B2](#).

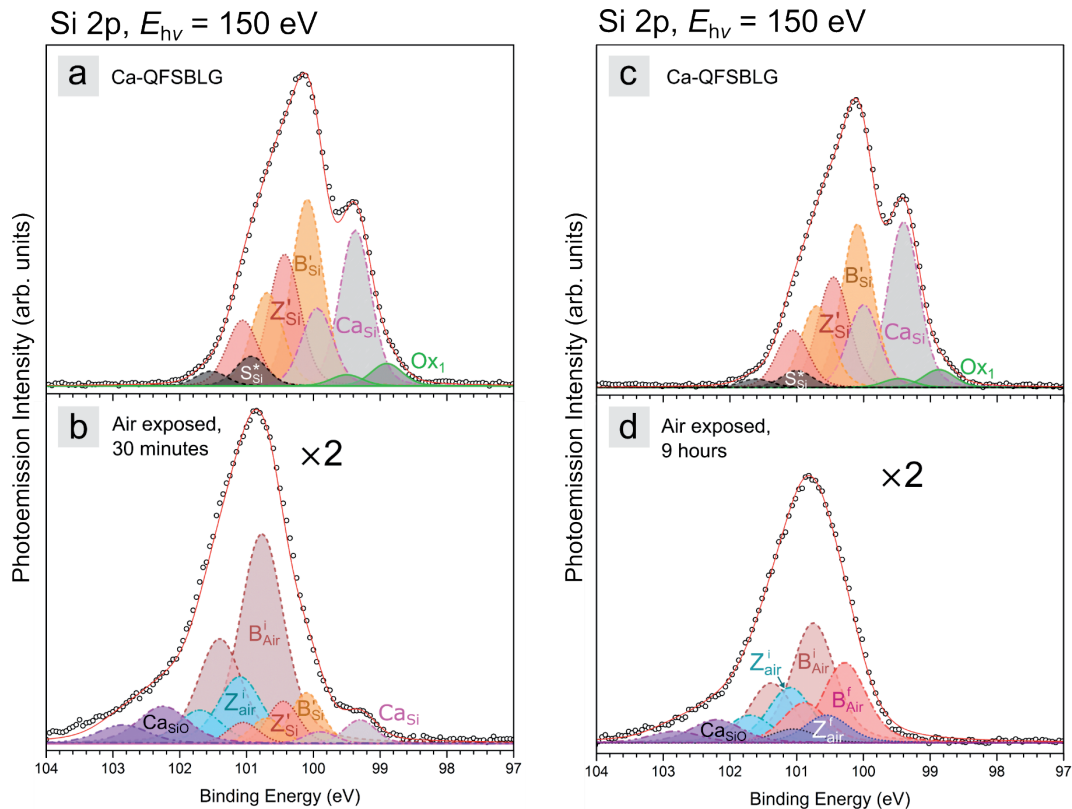
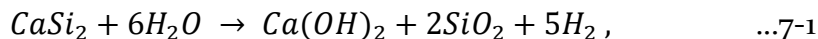


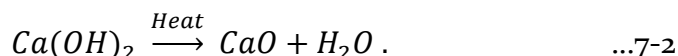
FIGURE 7.2: X-RAY PHOTOEMISSION SPECTRA SHOWING THE Si 2p CORE LEVEL OF SHORT-TERM AMBIENT AIR EXPOSED Ca-QFSBLG AT AN X-RAY ENERGY OF $E_{hv} = 150$ eV.

(a) Pristine Ca-QFSBLG showing the same components from [Figure 5.4c-d](#). (b) Effects of 30-minute ambient air exposure on Ca-QFSBLG. Component Ca_{Si} (Ca -silicide) has almost disappeared. Components B'_{air} and Z'_{air} (the Si 2p component analogues of the similarly named C 1s components from [Figure 7.1c-d](#)) have arisen in place of components B'_{Si} and Z'_{Si} (which have been diminished in intensity). Component Ca_{SiO} is likely a calcium-silicate compound (see text for details). (c) 30-minute ambient air exposed Ca-QFSBLG sample EMLG#2 showing same components from [Figure 5.4c-d](#). (d) 9-hour ambient air exposed Ca-QFSBLG sample EMLG#3. Components Ca_{Si} , B'_{Si} and Z'_{Si} have disappeared, and components B'_{air}^f and Z'_{air}^f have arisen.

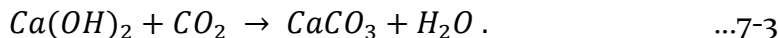
In the ensuing discussion, I will explore the expected ambient air reactions, and compare this with the above experimental observations in [Figure 7.1](#) and [Figure 7.2](#). The reaction of calcium silicide with water is well known [406]:



and forms calcium hydroxide, silicon dioxide and hydrogen gas. Here I have used the stoichiometry of $CaSi_2$ (close to the measured and theoretical values from [Chapter 5, Section 5.4.2.4](#) and [Section 5.4.4](#), respectively). This reaction is likely to have occurred upon exposure of Ca-QFSBLG to ambient atmosphere. Since the sample was heated between 723 – 773 K for at least 1 hour before measuring the core levels (to clean atmospheric contaminants), it is very likely that the $Ca(OH)_2$ decomposed [407]:

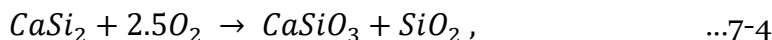


However, in the presence of CO_2 , $Ca(OH)_2$ reacts spontaneously in ambient air to form calcium carbonate [408]:



The temperature required to decompose $CaCO_3$ is much higher (> 1000 K [409]) than that used for sample cleaning in these experiments (see [Methods, Section 7.3.1.1](#)). Thus, there should be an *accumulation* of $CaCO_3$ over time (as we shall see in the proceeding section, this is indeed the case).

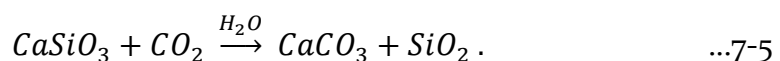
Additionally, in order to correctly fit the high binding energy side spectrum presented in [Figure 7.2b, d](#), component $CaSiO$ – located at $E_B = 102.23 \pm 0.05$ eV (obtained by averaging values in [Figure 7.2b](#) and [Figure 7.2d](#)) – was included. Component $CaSiO$ agrees well in binding energy with a calcium silicate (CS) or calcium silicate hydrate (CSH) compound, such as the minerals Wollastonite ($CaSiO_3$) [410-411], Xonotlite ($Ca_6Si_6O_{17}(OH)_2$) [412-414] or Foshagite ($Ca_4Si_3O_9(OH)_2$) [414]. The oxidation of $CaSi_2$ with O_2 yields Wollastonite [415]:



and thus, may suggest component $CaSiO$ comprises Wollastonite, although, this reaction typically occurs at high temperatures, and so it is unlikely to

occur here. Alternatively, the binding energy of component Ca_{SiO} is also in agreement with sub-stoichiometric silicon oxide ($\text{SiO}_{1.05}$) [416], and it is likely that silicon oxide was present from the oxidation of CaSi_2 (Equation 7-1), which forms silicon oxide.

The relative intensity of component Ca_{SiO} decreases upon increased exposure to ambient air, which is expected for CS and CSH materials as they react with ambient air (CO_2 and H_2O) [417-420]. The reaction of Wollastonite in ambient air proceeds as follows [417, 419]:



Thus, since a small decrease in relative intensity of component Ca_{SiO} is observed, it is tempting to assign the identity of component Ca_{SiO} to Wollastonite (or similar material). To further investigate whether component Ca_{SiO} was due to the formation of CS/CSH or silicon oxide, the O 1s core level was analysed, and is shown in Figure 7.3. Wollastonite has a binding energy of $E_B \approx 531.40$ eV [410], and is not present in Figure 7.3. Thus, I rule out Wollastonite in favour of a sub-stoichiometric silicon oxide, which has a binding energy of $E_B = 533.80 \pm 0.05$ eV in favourable agreement with the binding energy of Si-O compounds formed on top of SiC [421-422], and is thus labelled as component Si_{Ox} in Figure 7.3 to reflect this. The intensity discrepancy may be due to more than one species of silicon oxide being present (the extended high binding energy tail in Figure 7.2b suggests this, even though an additional component was not fit), which would decrease the overall intensity of component Ca_{SiO} in Figure 7.2b.

Figure 7.3 shows two additional components at $E_B = 532.58 \pm 0.08$ eV and 531.09 ± 0.09 eV (calculated taking the average and standard deviation of the values in Figure 7.3), labelled Ca_{OH} and Ca_{O} , respectively. Component Ca_{O} agrees with binding energy values for surface layers of calcium oxide [326], and thus I assign this component to calcium oxide (CaO). As discussed above, Equation 7-2 implies the creation of CaO after annealing, but also that one should observe the presence of $\text{Ca}(\text{OH})_2$ given the initial Ca-silicide oxidation (Equation 7-1). Thus, component Ca_{OH} is likely $\text{Ca}(\text{OH})_2$, since it is expected that this product is formed, and I find favourable binding energy agreement with previous literature values [330]. No presence of CaCO_3 after 9 hours of ambient air exposure is expected since no carbonates ($E_B \approx 290$ eV) were visible in the C 1s core level (Figure 7.1d). The photoelectron cross sections of the C 1s and O 1s core level at the prescribed X-ray energies are similar [143], ruling out any of the observable peaks in the O 1s as due to a metal carbonate. A table of values showing the fitting parameters is given in Table 7-1.

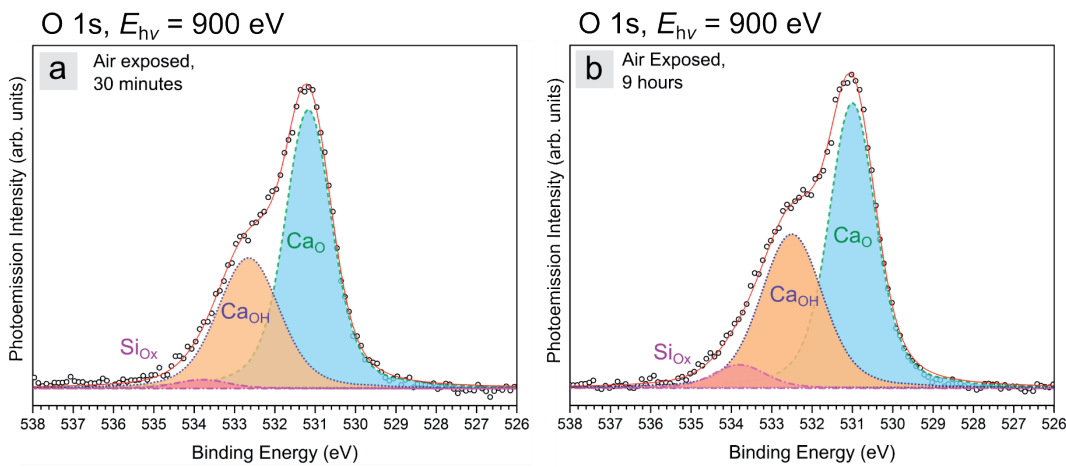


FIGURE 7.3: X-RAY PHOTOEMISSION SPECTRA SHOWING THE O 1S CORE LEVEL OF SHORT-TERM AMBIENT AIR EXPOSED Ca-QFSBLG AT AN X-RAY ENERGY OF $E_{hv} = 900$ eV.

(a) 30-minute ambient air exposure of Ca-QFSBLG showing components Ca_O , Ca_{OH} and SiO_x corresponding to calcium oxide, calcium hydroxide and silicon oxide, respectively. (b) 9-hour ambient air exposure of Ca-QFSBLG. Components Ca_O , Ca_{OH} and SiO_x have increased in relative intensity.

TABLE 7-1: FIT PARAMETERS FOR THE O 1S CORE LEVEL OF AMBIENT AIR EXPOSED Ca-QFSBLG AT AN X-RAY ENERGY OF $E_{hv} = 900$ eV.

The below table outlines the binding energy (E_B), relative intensity (RI) of each component as referenced to 30-minute ambient air exposed Ca-QFSBLG and the Gaussian width (W_G) and Lorentzian width (W_L) of the Voigt fit used.

Ca-QFSBLG, O 1s		(a) 30-minute Ambient Air Exposure			(b) 9-hour Ambient Air Exposure		
Component	E_{hv} (eV)	E_B (eV)	RI	W_G/W_L (eV)	E_B (eV)	RI	W_G/W_L (eV)
Ca_O	900	531.17	1	1.05/0.55	531.00	1.02	1.05/0.55
Ca_{OH}	900	532.65	0.47	1.50/0.55	532.50	0.55	1.50/0.55
SiO_x	900	533.80	0.03	1.20/0.55	533.80	0.09	1.20/0.55

SECO measurements and the calculated workfunction for Ca-QFSBLG prior to, and after 30 minutes of ambient air exposure are shown in [Figure 7.4](#). The calculated Ca-QFSBLG workfunction of $W_f = 3.76 \pm 0.05$ eV shown in [Figure 7.4a](#) agrees with the previous values for Ca-QFSBLG found in [Figure 5.13](#). [Figure 7.4b](#) shows the SECO results of the same sample after a 30-minute ambient air exposure. The workfunction of ambient air exposed Ca-QFSBLG increases to 4.04 ± 0.05 eV, in agreement with that of pristine EMLG ($W_f = 3.96 \pm 0.05$ eV). The oxidation of the underlying Ca-silicide decreases the concentration of n-type carriers, and this is also supported by the fact that the high binding energy asymmetry of the C 1s peak decreases after increasing exposure to ambient atmosphere (see [Figure 7.1c-d](#) and corresponding [Table B.2-6](#) and [Table B.2-8](#)).

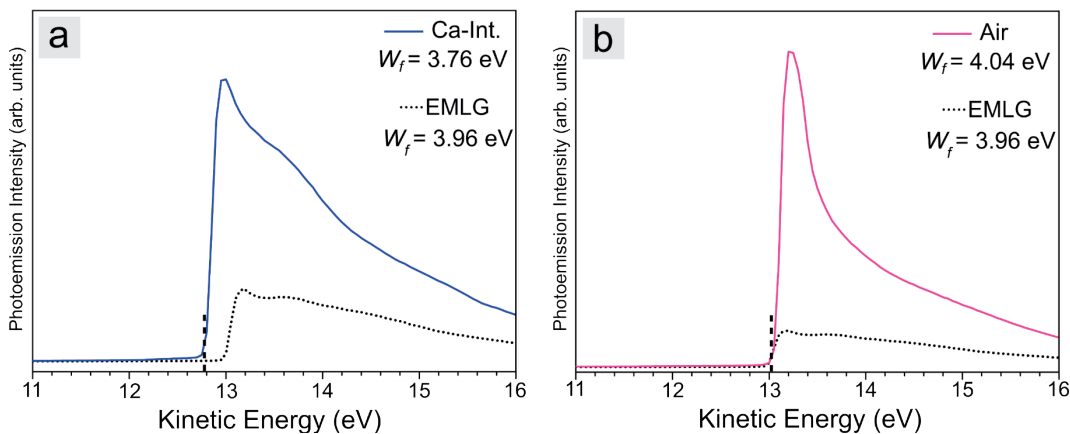


FIGURE 7.4: SECONDARY ELECTRON CUT-OFF (SECO) PHOTOEMISSION MEASUREMENTS SHOWING THE WORKFUNCTION OF Ca-QFSBLG EXPOSED TO AMBIENT AIR FOR 30 MINUTES.

(a) Ca-QFSBLG sample from [Figure 7.1c](#)/[Figure 7.2b](#) showing workfunction $W_f = 3.76 \pm 0.05$ eV compared with pristine EMLG ($W_f = 3.96 \pm 0.05$ eV) prior to Ca-intercalation. (b) Ca-QFSBLG sample exposed to ambient air for 30 minutes, workfunction has increased to $W_f = 4.04 \pm 0.05$ eV.

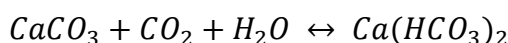
7.4.1.2 Long-Term Ambient Air Exposure

The Ca-QFSBLG sample from [Figure 5.4](#)/[Figure 5.5](#) was exposed to ambient air for ≈ 1 year, after which the sample was analysed with a lab based XPS and Raman mapping system (see [Methods](#), [Section 7.3.2](#) and [Section 7.3.3](#)).

[Figure 7.5a](#) shows a representative pristine EMLG spectrum (using the same growth process) from the lab based XPS that was used. The lab based XPS operates at an X-ray energy of $E_{hv} = 1486.6$ eV (Al $K\alpha$), making the measurements more bulk sensitive. This is easily observed upon inspection of the SiC component ‘Bc’ at lower binding energy, which does not show any asymmetry, unlike in [Figure 5.5](#) at lower E_{hv} which required a surface (‘Zc’) and bulk (‘Bc’) component to be fitted. Component G ($E_B = 284.73 \pm 0.1$ eV) represents the carbon atoms in the graphene layer, whereas S₁ and S₂ represent the carbon atoms the buffer layer components as described previously (see [Section 5.4.2.2](#)). The fit parameters of all components in [Figure 7.5](#) can be found in [Appendix B2, Table B.2-11](#).

[Figure 7.5b](#) shows the Ca-QFSBLG sample from [Figure 5.4](#)/[Figure 5.5](#) exposed to ambient air for 1 year. The C 1s core level now appears completely different from the C 1s spectrum of short-term air exposed Ca-QFSBLG ([Figure 7.1c-d](#)). Component B_{air}^f at $E_B = 282.50 \pm 0.1$ eV is in agreement with the same component found in the 9 hour ambient air exposed sample in [Figure 7.1d](#) and shows that the oxidation reaction reaches a stable (*i.e. final*) state. Component G'_{air} representing graphene ($E_B = 284.58 \pm 0.1$ eV) was fit using a BWF function, and used almost identical parameters to component G in [Figure 7.5a](#). There was no significant shift between component G'_{air} and G. Component sp₃ at $E_B = 285.72 \pm 0.1$ eV is in agreement with defected carbon in an ‘sp³’ configuration (and hence the name) [[423-424](#)]. Others have attributed this feature to a damaged hydrocarbon structure ($E_B = 285.60$ eV) [[425](#)]. Nonetheless, the feature is attributed to a defect. The shift I find between the sp² (graphene) and component sp₃ is $\Delta E_B = +1.14 \pm 0.1$ eV, which approximately agrees with the binding energy shift found in ref. [[423](#)] of $\approx +0.8$ eV.

[Figure 7.5b](#) also shows components at higher binding energy that were not present in the short-term air exposure. Components CO_3^{2-} and HCO_3^- at $E_B = 289.47 \pm 0.10$ eV and 290.50 ± 0.1 eV, represent carbonate and bicarbonate contributions, respectively [[426](#)]. Calcium carbonate ($CaCO_3$) is an expected final product of the oxidation reaction, as seen in [Equation 7-3](#). If excess CO_2 is present, then further reaction of the $CaCO_3$ with CO_2 and H_2O can occur to produce calcium bicarbonate in solution [[427](#)]:



...7-6

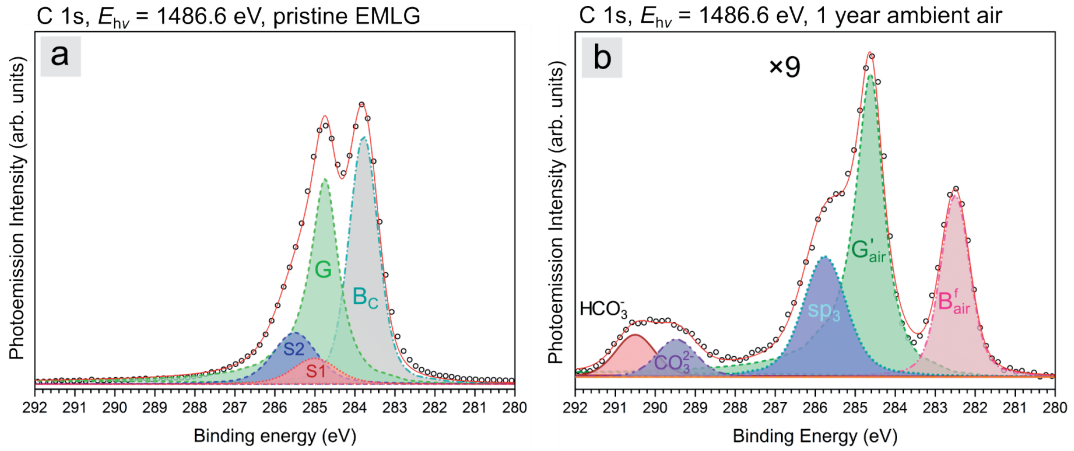


FIGURE 7.5: X-RAY PHOTOEMISSION SPECTRA SHOWING THE C 1s CORE LEVEL OF Ca-QFSBLG EXPOSED TO AMBIENT AIR FOR 1 YEAR.

(a) A sample of pristine EMLG (similarly synthesised, but from a different growth run from the ones used in this study) shown as a representative EMLG sample to compare against. Fitted curve comprises of components S₁, S₂ (buffer layer), G (graphene), B_c (SiC, bulk). (b) 1-year ambient air exposed Ca-QFSBLG sample showing components B_{air}^f (SiC bulk), G_{air}' (graphene), sp₃ (damaged graphene), CO₃²⁻ (carbonate) and HCO₃⁻ (bicarbonate).

The sample in Figure 7.5b was further analysed using Raman mapping spectroscopy, the results of which are shown in Figure 7.6. Figure 7.6a shows an overview of the area mapped, using the full width at half maximum of the 2D peak ($\text{FWHM}_{2\text{D}}$) for colour contrast. The 2D peak (which arises from the excitation of two phonons near the K point of the Brillouin zone [186]) width can determine the number of graphene layers [428-429], for instance, monolayer graphene (on silicon carbide, EMLG) corresponds to a $\text{FWHM}_{2\text{D}} \approx 46 \text{ cm}^{-1}$ [429]. Figure 7.6a shows visually that the $\text{FWHM}_{2\text{D}}$ of long-term ambient air exposed Ca-QFSBLG lies between 60 to 75 cm^{-1} (consistent with bilayer and trilayer graphene [429]), much above the monolayer graphene value. Figure 7.6b shows the averaged spectrum from the dashed region in Figure 7.6a, fitted with a Gaussian lineshape. In this region, the $\text{FWHM}_{2\text{D}} \approx 70 \text{ cm}^{-1}$, as expected. Upon comparison with a representative EMLG Raman map using similar parameters (see Figure 7.10), it is clear that Ca-QFSBLG has little or no regions with a $\text{FWHM}_{2\text{D}} \approx 40 \text{ cm}^{-1}$ which would indicate traces of monolayer graphene. Thus, this strongly suggests that the sample remains intercalated even after air exposure.

Furthermore, I do not observe step edges in the Raman map of [Figure 7.6a](#) (which would be present with EMLG – see [Figure 7.10](#)). Step edges on SiC typically grow multilayer graphene [84-85], but the features can be largely eliminated after hydrogen intercalation due to the flat terraces becoming bilayer graphene and the fact that the step edges lack a buffer layer. [Figure 7.6a](#) does not show any steps visible in the FWHM_{2D} map, and thus, is in further support of the sample remaining intercalated, even while the underlying calcium is oxidised.

[Figure 7.6c](#) shows an overview of the entire Raman spectrum averaged over the scans in the small dashed area shown in [Figure 7.6a](#), and is in agreement with defected graphene due to the presence of D ($\approx 1342 \text{ cm}^{-1}$), D' ($\approx 1616 \text{ cm}^{-1}$) and D+D' (2937 cm^{-1}) [181]. The presence of the G peak (arising from longitudinal optical (LO) excitations of the carbon ring at the Γ point [181]) at 1580 cm^{-1} , is associated with the formation of sp² bonded carbon, and agrees with bilayer or multilayer graphene on SiC [186]. I also observe a feature at $\approx 3244 \text{ cm}^{-1}$ which I attribute to the 2D' mode (a two phonon process) [181] and a feature at $\approx 2451 \text{ cm}^{-1}$ (D*) which is associated with a double resonance – inter-valley scattering of a phonon from the K to K' bands of graphene [430]. The interpretation of the D* feature is debated, and an alternate interpretation is that this arises from a combination of D (at $\approx 1350 \text{ cm}^{-1}$) and LA phonons (at $\approx 1100 \text{ cm}^{-1}$), and thus, arises from defects present in the graphene [181]. But since this feature is present in pristine EMLG (see [Figure 7.10](#)) and I observe no feature at $\approx 1100 \text{ cm}^{-1}$, I attribute the G, 2D' and D* peaks to Raman modes of non-defected (*i.e.* pristine) graphene.

The presence of the D peak can be used as a metric to predict crystallite sizes (L_a) in the graphite and graphene. This was first determined by Tuinstra and Koenig, which used the ratio of the D and G peak (I_D/I_G) to predict graphite crystallite size [183]. This equation was then generalised for any laser wavelength by Cançado *et al.* [431]. More recently, the intensity ratio of the D and D' peak ($I_D/I_{D'}$) was used to determine whether the defects in graphene (exfoliated flakes on SiO₂) were sp³ ($I_D/I_{D'} \approx 13$), vacancy ($I_D/I_{D'} \approx 7$) or grain boundary ($I_D/I_{D'} \approx 3.5$) related [432]. From [Figure 7.6c](#), I find that $I_D/I_{D'} \approx 2$, which suggests that the defects are from grain boundaries. Moreover, Zandiataashbar *et al.* [433] found using supported and suspended exfoliated graphene flakes, that for $I_D/I_G < 1$ and $I_{2D}/I_G > 1$, the graphene was dominated by sp³-type defects. The results in [Figure 7.6c](#) disagree with the regimes outlined in ref. [433], as in addition to finding $I_D/I_G \approx 0.32$ and $I_{2D}/I_G \approx 1.7$ (which is in agreement with sp³-type defects), I find $I_D/I_{D'} \approx 2$, which does not agree with the sp³-type defect regime. Thus, I tentatively ascribe the D peak to grain boundary ‘line type’ defects, which rules out defects from vacancies (from which a difference formula for the inter-defect distance, L_D , would need to be used, see [Section 7.4.2.2](#), or ref. [434]). The size of the resultant graphene crystallites can thus be found using [431]:

$$L_a(nm) \cong \frac{560}{E_L^4} \left[\frac{I_D}{I_G} \right]^{-1}, \quad \dots 7-7$$

where the crystalline size in nanometres of the graphene is given by L_a , E_L is the energy of the laser excitation in eV, I_D is the intensity of the D peak and I_G is the intensity of the G peak. [Equation 7-7](#) yields a value for the crystallite size of $L_a \approx 59$ nm. It is interesting to note that the C 1s core level data from [Figure 7.5b](#) suggests that the defected carbon quantity could be quite high since the defected component is comparable in size to the graphene peak, but only a relatively small defect peak is observed in the Raman spectrum of [Figure 7.6](#). To ascertain the quantitative relationship between crystallite size from the D peak in the Raman spectra and the presence of component sp_3 in the XPS spectra requires further work. For instance, it seems as though the presence of component sp_3 in the XPS measurements, is connected to observation of the D peak in Raman measurements, but that there is a discrepancy between the relative peak areas. Nonetheless, both XPS and Raman results show that after oxidation of the underlying Ca-silicide in Ca-QFSBLG, defects in the graphene form.

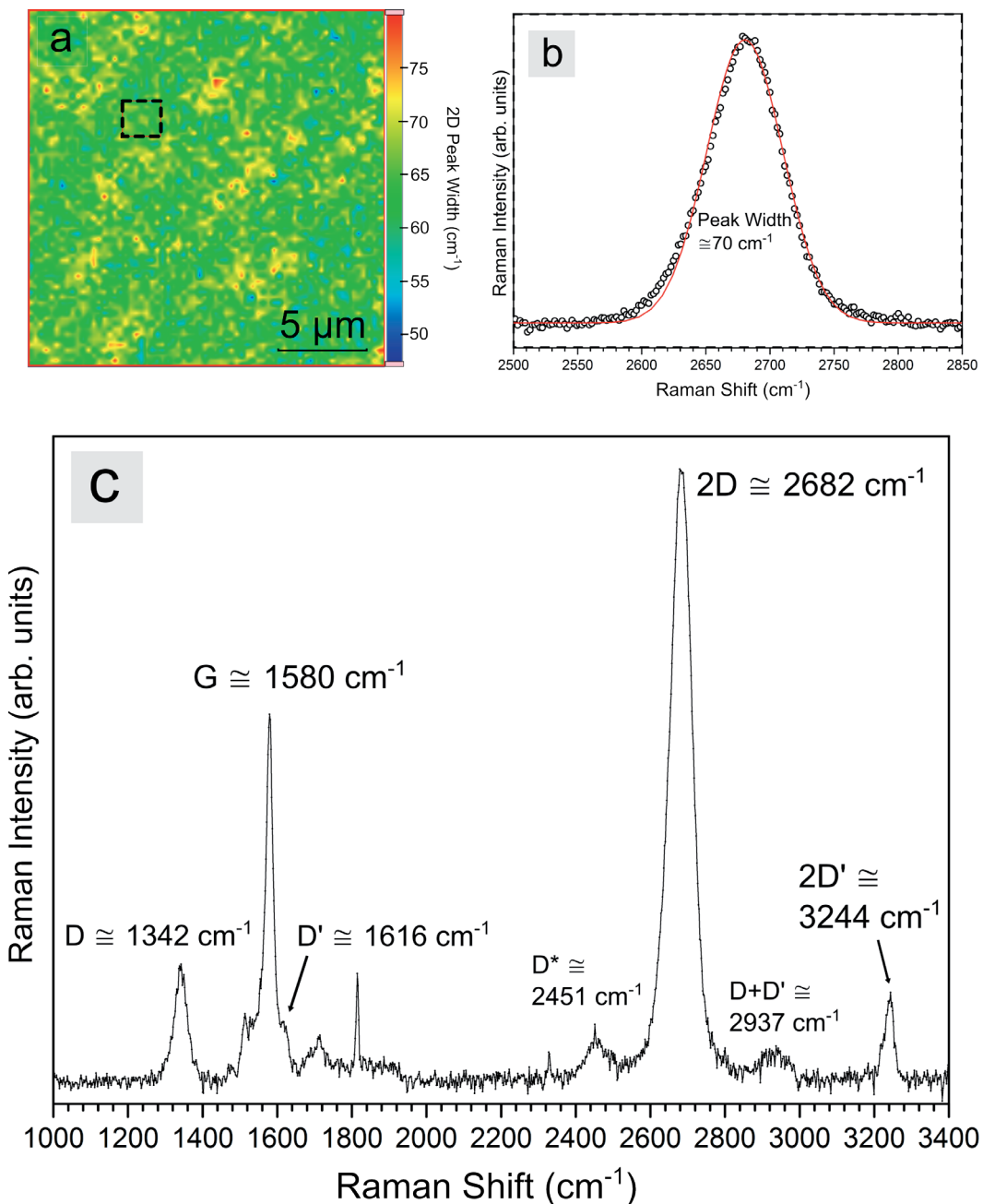


FIGURE 7.6: RAMAN MAPPING SPECTROSCOPY OF CA-QFSBLG EXPOSED TO AMBIENT AIR FOR 1 YEAR.

(a) Raman map ($20.1 \times 20.1 \mu\text{m}^2$) of the '2D' peak width (full width at half maximum, $\text{FWHM}_{2\text{D}}$). **(b)** $\text{FWHM}_{2\text{D}}$ averaged from the dashed area in (a) and fit with a Gaussian, showing FWHM equal to $\approx 70 \text{ cm}^{-1}$. **(c)** Full spectrum from the average of the dotted area in (a) showing relevant peaks in spectrum. A prominent D peak is visible at $\approx 1342 \text{ cm}^{-1}$.

7.4.2 Ambient Air Exposure of Magnesium-Intercalated Quasi-Freestanding Bilayer Graphene on SiC(0001) (Mg-QFSBLG)

In this section, I present and discuss results on the effects of short- and long-term ambient air exposures of Mg-QFSBLG after \approx 6 hours and \approx 8 months, respectively. I find that Mg-QFSBLG is quite stable after short-term ambient air exposures, with a significant amount of the original Mg-silicide remaining (unlike Ca-QFSBLG, in which the Ca-silicide almost completely disappeared after 30 minutes). For long-term exposures of 8 months, Raman mapping spectroscopy results show that (in contrast to Ca-QFSBLG), Mg-QFSBLG not only remains quasi-freestanding, but that no significant defect formation is observed. Further details on the long-term ambient air exposure experiments can be found in the [Chapter 8, Section 8.5.1](#).

7.4.2.1 Short-Term Ambient Air Exposure

[Figure 7.7](#) shows the Si 2p and C 1s core levels of Mg-QFSBLG exposed to ambient air for 6 hours. [Figure 7.7a](#) shows the Si 2p core level of Mg-QFSBLG directly after exposure to ambient air for 6 hours where it is observed that all the original components from pristine Mg-QFSBLG in [Figure 6.4c-d](#) remain in the same binding energy location (see [Appendix C1, Table C.1-4](#)). In particular, component Mg_{Si} which represents the Mg-silicide compound found in [Chapter 6](#), remains the dominant peak in the spectrum. Thus, after 6 hours of ambient air exposure, there remains a significant amount of Mg-silicide underneath the graphene, which is largely pristine.

The oxidation resilience of Mg-QFSBLG in ambient air is further supported in [Figure 7.7b](#), which shows the C 1s core level of Mg-QFSBLG directly after exposure to ambient air for 6 hours. No obvious changes are observed between the spectrum in [Figure 7.7b](#), and the pristine Mg-QFSBLG in [Figure 6.5c-d](#). In contrast, changes were observed in the case of Ca-QFSBLG (see [Figure 7.1](#)), so if a significant oxidation reaction was taking place, the SiC components B_C ($E_B = 282.61 \pm 0.05$ eV) and Z_C ($E_B = 282.94 \pm 0.05$ eV) would be expected to undergo a shift in E_B as a consequence. No observation of any additional components in the C 1s core level, or any shift in the original components was observed. In the case of Ca-QFSBLG (see [Figure 7.1](#)), the original SiC components (*i.e.* B_C and Z_C) were also diminished in intensity. The intensity of the spectra in [Figure 7.7a-b](#) is significantly lower than in [Figure 6.4c-d](#) (signified by the $\times 3$ magnification factor), but this was thought to be due to atmospheric contaminants. [Figure 7.7c-d](#) shows the same spectra from [Figure 7.7a-b](#) after a short anneal in UHV (see [Methods Section 7.3.1.2](#)), and is in support of atmospheric contamination being at least partially

responsible for this signal intensity decrease. The fit parameters for the C 1s core level are shown in [Table C.1-5](#).

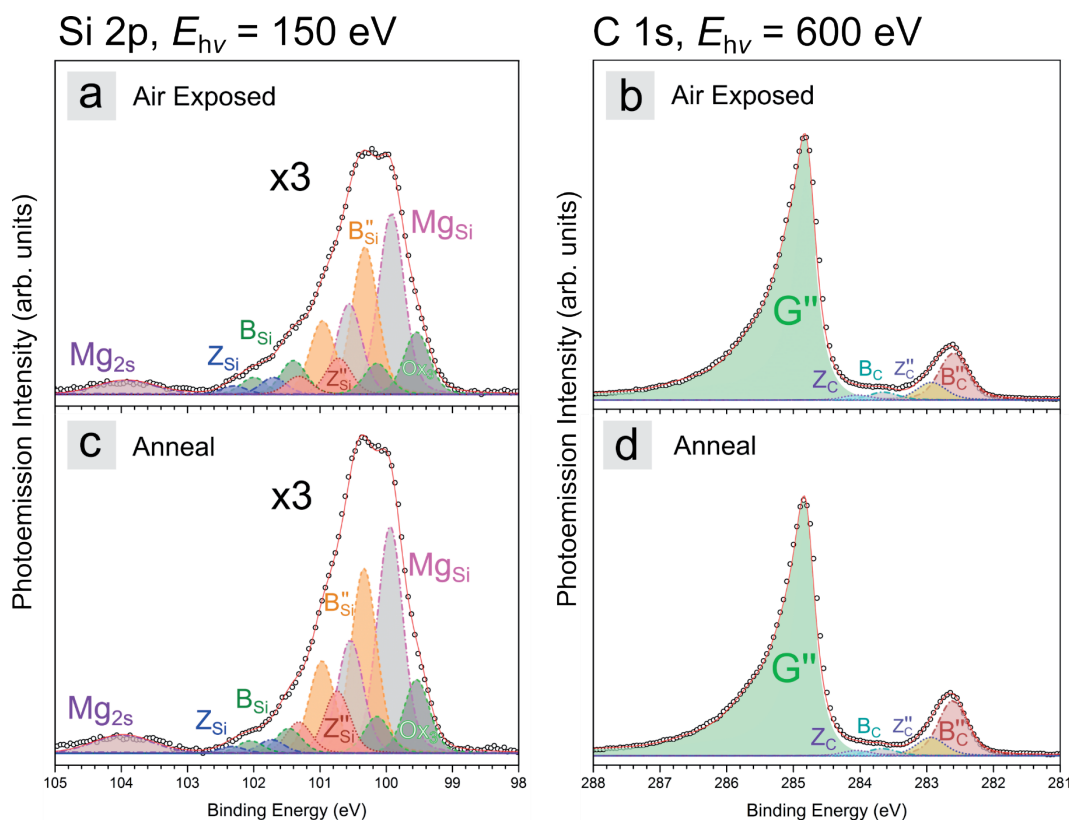


FIGURE 7.7: X-RAY PHOTOEMISSION SPECTRA SHOWING THE Si 2p AND C 1s CORE LEVELS OF Mg-QFSBLG AFTER SHORT-TERM (6-HOUR) EXPOSURES TO AMBIENT AIR, AT X-RAY ENERGIES OF $E_{hv} = 150 \text{ eV}$ AND 600 eV , RESPECTIVELY.

(a) The Si 2p core level of 6-hour air exposed Mg-QFSBLG showing all components. Component Mg_{Si} which represents Mg-silicide is still the dominant component. **(b)** The C 1s core level of 6-hour air exposed Mg-QFSBLG showing all components. No significant change from [Figure 6.5](#) is observed, in support of no significant oxidation taking place. **(c)** The Si 2p core level after further annealing to 623 K for 1.5 hours in UHV. Some intensity is regained in the signal, suggesting atmospheric contaminants were present. The y-scale of (a) and (c) have been magnified $\times 3$ in comparison to [Figure 6.4c](#). **(d)** The C 1s core level after further annealing to 623 K for 1.5 hours in UHV.

[Figure 7.8](#) shows the O 1s core level of Mg-QFSBLG after exposure to ambient air for 6 hours. In green (“Air Expose”, bottom curve) the spectrum directly after air exposure is shown. The pink (“Anneal”, top) curve shows the spectrum after annealing at 623 K for 1.5 hours in UHV. The O 1s spectra are compared to the pristine EMLG starting sample, shown as the dotted line. Upon comparison of the spectra, it is observed that annealing causes a decrease in the intensity of the O 1s signal in comparison to the pristine EMLG baseline, which would be expected if atmospheric contaminants were removed. Furthermore, the intensity of the spectra is very near to the noise level, as was observed in the 1st and 2nd Ca-intercalation of EMLG (see [Figure 5.6](#)). Thus, it is expected that these levels of oxidation are *not* significant, *i.e.* effects from such a small amount of oxidation, and thus, the oxidation products, are not directly observable in the Si 2p and C 1s core levels.

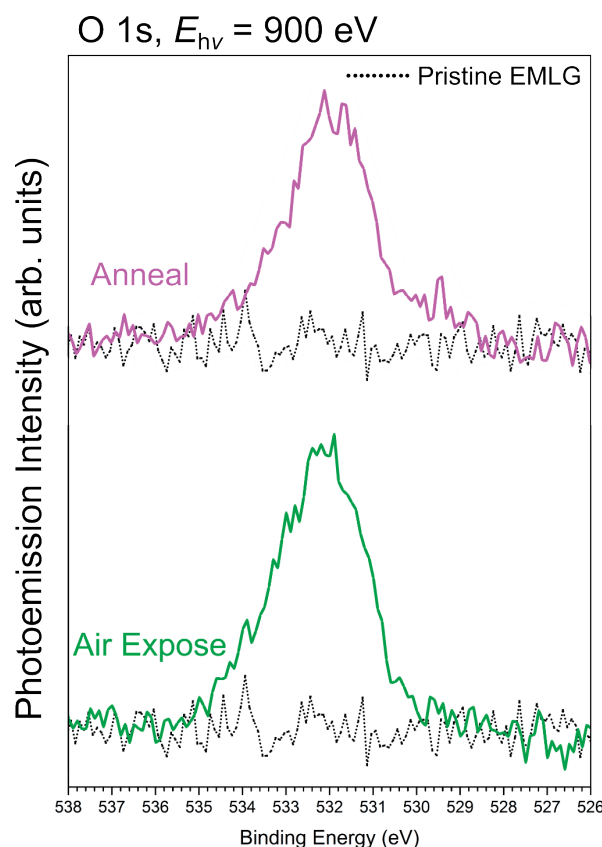


FIGURE 7.8: X-RAY PHOTOEMISSION SPECTRA SHOWING THE O 1S CORE LEVEL OF Mg-QFSBLG EXPOSED AFTER SHORT-TERM (6-HOUR) EXPOSURES TO AMBIENT AIR, AT AN X-RAY ENERGY OF $E_{hv} = 900$ eV.

The bottom “Air Expose” green curve shows the Mg-QFSBLG O 1s spectrum directly after air exposure. The top “Anneal” pink curve shows the Mg-QFSBLG O 1s spectrum after a 1.5-hour, 623 K anneal in UHV. Both spectra are compared against pristine EMLG which did not show oxygen contamination (dotted black line).

7.4.2.2 Long-Term Ambient Air Exposure – Raman Spectroscopy

To further understand the effects of long-term ambient air exposures on Mg-QFSBLG, an Mg-QFSBLG sample was exposed to ambient air for ≈ 8 months, and analysed with Raman mapping spectroscopy, the results of which are shown in [Figure 7.9](#).

[Figure 7.9a](#) shows an overview of the mapped area using Raman spectroscopy, coloured by the width of the 2D peak (the width was measured from 50% of the peak height, *i.e.* full width at half maximum). As can be clearly seen, the 2D peak width is approximately $50 - 80 \text{ cm}^{-1}$, indicating that the sample is $2 - 3$ layers of graphene, and contains no monolayer graphene [429] – as was observed with Ca-QFSBLG. [Figure 7.9b](#) shows the averaged spectrum from the small dash-dotted region in [Figure 7.9a](#), showing clearly the width of the averaged 2D peak region as $\approx 74 \text{ cm}^{-1}$, which is closer to trilayer graphene ($\approx 73 \text{ cm}^{-1}$) than monolayer graphene ($\approx 43 \text{ cm}^{-1}$) [429], and close to the value observed for Ca-QFSBLG in [Figure 7.6a-b](#). This is in stark contrast to pristine epitaxial monolayer graphene in [Figure 7.10a-b](#), which shows large monolayer regions with a 2D peak width of $\approx 37 \text{ cm}^{-1}$ (with exception of the step edges, which are known to have additional layers of graphene [84-85]).

[Figure 7.9c](#) shows the averaged Raman spectrum from the entire area in [Figure 7.9a](#). Here, the G and 2D peak are located at $\approx 1585 \text{ cm}^{-1}$ and $\approx 2700 \text{ cm}^{-1}$, consistent with that of bilayer/multilayer graphene on SiC(0001) [186]. Additionally, the Raman spectrum in [Figure 7.9c](#) shows a small feature centred on the D peak at $\approx 1350 \text{ cm}^{-1}$, which is evident after background subtraction. Fromm *et al.* [435] attributed this broad peak to the buffer layer periodicity, and not a feature associated necessarily with defects. (This observation agrees with the buffer layer component still present in the C 1s core level – see [Chapter 8, Figure 8.9](#) for further details). There also exists a feature at $\approx 2450 \text{ cm}^{-1}$ (D^*) which is associated with a double resonance – inter-valley scattering of a phonon from the K to K' bands of graphene [430]. The interpretation of the D^* feature is debated, and an alternate interpretation is that this arises from a combination of D (at $\approx 1350 \text{ cm}^{-1}$) and LA phonons (at $\approx 1100 \text{ cm}^{-1}$), and thus, may arise from defects present in the graphene [181] (see [Section 7.4.1.2](#) for further details). If so, these defects could either be from line defects (such as grain boundaries), in which case [Equation 7-7](#) can be used. In contrast, the defects could be associated with point defects (since $I_D/I_G \ll 1$ and $I_{2D}/I_G < 1$, these could be vacancies for example [433]); then the formula would take the form [434]:

$$L_D^2 (\text{nm}^2) = \frac{4.3 \times 10^3}{E_L^4} \left[\frac{I_D}{I_G} \right]^{-1}, \quad \dots 7-8$$

and

$$n_D \text{ (cm}^{-2}\text{)} = \frac{10^{14}}{\pi L_D^2}. \quad \dots 7\text{-9}$$

Where L_D is the point inter-defect distance, n_D is the density of defects, E_L is the energy of the laser excitation in eV, I_D is the intensity of the D peak and I_G is the intensity of the G peak. Using [Equation 7-8](#) and [Equation 7-9](#) yields $L_D \approx 300$ nm and $n_D \approx 3.5 \times 10^9$ defects/cm². Using the same equations on the pristine EMLG sample in [Figure 7.10c](#), $L_D \approx 400$ nm and $n_D \approx 1.9 \times 10^9$ defects/cm² and thus, demonstrates that the graphene is not significantly (if at all) defected by the intercalation of, and subsequent oxidation of Mg underneath the graphene. This is in contrast to the intercalation of cobalt [310], iron [309] and oxygen [398] (and Ca, see [Section 7.4.1.2](#)) underneath graphene on silicon carbide, which have been found to induce a prominent D-peak after intercalation. Further details regarding the long-term ambient air exposure of Mg-QFSBLG can be found in [Chapter 8, Section 8.5.1](#) (where it is shown that the Mg-QFSBLG does in fact oxidise, *i.e.* no Mg-silicide remains), but as can be seen in [Figure 7.9](#), the graphene remains defect free even after intercalation *and* complete Mg-silicide oxidation after long term exposures to ambient atmosphere, which was not the case for Ca-QFSBLG.

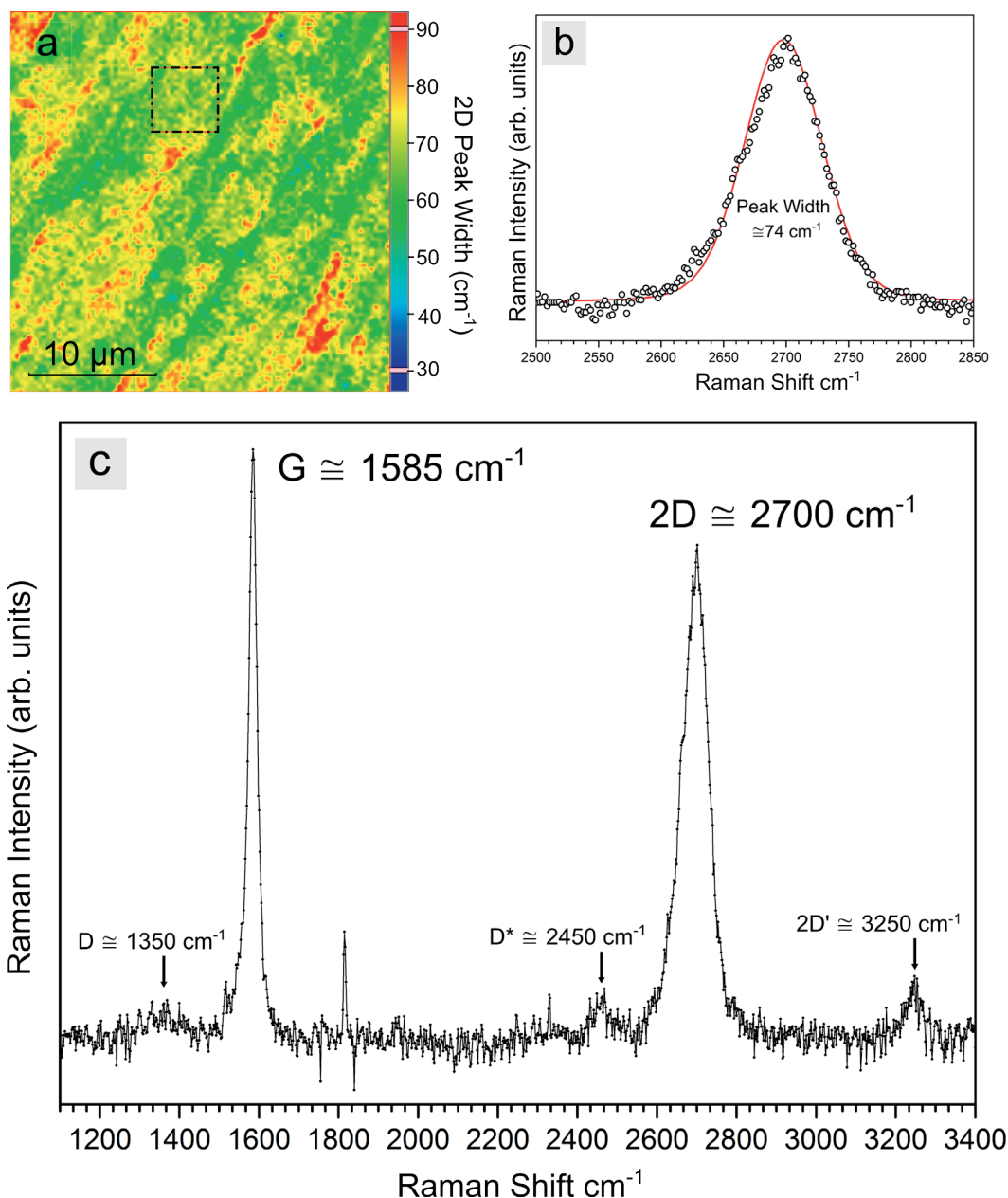


FIGURE 7.9: RAMAN MAPPING SPECTROSCOPY OF $30.3 \times 30.3 \mu\text{m}$ AREA USING A 9.6 mW 532 NM LASER, 16 AVERAGES, 0.25 s EXPOSURE AND $0.3 \mu\text{m}$ PIXEL SIZE.

(a) The 2D peak width (at 50% peak height) of the entire mapped area. As can be clearly seen, the 2D peak width lies between $50 - 90 \text{ cm}^{-1}$, signifying all graphene is >1 layer. (b) Collated spectra in the dash-dotted region in (a), averaged and fit with a Voigt function, showing the representative 2D peak from this region. The peak width is $\approx 74 \text{ cm}^{-1}$. (c) All spectra from the map in (a) averaged, background subtracted, flattened and displayed from $1100 - 3400 \text{ cm}^{-1}$ showing D , G , D^* , $2D$ and $2D'$ peaks.

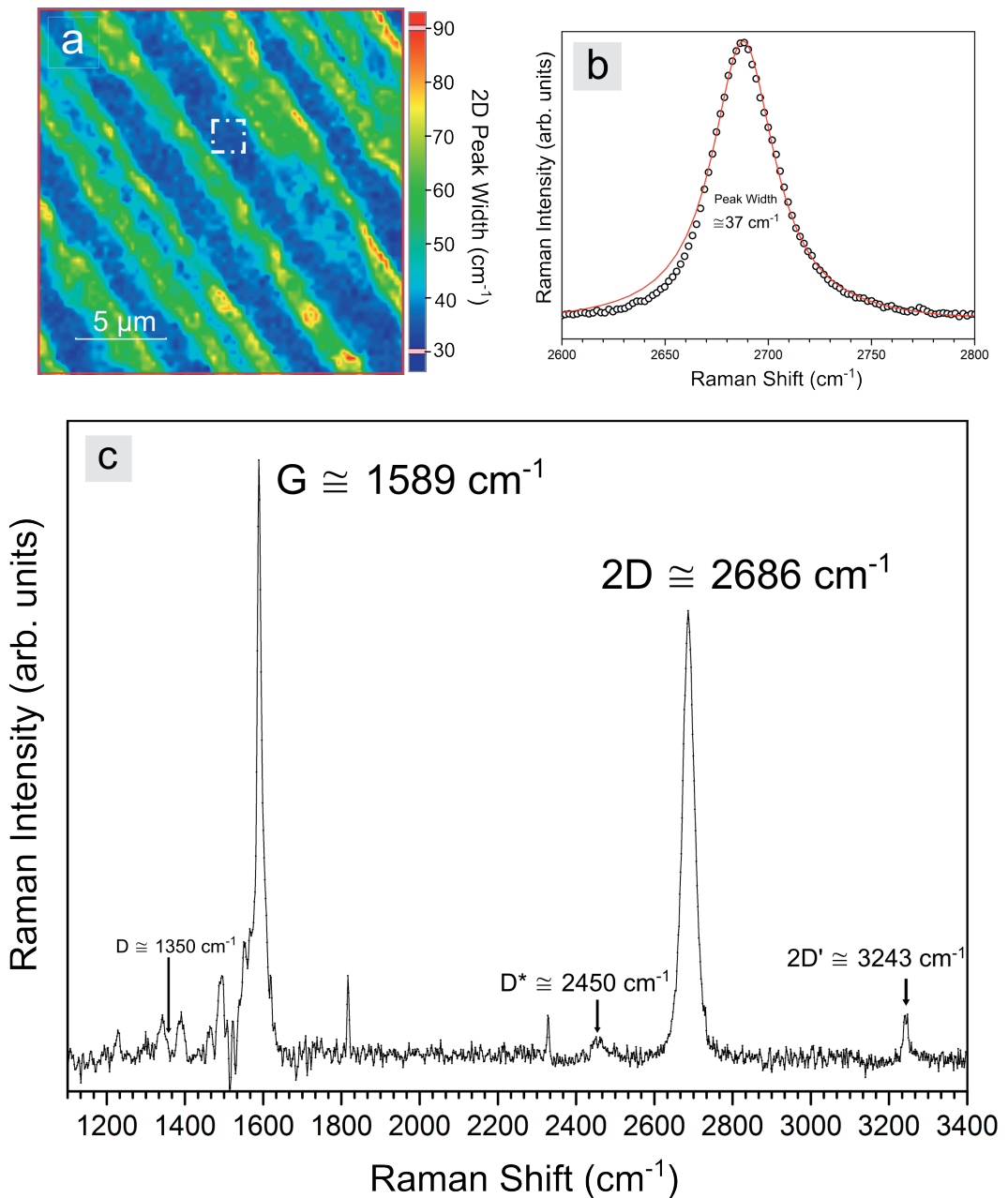


FIGURE 7.10: RAMAN MAPPING SPECTROSCOPY OF $20.1 \times 20.1 \mu\text{m}^2$ AREA USING A 9.6 mW 532 NM LASER, 8 AVERAGES, 0.25 s EXPOSURE AND 0.3 μm PIXEL SIZE.

(a) The 2D peak width (at 50% peak height) of the mapped area. There are 2 distinct regions, $30 - 50 \text{ cm}^{-1}$ (monolayer) and $> 50 \text{ cm}^{-1}$ (bilayer or trilayer). The bilayer/trilayer regions are typically on step edges. (b) Collated spectra in the dash-dotted region in (a) averaged and fit with a Lorentzian function, showing the representative 2D peak from this region. The peak width is $\approx 37 \text{ cm}^{-1}$. (c) All spectra from the map in (a) averaged, background subtracted, flattened and displayed from 1100 – 3400 cm^{-1} showing D , G , D^* , 2D and 2D' peaks. Uncertainty in the peak location was estimated as $\pm 2 \text{ cm}^{-1}$.

7.5 Conclusion

While many elements have been intercalated underneath graphene on silicon carbide, the details of what occurs after ambient air exposure are rarely, if ever reported in literature. Here, I have explored the ambient air effects on the chemical and electronic structure of two related intercalated samples, Ca-QFSBLG and Mg-QFSBLG. I have shown that as expected, Ca-QFSBLG is not air stable, and oxidises rapidly in ambient air to produce calcium hydroxide, and finally, after long term exposures of 1-year, significant amounts of calcium carbonate. While ambient air reacted Ca-QFSBLG remains quasi-freestanding after long-term oxidation, the graphene is found to be significantly defected, with defect signatures appearing in both the XPS and Raman spectra.

In contrast to Ca-QFSBLG, Mg-QFSBLG remained relatively un-reacted after short term exposures up to 6 hours, where XPS measurements showed much of the original Mg-silicide remaining after this time, along with no major changes to the Si 2p or C 1s core levels which could suggest the formation of oxidation products. After long-term exposures of 8 months, Raman mapping spectroscopy showed that not only did the Mg-QFSBLG remain quasi-freestanding, but that the Mg-QFSBLG did not contain a significant amount of graphene defects – a considerable improvement over Ca-QFSBLG.

In summation, it is expected that this study will inspire further investigation into the air-stability of other intercalants, to ultimately yield an even higher n-type doped, low workfunction, and air stable quasi-freestanding graphene. As it currently stands, Mg-QFSBLG represents one of the most highly n-type doped, low workfunction, and air stable intercalated graphenes in the literature, and should be used as a steppingstone toward the discovery of even more highly n-type, and air-stable intercalants.

8

Chapter

Outlook and Concluding Remarks

"I have not the smallest molecule of faith in aerial navigation other than ballooning"
- LORD KELVIN
(SIR WILLIAM THOMPSON)

8.1 Introduction

Lord Kelvin, famed physicist, engineer, and inventor – most known to physics students as the man whose name bears the standardised unit of temperature, the kelvin, K – and many others like him throughout history – have made predictions which have turned out to be incorrect [436]. Thus, in this outlook chapter, I will not attempt to give broad overarching predictions of the future of 2D materials (or any field for that matter), as it is almost impossible to make these predictions accurate or insightful! But I will outline here some of my thoughts on the importance of the findings in this thesis, and possibly where these findings could be expanded upon if one so chooses.

In his final address, Lord Kelvin stated [437]:

"One word characterises the most strenuous efforts for the advancement of science that I have made perseveringly through 55 years ; that word is failure ; I know no more of electric and magnetic force, or of the relations between ether, electricity and ponderable matter, or of chemical affinity, than I knew and tried to teach my students natural philosophy 50 years ago in my first session as professor."

Much of Lord Kelvin's sentiment in 1896 still resonates with me (and I am sure many other young scientists). The scientific endeavour is surely filled more with failure than success. In all instances, failure is just as important as success, and represents the small and winding road to discovery. This is in my opinion what Lord Kelvin was trying to convey. In terms of the document before you, a physics doctoral thesis is not the end of one's journey, but

simply the beginning (if one so chooses) of a long winding journey into the world of physics, discovery and as Lord Kelvin referred to it - failure.

In the following chapter, I will present the outlook of each previous experimental chapter in this thesis in order, beginning with additional discussion and experiments on monolayer WS₂, followed by Ca-QFSBLG, Mg-QFSBLG and finally, how the oxidation of Ca-QFSBLG and Mg-QFSBLG is not necessarily a failure, or of no value. In many cases, the experiments presented in this chapter I first thought were failures, but as I shall soon reveal, there is much that can be learned from failures! Thus, the preliminary data from the experiments presented in this chapter should, at the very least, provoke further reflection on the topics already presented. Lastly, I will offer my concluding remarks for the chapter and thesis.

8.2

Oxidation of Monolayer WS₂ Is a Photoinduced Process

In [Section 8.2.1](#), I will first outline the proposed photo-oxidation mechanism and reaction pathway which was alluded to in [Chapter 4](#). There is now overwhelming evidence that the oxidation of WS₂ (and other similar S-TMDs) should occur *via* Förster resonance energy transfer (FRET) or an electron transfer type mechanism after photoexcitation.

[Section 8.2.2](#) will discuss key annealing experiments in which the threshold temperature for thermal decomposition of WS₂ is determined to lie between 150 – 220 °C – a much higher value than what is known in literature. The key difference with the experiments I show in this section is that the WS₂ is annealed in darkness – unlike the results of previous experiments, which did not control for light exposure (which may have produced false positives [[207](#), [219-220](#)]). Thus, to prevent oxidation from light, the samples were kept in darkness after growth and during the annealing experiments.

8.2.1

Proposed Photo-Oxidation Mechanism and Reaction Pathway

The low irradiance light exposure experiments (see [Figure 4.13](#)) have shown that the physical mechanism of oxidation in ambient conditions of monolayer WS₂ is not due to heating [[207](#), [219-222](#)], substrate electric field effects [[208](#)] or the overcoming of a ‘threshold’ radiant energy (fluence) [[22](#)] for chemical reaction – but is due to photo-oxidation. Under the right ambient conditions (*i.e.* in the presence of water and oxygen), only light

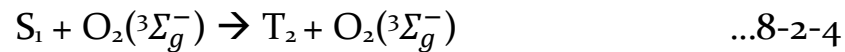
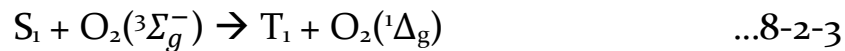
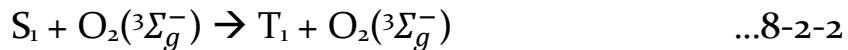
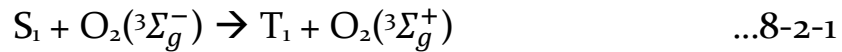
energetic enough to excite an optical bandgap transition is needed to cause oxidation – and this is clearly shown after comparison of the 532 nm and 660 nm light exposure experiments with the 760 nm light experiment in which there was no oxidation after 7 days – and the dark standard, which also showed no oxidation after 14 days. The rate of reaction should then proceed proportionally to the number of above optical bandgap photons absorbed by the WS₂. Since there is evidence to suggest that oxidation on the basal plane begins at sulphur vacancies [207], the number of sulphur vacancies would also determine the rate and extent of the oxidation (as well as the concentration of water and oxygen). Whether the oxidation reaction could proceed in the basal plane of the crystal *in the absence of sulphur vacancies on the basal plane* remains an open question, and one that is worthwhile pursuing. One way in which this could be investigated is by ‘healing’ any sulphur vacancies after growth *via* annealing in a sulphur rich environment [438] (see also below, [Section 8.2.2](#)) or chemical treatment [439]. Furthermore, since oxidation quenches the WS₂ PL response [207] (see also [Appendix A2](#)), this would decrease the oxidation rate as it progressed, further adding complexity to calculations or predictions of the oxidation rate.

As was noted in [Chapter 4](#), the phenomenon of photo-oxidation in direct band gap semiconductors is not a new observation. The body of work on photo-induced oxidation of semiconductors (especially direct bandgap semiconductors) serves as a useful guide in predicting the chemical reactions involved in the oxidation of WS₂ (and related family of S-TMDs). It suggests one of either two fundamental physical processes, both involving one or more reactive oxygen species (ROS), that is, singlet oxygen (O₂(¹Δ_g)), hydroxyl radicals ('OH), superoxide radicals ('O₂⁻) and/or hydrogen peroxide (H₂O₂).

The first possible reaction pathway is given by the generation of O₂(¹Δ_g) in a physical process called Förster resonance energy transfer (FRET) [440]. The process for FRET is generally that a molecule in the ground state (S₀), is photo-excited to its excited singlet state (S₁) and in the presence of oxygen (O₂(³Σ_g⁻), triplet oxygen, ground state of oxygen, O₂), undergoes an intersystem crossing (ISC), converting into the triplet excited state (T₁) which is then able to resonantly transfer energy (*i.e.* total energy is conserved) [440] to O₂(³Σ_g⁻), converting it to O₂(¹Δ_g) [441]. In fact, singlet oxygen creation is favoured in nature, as energy transfer to triplet oxygen is allowed in both the excited triplet and singlet states, and is thus ubiquitous in many molecules photo-excited in the presence of oxygen (provided the S₁/T₁ state of the molecule is > 94 kJ mol⁻¹, or 0.974 eV) [441]. The low irradiance light experiments shown in [Chapter 4, Section 4.4.3](#) showed that monolayer WS₂ oxidised when exposed to wavelengths of light at 532 nm (2.33 eV) and 660 nm (≈ 1.88 eV). At 1.88 eV, the exciton, which was found to lie between 1.95 – 2.04 eV, cannot be excited. While this may not completely rule out oxidation *via* a pathway involving the exciton, it does demonstrate that lower energy excitations from trions (invariably *negative* trions for WS₂ grown on SiO₂, sapphire or exfoliated, due to the dominant defect being sulphur vacancies

[195] – see Chapter 4, Discussion) are sufficient to begin oxidation of monolayer WS₂. Whether trions are the dominant quasiparticle involved in the oxidation reaction remains an open question, but could be investigated for instance using gated measurements to tune the carriers in WS₂, while the WS₂ is illuminated with above bandgap light.

Vaclavkova *et al.* [202] have recently probed the nature of bright trions in hBN encapsulated WS₂ and found that at temperatures below 60 K, the triplet state trion dominates, though at temperatures exceeding 60K, the singlet trion dominates. Thus, at room temperature, most if not all bright trions in WS₂ will be in the singlet (S₁) excited state. FRET may then be able to proceed as an ‘enhanced ISC’ process outlined in Equations 8-2-1 – 8-2-4 [441].



Since the energy of the excited singlet state in WS₂ is >1.88 eV, Equations 8-2-1 – 8-2-3 should apply, and the excited singlet state should undergo an ISC to a T₁ state. In Equation 8-2-3 for instance, this involves the excitation of O₂(³Σ_g⁻) to O₂(¹Δ_g) directly. FRET has also recently been suggested by Ding *et al.* [247], in which an O₂(¹Δ_g) sensitive molecular probe was used to find that under white light illumination, chemically exfoliated MoS₂ quantum dots produced O₂(¹Δ_g). Singlet oxygen generation is also observed in other material systems – for example photo-oxidation was observed in (direct bandgap) CdSe/ZnS quantum dots (QDs), where it was found that singlet oxygen (¹Δ_g) was produced upon PL of the QDs, which led to their oxidation in solution [442].

Although, the presence of O₂(¹Δ_g) on its own does not confirm FRET as the oxidation pathway of WS₂. For example, TiO₂ catalyses the reaction of O₂ and H₂O via the photocatalytic effect, which involves the transfer of electrons and holes to molecules such as O₂(³Σ_g⁻) and H₂O. The reaction in this case is termed the hydrogen evolution reaction (HER), as it generates hydrogen gas. Intermediary steps in this reaction produce a range of diverse ROS’s through oxidation/reduction reactions (*i.e.* electron transfer), including, but not limited to O₂(¹Δ_g) [252, 443-444]. In the same way that TiO₂ catalyses the HER, S-TMDs, and in particular MoS₂ and WS₂ have also been investigated

for their ability to catalyse the HER [445-447]. The photocatalysis of O₂/H₂O by WS₂ may explain the observed oxidation of WS₂ in ambient conditions and the presence of O₂(¹Δ_g).

Thus, the presence of O₂(¹Δ_g) on its own cannot prove the presence of FRET or the photocatalytic effect. For instance, in the case of thin layers/monolayers of black phosphorous (a 2D ‘monochalcogen’ layered material consisting entirely of phosphorous ‘phosphorene’, known to undergo significant and rapid oxidation in ambient [253]), ·OH, ·O₂⁻, and O₂(¹Δ_g) has been measured upon illumination with UV and near UV light [253, 448]. Favron *et al.* [253] subsequently deduced that the mechanism for oxidation in black phosphorous was electron transfer to oxygen molecules. But the reaction has been found to be more complex, requiring water as a ‘catalyst’ in order to progress [253] (and of course, light of suitable wavelength – though for black phosphorus, oxidation in darkness and in the presence of water has also been found to occur [449]). The same was observed in GaAs, where it was found that appreciable oxidation could only be achieved with oxygen *and* water. S-TMDs are no different, and reports on their oxidation have determined that water is essential for the oxidation reaction [22, 207, 258]. Nonetheless, experiments to elucidate the precise mechanism of ambient air oxidation in WS₂ (and other S-TMDs) is the subject of future work. For example, O₂(¹Δ_g) generation *via* FRET should be more efficient in direct bandgap materials, thus indirect bandgap S-TMDs should be expected to oxidize at a slower rate in comparison with direct bandgap S-TMD materials. This may be the case for WSe₂ (an indirect bandgap monolayer S-TMD) [450], and it would be of interest to see if this material oxidizes less rapidly than WS₂.

Whatever the mechanism may be, SO₄²⁻ signatures in oxidised WS₂ have been measured by X-ray photoelectron and Raman spectroscopy [22], implying SO₄²⁻ is a product in the final reaction. This was also found in the case of MoS₂, whereby SO₄²⁻ was produced upon oxidation [256, 258, 268]. In fact, sulfuric acid production from S-TMD oxidation has been reported since some of the first oxidation studies in 1955, though of course, the role of light in past experiments was not fully understood (and thus not controlled) [258]. The presence of H₂SO₄ may explain the observed micro ‘droplets’ seen in [Figure 4.10g-h](#), similar to the observation made by Budania *et al.* [257] after imaging multilayers of MoS₂ with AFM. This is similarly observed in black phosphorous, whereby small droplets form upon oxidation [448], and are thought to contain phosphoric acid [253, 448]. Not all oxidation islands were observed to have a liquid drop, which may be due to the absence of excess H₂O.

Nonetheless, I have demonstrated in [Chapter 4](#) (and re-iterated here) that the observed ambient air oxidation of S-TMDs is photo-induced, *i.e.* a photo-oxidation mechanism. The particulars of the precise chemical reaction pathway and reaction products will require further investigation to

completely understand, though it is my hope that the insights presented here spurs others to also investigate S-TMD oxidation chemistry further.

8.2.2 Finding the Threshold Temperature of Oxidation for WS₂

Since oxidation studies on S-TMDs began in 1955, it has been well known that bulk S-TMDs will oxidise when heated in ambient atmosphere [258]. More recently, oxidation of S-TMDs in the context of *monolayer* S-TMDs (especially those grown synthetically by CVD) have been investigated. Recent reports have attributed oxidation due to heating beginning from 80 °C [207] to as high as 250 °C [219]. Although in all past reports, the role of light in the oxidation of S-TMDs was not appreciated. In [Chapter 4, Section 4.4.5](#) the effects of heating in darkness were presented and showed that heating at 80 °C for 2 hours (6 times longer time scale than in ref. [207]) did not produce any observable oxidation (as judged with the LSCM), in contrast to ref. [207]. This finding suggests that previous experiments may have been compromised by light exposure prior to or during annealing (*via* ambient light, or analysis techniques such as optical microscopy or PL), which caused oxidation to unknowingly occur *via* photooxidation rather than thermal oxidation. Thus, a precise value for the threshold temperature of oxidation for monolayer WS₂ – which is technologically relevant to device manufacture and reliability – is lacking in the literature. The following section presents some of my preliminary results for experiments investigating the threshold temperature of oxidation for WS₂ in the *absence* of light, but further work is necessary.

To find the critical (threshold) temperature at which oxidation begins, a set of ambient air annealing experiments in darkness were devised. The samples used for these ambient air annealing experiments were grown differently to the samples used in the photo-oxidation study in [Chapter 4](#). In order to try and minimise sulphur defects, the concentration of sulphur during growth was kept high until the H₂ gas source was turned off and the furnace fully opened (*i.e.* the ‘anneal time’ or the time the sulphur was kept at its maximum temperature of 200 °C was extended from 5 minutes to 12 – 15 minutes). Sulphur annealing has been recently shown to ‘heal’ defects [438]. The possible effects of this will be analysed in the context of the ambient air annealing results in the following discussion.

Thus, the heating experiments tested the critical temperature for oxidation **and** whether the oxidation could proceed on the basal plane after increased sulphur concentration, with the notion that an increased sulphur concentration could help ‘heal’ the basal plane of sulphur defects. Of course, it is impossible to test for 2 variables at the same time, and so the preliminary results here need further work, but nonetheless, show promising results. The results showing the heating at various temperatures (in darkness) of these

samples are shown in [Figure 8.1](#). It was important to exclude light from these experiments, as the results from [Chapter 4](#) have demonstrated that light is capable of beginning the oxidation reaction in ambient conditions. As mentioned, it is thus very possible that every oxidation study of monolayer WS₂ and similar materials has been contaminated by the fact that these materials were already oxidised (as they were exposed to light and O₂/H₂O [[451](#)]), or were oxidised by the very technique used to investigate if oxidation had taken place (Raman/PL spectroscopy or optical microscopy) creating false positives. The work presented here thus offers a unique insight into the oxidation of WS₂, as one can eliminate oxidation from occurring before heating (eliminating false positives). The results shown in [Figure 4.16](#) and [Figure 8.1](#) were obtained using an LSCM, which has a maximum resolution of ≈ 120 nm, but due to the high contrast between oxidised and un-oxidised WS₂ (see [Chapter 3, Section 3.8](#)), the smallest detectable features in [Figure 4.10e-f](#) were between 50 – 120 nm in size. It is possible that oxidation was present, though beyond the resolving capabilities of the LSCM. To circumvent this, the samples were annealed for 3 hours at the quoted temperatures.

[Figure 8.1](#) shows that monolayer WS₂ remains visually (with the LSCM) un-oxidised at temperatures below 150 °C. In [Figure 8.1a-b](#), the grain boundaries (or ‘grain walls’ which refer to thicker, i.e. few nanometre sized grain boundaries [[452](#)]) which exist between the triangular single crystals of WS₂ appear ‘white’ or ‘invisible’, suggesting that these regions are not oxidised. It has been observed previously that heat treatments are able to rapidly oxidise grain boundaries, and typically these regions are the first to become visibly oxidised [[219-220](#)]. Nakanishi *et al.* [[453](#)] investigated the grain boundaries of monolayer MoS₂ and found that certain orientations of grain boundaries were more prone to oxidation than others when heating was applied. The fact that some grain boundaries did oxidise suggests that these grain boundaries contained defects, which may contain a greater number of sulphur vacancies, or lower the energy barrier for reaction. In [Figure 8.1c](#), it is shown that increasing the temperature to 220 °C results in the grain boundaries appearing black (see through to substrate), indicating that oxidation has occurred. [Figure 8.1d](#) is the result of a standard-grown crystal undergoing the same heating process as in [Figure 8.1c](#). It is immediately observable that this crystal also has begun to oxidise along the edges.

These results are in contrast to those of Wu *et al.* [[222](#)] which found no visible change of MoS₂ few-layer samples at 260 °C and 300 °C, and many other past reports which found oxidation occurring at higher temperatures (see reference [[454](#)] for brief review). Lower temperatures have been reported historically, but these samples may have already undergone oxidation (by being subject to ambient conditions), as was observed by Perrozzi *et al.* [[451](#)], which noted oxidation occurring in the 25 – 150 °C temperature range. I find here that the temperature that induces oxidation lies between 150 °C and 220 °C, and that no oxidation is observed at lower annealing temperatures. This temperature is closer to the threshold oxidation temperatures of bulk MoS₂

(100 °C) found using Raman spectroscopy [454]. It should be noted that the role of light in oxidation for all these past reports has not been acknowledged.

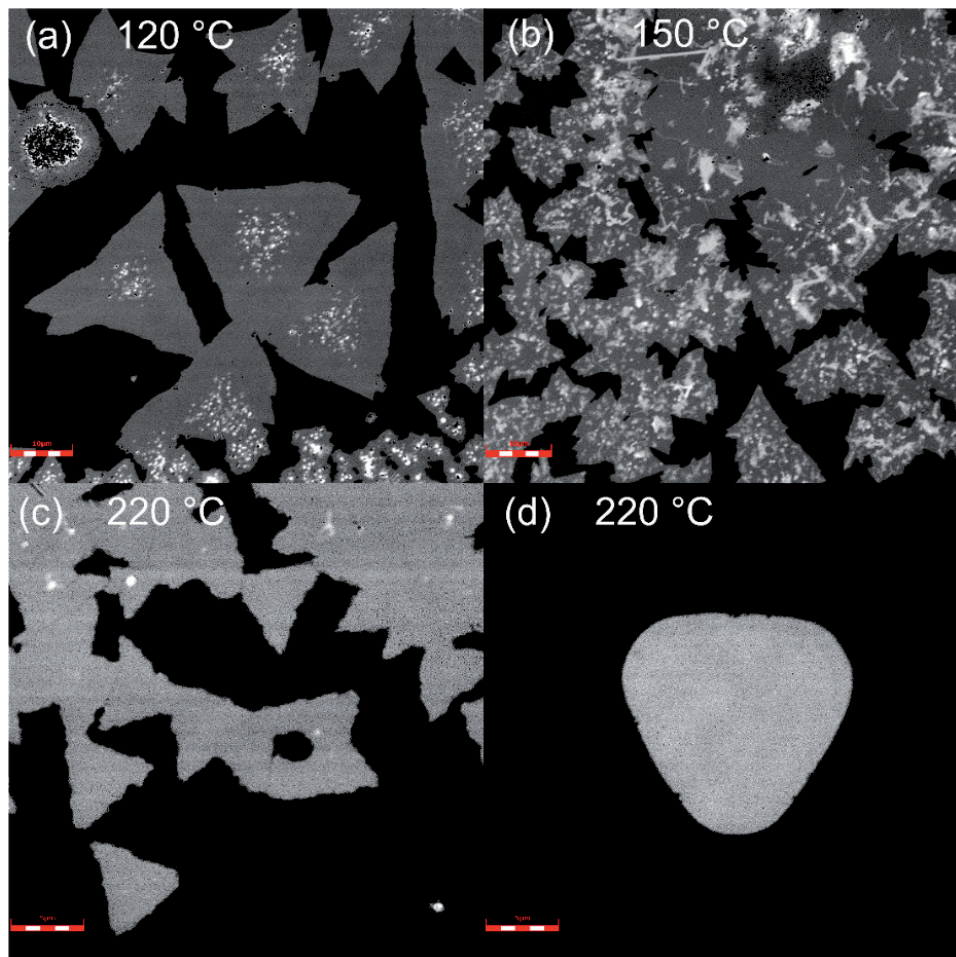


FIGURE 8.1: FINDING THE THRESHOLD TEMPERATURE OF OXIDATION: HEATING WS₂ IN THE ABSENCE OF LIGHT.

(a-c) Sister samples of WS₂ grown in a sulphur rich environment. **(a)** WS₂ heated to 120 °C for 3 hours. No signs of oxidation observed. Scale bar = 10 µm. **(b)** WS₂ heated to 150 °C for 3 hours. No signs of oxidation observed. Scale bar = 10 µm. **(c)** WS₂ heated to 220 °C for 3 hours. Grain boundaries are now visible, and edges are jagged, suggesting the WS₂ has oxidised. Scale bar = 5 µm. **(d)** WS₂ grown using standard method and heated to 220 °C for 3 hours. Crystal has oxidised on the edges. Scale bar = 5 µm.

Moreover, no oxidation of the basal plane was observed in both the standard growths and increased sulphur concentration growth crystals. Thus, increasing the sulphur concentration during growth had inconclusive effects on the oxidation dynamics of WS₂. A systematic experiment is needed to determine whether increasing the sulphur concentration during growth leads to more oxidation resistant WS₂ crystals (for example, repeating the

experiment at higher temperatures to compare whether the crystals will develop defects on the basal plane), but these results are promising.

The results presented in this section suggest that the thermal oxidation literature of WS₂ has not been fully explored, and that a precise temperature at which thermal oxidation begins in monolayer WS₂ is not yet experimentally known. Here, I have presented data that implies that the threshold temperature at which thermal oxidation of monolayer WS₂ in ambient air (and the absence of light) begins, lies in the range of 150 °C to 220 °C; but further work is necessary to pinpoint the precise onset of the thermal oxidation temperature. Further work would also crucially include Raman and PL analysis on sister samples to avoid as much as possible light exposure. This temperature would be of technological significance, as it would enable the cleaning of thin layers of WS₂ in ambient air while preventing oxidation, and also indicate the upper operating temperature of S-TMD transistors in ambient atmosphere. Here, it has been shown that annealing at 150 °C already enables at the least the removal of water (and other common lab solvents), and should permit the cleaning of WS₂ without use of a UHV chamber, provided the WS₂ (or other S-TMD) is protected from light.

8.3 Ca-Intercalated Quasi Freestanding Bilayer Graphene (Ca-QFSBLG)

In [Chapter 5](#), it was found that the calcium in Ca-intercalated graphene on 6H-SiC(0001) (Ca-QFSBLG) does not insert between the carbon layers, but preferentially at the SiC-buffer layer interface, strongly interacting with the Si surface to form a compound closely matching a Ca-silicide. Past experimental and theoretical reports have suggested that Ca intercalates between carbon layers, forming a C_6CaC_6 or similar structure. In the past, this structure has been thought to be the source of electrons to the Ca-intercalated graphene on SiC system, and thus, the origin of superconductivity in Ca-intercalated graphene on SiC.

In this outlook chapter, I will provide further details on the nanostructure of Ca deposited on the surface of epitaxial graphene on SiC – an experiment in which the details are largely lacking in the literature. I find that calcium assumes a (111) orientation when deposited on graphene on 6H-SiC(0001). I shall explore potential effects of the substrate, and suggest further experiments that could elucidate whether SiC substrate or the graphene itself plays a dominant role in the determination of the orientation of Ca on the surface of epitaxial graphene.

Moreover, I will discuss the need for further experiments to test whether Ca-QFSBLG is superconducting. The Ca-intercalation of epitaxial monolayer graphene (and bilayer graphene – see the Ca-intercalated H-QFSBLG results in [Appendix B4](#)) has raised important questions regarding the position of intercalated calcium in epitaxial graphene systems [[18-19](#), [23-24](#), [272](#)], and thus, the underlying mechanism of superconductivity in recent experiments on Ca-intercalated bilayer graphene [[19](#)].

8.3.1 Surface Deposition of Calcium on Epitaxial Graphene on 6H-SiC(0001)

For the calcium deposition shown in [Figure 8.2](#), ≈ 1 monolayer of calcium (as judged by a quartz crystal monitor, Createc) was deposited on the surface of the EMLG while the sample was at an elevated temperature of ≈ 423 K. Temperatures were measured using a single-colour pyrometer (LumaSense Technologies, IMPAC 8 Pro series). After Ca deposition (≈ 2 minutes 30 seconds with the effusion cell at ≈ 623 K) the sample was immediately allowed to cool for 15 minutes in UHV (heater turned off), after which the sample was rapidly cooled to ≈ 77 K in the STM. [Figure 8.2a](#) shows a magnified view of

the graphene surface directly after Ca deposition. [Figure 8.2b](#) shows the approximate height (from the line in [Figure 8.2a](#)) of the larger Ca-islands as ≈ 1.18 nm, in agreement with 2 layers of Ca metal rather than 1 monolayer as judged by the crystal quartz monitor (the accepted lattice parameter of Ca is 0.55884 ± 0.00002 nm, yielding 1.11768 ± 0.00004 nm for 2 layers [455]).

[Figure 8.2c](#) shows a zoomed-out image of the Ca decorated surface, and [Figure 8.2d](#) shows an even further zoomed-out image of the Ca-decorated surface. Upon closer inspection of [Figure 8.2d](#), I observe a feature (green circle) that appears to be surface damage, which may have been caused by Ca-deposition, or been present before intercalation, and requires further investigation to determine whether Ca deposition itself is the cause.

Nonetheless, [Figure 8.2](#) shows definitively, that the growth of Ca on graphene is a Volmer-Weber process – in agreement with recent findings [290]. But unlike ref. [290] (which used multilayer graphene on 6H-SiC(0001)), I observe that the Ca islands formed in [Figure 8.2](#) are hexagonal, suggesting the Ca is in the (1 1 1) orientation (since Ca is an FCC lattice [456]). In fact, the hexagonal crystallisation of calcium has been described as far back as H. Moissan (after which moissanite – silicon carbide – is named) who observed calcium crystallising in hexagonal tablets, “*Le calcium cristallise en tablettes hexagonales*” [457], causing it initially to be mistakenly identified to possess a hexagonal lattice structure [456]. Recently, Kong *et al.* [458] have found that the ionicity of an underlying material has the ability to influence the epitaxial growth of materials above monolayer, bilayer and trilayer graphene – dependent on the strength of the ionicity of the underlying substrate. In this study, graphene was transferred on top of a GaAs substrate (GaAs has an ‘ionicity’ or ionic bonding character of 31%), and then GaAs was epitaxially grown on top of the graphene, *i.e.* the GaAs grown on graphene assumed the epitaxy of the underlying GaAs substrate. With increasing substrate ionicity, the “ionic field” can penetrate through more layers of graphene. 6H-SiC has an ionicity of approximately 40% [459], and so the effect should be more prominent on 6H-SiC substrates. Thus, it is interesting to note that the calcium orientates into hexagonal shapes, and may suggest the 6H-SiC(0001) (which has hexagonal symmetry) may influence the orientation of the calcium, and *not* the graphene.

To test whether the Ca is aligning with and growing epitaxially with the SiC bulk (due to the ionic field) or with the graphene, two experiments could be conducted. The first would be to repeat the experiment using graphene on 3C-SiC(001) [460], which is cubic rather than hexagonal, and observe whether the calcium grows in the cubic orientation. In fact, 3C-SiC has an ionicity of 0.61 – 0.66 [461-462] exceeding that of 6H-SiC, and so the effect should be even more pronounced. The second would be to repeat the experiment using graphite (*I* was not able to find evidence of previous STM studies) on SiC (*i.e.* > 3 layers of graphene) to see whether the same orientation arises (here

the thicker graphene layers would attenuate the crystal field). In either experiment, the effect of the 6H-SiC substrate (if any) would be elucidated.

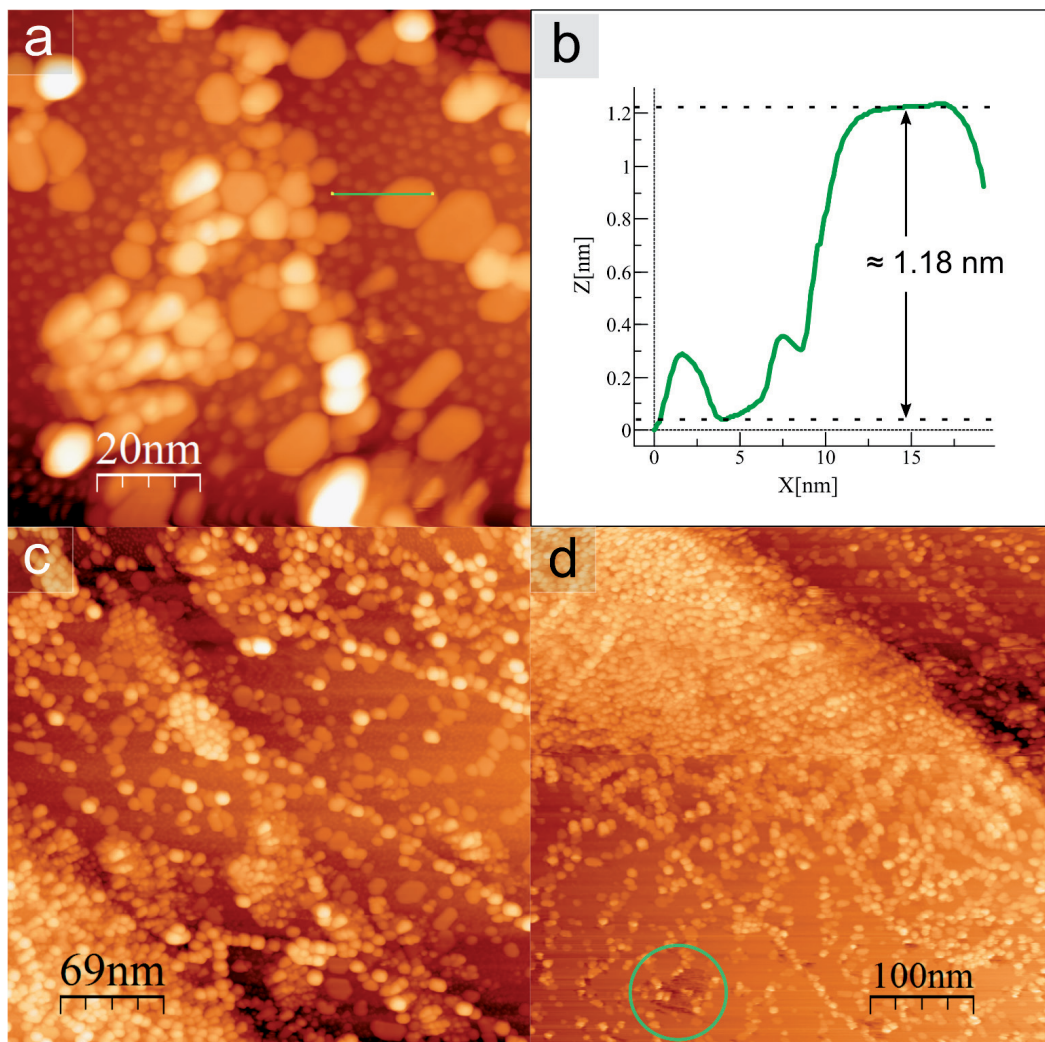


FIGURE 8.2: ROOM TEMPERATURE CALCIUM DEPOSITION (≈ 1 MONOLAYER) ON THE SURFACE OF EPITAXIAL GRAPHENE ON 6H-SiC(0001).

(a) Magnified view of Ca deposited on epitaxial graphene showing Volmer-Weber growth and uneven island height (1 V, 100 pA, 77 K). **(b)** Height profile taken from line in (a) showing height of larger Ca-islands as ≈ 1.18 nm. **(c)** Zoom-out showing larger area of Ca deposited surface (1 V, 100 pA, 77 K). **(d)** Large area scan of Ca-deposited surface. Feature outlined by green circle shows what appears to be surface damage (0.2 V, 200 pA, 77 K).

8.3.2 Is Ca-QFSBLG a Superconductor?

Previous experiments by Ichinokura *et al.* [19] measured Ca-intercalated bilayer graphene on 6H-SiC(0001). As was learned in [Chapter 5](#) and [Appendix B4](#), calcium prefers to intercalate at the SiC-buffer layer interface, rather than between the buffer layer-graphene interface in EMLG, or graphene-graphene interface in the case of H-QFSBLG. Ichinokura *et al.* [19] assumed that the calcium intercalated between the graphene sheets, and this may not be correct since I found no evidence that suggested that Ca intercalated in any significant amount between the layers of graphene in *both* the EMLG and H-QFSBLG. There is already evidence to suggest that the assumption of Ichinokura *et al.* [19] regarding the location of the intercalated calcium is incorrect, since Endo *et al.* [24] repeated the intercalation procedure in ref. [19], and suggested that the Ca intercalated between the buffer layer and 1st (bottom) graphene layer, not between the 1st and 2nd (top) graphene layer as originally claimed; already adding doubt to the intercalant residing between the graphene layers.

Thus, the experiment of Ichinokura *et al.* [19] should be repeated, and the location of the Ca-intercalant found using XPS, similarly to what has been shown in this thesis. This would confirm the precise position of the Ca, prior to measurement of the resistivity at low temperature to find T_C.

8.4 Mg-Intercalated Quasi Freestanding Bilayer Graphene (Mg-QFSBLG)

In this section, I will discuss further some of the concepts and results regarding the Mg-QFSBLG work presented in [Chapter 6](#).

In [Section 8.4.1](#), I explore the stoichiometry of the newly created Mg-silicide compound using recent density functional theory calculations from collaborators [26], and suggest future experiments which may be able to determine this ratio experimentally.

It was noted in [Chapter 6](#) and [Appendix C3](#) that magnesium was unable to displace the hydrogen underneath H-QFSBLG to form Mg-QFSBLG. While a null result, this has technological implications, and I will discuss these further in [Section 8.4.2](#).

Finally, in [Section 8.4.3](#), I will present preliminary results that explore the intercalation mechanism of Mg (and indeed all other similar intercalants) *via* the Mg-intercalation of a femto-second pulsed laser patterned EMLG sample. The artificial creation of voids in the sample is found to increase the rate at which intercalation occurs in the EMLG sample, and suggests that intercalation occurs solely through openings in the graphene (*i.e.* caused by cuts in the graphene due to handling). Thus, artificial void creation can increase the intercalation efficiency – especially regarding difficult-to-intercalate (*i.e.* high vapour pressure) materials such as magnesium – making this an attractive technique for device applications.

8.4.1 Density Functional Theory Calculations of the Mg-QFSBLG Structure

The XPS spectra and STM micrographs of Mg-QFSBLG (see [Figure 6.4](#), [Figure 6.5](#) and [Figure 6.8](#)) showed that the magnesium intercalated underneath the buffer layer. Furthermore, the LEED patterns shown in [Figure 6.3](#) implied that magnesium ordered in a $(\sqrt{3}\times\sqrt{3})R30^\circ$ with respect to the SiC surface, which suggests a surface with 1 Mg per 3 Si.

To investigate the resulting structure, collaborators carried out similar density functional theory (DFT) calculations to those in [Chapter 5](#), [Section 5.4.4](#) (for Ca-QFSBLG) [26], using the structure determined from LEED as a starting point. The calculated structure of Mg-QFSBLG is shown in [Figure 8.3](#), and was found to be energetically stable. [Figure 8.3a](#) shows that the former buffer layer is raised to lie 0.451 nm above the surface Si atoms, a change in height (Δh), compared to pristine EMLG, of approximately 0.24 nm

(using the known value for buffer layer – Si distance of 0.21 nm [49]). Since no experimental data was obtained with the STM showing partial Mg-intercalation, the theoretical prediction for the change in height after Mg-intercalation was not able to be supported by experiment.

Figure 8.3b shows the top down view of the calculated Mg-QFSBLG unit cell. The ratio of Mg : Si is 1 : 3, or MgSi_3 . The stoichiometry of the magnesium and silicon could be experimentally determined with XPS provided that the kinetic energies of the core levels are greater than 150 eV (see [Chapter 5, Section 5.4.2.4](#)). This could be achieved for example using a synchrotron, or lab-based XPS system, but was impossible to determine from the Mg 2p core level shown in [Chapter 6 Section 6.4.2.3](#) due to the kinetic energy being << 150 eV. This was not obtained due to time considerations in the experiment. Thus, I leave this experimental determination to future work.

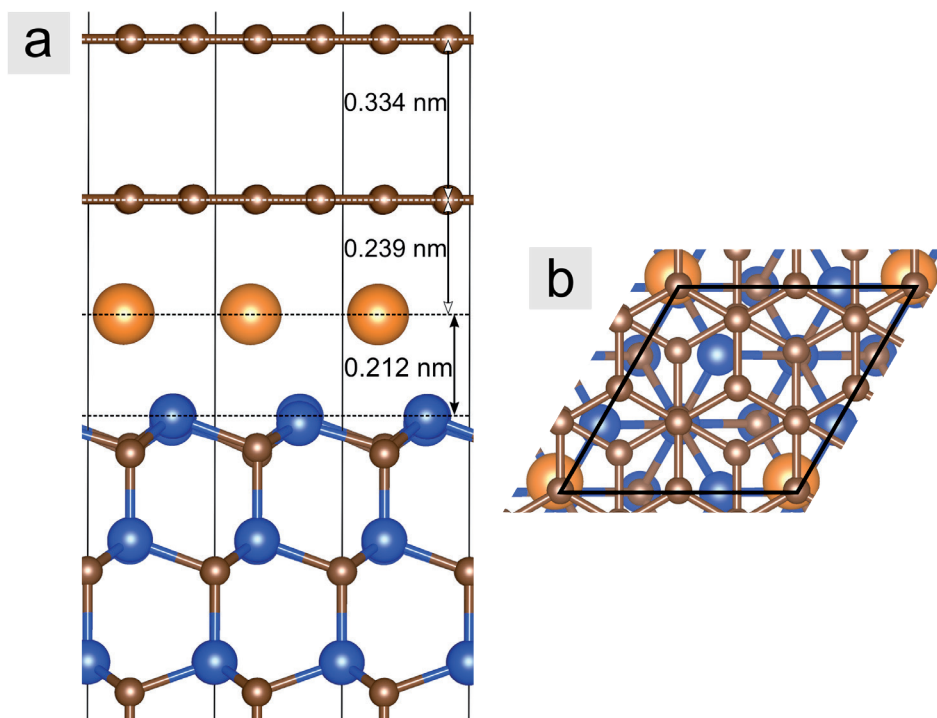


FIGURE 8.3: DENSITY FUNCTIONAL THEORY CALCULATIONS OF THE Mg-QFSBLG STRUCTURE.

(a) Side-on view of Mg-QFSBLG structure showing vertical distances between atomic planes. (b) Top down view of unit cell of Mg-QFSBLG showing the ratio of Mg : Si as 1 : 3. Brown (small) = carbon, blue (medium) = silicon, orange (large) = magnesium.

8.4.2 Using the Relative Reactivity of Intercalants for Device Fabrication

Typically, intercalation publications only attempt the intercalation of a single intercalant. If more than two atomic species are intercalated, these intercalants are typically complementary to one another and are used to form binary compounds – such as the intercalation and growth of SnGe [304], GaN [463] or MoS₂ [464] layers underneath graphene on silicon carbide. It is well known that confinement can alter chemical reactivity [465-467]. Less explored (in fact I could not find previous publications on the topic) is whether one intercalant is able to displace another intercalant. Yet this ‘relative reactivity’ knowledge could prove extremely useful, as I explain below.

In this thesis, I have presented results which have begun exactly this type of characterisation. For instance, I found (see [Appendix B4](#)) that calcium was able to displace the intercalated hydrogen underneath H-QFSBLG, forming Ca-Si bonds. On the other hand, magnesium was *unable* to displace the hydrogen and intercalate H-QFSBLG, but did intercalate EMLG (see [Appendix C3](#)). Although this was a null result, the fact that the Mg was unable to intercalate the H-QFSBLG is technologically relevant, since if one could selectively remove the intercalated hydrogen (through heating for example), then these areas would be selectively intercalated without disrupting the H-Si bonds of the existing H-QFSBLG regions. Since Mg-QFSBLG is highly n-type doped, and H-QFSBLG is p-type doped, this could set up atomically sharp n-p junctions, and could be interesting for pursuing device applications.

This is the subject of future work, and it is hoped continued efforts will yield a more detailed description of the chemical reactivity of intercalants *with respect to each other*, and not limited to the reactivity of the intercalant with the underlying silicon carbide.

8.4.3 Intercalation Mechanism and Increasing Intercalation Efficiency

One question that has remained in the literature (and this work) is, “*how does calcium/magnesium (or any other intercalant) intercalate epitaxial graphene?*”. Previous publications have endeavoured to explore the mechanism of intercalation, and have found that there exist at least 4 general mechanisms which are dependent on the specific intercalant [468]: intercalation facilitated by (1) large (multi-atomic) voids, *i.e.* discontinuities in the graphene [339, 355, 469-470]; (2) wrinkles with nano-sized defects [463, 471]; (3) existing point defects [472-474]; and finally (4) defects created by the

intercalant itself [470, 475-476]. The mechanism of (2) and (3) is expected to be quite similar since the nano-sized defects can be considered point defects (and so only mechanism (2) will be discussed here).

In the case of mechanism (1), Sorger *et al.* [339] found that hydrogen intercalation was facilitated around graphene voids after the fabrication of artificial holes in the graphene *via* oxygen plasma etching. The holes in this case had a diameter of ≈ 200 nm, and were spaced ≈ 2 μm apart. Sutter, Safowski and Sutter [469] found that monolayer graphene micro-islands on Ru(0001) could be intercalated by oxygen, and that the intercalation progressed from the outside of the flake toward the inside. Furthermore, Jin *et al.* [470] found that Pb atoms intercalated monolayer graphene on Ru(0001) from the edges, similarly to oxygen.

For mechanism (2), Petrović *et al.* [471] found that Cs intercalation of graphene on Ir(111) was favoured at graphene wrinkle sites, where there are thought to exist nano-sized defects that facilitate intercalation. Wrinkle-intercalation was also observed by Zakaria *et al.* [463] after the intercalation of GaN. In both cases, intercalation was found in the immediate area surrounding the wrinkle sites.

For mechanism (4), theoretical calculations by Boukhvalov and Katsnelson [475] have implied that certain transition metals are able to reduce the formation energy of vacancy defects. This was subsequently experimentally observed by Jin *et al.* [470] and Sicot *et al.* [476] in the case of Ni intercalation of graphene on Ru(0001) and Cu intercalation of graphene on Ir(111), respectively. These defects can be ‘healed’ after annealing [470, 474, 477].

Furthermore, there is evidence to suggest that the intercalation mechanism depends on the specific intercalant. For example, Jin *et al.* [470] observed that the mechanism of intercalation for graphene islands grown on Ru(0001) was different for Ni and Pb. The Ni preferred to intercalate through the graphene by creating defects (mechanism (4)), whereas the Pb could only intercalate from the edges of the graphene (mechanism (1)). The fact that Ni (and elements such as Si [477]) are able to create defects in the graphene implies that these elements are able to bond with carbon to create these types of defects for intercalation [470].

This suggests that the intercalation of Mg will follow one of two major pathways underneath the graphene. Either it will create defects and intercalate, or it will intercalate starting from the edges using existing defects in the graphene. To test which of these hypotheses is correct, an EMLG sample was fabricated with intentional defects, to study whether these defects increased the speed of intercalation. For the intentionally defected sample, an EMLG sample was fabricated (by collaborators at the U.S. Naval Research Laboratory) with etched lines using laser ablation, as is shown in the schematic of Figure 8.4. The laser used had a power of 5 mW, centre

wavelength of 800 nm, and was pulsed at ≈ 50 femtoseconds. Each line was written at $\approx 20 \mu\text{m s}^{-1}$. Further details regarding patterning can be found in ref. [478]. A schematic of the sample is shown in Figure 8.4, and illustrates 13 laser ablated lines of $\approx 2 \mu\text{m}$ width in the centre of the EMLG sample.

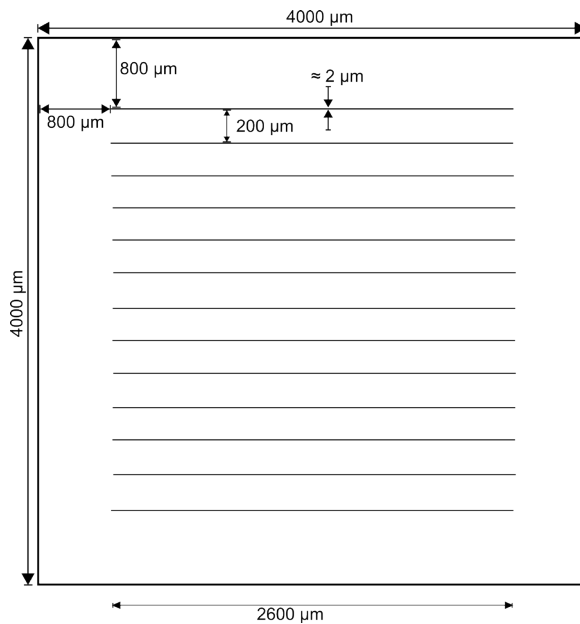


FIGURE 8.4: SCHEMATIC OF LASER PATTERNED EPITAXIAL MONOLAYER GRAPHENE ‘DEFECTED’ SAMPLE.

Showing etched lines (void of graphene) of $2 \mu\text{m}$ width using a $50\times$ objective and ≈ 50 femtosecond pulses from a 5 mW Ti:sapphire laser at 800 nm centre wavelength.

Void-mediated intercalation should be enhanced by the increased density of voids, and can be directly measured using XPS. Thus, creating artificial voids in the graphene would increase the speed of Mg intercalation if Mg intercalation proceeds *via* voids, but if Mg intercalation proceeds *via* defect creation, the voids should not influence the intercalation process.

The experiment was set up as follows, two EMLG samples were mounted on the same sample holder – one pristine EMLG sample and one laser patterned (which I designate ‘EMLG-p’). The sample was then Mg-intercalated in a stepwise fashion, consisting of 3 steps. In the first Mg-intercalation step, ≈ 15 nm of Mg was deposited on the sample (cell temperature 673 K , 20 minutes of Mg flux exposure), which was then heated to 463 K for ≈ 1.5 hours. For the 2^{nd} Mg-intercalation, ≈ 15 nm of Mg was deposited on the sample (cell temperature 673 K , 20 minutes of Mg flux exposure), which was then heated to 623 K for ≈ 1.5 hours. For the 3^{rd} Mg-intercalation, ≈ 15 nm of Mg was deposited on the sample (cell temperature 673 K , 20 minutes of Mg flux exposure), which was then heated to 623 K for ≈ 1.5 hours.

[Figure 8.5a-b](#) shows the C 1s core level of pristine EMLG and pristine EMLG-p. No major differences between the two spectra are observable, and furthermore, match closely with the spectra already presented in [Chapter 5](#) and [Chapter 6](#) (see [Figure 5.5](#) and [Figure 6.5](#)). All fit parameters can be found in [Appendix C1](#). As was observed in [Chapter 5](#), [Chapter 6](#) and [Chapter 7](#), the shift in the SiC components Z_C and B_C were a tell-tale sign of changes at the SiC surface, correlated directly to intercalation and the formation of an alkali metal silicide. Thus, analysis of the shift in this component gives an indication of the extent of intercalation, since a completely intercalated sample should have no observable Z_C and B_C components. After the 1st Mg-intercalation shown in [Figure 8.5c-d](#), differences between EMLG and EMLG-p are visible. Even though both samples were subjected to approximately the same deposition and annealing conditions, clearly the laser patterned sample (EMLG-p) has intercalated more than the un-patterned sample (EMLG) since components Z_C/B_C have mostly disappeared. This observation is repeated for the 2nd Mg-intercalation ([Figure 8.5e-f](#)) and the 3rd Mg-intercalation ([Figure 8.5g-h](#)), in which component B_C is not attenuated as much in EMLG compared to EMLG-p. Furthermore, the shape of the C 1s peak clearly changes to more highly doped in EMLG-p after the 1st Mg-intercalation, whereas the EMLG sample retains the characteristic ‘bulge’ related to the buffer layer.

These results imply that the main mechanism of Mg-intercalation is *via* voids in the graphene/buffer layer, and intercalation proceeds *via* mechanism (1). In fact, the density of lines is much lower in sample EMLG-p than the patterned sample by Sorger *et al.* [339] which patterned 0.2 μm diameter circular voids in EMLG spaced between 0.3 – 1 μm apart. Sample EMLG-p on the other hand, has 2 μm × 2600 μm rectangular voids spaced 200 μm away from each other (and thus, extending over many terraces). Even with this low density of voids, a drastic change in the Mg-intercalation speed is observed in comparison to pristine EMLG.

Furthermore, this suggests that Mg-intercalation efficiency (and similar elements that intercalate using mechanism (1), *i.e.* voids) can be increased by the patterning or scratching of the graphene at the edges of the sample. This is especially important for high vapour pressure elements such as Mg which are difficult to intercalate. Recently, antimony was intercalated underneath buffer layer only on 6H-SiC(0001) to form quasi-freestanding graphene [322]. Since Sb has a high vapour pressure, an overpressure of argon was used to prevent the Sb boiling off before intercalation could occur. In fact, Mg has a higher vapour pressure than Sb [360], but this method was not needed for intercalation in this case. It would be interesting to extend this method to other high vapour pressure elements to see if intercalation speed and efficiency is increased. Here I have shown that patterning on its own can speed up the intercalation of high vapour pressure elements so that high pressure intercalation is not necessary. Further results (LEED, XPS) on the step-wise Mg-intercalation can be found in [Appendix C4](#).

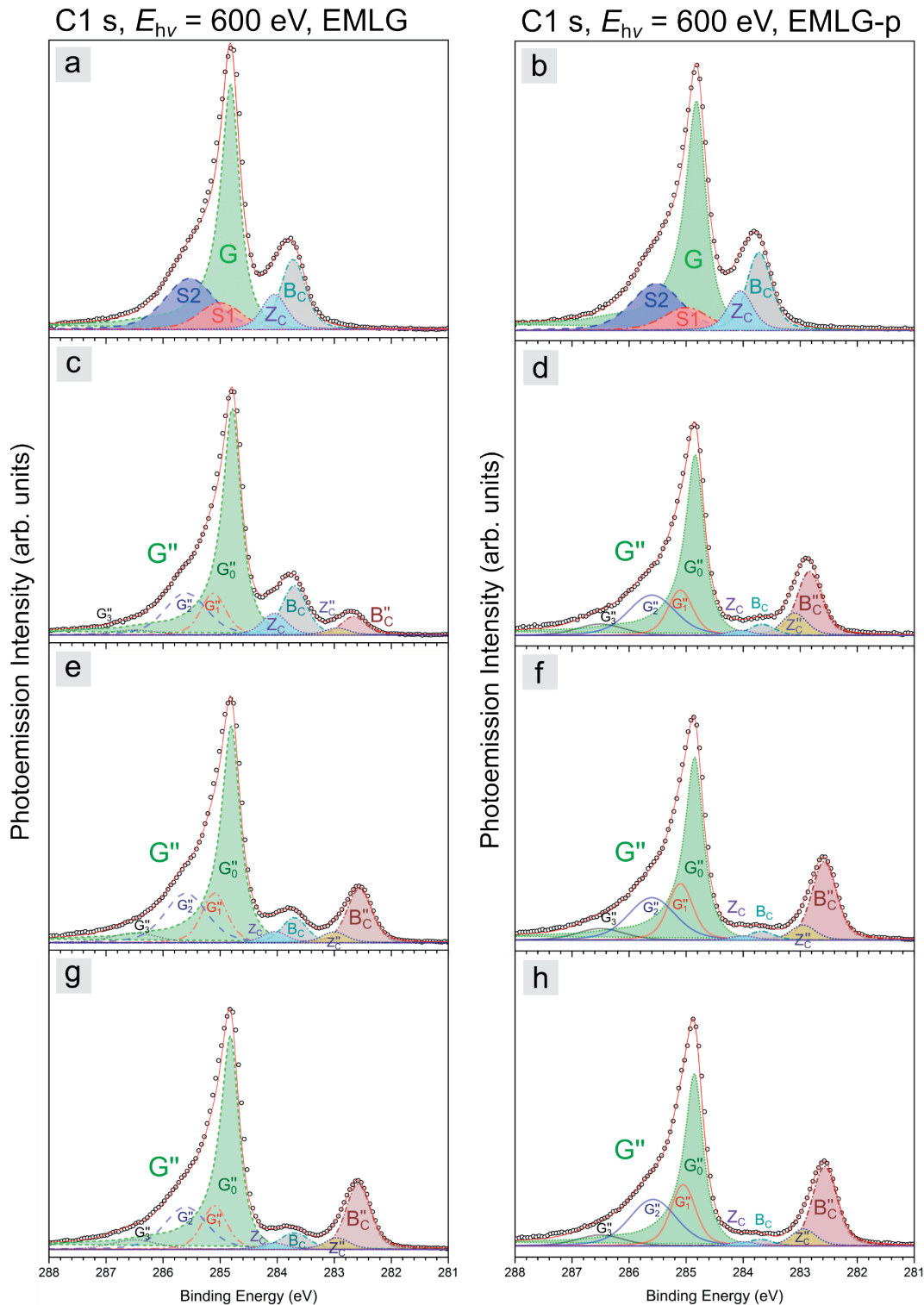


FIGURE 8.5: X-RAY PHOTOEMISSION SPECTRA SHOWING THE C 1s CORE LEVELS OF STEPWISE Mg-INTERCALATED PRISTINE AND LASER PATTERNED EPITAXIAL MONOLAYER GRAPHENE (EMLG) SAMPLES AT AN X-RAY ENERGY OF $E_{hv} = 600$ eV.

(a) Pristine EMLG showing components S_1/S_2 (buffer layer), G (graphene), Z_c (SiC) and B_c (Bulk SiC). (b) Laser patterned EMLG (EMLG-p). (c, d) 1st Mg-intercalation. (e, f) 2nd Mg-intercalation. (g, h) 3rd Mg-intercalation. See text or [Chapter 6](#) for component definitions. See [Table C.1-7](#) and [Table C.1-8](#) for component values.

8.5 Oxidation of Ca-QFSBLG and Mg-QFSBLG

In this section, I will present preliminary results on the long-term ambient air exposure of the Mg-QFSBLG sample that was presented in Chapter 7 (fabricated *via* a three-step Mg-intercalation, see [Methods 7.3.1.2](#) and [Figure 8.5](#) for more details). I show that Mg-QFSBLG is unstable in air for long-term ambient air exposures of 8 months, and explore the possible oxidation reactions that may be taking place *via* XPS. To find the precise point in time at which all the Mg-silicide is oxidised requires further work, and it is likely that Mg-QFSBLG could oxidise within shorter ambient air exposures. But the oxidation is found to be likely initiated by moisture, and thus, anhydrous environments should be beneficial in protection from oxidation.

Furthermore, the general technological usefulness of ambient air sensitive intercalants which follow well-known chemical reaction pathways for use in gas sensing are discussed. While more research in this field is required, the Ca- and Mg-intercalation oxidation experiments have revealed that one can easily measure conductivity changes in the overlaying graphene while ambient air reactions are occurring underneath the graphene. This opens exciting device applications in which the gas sensor can be tuned depending on the specific air-reactiveness of the intercalant.

8.5.1 Long-term Ambient Air Stability of Mg-QFSBLG

The short-term ambient air exposure results in [Chapter 7](#) showed that some oxidation *was* taking place in Mg-QFSBLG after 6 hours of ambient air exposure, but that this oxidation was so low in concentration, that the effects were almost non-existent in the Si 2p, C 1s and O 1s core level spectra. Thus, to further analyse the oxidation of Mg-QFSBLG, longer ambient air exposures were required. Even so, the structure of the Mg-intercalated graphene *remains bilayer* even after oxidation (see [Chapter 7, Section 7.4.2.2](#)). [Figure 8.6](#) shows the C 1s and Si 2p core levels of 8-month ambient air exposed Mg-QFSBLG, which were obtained using a lab-based XPS using Al K α X-rays (see [Methods, Section 7.3.2](#)). It should be noted here that the lab based XPS does not have a heating stage, so samples were unable to be annealed to remove atmospheric contaminants. [Figure 8.6a-b](#) shows the C 1s and Si 2p core levels, respectively, of a representative pristine EMLG sample (that was not used for intercalation) which was grown using the same method and equipment as the Mg-intercalated EMLG samples. Although lacking the surface sensitivity of the synchrotron based XPS technique, many of the same components are

still resolvable, and agree in binding energy with the values found from the synchrotron. Thus, atmospheric contaminants do not affect greatly the measurement. The fit parameters for all components can be found in [Table 8-1](#) and [Table 8-2](#).

[Figure 8.6c-d](#) show the C 1s and Si 2p core levels of Mg-QFSBLG exposed to ambient atmosphere for 8 months. The C 1s core level in [Figure 8.6c](#) shows that component B_C from pristine EMLG still exists, which is expected since the Mg-intercalation was more partial in this sample than the other Mg-QFSBLG sample analysed in [Chapter 6](#) (see [Figure 6.5](#) and [Figure 8.5](#) for comparison). Component B_C'' that was initially formed upon Mg-intercalation has shifted in binding energy, $\Delta E_B = 0.52 \pm 0.15$ eV, to higher binding energy (now labelled component B_C^{air}), suggesting that a chemical reaction has occurred at the SiC surface (as was the case with Ca-QFSBLG). The Si 2p core level in [Figure 8.6c](#) shows an additional component to the original SiC bulk component B_{Si} , which I label $B_{\text{Si}}^{\text{air}}$, and is located at $E_B = 100.83 \pm 0.1$ eV, $\Delta E_B = 0.51 \pm 0.15$ eV. The equivalence in energy separation between components B_C^{air} and $B_{\text{Si}}^{\text{air}}$ is in strong support that these components are resultant from the same process – *i.e.* an oxidation of the intercalated Mg-Si layer resulting in an altered SiC surface. The oxidation of the intercalated Mg is clearer after analysis of the O 1s core level, shown in [Figure 8.7](#).

Furthermore, the characteristic ‘highly doped’ graphene C 1s lineshape which was observed for pristine Mg-QFSBLG (see [Chapter 6, Section 6.4.4.1](#)) is no longer apparent in 8-month ambient air exposed Mg-QFSBLG (component G_{air}'' in [Figure 8.6c](#)). Thus, it is likely that long-term ambient exposed Mg-QFSBLG is relatively low-doped compared to its initial highly n-type doped ‘pristine’ state, similar to the scenario of ambient air oxidised Ca-QFSBLG (see [Figure 7.4](#)). In contrast, there exists no evidence that indicates damage to the Mg-QFSBLG after oxidation, which was the case after oxidation of Ca-QFSBLG (component sp_3 in [Figure 7.5b](#)). Furthermore, the pristine bulk component B_C , and the buffer layer components S_1 and S_2 are still observable, which is likely due to the fact that this EMLG sample (three-step Mg-intercalation) was more partially intercalated (see [Figure 8.5](#)).

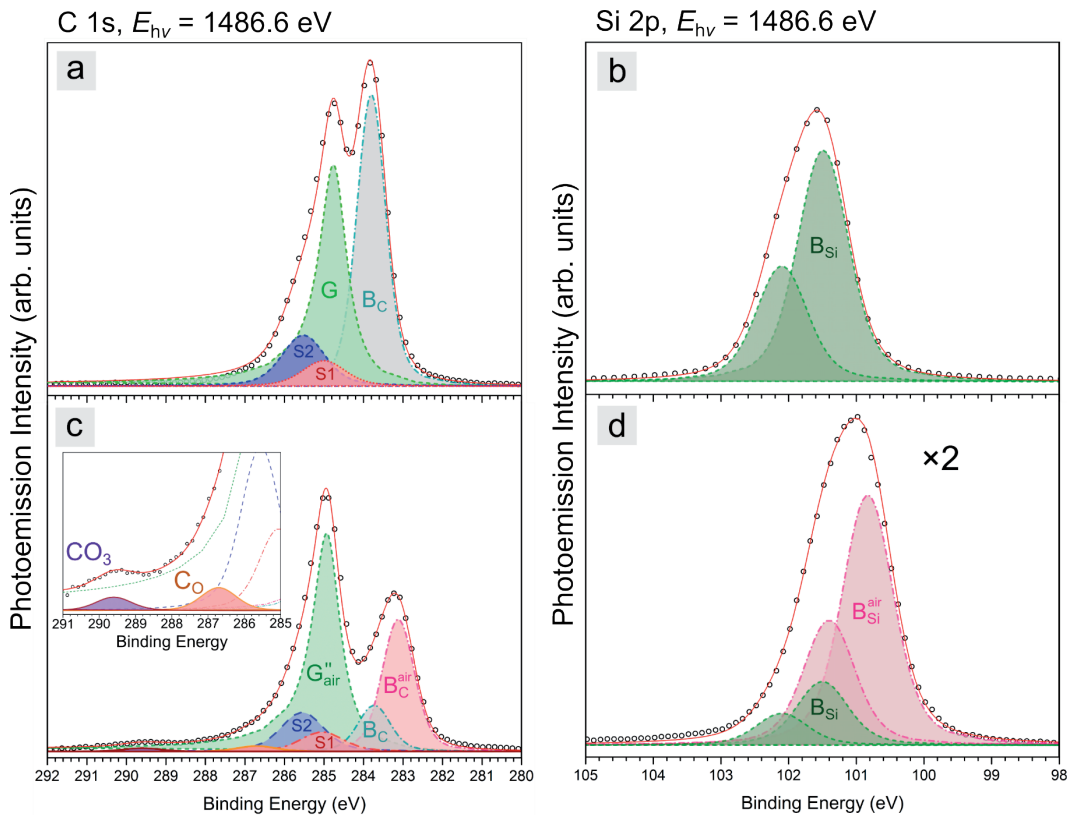


FIGURE 8.6: X-RAY PHOTOEMISSION SPECTRA SHOWING THE C 1s AND Si 2p CORE LEVELS OF LONG-TERM (8 MONTHS) AMBIENT AIR EXPOSED Mg-QFSBLG AT AN X-RAY ENERGY OF $E_{hv} = 1486.6$ eV.

(a) C 1s core level of pristine EMLG showing buffer layer (S_1 , S_2), graphene (G) and bulk SiC (B_C) components. (b) Si 2p core level of pristine EMLG showing bulk SiC (B_{Si}) component. (c) C 1s core level of 8-month air exposed Mg-QFSBLG showing buffer layer (S_1 , S_2), graphene (G''_{air}), EMLG SiC bulk (B_C) and shifted SiC bulk (B_C^{air}) components. (d) Si 2p core level of 8-month air exposed Mg-QFSBLG showing EMLG bulk SiC (B_{Si}) and shifted SiC bulk (B_{Si}^{air}) components. Components B_C^{air} and B_{Si}^{air} are resultant from ambient air reaction (oxidation). The intensity scale in (d) is magnified $\times 2$ from (b).

TABLE 8-1: Si 2p CORE LEVEL FIT PARAMETERS FOR ALL COMPONENTS IN FIGURE 8.6.

The below table outlines the binding energy (E_B) of the $2p_{3/2}$ and $2p_{1/2}$ lines, as well as the Gaussian width (W_G) and Lorentzian width (W_L) of the Voigt fits for pristine EMLG and long-term (8 months) ambient air exposed Mg-QFSBLG

EMLG, Si 2p		(b) Pristine EMLG			(d) 8 Months Air-Exposure, Mg-QFSBLG		
Component	E_{hv} (eV)	E_B (eV) $2p_{3/2}$	E_B (eV) $2p_{1/2}$	W_G/W_L (eV)	E_B (eV) $2p_{3/2}$	E_B (eV) $2p_{1/2}$	W_G/W_L (eV)
B _{Si}	1486.6	101.49	102.10	0.7/0.35	101.50	102.10	0.7/0.35
B _{Si} ^{air}	1486.6	-	-	-	100.83	101.40	0.70.35

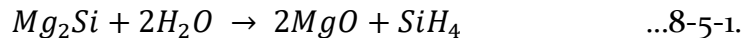
TABLE 8-2: C 1s CORE LEVEL FIT PARAMETERS FOR ALL COMPONENTS IN FIGURE 8.6.

The below table outlines both the binding energy (E_B), as well as the Gaussian width (W_G) and Lorentzian width (W_L) of the Voigt fits for pristine EMLG and long-term (8 months) ambient air exposed Mg-QFSBLG.

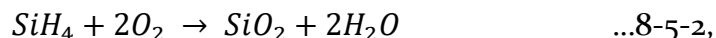
EMLG, C 1s		(a), Pristine EMLG		(c) 8 Months Air-Exposure	
Component	E_{hv} (eV)	E_B (eV)	Q/W_L or W_G/W_L (eV)	E_B (eV)	Q/W_L or W_G/W_L (eV)
G	1486.6	284.73	14/0.43	-	-
S ₁	1486.6	285.00	1/0.5	285.05	1/0.5
S ₂	1486.6	285.52	1/0.5	285.55	1/0.5
B _C	1486.6	283.80	0.7/0.3	283.73	0.8/0.3
B _{air} ["]	1486.6			283.12	0.8/0.3
G _{air} ["]	1486.6			284.90	14/0.43
C _O	1486.6			286.71	1/0.3
CO ₃	1486.6			289.60	1/0.3

Since components B_C^{air} and $B_{\text{Si}}^{\text{air}}$ were observed *after* exposure to ambient, it implies that there is a reaction occurring that alters the electronic structure between the SiC surface and graphene. In the following discussion, I will explore the likely chemical reactions occurring, and finally compare this to the C 1s and O 1s core levels of 8-month ambient air exposed Mg-QFSBLG.

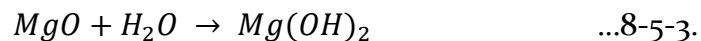
It is well known that magnesium silicide reacts readily with H_2O [479-480]:



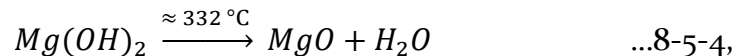
In the presence of O_2 , SiH_4 will spontaneously react [479]:



forming silicon dioxide and water. In the presence of excess H_2O , MgO (being hydroscopic) reacts in ambient [479]:



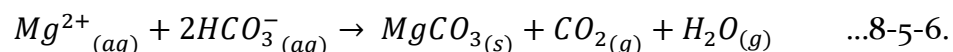
This reaction is reversible, and upon heating to 332°C [479] – 380°C [481]:



the magnesium hydroxide reverts to magnesium oxide (and water). Furthermore, it has been demonstrated that the oxidation of magnesium in O_2 [482] and H_2O [483] environments at room temperature, can produce magnesium carbonate (MgCO_3). Although MgCO_3 was not the dominant oxidation species in these reactions, $\text{Mg(HCO}_3)_2$ is able to form *via* the carbonisation of aqueous Mg(OH)_2 [479]:



This forms magnesium bicarbonate, but upon drying, converts to MgCO_3 [479]:



[Equation 8-5-5](#) and [Equation 8-5-6](#) suggest that both magnesium carbonate and/or magnesium bicarbonate may be present after ambient air exposure. Thus, after ambient air exposure it is expected that the magnesium oxidation

products will include observable amounts of MgO , Mg(OH)_2 and $\text{MgCO}_3/\text{Mg(HCO}_3)_2$. Other oxidation reactants and products such as H_2O and small amounts of SiO_2 are also expected (Equation 8-5-2).

Upon closer inspection of the C 1s core level at higher binding energy, magnified in the inset of Figure 8.6c, two additional components that were *not visible* in pristine EMLG (Figure 8.6a) which I label C_O and CO_3 are *visible* after long-term ambient air exposure of Mg-QFSBLG. Component C_O at $E_\text{B} = 286.71 \pm 0.10$ eV is in good agreement with literature values for a compound with C-O bonding [424, 484]. Since component C_O is not visible in pristine samples (Figure 8.6a), then it must arise after ambient air reaction of Mg-QFSBLG. Component CO_3 at $E_\text{B} = 289.60 \pm 0.1$ eV is in favourable agreement with MgCO_3 [482, 485].

Prior to measuring the air exposed Mg-QFSBLG sample, the O 1s core level for pristine EMLG was measured, and is shown in Figure 8.7a. Since the lab-based source does not have the ability to anneal samples, the O 1s spectrum of pristine EMLG contains oxygen contamination species (samples were able to be annealed in UHV at the synchrotron, and so oxygen contamination was not observed at the synchrotron). The spectrum in Figure 8.7a was deconvolved into two components labelled Ac and H_2O . Component Ac at $E_\text{B} = 533.90 \pm 0.1$ eV likely represents adventitious carbon contamination [484], whereas component H_2O at $E_\text{B} = 532.40 \pm 0.1$ eV agrees with literature values representing water contamination [484, 486].

Long-term (8-month) ambient air exposed Mg-QFSBLG shown in Figure 8.7b, reveals the presence of at least 3 components. Component MgO at $E_\text{B} = 531.10 \pm 0.1$ eV is in excellent agreement with literature values for magnesium oxide (MgO) [482, 487-488]. The higher binding energy component MgOH at $E_\text{B} = 532.55 \pm 0.1$ eV is in agreement with magnesium hydroxide [377, 488]. Component MgCO at $E_\text{B} = 533.75 \pm 0.1$ eV is in approximate agreement with literature values for MgCO_3 [482-483]. Further complicating the analysis is the possible presence of SiO_x (see Equation 8-5-2) which possesses a similar binding energy of ≈ 533.80 eV [421-422]. But since SiO_x was not observed in the Si 2p core level in Figure 8.6d, its contribution to component MgCO should be small (the photoionization cross section at 1486.6 eV of the O 1s core level is ≈ 4 times greater than the Si 2p core level and ≈ 3 times greater than the C 1s core level [143]).

To summarise, I have shown that the Mg-silicide that was initially formed upon formation of Mg-QFSBLG, completely oxidises after 8 months of ambient air exposure. It is likely that the oxidation reaction is initiated by the presence of water, and proceeds in a stepwise fashion (similar to Ca-QFSBLG) forming magnesium oxide, magnesium hydroxide and magnesium bicarbonate/carbonate. Further work is needed to ascertain whether oxidation could proceed given the absence of water, and the precise longevity of Mg-QFSBLG in controlled humidity environments. Nonetheless, these

preliminary results have already shown that Mg-QFSBLG may slowly react with moisture.

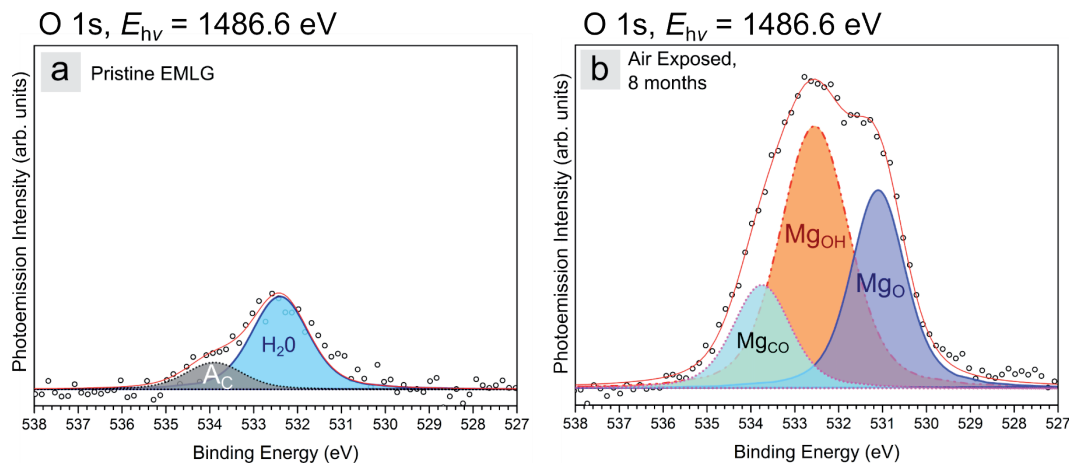


FIGURE 8.7: X-RAY PHOTOEMISSION SPECTRA AT AN X-RAY ENERGY OF $E_{hv} = 1486.6$ eV OF THE O 1s CORE LEVEL OF PRISTINE EMLG AND LONG-TERM (8-MONTH) AMBIENT AIR EXPOSED Mg-QFSBLG.

(a) Pristine EMLG, not annealed showing surface contamination from adventitious carbon (A_C) and water (H_2O). (b) Mg-QFSBLG exposed to ambient air for 8 months showing significant oxidation corresponding to magnesium oxide (MgO), magnesium hydroxide ($Mg(OH)_2$) and magnesium carbonate ($MgCO_3$) species.

TABLE 8-3: O 1s CORE LEVEL FIT PARAMETERS FOR ALL COMPONENTS IN FIGURE 8.10. The below table outlines both the binding energy (E_B), as well as the Gaussian width (W_G) and Lorentzian width (W_L) of the Voigt fits for pristine EMLG and long-term (8 months) ambient air exposed Mg-QFSBLG.

EMLG/Mg-QFSBLG O 1s		(a) Pristine EMLG		(b) 8-month Ambient Air Exposure	
Component	E_{hv} (eV)	E_B (eV)	W_G/W_L (eV)	E_B (eV)	W_G/W_L (eV)
H ₂ O	1486.6	532.4	1.2/0.6		
A _C	1486.6	533.9	1.2/0.6		
MgO	1486.6			531.10	1.1/0.6
MgOH	1486.6			532.55	1.5/0.6
MgCO	1486.6			533.75	1.2/0.6

8.5.2 Gas Sensors: Utilising Ambient Air Reacted Intercalated Compounds

I have shown that Ca-intercalation and Mg-intercalation alters the physical and electrical properties of the epitaxial graphene – epitaxial monolayer graphene becomes a quasi-freestanding bilayer (Ca-QFSBLG/Mg-QFSBLG, physical), the carrier density is increased and the work function is lowered (more n-type, electrical). Upon ambient air exposure, it is likely that the graphene remains quasi-freestanding (see Raman maps in [Figure 7.6](#) and [Figure 7.9](#)), but that the electrical properties are significantly altered due to the oxidation of the underlying Ca-silicide/Mg-silicide. In the case of Ca-QFSBLG, these electrical changes manifest in the form of workfunction decreases ([Figure 7.4](#)), changes in the shape of the graphene peak signifying a decrease in the number of charge carriers ([Figure 7.2](#)), and the creation of defects in the graphene ([Figure 7.5](#) and [Figure 7.6](#)). In summation, these effects should lower the conductivity of the graphene [489]. Thus, the reaction of calcium with H₂O (forming Ca(OH)₂) and then CO₂ (forming CaCO₃/CaHCO₃) can be monitored using an electrical device such as a Hall bar, 4 probe or simple 2 probe device to create a specialised (and specific to the intercalant) gas sensor. Since the oxidation reaction of Ca-silicide follows a well-known path, the sensor could be calibrated for the detection of H₂O and CO₂ through changes in resistivity/conductivity. Although this sensor might not be useful at ambient for the detection of H₂O (the Ca-silicide is almost completely reacted after 30 minutes), the reaction with CO₂ may be much slower (no carbonates were observed after 9 hours), and thus may be more useful as a CO₂ detector at ambient. Alternatively, this type of detector may find use in UHV, inert or low earth orbit/outer space environments as a H₂O and CO₂ sensor. Since CaCO₃ can be converted back to CaO via heating at ≈ 1073 K, it is possible that the sensor could be recycled. This should also be the case for sensors made from Mg-QFSBLG. Furthermore, this opens an exciting opportunity in gas sensing, whereby the graphene gas sensor can be ‘tuned’ or made specific by reactions dependent on the intercalant. Investigation into alternative intercalants that are reactive with other gas species should be conducted.

The exploration of reactive intercalated graphene for gas detection – where the sensing medium is in fact buried underneath the graphene – has not been previously explored in detail, but may offer benefits over traditional gas sensing *via* the increase in reaction specificity. Here, the benefit of the graphene comes in two forms: (1) The graphene offers some protection to the underlying sensing medium (the intercalant in this case) and (2) The graphene is a conductive medium in which integrated electronics and circuitry can be constructed from. The oxidation and reaction chemistry of intercalants underneath graphene offers a rich and untapped chemical playground, which may lead to developments regarding unique and extremely gas-specific sensors.

8.6 Concluding Remarks

In [Chapter 4](#), I looked at the ambient air oxidation of monolayer WS₂ and found that monolayers of WS₂ oxidise significantly when exposed to the ambient atmosphere, and light. In other words, the primary oxidation route for monolayer WS₂ was a photooxidation pathway. In the absence of light, I found that monolayer WS₂ was extremely stable, with no major oxidation visible after 10 months of ambient air exposure. This photooxidation mechanism by which transition metal dichalcogenides oxidise in ambient has eluded the scientific literature since at least 1955 [[258](#)] when oxidation studies began. I will outline below some experiments which should be conducted (or that I would have conducted if time permitted):

- 1) It would be prudent to extend this photo-induced oxidation study to the entire suite of semiconducting transition metal dichalcogenides, especially MoS₂, MoSe₂ and WSe₂.
- 2) The oxidation rate of the reaction should be determined. Since the oxidation in ambient is initiated by photoexcitation, as the S-TMD oxidises, so to the photoluminescent intensity will decrease or ‘quench’ (see [Figure A.2-1](#)) and thus, decrease the rate of oxidation.
- 3) The precise temperature at which monolayer WS₂ (or any other S-TMD) oxidises in ambient atmosphere should be determined, as this metric is of fundamental importance for device fabrication.

The preliminary results I have presented in [Section 8.2](#) have begun to answer some of these questions, and provide a good starting point for further experimentation. Some questions that remain are, “Is it possible to fabricate a WS₂ monolayer with no sulphur vacancies?”, and “Given no sulphur vacancies on the surface, would photooxidation proceed on the basal plane in ambient atmosphere?”.

In [Chapter 5](#), I investigated the physical and electronic structure of Ca-QFSBLG and found that Ca-intercalation was energetically favoured underneath the buffer layer, preferentially forming Ca-QFSBLG (instead of intercalating between the carbon layers or not disrupting the buffer layer bonding). The electronic structure was probed using SECO and comparisons of the experimental C 1s core level lineshape to the theoretical C 1s core level lineshape for highly doped quasi-freestanding bilayer graphene. SECO measurements showed that the work function *decreased* from EMLG, implying n-type doping. Comparisons to the theory of highly doped bilayer graphene also corroborated these results, and showed Ca-QFSBLG likely had a doping of at least 10¹⁴ carriers cm⁻². These findings are important, because

it shows that highly n-type doped graphene can be obtained when the Ca resides entirely underneath the buffer layer, and, that prior works which assumed Ca intercalated only between graphene layers for similar systems are likely erroneous.

In [Section 8.3.1](#) I presented further work on the surface deposition of Ca, which can form hexagonal monolayer/bilayers of Ca on the graphene surface. Whether the orientation of the Ca is affected by the SiC or graphene remains an open question, though a simple experiment was proposed to answer this question.

Furthermore, the fact that the Ca intercalates underneath the buffer layer already motivates further theoretical study into whether Ca-QFSBLG could become superconducting. In [Section 8.3.2](#) it was asked whether previous works which observed superconductivity were measuring the superconductivity of Ca-QFSBLG, or graphene with Ca intercalated between the graphene layers? This is a fundamentally important question, which may lead to the re-interpretation of past experimental and theoretical results.

In [Chapter 6](#), I investigated the physical and electronic structure of Mg-QFSBLG. While this material has not been studied before, I found that Mg-intercalation of EMLG yielded a highly n-type doped, low workfunction and freestanding bilayer graphene, similar to the Ca-QFSBLG case. [Section 8.4](#) sought to expand further upon some of the material in [Chapter 6](#).

In [Section 8.4.1](#), I showed recent density functional theory calculations undertaken by collaborators that were able to determine the Mg:Si ratio as 1:3. To experimentally determine this ratio, further XPS experiments are needed.

Moreover, it was shown ([Appendix C3](#)) that magnesium could not intercalate H-QFSBLG. Although a non-result, I discussed in [Section 8.4.2](#) how such an effect could prove extremely useful, as the discovery of intercalants that do not displace other intercalants that lead to an *opposite* doping induced in the graphene could prove technologically important. It allows the fabrication of n- and p-type junctions at the wafer scale, permitted one can pattern the already intercalated sample (*i.e.* selectively remove intercalants). Possible methods for doing this were explored and continued efforts to further develop these devices and collate a list of compatible intercalant chemistries is desired.

Furthermore, in [Section 8.4.3](#) I presented preliminary results that showed how to increase the magnesium intercalation efficiency of graphene on silicon carbide *via* the patterning of artificial voids in the graphene. This also demonstrated that low density defects could cause remarkable effects on the intercalation speed, and thus, I postulated that the mechanism of Mg-

intercalation is through such defects. These results already prompt utilisation of this technique in device manufacture.

In [Chapter 7](#), I showed for the first time the ambient air oxidation behaviour of Ca-QFSBLG and Mg-QFSBLG. In the case of Ca-QFSBLG, the results of a short-term (30 minutes and 9 hours) and long-term (\approx 1 year) ambient air exposure were shown. It was found that the underlying Ca-silicide of Ca-QFSBLG rapidly oxidises to form $\text{Ca}(\text{OH})_2$ and CaO (most likely from heating $\text{Ca}(\text{OH})_2$). After long-term air exposures, CaCO_3 was formed. In the case of Mg-QFSBLG, short-term (6-hour) ambient air exposures did not significantly oxidise the underlying Mg-silicide. For both Ca-QFSBLG and Mg-QFSBLG, Raman mapping spectroscopy showed that they remained quasi-freestanding, despite reaction with ambient.

In [Section 8.5.1](#), I showed in more detail some of the preliminary results regarding the long-term (\approx 8 months) ambient air oxidation of Mg-QFSBLG. It was found that Mg-QFSBLG likely follows a similar oxidation pathway to Ca-QFSBLG, though in contrast, no significant amounts of MgCO_3 are formed. Although the information in this section is useful, a thorough and systematic experiment is required to find the exact timeframe after which no Mg-silicide exists (as was done with Ca-QFSBLG). Moreover, it was postulated that the oxidation reaction should proceed only with significant amounts of water, so controlled experiments over a range of humidity levels should be undertaken.

Furthermore, [Section 8.5.2](#) discussed an unforeseen technological application of Ca- and Mg-intercalated graphene, in which the sensing medium could be determined and tuned by the intercalant itself. In the case of Mg-QFSBLG and Ca-QFSBLG, the oxidation of the underlying intercalant could be used to sense oxygen, water and/or carbon dioxide by measuring the conductance changes in the graphene over time. Although promising, further development and testing of these types of ‘intercalated graphene gas sensors’ is required. Nonetheless, if realised, these devices could be useful for gas sensing applications in UHV and low earth orbit/outer space environments, and thus, of interest to the broader scientific community.

It is my hope that this dissertation has made it clear that continued efforts toward the research of the ambient air reaction of S-TMDs and intercalated graphene is likely to yield beneficial technological outcomes for the field of 2D materials, as was observed in the case of silicon and the silicon transistor.

And finally, as Lord Kelvin put it:

“Something of sadness must come of failure ; but in the pursuit of science, inborn necessity to make the effort brings with it much of the certaminis gaudia [joyful struggle] – and saves the naturalist from being wholly miserable, perhaps even allows him to be fairly happy, in his daily work.”

And if you have made it this far, I want to thank you for taking the time to read my doctoral thesis. It has been a 4-year long odyssey into the world of experimental physics, finally culminating in the thesis before you. It is my hope that this thesis spurs further work on the topics presented here, while I take a short break before my next scientific endeavour, wherever *and* whatever that may be!

- *J. C. Kotsakidis,*

Melbourne, Australia, 2020.

B

Bibliography

1. Riordan, M. In *The Road to Silicon Was Paved with Germanium*, Silicon Materials Science and Technology: Proceedings of the Eighth International Symposium on Silicon Materials Science and Technology, The Electrochemical Society: 1998; p 134.
2. Chabal, Y. J., *Fundamental Aspects of Silicon Oxidation*. Springer Science & Business Media: 2012; Vol. 46.
3. Novoselov, K. S.; Geim, A. K.; Morozov, S. V.; Jiang, D.; Zhang, Y.; Dubonos, S. V.; Grigorieva, I. V.; Firsov, A. A., Electric Field Effect in Atomically Thin Carbon Films. *Science* **2004**, *306* (5696), 666-669.
4. Novoselov, K.; Jiang, D.; Schedin, F.; Booth, T.; Khotkevich, V.; Morozov, S.; Geim, A., Two-Dimensional Atomic Crystals. *PNAS* **2005**, *102* (30), 10451-10453.
5. Geim, A. K., Nobel Lecture: Random Walk to Graphene. *Rev. Mod. Phys.* **2011**, *83* (3), 851.
6. Joensen, P.; Frindt, R.; Morrison, S. R., Single-Layer MoS₂. *Materials research bulletin* **1986**, *21* (4), 457-461.
7. Mak, K. F.; Lee, C.; Hone, J.; Shan, J.; Heinz, T. F., Atomically Thin MoS₂: A New Direct-Gap Semiconductor. *Phys. Rev. Lett.* **2010**, *105* (13), 136805.
8. Splendiani, A.; Sun, L.; Zhang, Y.; Li, T.; Kim, J.; Chim, C.-Y.; Galli, G.; Wang, F., Emerging Photoluminescence in Monolayer MoS₂. *Nano Lett.* **2010**, *10* (4), 1271-1275.
9. Geim, A. K.; Novoselov, K. S., The Rise of Graphene. *Nat. Mater.* **2007**, *6* (3), 183-191.

10. Zeng, M.; Xiao, Y.; Liu, J.; Yang, K.; Fu, L., Exploring Two-Dimensional Materials Toward the Next-Generation Circuits: from Monomer Design to Assembly Control. *Chem. Rev.* **2018**, *118* (13), 6236-6296.
11. Randviir, E. P.; Brownson, D. A.; Banks, C. E., A Decade of Graphene Research: Production, Applications and Outlook. *Materials Today* **2014**, *17* (9), 426-432.
12. Choi, W.; Choudhary, N.; Han, G. H.; Park, J.; Akinwande, D.; Lee, Y. H., Recent Development of Two-Dimensional Transition Metal Dichalcogenides and Their Applications. *Materials Today* **2017**, *20* (3), 116-130.
13. Koppens, F.; Mueller, T.; Avouris, P.; Ferrari, A.; Vitiello, M.; Polini, M., Photodetectors Based on Graphene, Other Two-Dimensional Materials and Hybrid Systems. *Nat. Nanotechnol.* **2014**, *9* (10), 780.
14. Fiori, G.; Bonaccorso, F.; Iannaccone, G.; Palacios, T.; Neumaier, D.; Seabaugh, A.; Banerjee, S. K.; Colombo, L., Electronics Based on Two-Dimensional Materials. *Nat. Nanotechnol.* **2014**, *9* (10), 768.
15. Choi, W.; Lahiri, I.; Seelaboyina, R.; Kang, Y. S., Synthesis of Graphene and Its Applications: A Review. *Critical Reviews in Solid State and Materials Sciences* **2010**, *35* (1), 52-71.
16. Mak, K. F.; Shan, J., Photonics and Optoelectronics of 2D Semiconductor Transition Metal Dichalcogenides. *Nat. Photonics* **2016**, *10* (4), 216-226.
17. Kotsakidis, J. C.; Zhang, Q.; Vazquez de Parga, A. L.; Currie, M.; Helmerson, K.; Gaskill, D. K.; Fuhrer, M. S., Oxidation of Monolayer WS₂ in Ambient Is a Photoinduced Process. *Nano Lett.* **2019**, *19* (8), 5205-5215.
18. Kanetani, K.; Sugawara, K.; Sato, T.; Shimizu, R.; Iwaya, K.; Hitosugi, T.; Takahashi, T., Ca Intercalated Bilayer Graphene as a Thinnest Limit of Superconducting C₆Ca. *PNAS* **2012**, *109* (48), 19610-19613.
19. Ichinokura, S.; Sugawara, K.; Takayama, A.; Takahashi, T.; Hasegawa, S., Superconducting Calcium-Intercalated Bilayer Graphene. *ACS nano* **2016**, *10* (2), 2761.
20. Bao, W.; Wan, J.; Han, X.; Cai, X.; Zhu, H.; Kim, D.; Ma, D.; Xu, Y.; Munday, J. N.; Drew, H. D.; Fuhrer, M. S.; Hu, L., Approaching the Limits of Transparency and Conductivity in Graphitic Materials Through Lithium Intercalation. *Nat. Commun.* **2014**, *5* (1), 1-9.

21. Roche, B.; Voisin, B.; Jehl, X.; Wacquez, R.; Sanquer, M.; Vinet, M.; Deshpande, V.; Previtali, B., A Tunable, Dual Mode Field-Effect or Single Electron Transistor. *Appl. Phys. Lett.* **2012**, *100* (3), 032107.
22. Atkin, P.; Lau, D.; Zhang, Q.; Zheng, C.; Berean, K.; Field, M.; Ou, J.; Cole, I.; Daeneke, T.; Kalantar-Zadeh, K., Laser Exposure Induced Alteration of WS₂ Monolayers in the Presence of Ambient Moisture. *2D Mater.* **2017**, *5* (1), 015013.
23. McChesney, J. L.; Bostwick, A.; Ohta, T.; Seyller, T.; Horn, K.; González, J.; Rotenberg, E., Extended Van Hove Singularity and Superconducting Instability in Doped Graphene. *Phys. Rev. Lett.* **2010**, *104* (13), 136803.
24. Endo, Y.; Fukaya, Y.; Mochizuki, I.; Takayama, A.; Hyodo, T.; Hasegawa, S., Structure of Superconducting Ca-Intercalated Bilayer Graphene/SiC Studied Using Total-Reflection High-Energy Positron Diffraction. *Carbon* **2019**, *157*, 857-862.
25. Sernelius, B. E., Core-Level Spectra from Bilayer Graphene. *FlatChem* **2017**, *1*, 6-10.
26. Grubišić-Čabo, A.; Kotsakidis, J. C.; Yin, Y.; Tadich, A.; Haldon, M.; Solari, S.; di Bernardo, I.; Daniels, K. M.; Riley, J.; Huwald, E.; Edmonds, M. T.; Myers-Ward, R. L.; Medhekar, N. V.; Gaskill, D. K.; Fuhrer, M. S., Magnesium-Intercalated Graphene on SiC: Highly n-Doped Air-Stable Bilayer Graphene at Extreme Displacement Fields. *arXiv preprint arXiv:2005.02670* **2020**.
27. Wallace, P. R., The Band Theory of Graphite. *Physical Review* **1947**, *71* (9), 622.
28. Koshino, M.; Tsuneya, A., Electronic Properties of Monolayer and Multilayer Graphene. In *Physics of Graphene*, Aoki, H.; Dresselhaus, M. S., Eds. Springer Science & Business Media: 2013.
29. Neto, A. C.; Guinea, F.; Peres, N. M.; Novoselov, K. S.; Geim, A. K., The Electronic Properties of Graphene. *Rev. Mod. Phys.* **2009**, *81* (1), 109.
30. Novoselov, K. S.; Geim, A. K.; Morozov, S. V.; Jiang, D.; Katsnelson, M. I.; Grigorieva, I.; Dubonos, S.; Firsov; AA, Two-Dimensional Gas of Massless Dirac Fermions in Graphene. *nature* **2005**, *438* (7065), 197-200.

31. Ang, Y. S.; Chen, Y.; Tan, C.; Ang, L., Generalized High-Energy Thermionic Electron Injection at Graphene Interface. *Physical Review Applied* **2019**, *12* (1), 014057.
32. Bernal, J. D., The Structure of Graphite. *Proceedings of the Royal Society of London. Series A, Containing Papers of a Mathematical and Physical Character* **1924**, *106* (740), 749-773.
33. Mostaani, E.; Drummond, N.; Fal'Ko, V., Quantum Monte Carlo Calculation of the Binding Energy of Bilayer Graphene. *Phys. Rev. Lett.* **2015**, *115* (11), 115501.
34. Ohta, T.; Bostwick, A.; Seyller, T.; Horn, K.; Rotenberg, E., Controlling the Electronic Structure of Bilayer Graphene. *Science* **2006**, *313* (5789), 951-954.
35. Razado-Colambo, I.; Avila, J.; Vignaud, D.; Godey, S.; Wallart, X.; Woodruff, D.; Asensio, M., Structural Determination of Bilayer Graphene on SiC(0001) Using Synchrotron Radiation Photoelectron Diffraction. *Sci. Rep.* **2018**, *8* (1), 1-10.
36. McCann, E., Asymmetry Gap in the Electronic Band Structure of Bilayer Graphene. *Phys. Rev. B* **2006**, *74* (16), 161403.
37. McCann, E.; Abergel, D. S.; Fal'ko, V. I., The Low Energy Electronic Band Structure of Bilayer Graphene. *The European Physical Journal Special Topics* **2007**, *148* (1), 91-103.
38. McCann, E.; Fal'ko, V. I., Landau-Level Degeneracy and Quantum Hall Effect in a Graphite Bilayer. *Phys. Rev. Lett.* **2006**, *96* (8), 086805.
39. Zou, K.; Hong, X.; Zhu, J., Effective Mass of Electrons and Holes in Bilayer Graphene: Electron-Hole Asymmetry and Electron-Electron Interaction. *Phys. Rev. B* **2011**, *84* (8), 085408.
40. Ohta, T.; Bostwick, A.; McChesney, J. L.; Seyller, T.; Horn, K.; Rotenberg, E., Interlayer Interaction and Electronic Screening in Multilayer Graphene Investigated with Angle-Resolved Photoemission Spectroscopy. *Phys. Rev. Lett.* **2007**, *98* (20), 206802.
41. Wu, X.; Hu, Y.; Ruan, M.; Madiomanana, N. K.; Hankinson, J.; Sprinkle, M.; Berger, C.; De Heer, W. A., Half Integer Quantum Hall Effect in High Mobility Single Layer Epitaxial Graphene. *Appl. Phys. Lett.* **2009**, *95* (22), 223108.

42. Hwang, C.; Siegel, D. A.; Mo, S.-K.; Regan, W.; Ismach, A.; Zhang, Y.; Zettl, A.; Lanzara, A., Fermi Velocity Engineering in Graphene by Substrate Modification. *Sci. Rep.* **2012**, *2*, 590.
43. Moreau, E.; Godey, S.; Wallart, X.; Razado-Colambo, I.; Avila, J.; Asensio, M.-C.; Vignaud, D., High-Resolution Angle-Resolved Photoemission Spectroscopy Study of Monolayer and Bilayer Graphene on the C-face of SiC. *Phys. Rev. B* **2013**, *88* (7), 075406.
44. Nilsson, J.; Neto, A. C.; Peres, N.; Guinea, F., Electron-Electron Interactions and the Phase Diagram of a Graphene Bilayer. *Phys. Rev. B* **2006**, *73* (21), 214418.
45. Li, Z.; Henriksen, E.; Jiang, Z.; Hao, Z.; Martin, M. C.; Kim, P.; Stormer, H.; Basov, D. N., Band Structure Asymmetry of Bilayer Graphene Revealed by Infrared Spectroscopy. *Phys. Rev. Lett.* **2009**, *102* (3), 037403.
46. Shur, M.; Rumenantsev, S. L.; Levinstein, M. E., *SiC Materials and Devices*. World Scientific: 2006; Vol. 1.
47. Cheung, R., *Silicon Carbide Microelectromechanical Systems for Harsh Environments*. World Scientific: 2006.
48. Järrendahl, K.; Davis, R. F., Chapter 1 Materials Properties and Characterization of SiC. In *Semiconductors and Semimetals*, Soo Park, Y., Ed. Elsevier: 1998; Vol. 52, pp 1-20.
49. Emery, J. D.; Wheeler, V. D.; Johns, J. E.; McBriarty, M. E.; Detlefs, B.; Hersam, M. C.; Kurt Gaskill, D.; Bedzyk, M. J., Structural Consequences of Hydrogen Intercalation of Epitaxial Graphene on SiC (0001). *Appl. Phys. Lett.* **2014**, *105* (16), 161602.
50. Van Bommel, A.; Crombeen, J.; Van Tooren, A., LEED and Auger Electron Observations of the SiC(0001) Surface. *Surf. Sci.* **1975**, *48* (2), 463-472.
51. Charrier, A.; Coati, A.; Argunova, T.; Thibaudeau, F.; Garreau, Y.; Pinchaux, R.; Forbeaux, I.; Debever, J.-M.; Sauvage-Simkin, M.; Themlin, J.-M., Solid-State Decomposition of Silicon Carbide for Growing Ultra-Thin Heteroepitaxial Graphite Films. *J. Appl. Phys.* **2002**, *92* (5), 2479-2484.
52. Berger, C.; Song, Z.; Li, T.; Li, X.; Ogbazghi, A. Y.; Feng, R.; Dai, Z.; Marchenkov, A. N.; Conrad, E. H.; First, P. N.; de Heer, W. A., Ultrathin epitaxial graphite: 2D electron gas properties and a route toward graphene-based nanoelectronics. *J. Phys. Chem. B* **2004**, *108* (52), 19912-19916.

53. Emtsev, K.; Speck, F.; Seyller, T.; Ley, L.; Riley, J. D., Interaction, Growth, and Ordering of Epitaxial Graphene on SiC(0001) Surfaces: A Comparative Photoelectron Spectroscopy Study. *Phys. Rev. B* **2008**, *77* (15), 155303.
54. Gaskill, D. K.; Nyakiti, L., Formation of Epitaxial Graphene. In *Graphene Nanoelectronics: From Materials to Circuits* Murali, R., Ed. Springer-Verlag New York New York **2012**.
55. Seyller, T., Epitaxial Graphene on SiC(0001). In *Graphene Nanoelectronics: Metrology, Synthesis, Properties and Applications*, Raza, H., Ed. Springer Science & Business Media: Berlin Heidelberg, **2012**.
56. Forbeaux, I.; Themlin, J.-M.; Debever, J.-M., Heteroepitaxial Graphite on 6H-SiC(0001): Interface Formation Through Conduction-Band Electronic Structure. *Phys. Rev. B* **1998**, *58* (24), 16396.
57. Lilov, S., Thermodynamic Analysis of the Gas Phase at the Dissociative Evaporation of Silicon Carbide. *Comput. Mater. Sci.* **1993**, *1* (4), 363-368.
58. Varchon, F.; Mallet, P.; Veuillet, J.-Y.; Magaud, L., Ripples in Epitaxial Graphene on the Si-Terminated SiC (0001) Surface. *Phys. Rev. B* **2008**, *77* (23), 235412.
59. de Lima, L. H.; Handschak, D.; Schönbohm, F.; Landers, R.; Westphal, C.; de Siervo, A., The Atomic Structure of a Bare Buffer Layer on SiC(0001) Chemically Resolved. *Chemical communications* **2014**, *50* (88), 13571-13574.
60. Riedl, C.; Coletti, C.; Starke, U., Structural and Electronic Properties of Epitaxial Graphene on SiC(0001): A Review of Growth, Characterization, Transfer Doping and Hydrogen Intercalation. *J. Phys. D: Appl. Phys.* **2010**, *43* (37), 374009.
61. Goler, S.; Coletti, C.; Piazza, V.; Pingue, P.; Colangelo, F.; Pellegrini, V.; Emtsev, K. V.; Forti, S.; Starke, U.; Beltram, F., Revealing the Atomic Structure of the Buffer Layer Between SiC (0001) and Epitaxial Graphene. *Carbon* **2013**, *51*, 249-254.
62. Qi, Y.; Rhim, S.; Sun, G.; Weinert, M.; Li, L., Epitaxial Graphene on SiC(0001): More than just Honeycombs. *Phys. Rev. Lett.* **2010**, *105* (8), 085502.
63. Cavallucci, T.; Tozzini, V., Intrinsic Structural and Electronic Properties of the Buffer Layer on Silicon Carbide Unraveled by Density Functional Theory. *Sci. Rep.* **2018**, *8* (1), 1-10.

64. Varchon, F.; Feng, R.; Hass, J.; Li, X.; Nguyen, B. N.; Naud, C.; Mallet, P.; Veuillen, J.-Y.; Berger, C.; Conrad, E. H., Electronic Structure of Epitaxial Graphene Layers on SiC: Effect of the Substrate. *Phys. Rev. Lett.* **2007**, *99* (12), 126805.
65. Mattausch, A.; Pankratov, O., Ab initio Study of Graphene on SiC. *Phys. Rev. Lett.* **2007**, *99* (7), 076802.
66. Conrad, M.; Rault, J.; Utsumi, Y.; Garreau, Y.; Vlad, A.; Coati, A.; Rueff, J.-P.; Miceli, P.; Conrad, E., Structure and Evolution of Semiconducting Buffer Graphene Grown on SiC(0001). *Phys. Rev. B* **2017**, *96* (19), 195304.
67. Nevius, M.; Conrad, M.; Wang, F.; Celis, A.; Nair, M.; Taleb-Ibrahimi, A.; Tejeda, A.; Conrad, E., Semiconducting Graphene from Highly Ordered Substrate Interactions. *Phys. Rev. Lett.* **2015**, *115* (13), 136802.
68. Nair, M.; Palacio, I.; Celis, A.; Zobelli, A.; Gloter, A.; Kubsky, S.; Turmaud, J.-P.; Conrad, M.; Berger, C.; de Heer, W., Band Gap Opening Induced by the Structural Periodicity in Epitaxial Graphene Buffer Layer. *Nano Lett.* **2017**, *17* (4), 2681-2689.
69. Mammadov, S.; Ristein, J.; Koch, R. J.; Ostler, M.; Raidel, C.; Wanke, M.; Vasiliauskas, R.; Yakimova, R.; Seyller, T., Polarization Doping of Graphene on Silicon Carbide. *2D Mater.* **2014**, *1* (3), 035003.
70. Virojanadara, C.; Watcharinyanon, S.; Zakharov, A.; Johansson, L. I., Epitaxial Graphene on 6H-SiC and Li Intercalation. *Phys. Rev. B* **2010**, *82* (20), 205402.
71. Xia, C.; Johansson, L. I.; Zakharov, A.; Hultman, L.; Virojanadara, C., Effects of Al on Epitaxial Graphene Grown on 6H-SiC (0001). *Mater. Res. Express* **2014**, *1* (1), 015606.
72. Xia, C.; Johansson, L. I.; Niu, Y.; Zakharov, A. A.; Janzén, E.; Virojanadara, C., High Thermal Stability Quasi-Free-Standing Bilayer Graphene Formed on 4H-SiC(0 0 0 1) via Platinum Intercalation. *Carbon* **2014**, *79*, 631-635.
73. Jobst, J.; Waldmann, D.; Speck, F.; Hirner, R.; Maude, D. K.; Seyller, T.; Weber, H. B., Quantum Oscillations and Quantum Hall Effect in Epitaxial Graphene. *Phys. Rev. B* **2010**, *81* (19), 195434.
74. Bolotin, K. I.; Sikes, K.; Jiang, Z.; Klima, M.; Fudenberg, G.; Hone, J.; Kim, P.; Stormer, H., Ultrahigh Electron Mobility in Suspended Graphene. *Solid State Commun.* **2008**, *146* (9), 351-355.

75. Speck, F.; Jobst, J.; Fromm, F.; Ostler, M.; Waldmann, D.; Hundhausen, M.; Weber, H. B.; Seyller, T., The Quasi-Free-Standing Nature of Graphene on H-Saturated SiC(0001). *Appl. Phys. Lett.* **2011**, *99* (12), 122106.
76. Virojanadara, C.; Syväjarvi, M.; Yakimova, R.; Johansson, L.; Zakharov, A.; Balasubramanian, T., Homogeneous Large-Area Graphene Layer Growth on 6H-SiC(0001). *Phys. Rev. B* **2008**, *78* (24), 245403.
77. Emtsev, K. V.; Bostwick, A.; Horn, K.; Jobst, J.; Kellogg, G. L.; Ley, L.; McChesney, J. L.; Ohta, T.; Reshanov, S. A.; Röhrl, J., Towards Wafer-Size Graphene Layers by Atmospheric Pressure Graphitization of Silicon Carbide. *Nat. Mater.* **2009**, *8* (3), 203-207.
78. Lew, K. K.; VanMil, B. L.; Myers-Ward, R. L.; Holm, R. T.; Eddy, C. R.; Gaskill, D. K., Etching of 4° and 8° 4H-SiC Using Various Hydrogen-Propane Mixtures in a Commercial Hot-Wall CVD Reactor. *Materials Science Forum* **2007**, *556*, 513-516.
79. VanMil, B. L.; Lew, K.-K.; Myers-Ward, R. L.; Holm, R. T.; Gaskill, D. K.; Eddy, C. R. In *Etch Rates for Si-Face 4H-SiC Using H₂ and a C₃H₈ Partial Pressure*, 2007 International Semiconductor Device Research Symposium, IEEE: 2007; pp 1-2.
80. VanMil, B. L.; Myers-Ward, R. L.; Tedesco, J. L.; Eddy, C. R.; Jernigan, G. G.; Culbertson, J. C.; Campbell, P. M.; McCrate, J. M.; Kitt, S. A.; Gaskill, D. K., Graphene Formation on SiC Substrates. *Materials Science Forum* **2009**, *615*, 211-214.
81. Tedesco, J. L.; VanMil, B.; Myers-Ward, R. L.; Culbertson, J.; Jernigan, G.; Campbell, P.; McCrate, J. M.; Kitt, S. A.; Eddy Jr, C.; Gaskill, D. K., Improvement of Morphology and Free Carrier Mobility Through Argon-Assisted Growth of Epitaxial Graphene on Silicon Carbide. *ECS Transactions* **2009**, *19* (5), 137.
82. Riedl, C.; Coletti, C.; Iwasaki, T.; Zakharov, A.; Starke, U., Quasi-Free-Standing Epitaxial Graphene on SiC Obtained by Hydrogen Intercalation. *Phys. Rev. Lett.* **2009**, *103* (24), 246804.
83. Virojanadara, C.; Yakimova, R.; Zakharov, A.; Johansson, L., Large Homogeneous Mono-/Bi-Layer Graphene on 6H-SiC(0001) and Buffer Layer Elimination. *J. Phys. D: Appl. Phys.* **2010**, *43* (37), 374010.
84. Ostler, M.; Deretzis, I.; Mammadov, S.; Giannazzo, F.; Nicotra, G.; Spinella, C.; Seyller, T.; La Magna, A., Direct Growth of Quasi-Free-Standing

Epitaxial Graphene on Nonpolar SiC Surfaces. *Phys. Rev. B* **2013**, *88* (8), 085408.

85. Daniels, K. M.; Jadidi, M. M.; Sushkov, A. B.; Nath, A.; Boyd, A. K.; Sridhara, K.; Drew, H. D.; Murphy, T. E.; Myers-Ward, R. L.; Gaskill, D. K., Narrow Plasmon Resonances Enabled by Quasi-Freestanding Bilayer Epitaxial Graphene. *2D Mater.* **2017**, *4* (2), 025034.
86. Bae, S.-H.; Zhou, X.; Kim, S.; Lee, Y. S.; Cruz, S. S.; Kim, Y.; Hannon, J. B.; Yang, Y.; Sadana, D. K.; Ross, F. M.; Park, H.; Kim, J., Unveiling the Carrier Transport Mechanism in Epitaxial Graphene for Forming Wafer-Scale, Single-Domain Graphene. *PNAS* **2017**, *114* (16), 4082-4086.
87. Wilson, J.; Yoffe, A., The Transition Metal Dichalcogenides Discussion and Interpretation of the Observed Optical, Electrical and Structural Properties. *Adv. Phys.* **1969**, *18* (73), 193-335.
88. Kolobov, A. V.; Tominaga, J., *Two-Dimensional Transition-Metal Dichalcogenides*. Springer: 2016; Vol. 239.
89. Verzhbitskiy, I.; Eda, G., Chalcogenide Nanosheets: Optical Signatures of Many-Body Effects and Electronic Band Structure. In *Inorganic Nanosheets and Nanosheet-Based Materials*, Nakato, T.; Kawamata, J.; Takagi, S., Eds. Springer: 2017.
90. Kam, K.; Parkinson, B., Detailed Photocurrent Spectroscopy of the Semiconducting Group VIB Transition Metal Dichalcogenides. *J. Phys. Chem.* **1982**, *86* (4), 463-467.
91. Baglio, J. A.; Calabrese, G. S.; Kamieniecki, E.; Kershaw, R.; Kubiak, C. P.; Ricco, A. J.; Wold, A.; Wrighton, M. S.; Zoski, G. D., Characterization of n-Type Semiconducting Tungsten Disulfide Photoanodes in Aqueous and Nonaqueous Electrolyte Solutions: Photo-Oxidation of Halides with High Efficiency. *J. Electrochem. Soc.* **1982**, *129* (7), 1461.
92. Kuc, A.; Zibouche, N.; Heine, T., Influence of Quantum Confinement on the Electronic Structure of the Transition Metal Sulfide TS₂. *Phys. Rev. B* **2011**, *83* (24), 245213.
93. Roldán, R.; Silva-Guillén, J. A.; López-Sancho, M. P.; Guinea, F.; Cappelluti, E.; Ordejón, P., Electronic Properties of Single-Layer and Multilayer Transition Metal Dichalcogenides MX₂ (M= Mo, W and X= S, Se). *Ann. Phys.* **2014**, *526* (9-10), 347-357.

94. Zhao, W.; Ribeiro, R. M.; Toh, M.; Carvalho, A.; Kloc, C.; Castro Neto, A.; Eda, G., Origin of Indirect Optical Transitions in Few-Layer MoS₂, WS₂, and WSe₂. *Nano Lett.* **2013**, *13* (11), 5627-5634.
95. Zhao, W.; Ribeiro, R. M.; Eda, G., Electronic Structure and Optical Signatures of Semiconducting Transition Metal Dichalcogenide Nanosheets. *Acc. Chem. Res.* **2015**, *48* (1), 91-99.
96. Yoffe, A., Low-Dimensional Systems: Quantum Size Effects and Electronic Properties of Semiconductor Microcrystallites (Zero-Dimensional Systems) and Some Quasi-Two-Dimensional Systems. *Adv. Phys.* **2002**, *51* (2), 799-890.
97. Liu, G.-B.; Xiao, D.; Yao, Y.; Xu, X.; Yao, W., Electronic Structures and Theoretical Modelling of Two-Dimensional Group-VIB Transition Metal Dichalcogenides. *Chem. Soc. Rev.* **2015**, *44* (9), 2643-2663.
98. Schutte, W.; De Boer, J.; Jellinek, F., Crystal Structures of Tungsten Disulfide and Diselenide. *Journal of Solid State Chemistry* **1987**, *70* (2), 207-209.
99. Wang, Q. H.; Kalantar-Zadeh, K.; Kis, A.; Coleman, J. N.; Strano, M. S., Electronics and Optoelectronics of Two-Dimensional Transition Metal Dichalcogenides. *Nat. Nanotechnol.* **2012**, *7* (11), 699-712.
100. Schmidt, H.; Giustiniano, F.; Eda, G., Electronic Transport Properties of Transition Metal Dichalcogenide Field-Effect Devices: Surface and Interface Effects. *Chem. Soc. Rev.* **2015**, *44* (21), 7715-7736.
101. Gutiérrez, H. R.; Perea-López, N.; Elías, A. L.; Berkdemir, A.; Wang, B.; Lv, R.; López-Urías, F.; Crespi, V. H.; Terrones, H.; Terrones, M., Extraordinary Room-Temperature Photoluminescence in Triangular WS₂ Monolayers. *Nano Lett.* **2012**, *13* (8), 3447-3454.
102. Bromley, R.; Murray, R.; Yoffe, A., The Band Structures of Some Transition Metal Dichalcogenides. III. Group VIA: Trigonal Prism Materials. *Journal of Physics C: Solid State Physics* **1972**, *5* (7), 759.
103. Hanbicki, A.; Currie, M.; Kiouseoglou, G.; Friedman, A.; Jonker, B., Measurement of High Exciton Binding Energy in the Monolayer Transition-Metal Dichalcogenides WS₂ and WSe₂. *Solid State Commun.* **2015**, *203*, 16-20.
104. Carvalho, A.; Ribeiro, R.; Neto, A. C., Band Nesting and the Optical Response of Two-Dimensional Semiconducting Transition Metal Dichalcogenides. *Phys. Rev. B* **2013**, *88* (11), 115205.

105. Duke, C., The Birth and Evolution of Surface Science: Child of the Union of Science and Technology. *PNAS* **2003**, *100* (7), 3858-3864.
106. Oura, K.; Lifshits, V.; Saranin, A.; Zotov, A.; Katayama, M., *Surface Science: An Introduction*. Springer-Verlag Berlin Heidelberg: 2013.
107. Young, R. D., Surface Microtopography. *PhT* **1971**, *24* (11), 42.
108. Young, R.; Ward, J.; Scire, F., The Topografiner: An Instrument for Measuring Surface Microtopography. *Rev. Sci. Instrum.* **1972**, *43* (7), 999-1011.
109. Lide, D. R., *A Century of Excellence in Measurements, Standards, and Technology*. CRC Press: 2001.
110. Binnig, G.; Rohrer, H.; Gerber, C.; Weibel, E., Tunneling Through a Controllable Vacuum Gap. *Appl. Phys. Lett.* **1982**, *40* (2), 178-180.
111. Binnig, G.; Rohrer, H., Scanning Tunneling Microscopy—From Birth to Adolescence. *Rev. Mod. Phys.* **1987**, *59* (3), 615.
112. Chen, C. J., *Introduction to Scanning Tunneling Microscopy*. Oxford University Press on Demand: 1993; Vol. 4.
113. Bransden, B. H.; Joachain, C. J., *Quantum Mechanics*. 2nd Edition ed.; Pearson Education: 2000.
114. Bardeen, J., Tunnelling from a Many-Particle Point of View. *Phys. Rev. Lett.* **1961**, *6* (2), 57.
115. Tersoff, J.; Hamann, D. R., Theory of the Scanning Tunneling Microscope. *Phys. Rev. B* **1985**, *31* (2), 805.
116. Gugel, D.; Niesner, D.; Eickhoff, C.; Wagner, S.; Weinelt, M.; Fauster, T., Two-Photon Photoemission from Image-Potential States of Epitaxial Graphene. *2D Mater.* **2015**, *2* (4), 045001.
117. Voigtländer, B., *Scanning Probe Microscopy: Atomic Force Microscopy and Scanning Tunneling Microscopy*. Springer: 2015.
118. Meyer, E.; Hug, H. J.; Bennewitz, R., *Scanning Probe Microscopy: The Lab on a Tip*. Springer Science & Business Media: 2003.

119. Farnsworth, H.; Schlier, R.; George, T.; Burger, R., Ion Bombardment-Cleaning of Germanium and Titanium as Determined by Low-Energy Electron Diffraction. *J. Appl. Phys.* **1955**, *26* (2), 252-253.
120. Pan, S.; Hudson, E. W.; Davis, J., ^3He Refrigerator Based Very Low Temperature Scanning Tunneling Microscope. *Rev. Sci. Instrum.* **1999**, *70* (2), 1459-1463.
121. Binnig, G.; Quate, C. F.; Gerber, C., Atomic Force Microscope. *Phys. Rev. Lett.* **1986**, *56* (9), 930.
122. Binnig, G.; Gerber, C.; Stoll, E.; Albrecht, T.; Quate, C., Atomic Resolution with Atomic Force Microscope. *EPL (Europhysics Letters)* **1987**, *3* (12), 1281.
123. Johnson, D.; Hilal, N.; Bowen, W. R., Basic Principles of Atomic Force Microscopy. In *Atomic force microscopy in process engineering*, Elsevier Ltd.: 2009; pp 1-30.
124. Rius, G.; Matsui, S.; Tanemura, M.; Lorenzoni, M.; Perez-Murano, F. In *Properties and Applications of Carbon Nanofibers for Atomic Force Microscopy*, 10th IEEE International Conference on Nano/Micro Engineered and Molecular Systems, IEEE: 2015; pp 571-574.
125. Lennard-Jones, J. E., On the Determination of Molecular Fields. II. From the Equation of State of Gas. *Proc. Roy. Soc. A* **1924**, *106*, 463-477.
126. Eaton, P.; West, P., *Atomic Force Microscopy*. Oxford University Press: 2010.
127. García, R.; Pérez, R., Dynamic Atomic Force Microscopy Methods. *Surface science reports* **2002**, *47* (6-8), 197-301.
128. Hertz, H., Ueber einen Einfluss des Ultravioletten Lichtes auf die Electrische Entladung. *Ann. Phys.* **1887**, *267* (8), 983-1000.
129. Lenard, P., Ueber die Lichtelektrische Wirkung. *Ann. Phys.* **1902**, *313* (5), 149-198.
130. Einstein, A., Über einem die Erzeugung und Verwandlung des Lichtes betreffenden heuristischen Gesichtspunkt. *Ann. Phys.* **1905**, *4*.
131. Nobel Media AB The Nobel Prize in Physics 1921. <https://www.nobelprize.org/prizes/physics/1921/summary/> (accessed 16/8/2020).

132. Planck, M., Ueber das Gesetz der Energieverteilung im Normalspectrum. *Ann. Phys.* **1901**, 309, 553.
133. Siegbahn, K.; Nordling, C.; Fahlman, A.; Nordberg, R.; Hamrin, K.; Hedman, J.; Johansson, G.; Bergmark, T.; Karlsson, S.; Lindgren, I.; Lindburg, B., ESCA. Atomic, Molecular and Solid State Structure Studied by Means of Electron Spectroscopy. . *Nova Acta Regiae Societatis Scientiarum Upsaliensis* **1967**, 20 (4).
134. Thomas, J., 1981 Nobel Prizes in Physics Kai Siegbahn. *Europhysics News* **1982**, 13 (2), 5-5.
135. Van der Heide, P., *X-ray Photoelectron Spectroscopy: An Introduction to Principles and Practices*. John Wiley & Sons: 2011.
136. Kumar, C. S., *Surface Science Tools for Nanomaterials Characterization*. Springer: 2015.
137. Helander, M.; Greiner, M.; Wang, Z.; Lu, Z., Pitfalls in Measuring Work Function Using Photoelectron Spectroscopy. *Appl. Surf. Sci.* **2010**, 256 (8), 2602-2605.
138. Hofmann, S., *Auger-and X-ray Photoelectron Spectroscopy in Materials Science: A User-Oriented Guide*. Springer Science & Business Media: Berlin Heidelberg 2012; Vol. 49.
139. Powell, C. J.; Jablonski, A., Progress in Quantitative Surface Analysis by X-ray Photoelectron Spectroscopy: Current Status and Perspectives. *J. Electron Spectrosc. Relat. Phenom.* **2010**, 178, 331-346.
140. Reilman, R. F.; Msezane, A.; Manson, S. T., Relative Intensities in Photoelectron Spectroscopy of Atoms and Molecules. *J. Electron Spectrosc. Relat. Phenom.* **1976**, 8 (5), 389-394.
141. Wagner, C.; Davis, L.; Zeller, M.; Taylor, J.; Raymond, R.; Gale, L., Empirical Atomic Sensitivity Factors for Quantitative Analysis by Electron Spectroscopy for Chemical Analysis. *Surf. Interface Anal.* **1981**, 3 (5), 211-225.
142. Seah, M. P.; Dench, W., Quantitative Electron Spectroscopy of Surfaces: A Standard Data Base for Electron Inelastic Mean Free Paths in Solids. *Surf. Interface Anal.* **1979**, 1 (1), 2-11.
143. Yeh, J.; Lindau, I., Atomic Subshell Photoionization Cross Sections and Asymmetry Parameters: $1 \leq Z \leq 103$. *At. Data Nucl. Data Tables* **1985**, 32 (1), 1-155.

144. Schultz, T.; Lenz, T.; Kotadiya, N.; Heimel, G.; Glasser, G.; Berger, R.; Blom, P. W.; Amsalem, P.; de Leeuw, D. M.; Koch, N., Reliable Work Function Determination of Multicomponent Surfaces and Interfaces: The Role of Electrostatic Potentials in Ultraviolet Photoelectron Spectroscopy. *Adv. Mater. Interfaces* **2017**, *4* (19), 1700324.
145. Mårtensson, N., 3 - ESCA. In *Treatise on Materials Science & Technology*, Tu, K. N.; Rosenberg, R., Eds. Elsevier: 1988; Vol. 27, pp 65-109.
146. Hüfner, S., *Photoelectron Spectroscopy: Principles and Applications*. Springer-Verlag Berlin Heidelberg: Heidelberg 2013.
147. Raether, H., Solid State Excitations by Electrons. In *Springer Tracts in Modern Physics, Volume 38*, Springer: 1965; pp 84-157.
148. Wertheim, G.; Citrin, P., Fermi Surface Excitations in X-Ray Photoemission Line Shapes from Metals. In *Photoemission in solids I*, Springer: 1978; pp 197-236.
149. Mahan, G., Excitons in Metals: Infinite Hole Mass. *Physical Review* **1967**, *163* (3), 612.
150. Anderson, P. W., Infrared Catastrophe in Fermi Gases with Local Scattering Potentials. *Phys. Rev. Lett.* **1967**, *18* (24), 1049.
151. Nozières, P.; De Dominicis, C., Singularities in the X-ray Absorption and Emission of Metals. III. One-Body Theory Exact Solution. *Physical Review* **1969**, *178* (3), 1097.
152. Decleva, P.; Fronzoni, G.; Kivimäki, A.; Ruiz, J. Á.; Svensson, S., Shake-Up Transitions in S 2p, S 2s and F 1s Photoionization of the SF₆ Molecule. *Journal of Physics B: Atomic, Molecular and Optical Physics* **2009**, *42* (5), 055102.
153. Shirley, D. A., High-Resolution X-Ray Photoemission Spectrum of the Valence Bands of Gold. *Phys. Rev. B* **1972**, *5* (12), 4709.
154. Végh, J., The Shirley Background Revised. *J. Electron Spectrosc. Relat. Phenom.* **2006**, *151* (3), 159-164.
155. Ratner, B. D.; Castner, D. G., Electron Spectroscopy for Chemical Analysis. In *Surface Analysis: The principal Techniques*, 2nd ed.; Vickerman, J. C.; Gilmore, I. S., Eds. 2009.

156. Watts, J. F.; Wolstenholme, J., *An Introduction to Surface Analysis by XPS and AES*. 2nd ed.; John Wiley & Sons 2020.
157. Doniach, S.; Šunjić, M., Many-Electron Singularity in X-ray Photoemission and X-ray Line Spectra from Metals. *Journal of Physics C: Solid State Physics* **1970**, *3* (2), 285.
158. Hüfner, S.; Wertheim, G., Core-Line Asymmetries in the X-Ray-Photoemission Spectra of Metals. *Phys. Rev. B* **1975**, *11* (2), 678.
159. Cowie, B.; Tadich, A.; Thomsen, L., The Current Performance of the Wide Range (90–2500 eV) Soft X-ray Beamline at the Australian Synchrotron. *AIP Conference Proceedings* **2010**, *1234* (1), 307–310.
160. Philippe, B.; Dedryvère, R. m.; Allouche, J.; Lindgren, F.; Gorgoi, M.; Rensmo, H. k.; Gonbeau, D.; Edström, K., Nanosilicon Electrodes for Lithium-Ion Batteries: Interfacial Mechanisms Studied by Hard and Soft X-ray Photoelectron Spectroscopy. *Chem. Mater.* **2012**, *24* (6), 1107–1115.
161. Davisson, C.; Germer, L. H., The Scattering of Electrons by a Single Crystal of Nickel. *Nature* **1927**, *119* (2998), 558–560.
162. Thomson, G. P.; Reid, A., Diffraction of Cathode Rays by a Thin Film. *Nature* **1927**, *119* (3007), 890–890.
163. De Broglie, L., Waves and Quanta. *Nature* **1923**, *112* (2815), 540–540.
164. Van Hove, M. A.; Weinberg, W. H.; Chan, C.-M., *Low-Energy Electron Diffraction: Experiment, Theory and Surface Structure Determination*. Springer Science & Business Media: 2012; Vol. 6.
165. De Broglie, L., The Wave Nature of the Electron. *Nobel lecture* **1929**, *12*, 244–256.
166. O'Connor, D. J.; Sexton, B. A.; Smart, R. S., *Surface Analysis Methods in Materials Science*. Springer Science & Business Media: 2013; Vol. 23.
167. Wehnelt, A., X. On the Discharge of Negative Ions by Glowing Metallic Oxides, and Allied Phenomena. *The London, Edinburgh, and Dublin Philosophical Magazine and Journal of Science* **1905**, *10* (55), 80–90.
168. Gaertner, G.; Den Engelsen, D., Hundred Years Anniversary of the Oxide Cathode—A Historical Review. *Appl. Surf. Sci.* **2005**, *251* (1–4), 24–30.

169. Wood, E. A., Vocabulary of Surface Crystallography. *J. Appl. Phys.* **1964**, *35* (4), 1306-1312.
170. Starke, U.; Schardt, J.; Bernhardt, J.; Franke, M.; Heinz, K., Stacking Transformation from Hexagonal to Cubic SiC Induced by Surface Reconstruction: A Seed for Heterostructure Growth. *Phys. Rev. Lett.* **1999**, *82* (10), 2107.
171. Starke, U.; Franke, M.; Bernhardt, J.; Schardt, J.; Reuter, K.; Heinz, K. In *Large Unit Cell Superstructures on Hexagonal SiC-Sufaces Studied by LEED, AES and STM*, Materials Science Forum, Trans Tech Publ: 1998; pp 321-326.
172. Riedl, C.; Starke, U.; Bernhardt, J.; Franke, M.; Heinz, K., Structural Properties of the Graphene-SiC(0001) Interface as a Key for the Preparation of Homogeneous Large-Terrace Graphene Surfaces. *Phys. Rev. B* **2007**, *76* (24), 245406.
173. Jones, A. C.; Hitchman, M. L., *Chemical Vapour Deposition: Precursors, Processes and Applications*. Royal society of chemistry: 2009.
174. Park, J.-H.; Sudarshan, T., *Chemical Vapor Deposition*. ASM International: 2001; Vol. 2.
175. Xu, Y.; Yan, X.-T., *Chemical Vapour Deposition: An Integrated Engineering Design for Advanced Materials*. Springer Science & Business Media: 2010.
176. Dobrovinskaya, E. R.; Lytvynov, L. A.; Pishchik, V., *Sapphire: Material, Manufacturing, Applications*. Springer Science & Business Media: 2009.
177. Cong, C.; Shang, J.; Wu, X.; Cao, B.; Peimyoo, N.; Qiu, C.; Sun, L.; Yu, T., Synthesis and Optical Properties of Large-Area Single-Crystalline 2D Semiconductor WS₂ Monolayer from Chemical Vapor Deposition. *Adv. Opt. Mater.* **2014**, *2* (2), 131-136.
178. Raman, C. V.; Krishnan, K. S., A New Type of Secondary Radiation. *Nature* **1928**, *121* (3048), 501-502.
179. Cardona, M.; Peter, Y. Y., *Fundamentals of Semiconductors*. Springer: 2005.
180. Smith, E.; Dent, G., *Modern Raman Spectroscopy: A Practical Approach*. John Wiley & Sons: 2019.

181. Ferrari, A. C.; Basko, D. M., Raman Spectroscopy as a Versatile Tool for Studying the Properties of Graphene. *Nat. Nanotechnol.* **2013**, *8* (4), 235.
182. Ferrari, A. C.; Robertson, J., Interpretation of Raman Spectra of Disordered and Amorphous Carbon. *Phys. Rev. B* **2000**, *61* (20), 14095.
183. Tuinstra, F.; Koenig, J. L., Raman Spectrum of Graphite. *J. Chem. Phys.* **1970**, *53* (3), 1126-1130.
184. Wu, J.-B.; Lin, M.-L.; Tan, P.-H., Raman Spectroscopy of Monolayer and Multilayer Graphenes. In *Raman Spectroscopy of Two-Dimensional Materials*, Tan, P.-H., Ed. Springer: 2018; Vol. 276.
185. Malard, L.; Pimenta, M. A.; Dresselhaus, G.; Dresselhaus, M., Raman Spectroscopy in Graphene. *Physics reports* **2009**, *473* (5-6), 51-87.
186. Röhrl, J.; Hundhausen, M.; Emtsev, K.; Seyller, T.; Graupner, R.; Ley, L., Raman Spectra of Epitaxial Graphene on SiC(0001). *Appl. Phys. Lett.* **2008**, *92* (20), 201918.
187. Patane, A.; Balkan, N., *Semiconductor Research: Experimental Techniques*. Springer-Verlag Berlin Heidelberg: 2012; Vol. 150.
188. Chernikov, A.; Berkelbach, T. C.; Hill, H. M.; Rigosi, A.; Li, Y.; Aslan, O. B.; Reichman, D. R.; Hybertsen, M. S.; Heinz, T. F., Exciton Binding Energy and Nonhydrogenic Rydberg Series in Monolayer WS₂. *Phys. Rev. Lett.* **2014**, *113* (7), 076802.
189. Mak, K. F.; He, K.; Lee, C.; Lee, G. H.; Hone, J.; Heinz, T. F.; Shan, J., Tightly Bound Trions in Monolayer MoS₂. *Nat. Mater.* **2013**, *12* (3), 207-211.
190. Arora, A.; Deilmann, T.; Reichenauer, T.; Kern, J.; de Vasconcellos, S. M.; Rohlfing, M.; Bratschitsch, R., Excited-State Trions in Monolayer WS₂. *Phys. Rev. Lett.* **2019**, *123* (16), 167401.
191. Kheng, K.; Cox, R.; d'Aubigné, M. Y.; Bassani, F.; Saminadayar, K.; Tatarenko, S., Observation of Negatively Charged Excitons X⁻ in Semiconductor Quantum Wells. *Phys. Rev. Lett.* **1993**, *71* (11), 1752.
192. Finkelstein, G.; Shtrikman, H.; Bar-Joseph, I., Optical Spectroscopy of a Two-Dimensional Electron Gas Near the Metal-Insulator Transition. *Phys. Rev. Lett.* **1995**, *74* (6), 976.
193. Koperski, M.; Molas, M. R.; Arora, A.; Nogajewski, K.; Slobodeniu, A. O.; Faugeras, C.; Potemski, M., Optical Properties of Atomically Thin

Transition Metal Dichalcogenides: Observations and Puzzles. *Nanophotonics* **2017**, *6* (6), 1289–1308.

194. Cui, Y.; Xin, R.; Yu, Z.; Pan, Y.; Ong, Z. Y.; Wei, X.; Wang, J.; Nan, H.; Ni, Z.; Wu, Y., High-Performance Monolayer WS₂ Field-Effect Transistors on High-κ Dielectrics. *Adv. Mater.* **2015**, *27* (35), 5230–5234.
195. Carozo, V.; Wang, Y.; Fujisawa, K.; Carvalho, B. R.; McCreary, A.; Feng, S.; Lin, Z.; Zhou, C.; Pereira-López, N.; Elías, A. L., Optical Identification of Sulfur Vacancies: Bound Excitons at the Edges of Monolayer Tungsten Disulfide. *Sci. Adv.* **2017**, *3* (4), e1602813.
196. Salehi, S.; Saffarzadeh, A., Atomic Defect States in Monolayers of MoS₂ and WS₂. *Surf. Sci.* **2016**, *651*, 215–221.
197. Mitioglu, A.; Plochocka, P.; Jadczyk, J.; Escoffier, W.; Rikken, G.; Kulyuk, L.; Maude, D., Optical Manipulation of the Exciton Charge State in Single-Layer Tungsten Disulfide. *Phys. Rev. B* **2013**, *88* (24), 245403.
198. Ross, J. S.; Wu, S.; Yu, H.; Ghimire, N. J.; Jones, A. M.; Aivazian, G.; Yan, J.; Mandrus, D. G.; Xiao, D.; Yao, W., Electrical Control of Neutral and Charged Excitons in a Monolayer Semiconductor. *Nat. Commun.* **2013**, *4* (1), 1–6.
199. Zhu, B.; Chen, X.; Cui, X., Exciton Binding Energy of Monolayer WS₂. *Sci. Rep.* **2015**, *5*, 9218.
200. Plechinger, G.; Nagler, P.; Kraus, J.; Paradiso, N.; Strunk, C.; Schüller, C.; Korn, T., Identification of Excitons, Trions and Biexcitons in Single-Layer WS₂. *physica status solidi (RRL)–Rapid Research Letters* **2015**, *9* (8), 457–461.
201. Ugeda, M. M.; Bradley, A. J.; Shi, S.-F.; Felipe, H.; Zhang, Y.; Qiu, D. Y.; Ruan, W.; Mo, S.-K.; Hussain, Z.; Shen, Z.-X., Giant Bandgap Renormalization and Excitonic Effects in a Monolayer Transition Metal Dichalcogenide Semiconductor. *Nat. Mater.* **2014**, *13* (12), 1091–1095.
202. Vaclavkova, D.; Wyzula, J.; Nogajewski, K.; Bartos, M.; Slobodeniuk, A.; Faugeras, C.; Potemski, M.; Molas, M., Singlet and Triplet Trions in WS₂ Monolayer Encapsulated in Hexagonal Boron Nitride. *Nanotechnology* **2018**, *29* (32), 325705.
203. Minsky, M., Memoir on Inventing the Confocal Scanning Microscope. *Scanning* **1988**, *10* (4), 128–138.

204. Maiman, T. H., Stimulated Optical Radiation in Ruby. *nature* **1960**, *187* (4736), 493-494.
205. Clarke, A.; Eberhardt, C.; Eberhardt, C. N., *Microscopy Techniques for Materials Science*. Woodhead Publishing: 2002.
206. Yacobi, B. G.; Kazmerski, L. L.; Holt, D., *Microanalysis of Solids*. Springer Science & Business Media: 2013.
207. Gao, J.; Li, B.; Tan, J.; Chow, P.; Lu, T.-M.; Koratkar, N., Aging of Transition Metal Dichalcogenide Monolayers. *ACS nano* **2016**, *10* (2), 2628-2635.
208. Kang, K.; Godin, K.; Kim, Y. D.; Fu, S.; Cha, W.; Hone, J.; Yang, E. H., Graphene-Assisted Antioxidation of Tungsten Disulfide Monolayers: Substrate and Electric-Field Effect. *Adv. Mater.* **2017**, *29* (18), 1603898.
209. Tongay, S.; Zhou, J.; Ataca, C.; Lo, K.; Matthews, T. S.; Li, J.; Grossman, J. C.; Wu, J., Thermally Driven Crossover from Indirect Toward Direct Bandgap in 2D Semiconductors: MoSe₂ versus MoS₂. *Nano Lett.* **2012**, *12* (11), 5576-5580.
210. Dong, N.; Li, Y.; Feng, Y.; Zhang, S.; Zhang, X.; Chang, C.; Fan, J.; Zhang, L.; Wang, J., Optical Limiting and Theoretical Modelling of Layered Transition Metal Dichalcogenide Nanosheets. *Sci. Rep.* **2015**, *5*, 14646.
211. Xiao, D.; Liu, G.-B.; Feng, W.; Xu, X.; Yao, W., Coupled Spin and Valley Physics in Monolayers of MoS₂ and other Group-VI Dichalcogenides. *Phys. Rev. Lett.* **2012**, *108* (19), 196802.
212. Zeng, H.; Dai, J.; Yao, W.; Xiao, D.; Cui, X., Valley Polarization in MoS₂ Monolayers by Optical Pumping. *Nat. Nanotechnol.* **2012**, *7* (8), 490.
213. Mak, K. F.; He, K.; Shan, J.; Heinz, T. F., Control of Valley Polarization in Monolayer MoS₂ by Optical Helicity. *Nat. Nanotechnol.* **2012**, *7* (8), 494.
214. Ye, Y.; Wong, Z. J.; Lu, X.; Ni, X.; Zhu, H.; Chen, X.; Wang, Y.; Zhang, X., Monolayer Excitonic Laser. *Nat. Photonics* **2015**, *9* (11), 733.
215. Tran, T. T.; Choi, S.; Scott, J. A.; Xu, Z. Q.; Zheng, C.; Seniutinas, G.; Bendavid, A.; Fuhrer, M. S.; Toth, M.; Aharonovich, I., Room-Temperature Single-Photon Emission from Oxidized Tungsten Disulfide Multilayers. *Adv. Opt. Mater.* **2017**, *5* (5), 1600939.

216. Yang, W.; Gan, L.; Li, H.; Zhai, T., Two-Dimensional Layered Nanomaterials for Gas-Sensing Applications. *Inorg. Chem. Front.* **2016**, *3* (4), 433-451.
217. Ly, T. H.; Chiu, M.-H.; Li, M.-Y.; Zhao, J.; Perello, D. J.; Cichocka, M. O.; Oh, H. M.; Chae, S. H.; Jeong, H. Y.; Yao, F., Observing Grain Boundaries in CVD-Grown Monolayer Transition Metal Dichalcogenides. *ACS nano* **2014**, *8* (11), 11401-11408.
218. Yamamoto, M.; Dutta, S.; Aikawa, S.; Nakaharai, S.; Wakabayashi, K.; Fuhrer, M. S.; Ueno, K.; Tsukagoshi, K., Self-Limiting Layer-by-Layer Oxidation of Atomically Thin WSe₂. *Nano Lett.* **2015**, *15* (3), 2067-2073.
219. Rong, Y.; He, K.; Pachios, M.; Robertson, A. W.; Bhaskaran, H.; Warner, J. H., Controlled Preferential Oxidation of Grain Boundaries in Monolayer Tungsten Disulfide for Direct Optical Imaging. *ACS nano* **2015**, *9* (4), 3695-3703.
220. Zhang, Y.; Zhang, Y.; Ji, Q.; Ju, J.; Yuan, H.; Shi, J.; Gao, T.; Ma, D.; Liu, M.; Chen, Y., Controlled Growth of High-Quality Monolayer WS₂ Layers on Sapphire and Imaging its Grain Boundary. *ACS nano* **2013**, *7* (10), 8963-8971.
221. Yamamoto, M.; Einstein, T. L.; Fuhrer, M. S.; Cullen, W. G., Anisotropic Etching of Atomically Thin MoS₂. *J. Phys. Chem. C* **2013**, *117* (48), 25643-25649.
222. Wu, J.; Li, H.; Yin, Z.; Li, H.; Liu, J.; Cao, X.; Zhang, Q.; Zhang, H., Layer Thinning and Etching of Mechanically Exfoliated MoS₂ Nanosheets by Thermal Annealing in Air. *Small* **2013**, *9* (19), 3314-3319.
223. Horcas, I.; Fernández, R.; Gomez-Rodriguez, J.; Colchero, J.; Gómez-Herrero, J.; Baro, A., WSXM: A Software for Scanning Probe Microscopy and a Tool for Nanotechnology. *Rev. Sci. Instrum.* **2007**, *78* (1), 013705.
224. Zhang, Q.; Lu, J.; Wang, Z.; Dai, Z.; Zhang, Y.; Huang, F.; Bao, Q.; Duan, W.; Fuhrer, M. S.; Zheng, C., Reliable Synthesis of Large-Area Monolayer WS₂ Single Crystals, Films, and Heterostructures with Extraordinary Photoluminescence Induced by Water Intercalation. *Adv. Opt. Mater.* **2018**, 1701347.
225. Sheng, Y.; Wang, X.; Fujisawa, K.; Ying, S.; Elias, A. L.; Lin, Z.; Xu, W.; Zhou, Y.; Korsunsky, A. M.; Bhaskaran, H.; Terrones, H.; Warner, J. H., Photoluminescence Segmentation Within Individual Hexagonal Monolayer Tungsten Disulfide Domains Grown by Chemical Vapor Deposition. *ACS Appl. Mater. Interfaces* **2017**, *9* (17), 15005-15014.

226. Peimyoo, N.; Shang, J.; Cong, C.; Shen, X.; Wu, X.; Yeow, E. K.; Yu, T., Nonblinking, Intense Two-Dimensional Light Emitter: Monolayer WS₂ Triangles. *ACS nano* **2013**, *7* (12), 10985-10994.
227. McCreary, K. M.; Hanbicki, A. T.; Singh, S.; Kawakami, R. K.; Jernigan, G. G.; Ishigami, M.; Ng, A.; Brintlinger, T. H.; Stroud, R. M.; Jonker, B. T., The Effect of Preparation Conditions on Raman and Photoluminescence of Monolayer WS₂. *Sci. Rep.* **2016**, *6*, 35154.
228. Liu, H.; Lu, J.; Ho, K.; Hu, Z.; Dang, Z.; Carvalho, A.; Tan, H. R.; Tok, E. S.; Sow, C. H., Fluorescence Concentric Triangles: A Case of Chemical Heterogeneity in WS₂ Atomic Monolayer. *Nano Lett.* **2016**, *16* (9), 5559-5567.
229. Zhang, Q.; Chang, Z.; Xu, G.; Wang, Z.; Zhang, Y.; Xu, Z. Q.; Chen, S.; Bao, Q.; Liu, J. Z.; Mai, Y. W.; Duan, W.; Fuhrer, M. S.; Zheng, C., Strain Relaxation of Monolayer WS₂ on Plastic Substrate. *Adv. Funct. Mater.* **2016**, *26* (47), 8707-8714.
230. Chow, P. K.; Jacobs-Gedrim, R. B.; Gao, J.; Lu, T.-M.; Yu, B.; Terrones, H.; Koratkar, N., Defect-Induced Photoluminescence in Monolayer Semiconducting Transition Metal Dichalcogenides. *ACS nano* **2015**, *9* (2), 1520-1527.
231. Su, L.; Yu, Y.; Cao, L.; Zhang, Y., Effects of Substrate Type and Material-Substrate Bonding on High-Temperature Behavior of Monolayer WS₂. *Nano Research* **2015**, *8* (8), 2686-2697.
232. Jadczak, J.; Kutrowska-Girzycka, J.; Kapuściński, P.; Huang, Y.; Wójs, A.; Bryja, L., Probing of Free and Localized Excitons and Trions in Atomically Thin WSe₂, WS₂, MoSe₂ and MoS₂ in Photoluminescence and Reflectivity Experiments. *Nanotechnology* **2017**, *28* (39), 395702.
233. Wang, Y.; Cong, C.; Yang, W.; Shang, J.; Peimyoo, N.; Chen, Y.; Kang, J.; Wang, J.; Huang, W.; Yu, T., Strain-Induced Direct-Indirect Bandgap Transition and Phonon Modulation in Monolayer WS₂. *Nano Research* **2015**, *8* (8), 2562-2572.
234. Conley, H. J.; Wang, B.; Ziegler, J. I.; Haglund Jr, R. F.; Pantelides, S. T.; Bolotin, K. I., Bandgap Engineering of Strained Monolayer and Bilayer MoS₂. *Nano Lett.* **2013**, *13* (8), 3626-3630.
235. Liu, Z.; Amani, M.; Najmaei, S.; Xu, Q.; Zou, X.; Zhou, W.; Yu, T.; Qiu, C.; Birdwell, A. G.; Crowne, F. J.; Vajtai, R.; Yakobson, B. I.; Xia, Z.; Dubey, M.; Ajayan, P. M.; Lou, J., Strain and Structure Heterogeneity in MoS₂ Atomic

Layers Grown by Chemical Vapour Deposition. *Nat. Commun.* **2014**, *5* (1), 1-9.

236. Island, J. O.; Kuc, A.; Diependaal, E. H.; Bratschitsch, R.; van der Zant, H. S.; Heine, T.; Castellanos-Gomez, A., Precise and reversible band gap tuning in single-layer MoSe₂ by uniaxial strain. *Nanoscale* **2016**, *8* (5), 2589-2593.
237. Yoo, Y.; Degregorio, Z. P.; Johns, J. E., Seed Crystal Homogeneity Controls Lateral and Vertical Heteroepitaxy of Monolayer MoS₂ and WS₂. *J. Am. Chem. Soc.* **2015**, *137* (45), 14281-14287.
238. Kim, I. S.; Sangwan, V. K.; Jariwala, D.; Wood, J. D.; Park, S.; Chen, K.-S.; Shi, F.; Ruiz-Zepeda, F.; Ponce, A.; Jose-Yacaman, M.; Dravid, V. P.; Marks, T. J.; Hersam, M. C.; Lauhon, L. J., Influence of Stoichiometry on the Optical and Electrical Properties of Chemical Vapor Deposition Derived MoS₂. *ACS nano* **2014**, *8* (10), 10551-10558.
239. Shi, B.; Zhou, D.; Fang, S.; Djebbi, K.; Feng, S.; Zhao, H.; Tlili, C.; Wang, D., Facile and Controllable Synthesis of Large-Area Monolayer WS₂ Flakes Based on WO₃ Precursor Drop-Casted Substrates by Chemical Vapor Deposition. *Nanomaterials* **2019**, *9* (4), 578.
240. Hu, Z.; Avila, J.; Wang, X.; Leong, J.; Zhang, Q.; Liu, Y.; Asensio, M.; Lu, J.; Carvalho, A.; Sow, C. H.; Neto, A. C., The Role of Oxygen Atoms on the Excitons at the Edges of Monolayer WS₂. *Nano Lett.* **2019**.
241. Zheng, C.; Xu, Z.-Q.; Zhang, Q.; Edmonds, M. T.; Watanabe, K.; Taniguchi, T.; Bao, Q.; Fuhrer, M. S., Profound Effect of Substrate Hydroxylation and Hydration on Electronic and Optical Properties of Monolayer MoS₂. *Nano Lett.* **2015**, *15* (5), 3096-3102.
242. Song, C.; Chen, H.; Fan, Y.; Luo, J.; Guo, X.; Liu, X., High-Work-Function Transparent Conductive Oxides with Multilayer Films. *Appl. Phys. Express* **2012**, *5* (4), 041102.
243. Hu, L.; Shan, X.; Wu, Y.; Zhao, J.; Lu, X., Laser Thinning and Patterning of MoS₂ with Layer-by-Layer Precision. *Sci. Rep.* **2017**, *7* (1), 15538.
244. Zhao, W.; Ghorannevis, Z.; Chu, L.; Toh, M.; Kloc, C.; Tan, P.-H.; Eda, G., Evolution of Electronic Structure in Atomically Thin Sheets of WS₂ and WSe₂. *ACS nano* **2012**, *7* (1), 791-797.
245. Bregnø, M.; Blazquez-Castro, A.; Westberg, M.; Breitenbach, T.; Ogilby, P. R., Direct 765 nm Optical Excitation of Molecular Oxygen in

- Solution and in Single Mammalian Cells. *J. Phys. Chem. B* **2015**, *119* (17), 5422-5429.
246. Blázquez-Castro, A., Direct $^1\text{O}_2$ Optical Excitation: A Tool for Redox Biology. *Redox biology* **2017**, *13*, 39-59.
247. Ding, X.; Peng, F.; Zhou, J.; Gong, W.; Slaven, G.; Loh, K. P.; Lim, C. T.; Leong, D. T., Defect Engineered Bioactive Transition Metals Dichalcogenides Quantum Dots. *Nat. Commun.* **2019**, *10* (1), 41.
248. Froehlicher, G.; Lorchat, E.; Berciaud, S., Charge Versus Energy Transfer in Atomically Thin Graphene-Transition Metal Dichalcogenide van der Waals Heterostructures. *Phys. Rev. X* **2018**, *8* (1), 011007.
249. Suzuki, T.; Ogawa, M., Degradation of Photoluminescence Intensity Caused by Excitation-Enhanced Oxidation of GaAs Surfaces. *Appl. Phys. Lett.* **1977**, *31* (7), 473-475.
250. Bermudez, V. M., Photoenhanced Oxidation of Gallium Arsenide. *J. Appl. Phys.* **1983**, *54* (11), 6795-6798.
251. Schafer, S.; Lyon, S., Optically Enhanced Oxidation of Semiconductors. *J. Vac. Sci. Technol.* **1981**, *19* (3), 494-497.
252. Nosaka, Y.; Nosaka, A. Y., Generation and Detection of Reactive Oxygen Species in Photocatalysis. *Chem. Rev.* **2017**, *117* (17), 11302-11336.
253. Favron, A.; Gaufrès, E.; Fossard, F.; Phaneuf-L'Heureux, A.-L.; Tang, N. Y.; Lévesque, P. L.; Loiseau, A.; Leonelli, R.; Francoeur, S.; Martel, R., Photooxidation and Quantum Confinement Effects in Exfoliated Black Phosphorus. *Nat. Mater.* **2015**, *14* (8), 826.
254. Shcherbakov, D.; Stepanov, P.; Weber, D.; Wang, Y.; Hu, J.; Zhu, Y.; Watanabe, K.; Taniguchi, T.; Mao, Z.; Windl, W.; Goldberger, J.; Bockrath, M.; Lau, C. N., Raman Spectroscopy, Photocatalytic Degradation, and Stabilization of Atomically Thin Chromium Tri-Iodide. *Nano Lett.* **2018**, *18* (7), 4214-4219.
255. Iwasaki, H.; Mizokawa, Y.; Nishitani, R.; Nakamura, S., X-Ray Photoemission Study of the Interaction of Oxygen and Air with Cleaved GaAs (110) Surfaces. *Jpn. J. Appl. Phys.* **1978**, *17* (2), 315.
256. Zhang, X.; Jia, F.; Yang, B.; Song, S., Oxidation of Molybdenum Disulfide Sheet in Water Under in situ Atomic Force Microscopy Observation. *J. Phys. Chem. C* **2017**, *121* (18), 9938-9943.

257. Budania, P.; Baine, P.; Montgomery, J.; McGeough, C.; Cafolla, T.; Modreanu, M.; McNeill, D.; Mitchell, N.; Hughes, G.; Hurley, P., Long-Term Stability of Mechanically Exfoliated MoS₂ Flakes. *MRS Commun.* **2017**, *7* (4), 813-818.
258. Ross, S.; Sussman, A., Surface Oxidation of Molybdenum Disulfide. *J. Phys. Chem.* **1955**, *59* (9), 889-892.
259. Wu, Z.; Yu, J.; Yuan, S., Strain-Tunable Magnetic and Electronic Properties of Monolayer CrI₃. *Phys. Chem. Chem. Phys.* **2019**.
260. Ye, M.; Zhang, D.; Yap, Y. K., Recent Advances in Electronic and Optoelectronic Devices Based on Two-Dimensional Transition Metal Dichalcogenides. *Electronics* **2017**, *6* (2), 43.
261. Rosenberger, M. R.; Chuang, H.-J.; McCreary, K. M.; Li, C. H.; Jonker, B. T., Electrical Characterization of Discrete Defects and Impact of Defect Density on Photoluminescence in Monolayer WS₂. *ACS nano* **2018**, *12* (2), 1793-1800.
262. Hong, J.; Hu, Z.; Probert, M.; Li, K.; Lv, D.; Yang, X.; Gu, L.; Mao, N.; Feng, Q.; Xie, L., Exploring Atomic Defects in Molybdenum Disulphide Monolayers. *Nat. Commun.* **2015**, *6*, 6293.
263. Addou, R.; Colombo, L.; Wallace, R. M., Surface Defects on Natural MoS₂. *ACS Appl. Mater. Interfaces* **2015**, *7* (22), 11921-11929.
264. Vancsó, P.; Magda, G. Z.; Pető, J.; Noh, J.-Y.; Kim, Y.-S.; Hwang, C.; Biró, L. P.; Tapasztó, L., The Intrinsic Defect Structure of Exfoliated MoS₂ Single Layers Revealed by Scanning Tunneling Microscopy. *Sci. Rep.* **2016**, *6*, 29726.
265. Edelberg, D.; Rhodes, D.; Kerelsky, A.; Kim, B.; Wang, J.; Zangiabadi, A.; Kim, C.; Abhinandan, A.; Ardelean, J.; Scully, M.; Scullion, D.; Embon, L.; Zu, R.; Santos, E. J. G.; Balicas, L.; Marianetti, C.; Barmak, K.; Zhu, X.; Hone, J.; Pasupathy, A. N., Hundredfold Enhancement of Light Emission via Defect Control in Monolayer Transition-Metal Dichalcogenides. *Nano Lett.* **2018**, *19* (7), 4371-4379.
266. Barja, S.; Refaelly-Abramson, S.; Schuler, B.; Qiu, D. Y.; Pulkkin, A.; Wickenburg, S.; Ryu, H.; Ugeda, M. M.; Kastl, C.; Chen, C.; Hwang, C.; Schwartzberg, A.; Aloni, S.; Mo, S.-K.; Ogletree, D. F.; Crommie, M. F. Y.; Oleg V.; Louie, S. G.; Neaton, J. B.; Weber-Bargioni, A., Identifying Substitutional Oxygen as a Prolific Point Defect in Monolayer Transition Metal

Dichalcogenides with Experiment and Theory. *Nat. Commun.* **2019**, *10* (1), 1-8.

267. KC, S.; Longo, R. C.; Wallace, R. M.; Cho, K., Surface Oxidation Energetics and Kinetics on MoS₂ Monolayer. *J. Appl. Phys.* **2015**, *117* (13), 135301.
268. Hu, K. H.; Hu, X. G.; Sun, X. J., Morphological Effect of MoS₂ Nanoparticles on Catalytic Oxidation and Vacuum Lubrication. *Appl. Surf. Sci.* **2010**, *256* (8), 2517-2523.
269. Afanasiev, P.; Lorentz, C., Oxidation of Nanodispersed MoS₂ in Ambient Air: The Products and the Mechanistic Steps. *J. Phys. Chem. C* **2019**.
270. Weller, T. E.; Ellerby, M.; Saxena, S. S.; Smith, R. P.; Skipper, N. T., Superconductivity in the Intercalated Graphite Compounds C₆Yb and C₆Ca. *Nat. Phys.* **2005**, *1* (1), 39-41.
271. Emery, N.; Hérold, C.; d'Astuto, M.; Garcia, V.; Bellin, C.; Marêché, J.; Lagrange, P.; Loupias, G., Superconductivity of Bulk CaC₆. *Phys. Rev. Lett.* **2005**, *95* (8), 087003.
272. Shimizu, R.; Sugawara, K.; Kanetani, K.; Iwaya, K.; Sato, T.; Takahashi, T.; Hitosugi, T., Charge-Density Wave in Ca-Intercalated Bilayer Graphene Induced by Commensurate Lattice Matching. *Phys. Rev. Lett.* **2015**, *114* (14), 146103.
273. Geim, A. K., Graphene: Status and Prospects. *Science* **2009**, *324* (5934), 1530-1534.
274. Lemme, M. C.; Echtermeyer, T. J.; Baus, M.; Kurz, H., A Graphene Field-Effect Device. *IEEE Electron Device Lett.* **2007**, *28* (4), 282-284.
275. Chen, W.; Chen, S.; Qi, D. C.; Gao, X. Y.; Wee, A. T. S., Surface Transfer p-type Doping of Epitaxial Graphene. *J. Am. Chem. Soc.* **2007**, *129* (34), 10418-10422.
276. Schedin, F.; Geim, A. K.; Morozov, S. V.; Hill, E.; Blake, P.; Katsnelson, M.; Novoselov, K. S., Detection of Individual Gas Molecules Adsorbed on Graphene. *Nat. Mater.* **2007**, *6* (9), 652-655.
277. Wang, H.; Wang, Q.; Cheng, Y.; Li, K.; Yao, Y.; Zhang, Q.; Dong, C.; Wang, P.; Schwingenschlögl, U.; Yang, W.; Zhang, X. X., Doping Monolayer Graphene with Single Atom Substitutions. *Nano Lett.* **2012**, *12* (1), 141-144.

278. Link, S.; Forti, S.; Stöhr, A.; Küster, K.; Rösner, M.; Hirschmeier, D.; Chen, C.; Avila, J.; Asensio, M.; Zakharov, A.; Wehling, T.; Lichtenstein, A.; Katsnelson, M.; Starke, U., Introducing Strong Correlation Effects into Graphene by Gadolinium Intercalation. *Phys. Rev. B* **2019**, *100* (12), 121407.
279. Rosenzweig, P.; Karakachian, H.; Link, S.; Küster, K.; Starke, U., Tuning the Doping Level of Graphene in the Vicinity of the Van Hove Singularity via Ytterbium Intercalation. *Phys. Rev. B* **2019**, *100* (3), 035445.
280. Li, K.; Feng, X.; Zhang, W.; Ou, Y.; Chen, L.; He, K.; Wang, L.-L.; Guo, L.; Liu, G.; Xue, Q.-K.; Ma, X., Superconductivity in Ca-Intercalated Epitaxial Graphene on Silicon Carbide. *Appl. Phys. Lett.* **2013**, *103* (6), 062601.
281. Khrapach, I.; Withers, F.; Bointon, T. H.; Polyushkin, D. K.; Barnes, W. L.; Russo, S.; Craciun, M. F., Novel Highly Conductive and Transparent Graphene-Based Conductors. *Adv. Mater.* **2012**, *24* (21), 2844-2849.
282. Li, Z.; Zhang, C.; Han, F.; Zhang, F.; Zhou, D.; Xu, S.; Liu, H.; Li, X.; Liu, J., Improving the Cycle Stability of FeCl_3 -Graphite Intercalation Compounds by Polar Fe_2O_3 Trapping in Lithium-ion Batteries. *Nano Research* **2019**, *12* (8), 1836-1844.
283. Dresselhaus, M. S.; Dresselhaus, G., Intercalation Compounds of Graphite. *Adv. Phys.* **2002**, *51* (1), 1-186.
284. Hannay, N.; Geballe, T.; Matthias, B.; Andres, K.; Schmidt, P.; MacNair, D., Superconductivity in Graphitic Compounds. *Phys. Rev. Lett.* **1965**, *14* (7), 225.
285. Ohta, T.; El Gabaly, F.; Bostwick, A.; McChesney, J. L.; Emtsev, K. V.; Schmid, A. K.; Seyller, T.; Horn, K.; Rotenberg, E., Morphology of Graphene Thin Film Growth on SiC(0001). *New J. Phys.* **2008**, *10* (2), 023034.
286. Profeta, G.; Calandra, M.; Mauri, F., Phonon-Mediated Superconductivity in Graphene by Lithium Deposition. *Nat. Phys.* **2012**, *8* (2), 131-134.
287. Gonzalez, J., Kohn-Luttinger Superconductivity in Graphene. *Phys. Rev. B* **2008**, *78* (20), 205431.
288. Nandkishore, R.; Levitov, L.; Chubukov, A., Chiral Superconductivity from Repulsive Interactions in Doped Graphene. *Nat. Phys.* **2012**, *8* (2), 158-163.

289. Gofron, K.; Campuzano, J.; Abrikosov, A.; Lindroos, M.; Bansil, A.; Ding, H.; Koelling, D.; Dabrowski, B., Observation of an "Extended" Van Hove Singularity in $\text{YBa}_2\text{Cu}_4\text{O}_8$ by Ultrahigh Energy Resolution Angle-Resolved Photoemission. *Phys. Rev. Lett.* **1994**, *73* (24), 3302.
290. Zhang, Y.; Zhang, H.; Cai, Y.; Song, J.; Qiao, D.; Chen, Q.; Hu, F.; Wang, P.; Huang, K.; He, P., Calcium Intercalation Underneath N-layer Graphene on 6H-SiC(0001). *Chem. Phys. Lett.* **2018**, *703*, 33-38.
291. Nyakiti, L.; Wheeler, V.; Garces, N.; Myers-Ward, R.; Eddy, C.; Gaskill, D., Enabling Graphene-Based Technologies: Toward Wafer-Scale Production of Epitaxial Graphene. *MRS Bull.* **2012**, *37* (12), 1149-1157.
292. Himpel, F.; McFeely, F.; Taleb-Ibrahimi, A.; Yarmoff, J.; Hollinger, G., Microscopic Structure of the SiO_2/Si Interface. *Phys. Rev. B* **1988**, *38* (9), 6084.
293. Gelius, U.; Asplund, L.; Basilier, E.; Hedman, S.; Helenelund, K.; Siegbahn, K., A High Resolution Multipurpose ESCA Instrument With X-ray Monochromator. *Nucl. Instrum. Methods Phys. Res., Sect. B* **1984**, *1* (1), 85-117.
294. Fedorov, A.; Verbitskiy, N.; Haberer, D.; Struzzi, C.; Petaccia, L.; Usachov, D.; Vilkov, O.; Vyalikh, D.; Fink, J.; Knupfer, M.; Büchner, B.; Grüneis, A., Observation of a Universal Donor-Dependent Vibrational Mode in Graphene. *Nat. Commun.* **2014**, *5*, 3257.
295. Despoja, V.; Šunjić, M., Theory of Core-Level Spectra in X-ray Photoemission of Pristine and Doped Graphene. *Phys. Rev. B* **2013**, *88* (24), 245416.
296. Sernelius, B. E., Core-Level Spectra from Graphene. *Phys. Rev. B* **2015**, *91* (4), 045402.
297. Kim, H.; Dugerjav, O.; Arvisbaatar, A.; Seo, J. M., Bifunctional Effects of the Ordered Si Atoms Intercalated Between Quasi-Free-Standing Epitaxial Graphene and SiC (0001): Graphene Doping and Substrate Band Bending. *New J. Phys.* **2015**, *17* (8), 083058.
298. Khademi, A.; Sajadi, E.; Dosanjh, P.; Bonn, D.; Folk, J. A.; Stöhr, A.; Starke, U.; Forti, S., Alkali Doping of Graphene: The Crucial Role of High-Temperature Annealing. *Phys. Rev. B* **2016**, *94* (20), 201405.
299. Coletti, C.; Riedl, C.; Lee, D. S.; Krauss, B.; Patthey, L.; von Klitzing, K.; Smet, J. H.; Starke, U., Charge Neutrality and Band-Gap Tuning of Epitaxial Graphene on SiC by Molecular Doping. *Phys. Rev. B* **2010**, *81* (23), 235401.

300. Kotsakidis, J. C.; Grubišić-Čabo, A.; Yin, Y.; Tadich, A.; Myers-Ward, R. L.; Dejarld, M.; Pavunny, S. P.; Currie, M.; Daniels, K. M.; Liu, C.; Edmonds, M. T.; Medhekar, N. V.; Gaskill, D. K.; Vázquez de Parga, A. L.; Fuhrer, M. S., Freestanding n-Doped Graphene via Intercalation of Calcium and Magnesium Into the Buffer Layer-SiC(0001) Interface. *Chem. Mater.* **2020**, *32* (15), 6464-6482.
301. Murata, Y.; Mashoff, T.; Takamura, M.; Tanabe, S.; Hibino, H.; Beltram, F.; Heun, S., Correlation Between Morphology and Transport Properties of Quasi-Free-Standing Monolayer Graphene. *Appl. Phys. Lett.* **2014**, *105* (22), 221604.
302. Watcharinyanon, S.; Virojanadara, C.; Osiecki, J.; Zakharov, A.; Yakimova, R.; Uhrberg, R.; Johansson, L. I., Hydrogen Intercalation of Graphene Grown on 6H-SiC(0001). *Surf. Sci.* **2011**, *605* (17-18), 1662-1668.
303. Speck, F.; Ostler, M.; Besendörfer, S.; Krone, J.; Wanke, M.; Seyller, T., Growth and Intercalation of Graphene on Silicon Carbide Studied by Low-Energy Electron Microscopy. *Ann. Phys.* **2017**, *529* (11), 1700046.
304. Kim, H.; Tsogtbaatar, N.; Tuvdendorj, B.; Lkhagvasuren, A.; Seo, J. M., Effects of Two Kinds of Intercalated In Films on Quasi-Free-Standing Monolayer Graphene Formed Above SiC(0001). *Carbon* **2020**, *159*, 229-235.
305. Schöpke, A.; Würz, R.; Schmidt, M., Epitaxial Growth of CaSi₂ on Si(111). *Surf. Interface Anal.* **2002**, *34* (1), 464-467.
306. Pi, T.-W.; Cheng, C.-P.; Wertheim, G., The Reaction of Si(001) with Magnesium and Calcium. *J. Appl. Phys.* **2011**, *109* (4), 043701-043701-7.
307. Sandin, A.; Jayasekera, T.; Rowe, J.; Kim, K. W.; Nardelli, M. B.; Dougherty, D. B., Multiple Coexisting Intercalation Structures of Sodium in Epitaxial Graphene-SiC Interfaces. *Phys. Rev. B* **2012**, *85* (12), 125410.
308. Fiori, S.; Murata, Y.; Veronesi, S.; Rossi, A.; Coletti, C.; Heun, S., Li-Intercalated Graphene on SiC (0001): An STM Study. *Phys. Rev. B* **2017**, *96* (12), 125429.
309. Gomoyunova, M.; Grebenyuk, G.; Davydov, V. Y.; Ermakov, I.; Eliseyev, I.; Lebedev, A.; Lebedev, S.; Lobanova, E. Y.; Smirnov, A.; Smirnov, D.; Pronin, I., Intercalation of Iron Atoms Under Graphene Formed on Silicon Carbide. *Phys. Solid State* **2018**, *60* (7), 1439-1446.
310. Grebenyuk, G.; Lobanova, E. Y.; Smirnov, D.; Eliseev, I.; Zubov, A.; Smirnov, A.; Lebedev, S.; Davydov, V. Y.; Lebedev, A.; Pronin, I., Cobalt

Intercalation of Graphene on Silicon Carbide. *Phys. Solid State* **2019**, *61* (7), 1316-1326.

311. Anderson, N. A.; Hupalo, M.; Keavney, D.; Tringides, M.; Vaknin, D., Intercalated Rare-Earth Metals Under Graphene on SiC. *J. Magn. Magn. Mater.* **2019**, *474*, 666-670.

312. Kim, H.; Dugerjav, O.; Lkhagvasuren, A.; Seo, J. M., Doping Modulation of Quasi-Free-Standing Monolayer Graphene Formed on SiC (0001) Through Sn_{1-x}Gex Intercalation. *Carbon* **2019**, *144*, 549-556.

313. Niu, Y.; Zakharov, A.; Yakimova, R., Metal-Dielectric Transition in Sn-Intercalated Graphene on SiC (0001). *Ultramicroscopy* **2017**, *183*, 49-54.

314. Emtsev, K. V.; Zakharov, A. A.; Coletti, C.; Forti, S.; Starke, U., Ambipolar Doping in Quasifree Epitaxial Graphene on SiC(0001) Controlled by Ge Intercalation. *Phys. Rev. B* **2011**, *84* (12), 125423.

315. Yurtsever, A.; Onoda, J.; Iimori, T.; Niki, K.; Miyamachi, T.; Abe, M.; Mizuno, S.; Tanaka, S.; Komori, F.; Sugimoto, Y., Effects of Pb Intercalation on the Structural and Electronic Properties of Epitaxial Graphene on SiC. *Small* **2016**, *12* (29), 3956-3966.

316. Briggs, N.; Gebeyehu, Z. M.; Vera, A.; Zhao, T.; Wang, K.; Duran, A. D. L. F.; Bersch, B.; Bowen, T.; Knappenberger, K. L.; Robinson, J. A., Epitaxial Graphene/Silicon Carbide Intercalation: A Minireview on Graphene Modulation and Unique 2D Materials. *Nanoscale* **2019**, *11* (33), 15440-15447.

317. Hönig, R.; Roese, P.; Shamout, K.; Ohkochi, T.; Berges, U.; Westphal, C., Structural, Chemical, and Magnetic Properties of Cobalt Intercalated Graphene on Silicon Carbide. *Nanotechnology* **2018**, *30* (2), 025702.

318. Virojanadara, C.; Zakharov, A.; Watcharinyanon, S.; Yakimova, R.; Johansson, L. I., A Low-Energy Electron Microscopy and X-Ray Photo-Emission Electron Microscopy Study of Li Intercalated into Graphene on SiC(0001). *New J. Phys.* **2010**, *12* (12), 125015.

319. Gierz, I.; Suzuki, T.; Weitz, R. T.; Lee, D. S.; Krauss, B.; Riedl, C.; Starke, U.; Höchst, H.; Smet, J. H.; Ast, C. R.; Klaus, K., Electronic Decoupling of an Epitaxial Graphene Monolayer by Gold Intercalation. *Phys. Rev. B* **2010**, *81* (23), 235408.

320. Wang, Z.-j.; Wei, M.; Jin, L.; Ning, Y.; Yu, L.; Fu, Q.; Bao, X., Simultaneous N-Intercalation and N-Doping of Epitaxial Graphene on 6H-

SiC (0001) Through Thermal Reactions with Ammonia. *Nano Research* **2013**, *6* (6), 399-408.

321. Oida, S.; McFeely, F.; Hannon, J.; Tromp, R.; Copel, M.; Chen, Z.; Sun, Y.; Farmer, D.; Yurkas, J., Decoupling Graphene from SiC (0001) via Oxidation. *Phys. Rev. B* **2010**, *82* (4), 041411.

322. Wolff, S.; Roscher, S.; Timmermann, F.; Daniel, M. V.; Speck, F.; Wanke, M.; Albrecht, M.; Seyller, T., Quasi-Freestanding Graphene on SiC (0001) by Ar-Mediated Intercalation of Antimony: A Route Toward Intercalation of High-Vapor-Pressure Elements. *Ann. Phys.* **2019**, *521* (11).

323. Delplancke, M.-P.; Powers, J. M.; Vandentop, G.; Salmeron, M.; Somorjai, G. A., Preparation and Characterization of Amorphous SiC:H Thin Films. *J. Vac. Sci. Technol., A* **1991**, *9* (3), 450-455.

324. Bebensee, F.; Voigts, F.; Maus-Friedrichs, W., The Adsorption of Oxygen and Water on Ca and CaO Films Studied with MIES, UPS and XPS. *Surf. Sci.* **2008**, *602* (9), 1622-1630.

325. Liu, P.; Kendelewicz, T.; Brown, G. E.; Parks, G. A.; Pianetta, P., Reaction of Water with Vacuum-Cleaved CaO(100) Surfaces: An X-Ray Photoemission Spectroscopy Study. *Surf. Sci.* **1998**, *416* (1-2), 326-340.

326. Van der Heide, P., Photoelectron Binding Energy Shifts Observed During Oxidation of Group IIA, IIIA and IVA Elemental Surfaces. *J. Electron Spectrosc. Relat. Phenom.* **2006**, *151* (2), 79-91.

327. Fuggle, J. C.; Mårtensson, N., Core-Level Binding Energies in Metals. *J. Electron Spectrosc. Relat. Phenom.* **1980**, *21* (3), 275-281.

328. Doveren, H. v.; Verhoeven, J. T., XPS Spectra of Ca, Sr, Ba and Their Oxides. *J. Electron Spectrosc. Relat. Phenom.* **1980**, *21* (3), 265-273.

329. Demri, B.; Muster, D., XPS Study of Some Calcium Compounds. *Journal of materials processing technology* **1995**, *55* (3-4), 311-314.

330. Dahle, S.; Voigts, F.; Maus-Friedrichs, W., In situ Preparation of Calcium Hydroxide Films. *Thin solid films* **2011**, *520* (1), 18-24.

331. Van Buuren, M.; Voermans, F.; VanKempen, H., Bonding in Mg₂Si Studied with X-Ray Photoelectron Spectroscopy. *J. Phys. Chem.* **1995**, *99* (23), 9519-9522.

332. Wicks, R.; Ingle, N., Characterizing the Detection System Nonlinearity, Internal Inelastic Background, and Transmission Function of an Electron Spectrometer for Use in X-Ray Photoelectron Spectroscopy. *Rev. Sci. Instrum.* **2009**, *80* (5), 053108.
333. Weng, L.; Vereecke, G.; Genet, M.; Bertrand, P.; Stone, W., Quantitative XPS. Part I: Experimental Determination of the Relative Analyser Transmission Function of Two Different Spectrometers — A Critical Assessment of Various Methods, Parameters Involved and Errors Introduced. *Surf. Interface Anal.* **1993**, *20* (3), 179–192.
334. Hemminger, C. S.; Land, T. A.; Christie, A.; Hemminger, J. C., An Empirical Electron Spectrometer Transmission Function for Applications in Quantitative XPS. *Surf. Interface Anal.* **1990**, *15* (5), 323–327.
335. Edgell, M.; Paynter, R.; Castle, J., High Energy XPS Using a Monochromated Ag L α Source: Resolution, Sensitivity and Photoelectric Cross Sections. *J. Electron Spectrosc. Relat. Phenom.* **1985**, *37* (2), 241–256.
336. Jiříček, P., Measurement of the Transmission Function of the Hemispherical Energy Analyser of ADES 400 Electron Spectrometer. *Czechoslovak Journal of Physics* **1994**, *44* (3), 261–267.
337. Rutter, G. M.; Guisinger, N.; Crain, J.; Jarvis, E.; Stiles, M. D.; Li, T.; First, P.; Stroscio, J. A., Imaging the Interface of Epitaxial Graphene with Silicon Carbide via Scanning Tunneling Microscopy. *Phys. Rev. B* **2007**, *76* (23), 235416.
338. Omidian, M.; Néel, N.; Manske, E.; Pezoldt, J.; Lei, Y.; Kröger, J., Structural and Local Electronic Properties of Clean and Li-Intercalated Graphene on SiC(0001). *Surf. Sci.* **2020**, 121638.
339. Sorger, C.; Hertel, S.; Jobst, J.; Steiner, C.; Meil, K.; Ullmann, K.; Albert, A.; Wang, Y.; Krieger, M.; Ristein, J.; Maier, S.; Weber, H. B., Gateless Patterning of Epitaxial Graphene by Local Intercalation. *Nanotechnology* **2014**, *26* (2), 025302.
340. Wong, S. L.; Huang, H.; Wang, Y.; Cao, L.; Qi, D.; Santoso, I.; Chen, W.; Wee, A. T. S., Quasi-Free-Standing Epitaxial Graphene on SiC (0001) by Fluorine Intercalation from a Molecular Source. *ACS nano* **2011**, *5* (9), 7662–7668.
341. Rutter, G. M.; Crain, J.; Guisinger, N.; Li, T.; First, P.; Stroscio, J., Scattering and Interference in Epitaxial Graphene. *Science* **2007**, *317* (5835), 219–222.

342. Simon, L.; Bena, C.; Vonau, F.; Aubel, D.; Nasrallah, H.; Habar, M.; Peruchetti, J., Symmetry of Standing Waves Generated by a Point Defect in Epitaxial Graphene. *The European Physical Journal B* **2009**, *69* (3), 351-355.
343. Susi, T.; Pichler, T.; Ayala, P., X-ray Photoelectron Spectroscopy of Graphitic Carbon Nanomaterials Doped with Heteroatoms. *Beilstein journal of nanotechnology* **2015**, *6* (1), 177-192.
344. Hassan, J.; Winters, M.; Ivanov, I.; Habibpour, O.; Zirath, H.; Rorsman, N.; Janzén, E., Quasi-Free-Standing Monolayer and Bilayer Graphene Growth on Homoepitaxial On-Axis 4H-SiC (0001) Layers. *Carbon* **2015**, *82*, 12-23.
345. Forti, S.; Starke, U., Epitaxial Graphene on SiC: From Carrier Density Engineering to Quasi-Free Standing Graphene by Atomic Intercalation. *J. Phys. D: Appl. Phys.* **2014**, *47* (9), 094013.
346. Hwang, E.; Sarma, S. D., Dielectric Function, Screening, and Plasmons in Two-Dimensional Graphene. *Phys. Rev. B* **2007**, *75* (20), 205418.
347. Mammadov, S.; Ristein, J.; Krone, J.; Raidel, C.; Wanke, M.; Wiesmann, V.; Speck, F.; Seyller, T., Work Function of Graphene Multilayers on SiC(0001). *2D Mater.* **2017**, *4* (1), 015043.
348. Fomenko, V., *Handbook of Thermionic Properties*. Plenum Press Data Division, New York: 1966.
349. Gaudart, L.; Rivoira, R., Propriétés Photoélectriques des Couches Minces de Calcium. *Applied optics* **1971**, *10* (10), 2336-2343.
350. Gaudart, L.; Renucci, P.; Rivoira, R., Work Functions and Structures of Alkaline-Earth Thin Films. *J. Appl. Phys.* **1978**, *49* (7), 4105-4110.
351. Liu, Y.; Merinov, B. V.; Goddard, W. A., Origin of Low Sodium Capacity in Graphite and Generally Weak Substrate Binding of Na and Mg Among Alkali and Alkaline Earth Metals. *PNAS* **2016**, *113* (14), 3735-3739.
352. Watcharinyanon, S.; Johansson, L. I.; Xia, C.; Virojanadara, C., Changes in Structural and Electronic Properties of Graphene Grown on 6H-SiC(0001) Induced by Na Deposition. *J. Appl. Phys.* **2012**, *111* (8), 083711.
353. Moriwake, H.; Kuwabara, A.; Fisher, C. A.; Ikuhara, Y., Why is Sodium-Intercalated Graphite Unstable? *RSC advances* **2017**, *7* (58), 36550-36554.
354. Walter, A. L.; Jeon, K.-J.; Bostwick, A.; Speck, F.; Ostler, M.; Seyller, T.; Moreschini, L.; Kim, Y. S.; Chang, Y. J.; Horn, K.; Rotenberg, E., Highly p-

- Doped Epitaxial Graphene Obtained by Fluorine Intercalation. *Appl. Phys. Lett.* **2011**, *98* (18), 184102.
355. Xia, C.; Watcharinyanon, S.; Zakharov, A.; Yakimova, R.; Hultman, L.; Johansson, L. I.; Virojanadara, C., Si Intercalation/Deintercalation of Graphene on 6H-SiC(0001). *Phys. Rev. B* **2012**, *85* (4), 045418.
356. Silly, M.; D'Angelo, M.; Besson, A.; Dappe, Y. J.; Kubsky, S.; Li, G.; Nicolas, F.; Pierucci, D.; Thomasset, M., Electronic and Structural Properties of Graphene-Based Metal-Semiconducting Heterostructures Engineered by Silicon Intercalation. *Carbon* **2014**, *76*, 27-39.
357. Rosenzweig, P.; Starke, U., Large-Area Synthesis of a Semiconducting Silver Monolayer via Intercalation of Epitaxial Graphene. *Phys. Rev. B* **2020**, *101* (20), 201407.
358. Stöhr, A.; Forti, S.; Link, S.; Zakharov, A. A.; Kern, K.; Starke, U.; Benia, H. M., Intercalation of Graphene on SiC(0001) Via Ion Implantation. *Phys. Rev. B* **2016**, *94* (8), 085431.
359. Chapman, J.; Su, Y.; Howard, C.; Kundys, D.; Grigorenko, A.; Guinea, F.; Geim, A.; Grigorieva, I.; Nair, R., Superconductivity in Ca-Doped Graphene Laminates. *Sci. Rep.* **2016**, *6* (1), 1-6.
360. Honig, R. E., Vapor Pressure Data for the Solid and Liquid Elements. *RCA review* **1962**, *23* (12), 567.
361. Park, H.; Singh, L. T.; Lee, P.; Kim, J.; Ryu, M.; Hwang, C.-C.; Kim, K. S.; Chung, J., Observation of Mg-Induced Structural and Electronic Properties of Graphene. *Appl. Phys. Lett.* **2016**, *109* (19), 193104.
362. Kawaguchi, M.; Kurasaki, A., Intercalation of Magnesium Into a Graphite-Like Layered Material of Composition BC₂N. *Chemical Communications* **2012**, *48* (55), 6897-6899.
363. Bucur, C. B., *Challenges of a Rechargeable Magnesium Battery: A Guide to the Viability of this Post Lithium-Ion Battery*. Springer International Publishing Cham, Switzerland, 2017.
364. God, C.; Bitschnau, B.; Kapper, K.; Lenhardt, C.; Schmuck, M.; Mautner, F.; Koller, S., Intercalation Behaviour of Magnesium into Natural Graphite Using Organic Electrolyte Systems. *RSC advances* **2017**, *7* (23), 14168-14175.
365. Xu, W.; Zhang, H.; Lerner, M. M., Graphite Intercalation by Mg Diamine Complexes. *Inorganic chemistry* **2018**, *57* (14), 8042-8045.

366. Broekman, L.; Tadich, A.; Huwald, E.; Riley, J.; Leckey, R.; Seyller, T.; Emtsev, K.; Ley, L., First Results from a Second Generation Toroidal Electron Spectrometer. *J. Electron Spectrosc. Relat. Phenom.* **2005**, *144*, 1001-1004.
367. Brause, M.; Braun, B.; Ochs, D.; Maus-Friedrichs, W.; Kempfer, V., Surface Electronic Structure of Pure and Oxidized Non-Epitaxial Mg₂Si Layers on Si (m). *Surf. Sci.* **1998**, *398* (1-2), 184-194.
368. Wigren, C.; Andersen, J.; Nyholm, R.; Karlsson, U. O., Epitaxial Silicide Formation in the Mg/Si (111) System. *Surf. Sci.* **1993**, *289* (3), 290-296.
369. Brennan, B.; McDonnell, S.; Hughes, G., Photoemission Studies of the Initial Interface Formation of Ultrathin MgO Dielectric Layers on the Si(111) Surface. *Thin Solid Films* **2010**, *518* (8), 1980-1984.
370. Casey, P.; Hughes, G., High Resolution Photoemission Study of the Formation and Thermal Stability of Mg Silicide on Silicon. *Thin Solid Films* **2011**, *519* (6), 1861-1865.
371. Schmuelling, G.; Winter, M.; Placke, T., Investigating the Mg-Si Binary System via Combinatorial Sputter Deposition as High Energy Density Anodes for Lithium-Ion Batteries. *ACS Appl. Mater. Interfaces* **2015**, *7* (36), 20124-20133.
372. Schröder, U. A.; Petrović, M.; Gerber, T.; Martínez-Galera, A. J.; Gränäs, E.; Arman, M. A.; Herbig, C.; Schnadt, J.; Kralj, M.; Knudsen, J.; Michely, T., Core Level Shifts of Intercalated Graphene. *2D Mater.* **2016**, *4* (1), 015013.
373. Richter, K., Spectral Properties of the Al and Mg K α 1 Lines Determined by the PAX Method. *Surf. Interface Anal.* **1990**, *15* (11), 705-707.
374. Schweppe, J.; Deslattes, R.; Mooney, T.; Powell, C., Accurate Measurement of Mg and Al K $\alpha_{1,2}$ X-Ray Energy Profiles. *J. Electron Spectrosc. Relat. Phenom.* **1994**, *67* (3), 463-478.
375. Powell, C. J., Recommended Auger Parameters for 42 Elemental Solids. *J. Electron Spectrosc. Relat. Phenom.* **2012**, *185* (1-2), 1-3.
376. An, K.; Park, R.; Kim, J.; Park, C.; Kim, C.; Chung, J.; Kinoshita, T.; Kakizaki, A., Photoemission Study for Mg/Si(111) 1x1 Surface. *J. Electron Spectrosc. Relat. Phenom.* **1996**, *80*, 165-168.

377. Fotea, C.; Callaway, J.; Alexander, M. R., Characterisation of the Surface Chemistry of Magnesium Exposed to the Ambient Atmosphere. *Surf. Interface Anal.* **2006**, *38* (10), 1363-1371.
378. Kurth, M.; Graat, P., Quantitative Analysis of the Plasmon Loss Intensities in X-Ray Photoelectron Spectra of Magnesium. *Surf. Interface Anal.* **2002**, *34* (1), 220-224.
379. Orlita, M.; Faugeras, C.; Plochocka, P.; Neugebauer, P.; Martinez, G.; Maude, D. K.; Barra, A.-L.; Sprinkle, M.; Berger, C.; De Heer, W. A.; Potemski, M., Approaching the Dirac Point in High-Mobility Multilayer Epitaxial Graphene. *Phys. Rev. Lett.* **2008**, *101* (26), 267601.
380. Sprinkle, M.; Siegel, D.; Hu, Y.; Hicks, J.; Tejeda, A.; Taleb-Ibrahimi, A.; Le Fèvre, P.; Bertran, F.; Vizzini, S.; Enriquez, H., First Direct Observation of a Nearly Ideal Graphene Band Structure. *Phys. Rev. Lett.* **2009**, *103* (22), 226803.
381. Miller, D. L.; Kubista, K. D.; Rutter, G. M.; Ruan, M.; de Heer, W. A.; First, P. N.; Stroscio, J. A., Observing the Quantization of Zero Mass Carriers in Graphene. *Science* **2009**, *324* (5929), 924-927.
382. Siegel, D. A.; Park, C.-H.; Hwang, C.; Deslippe, J.; Fedorov, A. V.; Louie, S. G.; Lanzara, A., Many-Body Interactions in Quasi-Freestanding Graphene. *PNAS* **2011**, *108* (28), 11365-11369.
383. Dimitrakopoulos, C.; Lin, Y.-M.; Grill, A.; Farmer, D. B.; Freitag, M.; Sun, Y.; Han, S.-J.; Chen, Z.; Jenkins, K. A.; Zhu, Y.; Liu, Z.; McArdle, T. J.; Ott, J. A.; Wisniewski, R.; Avouris, P., Wafer-Scale Epitaxial Graphene Growth on the Si-Face of Hexagonal SiC(0001) for High Frequency Transistors. *J. Vac. Sci. Technol., B: Nanotech. Microelectron.: Mat. Process., Meas., Phenom.* **2010**, *28* (5), 985-992.
384. Robinson, J. A.; Trumbull, K. A.; LaBella III, M.; Cavalero, R.; Hollander, M. J.; Zhu, M.; Wetherington, M. T.; Fanton, M.; Snyder, D. W., Effects of Substrate Orientation on the Structural and Electronic Properties of Epitaxial Graphene on SiC(0001). *Appl. Phys. Lett.* **2011**, *98* (22), 222109.
385. Min, H.; Sahu, B.; Banerjee, S. K.; MacDonald, A., Ab initio Theory of Gate Induced Gaps in Graphene Bilayers. *Phys. Rev. B* **2007**, *75* (15), 155115.
386. Castro, E. V.; Novoselov, K.; Morozov, S.; Peres, N.; Dos Santos, J. L.; Nilsson, J.; Guinea, F.; Geim, A.; Neto, A. C., Biased Bilayer Graphene: Semiconductor with a Gap Tunable by the Electric Field Effect. *Phys. Rev. Lett.* **2007**, *99* (21), 216802.

387. Gava, P.; Lazzeri, M.; Saitta, A. M.; Mauri, F., Ab initio Study of Gap Opening and Screening Effects in Gated Bilayer Graphene. *Phys. Rev. B* **2009**, *79* (16), 165431.
388. Zhang, Y.; Tang, T.-T.; Girit, C.; Hao, Z.; Martin, M. C.; Zettl, A.; Crommie, M. F.; Shen, Y. R.; Wang, F., Direct Observation of a Widely Tunable Bandgap in Bilayer Graphene. *Nature* **2009**, *459* (7248), 820-823.
389. Taychatanapat, T.; Jarillo-Herrero, P., Electronic Transport in Dual-Gated Bilayer Graphene at Large Displacement Fields. *Phys. Rev. Lett.* **2010**, *105* (16), 166601.
390. Kanayama, K.; Nagashio, K., Gap State Analysis in Electric-Field-Induced Band Gap for Bilayer Graphene. *Sci. Rep.* **2015**, *5* (1), 1-9.
391. Schafhäutl, C., Ueber die Verbindungen des Kohlenstoffes mit Silicium, Eisen und anderen Metallen, welche die verschiedenen Gattungen von Roheisen, Stahl und Schmiedeeisen bilden. *Journal für Praktische Chemie* **1840**, *21* (1), 129-157.
392. Inagaki, M., Applications of Graphite Intercalation Compounds. *J. Mater. Res.* **1989**, *4* (6), 1560-1568.
393. Matsumoto, R.; Arakawa, M.; Yoshida, H.; Akuzawa, N., Alkali-Metal-Graphite Intercalation Compounds Prepared from Flexible Graphite Sheets Exhibiting High Air Stability and Electrical Conductivity. *Synthetic metals* **2012**, *162* (23), 2149-2154.
394. Matsumoto, R.; Akuzawa, N., Structure and Stability of n-and p-Type Intercalated Multilayer Graphene Using Cs-C₂H₄, FeCl₃ and MoCl₅. *Materials Today Communications* **2019**, *20*, 100532.
395. Zhao, W.; Tan, P. H.; Liu, J.; Ferrari, A. C., Intercalation of Few-Layer Graphite flakes with FeCl₃: Raman Determination of Fermi Level, Layer by Layer Decoupling, and Stability. *J. Am. Chem. Soc.* **2011**, *133* (15), 5941-5946.
396. Katagiri, M.; Miyazaki, H.; Matsumoto, R.; Kajita, A.; Sakai, T., Intercalation Doping of Narrow Multilayer Graphene Interconnects with Sub-100 nm Widths. *Jpn. J. Appl. Phys.* **2017**, *56* (7S2), 07KD01.
397. Politou, M.; Wu, X.; Asselberghs, I.; Contino, A.; Soree, B.; Radu, I.; Huyghebaert, C.; Tokei, Z.; De Gendt, S.; Heyns, M., Evaluation of Multilayer Graphene for Advanced Interconnects. *Microelectron. Eng.* **2017**, *167*, 1-5.

398. Ostler, M.; Koch, R. J.; Speck, F.; Fromm, F.; Vita, H.; Hundhausen, M.; Horn, K.; Seyller, T. In *Decoupling the Graphene Buffer Layer from SiC(0001) via Interface Oxidation*, Materials Science Forum, Trans Tech Publ: 2012; pp 649-652.
399. Forti, S.; Emtsev, K.; Coletti, C.; Zakharov, A.; Riedl, C.; Starke, U., Large-Area Homogeneous Quasifree Standing Epitaxial Graphene on SiC(0001): Electronic and Structural Characterization. *Phys. Rev. B* **2011**, *84* (12), 125449.
400. Giovannetti, G.; Khomyakov, P.; Brocks, G.; Karpan, V. v.; Van den Brink, J.; Kelly, P. J., Doping Graphene with Metal Contacts. *Phys. Rev. Lett.* **2008**, *101* (2), 026803.
401. Forti, S.; Link, S.; Stöhr, A.; Niu, Y.; Zakharov, A. A.; Coletti, C.; Starke, U., Semiconductor to Metal Transition in Two-Dimensional Gold and its van der Waals Heterostack with Graphene. *Nat. Commun.* **2020**, *11* (1), 1-7.
402. Bersch, B.; Briggs, N.; Wang, Y.; Jiang, J.; Wang, K.; Dong, C.; Subramanian, S.; Fu, M.; Zou, Q.; Chuang, Y.-W.; Gai, Z.; Li, A.-P.; Zhu, J.; Chang, C.-Z.; Crespi, V. H.; Robinson, J. A., An Air-Stable and Atomically Thin Graphene/Gallium Superconducting Heterostructure. *arXiv preprint arXiv:1905.09938* **2019**.
403. Wang, F.; Shepperd, K.; Hicks, J.; Nevius, M.; Tinkey, H.; Tejeda, A.; Taleb-Ibrahimi, A.; Bertran, F.; Le Fevre, P.; Torrance, D.; First, P. N.; De Heer, W. A.; Zakharov, A.; Conrad, E. H., Silicon Intercalation into the Graphene-SiC Interface. *Phys. Rev. B* **2012**, *85* (16), 165449.
404. Liu, Y.; Guo, J.; Zhu, E.; Liao, L.; Lee, S.-J.; Ding, M.; Shakir, I.; Gambin, V.; Huang, Y.; Duan, X., Approaching the Schottky-Mott Limit in van der Waals Metal-Semiconductor Junctions. *Nature* **2018**, *557* (7707), 696-700.
405. Riordan, M.; Hoddeson, L., Origins of the pn Junction. *IEEE spectrum* **1997**, *34* (6), 46-51.
406. Abe, S.; Nakayama, H.; Nishino, T.; Iida, S., Valence-electron spectral change and charge transfer mechanism of CaSi₂ during CaSi₂-H₂O reaction. *Appl. Surf. Sci.* **1997**, *113*, 562-566.
407. Halstead, P.; Moore, A., The Thermal Dissociation of Calcium Hydroxide. *Journal of the Chemical Society (Resumed)* **1957**, 3873-3875.

408. Han, S.-J.; Yoo, M.; Kim, D.-W.; Wee, J.-H., Carbon Dioxide Capture Using Calcium Hydroxide Aqueous Solution as the Absorbent. *Energy & Fuels* **2011**, *25* (8), 3825-3834.
409. Johnston, J., The Thermal Dissociation of Calcium Carbonate. *J. Am. Chem. Soc.* **1910**, *32* (8), 938-946.
410. Wagner, C.; Passoja, D.; Hillery, H.; Kinisky, T.; Six, H.; Jansen, W.; Taylor, J., Auger and Photoelectron Line Energy Relationships in Aluminum–Oxygen and Silicon–Oxygen Compounds. *J. Vac. Sci. Technol.*, **1982**, *21* (4), 933-944.
411. Okada, K.; Kameshima, Y.; Yasumori, A., Chemical Shifts of Silicon X-Ray Photoelectron Spectra by Polymerization Structures of Silicates. *J. Am. Ceram. Soc.* **1998**, *81* (7), 1970-1972.
412. Tanizawa, Y.; Suzuki, T., Effects of Silicate Ions on the Formation and Transformation of Calcium Phosphates in Neutral Aqueous Solutions. *J. Chem. Soc., Faraday Trans.* **1995**, *91* (19), 3499-3503.
413. Black, L.; Garbev, K.; Stumm, A., Structure, Bonding and Morphology of Hydrothermally Synthesised Xonotlite. *Advances in Applied Ceramics* **2009**, *108* (3), 137-144.
414. Black, L.; Garbev, K.; Stemmermann, P.; Hallam, K. R.; Allen, G. C., Characterisation of Crystalline CSH Phases by X-Ray Photoelectron Spectroscopy. *Cem. Concr. Res.* **2003**, *33* (6), 899-911.
415. Anderson, P. E.; Yee, K.; Homentowski, E.; Cheng, G.; Mehta, N.; Chen, G.; Stec III, D.; Hash, M. C.; Pearson, T.; Culter, R. A. *Effect of Chemistry and Particle Size on the Performance of Calcium Disilicide Primers. Part 1-Synthesis of Calcium Silicide (CaSi₂) by Rotary Atomization*; ARMY ARMAMENT RESEARCH DEVELOPMENT AND ENGINEERING CENTER PICATINNY ARSENAL ...: 2010.
416. Alfonsetti, R.; Lozzi, L.; Passacantando, M.; Picozzi, P.; Santucci, S., XPS Studies on SiO_x Thin Films. *Appl. Surf. Sci.* **1993**, *70*, 222-225.
417. Plattenberger, D. A.; Ling, F. T.; Tao, Z.; Peters, C. A.; Clarens, A. F., Calcium Silicate Crystal Structure Impacts Reactivity with CO₂ and Precipitate Chemistry. *Environmental Science & Technology Letters* **2018**, *5* (9), 558-563.
418. Longo, R. C.; Cho, K.; Brüner, P.; Welle, A.; Gerdes, A.; Thissen, P., Carbonation of Wollastonite(001) Competing Hydration: Microscopic

Insights from Ion Spectroscopy and Density Functional Theory. *ACS Appl. Mater. Interfaces* **2015**, *7* (8), 4706-4712.

419. Svensson, K.; Neumann, A.; Menezes, F. F.; Lempp, C.; Pöllmann, H., The Conversion of Wollastonite to CaCO_3 Considering its use for CCS Application as Cementitious Material. *Applied Sciences* **2018**, *8* (2), 304.
420. Gartner, E.; Hirao, H., A review of alternative approaches to the reduction of CO_2 emissions associated with the manufacture of the binder phase in concrete. *Cem. Concr. Res.* **2015**, *78*, 126-142.
421. Hornetz, B.; Michel, H.; Halbritter, J., ARXPS Studies of SiO_2 -SiC Interfaces and Oxidation of 6H SiC Single Crystal Si-(001) and C-(001) Surfaces. *J. Mater. Res.* **1994**, *9* (12), 3088-3094.
422. Watanabe, H.; Hosoi, T.; Kirino, T.; Kagei, Y.; Uenishi, Y.; Chanthaphan, A.; Yoshigoe, A.; Teraoka, Y.; Shimura, T., Synchrotron X-Ray Photoelectron Spectroscopy Study on Thermally Grown SiO_2 /4H-SiC(0001) Interface and its Correlation with Electrical Properties. *Appl. Phys. Lett.* **2011**, *99* (2), 021907.
423. Rousseau, B.; Estrade-Szwarcopf, H.; Thomann, A.-L.; Brault, P., Stable C-atom Displacements on HOPG Surface Under Plasma Low-Energy Argon-Ion Bombardment. *Applied Physics A* **2003**, *77* (3-4), 591-597.
424. Estrade-Szwarcopf, H., XPS Photoemission in Carbonaceous Materials: A “Defect” Peak Beside the Graphitic Asymmetric Peak. *Carbon* **2004**, *42* (8-9), 1713-1721.
425. Yang, D.-Q.; Sacher, E., Carbon 1s X-ray Photoemission Line Shape Analysis of Highly Oriented Pyrolytic Graphite: The Influence of Structural Damage on Peak Asymmetry. *Langmuir* **2006**, *22* (3), 860-862.
426. Stipp, S. L.; Hochella Jr, M. F., Structure and Bonding Environments at the Calcite Surface as Observed with X-Ray Photoelectron Spectroscopy (XPS) and Low Energy Electron Diffraction (LEED). *Geochimica et Cosmochimica Acta* **1991**, *55* (6), 1723-1736.
427. Kugelmass, I. N.; Shohl, A., The Determination of the Equilibria Involving Calcium, Hydrogen, Carbonate, Bicarbonate, and Primary, Secondary, and Tertiary Phosphate ions. *J. Biol. Chem.* **1924**, *58* (3), 649-666.
428. Ferrari, A. C.; Meyer, J.; Scardaci, V.; Casiraghi, C.; Lazzeri, M.; Mauri, F.; Piscanec, S.; Jiang, D.; Novoselov, K.; Roth, S., Raman Spectrum of Graphene and Graphene Layers. *Phys. Rev. Lett.* **2006**, *97* (18), 187401.

Bibliography

429. Lee, D. S.; Riedl, C.; Krauss, B.; von Klitzing, K.; Starke, U.; Smet, J. H., Raman Spectra of Epitaxial Graphene on SiC and of Epitaxial Graphene Transferred to SiO₂. *Nano Lett.* **2008**, *8* (12), 4320-4325.
430. Saito, R.; Hofmann, M.; Dresselhaus, G.; Jorio, A.; Dresselhaus, M., Raman Spectroscopy of Graphene and Carbon Nanotubes. *Adv. Phys.* **2011**, *60* (3), 413-550.
431. Cançado, L.; Takai, K.; Enoki, T.; Endo, M.; Kim, Y.; Mizusaki, H.; Jorio, A.; Coelho, L.; Magalhaes-Paniago, R.; Pimenta, M., General Equation for the Determination of the Crystallite Size L_a of Nanographite by Raman Spectroscopy. *Appl. Phys. Lett.* **2006**, *88* (16), 163106.
432. Eckmann, A.; Felten, A.; Mishchenko, A.; Britnell, L.; Krupke, R.; Novoselov, K. S.; Casiraghi, C., Probing the Nature of Defects in Graphene by Raman Spectroscopy. *Nano Lett.* **2012**, *12* (8), 3925-3930.
433. Zandiatashbar, A.; Lee, G.-H.; An, S. J.; Lee, S.; Mathew, N.; Terrones, M.; Hayashi, T.; Picu, C. R.; Hone, J.; Koratkar, N., Effect of Defects on the Intrinsic Strength and Stiffness of Graphene. *Nat. Commun.* **2014**, *5* (1), 1-9.
434. Cançado, L. G.; Jorio, A.; Ferreira, E. M.; Stavale, F.; Achete, C. A.; Capaz, R. B.; Moutinho, M. V. d. O.; Lombardo, A.; Kulmala, T.; Ferrari, A. C., Quantifying Defects in Graphene via Raman Spectroscopy at Different Excitation Energies. *Nano Lett.* **2011**, *11* (8), 3190-3196.
435. Fromm, F.; Oliveira Jr, M.; Molina-Sanchez, A.; Hundhausen, M.; Lopes, J.; Riechert, H.; Wirtz, L.; Seyller, T., Contribution of the Buffer Layer to the Raman Spectrum of Epitaxial Graphene on SiC(0001). *New J. Phys.* **2013**, *15* (4), 043031.
436. Leinhard, J. H. No. 1233: Baden Baden-Powell
<https://uh.edu/engines/epi1233.htm> (accessed 18/8/2020).
437. Gray, A., Lord Kelvin's Jubilee. *Nature* **1896**, *54* (1391), 173-181.
438. Chee, S.-S.; Oh, C.; Son, M.; Son, G.-C.; Jang, H.; Yoo, T. J.; Lee, S.; Lee, W.; Hwang, J. Y.; Choi, H., Sulfur Vacancy-Induced Reversible Doping of Transition Metal Disulfides via Hydrazine Treatment. *Nanoscale* **2017**, *9* (27), 9333-9339.
439. Roy, S.; Choi, W.; Jeon, S.; Kim, D.-H.; Kim, H.; Yun, S. J.; Lee, Y.; Lee, J.; Kim, Y.-M.; Kim, J., Atomic Observation of Filling Vacancies in Monolayer Transition Metal Sulfides by Chemically Sourced Sulfur Atoms. *Nano Lett.* **2018**, *18* (7), 4523-4530.

440. Förster, T., Mechanisms of Energy Transfer. In *Comprehensive Biochemistry*, Elsevier: 1967; Vol. 22, pp 61-80.
441. Schweitzer, C.; Schmidt, R., Physical Mechanisms of Generation and Deactivation of Singlet Oxygen. *Chem. Rev.* **2003**, *103* (5), 1685-1758.
442. Yamashita, S. i.; Hamada, M.; Nakanishi, S.; Saito, H.; Nosaka, Y.; Wakida, S. i.; Biju, V., Auger Ionization Beats Photo-Oxidation of Semiconductor Quantum Dots: Extended Stability of Single-Molecule Photoluminescence. *Angew. Chem. Int. Ed.* **2015**, *54* (13), 3892-3896.
443. Nosaka, Y.; Daimon, T.; Nosaka, A. Y.; Murakami, Y., Singlet Oxygen Formation in Photocatalytic TiO₂ Aqueous Suspension. *Phys. Chem. Chem. Phys.* **2004**, *6* (11), 2917-2918.
444. Daimon, T.; Hirakawa, T.; Kitazawa, M.; Suetake, J.; Nosaka, Y., Formation of Singlet Molecular Oxygen Associated with the Formation of Superoxide Radicals in Aqueous Suspensions of TiO₂ Photocatalysts. *Appl. Catal., A* **2008**, *340* (2), 169-175.
445. Zhuang, H. L.; Hennig, R. G., Computational Search for Single-Layer Transition-Metal Dichalcogenide Photocatalysts. *J. Phys. Chem. C* **2013**, *117* (40), 20440-20445.
446. Ding, Q.; Song, B.; Xu, P.; Jin, S., Efficient Electrocatalytic and Photoelectrochemical Hydrogen Generation Using MoS₂ and Related Compounds. *Chem* **2016**, *1* (5), 699-726.
447. Wu, Z.; Fang, B.; Bonakdarpour, A.; Sun, A.; Wilkinson, D. P.; Wang, D., WS₂ Nanosheets as a Highly Efficient Electrocatalyst for Hydrogen Evolution Reaction. *Appl. Catal., B* **2012**, *125*, 59-66.
448. Ahmed, T.; Balendhran, S.; Karim, M. N.; Mayes, E. L.; Field, M. R.; Ramanathan, R.; Singh, M.; Bansal, V.; Sriram, S.; Bhaskaran, M., Degradation of Black Phosphorus is Contingent on UV-Blue Light Exposure. *npj 2D Mater. Appl.* **2017**, *1* (1), 18.
449. Hu, Z.; Li, Q.; Lei, B.; Zhou, Q.; Xiang, D.; Lyu, Z.; Hu, F.; Wang, J.; Ren, Y.; Guo, R., Water-Catalyzed Oxidation of Few-Layer Black Phosphorous in a Dark Environment. *Angew. Chem. Int. Ed.* **2017**, *56* (31), 9131-9135.
450. Hsu, W.-T.; Lu, L.-S.; Wang, D.; Huang, J.-K.; Li, M.-Y.; Chang, T.-R.; Chou, Y.-C.; Juang, Z.-Y.; Jeng, H.-T.; Li, L.-J., Evidence of Indirect Gap in Monolayer WSe₂. *Nat. Commun.* **2017**, *8* (1), 929.

451. Perrozzi, F.; Emamjomeh, S.; Paolucci, V.; Taglieri, G.; Ottaviano, L.; Cantalini, C., Thermal Stability of WS₂ Flakes and Gas Sensing Properties of WS₂/WO₃ Composite to H₂, NH₃ and NO₂. *Sensors and Actuators B: Chemical* **2017**, *243*, 812-822.
452. Jia, Z.; Hu, W.; Xiang, J.; Wen, F.; Nie, A.; Mu, C.; Zhao, Z.; Xu, B.; Tian, Y.; Liu, Z., Grain Wall Boundaries in Centimeter-Scale Continuous Monolayer WS₂ Film Grown by Chemical Vapor Deposition. *Nanotechnology* **2018**, *29* (25), 255705.
453. Nakanishi, T.; Yoshida, S.; Murase, K.; Taniguchi, T.; Watanabe, K.; Shinohara, H.; Kitaura, R., The Atomic and Electronic Structure of 0° and 60° Grain Boundaries in MoS₂. *Frontiers in Physics* **2019**, *7*, 59.
454. Windom, B. C.; Sawyer, W.; Hahn, D. W., A Raman Spectroscopic Study of MoS₂ and MoO₃: Applications to Tribological Systems. *Tribology Letters* **2011**, *42* (3), 301-310.
455. Bernstein, B.; Smith, J., Coefficients of Thermal Expansion for Face-Centered Cubic and Body-Centered Cubic Calcium. *Acta Crystallographica* **1959**, *12* (5), 419-420.
456. Hull, A., The Crystal Structure of Calcium. *Physical Review* **1921**, *17* (1), 42.
457. Moissan, H., Recherches sur le Calcium et ses Composes. *Annales de Chimie et de Physique* **1899**, *XVIII* (7), 289-343.
458. Kong, W.; Li, H.; Qiao, K.; Kim, Y.; Lee, K.; Nie, Y.; Lee, D.; Osadchy, T.; Molnar, R. J.; Gaskill, D. K.; Myers-Ward, R. L.; Daniels, K. M.; Zhang, Y.; Sundram, S.; Yu, Y.; Bae, S.-H.; Rajan, S.; Shao-Horn, Y.; Cho, K.; Ougazzaden, A.; Grossman, J. C.; Kim, J., Polarity Governs Atomic Interaction Through Two-Dimensional Materials. *Nat. Mater.* **2018**, *17* (11), 999-1004.
459. Christensen, N.; Satpathy, S.; Pawlowska, Z., Bonding and Ionicity in Semiconductors. *Phys. Rev. B* **1987**, *36* (2), 1032.
460. Aristov, V. Y.; Urbanik, G.; Kummer, K.; Vyalikh, D. V.; Molodtsova, O. V.; Preobrajenski, A. B.; Zakharov, A. A.; Hess, C.; Hänke, T.; Buchner, B., Graphene Synthesis on Cubic SiC/Si Wafers. Perspectives for Mass Production of Graphene-Based Electronic Devices. *Nano Lett.* **2010**, *10* (3), 992-995.

461. Churcher, N.; Kunc, K.; Heine, V., Ground State Properties of the Group IV Ionic Compound Silicon Carbide. *Solid State Commun.* **1985**, *56* (2), 177-180.
462. Willatzen, M.; Cardona, M.; Christensen, N., Relativistic Electronic Structure, Effective Masses, and Inversion-Asymmetry Effects of Cubic Silicon Carbide (β C-SiC). *Phys. Rev. B* **1995**, *51* (19), 13150.
463. Al Balushi, Z. Y.; Wang, K.; Ghosh, R. K.; Vilá, R. A.; Eichfeld, S. M.; Caldwell, J. D.; Qin, X.; Lin, Y.-C.; DeSario, P. A.; Stone, G.; Subramanian, S.; Paul, D. F.; Wallace, R. M.; Datta, S.; Redwing, J. M.; Robinson, J. A., Two-Dimensional Gallium Nitride Realized via Graphene Encapsulation. *Nat. Mater.* **2016**, *15* (11), 1166-1171.
464. Michałowski, P. P.; Knyps, P.; Ciepielewski, P.; Caban, P. A.; Dumiszewska, E.; Kowalski, G.; Tokarczyk, M.; Baranowski, J. M., Growth of Highly Oriented MoS₂ via an Intercalation Process in the Graphene/SiC(0001) System. *Phys. Chem. Chem. Phys.* **2019**, *21* (37), 20641-20646.
465. Pan, X.; Bao, X., The Effects of Confinement Inside Carbon Nanotubes on Catalysis. *Acc. Chem. Res.* **2011**, *44* (8), 553-562.
466. Fu, Q.; Bao, X., Surface Chemistry and Catalysis Confined Under Two-Dimensional Materials. *Chem. Soc. Rev.* **2017**, *46* (7), 1842-1874.
467. Grommet, A. B.; Feller, M.; Klajn, R., Chemical Reactivity Under Nanoconfinement. *Nat. Nanotechnol.* **2020**, 1-16.
468. Schumacher, S.; Huttmann, F.; Petrović, M.; Witt, C.; Förster, D. F.; Vo-Van, C.; Coraux, J.; Martinez-Galera, A. J.; Sessi, V.; Vergara, I.; Rückamp, R.; Grüninger, M.; Schleheck, N.; Meyer zu Heringdorf, F.; Ohresser, P.; Kralj, M.; Wehling, T. O.; Michely, T., Europium Underneath Graphene on Ir(111): Intercalation Mechanism, Magnetism, and Band Structure. *Phys. Rev. B* **2014**, *90* (23), 235437.
469. Sutter, P.; Sadowski, J. T.; Sutter, E. A., Chemistry Under Cover: Tuning Metal-Graphene Interaction by Reactive Intercalation. *J. Am. Chem. Soc.* **2010**, *132* (23), 8175-8179.
470. Jin, L.; Fu, Q.; Yang, Y.; Bao, X., A Comparative Study of Intercalation Mechanism at Graphene/Ru(0001) Interface. *Surf. Sci.* **2013**, *617*, 81-86.
471. Petrović, M.; Rakić, I. Š.; Runte, S.; Busse, C.; Sadowski, J.; Lazić, P.; Pletikosić, I.; Pan, Z.-H.; Milun, M.; Pervan, P.; Atodiresei, N.; Brako, R.;

- Šokčević, D.; Valla, T.; Michely, T.; Kralj, M., The Mechanism of Caesium Intercalation of Graphene. *Nat. Commun.* **2013**, *4* (1), 1-8.
472. Kaloni, T. P.; Kahaly, M. U.; Cheng, Y.; Schwingenschlögl, U., Mechanism of Si Intercalation in Defective Graphene on SiC. *J. Mater. Chem.* **2012**, *22* (44), 23340-23343.
473. Song, J.; Ouyang, B.; Medhekar, N., Energetics and Kinetics of Li Intercalation in Irradiated Graphene Scaffolds. *ACS Appl. Mater. Interfaces* **2013**, *5* (24), 12968-12974.
474. Sicot, M.; Leicht, P.; Zusan, A.; Bouvron, S.; Zander, O.; Weser, M.; Dedkov, Y. S.; Horn, K.; Fonin, M., Size-Selected Epitaxial Nanoislands Underneath Graphene Moiré on Rh(111). *ACS nano* **2012**, *6* (1), 151-158.
475. Boukhvalov, D.; Katsnelson, M., Destruction of Graphene by Metal Adatoms. *Appl. Phys. Lett.* **2009**, *95* (2), 023109.
476. Sicot, M.; Fagot-Revurat, Y.; Kierren, B.; Vasseur, G.; Malterre, D., Copper Intercalation at the Interface of Graphene and Ir(111) Studied by Scanning Tunneling Microscopy. *Appl. Phys. Lett.* **2014**, *105* (19), 191603.
477. Cui, Y.; Gao, J.; Jin, L.; Zhao, J.; Tan, D.; Fu, Q.; Bao, X., An Exchange Intercalation Mechanism for the Formation of a Two-Dimensional Si Structure Underneath Graphene. *Nano Research* **2012**, *5* (5), 352-360.
478. Nath, A.; Currie, M.; Boyd, A. K.; Wheeler, V. D.; Koehler, A. D.; Tadjer, M. J.; Robinson, Z. R.; Sridhara, K.; Hernandez, S. C.; Wollmershauser, J. A.; Robinson, J. T.; Myers-Ward, R. L.; Rao, M. V.; Gaskill, D. K., In Search of Quantum-Limited Contact Resistance: Understanding the Intrinsic and Extrinsic Effects on the Graphene-Metal Interface. *2D Mater.* **2016**, *3* (2), 025013.
479. Ropp, R. C., *Encyclopedia of the Alkaline Earth Compounds*. Newnes: 2012.
480. Mito, Y.; Ogino, A.; Konno, S.; Udono, H., Influence of Humidity, Volume Density, and MgO Impurity on Mg₂Si Thermoelectric-Leg. *J. Electron. Mater.* **2017**, *46* (5), 3103-3108.
481. Gill, A., The Thermal Dehydration or Decomposition of Certain Minerals and Salts. *Canadian Journal of Research* **1934**, *10* (6), 703-712.
482. Fournier, V.; Marcus, P.; Olefjord, I., Oxidation of Magnesium. *Surf. Interface Anal.* **2002**, *34* (1), 494-497.

483. Santamaria, M.; Di Quarto, F.; Zanna, S.; Marcus, P., Initial Surface Film on Magnesium Metal: A Characterization by X-Ray Photoelectron Spectroscopy (XPS) and Photocurrent Spectroscopy (PCS). *Electrochimica Acta* **2007**, *53* (3), 1314-1324.
484. Landoulsi, J.; Genet, M. J.; Fleith, S.; Touré, Y.; Liascukiene, I.; Méthivier, C.; Rouxhet, P. G., Organic Adlayer on Inorganic Materials: XPS Analysis Selectivity to Cope with Adventitious Contamination. *Appl. Surf. Sci.* **2016**, *383*, 71-83.
485. Khairallah, F.; Glisenti, A., XPS Study of MgO Nanopowders Obtained by Different Preparation Procedures. *Surface Science Spectra* **2006**, *13* (1), 58-71.
486. Yamamoto, S.; Bluhm, H.; Andersson, K.; Ketteler, G.; Ogasawara, H.; Salmeron, M.; Nilsson, A., In Situ X-Ray Photoelectron Spectroscopy Studies of Water on Metals and Oxides at Ambient Conditions. *Journal of Physics: Condensed Matter* **2008**, *20* (18), 184025.
487. Chen, C.; Splinter, S.; Do, T.; McIntyre, N., Measurement of Oxide Film Growth on Mg and Al Surfaces over Extended Periods Using XPS. *Surf. Sci.* **1997**, *382* (1-3), L652-L657.
488. Liu, M.; Zanna, S.; Ardelean, H.; Frateur, I.; Schmutz, P.; Song, G.; Atrens, A.; Marcus, P., A First Quantitative XPS Study of the Surface Films Formed, by Exposure to Water, on Mg and on the Mg-Al Intermetallics: Al_3Mg_2 and $\text{Mg}_{17}\text{Al}_{12}$. *Corrosion Science* **2009**, *51* (5), 1115-1127.
489. Banhart, F.; Kotakoski, J.; Krasheninnikov, A. V., Structural Defects in Graphene. *ACS nano* **2011**, *5* (1), 26-41.
490. Önneby, C.; Pantano, C. G., Silicon Oxycarbide Formation on SiC Surfaces and at the SiC/SiO₂ Interface. *J. Vac. Sci. Technol., A* **1997**, *15* (3), 1597-1602.
491. Soukiassian, P.; Amy, F., Silicon Carbide Surface Oxidation and SiO₂/SiC Interface Formation Investigated by Soft X-Ray Synchrotron Radiation. *J. Electron Spectrosc. Relat. Phenom.* **2005**, *144*, 783-788.
492. Johansson, L.; Owman, F.; Mårtensson, P., High-Resolution Core-Level Study of 6H-SiC(0001). *Phys. Rev. B* **1996**, *53* (20), 13793.
493. Amy, F.; Soukiassian, P.; Hwu, Y.; Brylinski, C., Identification of the 6H-SiC(0001) 3×3 Surface Reconstruction Core-Level Shifted Components. *Surf. Sci.* **2000**, *464* (1), L691-L696.

Bibliography

494. Rich, D.; Miller, T.; Samsavar, A.; Lin, H.; Chiang, T.-C., Adsorption and Growth of Sn on Si(100) From Synchrotron Photoemission Studies. *Phys. Rev. B* **1988**, *37* (17), 10221.
495. Black, L.; Garbev, K.; Stemmermann, P.; Hallam, K. R.; Allen, G. C., X-Ray Photoelectron Study of Oxygen Bonding in Crystalline C-S-H Phases. *Phys. Chem. Miner.* **2004**, *31* (6), 337-346.
496. Gruschwitz, M.; Schletter, H.; Schulze, S.; Alexandrou, I.; Tegenkamp, C., Epitaxial Graphene on 6H-SiC(0001): Defects in SiC Investigated by STEM. *Physical Review Materials* **2019**, *3* (9), 094004.
497. Ristein, J.; Mammadov, S.; Seyller, T., Origin of Doping in Quasi-Free-Standing Graphene on Silicon Carbide. *Phys. Rev. Lett.* **2012**, *108* (24), 246104.
498. Eigler, D. M.; Schweizer, E. K., Positioning Single Atoms with a Scanning Tunnelling Microscope. *Nature* **1990**, *344* (6266), 524-526.

A

Appendix A Tungsten Disulphide

A1. MATLAB Code for WS₂ PL Peak Mapping

```
% Script that reads in Witec maps and sorts the data based on spectral
% position rather than CCD counts in a spectral range.
% Created by Jimmy C. Kotsakidis
% Date started: 12/03/18
% V1.0

clear variables
clc
close all

%-----
Data = load('Scan_ooo_Spec.Data 1_F.txt'); %Load data here

% This loads the x variable in column 1, and the y data in the rest of
% the
% columns

x = Data(:,1);

% fundamental physical constants to convert to eV

h = 4.135667662E-15; % eV/s
c = 299792458; %m/s

% x is in wavelengths, to convert to eV

x = (h*c)./(x*1E-9);
```

```

y = Data(:,2:end);

%step size of x

x_step = x(1) - x(2);

%user defined input range of data

x_upper = input('Please input upper energy range number value
[eV]\n')
x_lower = input('Please input lower energy range number value
[eV]\n')

%Define smaller range of x - set energy limits

x_value_upper = find(x<(x_upper+(x_step/2)) & x>(x_upper-
(x_step/2)));
dimension = size(x_value_upper);

if dimension(1) > 1
    x_value_upper = x_value_upper(1);
end

x_value_lower = find(x<(x_lower+(x_step/2)) & x>(x_lower-
(x_step/2)));
dimension = size(x_value_lower);

if dimension(1) > 1
    x_value_lower = x_value_lower(1);
end

%define the map size.

spectral_map = zeros(1,length(y(1,:)));

for z = 1:length(y(1,:)) %Peak finding algorithm

    a = y(:,z);

```

```

a = a(x_value_upper:x_value_lower);

max_val = max(a); %finds max value in y in range of interest, 1.92-2.08eV.

location = find(a==max(a)); %finds location of max value in y

%typically there will be more than 1 maxima, will average it out
true_location = round(mean(location));

x_modified_range = x(x_value_upper:x_value_lower);

energy_of_peak = x_modified_range(location(1,1)); %correlates this
to energy in x.

spectral_map(1,z) = energy_of_peak;

end

%adjust scale bar to ones liking

scale_min = x(x_value_lower);
scale_max = x(x_value_upper);

clims = [scale_min scale_max];

% convert spectral_map into a 2D matrix

spectral_map_2D = vec2mat(spectral_map,sqrt(length(y(:,1))));

%spectral_map_2D = (reshape(spectral_map,[28,24]));

figure()
imagesc(spectral_map_2D,clims)
colorbar

```

A2. Photoluminescence Quenching of WS₂ After Oxidation

In [Chapter 4](#), photoluminescence maps of pristine WS₂ were shown, and it is expected that the conversion of WS₂ to WO_x ($1 < x \leq 3$) should result in a decreased PL response, as was observed by Gao *et al.* [[207](#)]. [Figure A.2-1](#) shows the photoluminescent (PL) mapping results for crystals grown similarly to those in [Chapter 4](#). The PL maps in [Figure A.2-1a-b](#) were taken with the same setup and similar parameters to the PL map in [Figure 4.10a-b](#): 532 nm laser at 350 μ W (this measurement was taken before the objective, so the power is likely $\approx 70 \mu$ W lower), $53 \times 53 \mu\text{m}^2$, 100 points per line and ≈ 24 s integration time (see [Methods Section 4.3.2](#)). It is immediately apparent upon comparison of [Figure A.2-1a-b](#) and [Figure 4.10a](#), that the photoluminescence intensity from the oxidised crystals in [Figure A.2-1](#) is severely diminished, or ‘quenched’ after oxidation. This is especially apparent along the three-fold symmetric lines extending outwards from the centre of the crystal, which were shown to harbour a greater concentration of oxidation ‘islands’ in [Chapter 4](#). The observation of little to no PL in these three-fold symmetric regions is in agreement with the LSCM and AFM observations in [Chapter 4](#) of more tungsten oxide in these regions.

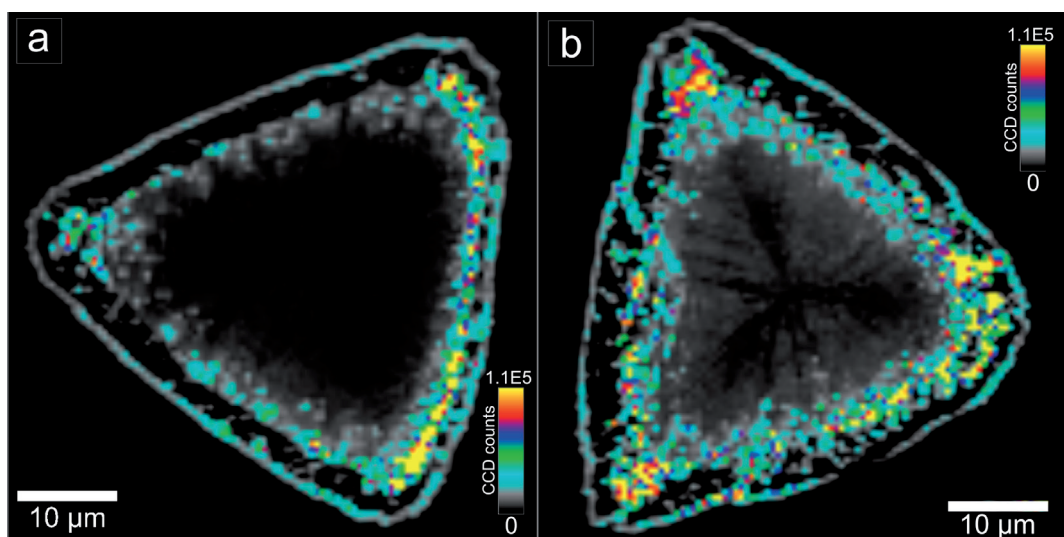


FIGURE A.2-1: PHOTOLUMINESCENCE (PL) MAPPING SPECTROSCOPY MEASUREMENT OF MONOLAYER WS₂ AFTER OXIDATION SHOWING PL INTENSITY.

(a-b) Similarly grown WS₂ crystals to the sample in [Figure 4.10](#) showing effects of oxidation. The PL intensity of the crystal has been severely quenched, especially along the 3-fold symmetric lines which possesses greater amounts of oxidation.

B

Appendix B Calcium Intercalation

B1. Functions used for the fitting of XPS components

The graphene peaks are fit using a Breit-Wigner-Fano (BWF) function described by:

$$y = y_0 + \frac{H \left(1 + \frac{x - x_c}{QW_L} \right)^2}{1 + \left(\frac{x - x_c}{W_L} \right)^2} \quad (B1.1)$$

where y_0 is the baseline, x_c is the peak centre, H is the height (counts per second, cps), W_L is the width (in eV) of the Lorentzian contribution and Q is the Asymmetry parameter. As $Q \rightarrow \infty$, the BWF lineshape becomes Lorentzian. This function thus represents an asymmetric transformation of the Lorentzian profile.

For all other non-graphene peaks, a Voigt profile in was implemented:

$$y = y_0 + A \frac{2\ln 2}{\pi^{\frac{3}{2}}} \frac{W_L}{W_G^2} \int_{-\infty}^{\infty} \frac{e^{-t^2}}{(\sqrt{\ln 2}) \frac{W_L}{W_G})^2 + ((\sqrt{4\ln 2}) \frac{x - x_c}{W_G} - t)^2} dt \quad (B1.2)$$

Where y_0 is the baseline, x_c is the peak centre, A is the area, W_G is the Gaussian full width at half maximum (FWHM, in eV) and W_L is the Lorentzian FWHM (in eV). The Voigt FWHM was calculated as:

$$FWHM = 0.5346W_L + \sqrt{0.2166W_L^2 + W_G^2} \quad (B1.3)$$

The RI ratio (RI_R) in the main text is calculated via:

$$RI_R = \frac{RI \text{ (lower } E_{hv})}{RI \text{ (higher } E_{hv})} \quad (B1.4)$$

Where RI is the relative intensity of the component, referenced to the suitable bulk component (B_{Si}/B_C for EMLG, B_{Si}^H/B_C^H for H-QFSBLG – see [Table B.2-1 – Table B.2-5](#)).

B2. Complete C 1s and Si 2p Table of Values for Ca-intercalation Experiments

TABLE B.2-1: Si 2p CORE LEVEL FIT PARAMETERS FOR COMPONENTS IN FIGURE 5.4 AND FIGURE B.3-4.

Table gives binding energies of both $2p_{3/2}$ and $2p_{1/2}$ peaks are given, as well as the relative intensity (RI) of the $2p_{3/2}$ peaks as referenced to the bulk Si peak ' B_{Si} ' corresponding to pristine SiC prior to Ca intercalation. W_G refers to the Gaussian FWHM for the Voigt fit (which was fixed to one of two values, except for component Ox_2), whereas the Lorentzian FWHM (W_L) was kept constant at 0.1 eV in all fits. Dash line corresponds to no observation.

TABLE B.2-2: Si 2p CORE LEVEL FIT PARAMETERS FOR COMPONENTS SHOWN IN FIGURE 5.4 AND FIGURE B.3-4.

Binding energies of both $2p_{3/2}$ and $2p_{1/2}$ peaks are given, as well as the relative intensity (RI) of the $2p_{3/2}$ peaks as referenced to the bulk Si peak ' B_{Si} ' (see Table B.2-1) corresponding to pristine SiC prior to Ca intercalation. W_G refers to the Gaussian FWHM for the Voigt fit, whereas the Lorentzian FWHM was set at 0.1 eV. A dash indicates that the quantity could not be measured.

EMLG, Si 2p		(a), (b), Pristine EMLG			
Component	E_{hv} (eV)	E_B (eV) $2p_{3/2}$	E_B (eV) $2p_{1/2}$	RI	W_G (eV)
A_o	150	99.20	99.80	0.016	0.5
	600	-	-	-	-
A_i	150	100.38	100.98	0.036	0.5
	600	100.30	100.94	0.018	0.5
A_2	150	100.96	101.56	0.071	0.5
	600	100.96	101.56	0.042	0.5

Complete C 1s and Si 2p Table of Values for Ca-intercalation Experiments

TABLE B.2-3: C 1s CORE LEVEL FIT PARAMETERS FOR PRISTINE AND Ca-INTERCALATED EMLG COMPONENTS SHOWN IN FIGURE 5.5 AND FIGURE B.3-1. Binding energy (E_B), relative intensity (RI) and asymmetry/Lorentzian FWHM (Q/W_L (eV)) parameters for all peaks. The RI values are referenced to the bulk SiC component ' B_C '. The 'G' component height was approximated using the BWF fit (i.e. G_o). All SiC related components were fit using Voigt functions with $W_G = 0.4$ eV and $W_L = 0.2$ eV. Buffer layer components S_1 and S_2 were fit using wider Voigt functions. A dash indicates that a measurement was not possible.

EMLG, C 1s		(a), (b), Pristine EMLG			(c), (d) 1 st Ca Intercalation			(e), (f) 2 nd Ca Intercalation		
Component	E_{hv} (eV)	E_B (eV)	RI	Q/W_L or W_L/W_G (eV)	E_B (eV)	RI	Q/W_L or W_L/W_G (eV)	E_B (eV)	RI	Q/W_L or W_L/W_G (eV)
S ₂	330	285.48	5.63	0.4/0.8						
	600	285.55	0.48	0.4/0.8						
S ₁	330	285	2.62	0.4/0.7						
	600	285	0.25	0.4/0.7						
G	330	284.83	35.0	12/0.2						
	600	284.82	2.47	9/0.2						
G'	330				284.88	30.94	9/0.2	284.89	26.75	9/0.2
	600				284.86	2.37	9/0.2	284.88	2.09	9/0.2
Z _C	330	284.05	0.75	0.2/0.4	284.05	0.17	0.2/0.4	284.05	0.18	0.2/0.4
	600	284.05	0.43	0.2/0.4	-	-	-	284.05	0.02	0.2/0.4
Z' _C	330				282.7	0.28	0.2/0.4	282.70	0.31	0.2/0.4
	600				282.65	0.22	0.2/0.4	282.73	0.22	0.2/0.4
B _C	330	283.7	1	0.2/0.4	283.7	0.30	0.2/0.4	283.77	0.29	0.2/0.4
	600	283.71	1	0.2/0.4	283.71	0.03	0.2/0.4	283.78	0.04	0.2/0.4
B' _C	330				282.28	0.62	0.2/0.4	282.35	0.52	0.2/0.4
	600				282.30	0.82	0.2/0.4	282.38	0.77	0.2/0.4
S _C [*]	330				283.25	0.41	0.2/0.4	283.27	0.66	0.2/0.4
	600				283.25	0.06	0.2/0.4	283.27	0.08	0.2/0.4

TABLE B.2-4: Si 2p CORE LEVEL FIT PARAMETERS FOR PRISTINE AND Ca-INTERCALATED H-QFSBLG COMPONENTS SHOWN IN FIGURE B.4-2.

Both $2p_{3/2}$ and $2p_{1/2}$ binding energies are presented, as well as the relative intensity (RI) of the peaks as referenced to the bulk SiC component, B_{Si}^H ($2p_{3/2}$ peak) corresponding to pristine SiC underneath H-QFSBLG prior to Ca-intercalation. W_G refers to the Gaussian FWHM for the Voigt fit, whereas the Lorentzian FWHM (W_L) was kept constant at 0.1 eV in all fits.

H-QFSBLG, Si 2p		(a), (b), Pristine H-QFSBLG				(c), (d) 1 st Ca Intercalation				(e), (f) 2 nd Ca Intercalation			
Component	E_{hv} (eV)	E_B (eV) $2p_{3/2}$	E_B (eV) $2p_{1/2}$	RI	W_G (eV)	E_B (eV) $2p_{3/2}$	E_B (eV) $2p_{1/2}$	RI	W_G (eV)	E_B (eV) $2p_{3/2}$	E_B (eV) $2p_{1/2}$	RI	W_G (eV)
B_{Si}^H	150	100.31	100.92	1	0.4								
	600	100.25	100.88	1	0.4								
H_{Si}	150	100.64	101.24	0.263	0.4								
	600	100.57	101.17	0.309	0.4								
B_{Si}	150					100.10	100.70	0.211	0.5	100.08	100.68	0.184	0.5
	600					100.08	100.68	0.758	0.5	100.08	100.68	0.715	0.5
Z_{Si}	150					100.48	101.11	0.099	0.5	100.45	101.10	0.086	0.5
	600					100.55	101.15	0.078	0.5	100.50	101.10	0.101	0.5
S_{Si}^*	150					100.97	101.57	0.026	0.5	100.97	101.6	0.034	0.5
	600					100.97	101.57	0.031	0.5	100.95	101.55	0.031	0.5
Ca_{Si}	150					99.33	99.93	0.224	0.5	99.30	99.90	0.203	0.5
	600					99.25	99.85	0.086	0.5	99.24	99.84	0.091	0.5

Complete C 1s and Si 2p Table of Values for Ca-intercalation Experiments

TABLE B.2-5: C 1s CORE LEVEL FIT PARAMETERS FOR PRISTINE AND Ca-INTERCALATED H-QFSBLG SHOWN IN FIGURE B.4-1.

Binding energies (E_B) and asymmetry/Lorentzian FWHM (Q/W_L) parameters for H-QFSBLG components are shown. The relative intensities (RI) are referenced to the bulk SiC component ' B_{Si}^H '. All SiC related components were fit with Voigt function, and graphene functions fit with BWF (asymmetric) functions.

H-QFSBLG, C 1s		(a), (b), Pristine H-QFSBLG			(c), (d) 1 st Ca Intercalation			(e), (f) 2 nd Ca Intercalation		
Component	E_{hv} (eV)	E_B (eV)	RI	Q/W_L or W_L/W_G (eV)	E_B (eV)	RI	Q/W_L or W_L/W_G (eV)	E_B (eV)	RI	Q/W_L or W_L/W_G (eV)
G^H	330	284.36	51.85	18/0.135						
	600	284.37	3.611	11/0.15						
G'	330				284.89	24.91	9/0.2	284.90	23.37	9/0.2
	600				284.87	1.859	9/0.2	284.89	1.836	9/0.2
B_C	330	283.65	0.160	0.2/0.4	283.70	0.226	0.2/0.4	283.72	0.264	0.2/0.4
	600	283.70	0.021	0.2/0.4	283.71	0.028	0.2/0.4	283.70	0.035	0.2/0.4
B_C'	330				282.32	0.566	0.2/0.4	282.30	0.519	0.2/0.4
	600				282.32	0.75	0.2/0.4	282.32	0.753	0.2/0.4
S_C^*	330	283.24	0.231	0.2/0.4	283.25	0.283	0.2/0.4	283.25	0.462	0.2/0.4
	600	283.30	0.035	0.2/0.4	283.20	0.046	0.2/0.4	283.23	0.063	0.2/0.4
Z_C	330				284.05	0.113	0.2/0.4	284.05	0.160	0.2/0.4
	600				284.05	0.011	0.2/0.4	284.05	0.018	0.2/0.4
Z_C'	330				282.68	0.198	0.2/0.4	282.68	0.179	0.2/0.4
	600				282.67	0.183	0.2/0.4	282.67	0.176	0.2/0.4
H_C	330	282.85	0.259	0.2/0.4						
	600	282.85	0.183	0.2/0.4						
B_C^H	330	282.56	1	0.2/0.4						
	600	282.56	1	0.2/0.4						

TABLE B.2-6: C 1s CORE LEVEL FIT PARAMETERS FOR SAMPLE EMLG#2 USED IN AMBIENT AIR EXPOSURE EXPERIMENTS SHOWN IN FIGURE 7.1a-c.

Binding energies (E_B) and asymmetry/Lorentzian FWHM (Q/W_L) parameters for components are shown. All SiC related components were fit with Voigt function, and graphene functions fit with BWF (asymmetric) functions.

EMLG, C 1s Ambient Air		(a) Pristine EMLG		(b) Pristine Ca-QFSBLG		(c) Ambient Air (30 min) Exposure of Ca-QFSBLG	
Component	E_{hv} (eV)	E_B (eV)	Q/W_L or W_L/W_G (eV)	E_B (eV)	Q/W_L or W_L/W_G (eV)	E_B (eV)	Q/W_L or W_L/W_G (eV)
S ₂	600	285.53	0.4/0.8				
S ₁	600	285.05	0.4/0.7				
G	600	284.79	9/0.21				
G'	600			284.85	9/0.2	284.80	12/0.2
Z _C	600	284.02	0.2/0.4				
Z'_C	600			282.75	0.2/0.4	282.75	0.2/0.4
Z _{air} ⁱ						283.30	0.2/0.4
B _C	600	283.70	0.2/0.4	283.72	0.2/0.4		0.2/0.4
B'_C	600			282.43	0.2/0.4	282.40	0.2/0.4
B _{air} ⁱ	600					282.96	0.2/0.4
S _C [*]	600			283.22	0.2/0.4		

TABLE B.2-7: Si 2p CORE LEVEL FIT PARAMETERS FOR PRISTINE Ca-QFSBLG AND 30-MINUTE AMBIENT AIR EXPOSED Ca-QFSBLG, FABRICATED FROM SAMPLE EMLG#2 ([FIGURE 7.2a, c](#)).

Table gives binding energies of both $2p_{3/2}$ and $2p_{1/2}$ peaks. W_G refers to the Gaussian FWHM for the Voigt fit (which was fixed to one of two values, except for component Ox_2), whereas the Lorentzian FWHM (W_L) was kept constant at 0.1 eV in all fits.

Ca-QFSBLG, Si 2p		(a) Pristine Ca-QFSBLG			(c) 30-minute Ambient Air Exposure		
Component	E_{hv} (eV)	E_B (eV) $2p_{3/2}$	E_B (eV) $2p_{1/2}$	W_G (eV)	E_B (eV) $2p_{3/2}$	E_B (eV) $2p_{1/2}$	W_G (eV)
Ox_1	150	98.90	99.50	0.5			
B_{Si}^i	150	100.09	100.69	0.5	100.10	100.70	0.5
B_{air}^i	150				100.77	101.40	0.6
Z_{Si}^i	150	100.43	101.06	0.5	100.45	101.05	0.5
Z_{air}^i	150				101.10	101.70	0.6
S_{Si}^*	150	100.93	101.53	0.5			
$CaSi$	150	99.37	99.94	0.5	99.30	99.90	0.5
$CaSiO$	150				102.25	102.85	0.7

TABLE B.2-8: C 1s CORE LEVEL FIT PARAMETERS FOR Ca-INTERCALATED SAMPLE EMLG#3 (Ca-QFSBLG) USED IN AMBIENT AIR EXPOSURE EXPERIMENTS SHOWN IN [FIGURE 7.1d](#).

Binding energies (E_B) and asymmetry/Lorentzian FWHM (Q/W_L) parameters for components are shown. All SiC related components were fit with Voigt function, and graphene functions fit with BWF (asymmetric) functions.

Ca-QFSBLG, C 1s		(d) Ambient Air (9-hour) Exposure of Ca-QFSBLG	
Component	E_{hv} (eV)	E_B (eV)	Q/W_L or W_L/W_G (eV)
G'	600	284.77	12/0.2
Z _{air} ^f	600	282.95	0.2/0.4
Z _{air} ⁱ	600	283.28	0.2/0.4
B _{air} ^f	600	282.60	0.2/0.4
B _{air} ⁱ	600	282.90	0.2/0.4

Complete C 1s and Si 2p Table of Values for Ca-intercalation Experiments

TABLE B.2-9: Si 2p CORE LEVEL FIT PARAMETERS FOR PRISTINE Ca-QFSBLG AND 30-MINUTE AMBIENT AIR EXPOSED Ca-QFSBLG, FABRICATED FROM SAMPLE EMLG#2 (FIGURE 7.2b, d).

Table gives binding energies of both $2p_{3/2}$ and $2p_{1/2}$ peaks. W_G refers to the Gaussian FWHM for the Voigt fit (which was fixed to one of two values, except for component Ox_2), whereas the Lorentzian FWHM (W_L) was kept constant at 0.1 eV in all fits.

EMLG, Si 2p		(b) Pristine Ca-QFSBLG			(d) 9-hour Ambient Air Exposure		
Component	E_{hv} (eV)	E_B (eV) $2p_{3/2}$	E_B (eV) $2p_{1/2}$	W_G (eV)	E_B (eV) $2p_{3/2}$	E_B (eV) $2p_{1/2}$	W_G (eV)
Ox_1	150	98.87	99.47	0.5			
B'_{Si}	150	100.09	100.70	0.5			
B^i_{air}	150				100.75	101.38	0.6
B^f_{air}	150				100.28	101.88	0.6
Z'_{Si}	150	100.45	101.06	0.5			
Z^i_{air}	150				101.10	101.70	0.6
Z^f_{air}	150				100.55	101.05	0.6
S^*_{Si}	150	101.00	101.61	0.5			
$CaSi$	150	99.40	100.00	0.5			
$CaSiO$	150				102.20	102.82	0.7

TABLE B.2-10: C 1S CORE LEVEL FIT PARAMETERS FOR PHENOMENOLOGICAL PLASMON COMPONENTS IN FIGURE 7.1b-d.

Components G_1 , G_2 and G_3 comprised the phenomenological fit to the plasmon losses. The fit parameters shown are binding energy (E_B), relative intensity (RI), and full width at half maximum (FWHM). All components were fit using Voigt functions. The RI was referenced to the corresponding pristine EMLG bulk peak B_C .

Ca-QFSBLG, C 1s		(b) Pristine Ca-QFSBLG			(c) 30-minute Ambient Air exposure			(d) 9-hour Ambient Air Exposure		
Component	E_{hv} (eV)	E_B (eV)	RI	FWHM (eV)	E_B (eV)	RI	FWHM (eV)	E_B (eV)	RI	FWHM (eV)
G_1	600	285.25	0.510	0.78	285.2	0.400	0.78	285.2	0.350	0.78
G_2	600	285.85	0.253	0.87	285.9	0.125	0.87	285.9	0.099	0.87
G_3	600	286.62	0.100	1.1	286.7	0.063	1.1	286.75	0.048	1.1

TABLE B.2-11: C 1s CORE LEVEL FIT PARAMETERS FOR PRISTINE EMLG AND SEPARATE Ca-QFSBLG SAMPLE (SAME SAMPLE FROM TABLE B.2-1/TABLE B.2-3) AFTER EXPOSURE TO THE AMBIENT AIR FOR 1 YEAR (FIGURE 7.5).

Binding energies (E_B) and asymmetry/Lorentzian FWHM (Q/W_L) parameters for components are shown. All SiC related components were fit with Voigt function, and graphene functions fit with BWF (asymmetric) functions.

EMLG, C 1s Ambient Air		(a) Pristine EMLG		(b) Ambient Air (1-year) Exposure of Ca-QFSBLG	
Component	E_{hv} (eV)	E_B (eV)	Q/W_L or W_G/W_L (eV)	E_B (eV)	Q/W_L or W_G/W_L (eV)
S ₂	1486.6	285.50	1.0/0.5		
S ₁	1486.6	285.00	1.0/0.5		
G	1486.6	284.72	14/0.43		
B _C	1486.6	283.78	0.7/0.3		
B _{air} ^f	1486.6			282.50	0.7/0.3
G _{air} '	1486.6			284.59	14/0.43
sp ₃	1486.6			285.76	1.0/0.5
CO ₃ ²⁻	1486.6			289.47	1.0/0.3
HCO ₃ ⁻	1486.6			290.50	1.0/0.3

B3. Complete C 1s and Si 2p XPS Spectra for Ca-QFSBLG Fabricated from Pristine EMLG

The Ca-intercalation results shown in the Si 2p and C 1s core levels of [Figure 5.4](#) and [Figure 5.5](#), respectively, had an intermediary intercalation step, shown in [Figure B.3-1](#) and [Figure B.3-2](#). Furthermore, [Figure B.3-1](#) illustrates the phenomenological method used for fitting the doped graphene peak caused by plasmon losses [25, 296]. In order to fit these plasmon losses, use of a series of monotonically decreasing (in intensity) peaks – labelled G₀, G₁, G₂ and G₃ (these peaks comprise component G' in [Figure 5.5](#) of the manuscript) to account for the graphene (G₀) and plasmon losses (G₁ – G₃), respectively – was implemented. The fit parameters of the plasmon loss components can be found in [Table B.3-1](#). It should be stated here that component G' in [Table B.2-3](#) and [Table B.2-5](#) refer to the G₀ peak position (since this was aligned with the graphene peak). The asymmetry parameter (Q) also references the BWF fit of the G₀ peak (and is thus not shown in [Table B.3-1](#)). The peak parameters for all other C 1s components can be found in [Table B.2-3](#).

TABLE B.3-1: PHENOMENOLOGICAL PLASMON LOSS FIT PARAMETERS FOR Ca-QFSBLG IN [FIGURE B.3-1](#).

Components G₁, G₂ and G₃ comprised the phenomenological fit to the plasmon losses. The fit parameters shown are binding energy (E_B), relative intensity (RI), and full width at half maximum (FWHM). All components were fit using Voigt functions using [Equation B1.2](#).

EMLG, C 1s		(a), (b), 1 st Ca Intercalation			(c), (d) 2 nd Ca Intercalation		
Component	E _{hv} (eV)	E _B (eV)	RI	FWHM (eV)	E _B (eV)	RI	FWHM (eV)
G ₁	330	285.2	4.21	0.78	285.2	4.11	0.78
	600	285.25	0.53	0.78	285.25	0.51	0.78
G ₂	330	285.8	2.70	0.87	285.785	3.46	0.87
	600	285.95	0.28	0.87	285.95	0.30	0.87
G ₃	330	286.5	0.74	1.1	286.5	1.05	1.1
	600	286.8	0.11	1.1	286.8	0.13	1.1

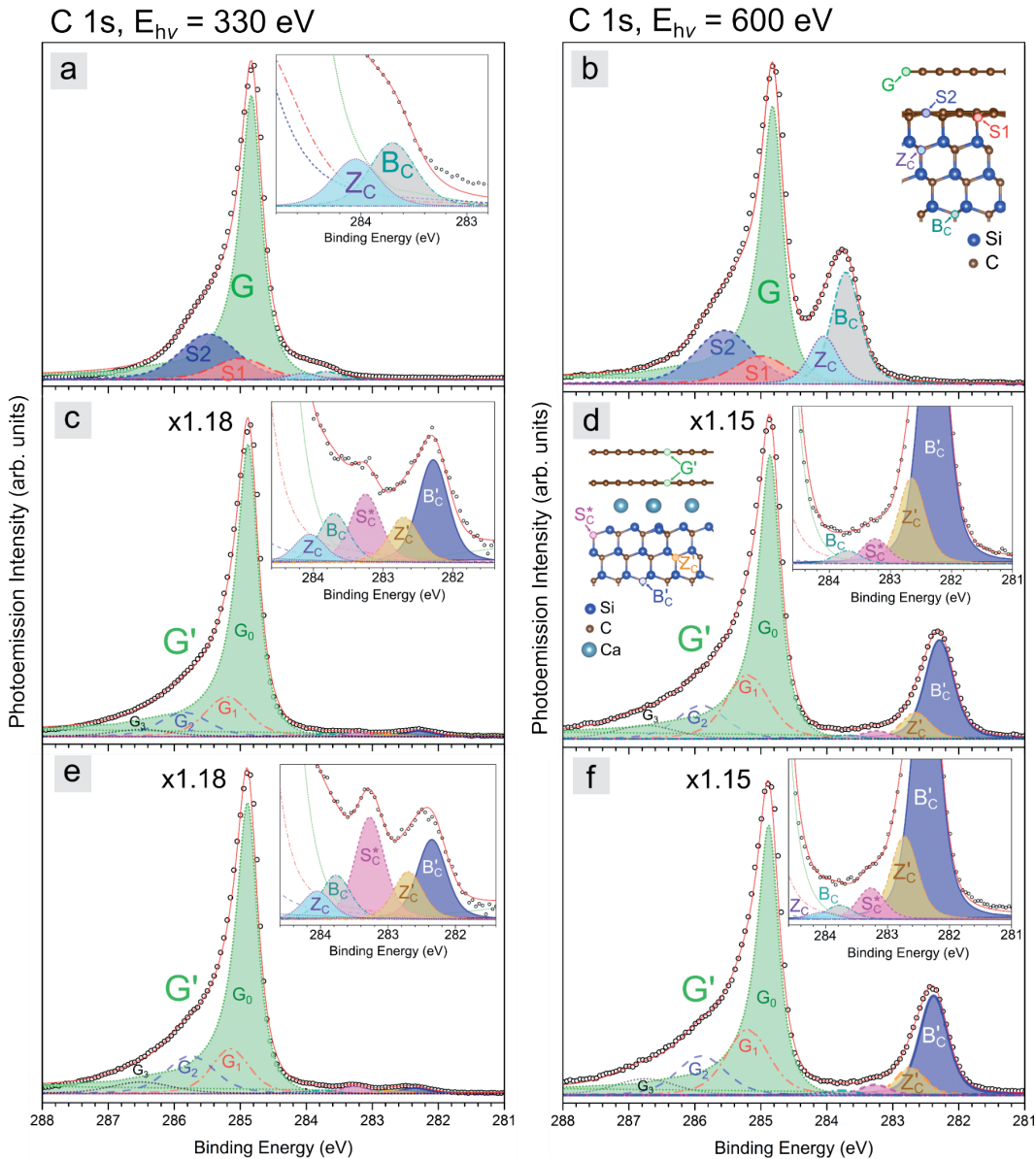


FIGURE B.3-1: X-RAY PHOTOEMISSION SPECTRA SHOWING THE C 1s CORE LEVEL OF PRISTINE EMLG AND Ca-QFSBLG AT TWO X-RAY ENERGIES, $E_{hv} = 330$ eV (LEFT, SURFACE SENSITIVE) AND $E_{hv} = 600$ eV (RIGHT, BULK SENSITIVE) SHOWING ALL Ca-INTERCALATION STEPS AND PHENOMENOLOGICAL FITS FOR THE G' PEAK.

(a, b) *pristine EMLG*. (c, d) *1st Ca-intercalation, Ca-QFSBLG*. (e, f) *2nd Ca-intercalation, Ca-QFSBLG*. Corresponding atomic locations of the components are found in the insets. (c)/(e) and (d)/(f) are magnified $\times 1.18$ and $\times 1.15$ times from (a) and (b), respectively. See [Chapter 5, Section 5.4.2](#) for further component details.

I note here that the observation of component S_C^* was not always obvious. Two additional pristine epitaxial monolayer graphene on 6H-SiC(0001) sister samples (samples grown in the same growth run, from the same wafer) were Ca-intercalated at the Australian Synchrotron, which I shall call EMLG#2 and EMLG#3. For EMLG#2, approximately 6 nm of calcium was deposited, and the sample was then annealed at ≈ 741 K for 2 hours. For EMLG#3, approximately 6 nm of calcium was deposited, and the sample annealed at ≈ 723 K for 2 hours. [Figure B.3-2](#) shows the C 1s and Si 2p core levels at $E_{hv} = 330$ eV and 150 eV, respectively. It is interesting to note that in these samples, component S_C^* is not as prominent as in [Figure B.3-1](#). The only difference I can ascertain between EMLG#2, EMLG#3 and the sample shown in the main manuscript, is the amount of Ca deposited on the surface (and thus amount of Ca intercalated). This is also obvious from the relative intensity of component B_C' , which is much lower than in the case of [Figure B.3-1](#) (as was mentioned previously, component B_C' is intimately connected with the intercalation extent, since this component is shifted when the chemical environment of the SiC surface is altered). Thus, it is likely that the higher concentration of metallic Ca (which is quite reactive) underneath the graphene is responsible for the formation of component S_C^* , which I attribute to sub-stoichiometric SiC [323]. The mechanism, which could involve the reaction of surface SiC layers to form Ca-Si compounds is likely complicated, and requires further investigation.

[Figure B.3-3](#) shows the SECO measurements from the omitted 1st Ca-intercalation step shown in [Figure B.3-1c-d](#) ([Figure B.3-3a](#)) as well as the two Ca-intercalated samples EMLG#2 ([Figure B.3-3b](#)) and EMLG#3 ([Figure B.3-3c](#)). To within error (± 0.05 eV), no significant difference in the workfunction, W_f , is observed between the 1st Ca-intercalation step of the sample shown in the manuscript, or Ca-intercalated EMLG#2 and EMLG#3. This further demonstrates that the intercalation process was repeatable, and that the samples were similar, since the workfunction measurements were consistent across different samples and separate intercalation experiments.

Complete C 1s and Si 2p XPS Spectra for Ca-QFSBLG Fabricated from
Pristine EMLG

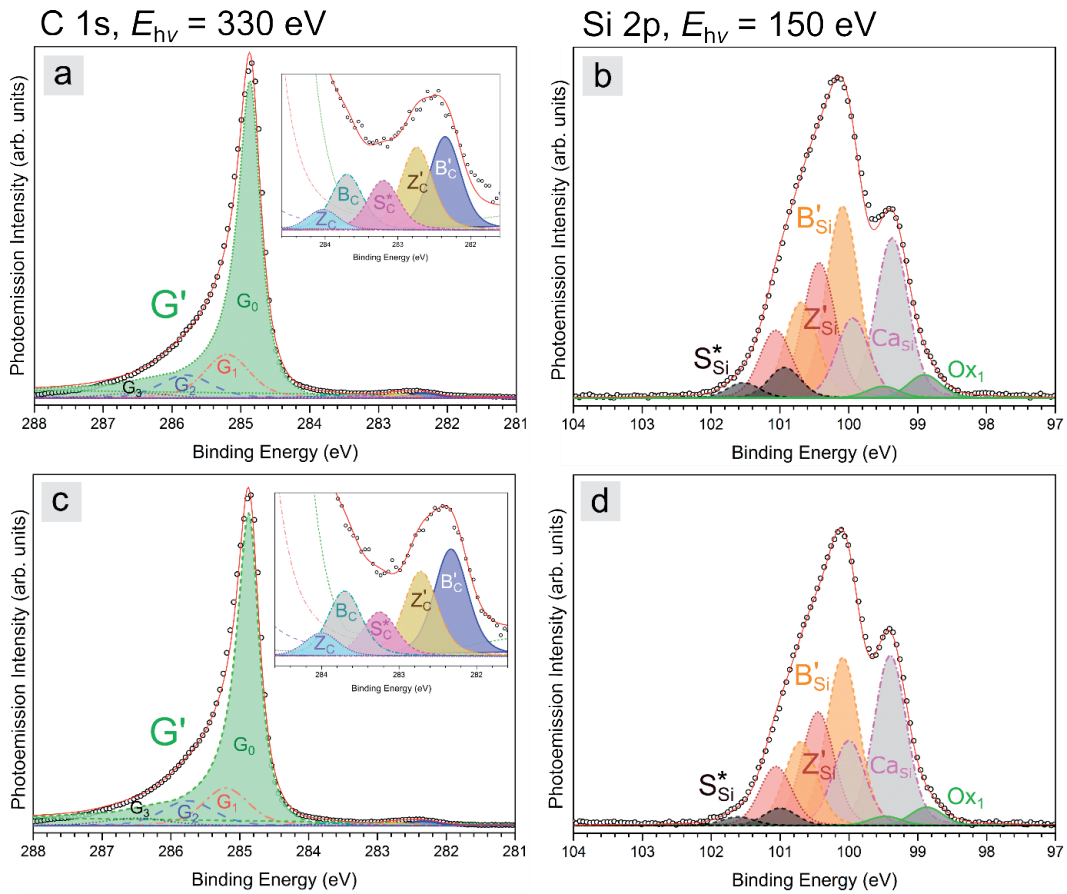


FIGURE B.3-2: X-RAY PHOTOEMISSION SPECTRA OF THE C 1s AND Si 2p CORE LEVELS OF CA-QFSBLG (SAMPLES EMLG#2 AND EMLG#3) AT AN X-RAY ENERGY OF $E_{hv} = 330$ eV AND 150 eV, RESPECTIVELY.

(a) C 1s core level of EMLG#2 showing all components, and (diminished) presence of component S_C^* . (b) Si 2p core level of EMLG#2 showing the formation of Ca-silicide, component Ca_{Si} . (c) C 1s core level of EMLG#3 showing all components, and (diminished) presence of component S_C^* . (d) Si 2p core level of EMLG#3 showing the formation of Ca-silicide, component Ca_{Si} .

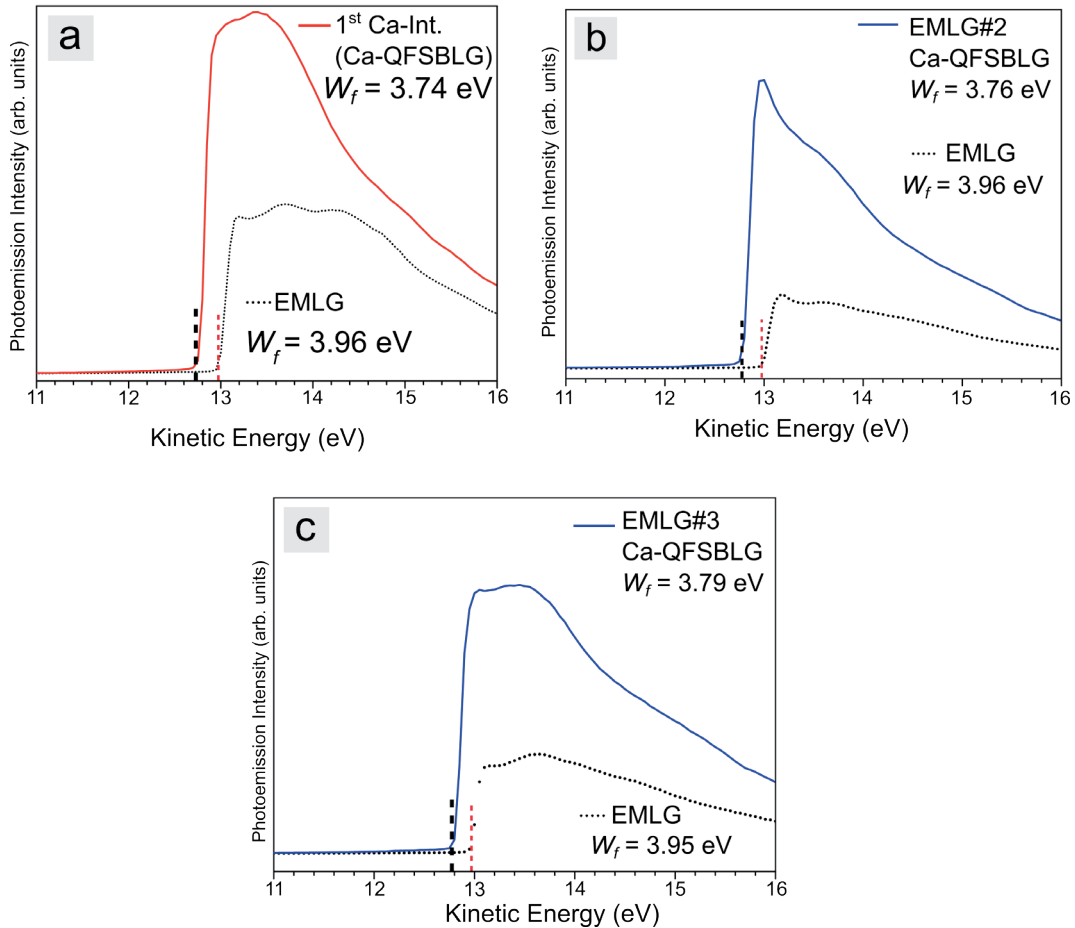


FIGURE B.3-3: SECONDARY ELECTRON CUT-OFF PHOTOEMISSION (SECO) MEASUREMENTS SHOWING THE WORKFUNCTION (W_f) OF THE OMITTED 1ST Ca-INTERCALATION STEP AND EMLG#2 AND EMLG#3 COMPARED TO THEIR PROSPECTIVE PRISTINE EMLG STARTING SAMPLES.

(a) SECO measurements of the 1st Ca-intercalation step of Figure B.3-1c-d showing a $W_f = 3.74$ eV. (b) SECO measurements after Ca-intercalation of EMLG#2, showing a $W_f = 3.76$ eV. (c) SECO measurements after Ca-intercalation of EMLG#3 showing a $W_f = 3.79$ eV.

Figure B.3-4 shows the Si 2p spectra of Ca-intercalated graphene and includes the 1st intercalation step that was omitted in Chapter 5. The changes from the 1st to 2nd Ca-intercalation are minor, and the general interpretation presented in Chapter 5 does not significantly alter, although analysis of these small changes is insightful. For instance, in Figure B.3-4a-b, it is observable that the lineshape of the Si 2p spectrum is broadened by components existing at the high and low binding energy extrema of the spectrum. On the high binding energy side, component Ox_o located at $E_B = 102.95 \pm 0.05$ eV matches closely in binding energy to a silicon oxide compound, in either an Si⁺² or Si⁺³ oxidation state [421-422, 490-491]. Component Ox_o has RI_R = 2, consistent

with a surface oxide formed on top of the SiC, likely the result of oxygen contamination present before or during graphene growth. The low binding energy side of the spectrum is magnified in the inset of [Figure B.3-4a](#) and shows 3 components – A_o, A₁ and A₂. These are surface components ($RI_R >> 1$) and are most likely silicon adatoms [491-493] (A₂, A₁) and excess silicon (A_o) [82]. For instance, component A_o corresponds well to pure silicon ($E_B = 99.2 \pm 0.05$ eV) [494], which may be due to Si left behind upon incomplete Si sublimation during graphene growth. Components A₁ and A₂ which reside at a slightly higher binding energy, are most likely silicon adatom components bonded to the bulk SiC (see ref. [493] for example Si adatom structure and refs. [491-492] for discussion).

Furthermore, components Ox₁ ($E_B = 98.83 \pm 0.05$ eV) and Ox₂ ($E_B = 97.45 \pm 0.05$ eV) arise after Ca-intercalation. After the 1st Ca-intercalation, shown in [Figure B.3-4c-d](#), component Ox₁ is dominant, but after the 2nd Ca-intercalation, component Ox₁ decreases in intensity, while component Ox₂ dominates in intensity. This may suggest that these components are interrelated. For instance, it is known that Ca-silicide compounds can exist in varying stoichiometries. The binding energy of Ox₁ agrees well with a silicon *deficient* (or Ca-rich) Ca-silicide, and component Ox₂ is in approximate agreement with a more Ca-rich silicide [306]. This agrees with the fact that an excess of calcium was deposited on the surface during the experiment. An alternate hypothesis may be that the Ca reacted with the initial surface oxygen contamination (component Ox_o – see [Figure B.3-4a-b](#)) to produce Ox₂, as component Ox₂ was not observed to occur in any H-QFSBLG samples (see [Appendix B4](#)), which did not have the surface oxide contaminant component Ox_o. Although this is unlikely, as Ca-silicates typically have higher binding energies [495].

Nonetheless these components are in small concentration (on the order of a few % of the original B_{Si} reference component) and thus, I presume they do not affect the presented results greatly. It should be further emphasized that components Ox_o, Ox₂, A_o, A₁ and A₂ were not observed to exist in the Si 2p core level spectra of the H-QFSBLG samples after Ca-intercalation, the results of which are almost identical to those presented here, and shown in the proceeding section. Thus, one can be certain that these additional ‘contamination’ components did not alter the interpretation of the results significantly. All curve fit parameters for the Si 2p core level in [Figure B.3-4](#) can be found in [Table B.2-1](#) and [Table B.2-2](#).

I note here that the binding energy location of Z_{Si} ($E_B = 101.83 \pm 0.05$ eV) agrees with prior literature values for this component [297, 304]. In ref. [297], this component was attributed to Si atoms at the surface of the SiC substrate involved in bonding to the buffer layer, yet upon changing the beam energy, no significant alteration of the relative intensity was found. In the results I have presented in this thesis, the same effect is observed, and so, it may be the case that component Z_{Si} extends further into the SiC bulk. This is also

likely the case for component Z_C , as it was fit using a BWF lineshape which is only partially able to capture the physics of the graphene lineshape (see [Chapter 5, Section 5.4.5.1](#) for further details). Thus, if component G was broadened, and had larger contributions to the spectrum at lower binding energy, this would decrease the RI of component Z_C at $E_{hv} = 330$ eV, making this value closer to Z_{Si} (and less surface sensitive). More recently, Gruschwitz *et al.* [496] have investigated the surface and sub-surface structure of the 6H-SiC(0001) substrate after graphene growth and have found that the first 3 bilayers of the top surface are deficient in Si. Thus, it is possible that the anomalous Z_{Si} and Z_C components found in this thesis and ref. [297], are resultant from these Si-deficient layers, and explains why these signals extend beyond the surface into the bulk region.

In summation, Z_C and Z_{Si} likely behave similarly to the change in X-ray energy, but the reason why no or little change is observed after changing the X-ray energy from surface sensitive to bulk sensitive requires further investigation. I have put forward here that these components may be due to silicon deficiencies in the top three bilayers of the SiC substrate present after graphene synthesis. Nonetheless, the subtleties associated with the RI of these components does not in any way affect the main conclusions drawn from the XPS of the Ca-QFSBLG or Mg-QFSBLG samples.

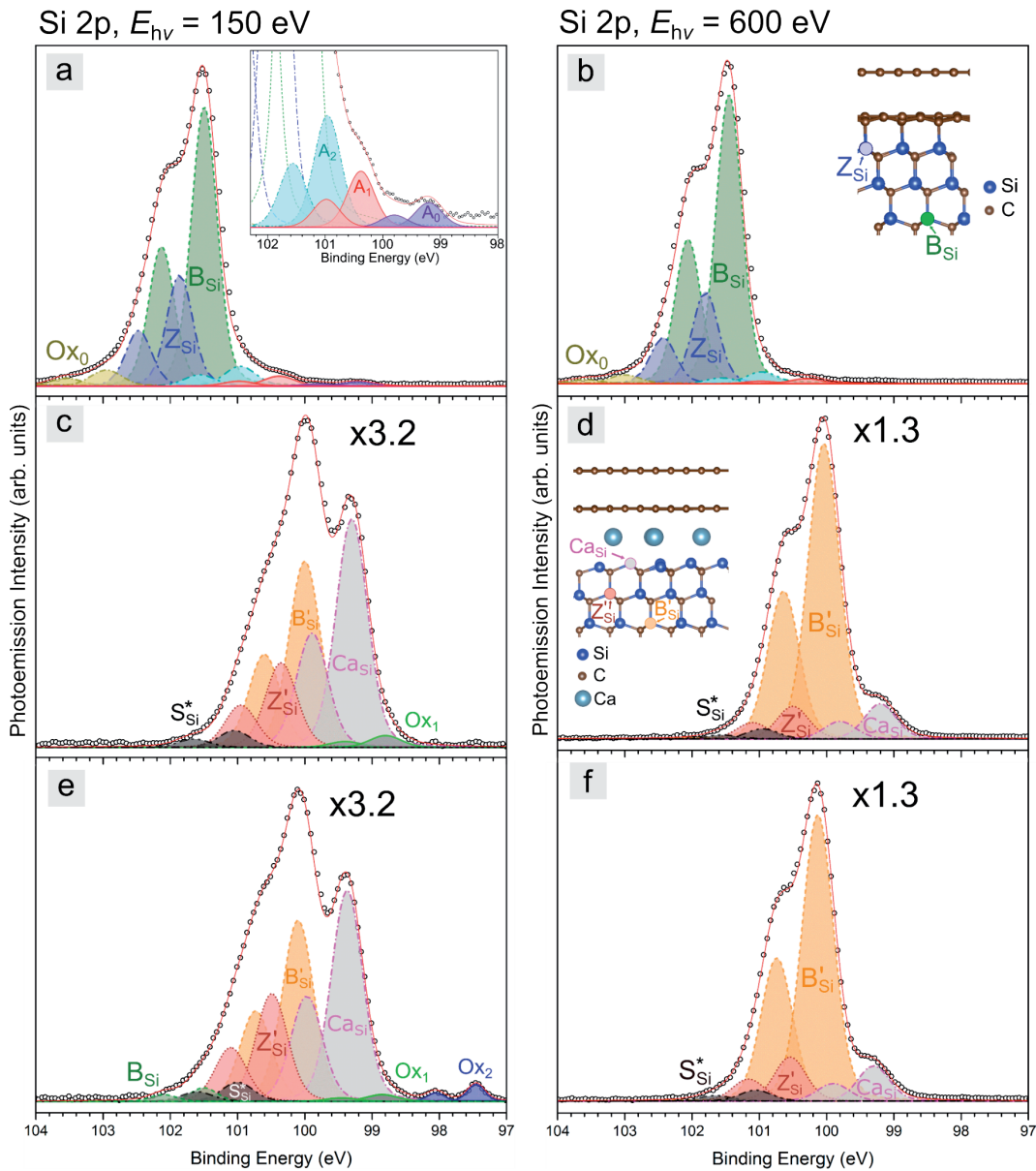


FIGURE B.3-4: X-RAY PHOTOEMISSION SPECTRA OF THE Si 2P CORE LEVEL OF PRISTINE EMLG AND Ca-QFSBLG AT TWO X-RAY ENERGIES, $E_{hv} = 150$ eV (LEFT, SURFACE SENSITIVE) AND $E_{hv} = 600$ eV (RIGHT, BULK SENSITIVE) SHOWING THE 1ST Ca-INTERCALATION STEP THAT WAS OMITTED FROM FIGURE 5.4 OF THE MANUSCRIPT.

(a, b) pristine EMLG. (c, d) 1st Ca-intercalation step (Ca-QFSBLG). (e, f) 2nd Ca-intercalation step (Ca-QFSBLG). The photoemission intensity scales in (c)/(e) and (d)/(f) are magnified $\times 3.2$ and $\times 1.3$ times from (a) and (b), respectively. Components Z_{Si} , Ox_2 and B_{Si} increase in intensity and there is a subsequent decrease in intensity of component Ox_1 upon comparison with the 1st Ca-intercalation step.

B4. Fabrication of Ca-QFSBLG from H-QFSBLG

The experiments conducted on pristine EMLG samples were repeated with pristine hydrogen intercalated ‘quasi-freestanding’ bilayer graphene (H-QFSBLG) samples (see [Chapter 2, Section 2.2.2](#)) in order to understand whether the Ca could intercalate H-QFSBLG, given the presence of another intercalant - hydrogen. The EMLG and H-QFSBLG samples were mounted together on the same holder (see [Section 5.3.4](#) in the [Methods of Chapter 5](#) for details). Since H-QFSBLG is already intercalated, the buffer layer components S₁ and S₂ are not present, simplifying the XPS analysis. As was later discovered, the H-QFSBLG samples also had the benefit of having no (measurable) initial oxygen contamination, and greatly aided in the analysis of EMLG samples by acting as standards (narrow linewidths). As in [Chapter 5](#), this section will follow the same logical flow by presenting first the X-ray photoemission spectra for the C 1s and Si 2p core levels, followed by the workfunction measurements of pristine and Ca-intercalated H-QFSBLG, as well as the effects on the workfunction after the deposition of Ca on the surface of Ca-QFSBLG. For completeness, the O 1s and Ca 2p core levels will also be presented.

[Figure B.4-1](#) and [Figure B.4-2](#) show the XPS spectra for the C 1s and Si 2p core levels of Ca-intercalated H-QFSBLG, respectively. [Figure B.4-1a-b](#) shows the C 1s core levels of pristine H-QFSBLG. The graphene component G^H located at a binding energy of $E_B = 284.37 \pm 0.05$ eV ($RI_R = 14.4$), agrees well with prior measurements [69]. The graphene component was fit using a Breit-Wigner-Fano (BWF) lineshape [294], as this lineshape was found to fit the G component more accurately than the often used Doniach-Šunjić lineshape [157, 295].

Component B_C^H at $E_B = 282.56 \pm 0.05$ eV represents the SiC bulk of H-QFSBLG, and agrees well in energy with prior measurements [69, 303]. Component H_C located at 282.85 ± 0.05 eV has an $RI_R = 1.42$, signifying it is slightly more towards the surface than the bulk component B_C^H. The identity of component H_C is similar to component Z_C of pristine EMLG (see [Figure B.3-4](#)) [297], i.e. it is a more surface component of the SiC bulk, associated with the change in bonding environment of the SiC surface (in this case due to H-Si bonds). The binding energy distance between component H_C and Z_C is $\Delta E_B = 1.2 \pm 0.1$ eV, and the binding energy difference between the bulk component B_C^H, and the pristine EMLG bulk component, B_C, is $\Delta E_B = 1.14 \pm 0.1$ eV. These binding energy shifts are the result of differences in the chemical environment at the surface of the SiC(0001) (the initial shift brought about by band bending, see below), and further corroborates the assignment of component H_C as the shifted version of component Z_C.

The pristine H-QFSBLG samples differ from the pristine EMLG samples, as the SiC components B_{Si}^H/B_C^H , H_{Si}/H_C and the graphene component G^H are shifted to lower binding energies from components B_{Si}/B_C and component G in pristine EMLG. In the case of the graphene component, this is because H-QFSBLG samples are p-type doped,[75, 82] induced by polarization doping from the substrate (in this case 6H-SiC(0001)) [497]. The doping of the SiC substrate (*i.e.* n-type or intrinsic) does have a small effect on the doping of the graphene, and it is found that graphene grown on n-type SiC is less p-doped [82, 302] than graphene grown on intrinsic SiC (or semi-insulating SiC as in our case), in agreement with the results presented here.[69] The shift of the SiC components B_{Si}^H/B_C^H and H_{Si}/H_C to lower binding energy is often observed in the intercalation of graphene on silicon carbide systems, and is caused by significant band bending upon intercalation [71-72, 82, 297, 312, 320-322].

Component B_C at $E_B = 283.70 \pm 0.05$ eV aligns in energy with the bulk SiC component from EMLG on SiC (0001) and suggests that the H-QFSBLG is not completely hydrogen intercalated, but rather is partially intercalated, in agreement with the LEED results in Fig. 1b and prior studies [301]. The RI_R (as referenced to component B_C^H) is $RI_R = 7.62$.

Component S_C^* at $E_B = 283.25 \pm 0.05$ eV has $RI_R = 6.6$. Its E_B location aligns well with sub-stoichiometric values of SiC [323], induced in the top layers of SiC and thus, may be due to incomplete H-intercalation [301]. As in the EMLG sample, component S_C^* increased in intensity after each intercalation step, clearly shown in Figs. S4c and d. Since component S_C^* was not present in pristine EMLG, this implies that component S_C^* is an intercalation specific component, and may arise as a product of intercalation itself.

Figure B.4-1c-d show the C 1s spectrum of H-QFSBLG after the 1st Ca-intercalation. Several features can be seen which differ from the pristine H-QFSBLG sample. Firstly, the SiC bulk peak B_C^H and the associated surface component of the SiC bulk, H_C , has been shifted to lower binding energy – labelled as components B_C' ($E_B = 232.31 \pm 0.05$ eV) and Z_C' ($E_B = 282.68 \pm 0.05$ eV), respectively. The prospective shifts in E_B are -1.39 ± 0.1 eV ($B_C \rightarrow B_C'$), -1.37 ± 0.1 eV ($Z_C \rightarrow Z_C'$), -0.25 ± 0.1 eV ($B_C^H \rightarrow B_C'$) and -0.17 ± 0.1 eV ($H_C \rightarrow Z_C'$), in agreement with our assignment of these components to binding energy shifted components B_C and Z_C , caused by a significant change to the buffer layer – SiC interface.

In contrast, the G^H peak has shifted to higher binding energy to become the G' peak at $E_B = 284.89 \pm 0.05$ eV, in agreement with the binding energy location of the G' peak for Ca-intercalated EMLG (Ca-QFSBLG). The shift to higher binding energy is typically associated with n-type doping of graphene, though it is important to note that this shift in binding energy is not directly proportional to the shift in the Fermi level (E_F) [25, 372].

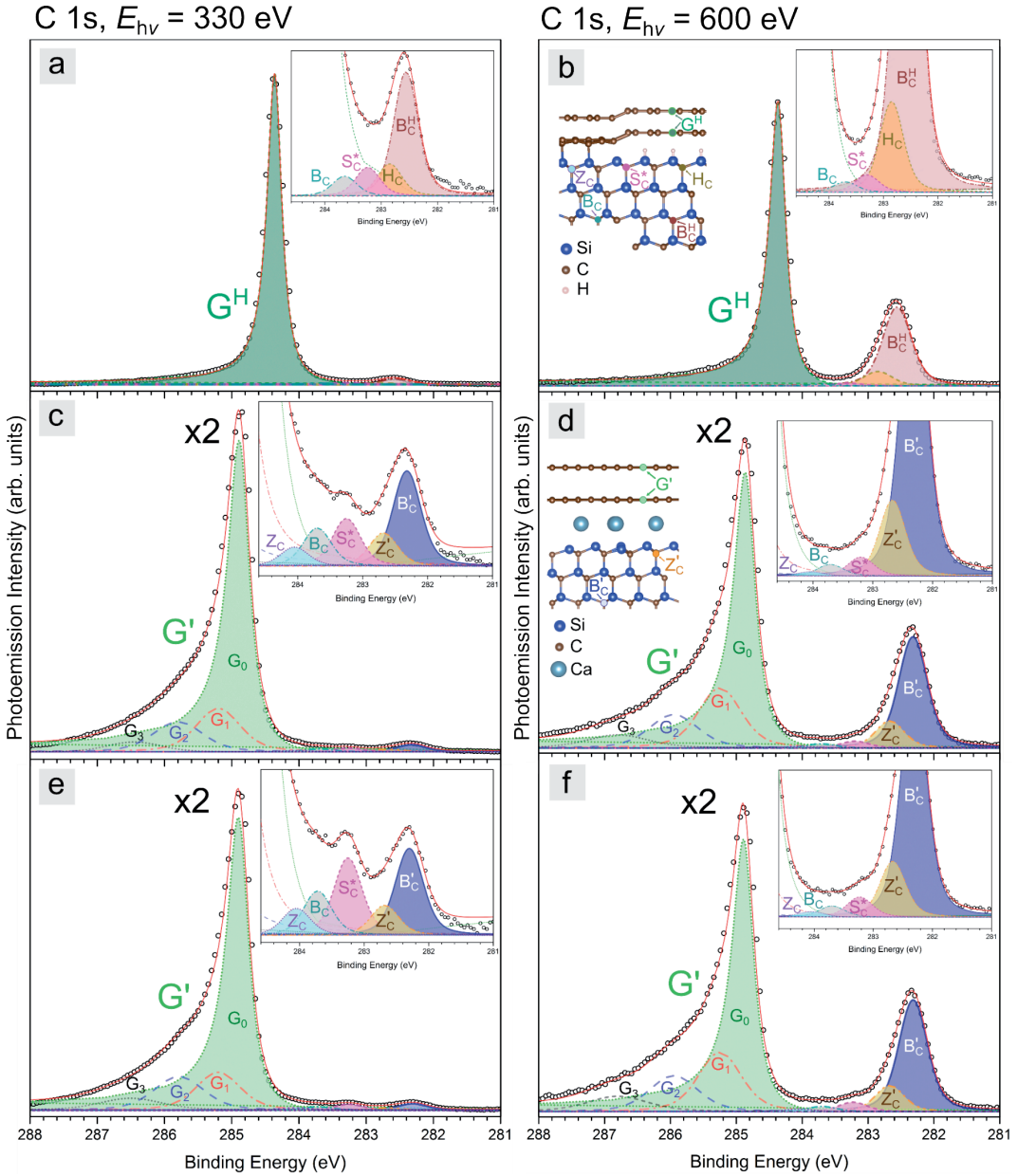


FIGURE B.4-1: X-RAY PHOTOEMISSION SPECTRA SHOWING THE C 1s CORE LEVELS OF PRISTINE H-QFSBLG AND Ca-QFSBLG AT BEAM ENERGIES OF $E_{hv} = 330$ eV (LEFT, SURFACE SENSITIVE) AND $E_{hv} = 600$ eV (RIGHT, BULK SENSITIVE).

(a), (b) Pristine H-QFSBLG showing components G^H , B_C , S_C^* , H_C and B_C^H (see text for details). Component G (graphene) was fit with a BWF function. All other peaks were fit with Voigt functions. (c), (d) After the 1st Ca-intercalation component G becomes G' , and 3 new components – Z_C , Z'_C and B'_C – are observed. The y-scale is magnified $\times 2$ from panels a and b. (e), (f) After the 2nd Ca-intercalation, all components stay relatively constant, except for component S_C^* , which grows in intensity. The y-scale is magnified $\times 2$ from panels (a) and (b).

TABLE B.4-1: PHENOMENOLOGICAL FIT PARAMETERS FOR Ca-QFSBLG IN FIGURE B.4-1.

Components comprising the phenomenological G' fits approximating the 2D plasmon losses from highly doped graphene. All binding energies (E_B) and peak parameters (RI, FWHM) are shown below. All components were fit with Voigt functions.

C 1s		(a), (b), 1 st Ca Intercalation			(c), (d) 2 nd Ca Intercalation		
Component	E_{hv} (eV)	E_B (eV)	RI	FWHM (eV)	E_B	RI	FWHM (eV)
G_1	330	285.2	3.46	0.78	285.2	3.02	0.78
	600	285.25	0.40	0.78	285.25	0.40	0.78
G_2	330	285.8	2.67	0.87	285.785	2.67	0.87
	600	285.95	0.22	0.87	285.95	0.24	0.87
G_3	330	286.5	0.95	1.1	286.5	0.95	1.1
	600	286.8	0.09	1.1	286.8	0.10	1.1

Figure B.4-2 shows the Si 2p core levels of pristine H-QFSBLG and Ca-QFSBLG at beam energies of $E_{hv} = 150$ eV (surface sensitive) and $E_{hv} = 600$ eV (bulk sensitive). Figure B.4-2a, b shows the pristine H-QFSBLG sample, where peak deconvolution yields 2 peaks – component B_{Si}^H ($E_B = 100.90 \pm 0.05$ eV) originating from the SiC bulk, and component H_{Si} ($E_B = 101.21 \pm 0.05$ eV) which originates from the changed SiC surface environment (band bending) from H-intercalation [82]. Here, components B_{Si}^H and H_{Si} are related to the components B_C^H and H_C from the C 1s spectra (see Figure B.4-1), but the elemental contributions are distinguished by the subscripts ‘Si’ and ‘C’ to signify that the components originate from different core levels (even though they are from the same compound / bonding environment). The spacing between these components is 0.31 ± 0.1 eV, which agrees with the E_B separation between B_C^H and H_C components in the C 1s core level data (Figure B.4-1a, b) of 0.29 ± 0.1 eV and thus justifies our assignment of these same components in the Si 2p core level data.

Unlike the fits to the C 1s core level spectra in Figure B.4-1, additional components corresponding to different SiC stoichiometries (S_{Si}^*) or from incomplete intercalation (B_{Si} , Z_{Si}) were not fit in the Si 2p core level spectra of Figure B.4-2a, b. There are two reasons for this – firstly, these components are not shifted greatly in energy from components B_{Si}^H and H_{Si} . Since the Si 2p core level peaks are split due to spin-orbit interactions, smaller peaks such as B_{Si} and S_{Si}^* are hidden under the 2p_{1/2} peaks of the B_{Si}^H and H_{Si} components which are close in binding energy. Secondly, these components are not high in concentration, and are unnecessary in obtaining a good fit to the data (i.e.

to maintain an intensity ratio of precisely 0.5 and spin orbit splitting of 0.61 ± 0.02 eV). This contrasts with the C 1s core level spectra in [Figure B.4-1](#), in which these components (S_{Si}^* , B_{Si} , Z_{Si}) were not masked by other components and thus, were required to explain the data.

[Figure B.4-2c, d](#) shows the Si 2p core levels after the 1st Ca-intercalation. The components B_{Si}^H and H_{Si} have now been replaced by a series of 4 components. Starting from the lower binding energy side, component C_{Si} at $E_B = 99.28 \pm 0.05$ eV is in agreement with the E_B value found for EMLG and thus, is a Ca-Si compound closely matching that of a Ca-silicide [[305-306](#)].

Components B_{Si}' ($E_B = 100.08 \pm 0.05$ eV), Z_{Si}' ($E_B = 100.50 \pm 0.05$ eV) and S_{Si}' ($E_B = 100.97 \pm 0.05$ eV) are SiC components that shifted in energy by 0.42 ± 0.1 eV ($B_{Si}' \rightarrow Z_{Si}'$) and 0.89 ± 0.1 eV ($B_{Si}' \rightarrow S_{Si}'$). This agrees with the energy shifts in Fig. S4 which are 0.37 ± 0.1 eV ($B_C \rightarrow Z_C$) and 0.94 ± 0.1 eV ($B_C \rightarrow S_C^*$), justifying our assignment of these components to both the C 1s and Si 2p core levels. Additionally, the surface sensitivity of the components that B_{Si}' is $RI_R \approx 0.27$, in agreement with the C 1s core level data in Fig. S4e, f (*i.e.* that B_C has an $RI_R < 1$, and that it has the lowest RI_R of all the components). The RI_R of the other components are 1.06, 0.97 and 2.42 for Z_{Si}' , S_{Si}' and C_{Si} , respectively. Thus, component B_{Si}' is deeper in the bulk than components Z_{Si}' and S_{Si}' , which are in comparable locations closer to the surface (as was found from the C 1s core levels). Component C_{Si} lies on the surface of the SiC, above the other components. The approximate atom locations for all components is shown in [Figure B.4-1](#) and [Figure B.4-2](#).

[Figure B.4-2e, f](#) shows the results of the 2nd Ca-intercalation in which little change in the components can be seen, except for the RI_R of component S_{Si}' ($RI_R \approx 1$), which has increased in amplitude (slightly), in agreement with the increase in amplitude observed for the C 1s core level of the same component (S_C^* , see [Figure B.4-1](#)) after the 2nd Ca-intercalation. This was not observed for the Ca-intercalated EMLG sample in [Figure 5.4](#) and [Figure 5.5](#) of the main text. Although as in the Ca-intercalated EMLG case, I find that there is a large discrepancy between the RI_R of S_C^* and S_{Si}' of ≈ 6 in the Ca-intercalated QFSBLG samples, in good agreement with the discrepancy found from Ca-intercalated EMLG. I attribute this effect to a non-stoichiometric carbon rich SiC compound [[323](#)], from which the carbon signal outweighs the Si signal yielding erroneous RI_R values.

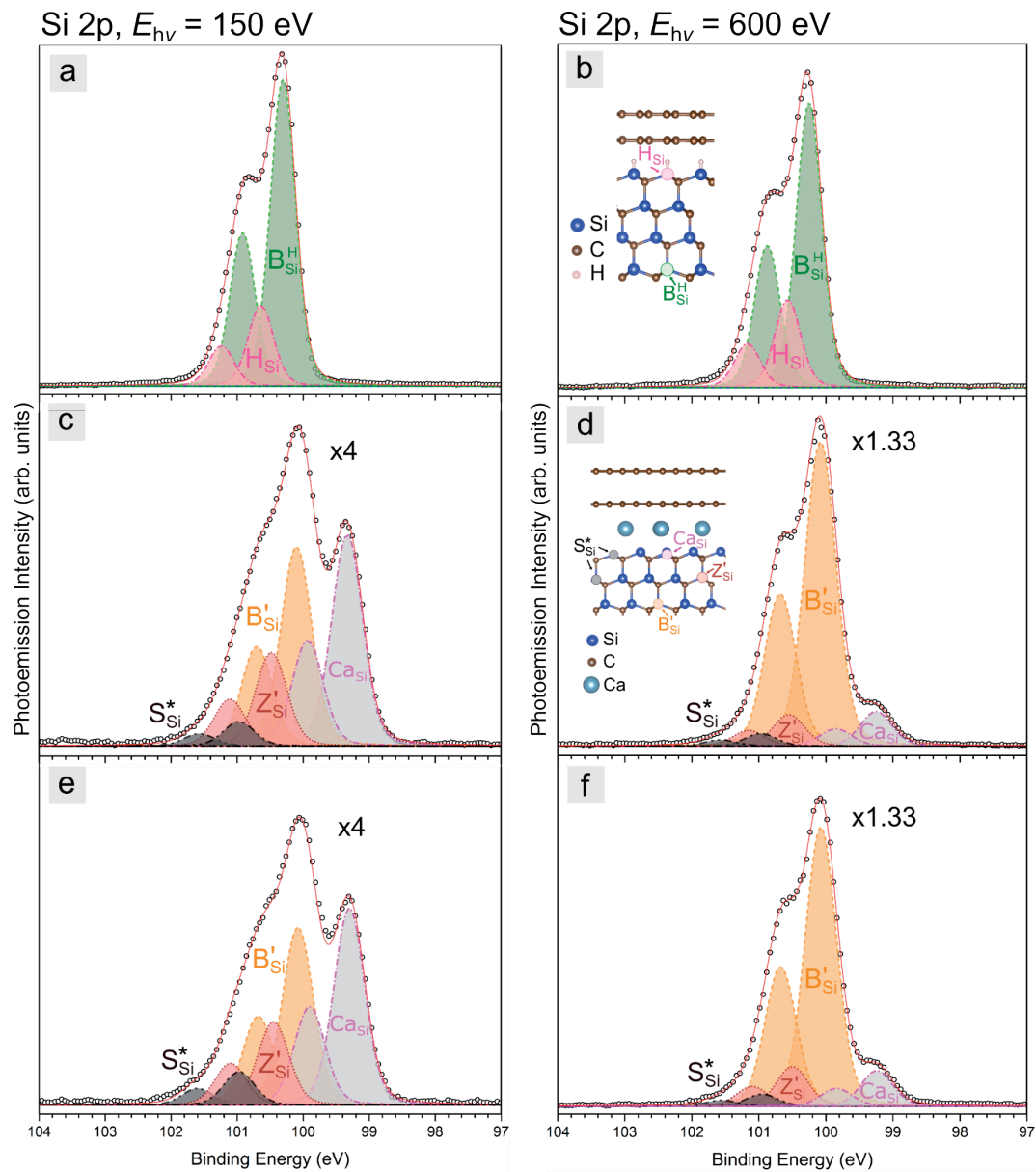


FIGURE B.4-2: X-RAY PHOTOEMISSION SPECTRA SHOWING THE Si 2p CORE LEVELS OF PRISTINE H-QFSBLG AND Ca-INTERCALATED H-QFSBLG (Ca-QFSBLG) AT BEAM ENERGIES OF $E_{hv} = 150$ eV (SURFACE SENSITIVE) AND $E_{hv} = 600$ eV (BULK SENSITIVE).

(a), (b) Pristine H-QFSBLG showing bulk SiC components B_{Si}^H and H_{Si} . (c), (d) Ca-QFSBLG (1st Ca intercalation of H-QFSBLG sample) showing components S_{Si}^* , Z'_{Si} , B'_{Si} and Ca_{Si} arise after Ca-intercalation. (e), (f) Ca-QFSBLG (2nd Ca-intercalation). Component S_{Si}^* has increased in intensity in (e), otherwise little change is observed after the 2nd Ca-intercalation step. Inset of (b) and (d) shows approximate atomic position of components determined from RI_R values.

Figure B.4-3 shows the Si 2p core levels at $E_{hv} = 150$ eV of two pristine H-QFSBLG samples (**Figure B.4-3a-b**) that were independently Ca-intercalated (**Figure B.4-3c-d**) in two separate experiments at the Australian Synchrotron (*i.e.* the Ca-intercalation experiment was performed 3 separate times with sister samples). For sample H-QFSBLG#2, approximately 6 nm of calcium was deposited, and the sample was then annealed at ≈ 741 K for 2 hours. For sample H-QFSBLG#3, approximately 6 nm of calcium was deposited, and the sample annealed at ≈ 723 K for 2 hours. As can be seen in **Figure B.4-3c-d**, the difference between these Ca-intercalated H-QFSBLG samples and those presented in **Figure 5.4** is the presence of component Ox_1 , which was not found in the sample intercalated in **Figure B.4-2**. Anneal temperature and time did not vary greatly between the experiments, and so this does not explain the observation of component Ox_1 in these samples. It is thought that component Ox_1 represents a different Ca-silicide stoichiometry (one that is Ca-rich), and if this is the case, we would expect the amount of deposited Ca to be important in its creation (*i.e.* an excess of intercalated Ca would be necessary). I did observe a non-uniformity in Ca deposition on the holder itself, (which manifested as a non-uniformity in the LEED spectra, see **Figure 5.3** and discussion) and amounted to less Ca deposition on the H-QFSBLG sample in **Figure 5.3**. Thus, the decreased amount of Ca on the surface may explain the absence of component Ox_1 .

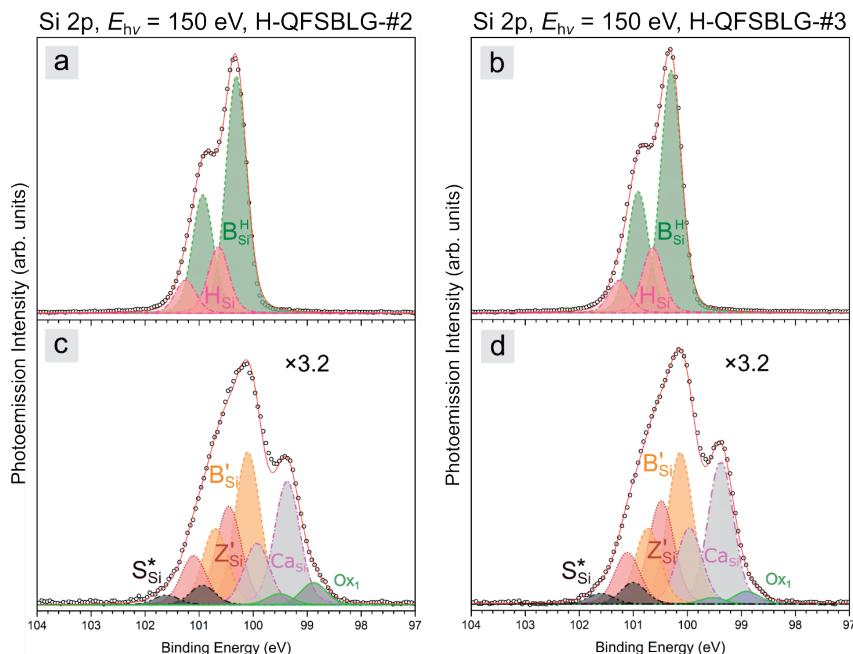


FIGURE B.4-3: X-RAY PHOTOELECTRON SPECTRA SHOWING Si 2p CORE LEVELS AT AN X-RAY ENERGY OF $E_{hv} = 150$ eV OF TWO SEPARATE (SISTER) PRISTINE H-QFSBLG SAMPLES USED FOR CA-INTERCALATION EXPERIMENTS.

(**a**), (**b**) *Pristine samples (named sample #2 and sample #3) prior to Ca-intercalation.* (**c**) *Ca-intercalated sample #2 showing presence of component Ox_1 .* (**d**) *Ca-intercalated sample #3 showing presence of component Ox_1 .*

[Figure B.4-4](#) shows the photoemission spectra for the O 1s core level of the same Ca-QFSBLG sample shown in [Figure B.4-1](#) and [Figure B.4-2](#). Small amounts of oxygen contamination are visible, and most likely this signal emanates from oxidised Ca that was adhered to the surface of the graphene and was not sublimated after annealing. The results shown in [Figure B.4-4](#) are almost identical to those shown in [Figure 5.6](#) in the main text.

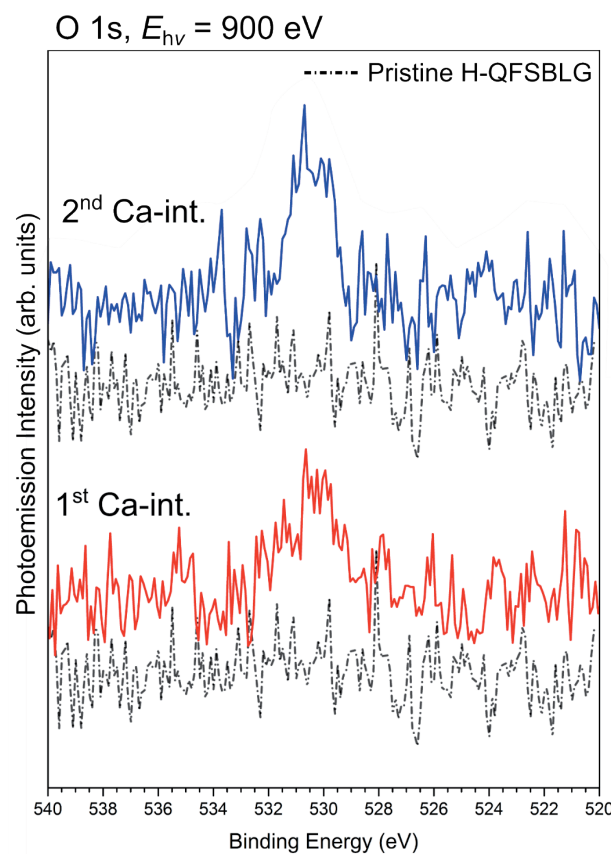


FIGURE B.4-4: X-RAY PHOTOEMISSION SPECTRA SHOWING THE O 1s CORE LEVEL OF Ca-QFSBLG COMPARED TO PRISTINE EMLG AT AN X-RAY ENERGY OF $E_{hv} = 900$ eV. Here, the O 1s core level after the 1st Ca-intercalation (1st Ca-int.) is shown in red at the bottom, while the 2nd Ca-intercalation is shown in blue at the top of the plot. Both data curves are compared to pristine H-QFSBLG which has no oxidation present.

[Figure B.4-5](#) shows the X-ray photoemission data for the Ca 2p core level of Ca-intercalated H-QFSBLG (*i.e.* Ca-QFSBLG), and is almost identical to the photoemission data from the Ca 2p core level of Ca-intercalated EMLG (Ca-QFSBLG) shown in [Figure 5.8](#). [Figure B.4-5a](#) shows the 1st Ca-intercalation, whereas [Figure B.4-5b](#) shows the 2nd Ca-intercalation.

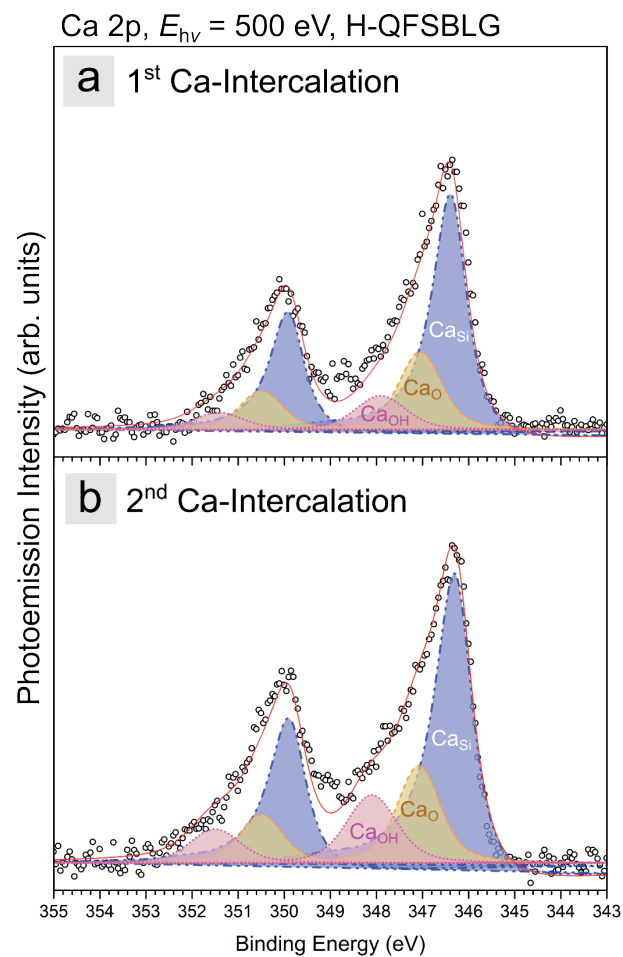


FIGURE B.4-5: X-RAY PHOTOEMISSION SPECTRA SHOWING THE Ca 2p CORE LEVEL OF Ca-INTERCALATED H-QFSBLG (Ca-QFSBLG) AT AN X-RAY ENERGY OF $E_{hv} = 500$ eV.

Ca-intercalated H-QFSBLG (Ca-QFSBLG) showing 3 components. Casi (blue) = Ca-Si compound, Cao (yellow) = Calcium oxide containing compound, CaOH (Red) = Ca-hydroxide compound. (a) 1st Ca-intercalation. (b) 2nd Ca-intercalation.

TABLE B.4-2: Ca 2p CORE LEVEL FIT PARAMETERS FOR Ca-INTERCALATED H-QFSBLG ([FIGURE B.4-5](#))

Table shows components Cas_i = Ca-silicide, CaO = Ca-oxide and CaOH = Ca-hydroxide, $2p_{1/2}$ to $2p_{3/2}$ binding energy difference and Lorentzian FWHM (W_L)/Gaussian FWHM (W_G) of the Voigt functions used to fit the components.

H-QFSBLG, Ca 2p		(c), H-QFSBLG, 1 st Ca-Intercalation					(d), H-QFSBLG 2 nd Ca-Intercalation				
Component	E_{hv} (eV)	E_B (eV) $2p_{3/2}$	E_B (eV) $2p_{1/2}$	$2p_{1/2} - 2p_{3/2}$ (eV)	W_L/W_G (eV)	E_B (eV) $2p_{3/2}$	E_B (eV) $2p_{1/2}$	$2p_{1/2} - 2p_{3/2}$ (eV)	W_L/W_G (eV)		
Cas_i	500	346.35	349.95	3.60	0.3/0.65	346.32	349.87	3.55	0.3/0.65		
CaO	500	347.05	350.55	3.50	0.3/0.8	347.09	350.55	3.46	0.3/0.8		
CaOH	500	348.00	351.50	3.50	0.5/1.0	348.00	351.50	3.50	0.5/1.0		

To estimate the direction of the shift in E_F (*i.e.* did Ca-intercalation make H-QFSBLG more n-type or more p-type), the workfunction shift was measured using secondary electron cut-off (SECO) photoemission spectroscopy. The results of the SECO measurements for each intercalation step are shown in [Figure B.4-6](#). After the 2nd Ca-intercalation, $W_f = 3.67 \pm 0.05$ eV ([Figure B.4-6c](#)), which is in agreement with the final value of Ca-intercalated EMLG ($W_f = 3.68 \pm 0.05$ eV, [Figure 5.13b](#)). The initial W_f of 4.40 ± 0.05 eV for H-QFSBLG is higher than that of EMLG, and agrees well with prior measurements [[16](#)]. The change in workfunction from H-QFSBLG to Ca-QFSBLG is then $\Delta W_f = -0.73 \pm 0.1$ eV, and suggests significant n-type doping, as was the case with Ca-intercalated EMLG.

Furthermore, [Figure B.4-7](#) shows the deposition of ≈ 0.6 nm of Ca on the surface of the same Ca-QFSBLG sample shown in [Figure B.4-6c](#). The results here are identical to those of [Figure 5.14](#), and it is found that the workfunction of the graphene shifts to $W_f = 3.11 \pm 0.05$ eV, while a metallic calcium peak appears at 2.34 ± 0.05 eV.

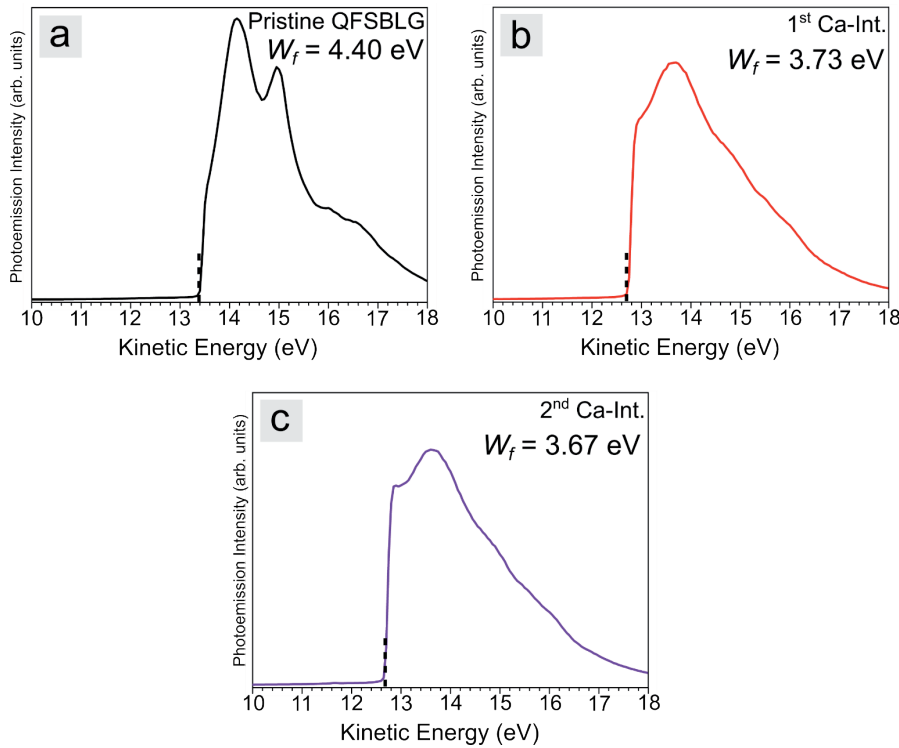


FIGURE B.4-6: SECONDARY ELECTRON CUT-OFF (SECO) PHOTOEMISSION MEASUREMENTS SHOWING THE WORKFUNCTION (W_f) OF PRISTINE AND Ca-INTERCALATED H-QFSBLG (Ca-QFSBLG).

(a) SECO measurements of pristine H-QFSBLG showing $W_f = 4.40 \pm 0.05 \text{ eV}$.
(b) SECO measurements of 1st Ca-intercalation showing $W_f = 3.73 \pm 0.05 \text{ eV}$.
(c) SECO measurements of 2nd Ca-intercalation showing $W_f = 3.67 \pm 0.05 \text{ eV}$. Dashed vertical line is point of W_f reading from line intersection method.

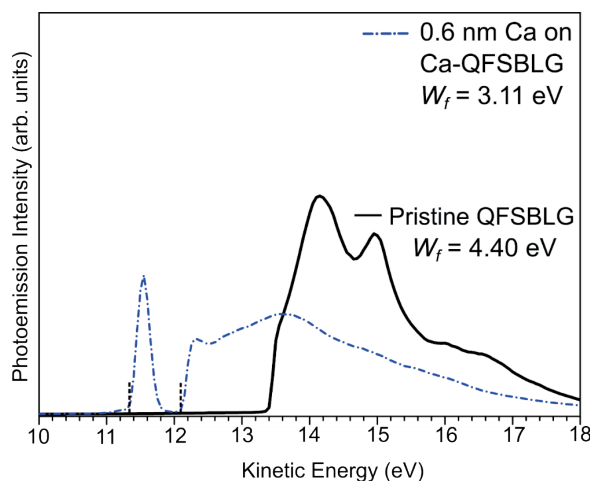


FIGURE B.4-7: SECO MEASUREMENTS SHOWING THE WORKFUNCTION (W_f) OF Ca-QFSBLG (SAMPLE FROM FIGURE B.4-6) AFTER DEPOSITION OF 0.6 nm OF CALCIUM ON THE SURFACE (DASH DOT, BLUE LINE) COMPARED TO PRISTINE EMLG (DOTTED, BLACK LINE). DASHED BLACK LINES SHOW W_f MEASUREMENT.

Upon comparison of LEED (see [Figure 5.3](#)), XPS and SECO results of Ca-intercalated H-QFSBLG with Ca-intercalated EMLG, it is found that the results of both are almost identical. Thus, it is very likely the case that the hydrogen that was initially intercalated underneath the graphene (H-QFSBLG) was displaced almost entirely by the calcium to form instead, Ca-intercalated quasi-freestanding bilayer graphene (Ca-QFSBLG). As with the Ca-QFSBLG formed from EMLG, I find that a Ca-Si layer closely matching a Ca-silicide is formed. To discover if there are truly differences between Ca-intercalated EMLG and Ca-intercalated H-QFSBLG, further experimentation is required, which is outside the scope of this dissertation. However, it is clear that the comparison of LEED, XPS and SECO results presented here yield no appreciable difference between the two types of starting samples, and thus, I conclude that the Ca-intercalation of EMLG or H-QFSBLG results in the same (structurally and electronically) Ca-QFSBLG samples.

B5. STM Surface Cleaning Procedure for Ca-QFSBLG

To image the surface of Ca-QFSBLG with the STM, it was necessary to clean the surface prior to scanning. It is well known [498] that the STM tip is able to exert forces upon adsorbate molecules or atoms.

[Figure B.5-1](#) shows how using the STM's ability to manipulate matter on the surface can clean a Ca contaminated graphene surface (utilised in [Figure 5.9](#) and [Figure 5.10](#) of this thesis), enabling scanning of the surface. The initial surface after Ca-intercalation is shown in [Figure B.5-1a](#) by using 1 V and 50 pA applied to the tip (PtIr in this case) and shows \approx 15 nm Ca islands scattered on the surface of the graphene. [Figure B.5-1b](#) shows the result of sweeping the scan window multiple times with 0.1 V and 50 pA applied to the tip. The tip interacts strongly with the Ca on the surface, and after a few passes ([Figure B.5-1c](#)) the excess Ca is swept to the sides of the scan window, while the tip retains its atomic resolution. [Figure B.5-1d](#) shows a magnified view of the cleaned area in [Figure B.5-1c](#). The cleaned area shown in [Figure B.5-1d](#) is the same Ca-QFSBLG area shown in [Figure 5.9](#) of the main text.

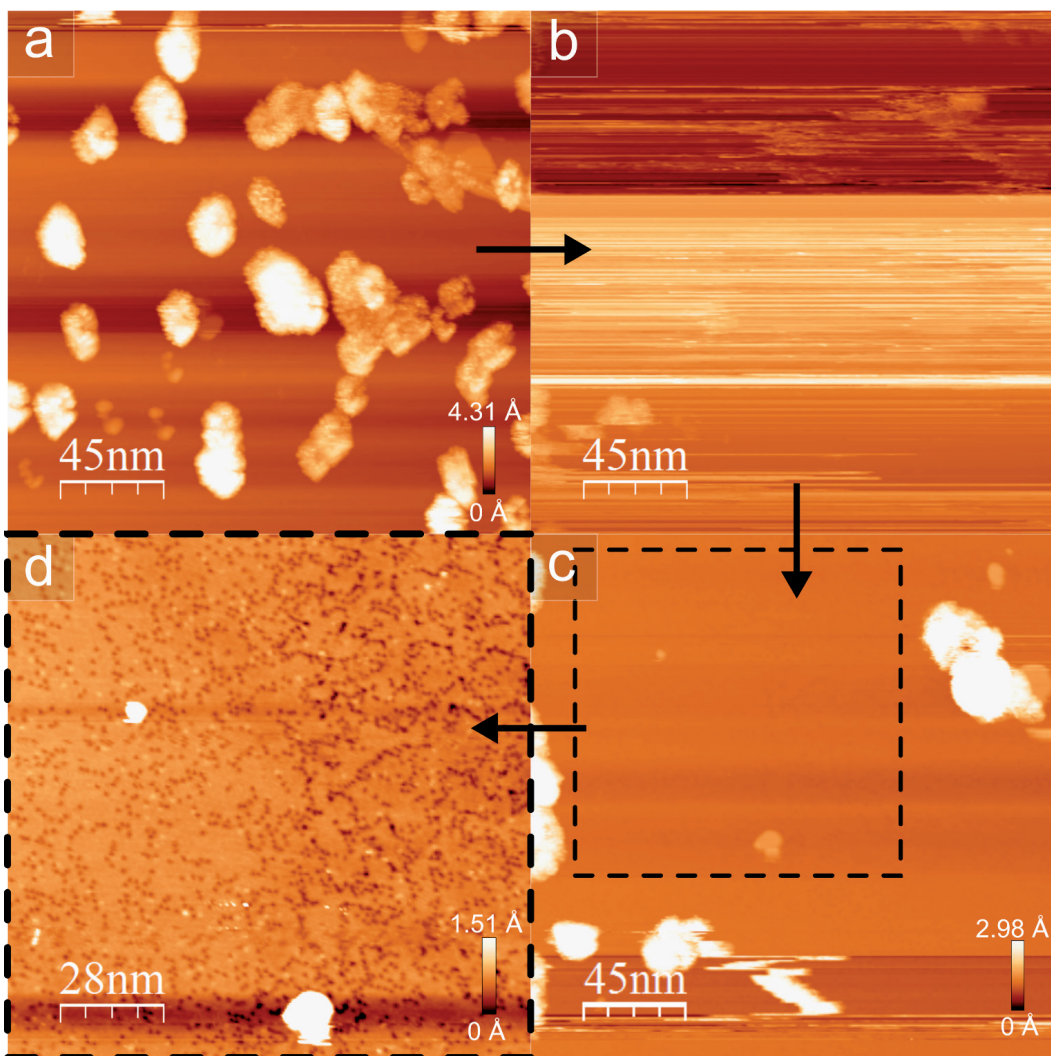


FIGURE B.5-1: CLEANING THE SURFACE OF Ca-QFSBLG FROM CALCIUM DEBRIS.

(a) Initial surface after the 2nd Ca-intercalation in the STM experiments (see Fig. 4, manuscript), (1 V, 50 pA). (b) Altering the voltage to 0.1V causes the tip to strongly interact with the Ca on the surface (0.1 V, 50 pA). (c) Continued scanning of the surface causes the excess Ca to be swept away with the STM tip (0.1 V, 50 pA). (d) Magnified view of dashed area in (c) showing surface topography of cleaned area (0.1 V, 50 pA).

C | Appendix C Magnesium Intercalation

C1. Tables of Values for Mg-intercalation Experiments

Below are the complete table of values for all X-ray photoemission spectra for the C 1s, Si 2p and Mg 2p core levels shown in [Chapter 6, 7, 8](#) and [Appendix C2](#)

TABLE C.1-1: Si 2p CORE LEVEL FIT PARAMETERS FOR ALL COMPONENTS IN FIGURE 6.4 AND FIGURE C.2-2.

Showing binding energy (E_B), relative intensity (RI), and Gaussian FWHM (W_G). All Lorentzian widths for the Voigt fits were set at 0.1 eV and kept constant. A dash indicates no measurement was possible, n/a = not applicable (Mg_{2s} is not a 2p component).

EMLG, Si 2p		(a), (b), Pristine EMLG				(c), (d) 1 st Mg Intercalation				(e), (f) 2 nd Mg Intercalation			
Component	E_{hv} (eV)	E_B (eV) 2p _{3/2}	E_B (eV) 2p _{1/2}	RI	W_G (eV)	E_B (eV) 2p _{3/2}	E_B (eV) 2p _{1/2}	RI	W_G (eV)	E_B (eV) 2p _{3/2}	E_B (eV) 2p _{1/2}	RI	W_G (eV)
Ox _o	150	102.9	103.50	0.068	0.5								
	600	102.8	103.40	0.046	0.5								
Z _{Si}	150	101.86	102.46	0.392	0.4	101.78	102.40	0.021	0.4	101.80	102.38	0.014	0.4
	600	101.80	102.38	0.401	0.4	101.75	102.35	0.059	0.4	101.74	102.34	0.035	0.4
B _{Si}	150	101.50	102.13	1	0.4	101.46	102.06	0.081	0.4	101.49	102.07	0.034	0.4
	600	101.46	102.09	1	0.4	101.44	102.04	0.152	0.4	101.43	102.03	0.076	0.4
B'' _{Si}	150					100.30	100.91	0.267	0.4	100.37	101.0	0.304	0.4
	600					100.27	100.91	0.713	0.4	100.33	100.96	0.817	0.4
Z'' _{Si}	150					100.68	101.28	0.041	0.4	100.74	101.34	0.061	0.4
	600					100.60	101.20	0.256	0.4	100.69	101.27	0.235	0.4
Mg _{Si}	150					99.91	100.52	0.385	0.4	99.98	100.59	0.446	0.4
	600					99.90	100.51	0.138	0.4	99.95	100.55	0.152	0.4
Ox ₃	150					99.53	100.13	0.128	0.4	99.58	100.19	0.115	0.4
	600					99.45	100.05	0.045	0.4	99.50	100.12	0.042	0.4
Mg _{2s}	150					103.91	n/a	n/a	1	103.97	n/a	n/a	1
	600					-	n/a	n/a	-	-	n/a	n/a	-

TABLE C.1-2: FIT PARAMETERS FOR Si 2p CORE LEVEL OF ADATOM COMPONENTS IN PRISTINE EMLG IN [FIGURE 6.4a-b](#) AND [FIGURE C.2-2a-b](#).
Showing binding energy (E_B), relative intensity (RI), and Gaussian FWHM (W_G). All components were fit with Voigt functions, with Lorentzian width of 0.1 eV.

EMLG, Si 2p		(a), (b), Pristine EMLG			
Component	E_{hv} (eV)	E_B (eV) 2p _{3/2}	E_B (eV) 2p _{1/2}	RI	W_G (eV)
A_0	150	99.2	99.8	0.009	0.5
	600	-	-	-	-
A_1	150	100.40	101.00	0.035	0.5
	600	100.40	101.00	0.017	0.5
A_2	150	101.00	101.60	0.068	0.5
	600	100.98	101.58	0.023	0.5

Magnesium Intercalation

TABLE C.1-3: C 1s CORE LEVEL FIT PARAMETERS FOR ALL COMPONENTS IN FIGURE 6.5 AND FIGURE C.2-1.

Showing binding energy (E_B), relative intensity (RI) and asymmetry/Lorentzian FWHM (Q/W_L) for BWF fits or Gaussian FWHM/Lorentzian FWHM (W_G/W_L) for Voigt fits.

EMLG, C 1s		(a), (b), Pristine EMLG			(c), (d) 1 st Mg Intercalation			(e), (f) 2 nd Mg Intercalation		
Component	E_{hv} (eV)	E_B (eV)	RI	Q/W_L or W_G/W_L (eV)	E_B (eV)	RI	Q/W_L or W_G/W_L (eV)	E_B (eV)	RI	Q/W_L or W_G/W_L (eV)
S2	330	285.48	5.563	0.8/0.4						
	600	285.54	0.550	0.8/0.4						
S1	330	285.05	2.636	0.7/0.3						
	600	285.01	0.281	0.7/0.3						
G	330	284.79	39.31	12/0.2						
	600	284.83	2.723	12/0.2						
G''	330				284.82	36.93	12/0.2	284.84	36.66	12/0.2
	600				284.83	2.882	9/0.2	284.82	2.898	9/0.2
Z _c	330	284.05	0.625	0.4/0.2						
	600	284.05	0.400	0.4/0.2	284.05	0.060	0.4/0.2	284.02	0.033	0.4/0.2
Z _c ''	330				282.95	0.238	0.4/0.2	282.90	0.375	0.4/0.2
	600				282.95	0.167	0.4/0.2	282.92	0.233	0.4/0.2
B _c	330	283.70	1	0.4/0.2	283.65	0.250	0.4/0.2	283.65	0.125	0.4/0.2
	600	283.74	1	0.4/0.2	283.69	0.187	0.4/0.2	283.65	0.100	0.4/0.2
B _c ''	330				282.59	0.913	0.4/0.2	282.64	0.900	0.4/0.2
	600				282.59	0.900	0.4/0.2	282.63	0.933	0.4/0.2

TABLE C.1-4: Si 2p CORE LEVEL FIT PARAMETERS OF ALL COMPONENT FOR Mg-QFSBLG AFTER SHORT-TERM AIR EXPOSURE IN FIGURE 7.7.

The Lorentzian width of the Voigt fits were kept constant at 0.1 eV. The binding energy (E_B) parameters, relative intensity (RI) and Gaussian width (W_G) for the Voigt fits are shown (note: Mg_{2s} is not an Mg 2p component).

EMLG, Si 2p		(a) Air Exposure				(c) Annealing			
Component	E_{hv} (eV)	E_B (eV) 2p _{3/2}	E_B (eV) 2p _{1/2}	RI	W_G (eV)	E_B (eV) 2p _{3/2}	E_B (eV) 2p _{1/2}	RI	W_G (eV)
Z _{Si}	150	101.7	102.3	0.010	0.4	101.73	102.333	0.008	0.4
B _{Si}	150	101.4	102	0.020	0.4	101.47	102.05	0.015	0.4
B'' _{Si}	150	100.32	100.96	0.088	0.4	100.34	100.97	0.110	0.4
Z'' _{Si}	150	100.72	101.32	0.022	0.4	100.74	101.32	0.037	0.4
Mg _{Si}	150	99.92	100.56	0.108	0.4	99.94	100.54	0.135	0.4
O ₃	150	99.54	100.14	0.037	0.4	99.54	100.14	0.044	0.4
Mg _{2s}	150	103.93	n/a	n/a	1.0	103.98	n/a	n/a	1.0

Magnesium Intercalation

TABLE C.1-5: C 1s CORE LEVEL FIT PARAMETERS OF ALL COMPONENTS FOR Mg-QFSBLG AFTER SHORT-TERM AIR EXPOSURE IN [FIGURE 7.7](#).
Showing binding energy (E_B), relative intensity (RI) and asymmetry/Lorentzian width (Q/W_L) for BWF fits or Gaussian FWHM/Lorentzian FWHM (W_G/W_L) for Voigt fits.

EMLG, C 1s		(b) Air Exposure			(d) Annealing		
Component	E_{hv} (eV)	E_B (eV)	RI	Q/W_L or W_G/W_L (eV)	E_B	RI	Q/W_L or W_G/W_L (eV)
G''	600	284.81	2.260	9/0.2	284.83	2.281	9/0.2
Z _C	600	284.04	0.050	0.4/0.2	284.05	0.053	0.4/0.2
Z _C ''	600	282.93	0.180	0.4/0.2	282.94	0.187	0.4/0.2
B _C	600	283.65	0.08	0.4/0.2	283.67	0.073	0.4/0.2
B _C ''	600	282.60	0.477	0.4/0.2	282.61	0.560	0.4/0.2

TABLE C.1-6: Mg 2p CORE LEVEL FITTING PARAMETERS FOR Mg-QFSBLG (Mg-INTERCALATED EMLG) COMPONENTS SHOWN IN [FIGURE 6.7](#).

Lorentzian FWHM was set to 0.1 eV for Voigt fits. Mg_M was fit with a Doniach-Šunjić profile, with Lorentzian FWHM set to 0.2 eV, and asymmetry set to -0.2.

EMLG, Mg 2p		(a) 1 st Mg Intercalation			(b) 2 nd Mg Intercalation		
Component	E_{hv} (eV)	E_B (eV) 2p _{3/2}	E_B (eV) 2p _{1/2}	W_G (eV)	E_B (eV) 2p _{3/2}	E_B (eV) 2p _{1/2}	W_G (eV)
Mg _M	100	49.72	49.95	-	-	-	-
Mg _{Si}	100	50.65	50.90	0.45	50.73	50.98	0.45
Mg _{Ox}	100	51.15	51.40	0.50	51.20	51.45	0.50
Mg _{OH}	100	51.70	51.95	0.50	51.72	51.97	0.50

Magnesium Intercalation

TABLE C.1-7: C 1s CORE LEVEL FIT PARAMETERS FOR ALL COMPONENTS IN FIGURE 8.8a, c, e, g (STEP-WISE Mg-INTERCALATION OF EMLG).

Showing binding energy (E_B), relative intensity (RI) and asymmetry/Lorentzian FWHM (Q/W_L) for BWF fits or Gaussian FWHM/Lorentzian FWHM (W_G/W_L) for Voigt fits.

EMLG, C 1s		(a) Pristine EMLG		(b) 1 st Mg-intercalation		(c) 2 nd Mg-intercalation		(d) 3 rd Mg-intercalation	
Component	E_{hv} (eV)	E_B (eV)	Q/W_L or W_L/W_G (eV)	E_B (eV)	Q/W_L or W_L/W_G (eV)	E_B (eV)	Q/W_L or W_L/W_G (eV)	E_B (eV)	Q/W_L or W_L/W_G (eV)
S ₂	600	285.53	0.4/0.8						
S ₁	600	285.00	0.3/0.7						
G	600	284.82	12/0.2						
G _o ["]	600			284.79	12/0.2	284.81	12/0.2	284.82	12/0.2
Z _C	600	284.05	0.2/0.4	284.05	0.2/0.4	284.04	0.2/0.4	284.05	0.2/0.4
Z _C ["]	600			282.95	0.2/0.4	283.00	0.2/0.4	282.95	0.2/0.4
B _C	600	283.72	0.2/0.4	283.70	0.2/0.4	283.70	0.2/0.4	283.70	0.2/0.4
B _C ["]	600			282.66	0.2/0.4	282.56	0.2/0.4	282.58	0.2/0.4
G ₁ ["]	600			285.12	0.2/0.4	285.10	0.2/0.4	285.10	0.2/0.4
G ₂ ["]	600			285.60	0.3/0.7	285.60	0.3/0.7	285.60	0.3/0.7
G ₃ ["]	600			286.50	0.3/0.8	286.50	0.3/0.8	286.50	0.3/0.8

TABLE C.1-8: C 1s CORE LEVEL FIT PARAMETERS FOR ALL COMPONENTS IN FIGURE 8.8b, d, f, h (STEP-WISE INTERCALATED PATTERNED EMLG).

Showing binding energy (E_B), relative intensity (RI) and asymmetry/Lorentzian FWHM (Q/W_L) for BWF fits or Gaussian FWHM/Lorentzian FWHM (W_G/W_L) for Voigt fits.

EMLG-p, C 1s		(a) Pristine EMLG-p		(b) 1 st Mg-intercalation		(c) 2 nd Mg-intercalation		(d) 3 rd Mg-intercalation	
Component	E_{hv} (eV)	E_B (eV)	Q/W_L or W_L/W_G (eV)	E_B (eV)	Q/W_L or W_L/W_G (eV)	E_B (eV)	Q/W_L or W_L/W_G (eV)	E_B (eV)	Q/W_L or W_L/W_G (eV)
S ₂	600	285.52	0.4/0.8						
S ₁	600	285.00	0.4/0.7						
G	600	284.82	9/0.22						
G _o ["]	600			284.84	10/0.2	284.85	10/0.2	284.86	10/0.2
Z _C	600	284.05	0.2/0.4	284.05	0.2/0.4	284.00	0.2/0.4	284.00	0.2/0.4
Z _C ["]	600			283.10	0.2/0.4	282.95	0.2/0.4	282.94	0.2/0.4
B _C	600	283.72	0.2/0.4	283.67	0.2/0.4	283.68	0.2/0.4	283.70	0.2/0.4
B _C ["]	600			282.84	0.2/0.4	282.58	0.2/0.4	282.57	0.2/0.4
G ₁ ["]	600			285.10	0.2/0.4	285.10	0.2/0.4	285.05	0.2/0.4
G ₂ ["]	600			285.60	0.3/0.8	285.60	0.3/0.8	285.58	0.3/0.8
G ₃ ["]	600			286.50	0.3/0.8	286.50	0./0.8	286.50	0.3/0.8

Magnesium Intercalation

TABLE C.1-9: Si 2p CORE LEVEL FIT PARAMETERS FOR ALL COMPONENTS IN FIGURE C.4-3.

Showing binding energy (E_B), relative intensity (RI), and Gaussian FWHM (W_G). All Lorentzian widths for the Voigt fits were set at 0.1 eV and kept constant. A dash indicates no measurement was possible, n/a = not applicable (Mg_{2s} is not a 2p component).

EMLG, Si 2p		(a), (b), Pristine EMLG				(c), (d) 1 st Mg Intercalation				(e), (f) 2 nd Mg Intercalation				(g), (h) 3 rd Mg Intercalation			
Component	E_{hv} (eV)	E_B (eV) 2p _{3/2}	E_B (eV) 2p _{1/2}	RI	W_G (eV)	E_B (eV) 2p _{3/2}	E_B (eV) 2p _{1/2}	RI	W_G (eV)	E_B (eV) 2p _{3/2}	E_B (eV) 2p _{1/2}	RI	W_G (eV)	E_B (eV) 2p _{3/2}	E_B (eV) 2p _{1/2}	RI	W_G (eV)
Ox _o	150	102.9	103.50	0.08	0.5	102.90	103.50	0.08	0.5	102.90	103.50	0.01	0.5				
	600	102.9	103.50	0.04	0.5	102.90	103.50	0.03	0.5	102.90	103.50	0.01	0.5				
Z _{Si}	150	101.87	102.47	0.43	0.4	101.85	102.44	0.29	0.4	101.81	102.42	0.12	0.4	101.79	102.4	0.05	0.4
	600	101.81	102.40	0.41	0.4	101.78	102.38	0.29	0.4	101.78	102.38	0.15	0.4	101.78	102.38	0.08	0.4
B _{Si}	150	101.50	102.14	1	0.4	101.49	102.14	0.63	0.4	101.47	102.10	0.30	0.4	101.50	102.10	0.12	0.4
	600	101.47	102.10	1	0.4	101.43	102.06	0.70	0.4	101.44	102.07	0.35	0.4	101.46	102.06	0.21	0.4
B'' _{Si}	150					100.31	100.91	0.08	0.4	100.27	100.90	0.24	0.4	100.31	100.95	0.29	0.4
	600					100.34	100.96	0.2	0.4	100.26	100.90	0.51	0.4	100.29	100.93	0.62	0.4
Z'' _{Si}	150					100.65	101.25	0.04	0.4	100.65	101.25	0.11	0.4	100.71	101.28	0.14	0.4
	600					100.65	101.25	0.09	0.4	100.62	101.22	0.19	0.4	100.65	101.23	0.23	0.4
Mg _{Si}	150					99.95	100.55	0.11	0.4	99.87	100.48	0.31	0.4	99.93	100.51	0.38	0.4
	600					99.83	100.46	0.04	0.4	99.89	100.49	0.13	0.4	99.91	100.51	0.15	0.4
Ox ₃	150					99.50	100.10	0.03	0.4	99.49	100.10	0.11	0.4	99.53	100.13	0.12	0.4
	600					99.42	100.03	0.03	0.4	99.42	100.03	0.04	0.4	99.45	100.05	0.04	0.4
Mg _{2s}	150					104.00	n/a	n/a	0.9	103.90	n/a	n/a	0.9	103.95	n/a	n/a	0.9
	600					-	n/a	n/a	-	-	n/a	n/a	-	-	n/a	n/a	-

TABLE C.1-10: FIT PARAMETERS FOR Si 2p CORE LEVEL OF ADATOM COMPONENTS IN FIGURE C.4-3.

Showing binding energy (E_B), relative intensity (RI), and Gaussian FWHM (W_G). All components were fit with Voigt functions, with Lorentzian width of 0.1 eV.

EMLG, Si 2p		(a), (b), Pristine EMLG				(c), (d), 1 st Mg intercalation				(e), (f), 2 nd Mg Intercalation			
Component	E_{hv} (eV)	E_B (eV) 2p _{3/2}	E_B (eV) 2p _{1/2}	RI	W_G (eV)	E_B (eV) 2p _{3/2}	E_B (eV) 2p _{1/2}	RI	W_G (eV)	E_B (eV) 2p _{3/2}	E_B (eV) 2p _{1/2}	RI	W_G (eV)
A_0	150	99.2	99.8	0.01	0.5								
	600	-	-	-	-								
A_1	150	100.46	101.06	0.05	0.5	100.46	101.10	0.02	0.5				
	600	100.45	101.05	0.02	0.5	-	-	-	-				
A_2	150	100.93	101.53	0.13	0.5	100.98	101.58	0.09	0.5	100.98	101.58	0.04	0.5
	600	100.98	101.58	0.07	0.5	100.98	101.58	0.04	0.5	100.93	101.53	0.02	0.5

C2. Complete C 1s and Si 2p XPS Spectra for Mg-QFSBLG

[Figure C.2-1](#) shows the C 1s XPS spectra of pristine ([Figure C.2-1a-b](#)) and Mg-intercalated EMLG (Mg-QFSBLG, [Figure C.2-1c-f](#)), and elucidates the 1st Mg-intercalation step and the plasmon loss components comprising the G" doped graphene component (G_o, G₁, G₂ and G₃) which were omitted from [Figure 6.5](#) in the main text.

[Figure C.2-1c-f](#) show the plasmon loss components, which are different to those of [Figure B.3-1](#) and [Figure B.4-1](#) (Ca-QFSBLG). This is thought to be due to the presence of a larger bulk component (B_C/Z_C) after Mg-intercalation as compared to Ca-intercalation (the Mg-intercalation was more partial than the Ca-intercalation), and is more apparent upon comparison of the spectra at different X-ray energies. For instance, at $E_{hv} = 330$ eV, the plasmon loss components decrease monotonically from G_o to G₃, as expected for plasmon losses. In this case, B_C is small in comparison to other bulk peaks. At $E_{hv} = 600$ eV, the plasmon loss components no longer decrease monotonically, and a larger bulk contribution (B_C) is observed. Since the energy location of components S₁ and S₂ are in similar E_B locations as components G₁ and G₂ and components B_C/Z_C are in relatively high proportions, it is likely that the plasmon loss components have a contribution from the buffer layer components S₁ and S₂. This is further supported by the fact that when the bulk component B_C decreases after the 2nd Mg-intercalation, plasmon loss peak G₂ also seems to decrease. Furthermore, this was not observed with the Ca-intercalation of EMLG ([Figure B.3-1](#) and [Figure B.4-1](#)), where the Ca-QFSBLG had less pronounced B_C/Z_C components after intercalation, in further agreement with the buffer-layer contribution hypothesis presented here explaining the anomaly in the plasmon loss peaks. The plasmon loss component peak details can be found in [Table C.2-1](#).

The incomplete Mg-intercalation of pristine EMLG is also supported by the Si 2p core level spectra shown in [Figure C.2-2](#) for pristine and Mg-intercalated spectra, showing again all Mg-intercalation steps (including the 1st Mg-intercalation step that was omitted in [Figure 6.4](#)). It can be clearly seen that components B_{Si} and Z_{Si} corresponding to the bulk of the original pristine EMLG are still present, even after the 2nd intercalation. This is consistent with the LEED data in [Figure 6.3](#) which showed the presence (albeit diminished) of a buffer layer. Nonetheless, as was mentioned in [Chapter 6](#), the intercalation of Mg was more difficult than that of Ca, and was attributed to the higher vapor pressure (causing rate of evaporation to exceed rate of intercalation), the decreased sticking coefficient (contributing to the Mg evaporating before intercalation) [351], decreased reactivity or a combination of these effects. Nonetheless these effects contributed to keeping the graphene surface relatively clean, and this can be seen by comparison of the

relative intensity of the XPS spectra, which shows Mg-intercalation caused less attenuation in the XPS spectra than Ca-intercalation. It will be noted here that it was difficult to fit component Z_C for the C 1s spectra at $E_{hv} = 330$ eV, and this was likely the result of the large asymmetry in the BWF fit (and large width of the plasmon components) coupled with the already low intensity of the component at this X-ray energy. However, component Z_C was observed in the Si 2p core levels at low beam energy, and this is likely because the photoionization cross-section of the Si 2p core level at $E_{hv} = 150$ eV is ≈ 5 times larger than the C 1s core level at $E_{hv} = 330$ eV [143], and, there are no other peaks in this region to obscure component Z_{Si} .

Furthermore, component Ox_3 at $E_B = 99.53 \pm 0.05$ eV is a surface ($RI_R \approx 2.73$) sensitive component, and this may suggest that it is either a Mg-silicate (i.e. the Mg has reacted with the available surface oxygen that was present as contamination in the sample, component Ox_o , to produce an Mg-Si-O compound) or another form of Mg-silicide. I can rule out that the component is a Mg-silicate, as prior studies have determined the binding energy of an Mg-silicate is much higher than what we observe ($E_B = 102 - 103$ eV) [369-370]. It is well known that magnesium silicide is only able to form in the stoichiometry Mg_2Si , but the extreme conditions under which this Mg-silicide is formed could facilitate the formation of a stable stoichiometry differing from that of Mg_2Si underneath graphene. Pi *et al.* [306] found that upon Mg deposition on Si(001), a sub-stoichiometric or ‘transition layer’ Mg-silicide formed in addition to Mg_2Si , the components separated by $\Delta E_B \approx 0.42$ eV. The binding energy separation between components Mg_{Si} and Ox_3 is $\Delta E_B = 0.41 \pm 0.1$ eV, in agreement with Pi *et al.* [306]. Also, the relative intensity of component Ox_3 decreased after 6 hours of ambient air exposure, but did not shift in binding energy. This is unlikely to occur for an already oxidized material, or a material that is not at least semi-stable. I note here that component Ox_3 remarkably resembles component Ox_i in the Ca-intercalated Si 2p core level (see Figure B.3-2), in which it was also implied that the component consisted of a sub-stoichiometric Ca-silicide.

Components B''_{Si} ($E_B = 100.32 \pm 0.05$ eV) and Z''_{Si} ($E_B = 100.69 \pm 0.05$ eV) are analogous to the bulk and sub-surface SiC components, respectively, from Ca-intercalation (B'_{Si} and Z'_{Si}), shifted in energy by surface band bending. We also observe in Figure C.2-2c-d the remnants of the original bulk components B_{Si} and Z_{Si} , and this was due to impartial Mg-intercalation, also supported by our LEED data in Figure 6.3 which still shows the (albeit diminished) presence of a buffer layer.

In addition to the similar change in shape and lack of peak shift of the graphene component G” (as was seen with Ca-intercalation), we see the creation of 2 new components, labelled Z''_C ($E_B = 282.93 \pm 0.05$ eV) and B''_C ($E_B = 282.61 \pm 0.05$ eV). The binding energy separation of these newly formed components and components B_C and Z_C are $\Delta E_B = 1.07 \pm 0.1$ eV ($B_C \rightarrow B''_C$) and $\Delta E_B = 1.11 \pm 0.1$ eV ($Z_C \rightarrow Z''_C$). The binding energy difference, ΔE_B , between

components B_C and Z_C is 0.36 ± 0.1 eV, and agrees well with the $\Delta E_B = 0.32 \pm 0.1$ eV of components B''_C and Z''_C . These ΔE_B values agree with those of the Si 2p core level components ([Figure 6.4c-d](#) / [Figure C.2-2c-f](#)) in which the binding energy separation is measured as $\Delta E_B = 1.14 \pm 0.1$ eV ($B_{Si} \rightarrow B''_{Si}$), 1.09 ± 0.1 eV ($Z_{Si} \rightarrow Z''_{Si}$), 0.37 ± 0.1 eV ($Z_{Si} \rightarrow B''_{Si}$) and 0.32 ± 0.1 eV ($Z_{Si} \rightarrow B_{Si}$).

Furthermore, I find that Z''_C is more surface-like ($RI_R = 1.5$) than B''_C ($RI_R = 1$), and that these values agree well with the pristine components Z_C ($RI_R = 1.6$) and B_C ($RI_R = 1$) from [Figure C.2-1a-b](#), suggesting these components are likely located in the same atomistic positions (inset, [Figure C.2-1d](#)). On the other hand, the surface sensitivity for the analogous Si 2p bulk components, Z''_{Si} and B''_{Si} are $RI_R \approx 0.23$ and $RI_R \approx 0.37$, respectively and for the pristine SiC bulk components Z_{Si} and B_{Si} are $RI_R \approx 1$ and $RI_R = 1$, respectively. This discrepancy between the Mg-intercalated and pristine RI_R may arise because the sample was not completely intercalated, but also highlights that Z''_{Si} is less of a surface component. This is relatively straightforward to understand using the atomic models in [Figure C.2-2b, d](#). Here, pristine EMLG component Z_{Si} is located at the surface of the SiC ([Figure C.2-2b](#)). Upon intercalation ([Figure C.2-2d](#)), component Z''_{Si} has been shifted towards the bulk due to the reaction of the surface silicon with Mg to form an Mg-Si layer.

I have shown that the components B''_C/B''_{Si} and Z''_C/Z''_{Si} of the SiC bulk and surface, respectively – shifted to lower binding energy from the original components B_C/B_{Si} and Z_C/Z_{Si} , respectively, *after* the intercalation of Mg. The formation of Mg-Si bonds changed in the chemical environment (akin to the B_C/B_{Si} and Z_C/Z_{Si} components in Ca-intercalation) at the surface of the SiC, and thus caused these components to shift. This is also observed in many other reports of graphene on SiC intercalation with various elements (see refs. [[71-72](#), [313](#)] for some examples). All component parameters for [Figure C.2-1](#) and [Figure C.2-2](#) can be found in [Table C.1-1](#) (Si 2p), [Table C.1-2](#) (Si 2p) and [Table C.1-3](#) (C 1s).

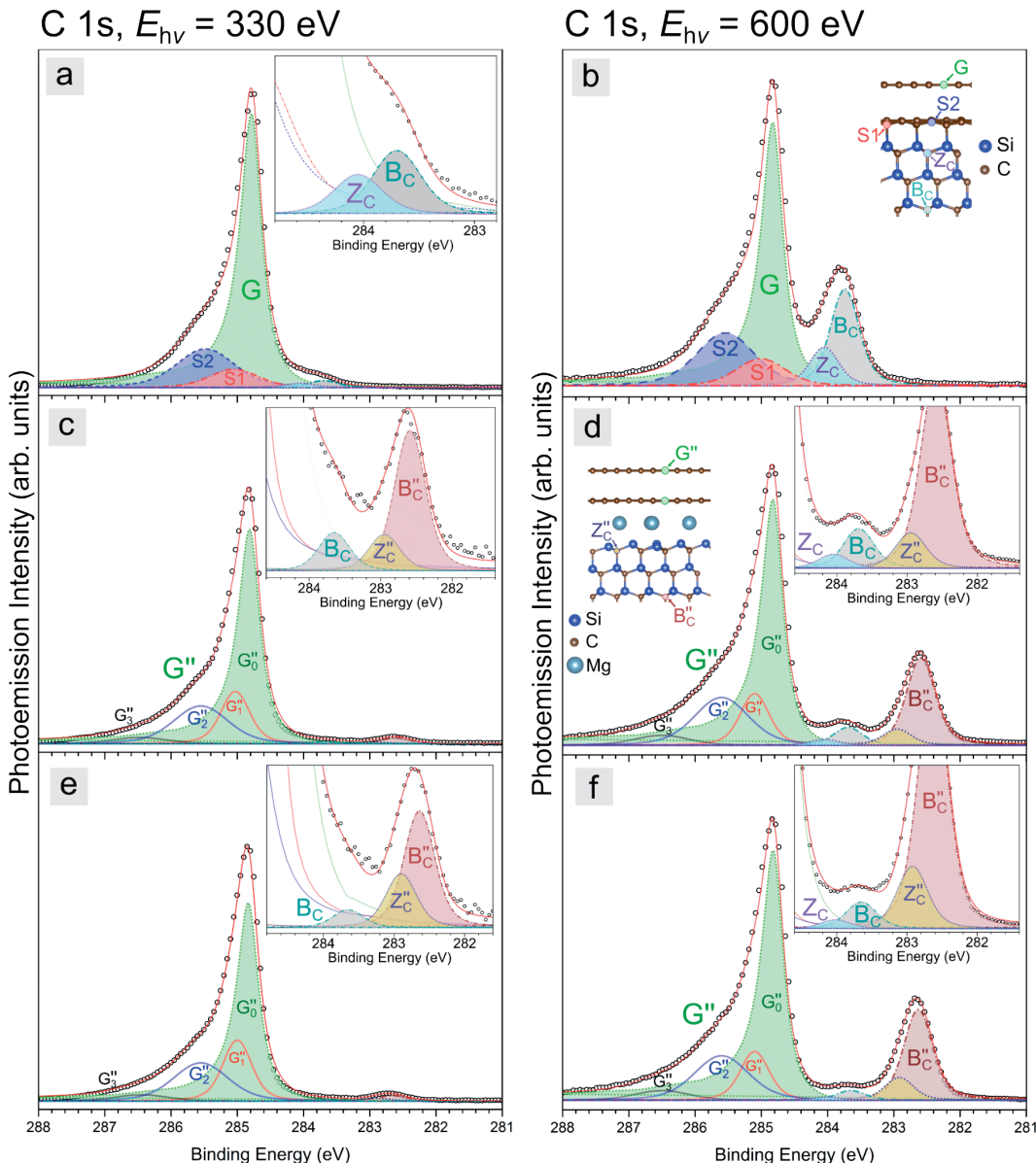


FIGURE C.2-1: X-RAY PHOTOEMISSION SPECTRA OF C 1s CORE LEVEL OF PRISTINE EPITAXIAL MONOLAYER GRAPHENE (EMLG) AND Mg-INTERCALATED QUASI-FREESTANDING GRAPHENE (Mg-QFSBLG) AT X-RAY ENERGIES OF 330 eV (SURFACE SENSITIVE) AND 600 eV (BULK SENSITIVE), SHOWING ALSO THE PLASMON LOSS PEAKS AND THE 1st Mg-INTERCALATION STEP THAT WERE OMITTED IN THE MAIN DISCUSSION.

(a, b) Pristine EMLG prior to Mg-intercalation showing buffer layer components S₂ and S₁. (c, d) 1st Mg-intercalation to create Mg-QFSBLG. (e, f) 2nd Mg-intercalation for the creation of Mg-QFSBLG. The Mg-intercalation was only partial as seen clearly by the presence of component B_C.

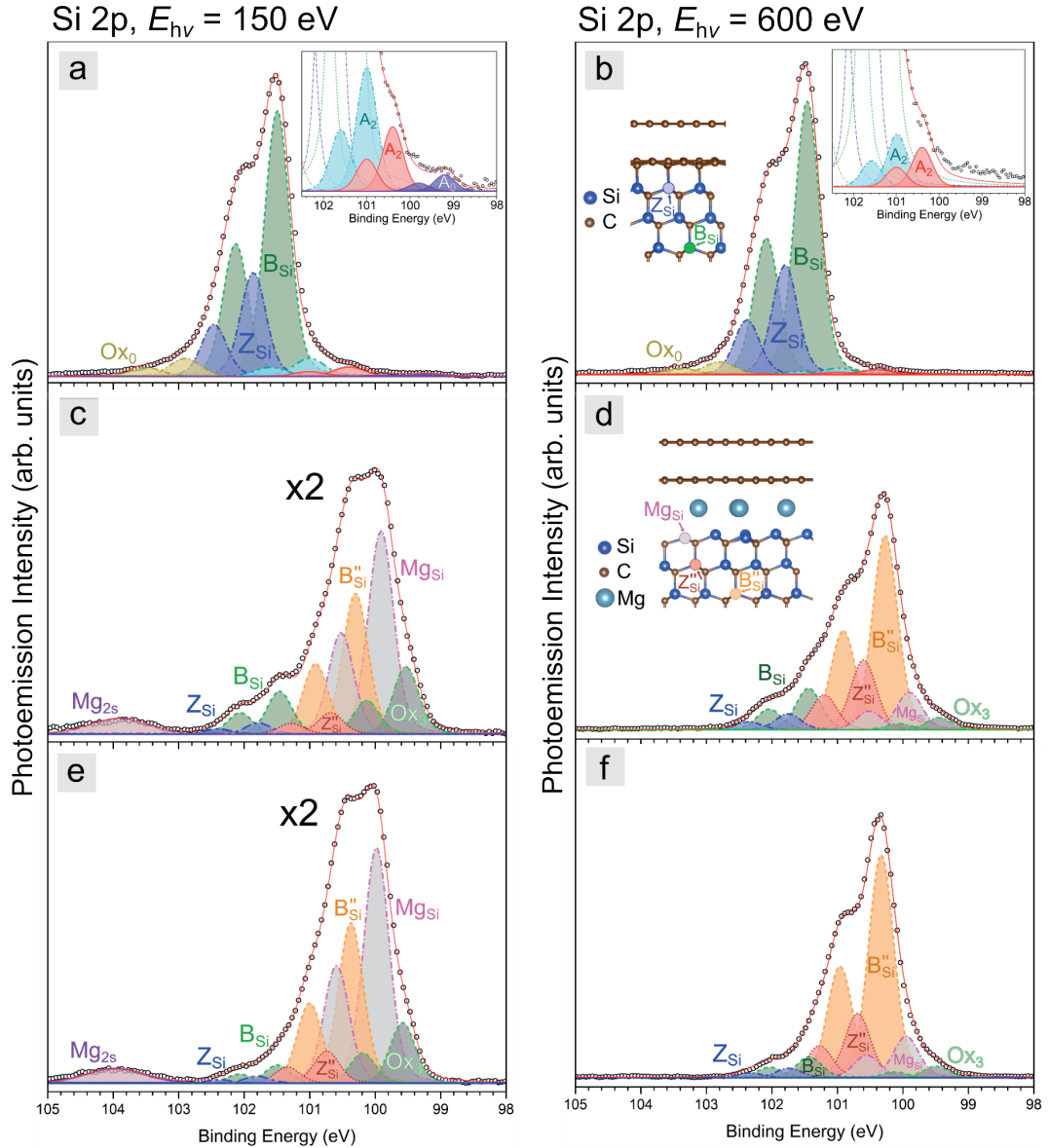


FIGURE C.2-2: X-RAY PHOTOEMISSION SPECTRA OF Si 2p CORE LEVEL OF PRISTINE EPITAXIAL MONOLAYER GRAPHENE (EMLG) AND Mg-INTERCALATED QUASI-FREESTANDING (Mg-QFSBLG) GRAPHENE AT X-RAY ENERGIES OF 150 eV (SURFACE SENSITIVE) AND 600 eV (BULK SENSITIVE), SHOWING ALSO THE 1ST Mg-INTERCALATION STEP THAT WAS OMITTED IN THE MAIN DISCUSSION.

(a), (b) Pristine EMLG prior to Mg-intercalation showing bulk (B_{Si}/Z_{Si}), adatom (A_0 , A_1 and A_2) and oxygen (Ox_0) components. (c), (d) 1st Mg-intercalation to create Mg-QFSBLG. Bulk components have shifted to lower binding energy and are now labelled with a double prime. Original bulk components are still present. (e), (f) 2nd Mg-intercalation to convert more regions to Mg-QFSBLG. The Mg-intercalation was only partial, seen clearly by the (slight) presence of the original bulk components.

TABLE C.2-1: PARAMETERS USED FOR THE VOIGT FITS OF THE PLASMON LOSS PEAKS FOR Mg-QFSBLG IN FIGURE C.2-1 SHOWING BINDING ENERGY (E_B), RELATIVE INTENSITY (RI) AND FULL WIDTH AT HALF MAXIMUM (FWHM). PARAMETERS FOR G_0 ARE SHOWN IN TABLE C.1-3 AS G'' .

EMLG, C 1s		(c), (d), 1 st Mg Intercalation			(e), (f) 2 nd Mg Intercalation		
Component	E_{hv} (eV)	E_B (eV)	RI	FWHM	E_B	RI	FWHM
G_1	330	285.03	7.50	0.52	285	8.75	0.52
	600	285.10	0.53	0.52	285.10	0.50	0.52
G_2	330	285.55	8.68	0.97	285.55	8.79	0.97
	600	285.60	0.49	0.97	285.60	0.46	0.97
G_3	330	286.47	0.02	0.97	286.45	0.02	0.97
	600	286.50	0.10	0.97	286.50	0.10	0.97

C3. The Mg-Intercalation of H-QFSBLG

EMLG and H-QFSBLG were mounted on the same sample holder (see) for every Ca- and Mg-intercalation. In this section I present findings on the attempted Mg-intercalation of H-QFSBLG. I find that while EMLG samples were Mg-intercalated to form Mg-QFSBLG, H-QFSBLG *could not* be intercalated. This is supported by LEED and XPS measurements, which I present below. The Mg-intercalation procedure is outlined in [Chapter 6, Section 6.3.1](#) (the sample used for XPS *not* SECO).

[Figure C.3-1](#) shows LEED images at an electron energy of 100 eV of pristine H-QFSBLG ([Figure C.3-1a](#)) and H-QFSBLG after multiple Mg-intercalations ([Figure C.3-1b](#)). It is clear that no visual presents itself after Mg-intercalation, implying that magnesium has been unsuccessful in intercalating H-QFSBLG. Although this may be the case, XPS measurements are needed to confirm that a reaction has not taken place, as small concentrations of Mg-silicide are not registered by LEED, even though the sample may be slowly converting to Mg-QFSBLG (as was observed, see [Appendix C4](#)).

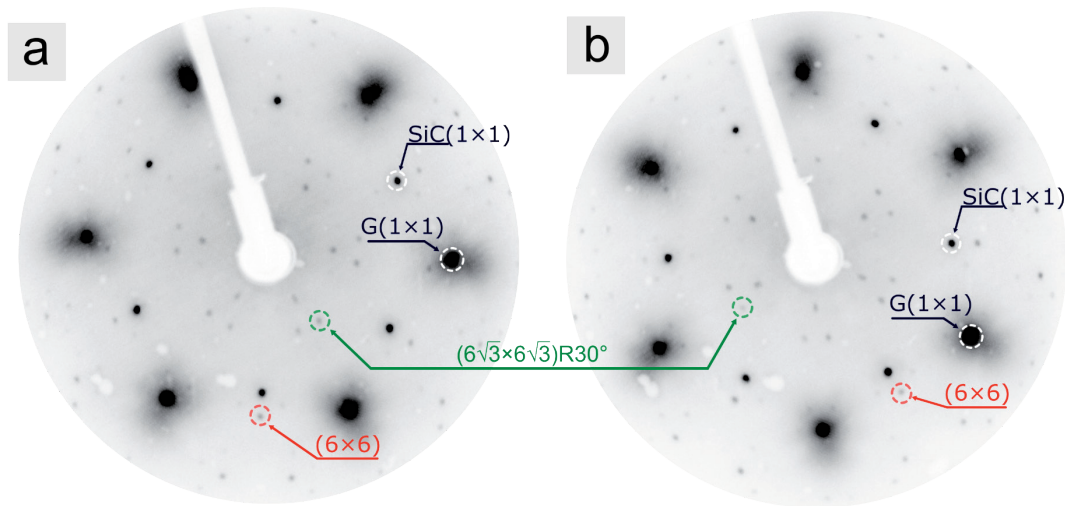


FIGURE C.3-1: LOW ENERGY ELECTRON DIFFRACTION PATTERN OF H-QFSBLG AT AN ELECTRON ENERGY OF 100 eV.

(a) Pristine H-QFSBLG showing graphene ($G(1\times 1)$), SiC ($SiC(1\times 1)$), $(6\sqrt{3}\times 6\sqrt{3})R30^\circ$ and (6×6) spots. The $(6\sqrt{3}\times 6\sqrt{3})R30^\circ$ and (6×6) spots are related to the buffer layer, and have a suppressed intensity in comparison with EMLG (Fig. 1a) due to H-intercalation de-coupling the buffer layer. (b) Mg-intercalated H-QFSBLG. No changes after Mg-intercalation were observed – the diffraction pattern is identical to pristine H-QFSBLG.

Figure C.3-2 shows the Si 2p and C 1s core level results before and after the attempted Mg-intercalation of H-QFSBLG. **Figure C.3-2a-b** show the Si 2p and C 1s core levels for pristine H-QFSBLG. The sample was intercalated at the same time as the EMLG sample shown in **Figure C.2-1** and **Figure C.2-2** (see **Chapter 6, Section 6.3.1**). **Figure C.3-2c-d** show the results after the 2nd Mg-intercalation - no change was observed in the Si 2p and C 1s core level spectra, respectively, apart from a small intensity decrease in the Si 2p core level. The results from the Si 2p and C 1s core level spectra show that no Mg intercalated these samples, although as can be observed in the Mg 2p spectra (Fig. S22), there may have been minute amounts of intercalation (at the detection limit of the synchrotron).

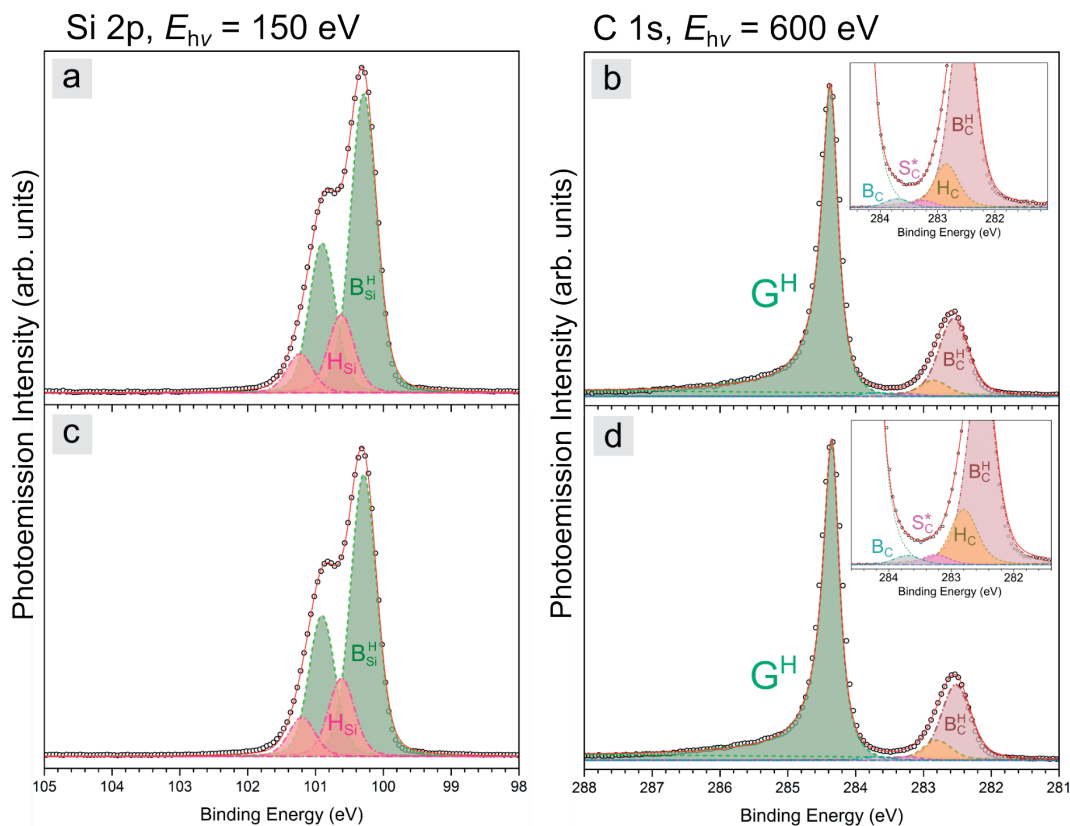


FIGURE C.3-2: X-RAY PHOTOEMISSION SPECTRA OF THE Si 2p AND C 1s CORE LEVELS OF THE ATTEMPTED Mg-INTERCALATION OF H-QFSBLG AFTER MULTIPLE INTERCALATION ATTEMPTS AT AN X-RAY ENERGY OF $E_{hv} = 150$ AND 600 eV, RESPECTIVELY.

- (a) Si 2p core level of pristine H-QFSBLG prior to Mg-intercalation attempts.
- (b) C 1s core level of pristine H-QFSBLG prior to Mg-intercalation attempts.
- (c) Si 2p core level after the 2nd Mg-intercalation attempt. (d) C 1s core level after the 2nd Mg-intercalation attempt. No evidence of intercalation was found in the C 1s or Si 2p core levels.

TABLE C.3-1: COMPONENT PARAMETERS FOR THE C 1s CORE LEVEL PHOTOEMISSION SPECTRA IN [FIGURE C.3-2b](#) AND [FIGURE C.3-2d](#) SHOWING BINDING ENERGY (E_B), ASYMMETRY/LORENTZIAN WIDTH (Q/W_L) OF THE BWF FIT OR GAUSSIAN WIDTH/LORENTZIAN WIDTH (W_G/W_L) OF THE VOIGT FIT.

H-QFSBLG, C 1s		(b), Pristine H-QFSBLG		(d) 2 nd Mg Intercalation	
Component	E_{hv} (eV)	E_B (eV)	Q/W_L or W_G/W_L (eV)	E_B (eV)	Q/W_L or W_G/W_L (eV)
G ^H	600	284.36	10/0.15	284.34	10/0.15
H _C	600	282.85	0.4/0.2	282.80	0.4/0.2
B _C ^H	600	282.56	0.4/0.2	282.52	0.4/0.2
B _C	600	283.70	0.4/0.2	283.70	0.4/0.2
S _C [*]	600	283.25	0.4/0.2	283.25	0.4/0.2

TABLE C.3-2: COMPONENT PARAMETERS FOR THE Si 2p CORE LEVEL PHOTOEMISSION SPECTRA IN [FIGURE C.3-2a](#) AND [FIGURE C.3-2c](#) SHOWING BINDING ENERGY (E_B), AND GAUSSIAN WIDTH/LORENTZIAN WIDTH (W_G/W_L) OF THE VOIGT FIT.

H-QFSBLG, Si 2p		(a) Pristine H-QFSBLG			(c) 2 nd Mg Intercalation		
Component	E_{hv} (eV)	E_B (eV) 2p _{3/2}	E_B (eV) 2p _{1/2}	W_G/W_L (eV)	E_B (eV) 2p _{3/2}	E_B (eV) 2p _{1/2}	W_G/W_L (eV)
B _{Si} ^H	150	100.29	100.90	0.4/0.1	100.34	100.97	0.4/0.1
H _{Si}	150	100.62	101.23	0.4/0.1	100.62	101.20	0.4/0.1

[Figure C.3-3](#) shows the results of the intercalation of pristine H-QFSBLG with Mg, and indicates that very little or no Mg-Si compound was produced. The photoionization cross section at $E_{hv} = 100$ eV for the Mg 2p core level is ≈ 1.3 and ≈ 35 times larger than the Si 2p and C 1s core levels at $E_{hv} = 150$ and 600 eV, respectively. Thus, this explains why there was no observable peaks in the Si 2p and C 1s core level spectra in [Figure C.3-2](#). It is possible that minute amounts of Mg may have intercalated, for example, at H vacancy sites which are known to exist in H-QFSBLG [301]. The component parameters can be found in [Table C.3-3](#).

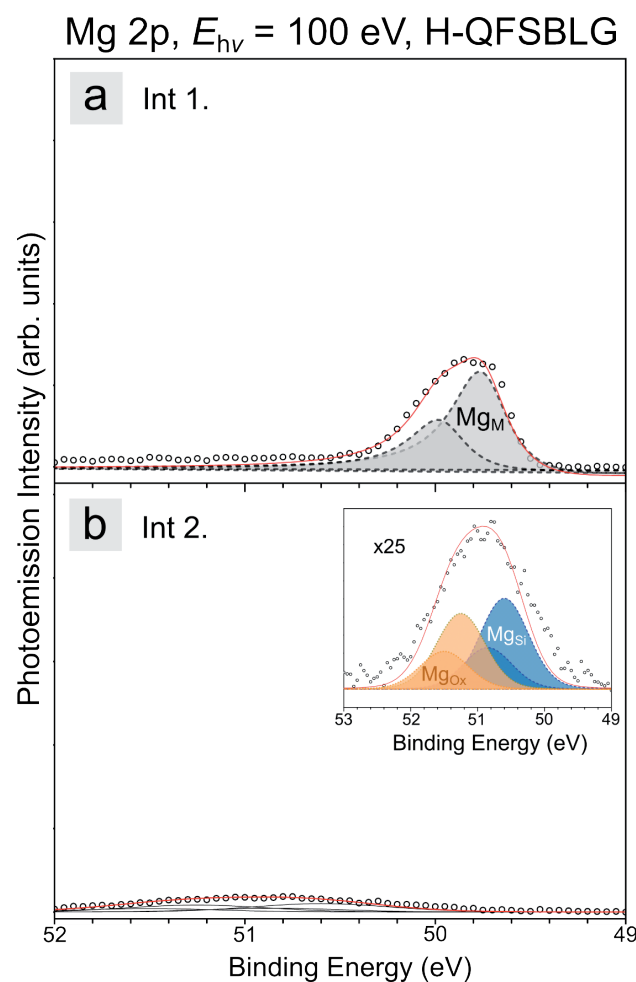


FIGURE C.3-3: X-RAY PHOTOEMISSION SPECTRA OF THE Mg 2p CORE LEVEL SHOWING BOTH ATTEMPTS OF THE Mg-INTERCALATION OF H-QFSBLG.

(a) *1st Mg intercalation showing excess metallic Mg (component Mg_M, dashed, grey) on the surface of the graphene, though no evidence of intercalation.* (b) *2nd Mg intercalation showing no Mg metal remaining on the surface. A small peak is visible, magnified by a factor of 25 in the inset and deconvolved showing Mg-silicide (Mg_{Si}, blue, dashed) and/or Mg-oxide (Mg_{Ox}, dotted, orange) components.*

TABLE C.3-3: FITTING PARAMETERS FOR THE Mg 2p CORE LEVEL (AT AN X-RAY ENERGY OF 100 eV) OF Mg-INTERCALATED H-QFSBLG IN [FIGURE C.3-3](#) SHOWING BINDING ENERGY (E_B), RELATIVE INTENSITY (RI) AND THE GAUSSIAN WIDTH (W_G)/LORENTZIAN WIDTH (W_L) FOR ALL PEAKS. Mg_M WAS FIT WITH A DONIACH-ŠUNJIĆ PROFILE, $W_L = 0.2$ eV, ASYMMETRY = -0.2.

H-QFSBLG, Mg 2p		(a) 1 st Mg-Intercalation			(c) 2 nd Mg-Intercalation		
Component	E_{hv} (eV)	E_B (eV) 2p _{3/2}	E_B (eV) 2p _{1/2}	W_G/W_L (eV)	E_B (eV) 2p _{3/2}	E_B (eV) 2p _{1/2}	W_G/W_L (eV)
Mg _M	100	49.74	49.96				
Mg _{Si}	100				50.60	50.85	0.8/o.1
Mg _{Ox}	100				51.25	51.50	0.8/o.1

[Figure C.3-4](#) shows the O 1s core level of H-QFSBLG after Mg-intercalations (1st Mg-intercalation, bottom curve, red; 2nd Mg-intercalation above curve, blue). In the 2nd Mg-intercalation, there is a small oxide peak evident. This may have been from excess Mg on the surface that was oxidised, and agrees with the presence of the oxide peak (component Mg_{Ox}) in the Mg 2p spectrum of [Figure C.3-3](#). This would also explain the Si 2p core level intensity decrease observed in [Figure C.2-2](#), as Mg debris on the surface of the graphene would attenuate the signal. After exposure to air for 6 hours ('Air Expose', green curve) there is a more significant oxide peak present, and implies that Mg was present either on just the surface, or both on the surface and intercalated underneath the graphene. Since the sample started oxidising in UHV, it is likely that Mg was on the surface. Nonetheless, whether the magnesium was intercalated or not, XPS and LEED are unable to offer conclusive evidence, and a more sensitive surface technique such as STM would need to be utilised to determine if the Mg is able to intercalate hydrogen vacancies in H-QFSBLG.

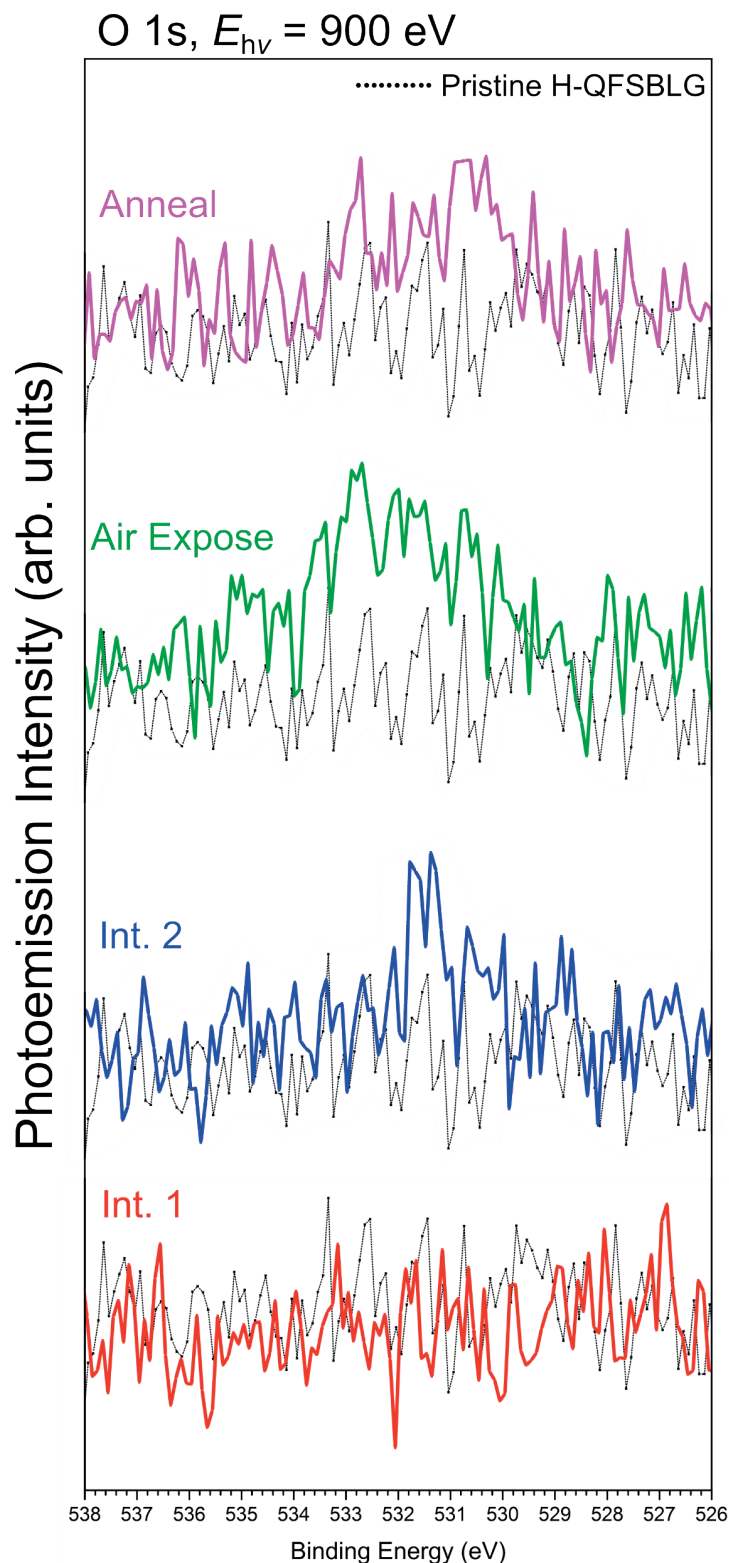


FIGURE C.3-4: X-RAY PHOTOEMISSION SPECTRA OF THE O 1s CORE LEVEL OF H-QFSBLG AFTER ATTEMPTED Mg-INTERCALATIONS AND SUBSEQUENT 6-HOUR AIR EXPOSURE AND ANNEAL AT 623 K FOR 1.5 HOURS.

C4. Step-Wise Mg-Intercalation of Epitaxial Monolayer Graphene on 6H-SiC(0001)

The step-wise Mg-intercalation of graphene on 6H-SiC(0001) was possible with Mg because of its higher vapour pressure, lower adhesion and decreased reactivity in comparison to Ca; ultimately increasing the difficulty of Mg-intercalation. In the stepwise Mg-intercalation experiment, two samples were used – a pristine EMLG sample, and a laser patterned EMLG sample named EMLG-p (see [Chapter 7, Section 7.3.1.2](#) for intercalation method and [Chapter 8, Section 8.4.3](#) for laser patterning details).

The LEED spot patterns were taken at an electron energy of 100 eV. [Figure C.4-1](#) shows the LEED spot patterns of pristine and Mg-intercalated EMLG. [Figure C.4-1a](#) shows the pristine EMLG spot pattern, in which the graphene ($G(1\times 1)$) and silicon carbide ($SiC(1\times 1)$) spots can be seen, as well as spot patterns arising from the buffer layer ($(6\sqrt{3}\times 6\sqrt{3})R30^\circ$ and (6×6)). [Figure C.4-1b-c](#) show the 1st and 2nd Mg-intercalation, respectively. No evidence of Mg-intercalation is present, since the buffer layer related spot patterns are still visible, and there are no $(\sqrt{3}\times\sqrt{3})R30^\circ$ spots with respect to the $SiC(1\times 1)$ spots ($SiC(\sqrt{3}\times\sqrt{3})R30^\circ$) visible, as was the case with the Mg-QFSBLG sample in [Chapter 6](#). Only after the 3rd Mg-intercalation step, shown in [Figure C.4-1d](#), are the $SiC(\sqrt{3}\times\sqrt{3})R30^\circ$ spots visible and buffer layer related spots been suppressed, suggesting Mg-QFSBLG has been formed. This contrasts with the EMLG-p sample in [Figure C.4-2](#) which shows evidence of the formation of Mg-QFSBLG after the 1st Mg-intercalation. After the 2nd Mg-intercalation shown in [Figure C.4-2c](#), the LEED spot pattern is what would be expected from Mg-QFSBLG. Furthermore, the $(6\sqrt{3}\times 6\sqrt{3})R30^\circ$ and (6×6) spots are almost entirely eliminated. Thus, the LEED data supports the C 1s core level spectra shown in [Figure 8.8](#), which demonstrated the EMLG-p sample intercalating faster and more completely than the standard EMLG sample.

Furthermore, the step-wise Mg-intercalated pristine EMLG sample was used to find the workfunction of Mg-QFSBLG in [Chapter 6, Section 6.4.4.2](#). The resulting Si 2p spectrum is shown in [Figure C.4-3](#) (see [Table C.1-9](#) and [Table C.1-10](#) for fit parameters) and demonstrates that this sample was less intercalated than the sample which was intercalated in 2 steps, as shown in [Figure C.2-2](#). The C 1s spectrum for this sample is shown in [Figure 8.5a, c, e, g](#) (see [Table C.1-7](#) for fit parameters).

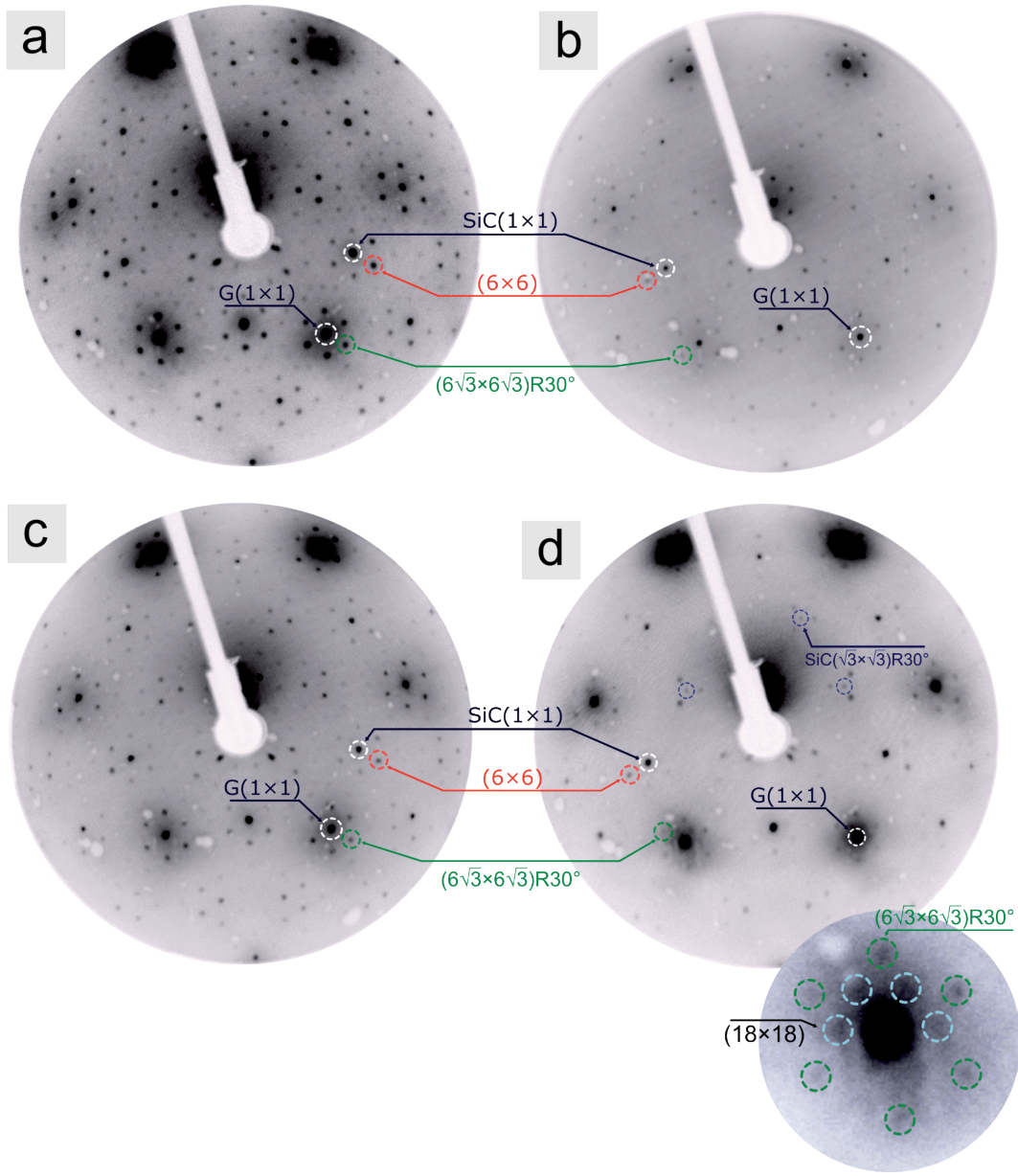


FIGURE C.4-1: LOW ENERGY ELECTRON DIFFRACTION AT AN ELECTRON ENERGY OF 100 eV OF PRISTINE AND Mg-INTERCALATED EPITAXIAL MONOLAYER GRAPHENE ON 6H-SiC(0001) (EMLG).

(a) Pristine EMLG showing diffraction spots due to the SiC bulk ($\text{SiC}(1\times 1)$), graphene ($\text{G}(1\times 1)$) and buffer layer ($(6\sqrt{3}\times 6\sqrt{3})\text{R}30^\circ$ and (6×6)). (b) 1st Mg-intercalation still shows presence of buffer layer, no evidence of an ordered Mg coordination is observed. (c) 2nd Mg-intercalation still shows presence of buffer layer and no evidence of the formation of a Mg-silicide. (d) 3rd Mg-intercalation showing the $(\sqrt{3}\times\sqrt{3})\text{R}30^\circ$ spots with respect to the $\text{SiC}(1\times 1)$ spots ($\text{SiC}(\sqrt{3}\times\sqrt{3})\text{R}30^\circ$) and evidence of the (18×18) spots that were observed with the Mg-QFSBLG sample in Figure 6.3. The suppression of $(6\sqrt{3}\times 6\sqrt{3})\text{R}30^\circ/(6\times 6)$ spots related to the buffer layer and increase in brightness of the $\text{G}(1\times 1)$ with respect to the $\text{SiC}(1\times 1)$ spots, as compared to pristine EMLG in (a) is apparent.

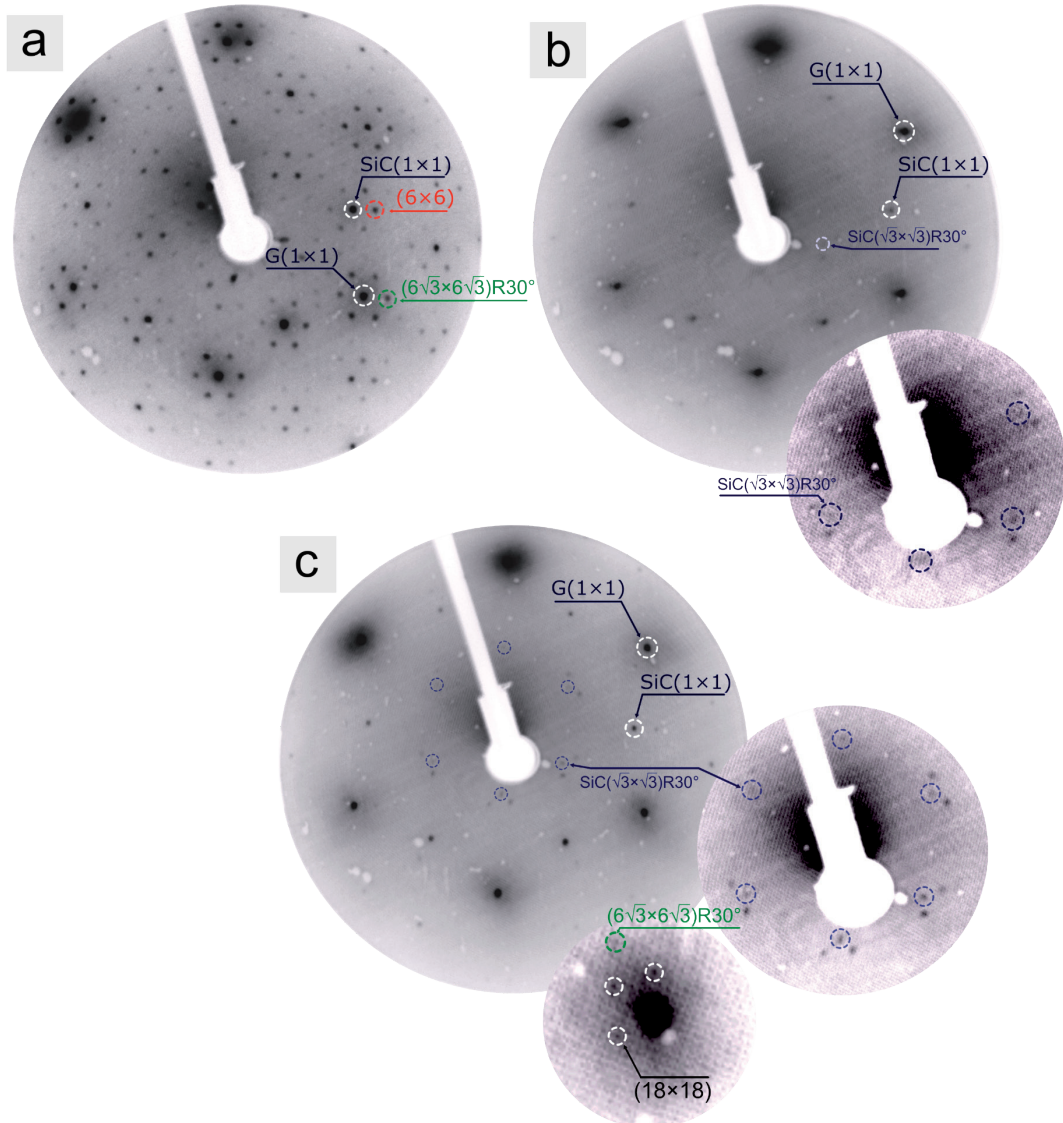


FIGURE C.4-2: LOW ENERGY ELECTRON DIFFRACTION AT AN ELECTRON ENERGY OF 100 eV OF PRISTINE AND Mg-INTERCALATED ‘PATTERNED’ EPITAXIAL MONOLAYER GRAPHENE ON 6H-SiC(0001) (EMLG-p).

(a) Pristine EMLG-p showing diffraction spots due to the SiC bulk ($\text{SiC}(1\times 1)$), graphene ($\text{G}(1\times 1)$) and buffer layer ($(6\sqrt{3}\times 6\sqrt{3})\text{R}30^\circ$ and (6×6)). **(b)** 1st Mg-intercalation of EMLG-p showing evidence of the $(\sqrt{3}\times\sqrt{3})\text{R}30^\circ$ spots with respect to the $\text{SiC}(1\times 1)$ spots ($\text{SiC}(\sqrt{3}\times\sqrt{3})\text{R}30^\circ$), suggesting in the 1st Mg-intercalation, Mg-QFSBLG has started to form in substantial quantity. **(c)** 2nd Mg-intercalation of EMLG-p showing more prominent $\text{SiC}(\sqrt{3}\times\sqrt{3})\text{R}30^\circ$ spots which suggest that Mg-QFSBLG has formed. In addition, partial (18×18) spots (around the $\text{G}(1\times 1)$ spots) are observed, as in Figure 6.3.

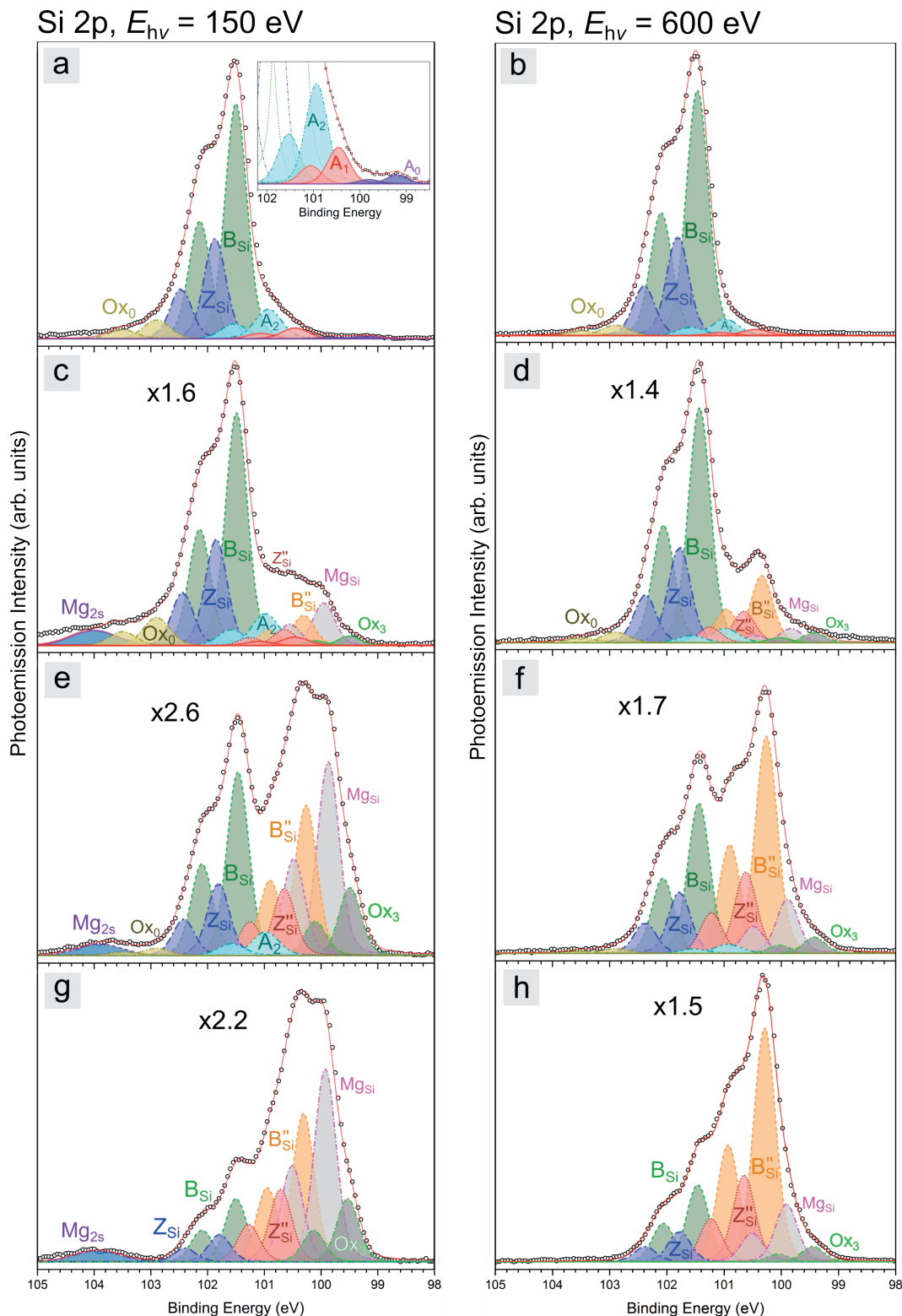


FIGURE C.4-3: X-RAY PHOTOEMISSION SPECTRA SHOWING THE Si 2p CORE LEVEL OF STEP-WISE Mg-INTERCALATED EMLG AT AN X-RAY ENERGY OF $E_{hv} = 150$ eV AND 600 eV, SEE FIGURE 6.10 AND FIGURE 8.5.

(a, b) Pristine EMLG. (c, d) 1st Mg-intercalation. (e, f) 2nd Mg-intercalation. (g, h) 3rd Mg-intercalation. Magnifications from (a) and (b) are given in (c, e, g) and (d, f, h), respectively. See text for component explanations.

C5. Raman Spectroscopy Map of Buffer Layer / EMLG Sister Sample Used in ARPES Study

[Figure C.5-1](#) shows a Raman map of a sister sample of the buffer layer/monolayer mixed sample that was used in the STM ([Figure 6.8](#)) and ARPES ([Figure 6.11](#)) studies. The colour map shown in [Figure C.5-1](#) illustrates the buffer layer regions in black, while monolayer is shown in blue/green and bilayer/trilayer is shown in orange/red. The buffer layer amount was estimated using ImageJ, the results of which are shown in [Figure C.5-2a](#). [Figure C.5-2b](#) shows [Figure C.5-1](#) overlaid with the calculated buffer layer areas of [Figure C.5-2a](#). The total calculated buffer layer amount is $\approx 50\%$ of the sample area in [Figure C.5-1](#). Immediately noticeable is that the regions do not perfectly exclude all graphene areas, and subsequently this yields a slight overestimation of the buffer layer amount.

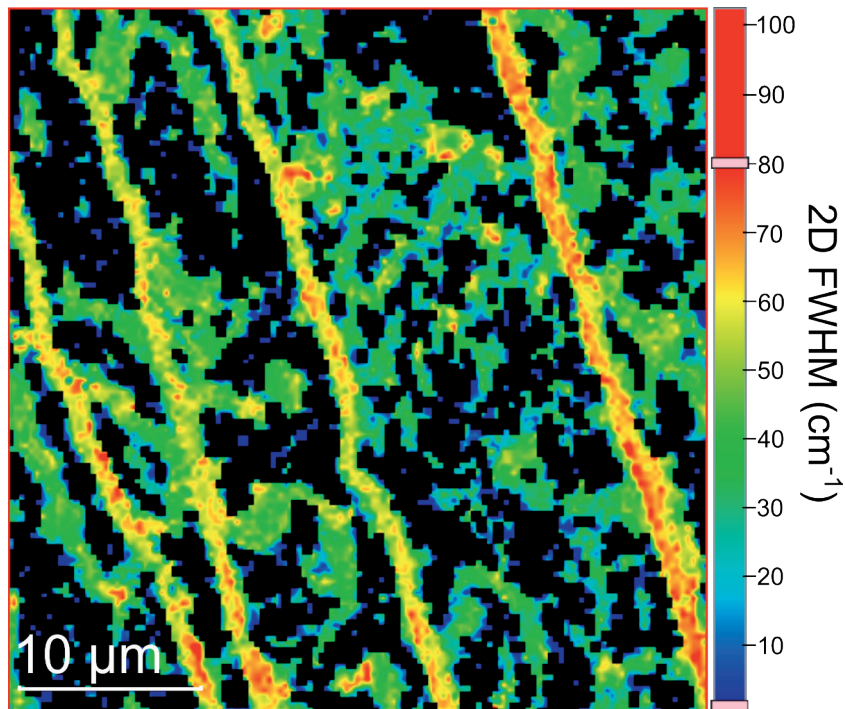


FIGURE C.5-1: RAMAN MAP OF EMLG/BUFFER LAYER SISTER SAMPLE SHOWN IN [FIGURE 6.8](#) AND [FIGURE 6.11](#).

The Raman map ($38.7 \times 38.7 \mu\text{m}$) was obtained using a 532 nm laser at 9.6 mW , with exposure time of 0.125 seconds, pixel size of $0.3 \mu\text{m}$ and 5 averages. Colour bar shows the full width at half maximum (FWHM) of the 2D peak. Black regions are buffer layer.

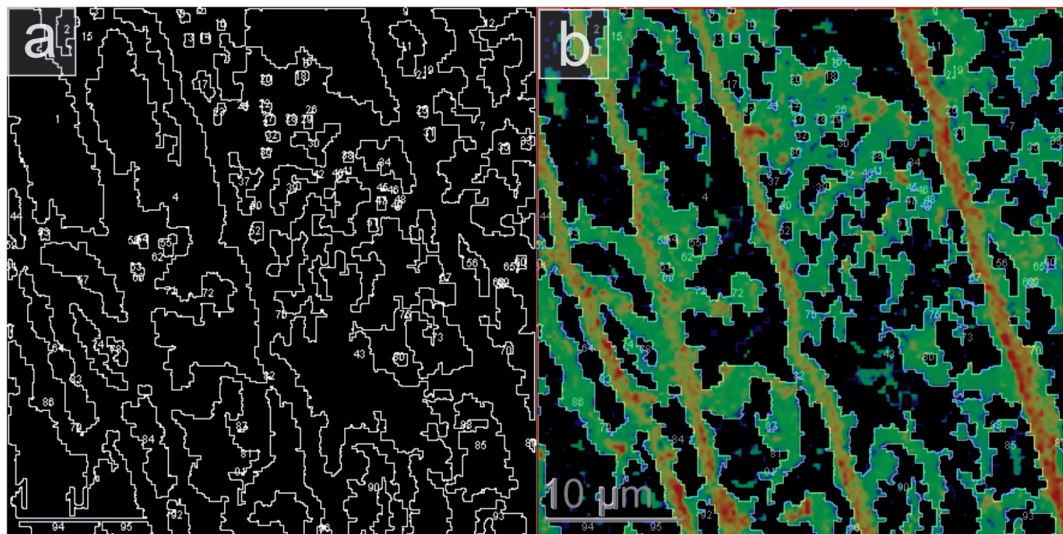


FIGURE C.5-2: CALCULATING THE APPROXIMATE AREA OF BUFFER LAYER ON THE SAMPLE USING IMAGEJ.

(a) The same image from Figure C.5-1 was threshold to outline the buffer layer regions. This resulted in a high fidelity estimation of these areas, though as can be seen in (b), not all monolayer regions were excluded, leading to a slight overestimation of the amount of buffer layer.

D

Appendix D Publications Arising from Thesis

Below are the peer-reviewed publications that have arisen from the completion of this thesis:

Kotsakidis, J. C., Zhang, Q., Vazquez de Parga, A. L., Currie, M., Helmerson, K., Gaskill, D. K., & Fuhrer, M. S. (2019). Oxidation of Monolayer WS₂ in Ambient Is a Photoinduced Process. *Nano letters*, 19(8), 5205-5215.

[Received: 17th April 2019, Published: 9th July 2019, © 2019 American Chemical Society]

Kotsakidis, J. C., Grubišić-Čabo, A., Yin, Yuefeng, Tadich, Anton, Myers-Ward, Rachael L., DeJarld, Matthew, Pavunny, Shojan P., Currie, Marc, Daniels, Kevin M., Liu, Chang, Edmonds, Mark T., Medhekar, Nikhil V., Gaskill, D. Kurt, Vázquez de Parga, Amadeo L., Fuhrer, M. S. (2020).

Freestanding n-Doped Graphene via Intercalation of Calcium and Magnesium Into the Buffer Layer - SiC(0001) Interface. *Chemistry of Materials*, 32 (15), 6464-6482.

[Received: 23rd April 2020, Published: 15th July 2020, © 2020 American Chemical Society]

Oxidation of Monolayer WS₂ in Ambient Is a Photoinduced Process

Jimmy C. Kotsakidis ^{*,†}, Quianhui Zhang [‡], Amadeo L. Vazquez de Parga, ^{§,||}, Marc Currie, [‡], Kristian Helmerson, [†], D. Kurt Gaskill, [‡], and Michael S. Fuhrer ^{*,†}

^{*}School of Physics and Astronomy and [‡]Department of Civil Engineering, Monash University, Victoria 3800, Australia

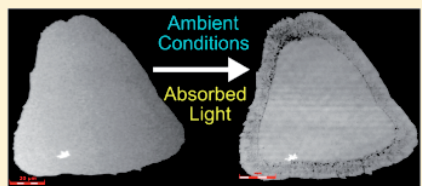
[§]Department Física de la Materia Condensada and Condensed Matter Physics Center (IFIMAC), Universidad Autónoma de Madrid, Cantoblanco 28049, Madrid, Spain

^{||}IMDEA Nanociencia, Cantoblanco 28049, Madrid, Spain

[†]U.S. Naval Research Laboratory, Washington DC 20375, United States

Supporting Information

ABSTRACT: We have studied the ambient air oxidation of chemical vapor deposition (CVD) grown monolayers of the semiconducting transition metal dichalcogenide (S-TMD) WS₂ using optical microscopy, laser scanning confocal microscopy (LSCM), photoluminescence (PL) spectroscopy, and atomic force microscopy (AFM). Monolayer WS₂ exposed to ambient conditions in the presence of light (typical laboratory ambient light for weeks or typical PL spectroscopy map) exhibits damage due to oxidation which can be detected with the LSCM and AFM, though may not be evident in conventional optical microscopy due to poorer contrast and resolution. Additionally, this oxidation was not random and was correlated with “high-symmetry” high intensity edges and red-shifted areas in the PL spectroscopy map, areas thought to contain a higher concentration of sulfur vacancies. In contrast, samples kept in ambient and darkness showed no signs of oxidation for up to 10 months. Low-irradiance/fluence experiments showed that samples subjected to excitation energies at or above the trion excitation energy (532 nm/2.33 eV and 660 nm/1.88 eV) oxidized in as little as 7 days, even for irradiances and fluences 8 and 4 orders of magnitude lower (respectively) than previously reported. No significant oxidation was observed for 760 nm/1.63 eV light exposure, which lies below the trion excitation energy in WS₂. The strong wavelength dependence and apparent lack of irradiance dependence suggests that ambient oxidation of WS₂ is initiated by photon-mediated electronic band transitions, that is, photo-oxidation. These findings have important implications for prior, present, and future studies concerning S-TMDs measured, stored, or manipulated in ambient conditions.



KEYWORDS: Transition metal dichalcogenides, tungsten disulfide, ambient air oxidation, photo-oxidation, defects, monolayer

Since the discovery of two-dimensional (2D) van der Waals materials such as graphene¹ and the semiconducting transition metal dichalcogenides (S-TMDs),² 2D physics has become more accessible to laboratories around the world, leading to an exponential increase of published papers year upon year.^{3,4} S-TMDs (and similarly graphene) possess radically different and useful properties in their 2D, monolayer form. Properties shared among some of the monolayer S-TMDs of family (Mo, W)(S, Se)₂ include a large direct bandgap,^{5–7} exceptional optical characteristics,⁸ and strong spin-orbit coupling along with broken inversion symmetry. This has led various groups to demonstrate the usefulness of S-TMDs in potential applications ranging from ultralow power electronics,¹⁰ valleytronics,^{11,12} photonics,¹³ and qubits¹⁴ to gas sensors.¹⁵

Understanding S-TMDs stability in ambient conditions and under light illumination, crucial for measurements and manipulations undertaken in those conditions, is essential for their development into potential applications. It is now well-known that monolayer and multilayer S-TMDs oxidize upon exposure to extreme conditions such as ultraviolet (UV) light

irradiation in moisture-rich conditions^{16,17} or elevated temperatures in ambient atmosphere.^{18–21} More recently, however, monolayer S-TMD oxidation has been reported in ambient conditions. For example, Gao et al.²² were among the first to report that WS₂ and MoS₂ had poor long-term stability in ambient conditions and observe that H₂O greatly sped up the oxidation process. Gao suggested oxidation began with oxygen substitution at sulfur vacancy sites and progressed via O or OH radicals, with H₂O acting as a “catalyst” lowering the energy barrier for reaction. In a subsequent report, Kang et al.²³ showed that oxidation was greatly suppressed, though not eliminated, when the monolayer S-TMD (in this case WS₂) was epitaxially grown on graphene compared to an oxide substrate. It was proposed that electric fields were necessary for WS₂ oxidation, although the detailed mechanism was unclear. Recently, Atkin et al.²⁴ determined that the oxidation reaction

Received: April 17, 2019

Revised: July 2, 2019

Published: July 9, 2019

could be initiated by laser light (440 nm) and proposed a fluence threshold ($>1.5 \times 10^{10} \text{ J m}^{-2}$) necessary for oxidation of monolayer WS₂. Atkin also found that H₂O was necessary for the oxidation reaction to proceed at any measurable rate (in agreement with Gao)²² and in addition found that sulfate was a likely reaction product.²⁴ Although these studies have identified important factors in the oxidation process, that is, ambient conditions, humidity, substrate, reaction products, and radiant exposure levels, a complete and fundamental understanding of the conditions under which oxidation takes place, and more critically the conditions that completely avoid oxidation in S-TMDs, is lacking.

In this work, we investigate ambient-exposed monolayers of the S-TMD WS₂ using standard characterization tools, optical microscopy, photoluminescence (PL) spectroscopy, and atomic force microscopy (AFM). Moreover, we also employ laser scanning confocal microscopy (LSCM), which serves as an integral tool in this work. By correlating AFM images with LSCM images, we are able to rapidly identify oxidized regions of monolayer WS₂, which may not be evident from optical microscopy or PL spectroscopy. Oxidation is visible in samples kept in ambient conditions and exposed to light characteristic of laboratory conditions (typical room light for weeks) or moderate laser powers in PL mapping spectroscopy but is not seen in as-grown samples or those stored in ambient conditions and darkness for up to ten months. We further explore the role of light by irradiating monolayer WS₂ samples with low-irradiance, visible light at 532, 660, and 760 nm. For WS₂ samples exposed to 532 and 660 nm light (above the threshold necessary for electronic excitation), oxidation is observed, whereas samples exposed to 760 nm light do not show appreciable oxidation (similar to those left in darkness). These results indicate that oxidation of WS₂ in ambient conditions requires photoexcitation, that is, oxidation is a wavelength-dependent, photoinduced process at odds with recent interpretations in literature.^{22–24} Furthermore, photo-induced oxidation occurs at irradiances and fluences of 8 and 4 orders of magnitude lower, respectively, than the irradiance and fluence thresholds proposed in ref 24, suggesting that the threshold for oxidation is extraordinarily low or absent. To our knowledge, a photo-oxidation mechanism in ambient conditions has not been previously described in detail for any member of the 2D S-TMD family of materials. The details of the oxidation reaction, likely Förster resonance energy transfer (FRET) and/or photocatalysis involving redox reactions with H₂O and O₂, requires further study. However, we expect the ambient air photo-oxidation of other direct bandgap S-TMDs (such as MoS₂) to occur similarly. These findings are important for future S-TMD based optoelectronic and electronic applications, as they establish important protocols for all researchers seeking to avoid damaging S-TMDs via oxidation.

Results. WS₂ is grown on c-sapphire (single side polished) in an atmospheric-pressure chemical vapor deposition (CVD) process described previously,²⁵ using mixtures of argon/hydrogen with WO₃ and sulfur powder precursors (see Methods and Figure S1 in the Supporting Information for details).

Figure 1a shows an LSCM micrograph of an as-grown monolayer WS₂ crystal, stored in darkness after growth for approximately one month, and exposed to laboratory and LSCM light for short durations before being stored again in darkness. Figure 1b shows LSCM and optical micrographs

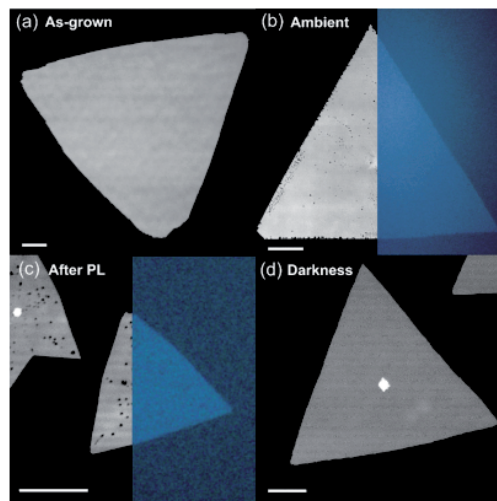


Figure 1. Laser scanning confocal micrograph (LSCM) of (a) CVD grown monolayer WS₂ exposed to minimal amounts of light before imaging with the LSCM approximately 1 month after growth. (b) WS₂ after approximately 19 days in ambient conditions, juxtaposed with an optical image of the same crystal. (c) WS₂ after routine photoluminescence spectroscopy, juxtaposed with an optical image of the same crystal, and (d) WS₂ crystals kept in darkness for approximately 10 months with brief exposure to ambient light. In the middle of this crystal is a crystal seed center, which was common throughout growths. Scale bars in all images are 10 μm .

taken on a similarly grown sample after approximately 19 days of exposure to ambient atmosphere and typical laboratory room lighting. The LSCM image (left side of Figure 1b) shows dark spots within the WS₂ crystal in Figure 1b, although these are not apparent in Figure 1a. These dark spots are difficult or impossible to observe in the optical micrograph of the same crystal, shown on the right side of Figure 1b (and similarly in Figure 1c). As discussed in more detail below, the dark spots correspond to the complete or partial oxidation of small ($<0.5 \mu\text{m}$) regions of WS₂ (i.e., WO_x where $x \leq 3$). This observation is consistent with recent reports on the ambient air oxidation of monolayer S-TMDs, which have recorded samples in laboratory conditions oxidizing in months²² to as little as weeks.²³ After the observation of dark spots/oxidation in Figure 1b, care was taken to not expose freshly grown samples to ambient UV light in the room, as this was thought to contribute to the oxidation of the WS₂.^{16,17} Thus, freshly grown crystals were stored in darkness. To understand the optical properties of our CVD grown WS₂ and investigate whether this could provide clues as to the causes of the observed oxidation in Figure 1b, samples were mapped using confocal PL spectroscopy (μ -PL). Figure 1c shows LSCM and optical micrographs of a monolayer WS₂ crystal after performing μ -PL of the sample, but otherwise the sample was protected from light, whereas Figure 1d shows a sister sample imaged with the LSCM after storage in darkness for 10 months. The conditions of the μ -PL imaging (excitation wavelength 532 nm, power 140 μW , irradiance $\sim 6.9 \times 10^8 \text{ W m}^{-2}$ with total fluence of $\sim 1.8 \times 10^5 \text{ J m}^{-2}$, see Methods for details) are similar to those routinely used for optical

Table 1. Summary of Wavelengths, Irradiances and Corresponding Fluences^a

wavelength (nm)	experiment/analysis	irradiance (W m^{-2})	fluence (J m^{-2})	oxidation visible?
415–700 (white light from LSCM)	LSCM	1.6×10^4	1.6×10^5	no
405 (blue)	LSCM	1.3×10^8	8.8×10^4	no
515 (green)	LED ^b	3	1.8×10^6	yes
532 (green)	LOW	3.8	2.3×10^6	yes
532 (green)	$\mu\text{-PL}$	6.9×10^8	1.8×10^8	yes
660 (red)	LOW	14.2	8.6×10^6	yes
760 (far red)	LOW	2.2	1.3×10^6	no ^c

^aSummary as well as if oxidation was visible with the LSCM for all experiments and analyses. LOW refers to low-irradiance experiments. ^bSee Supporting Information Section 10 for details. ^cSome crystals had signs of small amounts of oxidation. See Results and Supporting Information.

characterization of S-TMD crystals.²⁶ Table 1 shows all the irradiances and fluences used in this report. For the PL-exposed sample in Figure 1c, similar dark spots as in Figure 1b are evident with the LSCM micrographs, though are not obvious in the conventional optical micrograph shown on the right side of Figure 1c. The standard sample shown in Figure 1d, which remained in darkness, appears pristine (in Figure 1d, a bright spot in the middle of the WS₂ is evident; we identify this feature as a crystal seed center or multilayer WS₂, and not associated with oxidation). The results imply that light is responsible for the ambient air oxidation of monolayer WS₂. Considering that there are many reports using PL excitation conditions of S-TMDs on the same order of magnitude as that used in this report, the observation of oxidation after $\mu\text{-PL}$ was unexpected. Moreover, since the LSCM uses light to image the samples, it also carries a probability of oxidizing the WS₂. Thus, care was taken to ensure that the final step in the analysis was light exposure from the LSCM, and that sister samples (such as the one in Figure 1d) were used as standards to compare with the effects of any analysis/light exposure experiments that were undertaken. Yet even after two subsequent LSCM exposures, no oxidation is observed, the details of which can be found in the Supporting Information (Section 2, Figure S2). As will become clear, the advantages of LSCM characterization stem not only from its superior contrast and resolution but also from its inherent operation at low incident fluence, much lower than those found in PL experiments or under low-light illumination for days. The LSCM can operate in two modes, the first uses white light from an LED (optical micrographs in Figure 1b,c) and the second uses 405 nm light in a confocal laser scanning setup. In the case of the white light, the WS₂ is subjected to an irradiance of $\sim 1.6 \times 10^4 \text{ W m}^{-2}$ and fluence of $\sim 1.6 \times 10^5 \text{ J m}^{-2}$ (for 10 s exposures at 100 \times magnification). In the case of the 405 nm light, the irradiance and fluence were $\sim 1.3 \times 10^8 \text{ W m}^{-2}$ and $\sim 8.8 \times 10^4 \text{ J m}^{-2}$, respectively (see Methods for details).

Figure 2a–d shows the results of $\mu\text{-PL}$ on a different crystal on the same sample as in Figure 1c. Figure 2a shows the $\mu\text{-PL}$ intensity distribution of the WS₂ monolayer. It can be seen that the PL intensity on the edges is much brighter than that of the center, as is observed in many other reports.^{6,24,26–31} Also, the $\mu\text{-PL}$ shows a 3-fold rotationally symmetric pattern not only in the intensity map but also mirrored in the map of the peak photon energy (relating to the location of the exciton) shown in Figure 2b, that is, the two correlate with each other.²⁸ Figure 2c shows a representative spectrum from the central region of the crystal, deconvolved as two Voigt³² spectra identified as the exciton peak at approximately $2.03 \pm 0.01 \text{ eV}$ and smaller trion peak at $1.97 \pm 0.01 \text{ eV}$. A representative spectrum from the edge of the crystal is shown in Figure 2d and is similarly

deconvolved, showing a shifted exciton peak at approximately $1.96 \pm 0.01 \text{ eV}$ and trion peak at $1.91 \pm 0.01 \text{ eV}$. Figure 2c,d shows the heterogeneity of the optical characteristics of CVD grown monolayer WS₂ on sapphire; similar optical heterogeneity is found in all other samples. After $\mu\text{-PL}$ analysis, the sample was stored in darkness and then imaged with the LSCM as shown in Figure 2e. As in Figure 1c, the sample shows signs of oxidation, manifesting as small ($<0.5 \mu\text{m}$) dark spots, similar to those observed in previous reports using conventional light microscopy or atomic force microscopy.^{17,20–23,26}

To better understand the oxidized regions seen with the LSCM, the same sample was then imaged with AFM in intermittent-contact mode, shown in Figure 2f–h. Figure 2f shows an overview of the sample and the extent of the oxidation. AFM resolves more clearly the dark spots seen in LSCM as raised triangular “islands”. These triangular islands in S-TMDs have been observed before and identified as tungsten oxide in various oxidation states, WO_x ($x \leq 3$).^{17,23,24,26} We see that upon comparison of the $\mu\text{-PL}$ shown in Figure 2a,b and the after effects of oxidation seen in the LSCM and AFM micrographs of Figures 2e,f, respectively, that oxidation occurs more prevalently in some regions in a well-defined pattern, following the 3-fold symmetric pattern of lines extending from the center toward the vertices of the triangular crystal. Also, significant oxidation can be seen outside these areas, for example, in the region with red-shifted PL corresponding to the spectrum in Figure 2d. The inset of Figure 2f shows the height of the central part of the crystal as $\sim 0.5 \text{ nm}$ with the very edge of the crystal higher than that of the central part by $\sim 0.5 \text{ nm}$, with edge width of $\sim 0.32 \text{ nm}$ (see Supporting Information Figure S5). As can be seen in the inset of Figure 2f (and Figure S5), the edge is “granular” and contains local increases in height some of which are above or below 0.5 nm , the maximum of which was $\sim 1.3 \text{ nm}$ higher than the WS₂ basal plane (see Figure S5 in Supporting Information Section 4). In some samples (from different growth runs), this edge was also discernible under the LSCM (see Supporting Information Figure S4). This higher edge region correlates well to the increased edge PL intensity of the $\mu\text{-PL}$ map (Figure 2a) and thus we tentatively ascribe the bright edge in the PL spectrum to this physical feature observed with the AFM. Increased PL brightness around the edges of monolayer S-TMDs has also been reported on by others,^{6,24,26–31,33} and the effect is attributed to either differences in chemical composition on the edges of the crystal^{6,26–30,33} or to water intercalation at the edges of the S-TMDs.^{24,31,34}

Figure 2g,h shows higher-resolution AFM topography and phase images, respectively, of the triangular oxidation island feature outlined by the dotted black box in Figure 2f. The AFM

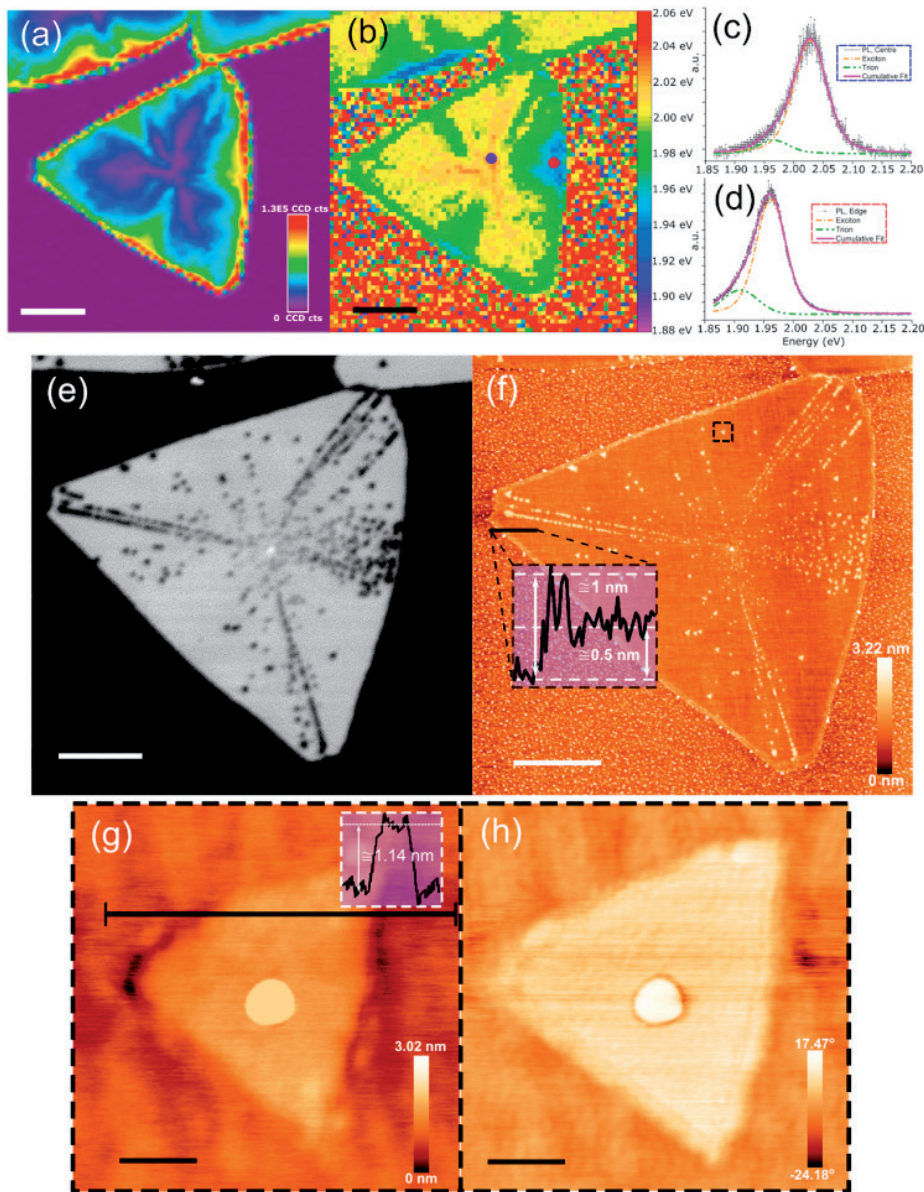


Figure 2. (a–d) μ -PL of monolayer WS_2 . (a) Map showing the intensity in charged-coupled device (CCD) counts (cts) (scale bar = 5 μm) and (b) shows the approximate location of the peak in intensity from (a) (scale bar = 5 μm). (c) PL spectrum obtained from the central spot (blue) in (b) with exciton and trion peak energies at 2.03 ± 0.01 and 1.97 ± 0.01 eV, respectively. (d) PL spectrum from the edge region (red spot) with exciton and trion peak energies of 1.96 ± 0.01 and 1.91 ± 0.01 eV respectively. (e,f) LSCM and AFM images showing oxidation of the same monolayer WS_2 crystal in Figure 2 after analysis with μ -PL (scale bars = 4 μm). In (e), an LSCM micrograph shows the oxidation as dark spots due to their altered transmittance. The morphology of these oxidation triangles was further investigated using AFM. In (f), the tapping mode AFM height micrograph shows unambiguously that these oxidation zones are raised, triangular, and aligned along the stress/strain lines of the crystal. Inset shows the measured height of the crystal. (g,h) A zoom-in of the boxed area (scale bars = 65 nm) in (f) of a triangular oxidation island. The AFM height image in (g) shows the height of this island is ~ 1.14 nm (inset) and the AFM phase image in (h) shows that the island is different in phase from the surrounding WS_2 . The AFM height (g) and phase (h) image both show a ‘droplet’ feature in the center of this triangular oxidation island.

topography image in Figure 2g shows that these triangular oxidation islands are not holes (as suggested by the LSCM in Figure 2e) but raised in topography by ≈ 1.14 nm above the surrounding WS_2 ; this is consistent with thicker WO_x remaining as the reaction product (see Supporting Information Section 3 for in-depth analysis of oxidation heights). The phase contrast between the oxidation island and WS_2 (Figure 2h) also indicates that the oxidized area is a different material. Additionally, thin films of WO_x have a higher transmittance than WS_2 at visible wavelengths (see Supporting Information Figures S4 and S5 for transmittance, reflectance, and absorptance of monolayer WS_2), explaining the dark (see-through to substrate) appearance of these regions under the LSCM.³⁵ It was observed that for some oxidation islands, there was a small (<60 nm), round, raised region in the middle of the oxidation island. This spot, seen more clearly with the enhanced contrast of the phase image in Figure 2h, suggests this feature is a liquid drop and could result from hygroscopic sulfur oxides.²⁴

The experiments thus far imply that visible light with wavelengths as long as 532 nm can cause oxidation of WS_2 in ambient at irradiances typically used for PL spectroscopy. To determine the physical mechanism of WS_2 oxidation, controlled, low-irradiance light exposure experiments were conducted with monolayer WS_2 samples at three specific wavelengths. The low irradiances used allow us to completely eliminate heating as a source of oxidation, and instead, focus on the wavelength dependence of the oxidation. The experiments used two lasers at 532 nm (2.33 eV) and 660 nm (1.88 eV) (see Methods for details and Supporting Information for laser spectra) and a halogen light (XGY-II) filtered at 760 nm (1.63 eV) with irradiances of approximately 3.8, 14.2, and 2.2 W m^{-2} , respectively. Previous experiments observed heating only at irradiances approximately 9 orders of magnitude higher (in MoS_2).³⁶ Figure 3a shows the absorptance spectrum of the WS_2 monolayers at ~ 293 K, determined via subtracting the measured transmission and reflectance spectra from the total light impinging on the sample (additional details in Methods). The absorptance spectrum is consistent with previous observations for monolayer WS_2 ^{37–39} and shows features characteristic of the “A” exciton at 619 ± 2 nm (2.003 ± 0.006 eV) and “B” exciton at 516 ± 2 nm (2.403 ± 0.009 eV), which arise from excitonic transitions in the spin-orbit split bands at K/K' points in the Brillouin zone. The observed spin-orbit splitting, Δ_{SO} , of 0.400 ± 0.015 eV is close to previously measured values for monolayer WS_2 .³⁸

The corresponding wavelengths used in the controlled low-irradiance light exposure experiments are highlighted and superimposed on Figure 3a. The 532 nm light was chosen to mimic the conditions found in the PL experiment, the 660 nm light was chosen as it is at the edge of the absorption of WS_2 (excites mainly the trion), and the 760 nm light was chosen as it is not significantly absorbed by monolayer WS_2 (i.e., photon induced electronic transitions are improbable). Light was shone constantly on the samples for 7 days in ambient atmosphere (ranging from $\sim 40\%$ to $\sim 60\%$ relative humidity) and they were subsequently imaged using the LSCM, giving a total fluence (uncorrected for absorptance) of 2.3×10^6 , 8.6×10^6 , and $1.3 \times 10^6 \text{ J m}^{-2}$ for the 532, 660, and 760 nm light, respectively. Note that these fluences are at least an order of magnitude larger than that of the LSCM.

Figure 3b–e shows the results of the low-irradiance experiments after 7 days of exposure to the different

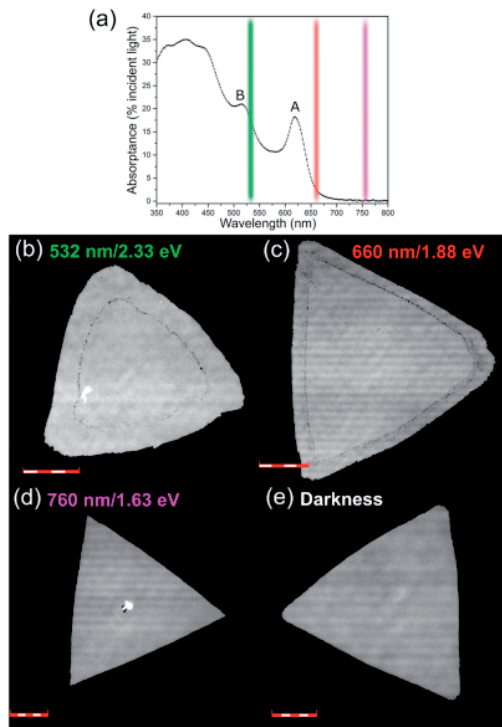


Figure 3. (a) Absorptance spectrum of monolayer WS_2 taken at ~ 293 K. Labels denote the A exciton at 619 ± 2 nm (2.003 ± 0.006 eV) and B exciton at 516 ± 2 nm (2.403 ± 0.009 eV). Color bands correspond to the wavelengths used for the low light exposure experiments, from left to right these are 532 nm (green), 660 nm (red) and 760 nm (purple). (b–d) Low-irradiance light exposure experiments. Laser scanning confocal micrographs of monolayer WS_2 after (b) 7 days exposure to green laser (532 nm/2.33 eV, 43.8 W m^{-2}) scale bar = $20 \mu\text{m}$, (c) 7 days of exposure to red light (660 nm/1.88 eV, 14.2 W m^{-2}) scale bar = $20 \mu\text{m}$, and (d) 7 days of exposure to far-red light (760 nm/1.63 eV, 2.2 W m^{-2}) scale bar = $10 \mu\text{m}$. (e) A standard sample kept in darkness for 2 weeks for comparison with light exposed samples, scale bar = $10 \mu\text{m}$.

wavelengths (b–d) or kept in darkness for 2 weeks (e) as imaged with the LSCM. In Figure 3b,c, small triangular islands on the edges and the interior of the WS_2 indicate that the 532 nm (b), and 660 nm (c) light caused significant oxidation of these samples. Figure 3d shows the results of 760 nm light exposure; no significant amount of oxidation can be detected, though on some crystals, minute traces of oxidation is observed (see Section 9 in Supporting Information). All samples (including those in Figure 3b–d) were exposed to small amounts of ambient light while mounting/removing the samples from the optical setup (and CVD furnace) and loading/measuring the samples for analysis with the LSCM. Additionally, the 760 nm exposure used a filter (see Methods) instead of a narrow wavelength source such as a laser, which may have further contributed to stray light exposure. As can be seen in Figure 3d, these brief ambient light exposures do not cause extensive oxidation (as observed with the LSCM)

compared to the exposures in **Figure 3b,c** which are severely oxidized. **Figure 3e** shows an LSCM image of a control sample kept in darkness for 2 weeks after growth; no oxidation in any samples kept in darkness was observed.

We also exposed the WS₂ monolayers to similar low-irradiance ($\sim 3 \text{ W m}^{-2}$) green ($\sim 515 \text{ nm}$) light in a nitrogen-filled glovebox environment with ultralow levels of O₂ and H₂O for 7 days. In contrast to the ultralow irradiance experiments in ambient conditions, the results show that no damage or adverse effects were observed (using the LSCM) on glovebox-exposed WS₂ (see Section 10 in **Supporting Information** for details); indicating that light-induced oxidation does not proceed in the absence of O₂ and H₂O.

Discussion. We have identified for the first time that the previously observed^{22–24} ambient oxidation of a monolayer S-TMD requires exposure to light that is able to excite electronic transitions within the WS₂, that is, the physical mechanism of oxidation in ambient is photo-oxidation. Although heating of TMDs in ambient has been shown to cause oxidation in S-TMDs,^{18–22} we can rule out heating as the cause of oxidation in our experiments, as we observe similar oxidation for long-time exposures at low-irradiance in **Figure 3b,c**. These low irradiances are approximately 8 orders of magnitude lower than the high-irradiance μ -PL exposure (**Figures 1c** and **2**) and are much below any levels that would cause measurable heating.³⁶ Furthermore, the LSCM uses higher irradiance than the green or red low-irradiance experiments, yet results in no significant oxidation. This implies that irradiance is not an important factor for oxidation. In contrast, fluence does appear to be essential for oxidation. Light exposure at 440 nm (2.82 eV) at high fluence ($>1.5 \times 10^{10} \text{ J m}^{-2}$) has been previously observed to cause oxidation of monolayer S-TMDs.²⁴ Here we find that lower photon energy light (down to the threshold for electronic excitation, 1.88 eV or 660 nm in WS₂) is sufficient for oxidation, using a fluence approximately 4 orders of magnitude lower ($\sim 2.3 \times 10^6 \text{ J m}^{-2}$ in **Figure 3b**) than previously reported. It should be noted, that by taking into account the absorptance of WS₂ (from **Figure 3a**), the actual amount of absorbed light (i.e., light that can excite electronic transitions) is lower by an order of magnitude for the 532 and 660 nm light and approximately zero for the 760 nm light (the uncorrected values of irradiance and fluence are quoted here for direct comparison with literature, see **Supporting Information** Section 6). In comparison, the LSCM images, which show no obvious signs of oxidation, were obtained using fluences of $\sim 8.8 \times 10^4 \text{ J m}^{-2}$. A summary of the irradiances, fluences, and whether oxidation was visible in each light exposure experiment is presented in **Table 1**. These observations suggest that a fluence threshold for oxidation is either nonexistent or extraordinarily low, and that oxidation will simply proceed at a rate that is proportional to the fluence and the efficacy in which the material generates excited carriers from optical excitation. Thus, depending on the resolution of the probe used, oxidation may not be observed, yet still be present even with brief exposures at low fluence.

The strong wavelength dependence of oxidation indicates a photoexcitation mechanism involving the WS₂ itself. We can rule out direct excitation of oxygen to create singlet oxygen (excited, reactive form of oxygen, see **Supporting Information**), which would occur at $760 \pm 10 \text{ nm}$ wavelength excitation,^{40,41} as we observe no oxidation in the low-irradiance 760 nm/1.63 eV experiment. The fact that the threshold photon energy (wavelength) corresponds well to the energy (wavelength)

threshold for electronic excitation (excitation of the trion), strongly suggests that oxidation instead occurs through a photoexcitation process, that is, photo-oxidation. The detailed mechanism, likely Förster resonance energy transfer (FRET) and/or photocatalysis reactions involving excited H₂O and/or O₂ species, requires further study (see **Supporting Information** Section 7 for more details). However, we also expect the ambient air photo-oxidation of other direct bandgap S-TMDs (such as MoS₂) to occur similarly due to very similar chemistry. For instance, Ding et al.⁴² have recently discovered singlet oxygen present in photoexcited solutions of MoS₂ quantum dots and have suggested FRET as the mechanism of oxidation. The necessity of photoexcited carriers for oxidation also explains the protection from oxidation of monolayer S-TMDs placed on graphene;²³ semimetallic graphene efficiently quenches the photoexcited carriers through nonradiative recombination, thus greatly reducing the available excited carriers for chemical reaction via FRET and/or photocatalysis.⁴³

We note at this point that the photo-oxidation of semiconductors (especially direct bandgap) is not a new observation, and has been reported on since at least 1977 in materials such as GaAs^{44–46} (see ref 45 and references therein) and with other direct bandgap semiconductors such as InP⁴⁶ and TiO₂.⁴⁷ Other 2D materials such as black phosphorus and the recently discovered 2D ferromagnet, CrI₃, have also been found to photo-oxidize (more rapidly compared to WS₂) when exposed to ambient conditions and light.^{48,49} In the ambient air photo-oxidation of black phosphorus and CrI₃, H₂O has been identified as a crucial reactant for oxidation. In the case of black phosphorus, oxidation required the presence of both adsorbed water and oxygen, even though the oxidation rate was found to only depend on the concentration of O₂.⁴⁸ This was also found with GaAs in which H₂O was found to have a “catalytic” effect on oxidation.⁵⁰ S-TMDs are no exception, and have also been found to only oxidize substantially in ambient with H₂O present,^{22,24,51–53} suggesting a similar mechanism may be responsible. The photo-oxidation of semiconductors is not limited to direct bandgap materials and has also been reported for silicon (note that CrI₃ also has an indirect bandgap),⁵⁴ although the effect was found to be less pronounced than for direct bandgap materials.⁴⁶ Thus, it is expected that even multilayers of S-TMDs will undergo ambient air photo-oxidation and indeed this has been reported by Budania et al.,⁵² who observed oxidation in exfoliated multilayer MoS₂ samples left in ambient conditions (though the role of light was not investigated). The photoinduced oxidation of semiconductors in ambient atmosphere seems to be a universal effect, yet not much attention has been paid to the mechanism in the 2D community, especially in regard to S-TMDs. Thus, we expect that past experiments may have been affected by photo-oxidation (see **Supporting Information** Section 8) since our results have shown that even for ultralow light exposures (see **Table 1**), that it only takes approximately days for there to be significant oxidation present. For example, oxidation may have affected past S-TMD electrical devices by increasing contact resistivity (WO_x has a larger bandgap), explaining at least in-part the large variation in measurements and lack of reproducibility from group to group and device to device.⁵⁵

Furthermore, we observe that oxidation does not occur randomly across individual monolayer WS₂ crystals but rather shows a preference for regions running roughly from the

centers to the vertices of triangular crystals, that is, arranged with 3-fold rotational symmetry around the crystal centers (**Figure 2e,f**), as well as the edges and red-shifted PL regions of the crystals (**Figures 1b, 3b,c, S10, S11b** and **Figure 2a,b,d**, respectively). The same 3-fold rotationally symmetric pattern is seen in the μ -PL (**Figure 2a,b**) and has been observed in our group previously,³¹ and by other groups.^{26–30} Recent work counting individual defects using conductive AFM has demonstrated that this 3-fold symmetric region has a higher defect density than surrounding areas of the single crystal.⁵⁶ Additionally, this 3-fold symmetric region has previously been shown to be preferentially oxidized under high-power laser irradiation and suggests that it contains a higher density of defects.²⁶ The observation of increased defect density has not been limited to the 3-fold symmetric areas. Carozo et al.⁵⁷ measured defect densities in CVD grown WS_2 using scanning transmission electron microscopy and found that the edges of single crystals typically have higher sulfur vacancies than the interior of the crystal. More recently, Hu et al.³³ analyzed CVD-grown WS_2 using PL and have found that the bright edges observed in PL are most likely due to oxygen chemically bonded to the edges. In regards to the red-shifted PL regions, it has been demonstrated that short duration plasma treatments can increase defect density in WS_2 , creating a neutral exciton peak that is red-shifted in energy ~ 0.1 eV below the “defect free” neutral exciton peak at ~ 2.03 eV (see **Figure 2c**).³² In that study, high-resolution transmission electron microscopy was performed and in conjunction with simulations, suggested that the red-shifted neutral exciton peak was due to single sulfur vacancies. These prior results suggest that the oxidation we observed in our experiments may have begun at 3-fold symmetric regions, edge sites, and red-shifted regions due to the increased defect densities contained there.

There is now overwhelming evidence that the most common structural defects present in S-TMDs are in the form of sulfur vacancies, and this is true (with the exception of atomic layer deposition grown samples)⁵⁸ whether the samples are exfoliated,^{58–60} grown via chemical vapor transport (CVT),⁶¹ or, as in our case, CVD.^{30,56–58} When sulfur vacancies are present on the surface of WS_2 , oxygen dissociative chemisorption in the these sites has been experimentally⁶² and theoretically⁶³ shown to be favorable. Thus, by forming the initial seed center, it is likely that sulfur vacancies chemisorbed with oxygen nucleate the oxidative growth of WO_x species.

In addition to the small (<250 nm) triangular oxide islands formed (**Figure 2e,f**), we observed with the AFM small (<65 nm) droplets in the centers of some of the triangular oxidation islands. The contents of these droplets are most likely aqueous H_3SO_4 (H_2SO_4 is hygroscopic) which forms one of the products in the oxidation of S-TMDs.^{24,51,53,64,65} Studies on the oxidation of MoS_2 have found traces of molybdic acid ($MoO_3 \cdot H_2O$ and $MoO_{3-x} \cdot xH_2O$, $x = 0.7–1$)^{51,65} though due to the low to negligible solubility of tungstic and molybdic oxides in water (or H_2SO_4),⁶⁵ it is unlikely that these droplets contain any significant quantities of tungstic acid. Not all triangular oxidation islands were observed to have a droplet in the middle of them, and this could be due to tungsten oxide forming in the absence of excess water.

However, the physical reasons behind the changes in PL intensity^{26–31} and peak position²⁸ observed in the PL of WS_2 (**Figure 2a–d**) remain unclear. In particular, some groups have considered strain from lattice mismatch between crystal and

substrate to explain changes in PL but, have subsequently ruled out this strain due to the persistence of the 3-fold symmetric pattern upon transfer of the crystal to another substrate, which is thought to relieve strain in as-grown crystals.^{26,29} Because oxidation was also observed in a region in which the exciton (and trion) emission peak was red-shifted (see **Figures 2a–d**), it may be that our measured red-shifted peak has contributions from both the trion and a defected neutral exciton (due to sulfur vacancies); further studies are required for confirmation. What is clear, is that our results indicate that the process of obtaining PL spectra in ambient conditions will necessarily form small oxide regions, and hence the analysis of the spectra could be affected by several associated mechanisms, for example, strain imparted to surrounding WS_2 developed during oxide formation.⁶⁶ However, there is reason to believe this issue can be mitigated as we have shown that illumination by light in a nitrogen atmosphere results in no measurable oxidation (see **Supporting Information** Section 10). Thus, performing PL in an inert environment is likely to be useful. Further work is needed, for example, by growing crystals and performing PL in an inert environment or vacuum, and then exposing these crystals to ambient and light in order to determine the effect of defected regions on PL. Additional work is also needed to confirm the nature of the oxidation mechanism (FRET or photocatalysis) and whether defects are necessary to initiate the oxidation, or whether it can proceed in a defect-free basal-plane of WS_2 in ambient with light exposure. Further elucidation of the oxidation mechanism would enable accurate prediction of the oxidation rate, which would be valuable in other aspects of S-TMD research and not limited to future oxidation studies.

Conclusion. Our work shows that the physical mechanism that causes the oxidation of WS_2 in ambient conditions is photoinduced, that is, a photo-oxidation mechanism. Oxidation is observed to not occur randomly but in 3-fold symmetric areas (as defined by μ -PL), edges, and areas in which there is an observed red-shift in exciton emission. It is thought that all these areas contain more defects in the form of sulfur vacancies where oxygen can attach and so provide a starting point from which oxidation can proceed. The fluence threshold that begins this photo-oxidation is at least 4 orders of magnitude lower than previously thought,²⁴ $<2.3 \times 10^6$ J m⁻². Photo-oxidation does not occur when the samples are left in darkness, nor is significant oxidation visible when the WS_2 is exposed to wavelengths that are not absorbed appreciably, as found in the low-irradiance 760 nm experiment. Taking into consideration that oxidation is only observed upon excitation of an electronic transition, it is likely that no fluence threshold exists and that oxidation occurs on a probabilistic basis. That is, lower light levels progress the reaction at much slower rates that are difficult to observe using the LSCM or AFM. Still, our study already places severe constraints on the processing and analysis of S-TMD films in ambient conditions, since exposure to typical room light for extended periods (days), or exposure to a single typical scanning PL or Raman spectroscopy measurement (minutes) may cause significant oxidative damage. Furthermore, we expect that these findings will guide the development of new nanofabrication techniques that completely avoid significant oxidation of S-TMDs, as the storage of S-TMDs in darkness or exposure to light that cannot excite electronic transitions should completely prevent progression of the oxidation reaction.

Methods. *Chemical Vapor Deposition.* An atmospheric-pressure CVD method was used to grow monolayer WS₂ on polished (single side) c-sapphire(0001) substrates (Shinkosha) in a 1 in. quartz tube furnace. The samples were determined to be monolayer from PL and AFM measurements, as presented in the main text. Before beginning the CVD process, the c-sapphire substrates were ultrasonicated in acetone and ethanol and then loaded into a 1 in. tube furnace in preparation for oxygen annealing. The samples were oxygen annealed by flowing oxygen at 50 sccm for at least 5 min over the sample after which the furnace was then ramped from 30 to 1050 °C in 30 min, held for 1 h, and then allowed to naturally cool to room temperature. After oxygen annealing, approximately 1.1 ± 0.1 g of sulfur powder ($\geq 99.5\%$, Sigma-Aldrich), and 2 ± 0.1 g of WO₃ powder ($\geq 99.9\%$, Sigma-Aldrich) were loaded in separate quartz boats. The sulfur was placed upstream and away from the central part of the furnace heating coils and under external heating coils (controlled by a separate temperature controller), whereas the WO₃ was loaded in the central part of the furnace along with the oxygen annealed substrates. A quartz test tube (approximately 22 mm in diameter) was placed against the substrate quartz boat (with the open-end facing outward) so as to restrict the flow of reactants. This helps increase the partial pressure of reactants over the substrates, thus promoting growth of WS₂. The furnace setup is illustrated in Supporting Information **Figure S1**. Argon was used as the carrier gas and flowed at 200 sccm, and H₂ was also added to the gas stream at 8 sccm after purging with argon for 10 min. The furnace and external heating coils were then heated to approximately 900 and 200 °C from 30 °C in 30 min, respectively and held for approximately 5 min at these temperatures. After cooling to 800 °C, the furnace lid was opened slightly, so as to rapidly cool the furnace. Between 600 and 500 °C, the furnace was fully opened, and the H₂ gas turned off. The sulfur was allowed to naturally cool from 200 °C to room temperature. The samples were removed and immediately stored in containers wrapped with aluminum foil and stored in a light-tight box.

Photoluminescence Spectroscopy. Crystals were analyzed using a WITec 300R spectrometer equipped with a 532 nm laser and power set at approximately 140 μW (as judged by an optical power meter after the 100× objective). The 2D confocal PL maps (μ-PL) were taken using the 100×/0.9 (Olympus MPLFLN) objective lens. A Gaussian beam profile was assumed, and the maximum irradiance estimated as $I = 8P/(\pi D^2)$, where P is the laser power and D is the diameter of the beam, estimated as $D = 1.22\lambda/NA \approx 721$ nm, where λ is the wavelength in nanometers and NA is the numerical aperture of the lens. The μ-PL map shown in **Figure 2a,b** took ~25 min to complete (75 × 75 pixels, ~0.27 s integration time per pixel). All PL measurements were taken at 20 °C ambient temperature and rel. humidity of 40–60%.

Laser Scanning Confocal Microscopy. Two different LSCM's were used. In **Figure 1b**, a Keyence VK-X200 system was employed. In all other LSCM figures, an Olympus OLS4100 system was used. These microscopes are also able to take standard optical images, as shown juxtaposed in **Figure 1b,c** in the main text, by use of a white LED. The white LED irradiance was calculated for the OLS4100 by first measuring the spectrum of the white LED, whose output was confined to the range 420–650 nm. A power meter was then used to measure the optical power exiting the 100×/0.95 objective lens. The responsivity of the power meter's silicon photo-

detector varies monotonically over this range of wavelengths; hence, we were able to place bounds on the power measurement by calibrating the responsivity at two extrema of the spectrum, 420 and 650 nm. The power was found to be bounded by $\approx 0.210 \pm 0.070$ mW. The field of view of the 100 × /0.95 is 128 μm, and the irradiance was then calculated using $I = 4P/(\pi D^2)$. For the blue laser at 405 nm, a power meter measured the maximum output as ~ 14 μW after the 100×/0.95 objective. The irradiance was then calculated assuming a Gaussian beam, similar to the photoluminescence setup. The time taken per scan varied depending on the magnification used, although the longest time of approximately 50 s (corresponding to unzoomed 100× magnification) was used to calculate the fluence, H , in which case the irradiance was multiplied by the total exposure time for each pixel, t : $H = 2Pt/(\pi r^2)$. The exposure time was calculated by dividing the total time for the scan (50 s) by the total number of pixels (1024 × 1024). The laser beam diameter is much larger than a pixel and so would result in the laser "spilling over" to multiple pixels. To estimate this effect, the area of the laser beam was divided by the area of a pixel to give ~ 14 . Thus, the calculated time was multiplied by 14 to estimate an upper limit to the true exposure time, yielding $\sim 8.8 \times 10^4$ J m⁻². A similar estimate is obtained by dividing the total energy delivered during the complete scan by the total area imaged.

Atomic Force Microscopy. A Bruker Dimension Icon AFM in tapping mode (in ambient and at ~ 20 °C) was used to obtain the atomic force micrographs. RTESPA-300 tips were used, and analysis was conducted using WSxM v4.0.⁶⁷ In **Figure 2f–h**, the image was flattened, and the contrast was enhanced. Bruker's own software was also used to analyze the height of the oxidized triangular islands (using the step height analysis function) and this data can be found in the Supporting Information.

Controlled Low-Light Irradiance/Fluence Experiments. Light sources were a 532 nm laser diode, 650 nm laser diode (measured to be 660 nm, see Supporting Information) and halogen light source (XGY-II) with appropriate bandpass filter at 760 nm ± 10 nm (Thorlabs FB760-10, OD 6+ 200 to 719 nm). The optical spectra of the laser sources can be found in the Supporting Information. A custom-built enclosure was used to shroud the experiment in darkness. In the enclosure, the optics used were an iris (Thorlabs ID25), beam steering mirrors, a circular linear variable neutral density filter, and a simple convex lens to expand the beam to an appropriate size. Samples were mounted onto a glass slide using double sided sticky tape. Standard samples (usually a sister sample from the same growth run) were kept in darkness for the entirety of the light exposure experiments. The irradiance and fluence for the sources were calculated similarly to the LSCM and PL sections above with the exception that the 760 nm light was assumed to be non-Gaussian (as in the white LED case with the LSCM), that is, $I = 4P/(\pi D^2)$. The diameters were measured as ~ 20 , ~ 12 , and ~ 30 mm. Values for the irradiance were calculated as 3.8, 14.2, and 2.2 W m⁻² for the 532, 660, and 760 nm light, respectively. Fluence values were then found by multiplying the irradiance by 604 800 s (seconds in 7 days) to give 2.3×10^6 , 8.6×10^6 , and 1.3×10^6 J m⁻² for the 532, 660, and 760 nm light, respectively.

Reflectance/Transmission/Absorptance Measurements and Calculations. The reflectance and transmission spectra of the WS₂ monolayer crystals were measured over 350–800 nm using a PerkinElmer Lambda 1050, equipped with an

integrating sphere. Samples grown on c-sapphire (Shinkosha) were mounted on clear glass microscope slides (Sail). Blank sapphire substrates (Shinkosha) mounted on clear glass microscope slides (Sail) from the same batches were also measured. This allowed the absorptance from only the WS₂ to be determined in the following way. The absorptance of the substrates, $A_s = 1 - T_s - R_s$, was subtracted from the absorptance of the WS₂ and substrate, given as $A_{WS_2+S} = 1 - T_{WS_2+S} - R_{WS_2+S}$, to yield the absorptance from only the WS₂ using the formula $A_{WS_2} = A_{WS_2+S} - A_s = (T_s - T_{WS_2+S}) + (R_s - R_{WS_2+S})$, where T_i and R_i are the measured transmittance and reflectance respectively of the substrate ($i = S$) and WS₂ plus substrate ($i = WS_2 + S$). The transmittance, reflectance, and absorptance of the WS₂ on the substrate and the substrate itself are shown in the [Supporting Information](#).

■ ASSOCIATED CONTENT

§ Supporting Information

The Supporting Information is available free of charge on the [ACS Publications website](#) at DOI: [10.1021/acs.nanolett.9b01599](https://doi.org/10.1021/acs.nanolett.9b01599).

Furnace setup is elucidated. The effects of multiple LSCM scans are visualized. Oxidation height analysis with AFM of triangular islands is presented. Details of the edges of WS₂ is analyzed further with LSCM and AFM. The spectra of the lasers used in the study are presented, and the transmittance reflectance and absorptance of the WS₂ on sapphire on glass are presented. Details of FRET and photocatalysis are given, and possible reaction products relating to the microscopic droplet feature seen in Figure 2g,h are discussed. The effects of heating monolayer WS₂ (in the absence of light) is presented. A crystal which underwent minute amounts of oxidation with the 760 nm experiment is presented. Finally, crystals exposed to green light in a nitrogen glovebox are compared with ambient air exposed samples ([PDF](#))

■ AUTHOR INFORMATION

Corresponding Authors

*E-mail (J.C.K.): Jimmy.Kotsakidis@monash.edu.
*E-mail (M.S.F.): Michael.Fuhrer@monash.edu.

ORCID

Jimmy C. Kotsakidis: [0000-0002-7167-5617](https://orcid.org/0000-0002-7167-5617)
Amadeo L. Vazquez de Parga: [0000-0003-0551-1603](https://orcid.org/0000-0003-0551-1603)

Author Contributions

J.C.K. and M.C. made the first observation with the LSCM, which was later developed further by J.C.K. with the help of D.K.G., M.S.F., A.L.V.P., and Q.Z. J.C.K. grew most of the samples, with some samples grown by Q.Z. AFM was conducted by J.C.K and Q.Z. PL was conducted by J.C.K. Low light irradiance/fluence laser experiments were conceived by J.C.K. and A.L.V.P. and carried out by J.C.K. Optical absorptance/transmittance/reflectance was conducted by J.C.K. and A.C. J.C.K. wrote the manuscript with significant editorial contributions from M.S.F., D.K.G., and A.L.V.P. The manuscript was written through contributions of all authors. All authors have given approval to the final version of the manuscript.

Funding

J.C.K. and M.S.F. acknowledge funding support from the Australian Research Council (DP150103837). D.K.G. and M.C. acknowledge funding from the Office of Naval Research (ONR). A.L.V.P. acknowledges the Ministerio de Economía y Competitividad (MINECO) Projects FOS2015-67367-C2-1-P, PGC2018-093291-B-I00, and Comunidad de Madrid project NMAT2d P2018/NMT-4511 for financial support. Q.Z. acknowledges funding support from the Australian Research Council (DE190101249).

Notes

The authors declare no competing financial interest.

■ ACKNOWLEDGMENTS

J.C.K. would like to thank A. Chesman for transmittance/reflectance/absorptance measurements and useful discussions, F. Shanks for use of the WITec PL/Raman system, as well as useful discussions, M. Greaves for time on the LSCM, S. Bhattacharyya for assistance with the glovebox, and S. Johnstone for assistance with equipment in the optical laboratory at Monash University. J.C.K. also acknowledges the hospitality of the U.S. Naval Research Laboratory (NRL) in which the initial investigations were performed. This work was performed in part at the Melbourne Centre for Nanofabrication (MCN) in the Victorian Node of the Australian National Fabrication Facility (ANFF).

■ ABBREVIATIONS

AFM, atomic force microscopy; CVD, chemical vapor deposition; PL, photoluminescence; μ -PL, confocal microphotoluminescence (mapping) spectroscopy; LSCM, laser scanning confocal microscope; FRET, Förster resonance energy transfer.

■ REFERENCES

- (1) Novoselov, K. S.; Geim, A. K.; Morozov, S. V.; Jiang, D.; Zhang, Y.; Dubonos, S. V.; Grigorieva, I. V.; Firsov, A. A. Electric Field Effect in Atomically Thin Carbon Films. *Science* **2004**, *306* (5696), 666–669.
- (2) Novoselov, K.; Jiang, D.; Schedin, F.; Booth, T.; Khotkevich, V.; Morozov, S.; Geim, A. Two-Dimensional Atomic Crystals. *Proc. Natl. Acad. Sci. U. S. A.* **2005**, *102* (30), 10451–10453.
- (3) Randvir, E. P.; Brownson, D. A.; Banks, C. E. A Decade of Graphene Research: Production, Applications and Outlook. *Mater. Today* **2014**, *17* (9), 426–432.
- (4) Choi, W.; Choudhary, N.; Han, G. H.; Park, J.; Akinwande, D.; Lee, Y. H. Recent Development of Two-Dimensional Transition Metal Dichalcogenides and Their Applications. *Mater. Today* **2017**, *20* (3), 116–130.
- (5) Mak, K. F.; Lee, C.; Hone, J.; Shan, J.; Heinz, T. F. Atomically Thin MoS₂: A New Direct-Gap Semiconductor. *Phys. Rev. Lett.* **2010**, *105* (13), 136805.
- (6) Gutiérrez, H. R.; Perea-López, N.; Elías, A. L.; Berkdemir, A.; Wang, B.; Lv, R.; López-Urías, F.; Crespi, V. H.; Terrones, H.; Terrones, M. Extraordinary Room-Temperature Photoluminescence in Triangular WS₂ Monolayers. *Nano Lett.* **2013**, *13* (8), 3447–3454.
- (7) Tongay, S.; Zhou, J.; Ataca, C.; Lo, K.; Matthews, T. S.; Li, J.; Grossman, J. C.; Wu, J. Thermally Driven Crossover from Indirect Toward Direct Bandgap in 2D Semiconductors: MoSe₂ versus MoS₂. *Nano Lett.* **2012**, *12* (11), 5576–5580.
- (8) Dong, N.; Li, Y.; Feng, Y.; Zhang, S.; Zhang, X.; Chang, C.; Fan, J.; Zhang, L.; Wang, J. Optical Limiting and Theoretical Modelling of Layered Transition Metal Dichalcogenide Nanosheets. *Sci. Rep.* **2015**, *5*, 14646.

Nano Letters

Letter

- (9) Xiao, D.; Liu, G.-B.; Feng, W.; Xu, X.; Yao, W. Coupled Spin and Valley Physics in Monolayers of MoS₂ and other Group-VI Dichalcogenides. *Phys. Rev. Lett.* **2012**, *108* (19), 196802.
- (10) Fiori, G.; Bonaccorso, F.; Iannaccone, G.; Palacios, T.; Neumaier, D.; Seabaugh, A.; Banerjee, S. K.; Colombo, L. Electronics Based on Two-Dimensional Materials. *Nat. Nanotechnol.* **2014**, *9* (10), 768.
- (11) Zeng, H.; Dai, J.; Yao, W.; Xiao, D.; Cui, X. Valley Polarization in MoS₂ Monolayers by Optical Pumping. *Nat. Nanotechnol.* **2012**, *7* (8), 490.
- (12) Mak, K. F.; He, K.; Shan, J.; Heinz, T. F. Control of Valley Polarization in Monolayer MoS₂ by Optical Helicity. *Nat. Nanotechnol.* **2012**, *7* (8), 494.
- (13) Ye, Y.; Wong, Z. J.; Lu, X.; Ni, X.; Zhu, H.; Chen, X.; Wang, Y.; Zhang, X. Monolayer Excitonic Laser. *Nat. Photonics* **2015**, *9* (11), 733.
- (14) Tran, T. T.; Choi, S.; Scott, J. A.; Xu, Z. Q.; Zheng, C.; Senintinas, G.; Bendavid, A.; Fuhrer, M. S.; Toth, M.; Aharonovich, I. Room-Temperature Single-Photon Emission from Oxidized Tungsten Disulfide Multilayers. *Adv. Opt. Mater.* **2017**, *5* (5), 1600939.
- (15) Yang, W.; Gan, L.; Li, H.; Zhai, T. Two-Dimensional Layered Nanomaterials for Gas-Sensing Applications. *Inorg. Chem. Front.* **2016**, *3* (4), 433–451.
- (16) Ly, T. H.; Chiu, M.-H.; Li, M.-Y.; Zhao, J.; Perello, D. J.; Cichocka, M. O.; Oh, H. M.; Chae, S. H.; Jeong, H. Y.; Yao, F.; et al. Observing Grain Boundaries in CVD-Grown Monolayer Transition Metal Dichalcogenides. *ACS Nano* **2014**, *8* (11), 11401–11408.
- (17) Yamamoto, M.; Dutta, S.; Aikawa, S.; Nakahara, S.; Wakabayashi, K.; Fuhrer, M. S.; Ueno, K.; Tsukagoshi, K. Self-Limiting Layer-by-Layer Oxidation of Atomically Thin WSe₂. *Nano Lett.* **2015**, *15* (3), 2067–2073.
- (18) Rong, Y.; He, K.; Pachos, M.; Robertson, A. W.; Bhaskaran, H.; Warner, J. H. Controlled Preferential Oxidation of Grain Boundaries in Monolayer Tungsten Disulfide for Direct Optical Imaging. *ACS Nano* **2015**, *9* (4), 3695–3703.
- (19) Zhang, Y.; Zhang, Y.; Ji, Q.; Ju, J.; Yuan, H.; Shi, J.; Gao, T.; Ma, D.; Liu, M.; Chen, Y.; et al. Controlled Growth of High-Quality Monolayer WS₂ Layers on Sapphire and Imaging its Grain Boundary. *ACS Nano* **2013**, *7* (10), 8963–8971.
- (20) Yamamoto, M.; Einstein, T. L.; Fuhrer, M. S.; Cullen, W. G. Anisotropic Etching of Atomically Thin MoS₂. *J. Phys. Chem. C* **2013**, *117* (48), 25643–25649.
- (21) Wu, J.; Li, H.; Yin, Z.; Li, H.; Liu, J.; Cao, X.; Zhang, Q.; Zhang, H. Layer Thinning and Etching of Mechanically Exfoliated MoS₂ Nanosheets by Thermal Annealing in Air. *Small* **2013**, *9* (19), 3314–3319.
- (22) Gao, J.; Li, B.; Tan, J.; Chow, P.; Lu, T.-M.; Koratkar, N. Aging of Transition Metal Dichalcogenide Monolayers. *ACS Nano* **2016**, *10* (2), 2628–2635.
- (23) Kang, K.; Godin, K.; Kim, Y. D.; Fu, S.; Cha, W.; Hone, J.; Yang, E. H. Graphene-Assisted Antioxidation of Tungsten Disulfide Monolayers: Substrate and Electric-Field Effect. *Adv. Mater.* **2017**, *29* (18), 1603898.
- (24) Atkin, P.; Lau, D.; Zhang, Q.; Zheng, C.; Berean, K.; Field, M.; Ou, J.; Cole, I.; Daenke, T.; Kalantar-Zadeh, K. Laser Exposure Induced Alteration of WS₂ Monolayers in the Presence of Ambient Moisture. *2D Mater.* **2018**, *5* (1), 015013.
- (25) Zhang, Q.; Lu, J.; Wang, Z.; Dai, Z.; Zhang, Y.; Huang, F.; Bao, Q.; Duan, W.; Fuhrer, M. S.; Zheng, C. Reliable Synthesis of Large-Area Monolayer WS₂ Single Crystals, Films, and Heterostructures with Extraordinary Photoluminescence Induced by Water Intercalation. *Adv. Opt. Mater.* **2018**, *6*, 1701347.
- (26) Sheng, Y.; Wang, X.; Fujisawa, K.; Ying, S.; Elias, A. L.; Lin, Z.; Xu, W.; Zhou, Y.; Korsunsky, A. M.; Bhaskaran, H.; et al. Photoluminescence Segmentation Within Individual Hexagonal Monolayer Tungsten Disulfide Domains Grown by Chemical Vapor Deposition. *ACS Appl. Mater. Interfaces* **2017**, *9* (17), 15005–15014.
- (27) Peimyoo, N.; Shang, J.; Cong, C.; Shen, X.; Wu, X.; Yeow, E. K.; Yu, T. Nonblinking, Intense Two-Dimensional Light Emitter: Monolayer WS₂ Triangles. *ACS Nano* **2013**, *7* (12), 10985–10994.
- (28) Cong, C.; Shang, J.; Wu, X.; Cao, B.; Peimyoo, N.; Qiu, C.; Sun, L.; Yu, T. Synthesis and Optical Properties of Large-Area Single-Crystalline 2D Semiconductor WS₂ Monolayer from Chemical Vapor Deposition. *Adv. Opt. Mater.* **2014**, *2* (2), 131–136.
- (29) McCreary, K. M.; Hanbicki, A. T.; Singh, S.; Kawakami, R. K.; Jernigan, G. G.; Ishigami, M.; Ng, A.; Brintlinger, T. H.; Stroud, R. M.; Jonker, B. T. The Effect of Preparation Conditions on Raman and Photoluminescence of Monolayer WS₂. *Sci. Rep.* **2016**, *6*, 35154.
- (30) Liu, H.; Lu, J.; Ho, K.; Hu, Z.; Dang, Z.; Carvalho, A.; Tan, H. R.; Tok, E. S.; Sow, C. H. Fluorescence Concentric Triangles: A Case of Chemical Heterogeneity in WS₂ Atomic Monolayer. *Nano Lett.* **2016**, *16* (9), 5559–5567.
- (31) Zhang, Q.; Chang, Z.; Xu, G.; Wang, Z.; Zhang, Y.; Xu, Z. Q.; Chen, S.; Bao, Q.; Liu, J. Z.; Mai, Y. W.; et al. Strain Relaxation of Monolayer WS₂ on Plastic Substrate. *Adv. Funct. Mater.* **2016**, *26* (47), 8707–8714.
- (32) Chow, P. K.; Jacobs-Gedrim, R. B.; Gao, J.; Lu, T.-M.; Yu, B.; Terrones, H.; Koratkar, N. Defect-Induced Photoluminescence in Monolayer Semiconducting Transition Metal Dichalcogenides. *ACS Nano* **2015**, *9* (2), 1520–1527.
- (33) Hu, Z.; Avila, J.; Wang, X.; Leong, J.; Zhang, Q.; Liu, Y.; Asensio, M.; Lu, J.; Carvalho, A.; Sow, C. H. The Role of Oxygen Atoms on the Excitons at the Edges of Monolayer WS₂. *Nano Lett.* **2019**, *19*, 4641.
- (34) Zheng, C.; Xu, Z.-Q.; Zhang, Q.; Edmonds, M. T.; Watanabe, K.; Taniguchi, T.; Bao, Q.; Fuhrer, M. S. Profound Effect of Substrate Hydroxylation and Hydration on Electronic and Optical Properties of Monolayer MoS₂. *Nano Lett.* **2015**, *15* (5), 3096–3102.
- (35) Song, C.; Chen, H.; Fan, Y.; Luo, J.; Guo, X.; Liu, X. High-Work-Function Transparent Conductive Oxides with Multilayer Films. *Appl. Phys. Express* **2012**, *5* (4), 041102.
- (36) Hu, L.; Shan, X.; Wu, Y.; Zhao, J.; Lu, X. Laser Thinning and Patterning of MoS₂ with Layer-by-Layer Precision. *Sci. Rep.* **2017**, *7* (1), 15538.
- (37) Zhao, W.; Ghorannevis, Z.; Chu, L.; Toh, M.; Kloc, C.; Tan, P.-H.; Eda, G. Evolution of Electronic Structure in Atomically Thin Sheets of WS₂ and WSe₂. *ACS Nano* **2013**, *7* (1), 791–797.
- (38) Hanbicki, A.; Currie, M.; Kiseoglou, G.; Friedman, A.; Jonker, B. Measurement of High Exciton Binding Energy in the Monolayer Transition-Metal Dichalcogenides WS₂ and WSe₂. *Solid State Commun.* **2015**, *203*, 16–20.
- (39) Zhu, B.; Chen, X.; Cui, X. Exciton Binding Energy of Monolayer WS₂. *Sci. Rep.* **2015**, *5*, 9218.
- (40) Bregnhoj, M.; Blazquez-Castro, A.; Westberg, M.; Breitenbach, T.; Ogilby, P. R. Direct 765 nm Optical Excitation of Molecular Oxygen in Solution and in Single Mammalian Cells. *J. Phys. Chem. B* **2015**, *119* (17), 5422–5429.
- (41) Blázquez-Castro, A. Direct 1O2 optical excitation: A tool for redox biology. *Redox Biol.* **2017**, *13*, 39–59.
- (42) Ding, X.; Peng, F.; Zhou, J.; Gong, W.; Slaven, G.; Loh, K. P.; Lim, C. T.; Leong, D. T. Defect Engineered Bioactive Transition Metals Dichalcogenides Quantum Dots. *Nat. Commun.* **2019**, *10* (1), 41.
- (43) Froehlicher, G.; Lorchat, E.; Berciaud, S. Charge Versus Energy Transfer in Atomically Thin Graphene-Transition Metal Dichalcogenide van der Waals Heterostructures. *Phys. Rev. X* **2018**, *8* (1), 011007.
- (44) Suzuki, T.; Ogawa, M. Degradation of Photoluminescence Intensity Caused by Excitation-Enhanced Oxidation of GaAs Surfaces. *Appl. Phys. Lett.* **1977**, *31* (7), 473–475.
- (45) Bermudez, V. M. Photoenhanced Oxidation of Gallium Arsenide. *J. Appl. Phys.* **1983**, *54* (11), 6795–6798.
- (46) Schafer, S.; Lyon, S. Optically Enhanced Oxidation of Semiconductors. *J. Vac. Sci. Technol.* **1981**, *19* (3), 494–497.

- (47) Nosaka, Y.; Nosaka, A. Y. Generation and Detection of Reactive Oxygen Species in Photocatalysis. *Chem. Rev.* **2017**, *117* (17), 11302–11336.
- (48) Favron, A.; Gaufrès, E.; Fossard, F.; Phaneuf-L'Heureux, A.-L.; Tang, N. Y.; Lévesque, P. L.; Loiseau, A.; Leonelli, R.; Francoeur, S.; Martel, R. Photooxidation and Quantum Confinement Effects in Exfoliated Black Phosphorus. *Nat. Mater.* **2015**, *14* (8), 826.
- (49) Shcherbakov, D.; Stepanov, P.; Weber, D.; Wang, Y.; Hu, J.; Zhu, Y.; Watanabe, K.; Taniguchi, T.; Mao, Z.; Windl, W.; et al. Raman Spectroscopy, Photocatalytic Degradation, and Stabilization of Atomically Thin Chromium Tri-Iodide. *Nano Lett.* **2018**, *18* (7), 4214–4219.
- (50) Iwasaki, H.; Mizokawa, Y.; Nishitani, R.; Nakamura, S. X-Ray Photoemission Study of the Interaction of Oxygen and Air with Cleaved GaAs (110) Surfaces. *Jpn. J. Appl. Phys.* **1978**, *17* (2), 315.
- (51) Zhang, X.; Jia, F.; Yang, B.; Song, S. Oxidation of molybdenum disulfide sheet in water under *in situ* atomic force microscopy observation. *J. Phys. Chem. C* **2017**, *121* (18), 9938–9943.
- (52) Budania, P.; Baine, P.; Montgomery, J.; McGeough, C.; Cafolla, T.; Modreanu, M.; McNeill, D.; Mitchell, N.; Hughes, G.; Hurley, P. Long-Term Stability of Mechanically Exfoliated MoS₂ Flakes. *MRS Commun.* **2017**, *7* (4), 813–818.
- (53) Ross, S.; Sussman, A. Surface Oxidation of Molybdenum Disulfide. *J. Phys. Chem.* **1955**, *59* (9), 889–892.
- (54) Wu, Z.; Yu, J.; Yuan, S. Strain-Tunable Magnetic and Electronic Properties of Monolayer CrI₃. *Phys. Chem. Chem. Phys.* **2019**, *21*, 7750.
- (55) Ye, M.; Zhang, D.; Yap, Y. K. Recent advances in electronic and optoelectronic devices based on two-dimensional transition metal dichalcogenides. *Electronics* **2017**, *6* (2), 43.
- (56) Rosenberger, M. R.; Chuang, H.-J.; McCreary, K. M.; Li, C. H.; Jonker, B. T. Electrical Characterization of Discrete Defects and Impact of Defect Density on Photoluminescence in Monolayer WS₂. *ACS Nano* **2018**, *12* (2), 1793–1800.
- (57) Carozo, V.; Wang, Y.; Fujisawa, K.; Carvalho, B. R.; McCreary, A.; Feng, S.; Lin, Z.; Zhou, C.; Perea-López, N.; Elías, A. L.; et al. Optical Identification of Sulfur Vacancies: Bound Excitons at the Edges of Monolayer Tungsten Disulfide. *Sci. Adv.* **2017**, *3* (4), e1602813.
- (58) Hong, J.; Hu, Z.; Probert, M.; Li, K.; Lv, D.; Yang, X.; Gu, L.; Mao, N.; Feng, Q.; Xie, L.; et al. Exploring Atomic Defects in Molybdenum Disulfide Monolayers. *Nat. Commun.* **2015**, *6*, 6293.
- (59) Addou, R.; Colombo, L.; Wallace, R. M. Surface Defects on Natural MoS₂. *ACS Appl. Mater. Interfaces* **2015**, *7* (22), 11921–11929.
- (60) Vancsó, P.; Magda, G. Z.; Pető, J.; Noh, J.-Y.; Kim, Y.-S.; Hwang, C.; Biró, L. P.; Tapasztó, L. The Intrinsic Defect Structure of Exfoliated MoS₂ Single Layers Revealed by Scanning Tunneling Microscopy. *Sci. Rep.* **2016**, *6*, 29726.
- (61) Edelberg, D.; Rhodes, D.; Kerelsky, A.; Kim, B.; Wang, J.; Zangiabadi, A.; Kim, C.; Abhinandan, A.; Ardelean, J.; Scully, M.; et al. Hundredfold Enhancement of Light Emission via Defect Control in Monolayer Transition-Metal Dichalcogenides. *NANO Lett.* **2019**, *19* (7), 4371–4379.
- (62) Barja, S.; Refaelly-Abramson, S.; Schuler, B.; Qiu, D. Y.; Pulkin, A.; Wickenburg, S.; Ryu, H.; Ugeda, M. M.; Kastl, C.; Chen, C.; et al. Identifying Substitutional Oxygen as a Prolific Point Defect in Monolayer Transition Metal Dichalcogenides with Experiment and Theory. *arXiv:1810.03364* **2018**.
- (63) KC, S.; Longo, R. C.; Wallace, R. M.; Cho, K. Surface Oxidation Energetics and Kinetics on MoS₂ Monolayer. *J. Appl. Phys.* **2015**, *117* (13), 135301.
- (64) Hu, K. H.; Hu, X. G.; Sun, X. J. Morphological Effect of MoS₂ Nanoparticles on Catalytic Oxidation and Vacuum Lubrication. *Appl. Surf. Sci.* **2010**, *256* (8), 2517–2523.
- (65) Afanasiev, P.; Lorentz, C. Oxidation of Nanodispersed MoS₂ in Ambient Air: The Products and the Mechanistic Steps. *J. Phys. Chem. C* **2019**, *123*, 7486.
- (66) Conley, H. J.; Wang, B.; Ziegler, J. I.; Haglund, R. F., Jr; Pantelides, S. T.; Bolotin, K. I. Bandgap Engineering of Strained Monolayer and Bilayer MoS₂. *Nano Lett.* **2013**, *13* (8), 3626–3630.
- (67) Horcas, I.; Fernández, R.; Gomez-Rodriguez, J.; Colchero, J.; Gómez-Herrero, J.; Baro, A. WSXM: A Software for Scanning Probe Microscopy and a Tool for Nanotechnology. *Rev. Sci. Instrum.* **2007**, *78* (1), 013705.

Freestanding n-Doped Graphene via Intercalation of Calcium and Magnesium into the Buffer Layer–SiC(0001) Interface

Jimmy C. Kotsakidis,* Antonija Grubisic-Cabo, Yuefeng Yin, Anton Tadich, Rachael L. Myers-Ward, Matthew DeJarl, Shojan P. Pavunny, Marc Currie, Kevin M. Daniels, Chang Liu, Mark T. Edmonds, Nikhil V. Medhekar, D. Kurt Gaskill, Amadeo L. Vazquez de Parga,* and Michael S. Fuhrer*



Cite This: <https://dx.doi.org/10.1021/acs.chemmater.0c01729>



Read Online

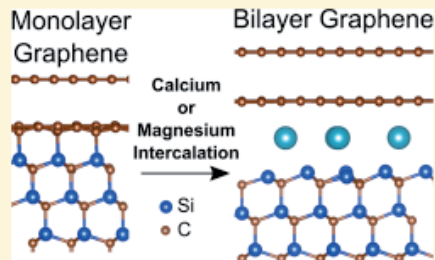
ACCESS |

Metrics & More

Article Recommendations

Supporting Information

ABSTRACT: The intercalation of epitaxial graphene on SiC(0001) with Ca has been studied extensively, yet precisely where the Ca resides remains elusive. Furthermore, the intercalation of Mg underneath epitaxial graphene on SiC(0001) has not been reported. Here, we use low energy electron diffraction, X-ray photoelectron spectroscopy, secondary electron cutoff photoemission, and scanning tunneling microscopy to elucidate the physical and electronic structures of both Ca- and Mg-intercalated epitaxial graphene on 6H-SiC(0001). We find that Ca intercalates underneath the buffer layer and bonds to the Si-terminated SiC surface, breaking the C–Si bonds of the buffer layer, i.e., “freestanding” the buffer layer to form Ca-intercalated quasi-freestanding bilayer graphene (Ca-QFSBLG). The situation is similar for the Mg-intercalation of epitaxial graphene on SiC(0001), where an ordered Mg-terminated reconstruction at the SiC surface is formed and Mg bonds to the Si-terminated SiC surface are found, resulting in Mg-intercalated quasi-freestanding bilayer graphene (Mg-QFSBLG). Ca-intercalation underneath the buffer layer has not been considered in previous studies of Ca-intercalated epitaxial graphene. Furthermore, we find no evidence that either Ca or Mg intercalates between graphene layers. However, we do find that both Ca-QFSBLG and Mg-QFSBLG exhibit very low work functions of 3.68 and 3.78 eV, respectively, indicating high n-type doping. Upon exposure to ambient conditions, we find Ca-QFSBLG degrades rapidly, whereas Mg-QFSBLG remains remarkably stable.



Graphene, the two-dimensional (2D) allotrope of carbon consisting of a network of hexagonally bonded carbon atoms,¹ possesses radically different properties than those of its bulk form (graphite), owing to its Dirac cone band structure at low energy.² In addition, considerable research has been conducted on the modification of graphene's properties via doping using techniques such as electrostatic gating,³ surface decoration,^{4,5} structure modification,⁶ and intercalation.⁷ Of these methods, intercalation (i.e., insertion of atomic or molecular species under or in between graphene layers) has proven a powerful method for achieving the highest doping levels in graphene.^{8–10} Thus, intercalation has enabled various investigations into the fundamental physics of superconductivity^{8,11,12} and many-body interactions^{8–10} as well as potential applications such as highly conductive and transparent electrodes¹³ and energy storage.¹⁴

Following the discovery of superconducting Ca-intercalated graphite (CaC₆)—which exhibits the highest superconducting transition temperature ($T_c = 11.5$ K) among the graphite intercalation compounds—intercalation of the alkaline-earth Ca has been of particular interest in attempts to achieve superconductivity¹² and extremely high doping in graphene.⁸

Superconductivity with a high T_c via conventional electron–phonon coupling¹⁵ or unconventional electron–electron coupling^{16,17} has been predicted in highly n-type doped graphene if the Fermi level (E_F) is shifted high into the conduction band near the Van Hove singularity. This scenario has analogies to the high- T_c cuprates, in which superconductivity is associated with the interaction between E_F and the Van Hove singularity.¹⁸ This physical scenario in graphene was first observed by McChesney et al.⁸ using submonolayer graphene on SiC(0001) intercalated with Ca (and the surface decorated with Ca and K), and it was subsequently suggested that the sample could exhibit superconductivity. More recently, the superconductivity of Ca-intercalated bilayer graphene was reported by Ichinokura et al.¹² with $T_c \approx 2$ K.

Received: April 23, 2020

Revised: July 13, 2020

Published: July 15, 2020

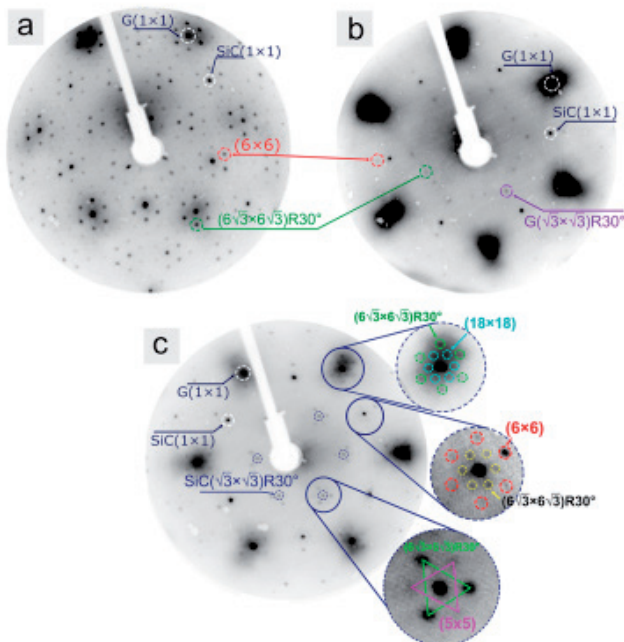


Figure 1. Low energy electron diffraction (LEED) patterns at electron energy of 100 eV. (a) Pristine epitaxial monolayer graphene on SiC(0001) (EMLG) showing graphene ($G(1 \times 1)$) and SiC ($SiC(1 \times 1)$) spots, as well as $(6\sqrt{3} \times 6\sqrt{3})R30^\circ$ and (6×6) spots arising from the buffer layer. (b) Ca-QFSBLG showing the emergence of $(\sqrt{3} \times \sqrt{3})R30^\circ$ spots with respect to the $G(1 \times 1)$ spots ($G(\sqrt{3} \times \sqrt{3})R30^\circ$). (c) Mg-QFSBLG with spots corresponding to a $(\sqrt{3} \times \sqrt{3})R30^\circ$ reconstruction relative to the $SiC(1 \times 1)$ spots ($SiC(\sqrt{3} \times \sqrt{3})R30^\circ$), along with (5×5) , (18×18) (around the $G(1 \times 1)$), and $(6\sqrt{3} \times 6\sqrt{3})R30^\circ/(6 \times 6)$ (around the $SiC(1 \times 1)$) spots. In both Ca-QFSBLG (b) and Mg-QFSBLG (c) we observe the suppression of $(6\sqrt{3} \times 6\sqrt{3})R30^\circ/(6 \times 6)$ spots related to the buffer layer and increase in brightness of the $G(1 \times 1)$ with respect to the $SiC(1 \times 1)$ spots, as compared to pristine EMLG in (a).

The Ca-intercalation experiments performed to date have utilized large-area graphene on SiC,^{8,11,12,19–21} as it enables a wide range of surface probes such as scanning tunneling microscopy (STM), low energy electron diffraction (LEED), X-ray photoelectron spectroscopy (XPS), and angle resolved photoemission spectroscopy (ARPES). Graphene synthesis on SiC occurs via the sublimation of Si, where the remaining C naturally forms a hexagonal carbon network. This first layer of carbon is often termed the “zero layer” or “buffer layer”²² and is partially bonded to the topmost silicon on SiC(0001). Continued sublimation forms another buffer layer beneath the first, releasing the C–Si bonds of the original buffer layer, which then becomes monolayer graphene.

The structure of Ca-intercalated graphene on SiC is less clear, with disagreement regarding the location of the intercalated Ca. For instance, McChesney et al.⁸ implied the position of the Ca intercalant in their partial monolayer graphene was between the first graphene layer and the buffer layer. Kanetani et al.¹⁹ and Ichinokura et al.¹² studied the Ca-intercalated bilayer graphene on SiC(0001), and based on LEED and reflection high energy electron diffraction data concluded that Ca was intercalated between the first and second graphene layers. A correction to this interpretation was recently published by Endo et al.,²⁰ in which it was determined that the Ca intercalant position for bilayer graphene on SiC was between the buffer layer and the first graphene layer.

The calcium intercalation of graphite^{23,24} and graphene^{8,12,19–21,25,26} has been extensively studied and can highly n-type dope these systems.⁸ On the other hand, the alkaline-earth magnesium has not been investigated as an intercalant in graphene on silicon carbide systems. Some reasons for this may be due to the well-known experimental knowledge that metallic magnesium does not intercalate graphite²⁷ and also may be exacerbated by magnesium’s well-known high vapor pressure.²⁸ More recent theoretical considerations have substantiated the difficulty of magnesium intercalation for a range of different materials (including graphite) and have implied that the difficulty of Mg intercalation is a result of its weak binding forces to the target substrate.²⁹ Thus, it is likely that for these reasons the intercalation of graphene on SiC with magnesium was not considered.

Despite these challenges, magnesium has been intercalated underneath graphene on Ni(111)³⁰ and between layers of a “graphite-like” material composed of boron, carbon and nitrogen.³¹ Furthermore, magnesium intercalation for energy storage applications has long been sought after to replace lithium.³² But in this case, magnesium forms part of an electrolyte or organic molecule.^{33,34} As a rule, it has generally been understood that Mg intercalation of pure carbon systems is not possible, but the fact that intercalation of graphene on SiC(0001) systems can occur at the buffer layer–SiC(0001) interface³⁵ implies that the “traditional” rules of intercalation

Chemistry of Materials

pubs.acs.org/cm

Article

from experiments with graphite in which the intercalant is inserted between graphite layers may not apply (as was the case with other substrates and modified materials^{30,31}).

In this communication, we present new findings on the intercalation structure of two alkaline-earth metals—Ca and Mg—via the intercalation of epitaxial monolayer graphene (EMLG) (and hydrogen intercalated “quasi-freestanding” bilayer graphene, “H-QFSBLG”—see Supporting Information Section 1.3) on 6H-SiC(0001). We show that Ca intercalates underneath the buffer layer of EMLG, bonding with the Si-terminated surface of the SiC(0001) and “quasi-freestanding” the buffer layer to create another graphene layer, i.e., forming quasi-freestanding bilayer graphene (QFSBLG) above the Ca–Si layer, which we term Ca-QFSBLG. The intercalated Ca forms a new ordered ($\sqrt{3} \times \sqrt{3}$)R30° interface reconstruction with respect to the graphene. The observations are supported by density functional theory (DFT) calculations, which show Ca under the buffer layer as the lowest energy configuration. In addition, we report for the first time on the intercalation of EMLG with Mg. Similar to Ca, Mg intercalates underneath the buffer layer of EMLG, bonding with the Si surface of SiC and freestanding the buffer layer to again form QFSBLG, which we term Mg-QFSBLG. Here, stronger Mg–Si interactions produce an ordered Mg-terminated ($\sqrt{3} \times \sqrt{3}$)R30° reconstruction with respect to the SiC rather than the graphene. As in the Ca-intercalation experiment, we find no evidence to suggest the formation of an Mg-carbide or intercalation of the Mg in between graphene layers. Both Ca- and Mg-intercalated systems result in the formation of bilayer graphene with exceptionally low work functions (3.68 and 3.78 eV, respectively). However, while the Ca-QFSBLG system is not air-stable, we find that the Mg-QFSBLG system shows remarkable stability to ambient conditions, with little change in photoemission spectra after ≈6 h of exposure to ambient conditions. Consequently, Mg intercalation could offer a possible route to highly electron doped, low work function, and air-stable graphene.

■ EXPERIMENTAL OVERVIEW

The EMLG samples were prepared using a previously described method (further details can be found in Methods).³⁶ The EMLG samples are majority monolayer, with inclusions of bilayer and trilayer regions. However, our conclusions are not affected by the number of graphene layers in the starting sample, as (1) the LEED and XPS analysis of the structure and chemistry at the intercalated buffer layer/SiC interface is insensitive to the number of graphene overlayers and (2) previous studies have shown that bilayer regions (step edges) of such samples do not include a buffer layer³⁷ and subsequent intercalation (with hydrogen) results in near-total conversion of the samples to QFSBLG.³⁸ Ca and Mg intercalation for XPS and LEED measurement was carried out at the Australian Synchrotron soft X-ray beamline end station under ultrahigh vacuum (UHV) conditions ($\approx 1 \times 10^{-10}$ mbar). Low temperature STM was carried out at Monash University on Ca-QFSBLG prepared in situ, under UHV ($\approx 1 \times 10^{-10}$ mbar). The Mg-QFSBLG sample analyzed with the STM was prepared by Mg intercalation at the Australian Synchrotron and then transferred in ambient air to the STM UHV chamber.

We have additionally studied Ca and Mg intercalation of H-QFSBLG, prepared using a previously described method (see Methods for details on growth).³⁸ We found no evidence for Mg intercalation of H-QFSBLG (see Supporting Information Section 2.3), but were able to intercalate Ca to transform H-

QFSBLG to Ca-QFSBLG, with substantially similar properties to Ca-QFSBLG formed from EMLG (discussed further in Supporting Information Section 1.3). Details of all experiments are found in Methods.

■ RESULTS AND DISCUSSION

Low Energy Electron Diffraction (LEED) of Ca- and Mg-Intercalated EMLG on SiC(0001). Figure 1 shows LEED images taken at an electron energy of 100 eV. Figure 1a shows a typical EMLG sample with graphene (G(1×1)) and SiC (SiC(1×1)) spots, as well as the expected ($6\sqrt{3} \times 6\sqrt{3}$)R30° and (6×6) spots which originate from the buffer layer–SiC interaction.³⁹ The Ca- and Mg-intercalated samples are shown in Figure 1b,c, respectively, and share important features. First, the relative intensities of the SiC(1×1) to the G(1×1) spots after Ca- and Mg-intercalation are greatly reduced. This is in contrast to the similar intensities of the G(1×1) and SiC(1×1) spots in pristine EMLG prior to intercalation (Figure 1a). Second, the ($6\sqrt{3} \times 6\sqrt{3}$)R30° spots are strongly suppressed in both the Ca- and Mg-intercalated samples (Figure 1b,c, respectively), when compared to pristine EMLG (Figure 1a). These observations are similar to the case of H-QFSBLG after H-intercalation of EMLG, which is known to decouple the buffer layer,⁴⁰ and, thus, suggests that the buffer layer of the EMLG is similarly decoupled after Ca/Mg-intercalation and transformed to QFSBLG (i.e., Ca/Mg-QFSBLG). Consequently, our LEED results present the first evidence that intercalation of Ca and Mg occurs between the SiC(0001) surface and the buffer layer, in disagreement with previous reports. We note that the weak ($6\sqrt{3} \times 6\sqrt{3}$)R30° spots after Ca/Mg-intercalation (seen in Figures 1b,c) are also observed after H-intercalation⁷ and likely result from incomplete (i.e., partial) intercalation.⁴¹

Furthermore, Figure 1b shows the emergence of ($\sqrt{3} \times \sqrt{3}$)R30° spots with respect to the G(1×1) spots after Ca-intercalation (which we label “G($\sqrt{3} \times \sqrt{3}$)R30°”). Previous Ca-intercalation studies¹⁹ also reported G($\sqrt{3} \times \sqrt{3}$)R30° spots and interpreted these as due to Ca atoms intercalating between the graphene layers. Yet the G($\sqrt{3} \times \sqrt{3}$)R30° spots are not definitive evidence for intercalation between the graphene layers, as their emergence has been observed after the intercalation of Yb in buffer-layer-only samples to form “quasi-freestanding” monolayer graphene on SiC.¹⁰ Thus, it is plausible that the G($\sqrt{3} \times \sqrt{3}$)R30° spots instead describe a Ca-QFSBLG structure. As we discuss further below, the prior interpretation is incorrect, and Ca (and Mg) indeed lie between the SiC(0001) surface and the buffer layer.

In contrast, the Mg-intercalated EMLG sample in Figure 1c shows the emergence of ($\sqrt{3} \times \sqrt{3}$)R30° spots with respect to the SiC(1×1) spots, not the G(1×1) spots (i.e., SiC($\sqrt{3} \times \sqrt{3}$)R30°). Such spots were observed by Stöhr et al.⁴² and Kim et al.⁴³ after intercalation of the buffer layer only on SiC with Bi and In, respectively, and by Xia et al.⁴⁴ after Si-intercalation of EMLG. The SiC($\sqrt{3} \times \sqrt{3}$)R30° spots have also been observed in the past with Si adatoms bonded via the dangling bonds of the Si surface of SiC.⁴⁵ Thus, the observation of these SiC($\sqrt{3} \times \sqrt{3}$)R30° spots strongly indicates that Mg has intercalated beneath the buffer layer, releasing the buffer layer–SiC bonds to create Mg-QFSBLG, in agreement with the disappearance of the ($6\sqrt{3} \times 6\sqrt{3}$)R30°/(6×6) and brightness increase in G(1×1) spots relative to the SiC(1×1) spots.

Also visible in Figure 1c are extra spots concentric around both the G(1×1) and SiC(1×1) spots. These spots are shown more clearly in the magnified and enhanced views in the right

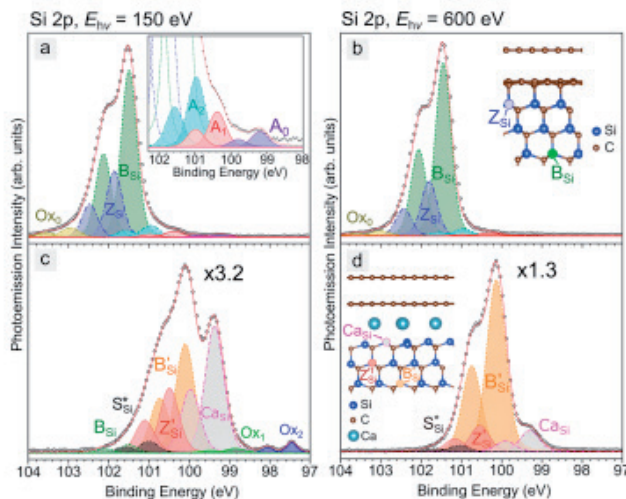


Figure 2. X-ray photoemission spectra showing the Si 2p core level of pristine epitaxial monolayer graphene on SiC(0001) (EMLG) and Ca-intercalated EMLG (Ca-QFSBLG) at two incident X-ray energies (E_{hv}): 150 eV (left, surface sensitive) and 600 eV (right, bulk substrate sensitive). (a, b) Pristine EMLG before intercalation showing all components. Component B_{Si} is the bulk component of SiC, whereas component Z_{Si} is a more surface SiC component. The approximate atom locations of components B_{Si} and Z_{Si} are shown in the inset of b. (c, d) EMLG after Ca-intercalation (Ca-QFSBLG) and new components Ca_{Si} , B'_{Si} , Z'_{Si} , and S'_{Si} . Components Z_{Si} and B_{Si} have been shifted to lower binding energy and are now labeled Z'_{Si} and B'_{Si} respectively. c has its y-scale magnified $\times 3.2$ from a, and d has its y-scale magnified $\times 1.3$ from b. The approximate atom positions of the components are shown in the inset of d; see text for further explanation of the components.

Table 1. Summary of the Fitting Parameters for the Major Components in Figure 2^a

EMLG, Si 2p		(a, b) pristine EMLG				(c, d) second Ca intercalation			
component	E_{hv} (eV)	E_B (eV) $2p_{3/2}$	E_B (eV) $2p_{1/2}$	RI	G_w (eV)	E_B (eV) $2p_{3/2}$	E_B (eV) $2p_{1/2}$	RI	G_w (eV)
B_{Si}	150	101.50	102.13	1	0.4	101.45	102.05	0.016	0.4
	600	101.45	102.06	1	0.4				
Z_{Si}	150	101.86	102.47	0.40	0.4	100.51	101.13	0.12	0.5
	600	101.80	102.43	0.32	0.4				
Ox_0	150	102.95	103.55	0.06	0.5	100.54	101.16	0.10	0.5
	600	102.95	103.55	0.03	0.5				
B'_{Si}	150					100.11	100.74	0.24	0.5
	600					100.13	100.74	0.68	0.5
Z'_{Si}	150					100.51	101.13	0.12	0.5
	600					100.54	101.16	0.10	0.5
S'_{Si}	150					101	101.63	0.02	0.5
	600					101.05	101.65	0.026	0.5
Ca_{Si}	150					99.37	99.97	0.24	0.5
	600					99.3	99.9	0.08	0.5
Ox_1	150					98.85	99.45	0.008	0.5
	600					*	*	*	*
Ox_2	150					97.45	98.05	0.02	0.25
	600					*	*	*	*

^aBoth the Si 2p_{3/2} and the 2p_{1/2} peak locations are given, as well as the relative intensity (RI) of the 2p_{3/2} peaks as referenced to the bulk SiC peak B_{Si} corresponding to pristine SiC prior to Ca intercalation. G_w refers to the Gaussian FWHM for the Voigt fit (which was fixed to one of two values, except for component Ox_2), whereas the Lorentzian FWHM (W_L) was kept constant at 0.1 eV in all fits. The dashes correspond to no observation.

inset of Figure 1c. In regards to the G(1 × 1) spots, the new concentric spots correspond to an (18 × 18) reconstruction, rotated 30° with respect to the (6 $\sqrt{3} \times 6\sqrt{3}$)R30° spots. Observation of the (18 × 18) spots is consistent with the expected expansion of the Moiré pattern from the interaction of graphene with SiC(0001) from (6 $\sqrt{3} \times 6\sqrt{3}$)R30° to (18 × 18) upon the ($\sqrt{3} \times \sqrt{3}$)R30° reconstruction of the surface (i.e., ($\sqrt{3} \times \sqrt{3}$)R30° × (6 $\sqrt{3} \times 6\sqrt{3}$)R30° = (18 × 18)). These LEED spots have been observed previously after the intercalation of Pt underneath graphene on SiC(0001), and their appearance was attributed to the concurrent formation of a Pt-silicide.⁴⁶ Similarly, we observe the appearance of (6 $\sqrt{3} \times 6\sqrt{3}$)R30° spots around the SiC(1 × 1) spots corresponding to the expansion of the (6 × 6) Moiré by the ($\sqrt{3} \times \sqrt{3}$)R30°

reconstruction. Also seen are (5×5) spots in **Figure 1c**, but these were not found to have significance regarding the Mg-intercalation structure.³⁹

LEED spot patterns have elucidated the overlaying symmetries resulting from Ca- and Mg-intercalation of EMLG and suggest that both Ca and Mg intercalate underneath the buffer layer to form Ca-QFSBLG and Mg-QFSBLG. Nonetheless, LEED alone cannot determine the chemistry occurring underneath the graphene, and so we turn to XPS. Below, we first discuss the Si 2p and then the C 1s XPS spectra of Ca-QFSBLG (discussion of the O 1s and Ca 2p core levels can be found in the Supporting Information, **Section 1.5**), before discussing the surface morphology of Ca-QFSBLG as imaged by STM and density functional theory calculations concerning the predicted structure of Ca-intercalated EMLG. This discussion will then be repeated for Mg-QFSBLG (without the theoretical consideration), which we will show shares many similarities with Ca-QFSBLG.

X-ray Photoelectron Spectroscopy of Ca-QFSBLG. Here we present and discuss the XPS results for the C 1s and Si 2p core levels for the same EMLG sample, the LEED of which is shown in **Figure 1b**. H-QFSBLG samples were also transformed to Ca-QFSBLG by the same intercalation method used for the EMLG samples and showed similar XPS spectral features—see **Supporting Information Section 1.3** for details.

Figure 2 shows the Si 2p core level XPS spectra—photoemission intensity as a function of binding energy, E_B —before and after Ca-intercalation. In all XPS spectra, experimental data points are shown as open black circles, and the final fit is overlaid as a red line. Each Si 2p component is comprised of $2p_{3/2}$ and $2p_{1/2}$ peaks colored identically to avoid confusion, and we quote only E_B values corresponding to the $2p_{3/2}$ peak. Fit parameters of the major components are given in **Table 1**; the full set of fit parameters (which includes the omitted first intercalation step) can be found in **Supporting Information Section 1.1**.

Figure 2a,b shows the Si 2p core level spectra of pristine EMLG. The tunability of the synchrotron source allowed different X-ray energies ($E_hv = 150$ eV, 600 eV) to be used in order to determine the surface and bulk nature of the various components and aided in spectrum deconvolution. Pristine EMLG shows two major components: B_{Si} ($E_B = 101.47 \pm 0.05$ eV) corresponds to “bulk” SiC^{7,47,48} and Z_{Si} ($E_B = 101.83 \pm 0.05$ eV) to surface Si bonded to the C in the buffer layer/zero layer.^{7,43,49} Further discussion concerning the component Z_{Si} can be found in **Supporting Information Section 1.2**. (The components corresponding to compounds present in both the Si 2p and the C 1s XPS spectra are designated using the same label, with different subscript labels, in order to distinguish the specific core level; i.e., B_{Si} and B_C are the bulk SiC signals in the Si 2p and C 1s spectra, respectively). We note here that the E_B value was calculated by averaging all measured values (including the values from the omitted first intercalation which can be found in the **Supporting Information Section 1.1**)—see **Methods** for further details. The corresponding atomic positions for the major components of pristine EMLG are shown schematically in the inset of **Figure 2b**. These positions are approximately determined by a calculation of the relative intensity ratio, RI_R , discussed in detail in **Methods**. The RI_R is a qualitative measure of surface sensitivity, with an $RI_R > 1$ indicating that the component is more toward the surface (see **Methods** and **Supporting Information Section 1.1**), and was calculated using the relative intensity (RI) referenced to the well-known bulk

component B_{Si} (or B_C in the case of C 1s spectra, see below), following closely the conventions used in ref 49. For instance, the RI_R of component Z_{Si} is 1.25 [$RI(150$ eV)/ $RI(600$ eV) = $0.4/0.32 = 1.25$] and implies a more surface origin for this component. Additional components— Ox_0 , A_0 , A_1 , and A_2 —are seen with intensities <8% relative to component B_{Si} and likely result from oxygen contamination (Ox_0) and silicon adatoms (A_0 , A_1 , A_2). These components, along with components Ox_1 and Ox_2 (which are thought to arise from differing Ca–Si stoichiometry), are in small concentration and, thus, are not significant for the determination of the general Ca-intercalated structure. We refer the reader to **Supporting Information Sections 1.2 and 1.3** for further discussion of these features.

Figure 2c,d shows the Si 2p XPS spectra of Ca-QFSBLG formed by Ca-intercalation of the sample in **Figure 2a,b**. We show here only the final Ca-intercalation step. The results of the intermediate intercalation step, which do not affect the conclusions presented here, can be found in **Supporting Information Section 1.2**. Nonetheless, immediately apparent in **Figure 2c,d** is the complete change in spectrum shape - the bulk (B_{Si}) and surface bulk (Z_{Si}) components have all but disappeared and have been replaced by several components at lower binding energies.

Component Ca_{Si} is highly surface-like, with an $RI_R = 4$. It is substantially shifted relative to component B_{Si} (and Z_{Si}) of pristine EMLG by $\Delta E_B = 2.18 \pm 0.11$ eV, suggesting a significant chemical change at the Si surface. Its binding energy of $E_B = 99.29 \pm 0.06$ eV is similar to that of a Ca-silicide.^{50,51} This is strong evidence for a Ca–Si bonding environment at the SiC surface underneath the graphene and buffer layer, and is in contrast with previous reports that Ca intercalates between the graphene layers,^{12,19} or between the buffer layer and the first graphene layer.^{8,20}

In fact, many previous reports on the intercalation of alkalis,^{52–54} transition metals,^{46,55,56} rare earths,^{9,10,57} and other elements^{49,58–60} have reported intercalation underneath the buffer layer (see ref 35 for a brief review of intercalation of graphene on SiC). Furthermore, many prior studies on the intercalation of graphene on SiC have specifically reported the formation of silicide-like compounds,^{46,56,60,61} and thus, it is not surprising that we observe a surface Si component matching closely in binding energy with that of a Ca-silicide. The observation of a Ca–Si interaction implies disruption of the Si–C bonds on the SiC(0001) surface with the C-rich buffer layer and is supported by the LEED intensity suppression of the $(6\sqrt{3} \times 6\sqrt{3})R30^\circ$ spots (which arise from the buffer layer) and an increase in the intensity of the G(1×1) spots relative to the SiC(1×1) spots which indicates decoupling of the buffer layer (see **Figure 1b**). Both XPS and LEED observations are consistent with the formation of a Ca–Si compound and a new graphene layer.

Two other major peak components in **Figure 2c,d** include components B'_{Si} and Z'_{Si} located at binding energies of $E_B = 100.07 \pm 0.05$ eV and $E_B = 100.48 \pm 0.07$ eV, respectively. These new components are shifted equally to lower binding energies relative to B_{Si} and Z_{Si} by -1.40 ± -0.10 eV ($B_{Si} \rightarrow B'_{Si}$) and -1.35 ± -0.12 eV ($Z_{Si} \rightarrow Z'_{Si}$) and are separated equally in binding energies; 0.36 ± 0.1 eV ($Z_{Si} \rightarrow B_{Si}$) and 0.41 ± 0.12 eV ($Z'_{Si} \rightarrow B'_{Si}$) to within error. The RI_R of these components suggests that B'_{Si} ($RI_R = 0.35$) is in the bulk, while Z'_{Si} ($RI_R = 1.1$) is closer to the surface. This situation is illustrated with the atomic model inset in **Figure 2d** and further supports that components B_{Si} (Z_{Si}) and B'_{Si} (Z'_{Si}) are simply binding energy-

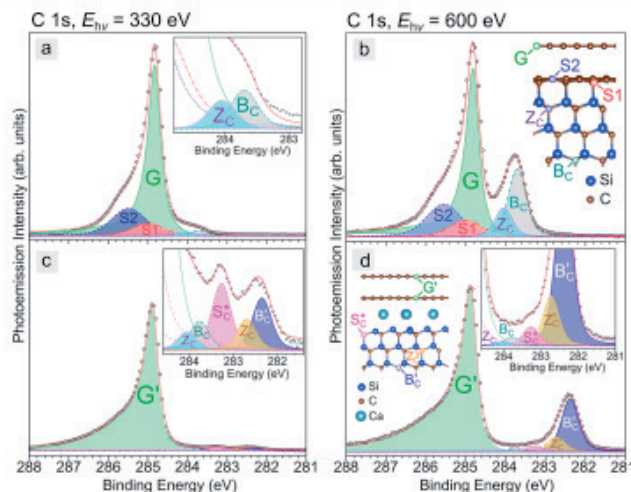


Figure 3. X-ray photoemission spectra showing the C 1s core level of pristine epitaxial monolayer graphene on SiC(0001) (EMLG) and Ca-intercalated EMLG (Ca-QFSBLG) at two X-ray energies, $E_{hv} = 330$ eV (left, surface sensitive) and $E_{hv} = 600$ eV (right, bulk substrate sensitive). (a, b) Pristine EMLG before Ca-intercalation showing deconvoluted components G (graphene), S₁/S₂ (carbon in the buffer layer), and Z_C/B_C (surface/bulk SiC). The SiC components at lower binding energy are more clearly seen in the magnified view of the inset of Figure 3a. The approximate atomic location of these components is shown in the inset of b (see text for details). (c, d) Ca-QFSBLG showing component G' (doped graphene). Three additional SiC components have emerged, S₂*, Z_C*, and B_C* related to the changed SiC conditions due to formation of a Ca–Si compound between SiC and the buffer layer. The SiC components at lower binding energy are magnified in the right insets. The approximate atom locations for the new components are shown in the left inset of d.

Table 2. Summary of the Fitting Parameters for the Major Components in Figure 3^a

EMLG, C 1s		(a, b) pristine EMLG			(c, d) second Ca intercalation		
component	E_{hv} (eV)	E_B (eV)	RI	Q/W_L or W_G/W_L (eV)	E_B (eV)	RI	Q/W_L or W_G/W_L (eV)
S ₂	330	285.48	5.63	0.8/0.4	284.89	26.75	9/0.2
	600	285.55	0.48	0.8/0.4			
S ₁	330	285.00	2.62	0.7/0.4	284.05	0.18	0.4/0.2
	600	285.00	0.25	0.7/0.4			
G	330	284.83	35.0	12/0.2	284.88	2.09	9/0.2
	600	284.82	2.47	9/0.2			
G'	330				284.89	26.75	9/0.2
	600				284.88	2.09	9/0.2
Z _C	330	284.05	0.75	0.4/0.2	284.05	0.18	0.4/0.2
	600	284.05	0.43	0.4/0.2	284.05	0.02	0.4/0.2
Z _C *	330				282.70	0.31	0.4/0.2
	600				282.73	0.22	0.4/0.2
B _C	330	283.7	1	0.4/0.2	283.77	0.29	0.4/0.2
	600	283.71	1	0.4/0.2	283.78	0.04	0.4/0.2
B _C *	330				282.55	0.52	0.4/0.2
	600				282.38	0.77	0.4/0.2
S _C *	330				283.27	0.66	0.4/0.2
	600				283.27	0.08	0.4/0.2

^aThe binding energy location (E_B) is stated, as well as the relative intensity (RI) of the 1s peaks as referenced to the bulk SiC peak B_C corresponding to pristine SiC prior to Ca-intercalation. Q refers to the asymmetry parameter of the graphene, which was fit using a Breit–Wigner–Fano (BWF) function. W_G refers to the gaussian FWHM for the Voigt fit, whereas the Lorentzian FWHM (W_L) was kept constant at 0.2 eV in all fits except for the buffer layer components S₁ and S₂.

shifted equivalents of each other. The shift to lower binding energy of the SiC components is typically observed in the intercalation of graphene on silicon carbide systems and is caused by significant band bending upon intercalant insertion beneath the buffer layer.^{7,46,49,58,59,62–64}

Figure 3 (component fit parameters shown in Table 2) shows the C 1s core level XPS spectra before and after Ca-intercalation of the same EMLG sample as Figure 1b (and Figure 2). An E_{hv} of 330 and 600 eV was used to characterize the surface and bulk components, respectively. Figure 3a,b shows the pristine EMLG sample prior to intercalation, consisting of five components.

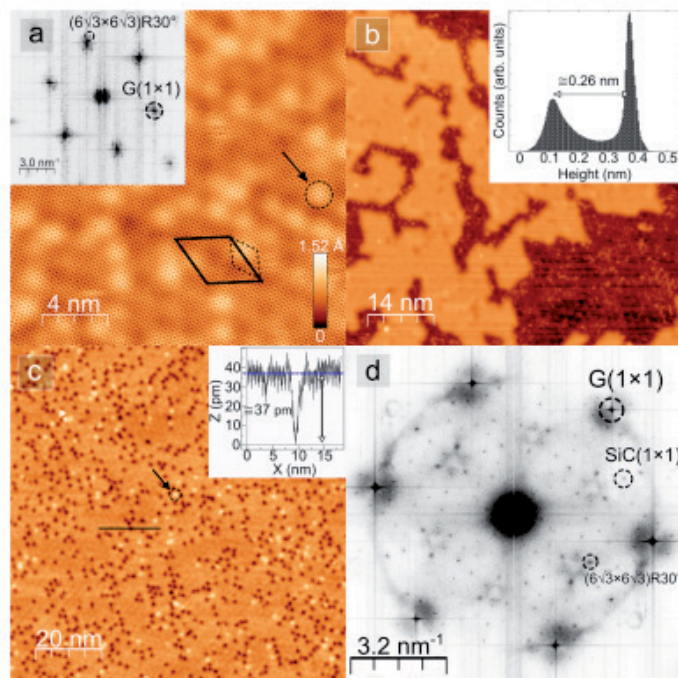


Figure 4. Scanning tunneling microscopy (STM) images of pristine epitaxial monolayer graphene (EMLG) before and after Ca-intercalation. (a) Pristine EMLG (1 V, 200 pA, 77 K) showing atomic resolution, along with real space ($6\sqrt{3} \times 6\sqrt{3}$)R30° (solid line) and (6 × 6) (dashed line) quasi-periodicities (Moiré). The bright spots correspond to silicon adatom features (dotted circle, arrow). Inset shows the fast Fourier transform (FFT) of the same image showing G(1 × 1) graphene spots with a measured lattice parameter of ≈ 0.25 nm and ($6\sqrt{3} \times 6\sqrt{3}$)R30° spots around G(1 × 1) spots. (b) First Ca-intercalation step (0.12 V, 300 pA, 4.6 K) showing formation of raised areas (Ca-QFSBLG). The height difference between these raised areas and the unintercalated graphene is 0.26 ± 0.01 nm (see inset). (c) After the second Ca-intercalation, Ca-QFSBLG formed on entire terraces (0.1 V, 400 pA, 4.6 K). Arrow and dotted circle show the postintercalation bright spot feature (different from the bright spot in a—see text). Inset shows a topographic line scan across one of the dark spots in the image, denoted by the solid black line. (d) FFT of c showing underlying symmetry of the Ca-QFSBLG surface and graphene (G(1 × 1)), SiC (SiC(1 × 1)), and ($6\sqrt{3} \times 6\sqrt{3}$)R30° spots.

Component G located at $E_B = 284.83 \pm 0.05$ eV corresponds to graphene, in agreement with prior reports.⁶⁵ All graphene-related peaks were fit using a Breit–Wigner–Fano line shape,⁶⁶ instead of the often used Doniach–Šunjić line shape,^{67,68} as the BWF line shape was found to more accurately describe our data (see Supporting Information Sections 1.1 and 1.3 for further details).

Components S1 ($RI_R = 10.48$) and S2 ($RI_R = 11.73$) are due to Si–C bonds from the buffer layer to the underlying SiC and C–C bonds in the buffer layer, respectively,^{7,65} and have an intensity ratio of $S2:S1 \approx 2:1$, in agreement with previous findings.⁶⁵ Additionally, two components at lower binding energy are resolved—components Z_C and B_C . These components are related to the carbon in the SiC surface and bulk, respectively. Component B_C at $E_B = 283.73 \pm 0.05$ eV ($RI_R = 1$, used as the RI reference) represents the well-known EMLG bulk component of SiC and agrees well in binding energy with prior measurements.^{47,65} We also find evidence for a surface-like component, Z_C , related to the carbon in SiC at $E_B = 284.05 \pm 0.05$ eV ($RI_R = 1.74$)—particularly evident from the asymmetry of the SiC peak in Figure 3b. Component Z_C has been fitted in previous reports in order to explain the different bonding environment of carbon toward the surface of the SiC.^{43,49} The

shift of Z_C relative to B_C of $\Delta E_B = 0.32 \pm 0.1$ eV is in agreement with the shift observed in the Si 2p spectra (Z_{Si} to B_{Si}) and suggests a similar chemical environment for these components. The inset in Figure 3a shows components Z_C and B_C more clearly at $E_{hv} = 150$ eV, and the inset of Figure 3b shows the approximate location of all the components in an atomic model.

Figure 3c,d shows the C 1s core level XPS spectra for the same sample after Ca-intercalation. It is immediately apparent that components S1 and S2 are no longer present, implying the absence (or near elimination of) bonding between the SiC and buffer layer. Moreover, although significantly suppressed in intensity, components B_C and Z_C are still present in the Ca-intercalated spectra. This is in agreement with the Si 2p core level spectra in Figure 2c,d (which showed the presence of component B_{Si}) and LEED (Figure 1b) suggesting partial intercalation, similar to that observed with hydrogen intercalation.⁴¹

The graphene peak, now labeled G' , located at $E_B = 284.88 \pm 0.05$ eV ($RI_R \approx 13$), is not shifted significantly (within measurement error) with respect to the original EMLG graphene component G ($E_B = 284.83 \pm 0.05$ eV), although from prior Ca-intercalation experiments,^{8,12} we expect significant n-type doping of the graphene. We do on the other hand

observe significant changes in the line shape of the graphene component, which is significantly broadened and more asymmetric. This increase in asymmetry of the G' peak is predicted to arise in highly doped graphene due to 2D plasmon losses^{69,70} (see Supporting Information Sections 1.2 and 1.4 and Methods for details on G' peak fitting) and suggests that the (n-type, as we shall soon discover) doping level of the graphene has increased significantly.

Nonetheless, we observe that the bulk component B_C and the associated surface component of the bulk, Z_C, have been shifted to lower binding energy—labeled as components B'_C ($E_B = 282.33 \pm 0.05$ eV, $RI_g \approx 0.72$) and Z'_C ($E_B = 282.70 \pm 0.05$ eV, $RI_g \approx 1.34$). The respective shifts in E_B are -1.40 ± 0.1 eV ($B_C \rightarrow B'_C$), -1.35 ± 0.1 eV ($Z_C \rightarrow Z'_C$), with a separation between components of 0.32 ± 0.1 eV ($Z_C \rightarrow B_C$) and 0.37 ± 0.1 eV ($Z'_C \rightarrow B'_C$). These shifts are in good agreement with the shifts in the Si 2p for the analogous Si 2p components in the preceding discussion and, thus, give confidence in our assignment of components B'_C/B'_{Si} and Z'_C/Z'_{Si} as the shifted components B_C/B_{Si} and Z_C/Z_{Si} brought about by band bending effects induced by the creation of a Ca–Si layer on the SiC(0001) surface. Approximate atom locations are shown in the atomic model inset of Figure 3d.

An additional component, which we label S_C* is evident in the Ca-intercalated spectra, located at $E_B = 283.26 \pm 0.05$ eV and shifted from component B_C by 0.47 ± 0.1 eV. An analogous component was observed in the Si 2p core level spectrum (Figure 2c,d), S_C* at $E_B = 101.01 \pm 0.05$ eV, shifted to higher binding energy from component B_{Si} by 0.47 ± 0.1 eV. This equivalence in binding energy shift across both core levels suggests that these components are from the same SiC compound. The E_B value of component S_C* agrees well with stoichiometric values of SiC.⁷¹ Indeed, judging from Figure 3c,d, we see that S_C* ($RI_g = 8.25$) is a surface component (hence the “S” assignment) and thus could be a result of SiC unreacted with Ca, yielding a C-rich SiC compound residing at the surface (and, thus, partly explaining the relatively smaller, $RI_g \approx 1$, in the Si 2p core level). Further discussion of component S_C* can be found in Supporting Information Section 1.2.

In summary, the Si 2p and C 1s core level spectra have yielded strong evidence for (1) a Ca–Si interaction at the surface of the SiC(0001) and (2) the elimination of buffer layer–SiC bonding. The formation of a Ca–Si compound is also supported by the Ca 2p spectra which can be found in Supporting Information Section 1.5. Coupled with the LEED results of Figure 1b, we conclude that Ca intercalates between the buffer layer and SiC(0001), bonding with the silicon at the SiC(0001) surface, disrupting the buffer layer–SiC bonding and converting the buffer layer into a new graphene layer.

Low Temperature Scanning Tunneling Microscopy of Ca-QFSBLG. Figure 4a shows an STM image of pristine EMLG prior to Ca-intercalation and transformation to Ca-QFSBLG. Apparent is the atomic resolution and Moiré pattern of the underlying buffer layer showing the $(6\sqrt{3} \times 6\sqrt{3})R30^\circ$ and associated (6×6) periodicity as expected.^{39,72,73} The inset in Figure 4a shows the fast Fourier transform (FFT) of the STM image. The graphene spots, labeled G(1×1), yield a lattice parameter of 0.253 ± 0.005 nm, in reasonable agreement with the lattice parameter of graphene (0.246 nm). In addition, we observe the $(6\sqrt{3} \times 6\sqrt{3})R30^\circ$ spots around the G(1×1) spots, in agreement with the pristine LEED images in Figure 1a. Another feature in Figure 4a is the bright spots (circled in Figure 4a) scattered randomly on the surface of the EMLG. These bright spots have been previously observed and have been

attributed to silicon adatoms on the surface of the SiC.⁷⁴ This is further strengthened by our interpretation that the spectral components A₀, A₁, and A₂, observed in the Si 2p photoemission spectra of pristine EMLG (Figure 2a,b), as corresponding to Si adatoms (see Supporting Information Section 1.2). Further STM data on the bright spots, including atomic resolution and height measurement, is presented in Supporting Information Section 1.6.

Figure 4b shows the same sample (from Figure 4a) after partial Ca intercalation as imaged with the STM at 0.12 V, 300 pA (see Supporting Information Section 1.6 for further details on Ca deposition). What is immediately apparent is that the surface is now covered by a network of raised “islanded” areas which no longer show the long-wavelength $(6\sqrt{3} \times 6\sqrt{3})R30^\circ$ modulation associated with the buffer layer. This observation is consistent with previous alkali^{52,53} and hydrogen⁷⁵ intercalation studies of graphene on SiC and indicates the formation of a freestanding structure. This observation is also consistent with the LEED data in Figure 1 and with the XPS data in Figures 2 and 3 which imply that the Si–C bonds that define the buffer layer are largely eliminated via the suppression of the $(6\sqrt{3} \times 6\sqrt{3})R30^\circ$ (6×6) spots and formation of a Ca–Si compound (component Ca_{Si})/elimination of components S1 and S2, respectively. The height of the newly formed feature is $\approx 0.26 \pm 0.01$ nm as judged by a histogram of heights from the STM image shown in the inset of Figure 4b. This is in agreement with the displacement measured by Fiori et al.⁵³ after the intercalation of Li atoms underneath the buffer layer and also agrees with the theoretical height increase for Ca-QFSBLG (see below).

Figure 4c shows an STM image of the same sample after another intercalation step, imaged at 0.1 V and 400 pA. Imaging the sample became increasingly challenging after each intercalation step due to the difficulty of removing excess Ca, which formed clusters on the graphene surface. A method for the removal of excess Ca on the surface using the STM tip was developed and resulted in atomically clean surfaces (see Supporting Information Section 1.6 for details). Nonetheless, Figure 4c shows that, after the second intercalation, entire terraces now lack the $(6\sqrt{3} \times 6\sqrt{3})R30^\circ$ modulation; we again interpret these as Ca-intercalated (i.e., Ca-QFSBLG) regions.

Figure 4d shows the FFT of the surface in Figure 4c and elucidates the underlying symmetry of the surface. Here we can see graphene spots (G(1×1)), SiC spots (SiC(1×1)), and the $(6\sqrt{3} \times 6\sqrt{3})R30^\circ$ symmetry that still exists, in agreement with the LEED from Figure 1. Notably, however, unlike the LEED results which showed $(\sqrt{3} \times \sqrt{3})R30^\circ$ spots with respect to the G(1×1) spots, Figure 4d shows no evidence of the $(\sqrt{3} \times \sqrt{3})R30^\circ$ symmetry. This provides strong evidence that the graphene bilayer created by Ca-intercalation is not itself intercalated with Ca to form CaC₆/C₆CaC₆,¹⁹ which has a unit cell that is $(\sqrt{3} \times \sqrt{3})R30^\circ$ with respect to the graphene. Thus, we conclude that Ca intercalation has formed quasi-freestanding bilayer graphene (i.e., Ca-QFSBLG), separated from the SiC surface by a Ca layer which has interacted strongly with the Si on the SiC(0001) surface. The $(\sqrt{3} \times \sqrt{3})R30^\circ$ spots observed in LEED indicate that the Ca underneath the QFSBLG is indeed in registry with the graphene; however, the STM measurements show that the perturbation of the $(\sqrt{3} \times \sqrt{3})R30^\circ$ Ca layer on the bilayer graphene unit is small.

The Ca-intercalated graphene areas in Figure 4b,c are different in appearance to the pristine EMLG starting sample in Figure 4a and contain “dark” and “bright” spots (different

from the "bright" spots attributed to Si adatoms prior to Ca-intercalation) on the surface (these spots are particularly evident on the uniform terrace in Figure 4c but can also be seen in the partially intercalated "island" areas in Figure 4b). The dark spots (which are not holes—see Supporting Information Section 1.6) have a height variation of <40 pm (see Figure 4c, inset) and, thus, are likely not due to the buffer layer corrugation which is ≈ 60 pm⁷³—in agreement with the height variation of similar features measured with STM after H-intercalation of graphene on SiC.⁴¹ In fact, similar "dark" features have been observed using STM after alkali,^{52,53} indium,⁴³ and hydrogen⁴¹ intercalation of graphene on silicon carbide. The observation of these features is, thus, intercalant *independent* and points to a universal underlying mechanism involving the SiC surface. In the case of H-intercalation, Murata et al.⁴¹ attributed these features to hydrogen vacancies, with a measured density ranging from $\approx 10^{11}$ to 10^{13} cm⁻² depending on the intercalation temperature used. Here we find that our dark spot density of $\approx 9 \times 10^{12}$ cm⁻² is within this range and agrees favorably with the dark spot density found after hydrogen intercalation.⁴¹ The density of the silicon adatoms (bright spots in Figure 4a) is on the order of 10^{13} cm⁻² for our measured data, whereas Rutter et al.⁷⁴ observed Si adatom densities on the order of 10^{14} cm⁻², in rough agreement with our numbers. Thus, we tentatively propose that the dark spots are Ca vacancies that are tied to Si adatom locations on the surface of the SiC. As for the postintercalation bright spots (arrow in Figure 4c), the height variation does not exceed ≈ 30 pm (see Supporting Information Section 1.6), and the density is $\approx 1 \times 10^{12}$ cm⁻², in approximate agreement with prior measurements on H-intercalated graphene on SiC.⁴¹ We note here that the postintercalation bright spots we observe after Ca-intercalation are likely not the same bright spots that were initially attributed to silicon adatom defects in the STM micrograph of pristine EMLG in Figure 4a. Previous reports have attributed these bright spots to defects⁴¹ or protrusions from intercalants bonded to the underlying graphene, rather than the SiC surface.⁷⁶ Since we do not observe electron scattering (i.e. standing waves) emanating from the postintercalation bright spots,^{77,78} our observations suggest the latter. Thus, we tentatively attribute these bright spots to excess metallic Ca that may be present on top of the underlying Ca-silicide. For further information on these postintercalation bright spot features, we refer the reader to Supporting Information Section 1.6. We mention here briefly that the STM of Ca-intercalated graphene has been previously conducted,^{19,21,25} but the bright and dark spot features shown in Figure 4b,c were not (to our best knowledge) reported.

The STM has elucidated the surface structure of Ca-intercalated EMLG on SiC(0001). In summation, we have found that Ca-QFSBLG has formed upon intercalation of Ca via elimination of EMLG's Moiré pattern and that no Ca-intercalation between the graphene layers occurred—consistent with our LEED (Figure 1b) and XPS (Figures 2 and 3) results.

Density Functional Theory of Ca-Intercalated Graphene on SiC(0001). Our results strongly imply that Ca-intercalation of EMLG occurs between the buffer layer and SiC(0001) surface to form Ca-QFSBLG and not between the buffer layer and graphene (or between graphene layers). To better understand this, we utilize DFT to investigate the energetics of Ca-intercalation.

Figure 5 shows schematics of the two structures modeled using DFT. Figure 5a,b shows side and top views of the first modeled structure, corresponding to Ca-QFSBLG, i.e., Ca

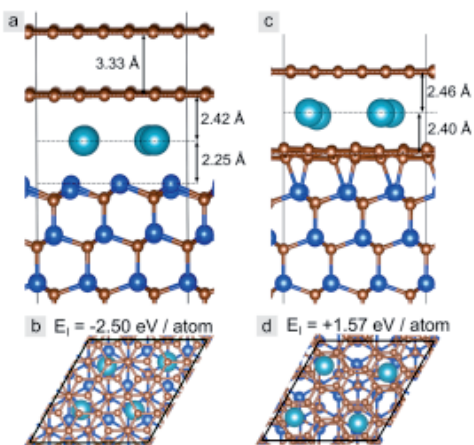


Figure 5. Atomic models (dark blue = Si, brown = C, light blue = Ca) of Ca-intercalated monolayer graphene on SiC(0001), showing the two possible intercalation regimes. (a) Side view of Ca-QFSBLG showing vertical distances and (b) top down view of Ca-QFSBLG showing the unit cell and approximate $(\sqrt{3} \times \sqrt{3})R30^\circ$ coordination of the Ca with respect to the graphene. The energy required for intercalation is $E_I = -2.50$ eV/atom (energetically favorable). (c) Side view of Ca intercalated between the first graphene layer and the buffer layer (SiC/Buffer/Ca/Graphene) showing distances and (d) top down view of Ca intercalated between the first graphene layer and the buffer layer showing the unit cell. In the case of (SiC/Buffer/Ca/Graphene) the coordination of the Ca was slightly larger than $(\sqrt{3} \times \sqrt{3})R30^\circ$. The energy required for intercalation is $E_I = +1.57$ eV/atom (not energetically favorable).

intercalated between the buffer layer–SiC interface to produce bilayer graphene from EMLG (SiC/Ca/Graphene/Graphene). The former buffer layer is raised to lie 0.467 nm above the surface Si atoms, a change in height (Δh), compared to pristine EMLG, of approximately 0.26 nm (using the known value for buffer layer–Si distance of 0.21 nm),⁷⁹ in excellent agreement with our experimentally measured value of $\Delta h = 0.26 \pm 0.01$ nm from STM. Figure 5c,d shows a second modeled structure, corresponding to Ca instead intercalated between the first graphene layer and the buffer layer (SiC/Buffer Layer/Ca/Graphene), a model that has been, up until now, thought to describe Ca-intercalation.²⁰ Using this model, the insertion of Ca gives a Δh of 0.153 nm when compared with pristine EMLG, which is not in agreement with our STM measurements (see Figure 4b, inset). The energy, E_p required to intercalate Ca was calculated (see Methods) yielding $E_I = -2.50$ and $+1.57$ eV/atom for Ca intercalated underneath the buffer layer and Ca intercalated between the first graphene layer and the buffer layer, respectively. Here, a negative value indicates the process is energetically favorable. Thus, DFT supports our experimental finding that the favored intercalation site for the Ca is between the SiC and the buffer layer.

It should be noted that our DFT results closely match the conclusions of Sandin et al.⁵² (which used Na as the intercalant) but disagree with a recent publication by Zhang et al.²¹ concerning Ca-intercalation. Sandin et al.⁵² concluded that a (SiC/Na/Graphene/Graphene) structure accurately describes Na-intercalation by comparing experimentally measured and theoretically calculated work function shifts. Zhang et al.²¹ used

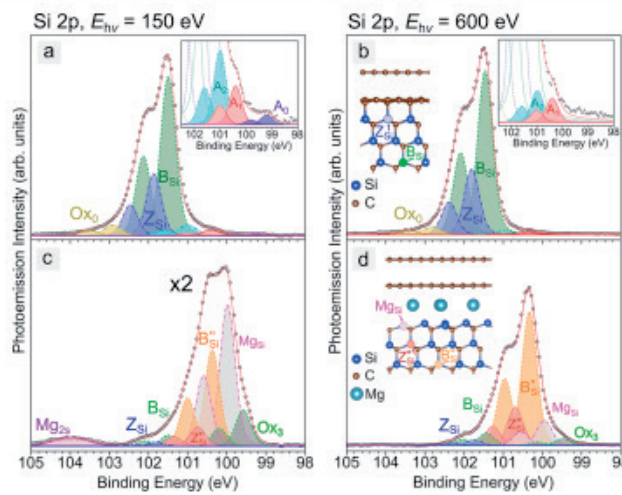


Figure 6. X-ray photoemission spectra showing the Si 2p core level of pristine epitaxial monolayer graphene on SiC(0001) (EMLG) and Mg-intercalated EMLG (Mg-QFSBLG) at X-ray energies $E_{hv} = 150$ eV (left, surface sensitive) and $E_{hv} = 600$ eV (right, bulk sensitive). (a, b) Pristine EMLG showing deconvolution of spectra into components (see main text for details). Right hand side inset in a and b show the magnified view of the lower binding energy components, and the left hand side inset in b shows the atomic model and approximate location of the EMLG spectral components. (c, d) After Mg-intercalation, Mg-QFSBLG is formed. Spectra are deconvoluted into components (see main text for details). Left hand side inset in d shows atomic model and approximate location of Mg-QFSBLG spectral components.

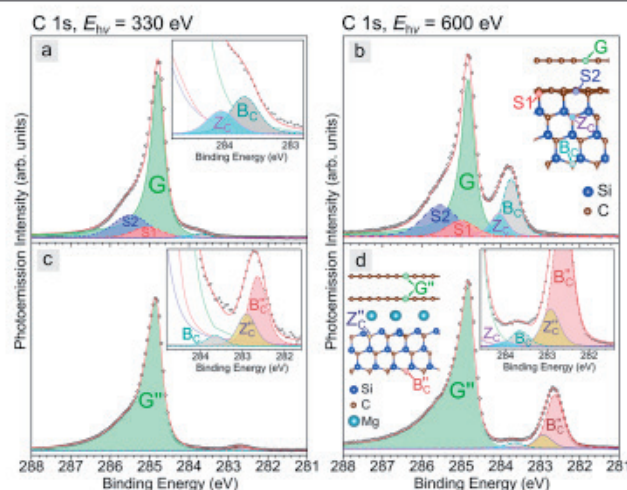


Figure 7. X-ray photoemission spectra for the C 1s core level of pristine epitaxial monolayer graphene on SiC(0001) (EMLG) and Mg-intercalated EMLG (Mg-QFSBLG) at X-ray energies of $E_{hv} = 330$ eV (left, surface sensitive) and $E_{hv} = 600$ eV (right, bulk sensitive). (a, b) Pristine EMLG prior to Mg-intercalation showing the graphene (G), buffer layer (S1, S2), and SiC (Z_C , B_C) components. Inset in a shows the magnified view of the Z_C and B_C components. Inset in b shows the approximate location of all the components with respect to an atomic model of EMLG. (c, d) After Mg-intercalation and the formation of Mg-QFSBLG showing new components, G'' (doped graphene), B_C'' (shifted bulk SiC component), and Z_C'' (shifted "surface" SiC component). Components Z_C and B_C are still present as the sample was only partially intercalated. Right hand side insets in c and d show a magnified view of components B_C'' and Z_C'' . Left hand side inset in d shows the approximate location of components B_C'' and Z_C'' .

STM and DFT calculations to find that low concentrations of Ca could intercalate in a "metastable" configuration underneath the buffer layer, although (SiC/buffer layer/Ca/Graphene) and (SiC/buffer layer/Graphene/Ca/Graphene) structures were found to be more energetically favorable—in stark disagreement

with our findings which suggest that the (SiC/Ca/Graphene/Graphene) structure is most stable. Furthermore, the change in height after intercalation in ref 21 was experimentally measured as 0.283 nm (theoretically calculated as 0.29 nm), and this

Table 3. Summary of the Fitting Parameters for the Major Components in Figure 6^a

EMLG, Si 2p		(a, b) pristine EMLG					(c, d) second Mg intercalation				
component	E_{b} (eV)	E_{B} (eV) 2p _{3/2}	E_{g} (eV) 2p _{1/2}	RI	W_G (eV)	E_{B} (eV) 2p _{3/2}	E_{B} (eV) 2p _{1/2}	RI	W_G (eV)		
O _x	150	102.90	103.50	0.068	0.5	101.80	102.38	0.014	0.4		
	600	102.80	103.40	0.046	0.5						
Z _{Si}	150	101.86	102.46	0.392	0.4	101.74	102.34	0.035	0.4		
	600	101.80	102.38	0.401	0.4						
B _{Si}	150	101.50	102.13	1	0.4	101.49	102.07	0.034	0.4		
	600	101.46	102.09	1	0.4						
B _{Si} *	150					100.37	101.0	0.304	0.4		
	600					100.33	100.96	0.817	0.4		
Z _{Si} *	150					100.74	101.34	0.061	0.4		
	600					100.69	101.27	0.235	0.4		
Mg _{Si}	150					99.98	100.59	0.446	0.4		
	600					99.95	100.55	0.152	0.4		
O _{x3}	150					99.58	100.19	0.115	0.4		
	600					99.50	100.12	0.042	0.4		
Mg _{Si}	150					103.97	n/a	n/a	1		
	600					-	n/a	n/a	-		

^aBoth 2p_{3/2} and 2p_{1/2} are stated, as well as the relative intensity (RI) of the 2p_{Mg} peaks as referenced to the bulk SiC peak B_{Si} corresponding to pristine SiC prior to Mg intercalation. W_G refers to the Gaussian FWHM for the Voigt fit (which was fixed to one of two values), whereas the Lorentzian FWHM (W_L) was kept constant at 0.1 eV in all fits. Component Mg_{Si} is not a 2p core level (see text). Dashes correspond to no observation; n/a = not applicable.

Table 4. Summary of the Fit Parameters of the Major Components in Figure 7^a

EMLG, C 1s		(a, b) pristine EMLG				(c, d) second Mg intercalation			
component	E_{b} (eV)	E_{B} (eV)	RI	Q/W _L or W _G /W _L (eV)	E_{B}	RI	Q/W _L or W _G /W _L (eV)		
S2	330	285.48	5.563	0.8/0.4	284.836	36.66	12/0.2		
	600	285.54	0.550	0.8/0.4					
S1	330	285.05	2.636	0.7/0.3	284.822	2.898	9/0.2		
	600	285.005	0.281	0.7/0.3					
G	330	284.787	39.31	12/0.2	282.90	0.375	0.4/0.2		
	600	284.830	2.723	12/0.2					
G*	330				284.836	36.66	12/0.2		
	600				284.822	2.898	9/0.2		
Z _C	330	284.05	0.625	0.4/0.2	284.02	0.033	0.4/0.2		
	600	284.05	0.400	0.4/0.2					
Z _C *	330				282.90	0.375	0.4/0.2		
	600				282.92	0.233	0.4/0.2		
B _C	330	283.70	1	0.4/0.2	283.65	0.125	0.4/0.2		
	600	283.74	1	0.4/0.2	283.65	0.100	0.4/0.2		
B _C *	330				282.64	0.900	0.4/0.2		
	600				282.63	0.933	0.4/0.2		

^aThe binding energy location (E_{b}) is stated, as well as the relative intensity (RI) of the 1s peaks as referenced to the bulk SiC peak B_C corresponding to pristine SiC prior to Mg intercalation. Q refers to the asymmetry parameter of the graphene (which was fit using a BWF function). W_G refers to the Gaussian FWHM for the Voigt fit, whereas the Lorentzian FWHM (W_L) was kept constant at 0.2 eV in all fits except those for buffer layer components S1 and S2. Dashes correspond to no observation.

disagrees with both of our experimental and theoretical results presented here.

X-ray Photoelectron Spectroscopy of Mg-QFSBLG. As in the Ca-intercalation case in the above sections, here we will focus on the Si 2p and C 1s core levels shown in Figures 6 and 7, respectively (O 1s and Mg 2p core levels can be found in Supporting Information Section 2.4). All relevant parameters for the component fits can be found in Table 3 (Si 2p) and Table 4 (C 1s). We shall note that the XPS results presented here, as in the Ca-intercalation case, are from the same sample analyzed initially with LEED (Figure 1c). Figure 6a,b shows the Si 2p core level of pristine EMLG sample prior to Mg-intercalation and are almost identical to the spectra obtained for the pristine EMLG

sample prior to Ca-intercalation in Figure 2a,b. Again, the RI's (and thus RI_R's) are referenced to the bulk of the SiC, components B_{Si}/B_C, and we retain the same nomenclature as in Figure 2a,b. All component binding energy locations and fit details can be found in the Supporting Information, Tables S10–S12, and since these components have not significantly changed, we refer the reader to the Supporting Information and preceding discussion of Figure 2a,b.

Figure 6 shows the Si 2p core level spectra before (Figure 6a,b) and after (Figure 6c,d) Mg-intercalation, showing drastic changes upon intercalation. We discuss again only the main components of the spectra and leave the discussion of nonessential components to the Supporting Information (see

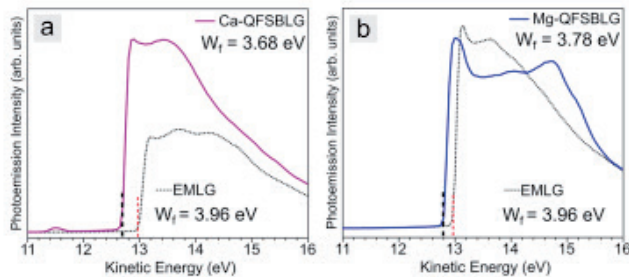


Figure 8. Secondary electron cutoff (SECO) photoemission measurements of pristine epitaxial monolayer graphene on SiC (EMLG) before and after Ca- and Mg-intercalation to form quasi-freestanding bilayer graphene on SiC (Ca-QFSBLG/Mg-QFSBLG). (a) Pristine EMLG (dotted line) and Ca-QFSBLG (solid purple line) showing work functions (W_f) of 3.96 and 3.68 eV, respectively. (b) Clean EMLG (dotted line) and Mg-QFSBLG (solid blue line) showing W_f of 3.96 and 3.78 eV, respectively.

Section 2.2). As we shall soon discover, the changes we observe in the XPS spectra amount to the creation of Mg-QFSBLG, and the XPS spectra are similar to the Ca-QFSBLG sample (with the exception that Mg could not displace the hydrogen in H-QFSBLG; see Supporting Information Section 2.3).

For instance, component Mg_{Si} located at $E_B = 99.94 \pm 0.05$ eV ($R_{I_R} \approx 2.9$) matches closely in binding energy to an Mg-silicide compound.^{51,80,81} We rule out this component arising from an oxide (i.e., from the reaction of Mg with any underlying silicon oxide to form a silicate⁸²), since silicon oxides reside at higher binding energy. Thus, our XPS results imply that our Mg deposition and annealing procedure has intercalated Mg between the buffer layer–SiC interface, producing an Mg–Si compound closely resembling an Mg-silicide and decoupling the buffer layer to form another graphene layer—similar to the Ca-intercalation case. This result complements the LEED results in Figure 1c and is also supported by Raman mapping spectroscopy data (see Supporting Information Section 2.5).

We also see the appearance of component Mg_{2s} at $E_B = 103.94 \pm 0.05$ eV. A similar component has been observed in previous XPS studies of magnesium silicide formation on Si(111) and Si(100), though its origin is controversial.^{80,83} The observation of a higher binding energy component in the Si 2p core level spectrum after Mg_2Si formation on Si(100) was attributed to plasmon losses from Mg 2s electrons.⁸³ However, in our experiment there is no observable Mg metal on the surface after the second Mg-intercalation (see the Mg 2p core level in Supporting Information Figure S23a,b), and thus, component Mg_{2s} cannot be caused by metallic plasmon losses. In the case of Mg_{Si} on Si(111), the higher binding energy component in the Si 2p spectrum ($E_B \approx 104$ eV, in agreement with our measurements) was attributed to satellite peaks from Mg 2s emission.⁸⁰ Satellite features can also (in addition to plasmons) be caused by polychromatic light and shake-up features. Since our experiment uses monochromatic light, we tentatively attribute this peak to a shake-up feature. Furthermore, component Mg_{2s} disappears into the signal noise level when $E_{hv} = 600$ eV, strongly implying that this component resides near the surface (i.e., is associated with the formation of the Mg-silicide). Further work is needed to confirm the origin of this feature, but its association with magnesium silicide formation lends support to our conclusion that Mg has intercalated at the buffer layer–SiC interface to interact with Si.

Figure 7a,b shows the pristine EMLG C 1s core level spectra, which are almost identical in nature to those of the Ca-

intercalation case in Figure 3a,b. Since the spectrum in Figure 7a,b is almost identical to that of Figure 3a,b, we refer the reader to the preceding discussion of Figure 3a,b and Supporting Information Sections 1.2 and 2.2 for further details.

As has been stated, the Mg-intercalation shown in Figure 6c,d shares similar features to the Ca-intercalation experiment. Upon comparison of Figure 7c,d with Figure 3c,d, we observe a similar change in shape and lack of peak shift of the graphene component G, now labeled G'', which we attribute to plasmonic effects due to high doping^{69,70} (see Supporting Information Section 1.4) and a reduction of the buffer layer contribution. Additionally, we observe that the new components B_{Si}''/B_C'' and Z_{Si}''/Z_C'' arise after intercalation in the Si 2p and C 1s core level spectra, respectively. These components are analogous to the shifted bulk (B_{Si}'/B_C') and subsurface (Z_{Si}'/Z_C') SiC components in Ca-QFSBLG (see Figures 2c,d and 3c,d), which arise from surface band bending caused by formation of an Mg layer underneath the buffer layer (analogous to Ca as in Figures 2 and 3). The shift of SiC components toward lower binding energy due to band bending at the SiC surface has been observed in many other graphene on SiC intercalation experiments.^{7,46,49,58,59,62–64} The relative shifts in binding energies among components B_{Si}'/B_C' , Z_{Si}'/Z_C' , B_{Si}''/B_C'' , and Z_{Si}''/Z_C'' can be found in Supporting Information Section 2.2 and further supports our assignment of these components.

After analysis of the C 1s and Si 2p XPS spectra, we find remarkable similarities between Ca- and Mg-intercalated graphene. In the case of Mg intercalation, we find (as in the Ca-intercalation case): (1) formation of an Mg–Si compound underneath the buffer layer at the SiC(0001) surface and (2) the disappearance or diminishment of the buffer layer contribution in the Mg-intercalated C 1s spectra. These conclusions are further strengthened by the LEED results in Figure 1c, and we conclude here that Mg intercalated between the buffer layer and SiC(0001), interacting strongly with the SiC surface and disrupting the buffer layer–SiC bonding to convert the buffer layer into a new graphene layer (Mg-QFSBLG).

Work Function Measurements of Ca- and Mg-QFSBLG. As noted above, we did not observe significant shifts in the binding energy of the graphene C 1s components upon either Ca- or Mg-intercalation. However, the shift in binding energy of the graphene component is not directly proportional to the shift in the Fermi level (E_F).^{70,84} The significant asymmetric broadening of the graphene C 1s component does suggest significant doping of the graphene, which would be expected

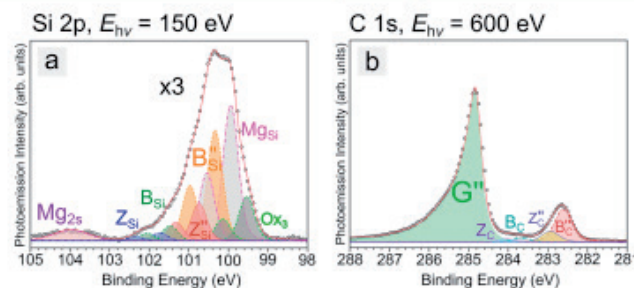


Figure 9. X-ray photoemission spectra showing the Si 2p and C 1s core levels of Mg-QFSBLG after ≈ 6 h of ambient air exposure (and after annealing in UHV) at X-ray energies of $E_{\text{hv}} = 150$ and 600 eV, respectively. (a) Si 2p core level, y -scale magnified $\times 3$ from Figure 6a. (b) C 1s core level. Component labels in a are the same as in Figure 6c,d, and labels in b are the same as in Figure 7c,d. Component Mg_{Si} (and O_{X_3}) in a has decreased in intensity relative to the other components causing the overall spectrum to change shape from Figure 6c,d. Component B_{C}^* has not shifted in binding energy.

upon intercalation of an electron donor such as Ca or Mg.⁸ A comparison between our experimentally measured C 1s data and the calculated line shape of highly doped graphene can be found in Supporting Information Section 1.4 and shows that the line shape of our data closely matches bilayer graphene doped with at least one layer at 10^{14} carriers cm^{-2} . To gain further experimental insight into the changes in doping upon intercalation, the work function (W_f) was measured using the secondary electron cutoff (SECO) photoemission technique, shown in Figure 8.

Figure 8a shows the W_f of pristine EMLG and Ca-intercalated graphene, i.e., Ca-QFSBLG (a -9 V potential was applied to the samples; see Methods). Our measured value for the W_f of pristine EMLG ($W_f = 3.96 \pm 0.05$ eV) is in approximate agreement with prior values.⁸⁵ After Ca-intercalation to form Ca-QFSBLG, the change in work function is $\Delta W_f = -0.28 \pm 0.1$ eV and strongly implies an increase in n-type doping.⁸⁶ In the case of Mg-intercalation to form Mg-QFSBLG, as shown in Figure 8b, the change in work function from EMLG is $\Delta W_f = -0.18 \pm 0.1$ eV, also implying a significant increase in n-type doping. Further discussion pertaining to the accuracy of the SECO measurements can be found in Supporting Information Section 1.2. The results for Ca-intercalated H-QFSBLG (to form Ca-QFSBLG) are shown in the Supporting Information Section 1.3 and are almost identical to the results obtained for Ca-intercalated EMLG shown here.

Air Stability of Mg-QFSBLG. All the experiments presented thus far have been conducted in UHV, and with few exceptions,⁸⁷ highly doped intercalated graphene is not typically stable in ambient conditions due to the high reactivity of the intercalants used. Whether the applications of such intercalated materials are superconductors, batteries, or highly transparent and conductive surfaces, air stability is an important consideration, significantly aiding in the technological implementation of these materials. As expected, we found our Ca-QFSBLG samples begin oxidation within 30 min of ambient exposure, manifesting in a radical change of the XPS spectra. Surprisingly, we find that our newly synthesized Mg-QFSBLG sample appears to be much more stable to air exposure.

Figure 9 shows the Si 2p and C 1s core level spectra for the same sample shown in Figures 6 and 7 after exposure to ambient atmosphere for ≈ 6 h, followed by reintroduction to vacuum and subsequent annealing to remove surface contaminants (see Methods). We do not observe a significant shift in any of the Si 2p or C 1s components for our Mg-intercalated sample (see

Supporting Information Tables S13 and S14), suggesting that Mg-intercalated graphene is remarkably stable in ambient conditions. Upon closer inspection, we observe that component Mg_{Si} has decreased in intensity with respect to the other Si 2p components, as compared to the spectrum before ambient exposure (Figure 6c) suggesting that there may have been some reaction with ambient conditions. Nonetheless, it appears that Mg-intercalation yields a very low work function (3.78 eV) yet relatively air-stable graphene.

Scanning Tunneling Microscopy of Mg-Intercalated Graphene on SiC(0001). A second EMLG sample was intercalated with Mg in UHV and then exposed to air for approximately 45 min during transfer to the low temperature UHV STM. Prior to scanning, the sample was annealed in UHV (see Methods). Figure 10 shows the STM topography map of the Mg-intercalated sample surface. The surface of the Mg-intercalation is almost identical to that of the Ca-intercalation sample in Figure 4c and does not show the $(6\sqrt{3} \times 6\sqrt{3})\text{R}30^\circ$ Moiré pattern characteristic of pristine EMLG (Figure 4a). This

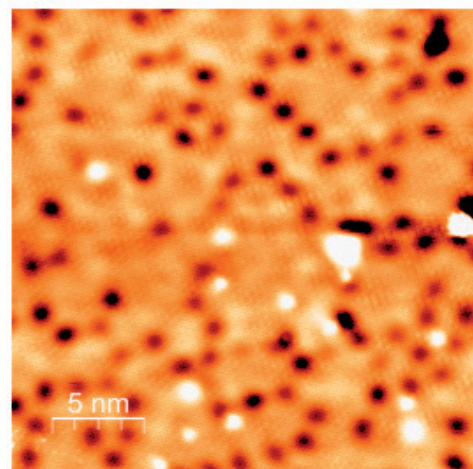


Figure 10. Scanning tunneling microscope (STM) micrograph of an Mg-QFSBLG sample exposed to air for ≈ 45 min before transferring to the STM (0.3 V, 200 pA, 77 K).

offers further support that Mg-QFSBLG is freestanding and furthermore, relatively air-stable, since the sample survived air exposure. The Mg-QFSBLG sample (**Figure 10**) also shows very similar postintercalation bright ($5 \times 10^{13} \text{ cm}^{-2}$) and dark ($4 \times 10^{14} \text{ cm}^{-2}$) spots as seen in **Figure 4b,c**, further supporting our claims that the dark and postintercalation bright spots are generic to graphenes intercalated at the SiC/buffer layer interface.

■ CONCLUSION

In this communication we report on the structure of graphene on SiC(0001) intercalated with either Ca or Mg. By combining LEED, XPS, and STM with DFT modeling, we show that the favored route for Ca intercalation is insertion at the buffer layer–SiC(0001) interface, forming an ordered ($\sqrt{3} \times \sqrt{3}$)R30° reconstruction relative to the graphene and strong chemical interactions with the Si-termination of SiC. The intercalated Ca breaks the buffer layer–SiC covalent bonding, freestands the buffer layer to form Ca-QFSBLG, and decreases the graphene work function, implying high n-type doping. Similarly, we find that the Mg intercalates EMLG samples at the buffer layer–SiC(0001) interface to form Mg-QFSBLG and also exhibits high n-type doping. Stronger chemical interaction between Si and Mg drives the formation of an ordered ($\sqrt{3} \times \sqrt{3}$)R30° reconstruction to the SiC. Unlike Ca-QFSBLG, Mg-QFSBLG exhibits remarkable air stability even after ≈ 6 h of ambient air exposure. This work shows the first successful (to our knowledge) Mg-intercalation of graphene on SiC(0001) to form a low work function (n-type doped) and highly air stable graphene, which may find potential applications in highly conductive and transparent electrodes.

Furthermore, we see no evidence of Ca or Mg intercalation between the graphene layers under the conditions for intercalation used here, consistent with the predictions of our DFT modeling. While we cannot rule out that further processing could result in additional intercalation between graphene layers, our results already prompt a re-examination of previous studies where it was assumed that Ca intercalated *only* between graphene layers and *not* at the buffer layer–SiC interface.^{8,12,19,20,25}

■ METHODS

Samples and Intercalation Procedure. Two types of graphene samples were used in the experiments—epitaxial monolayer graphene synthesized on semi-insulating 6H-SiC(0001) (EMLG)³⁶ and hydrogen intercalated bilayer graphene synthesized on semi-insulating 6H-SiC(0001) (H-QFSBLG).³⁶ H-QFSBLG results are discussed in Supporting Information Section 1.3. The 6H-SiC(0001) semi-insulating substrates nominally on-axis ($\approx 0.1^\circ$ offcut) were obtained from II-VI Incorporated. Prior to graphene synthesis, the 6H-SiC(0001) substrates were etched *in situ* (in an Aixtron/Epigress VP508 horizontal hot wall reactor) with high purity H₂ (200 mbar) at ≈ 1843 K. Epitaxial monolayer graphene was then synthesized in ≈ 20 min on these substrates while holding the temperature at ≈ 1843 K in an Ar atmosphere (100 mbar). This results in a sample with majority monolayer coverage on the SiC(0001) terraces, as well as regions of bilayer and small amounts of trilayer (see Supporting Information Figure S27 for Raman spectroscopic characterization of the layer number for a sister sample). To fabricate H-QFSBLG, H₂ was flowed at 80 slm (900 mbar) for 15–75 min upon cooling to 1223–1423 K.³⁶ Large area Hall measurements on batch samples of this type show sheet density and carrier concentration vary by 10–15%. Prior to measurement and intercalation, all samples were cleaned via annealing in UHV ($\approx 1 \times 10^{-10}$ mbar) between 673 and 773 K (determined with a single-color pyrometer and thermocouple) for approximately 8 h (for

XPS/LEED/SECO measurements). All alkaline earth metal depositions were undertaken while the samples were at room temperature.

The intercalation procedure at the Australian Synchrotron (in which the LEED, XPS, and SECO measurements were taken) is as follows. For Ca-intercalation, samples ($\approx 4 \text{ mm} \times 4 \text{ mm}$) were mounted on the same sample holder, consisting of two EMLG and two H-QFSBLG samples. Approximately 6 nm of Ca was deposited (as judged by a quartz crystal microbalance, QCM) using a WEZ effusion cell (MBE Komponenten) loaded with Ca metal (dendritic pieces, 99.99%, Sigma-Aldrich) in a pyrolytic boron nitride (PBN) crucible. The deposition required heating of the crucible to ≈ 698 K and exposure of 15 min to the Ca flux. After deposition, the sample was heated between ≈ 753 K for 1.5 h to intercalate and clean the sample surface. This procedure constituted the first intercalation step. This intercalation procedure was then repeated for the second intercalation step, except the anneal temperature was ≈ 736 K. All intercalation step data is shown Supporting Information Sections 1.2 and 2.2, whereas in the manuscript we show the results for only the pristine samples and final intercalation step.

For the Mg-intercalation, the samples were mounted similarly (1 EMLG, 1 H-QFSBLG), and an NTEZ effusion cell (MBE Komponenten) was used with a PBN crucible loaded with Mg (1/8-in. turnings, 99.95%, Sigma-Aldrich). In the first intercalation step, ≈ 7.5 nm was deposited onto the samples (cell temperature 673 K, 10 min of Mg flux exposure), which were then heated to ≈ 773 K for ≈ 2 h. Immediately afterward, ≈ 3.8 nm (cell temperature 673 K, 5 min of Mg flux exposure) of Mg was deposited before heating the sample to ≈ 773 K for ≈ 2 h. These steps constituted the first intercalation step. In the second intercalation step, the effusion cell was heated to 673 K, and the sample was exposed to 10 min of Mg flux before annealing at 623 K for 1.5 h. This sample was then exposed to ambient air for ≈ 6 h and annealed at ≈ 623 K for 1.5 h.

The Mg-QFSBLG sample in **Figure 8b** was a sister sample that was similarly intercalated at the Australian Synchrotron but this time in a three-step Mg-intercalation procedure with the final Mg-intercalation yielding similar results to the final (i.e., second) Mg-intercalation of the above sample. In the first Mg-intercalation step, ≈ 15 nm of Mg was deposited on the sample (cell temperature 673 K, 20 min of Mg flux exposure), which was then heated to 463 K for ≈ 1.5 h. For the second Mg-intercalation, ≈ 15 nm of Mg was deposited on the sample (cell temperature 673 K, 20 min of Mg flux exposure), which was then heated to 623 K for ≈ 1.5 h. For the third Mg-intercalation, ≈ 15 nm of Mg was deposited on the sample (cell temperature 673 K, 20 min of Mg flux exposure), which was then heated to 623 K for ≈ 1.5 h. See Supporting Information Figures S28 and S29 for the C 1s and Si 2p core levels, respectively.

The Mg-QFSBLG sample in **Figure 10** was fabricated via the intercalation of an EMLG sample. The same evaporator (NTEZ, PBN cell) and Mg source were used in a different UHV chamber. For this sample, the cell was heated to a temperature of 673 K, and the sample was exposed to the Mg flux for 25 min (≈ 18.8 nm) before heating to 623 K for 30 min. The sample was then taken from storage in the UHV chamber after ≈ 1 month and mounted onto an STM holder in ambient conditions (exposed for ~ 45 min) before being loaded into the STM chamber. The sample was cleaned at ≈ 673 K for ≈ 2 h before scanning.

The Ca-intercalated graphene sample studied by STM (**Figure 4**) was prepared as follows. An EMLG sample was cleaned in the CreaTec Fischer & Co GmbH STM UHV ($\approx 1 \times 10^{-10}$ mbar) chamber by annealing at ≈ 743 K for 1.2 h (all temperatures for the STM were determined with a single-color pyrometer). The depositions were carried out with a CreaTec effusion cell using a PBN crucible loaded with Ca (dendritic pieces, 99.99%, Sigma-Aldrich) that was baked at 473 K overnight prior to depositions. In the first intercalation (**Figure 4b**), ≈ 1 nm of Ca was deposited while the sample was held at room temperature (all thicknesses were determined with a CreaTec QCM). After deposition, the sample was heated to a temperature of 653 K and held for 10 min, after which the sample was ramped to ≈ 743 K and held at this temperature for 1.5 h to facilitate intercalation and remove excess surface Ca. For the second Ca-intercalation, another 1 nm of Ca was deposited after recalibration with the QCM. After deposition, the

Chemistry of Materials

pubs.acs.org/cm

Article

sample was heated to ≈ 653 K and held for 30 min and then ramped to ≈ 743 K and held for 1 h before allowing the sample to cool naturally.

Low Energy Electron Diffraction (LEED). LEED measurements were conducted at the Australian Synchrotron on the Soft X-ray beamline using an 8-in. LEED spectrometer (OCI Vacuum Micro-engineering Inc.). Initial measurement coordinates on pristine samples were recorded, and for each subsequent intercalation/deposition, the same measurement positions were recorded. All measurements were taken at an energy of 100 eV. In Figure 1a we show an example of a pristine EMLG, and Figure 1b,c shows a sister sample (grown in the same growth run) that was intercalated (hence the rotation of the sample). The LEED images in Figure 1 are color inverted in order to enhance visibility.

X-ray Photoelectron Spectroscopy (XPS). XPS data was taken at the soft X-ray beamline at the Australian Synchrotron,⁸⁸ equipped with a PHOIBOS 150 (9 channeltrons) detector. The pass energy of the analyzer was set at 10 eV for the O 1s core levels (energy step of 0.1 eV—see Supporting Information Sections 1.5 and 2.4) and 5 eV for all other core levels (energy step of 0.05 eV). Each recorded spectrum was energy calibrated using the Au 4f_{7/2} line at 84.0 eV from a Au foil in electrical contact with the sample. Inelastic contributions were removed from each XPS spectrum in the main manuscript by subtraction of a Shirley line shape (except for the Ca 2p spectra—see Supporting Information Section 1.5). The Si 2p spectra were obtained at $E_{\text{kr}} = 600$ eV (bulk sensitive) and 150 eV (surface sensitive) and were fit with Voigt functions with a Lorentzian full width at half-maximum (fwhm) of 0.1 eV and Gaussian fwhm of 0.4 or 0.5 eV. The Lorentzian fwhm, which was kept constant, was determined from pristine QFSBLG samples, as these samples were relatively pure and acted as standards in the experiment. Additionally, the area ratio of the Si 2p spin-orbit split peaks (and Mg 2p/Ca 2p core levels) was strictly kept as $2p_{1/2}:2p_{3/2} = 1:2$.⁸⁹ The spin-orbit splitting of the Si 2p core level after averaging and taking the standard deviation of all values was found to be 0.61 ± 0.02 eV, in excellent agreement with previously measured values.^{89,90}

The C 1s “graphene” peak (unintercalated) was fit with a Breit-Wigner–Fano (BWF) asymmetric line shape⁶⁶ (a type of asymmetric Lorentzian; see Supporting Information Section 1.1 for further details); as this line shape was found to fit component G more accurately than the often used Doniach–Šunjić line shape.⁶⁷ Upon intercalation, the doped graphene peak component G' was phenomenologically fit using a model that incorporated a BWF line shape convoluted with three Voigt functions (the details of which can be found in Supporting Information Sections 1.1, 1.2, and 2.2), to approximate the plasmon effects expected for a highly doped graphene line shape which was recently described.^{69,70} All C 1s core level SiC-related components were fit with Voigt line shapes using a Gaussian width of 0.4 eV and Lorentzian width of 0.2 eV⁴⁹ (resulting in a fwhm = 0.52 eV; all parameters are outlined in Table S3 and Table S12 in Supporting Information Sections 1.1 and 2.1, respectively). Care was taken to keep the Gaussian and Lorentzian contributions constant; i.e., the width of the Voigt functions did not change for the same components. Additionally, stringent conditions were placed on the binding energy location of the fitted peaks, which typically did not vary more than the uncertainty of the measurement, taken as ± 0.05 eV. The position of each component was calculated by averaging the available measurements (including the first intercalation step which was omitted in the main text—see Supporting Information, Sections 1.1 and 2.1) of the same component (in the same sample) across the various X-ray energies (E_{kr}). If the standard deviation was higher than the uncertainty in the measurement (i.e., > 0.05 eV), then the standard deviation was taken as the uncertainty in the measurement.

To qualitatively assess the surface sensitivity of the fitted components, the relative intensity (RI) was calculated by using the bulk SiC components of EMLG: $B_{\text{Si}}/B_{\text{C}}$ as the intensity reference (i.e., the RI of B_{Si} and $B_{\text{C}} = 1$). The RI ratio (RI_R) was then used as a qualitative metric of the surface sensitivity of a particular component by division of the lower E_{kr} RI with the RI of the same component at higher E_{kr} . In this regime, an $RI_R > 1$ signifies a more surface-like component, and an $RI_R \leq 1$ signifies a more bulk-like component.

Secondary Electron Cut-Off (SECO). SECO data (Figure 8) was taken at $E_{\text{kr}} = 100$ eV to find the work function (W_f) of the clean and intercalated graphene samples. The pass energy of the analyzer was set at 2 eV. A bias of -9 V was applied to the sample in order to effectively measure the low energy cutoff, and all samples were measured while perpendicular to the analyzer, as this is known to increase the accuracy of W_f measurement.⁹¹ The W_f was then determined by the intersection of two linear fits to the steep edge and background, as is common with SECO determinations of the W_f .^{92,93}

Scanning Tunneling Microscopy (STM). All STM images were taken with a CreaTec Fischer & Co GmbH low temperature STM. The micrographs shown in Figure 4a and Figure 10 were taken at 77 K, whereas the micrographs in Figure 4b,c were taken at 4.6 K. In Figure 4, a cut Pt–Ir tip was used, whereas an etched W tip was used in Figure 10. Micrographs were analyzed using WSxM.⁹⁴

Density Functional Theory (DFT). We use density functional theory (DFT) calculations as implemented in the Vienna ab initio Simulation Package (VASP) to calculate the intercalation energy of Ca on SiC and graphene.⁹⁵ The electron exchange and correlation is described using the Perdew–Burke–Ernzerhof (PBE) form of the generalized gradient approximation (GGA).⁹⁶ A semiempirical functional (DFT-D2) is employed to describe van der Waals interactions in the system.⁹⁷ The kinetic energy cutoff for the plane-wave basis set is set to 500 eV. We use a $9 \times 9 \times 1$ Γ -centered k-point mesh for sampling the Brillouin zone. In all cases, the SiC/graphene system is modeled by a supercell comprised of three layers of 3×3 SiC crystal along with $2\sqrt{3} \times 2\sqrt{3}$ graphene layers. The graphene is under a tensile strain of 7.6%. The intercalation energy (E_I) of Ca is calculated by

$$E_I = E(\text{SiC}/\text{graphene} + \text{Ca}) - E(\text{SiC}/\text{graphene}) - E(\text{Ca})$$

where $E(\text{SiC}/\text{graphene})$, $E(\text{Ca})$, and $E(\text{SiC}/\text{graphene} + \text{Ca})$ are the energy of the SiC/graphene heterostructure, the atomic energy of Ca in its bulk state, and the energy of the SiC/graphene system upon Ca intercalation, respectively. Here, a negative number signifies that the coordination is thermodynamically/energetically favorable, whereas a positive number signifies that the coordination is not energetically favorable.

ASSOCIATED CONTENT

Supporting Information

The Supporting Information is available free of charge at <https://pubs.acs.org/doi/10.1021/acs.chemmater.0c01729>.

Elucidation of all Ca- and Mg-intercalation steps of EMLG, along with detailed tables outlining parameters of the component fits including the omitted first intercalation steps; Ca-intercalation of H-QFSBLG—LEED, XPS (C 1s and Si 2p core level spectra), and SECO measurements; measured C 1s graphene line shapes for Ca- and Mg-intercalated EMLG (i.e. Ca- and Mg-QFSBLG) are compared to theoretical line shapes for highly doped graphene; O 1s and Ca 2p XPS spectra for Ca-intercalated EMLG and H-QFSBLG; STM micrographs of Ca deposition on top of EMLG, as well as the method for cleaning the graphene surface of excess Ca; detailed STM micrographs of the dark and post-intercalation bright features; C 1s and Si 2p core level spectra of the attempted Mg-intercalation of H-QFSBLG; O 1s and Mg 2p core level spectra of Mg-intercalated EMLG; Mg 2p spectra of H-QFSBLG; effect of long-term ambient exposure of Mg-QFSBLG via lab-based C 1s/Si 2p XPS spectra and Raman mapping spectra; and Si 2p and C 1s core levels of the Mg-intercalated sample in Figure 8b (PDF)

■ AUTHOR INFORMATION**Corresponding Authors**

Jimmy C. Kotsakidis — *School of Physics and Astronomy, Monash University, Melbourne, Victoria 3800, Australia; orcid.org/0000-0002-7167-5617; Email: jimmy.kotsakidis@monash.edu*

Michael S. Fuhrer — *School of Physics and Astronomy, Monash University, Melbourne, Victoria 3800, Australia; orcid.org/0000-0001-6183-2773; Email: michael.fuhrer@monash.edu*

Amadeo L. Vázquez de Parga — *Dep. Física de la Materia Condensada and Condensed Matter Physics Center (IFIMAC), Universidad Autónoma de Madrid, 28049 Madrid, Spain; IMDEA Nanociencia, 28049 Madrid, Spain; orcid.org/0000-0003-0551-1603; Email: alvazquezdeparga@uam.es*

Authors

Antonija Grubišić-Čabo — *School of Physics and Astronomy, Monash University, Melbourne, Victoria 3800, Australia; orcid.org/0000-0001-7683-0295*

Yuefeng Yin — *Department of Materials Science and Engineering, Monash University, Melbourne, Victoria 3800, Australia*

Anton Tadich — *Australian Synchrotron, Melbourne, Victoria 3168, Australia*

Rachael L. Myers-Ward — *U.S. Naval Research Laboratory, Washington D.C. 20375, United States*

Matthew DeJarlait — *U.S. Naval Research Laboratory, Washington D.C. 20375, United States*

Shojan P. Pavunny — *U.S. Naval Research Laboratory, Washington D.C. 20375, United States; orcid.org/0000-0003-4844-8675*

Marc Currie — *U.S. Naval Research Laboratory, Washington D.C. 20375, United States*

Kevin M. Daniels — *Institute for Research in Electronics and Applied Physics, University of Maryland, College Park, Maryland 20742, United States*

Chang Liu — *School of Physics and Astronomy, Monash University, Melbourne, Victoria 3800, Australia; orcid.org/0000-0002-0244-1999*

Mark T. Edmonds — *School of Physics and Astronomy, Monash University, Melbourne, Victoria 3800, Australia; orcid.org/0000-0001-8054-5470*

Nikhil V. Medhekar — *Department of Materials Science and Engineering, Monash University, Melbourne, Victoria 3800, Australia; orcid.org/0000-0003-3124-4430*

D. Kurt Gaskill — *Institute for Research in Electronics and Applied Physics, University of Maryland, College Park, Maryland 20742, United States; orcid.org/0000-0001-7106-3605*

Complete contact information is available at:
<https://pubs.acs.org/10.1021/acs.chemmater.0c01729>

Author Contributions

J.C.K. and A.L.V.P. performed the first Ca intercalations in the STM, from which a method was developed and guided future intercalation experiments at the Australian Synchrotron. J.C.K. suggested performing the Mg experiments and developed the method for Mg-intercalation based upon the Ca-intercalation method. J.C.K. wrote the experimental proposal (including the methods) for the Australian Synchrotron experiments with necessary assistance from A.T. and M.S.F. and some grammatical corrections from A.G.-C. The data at the Australian Synchrotron was collected by J.C.K., A.G.-C., A.L.V.P., A.T., C.L., and M.T.E. Ca and Mg crucibles were first loaded at Monash University and transported to the Australian Synchro-

tron by J.C.K. (under vacuum) and mounted with help from A.T. All starting samples were grown by D.K.G., R.L.M.-W., M.D., S.P.P., and K.M.D., and M.C. postprocessed the samples. S.P.P. and J.C.K. performed lab-based XPS, which was later analyzed by J.C.K. J.C.K. performed Raman spectroscopy measurements with the aid of D.K.G. and R.L.M.-W., which was analyzed by J.C.K. Y.Y. and N.V.M. performed the DFT calculations. J.C.K. composed the manuscript and created all the figures, with intellectual contributions from D.K.G. and M.S.F. The manuscript was written through contributions given by all authors. All authors have given approval to the final version of the manuscript.

Funding

J.C.K. acknowledges the Australian Government Research Training Program and the Monash Centre for Atomically Thin Materials (MCATM) for financial support. J.C.K. and M.S.F. acknowledge funding support from the Australian Research Council (ARC) Laureate Fellowship (FL120100038). J.C.K., M.S.F., N.V.M., and Y.Y. also acknowledge the ARC Centre of Excellence in Future Low-Energy Electronics (CE170100039) for financial support. N.V.M. and Y.Y. also gratefully acknowledge computational support from the Monash Campus Cluster, NCI computational facility and Pawsey Supercomputing Facility. A.L.V.P. acknowledges funding support from the Ministerio de Ciencia Innovación y Universidades project PGC2018-093291-B-I00 and Comunidad de Madrid Project NMAT2D-CM P2018/NMT-4511. D.K.G., R.L.M.-W., M.D., K.M.D., S.P.P., and M.C. acknowledge support by core programs at the U.S. Naval Research Laboratory funded by the Office of Naval Research. This research was undertaken (in part) on the soft X-ray beamline at the Australian Synchrotron, part of ANSTO.

Notes

The authors declare no competing financial interest.

■ ACKNOWLEDGMENTS

J.C.K. is pleased to acknowledge Glenn Jernigan (U.S. Naval Research Laboratory, NRL) for assistance with initial XPS data interpretation, experimental insight, and helpful discussions regarding preliminary data and lolanda Di Bernardo (Monash University) for helpful discussions regarding XPS data. J.C.K. also acknowledges the hospitality of NRL, at which some of the follow up experimental investigations were performed.

■ ABBREVIATIONS

Ca-QFSBLG, Ca-intercalated quasi-freestanding bilayer graphene; E_b , binding energy; E_{hv} , X-ray energy; EMLG, epitaxial monolayer graphene; H-QFSBLG, H-intercalated quasi-freestanding bilayer graphene; LEED, low energy electron diffraction; Mg-QFSBLG, Mg-intercalated quasi-freestanding bilayer graphene; SECO, secondary electron cutoff; STM, scanning tunneling microscopy; QFSBLG, quasi-freestanding bilayer graphene; XPS, X-ray photoelectron spectroscopy

■ REFERENCES

- (1) Novoselov, K. S.; Geim, A. K.; Morozov, S. V.; Jiang, D.; Zhang, Y.; Dubonos, S. V.; Grigorieva, I. V.; Firsov, A. A. Electric Field Effect in Atomically Thin Carbon Films. *Science* **2004**, *306* (5696), 666–669.
- (2) Geim, A. K. Graphene: Status and Prospects. *Science* **2009**, *324* (5934), 1530–1534.
- (3) Lemme, M. C.; Echtermeyer, T. J.; Baus, M.; Kurz, H. A Graphene Field-Effect Device. *IEEE Electron Device Lett.* **2007**, *28* (4), 282–284.

- (4) Chen, W.; Chen, S.; Qi, D. C.; Gao, X. Y.; Wee, A. T. S. Surface Transfer p-type Doping of Epitaxial Graphene. *J. Am. Chem. Soc.* **2007**, *129* (34), 10418–10422.
- (5) Schedin, F.; Geim, A. K.; Morozov, S. V.; Hill, E.; Blake, P.; Katsnelson, M.; Novoselov, K. S. Detection of Individual Gas Molecules Adsorbed on Graphene. *Nat. Mater.* **2007**, *6* (9), 652–655.
- (6) Wang, H.; Wang, Q.; Cheng, Y.; Li, K.; Yao, Y.; Zhang, Q.; Dong, C.; Wang, P.; Schwingenschlögl, U.; Yang, W.; Zhang, X. X. Doping Monolayer Graphene with Single Atom Substitutions. *Nano Lett.* **2012**, *12* (1), 141–144.
- (7) Riedl, C.; Coletti, C.; Iwasaki, T.; Zakharov, A.; Starke, U. Quasi-Free-Standing Epitaxial Graphene on SiC Obtained by Hydrogen Intercalation. *Phys. Rev. Lett.* **2009**, *103* (24), 246804.
- (8) McChesney, J. L.; Bostwick, A.; Ohta, T.; Seyller, T.; Horn, K.; González, J.; Rotenberg, E. Extended Van Hove Singularity and Superconducting Instability in Doped Graphene. *Phys. Rev. Lett.* **2010**, *104* (13), 136803.
- (9) Link, S.; Forti, S.; Stöhr, A.; Küster, K.; Rösner, M.; Hirschmeier, D.; Chen, C.; Avila, J.; Asensio, M.; Zakharov, A.; et al. Introducing Strong Correlation Effects into Graphene by Gadolinium Intercalation. *Phys. Rev. B* **2019**, *100* (12), 121407.
- (10) Rosenzweig, P.; Karakachian, H.; Link, S.; Küster, K.; Starke, U. Tuning the Doping Level of Graphene in the Vicinity of the Van Hove Singularity via Ytterbium Intercalation. *Phys. Rev. B* **2019**, *100* (3), 035445.
- (11) Li, K.; Feng, X.; Zhang, W.; Ou, Y.; Chen, L.; He, K.; Wang, L.-L.; Guo, L.; Liu, G.; Xue, Q.-K.; Ma, X. Superconductivity in Ca-Intercalated Epitaxial Graphene on Silicon Carbide. *Appl. Phys. Lett.* **2013**, *103* (6), 062601.
- (12) Ichinokura, S.; Sugawara, K.; Takayama, A.; Takahashi, T.; Hasegawa, S. Superconducting Calcium-Intercalated Bilayer Graphene. *ACS Nano* **2016**, *10* (2), 2761.
- (13) Khrapach, I.; Withers, F.; Bointon, T. H.; Polyushkin, D. K.; Barnes, W. L.; Russo, S.; Craciun, M. F. Novel Highly Conductive and Transparent Graphene-Based Conductors. *Adv. Mater.* **2012**, *24* (21), 2844–2849.
- (14) Li, Z.; Zhang, C.; Han, F.; Zhang, F.; Zhou, D.; Xu, S.; Liu, H.; Li, X.; Liu, J. Improving the Cycle Stability of FeCl₃-Graphite Intercalation Compounds by Polar Fe₂O₃ Trapping in Lithium-ion Batteries. *Nano Res.* **2019**, *12* (8), 1836–1844.
- (15) Profeta, G.; Calandra, M.; Mauri, F. Phonon-Mediated Superconductivity in Graphene by Lithium Deposition. *Nat. Phys.* **2012**, *8* (2), 131–134.
- (16) Gonzalez, J. Kohn-Luttinger Superconductivity in Graphene. *Phys. Rev. B* **2008**, *78* (20), 205431.
- (17) Nandkishore, R.; Leviton, L.; Chubukov, A. Chiral Superconductivity from Repulsive Interactions in Doped Graphene. *Nat. Phys.* **2012**, *8* (2), 158–163.
- (18) Gofron, K.; Campuzano, J.; Abrikosov, A.; Lindroos, M.; Bansil, A.; Ding, H.; Koelling, D.; Dabrowski, B. Observation of an "Extended" Van Hove Singularity in YBa₂Cu₃O₈ by Ultrahigh Energy Resolution Angle-Resolved Photoemission. *Phys. Rev. Lett.* **1994**, *73* (24), 3302.
- (19) Kanetani, K.; Sugawara, K.; Sato, T.; Shimizu, R.; Iwaya, K.; Hitosugi, T.; Takahashi, T. Ca Intercalated Bilayer Graphene as a Thinnest Limit of Superconducting Ca₆Ca. *Proc. Natl. Acad. Sci. U. S. A.* **2012**, *109* (48), 19610–19613.
- (20) Endo, Y.; Fukaya, Y.; Mochizuki, I.; Takayama, A.; Hyodo, T.; Hasegawa, S. Structure of Superconducting Ca-Intercalated Bilayer Graphene/SiC Studied Using Total-Reflection High-Energy Positron Diffraction. *Carbon* **2020**, *157*, 857–862.
- (21) Zhang, Y.; Zhang, H.; Cai, Y.; Song, J.; Qiao, D.; Chen, Q.; Hu, F.; Wang, P.; Huang, K.; He, P. Calcium Intercalation Underneath N-layer Graphene on 6H-SiC(0001). *Chem. Phys. Lett.* **2018**, *703*, 33–38.
- (22) Mattausch, A.; Pankratov, O. Ab initio Study of Graphene on SiC. *Phys. Rev. Lett.* **2007**, *99* (7), 076802.
- (23) Weller, T. E.; Ellerby, M.; Saxena, S. S.; Smith, R. P.; Skipper, N. T. Superconductivity in the intercalated graphite compounds C₆Yb and C₆Ca. *Nat. Phys.* **2005**, *1* (1), 39–41.
- (24) Emery, N.; Hérolé, C.; D'Astuto, M.; Garcia, V.; Bellin, C.; Maréché, J.; Lagrange, P.; Loupias, G. Superconductivity of Bulk CaC₆. *Phys. Rev. Lett.* **2005**, *95* (8), 087003.
- (25) Shimizu, R.; Sugawara, K.; Kanetani, K.; Iwaya, K.; Sato, T.; Takahashi, T.; Hitosugi, T. Charge-Density Wave in Ca-Intercalated Bilayer Graphene Induced by Commensurate Lattice Matching. *Phys. Rev. Lett.* **2015**, *114* (14), 146103.
- (26) Chapman, J.; Su, Y.; Howard, C.; Kundys, D.; Grigorenko, A.; Guinea, F.; Geim, A.; Grigorieva, I.; Nair, R. Superconductivity in Ca-Doped Graphene Laminates. *Sci. Rep.* **2016**, *6* (1), 23254.
- (27) Dresselhaus, M. S.; Dresselhaus, G. Intercalation Compounds of Graphite. *Adv. Phys.* **2002**, *51* (1), 1–186.
- (28) Honig, R. E. Vapor Pressure Data for the Solid and Liquid Elements. *RCA Review* **1962**, *23* (12), 567.
- (29) Liu, Y.; Merinov, B. V.; Goddard, W. A. Origin of Low Sodium Capacity in Graphite and Generally Weak Substrate Binding of Na and Mg Among Alkali and Alkaline Earth Metals. *Proc. Natl. Acad. Sci. U. S. A.* **2016**, *113* (14), 3735–3739.
- (30) Park, H.; Singh, L. T.; Lee, P.; Kim, J.; Ryu, M.; Hwang, C.-C.; Kim, K. S.; Chung, J. Observation of Mg-Induced Structural and Electronic Properties of Graphene. *Appl. Phys. Lett.* **2016**, *109* (19), 193104.
- (31) Kawaguchi, M.; Kurasaki, A. Intercalation of Magnesium Into a Graphite-Like Layered Material of Composition BC₂N. *Chem. Commun.* **2012**, *48* (55), 6897–6899.
- (32) Bucur, C. B. *Challenges of a Rechargeable Magnesium Battery: A Guide to the Viability of this Post Lithium-ion Battery*; Springer International Publishing: Cham, Switzerland, 2017.
- (33) God, C.; Bitschnau, B.; Kapper, K.; Lenhardt, C.; Schmuck, M.; Mautner, F.; Koller, S. Intercalation Behaviour of Magnesium into Natural Graphite Using Organic Electrolyte Systems. *RSC Adv.* **2017**, *7* (23), 14168–14175.
- (34) Xu, W.; Zhang, H.; Lerner, M. M. Graphite Intercalation by Mg Diamine Complexes. *Inorg. Chem.* **2018**, *57* (14), 8042–8045.
- (35) Briggs, N.; Gebeyehu, Z. M.; Vera, A.; Zhao, T.; Wang, K.; De La Fuente Duran, A.; Bersch, B.; Bowen, T.; Knappenberger, K. L.; Robinson, J. A. Epitaxial Graphene/Silicon Carbide Intercalation: A Minireview on Graphene Modulation and Unique 2D Materials. *Nanoscale* **2019**, *11* (33), 15440–15447.
- (36) Trammell, S. A.; Hernández, S. C.; Myers-Ward, R. L.; Zabetakis, D.; Stenger, D. A.; Gaskill, D. K.; Walton, S. G. Plasma-Modified, Epitaxial Fabricated Graphene on SiC for the Electrochemical Detection of TNT. *Sensors* **2016**, *16* (8), 1281.
- (37) Ostler, M.; Deretis, I.; Mammadov, S.; Giannazzo, F.; Nicotra, G.; Spinella, C.; Seyller, T.; La Magna, A. Direct Growth of Quasi-Free-Standing Epitaxial Graphene on Nonpolar SiC Surfaces. *Phys. Rev. B* **2013**, *88* (8), 085408.
- (38) Daniels, K. M.; Jadidi, M. M.; Sushkov, A. B.; Nath, A.; Boyd, A. K.; Sridhara, K.; Drew, H. D.; Murphy, T. E.; Myers-Ward, R. L.; Gaskill, D. K. Narrow Plasmon Resonances Enabled by Quasi-Free-standing Bilayer Epitaxial Graphene. *2D Mater.* **2017**, *4* (2), 025034.
- (39) Riedl, C.; Starke, U.; Bernhardt, J.; Franke, M.; Heinz, K. Structural Properties of the Graphene-SiC(0001) Interface as a Key for the Preparation of Homogeneous Large-Terrace Graphene Surfaces. *Phys. Rev. B* **2007**, *76* (24), 245406.
- (40) Riedl, C.; Coletti, C.; Starke, U. Structural and Electronic Properties of Epitaxial Graphene on SiC(0 0 0 1): A Review of Growth, Characterization, Transfer Doping and Hydrogen Intercalation. *J. Phys. D: Appl. Phys.* **2010**, *43* (37), 374009.
- (41) Murata, Y.; Mashoff, T.; Takamura, M.; Tanabe, S.; Hibino, H.; Beltram, F.; Heun, S. Correlation Between Morphology and Transport Properties of Quasi-Free-Standing Monolayer Graphene. *Appl. Phys. Lett.* **2014**, *105* (22), 221604.
- (42) Stöhr, A.; Forti, S.; Link, S.; Zakharov, A. A.; Kern, K.; Starke, U.; Benia, H. M. Intercalation of Graphene on SiC(0001) Via Ion Implantation. *Phys. Rev. B* **2016**, *94* (8), 085431.
- (43) Kim, H.; Tsogtbaatar, N.; Tuvdendorj, B.; Lkhagvasuren, A.; Seo, J. M. Effects of Two Kinds of Intercalated In Films on Quasi-Free-

- Standing Monolayer Graphene Formed Above SiC(0001). *Carbon* **2020**, *159*, 229–235.
- (44) Xia, C.; Watcharinyanon, S.; Zakharov, A.; Yakimova, R.; Hultman, L.; Johansson, L. I.; Virojanadara, C. Si Intercalation/Deintercalation of Graphene on 6H-SiC(0001). *Phys. Rev. B* **2012**, *85* (4), 045418.
- (45) Starke, U.; Schardt, J.; Bernhardt, J.; Franke, M.; Heinz, K. Stacking Transformation from Hexagonal to Cubic SiC Induced by Surface Reconstruction: A Seed for Heterostructure Growth. *Phys. Rev. Lett.* **1999**, *82* (10), 2107.
- (46) Xia, C.; Johansson, L. I.; Niu, Y.; Zakharov, A. A.; Janzen, E.; Virojanadara, C. High Thermal Stability Quasi-Free-Standing Bilayer Graphene Formed on 4H-SiC(0001) via Platinum Intercalation. *Carbon* **2014**, *79*, 631–635.
- (47) Watcharinyanon, S.; Virojanadara, C.; Osiecki, J.; Zakharov, A.; Yakimova, R.; Uhrberg, R.; Johansson, L. I. Hydrogen Intercalation of Graphene Grown on 6H-SiC(0001). *Surf. Sci.* **2011**, *605* (17–18), 1662–1668.
- (48) Speck, F.; Ostler, M.; Besendörfer, S.; Krone, J.; Wanke, M.; Seyller, T. Growth and Intercalation of Graphene on Silicon Carbide Studied by Low-Energy Electron Microscopy. *Ann. Phys.* **2017**, *529* (11), 1700046.
- (49) Kim, H.; Dugerjav, O.; Arvisbaatar, A.; Seo, J. M. Bifunctional Effects of the Ordered Si Atoms Intercalated Between Quasi-Free-Standing Epitaxial Graphene and SiC (0001): Graphene Doping and Substrate Band Bending. *New J. Phys.* **2015**, *17* (8), 083058.
- (50) Schöpke, A.; Würz, R.; Schmidt, M. Epitaxial Growth of CaSi₂ on Si (111). *Surf. Interface Anal.* **2002**, *34* (1), 464–467.
- (51) Pi, T.-W.; Cheng, C.-P.; Wertheim, G. The Reaction of Si(001) with Magnesium and Calcium. *J. Appl. Phys.* **2011**, *109* (4), 043701.
- (52) Sandin, A.; Jayasekera, T.; Rowe, J. E.; Kim, K. W.; Buongiorno Nardelli, M.; Dougherty, D. B. Multiple Coexisting Intercalation Structures of Sodium in Epitaxial Graphene-SiC Interfaces. *Phys. Rev. B* **2012**, *85* (12), 125410.
- (53) Fiori, S.; Murata, Y.; Veronesi, S.; Rossi, A.; Coletti, C.; Heun, S. Li-Intercalated Graphene on SiC (0001): An STM Study. *Phys. Rev. B* **2017**, *96* (12), 125429.
- (54) Virojanadara, C.; Watcharinyanon, S.; Zakharov, A.; Johansson, L. I. Epitaxial Graphene on 6H-SiC and Li Intercalation. *Phys. Rev. B* **2010**, *82* (20), 205402.
- (55) Gomoyunova, M.; Grebenyuk, G.; Davydov, V. Y.; Ermakov, I.; Eliseev, I.; Lebedev, A.; Lebedev, S.; Lobanova, E. Y.; Smirnov, A.; Smirnov, D.; Pronin, I. I. Intercalation of Iron Atoms Under Graphene Formed on Silicon Carbide. *Phys. Solid State* **2018**, *60* (7), 1439–1446.
- (56) Grebenyuk, G.; Lobanova, E. Y.; Smirnov, D.; Eliseev, I.; Zubov, A.; Smirnov, A.; Lebedev, S.; Davydov, V. Y.; Lebedev, A.; Pronin, I. Cobalt Intercalation of Graphene on Silicon Carbide. *Phys. Solid State* **2019**, *61* (7), 1316–1326.
- (57) Anderson, N. A.; Hupalo, M.; Keavney, D.; Tringides, M.; Vaknin, D. Intercalated Rare-Earth Metals Under Graphene on SiC. *J. Magn. Magn. Mater.* **2019**, *474*, 666–670.
- (58) Xia, C.; Johansson, L. I.; Zakharov, A.; Hultman, L.; Virojanadara, C. Effects of Al on Epitaxial Graphene Grown on 6H-SiC (0001). *Mater. Res. Express* **2014**, *1* (1), 015606.
- (59) Kim, H.; Dugerjav, O.; Lkhagvasuren, A.; Seo, J. M. Doping Modulation of Quasi-Free-Standing Monolayer Graphene Formed on SiC (0001) Through Sn_{1-x}Gex Intercalation. *Carbon* **2019**, *144*, 549–556.
- (60) Niu, Y.; Zakharov, A.; Yakimova, R. Metal-Dielectric Transition in Sn-Intercalated Graphene on SiC (0001). *Ultramicroscopy* **2017**, *183*, 49–54.
- (61) Höning, R.; Roese, P.; Shamout, K.; Ohkochi, T.; Berges, U.; Westphal, C. Structural, Chemical, and Magnetic Properties of Cobalt Intercalated Graphene on Silicon Carbide. *Nanotechnology* **2019**, *30* (2), 025702.
- (62) Wang, Z.-j.; Wei, M.; Jin, L.; Ning, Y.; Yu, L.; Fu, Q.; Bao, X. Simultaneous N-Intercalation and N-Doping of Epitaxial Graphene on 6H-SiC (0001) Through Thermal Reactions with Ammonia. *Nano Res.* **2013**, *6* (6), 399–408.
- (63) Oida, S.; McFeely, F.; Hannon, J.; Tromp, R.; Copel, M.; Chen, Z.; Sun, Y.; Farmer, D.; Yurkas, J. Decoupling Graphene from SiC (0001) via Oxidation. *Phys. Rev. B* **2010**, *82* (4), 041411.
- (64) Wolff, S.; Roscher, S.; Timmermann, F.; Daniel, M. V.; Speck, F.; Wanke, M.; Albrecht, M.; Seyller, T. Quasi-Freestanding Graphene on SiC (0001) by Ar-Mediated Intercalation of Antimony: A Route Toward Intercalation of High-Vapor-Pressure Elements. *Ann. Phys.* **2019**, *531* (11), 1900199.
- (65) Emtev, K.; Speck, F.; Seyller, T.; Ley, L.; Riley, J. D. Interaction, Growth, and Ordering of Epitaxial Graphene on SiC [0001] Surfaces: A Comparative Photoelectron Spectroscopy Study. *Phys. Rev. B* **2008**, *77* (15), 155303.
- (66) Fedorov, A.; Verbitskiy, N.; Haberer, D.; Struzzi, C.; Petaccia, L.; Usachov, D.; Vilkov, O.; Vyalikh, D.; Fink, J.; Knupfer, M.; et al. Observation of a Universal Donor-Dependent Vibrational Mode in Graphene. *Nat. Commun.* **2014**, *5*, 3257.
- (67) Despoja, V.; Šunjić, M. Theory of Core-Level Spectra in X-ray Photoemission of Pristine and Doped Graphene. *Phys. Rev. B* **2013**, *88* (24), 245416.
- (68) Domínguez, S.; Šunjić, M. Many-Electron Singularity in X-ray Photoemission and X-ray Line Spectra from Metals. *J. Phys. C: Solid State Phys.* **1970**, *3* (2), 285.
- (69) Semelius, B. E. Core-Level Spectra from Graphene. *Phys. Rev. B* **2015**, *91* (4), 045402.
- (70) Semelius, B. E. Core-Level Spectra from Bilayer Graphene. *FlatChem.* **2017**, *1*, 6–10.
- (71) Delplancke, M.-P.; Powers, J. M.; Vandentop, G.; Salmeron, M.; Somorjai, G. A. Preparation and Characterization of Amorphous SiC:H Thin Films. *J. Vac. Sci. Technol., A* **1991**, *9* (3), 450–455.
- (72) Varchon, F.; Mallet, P.; Veullien, J.-Y.; Magaud, L. Ripples in Epitaxial Graphene on the Si-Terminated SiC (0001) Surface. *Phys. Rev. B* **2008**, *77* (23), 235412.
- (73) Goler, S.; Coletti, C.; Piazza, V.; Pingue, P.; Colangelo, F.; Pellegrini, V.; Emtev, K. V.; Forti, S.; Starke, U.; Beltram, F.; Heun, S. Revealing the Atomic Structure of the Buffer Layer Between SiC (0001) and Epitaxial Graphene. *Carbon* **2013**, *51*, 249–254.
- (74) Rutter, G. M.; Guisinger, N.; Crain, J.; Jarvis, E.; Stiles, M. D.; Li, T.; First, P.; Stroscio, J. A. Imaging the Interface of Epitaxial Graphene with Silicon Carbide via Scanning Tunneling Microscopy. *Phys. Rev. B* **2007**, *76* (23), 235416.
- (75) Sorger, C.; Hertel, S.; Jobst, J.; Steiner, C.; Meil, K.; Ullmann, K.; Albert, A.; Wang, Y.; Krieger, M.; Ristein, J.; et al. Gateless Patterning of Epitaxial Graphene by Local Intercalation. *Nanotechnology* **2015**, *26* (2), 025302.
- (76) Wong, S. L.; Huang, H.; Wang, Y.; Cao, L.; Qi, D.; Santos, I.; Chen, W.; Wee, A. T. S. Quasi-Free-Standing Epitaxial Graphene on SiC (0001) by Fluorine Intercalation from a Molecular Source. *ACS Nano* **2011**, *5* (9), 7662–7668.
- (77) Rutter, G. M.; Crain, J.; Guisinger, N.; Li, T.; First, P.; Stroscio, J. Scattering and Interference in Epitaxial Graphene. *Science* **2007**, *317* (5835), 219–222.
- (78) Simon, L.; Bena, C.; Vonau, F.; Aubel, D.; Nasrallah, H.; Habar, M.; Peruchetti, J. Symmetry of Standing Waves Generated by a Point Defect in Epitaxial Graphene. *Eur. Phys. J. B* **2009**, *69* (3), 351–355.
- (79) Emery, J. D.; Wheeler, V. D.; Johns, J. E.; McBriarty, M. E.; Detlefs, B.; Hersam, M. C.; Kurt Gaskill, D.; Bedzyk, M. J. Structural Consequences of Hydrogen Intercalation of Epitaxial Graphene on SiC (0001). *Appl. Phys. Lett.* **2014**, *105* (16), 161602.
- (80) Brause, M.; Braun, B.; Ochs, D.; Maus-Friedrichs, W.; Kempfer, V. Surface Electronic Structure of Pure and Oxidized Non-Epitaxial Mg₂Si Layers on Si (111). *Surf. Sci.* **1998**, *398* (1–2), 184–194.
- (81) Wigren, C.; Andersen, J.; Nyholm, R.; Karlsson, U. O. Epitaxial Silicide Formation in the Mg/Si (111) System. *Surf. Sci.* **1993**, *289* (3), 290–296.
- (82) Casey, P.; Hughes, G. High Resolution Photoemission Study of the Formation and Thermal Stability of Mg Silicide on Silicon. *Thin Solid Films* **2011**, *519* (6), 1861–1865.

- (83) Van Buuren, M.; Voermans, F.; VanKempen, H. Bonding in Mg₂Si Studied with X-Ray Photoelectron Spectroscopy. *J. Phys. Chem.* 1995, 99 (23), 9519–9522.
- (84) Schröder, U. A.; Petrović, M.; Gerber, T.; Martinez-Galera, A. J.; Gránás, E.; Arman, M. A.; Herbig, C.; Schnadt, J.; Kralj, M.; Knudsen, J.; Michely, T. Core Level Shifts of Intercalated Graphene. *2D Mater.* 2017, 4 (1), 015013.
- (85) Gugel, D.; Niesner, D.; Eickhoff, C.; Wagner, S.; Weinelt, M.; Fauster, T. Two-Photon Photoemission from Image-Potential States of Epitaxial Graphene. *2D Mater.* 2015, 2 (4), 045001.
- (86) Mammadov, S.; Ristein, J.; Krone, J.; Raidel, C.; Wanke, M.; Wiesmann, V.; Speck, F.; Seyller, T. Work Function of Graphene Multilayers on SiC(0001). *2D Mater.* 2017, 4 (1), 015043.
- (87) Wehenkel, D. J.; Bointon, T. H.; Booth, T.; Boggild, P.; Craciun, M. F.; Russo, S. Unforeseen High Temperature and Humidity Stability of FeCl₃ Intercalated Few Layer Graphene. *Sci. Rep.* 2015, 5, 7609.
- (88) Cowie, B.; Tadich, A.; Thomsen, L. The Current Performance of the Wide Range (90–2500 eV) Soft X-ray Beamline at the Australian Synchrotron. *AIP Conference Proceedings*; American Institute of Physics: 2010; pp 307–310.
- (89) Himpsel, F.; McFeely, F.; Taleb-Ibrahimi, A.; Yarmoff, J.; Hollinger, G. Microscopic Structure of the SiO₂/Si Interface. *Phys. Rev. B* 1988, 38 (9), 6084.
- (90) Gelius, U.; Asplund, L.; Basilier, E.; Hedman, S.; Helenelund, K.; Siegbahn, K. A High Resolution Multipurpose ESCA Instrument With X-ray Monochromator. *Nucl. Instrum. Methods Phys. Res., Sect. B* 1984, 1 (1), 85–117.
- (91) Helander, M.; Greiner, M.; Wang, Z.; Lu, Z. Pitfalls in Measuring Work Function Using Photoelectron Spectroscopy. *Appl. Surf. Sci.* 2010, 256 (8), 2602–2605.
- (92) Schultz, T.; Lenz, T.; Kotadiya, N.; Heimel, G.; Glasser, G.; Berger, R.; Blom, P. W.; Amsalem, P.; de Leeuw, D. M.; Koch, N. Reliable Work Function Determination of Multicomponent Surfaces and Interfaces: The Role of Electrostatic Potentials in Ultraviolet Photoelectron Spectroscopy. *Adv. Mater. Interfaces* 2017, 4 (19), 1700324.
- (93) Coletti, C.; Riedl, C.; Lee, D. S.; Krauss, B.; Patthey, L.; von Klitzing, K.; Smet, J. H.; Starke, U. Charge Neutrality and Band-Gap Tuning of Epitaxial Graphene on SiC by Molecular Doping. *Phys. Rev. B* 2010, 81 (23), 235401.
- (94) Horcas, I.; Fernández, R.; Gomez-Rodriguez, J.; Colchero, J.; Gómez-Herrero, J.; Baro, A. WSXM: A Software for Scanning Probe Microscopy and a Tool for Nanotechnology. *Rev. Sci. Instrum.* 2007, 78 (1), 013705.
- (95) Kresse, G.; Furthmüller, J. Efficiency of ab-initio Total Energy Calculations for Metals and Semiconductors Using a Plane-Wave Basis Set. *Comput. Mater. Sci.* 1996, 6 (1), 15–50.
- (96) Perdew, J. P.; Burke, K.; Ernzerhof, M. Generalized Gradient Approximation Made Simple. *Phys. Rev. Lett.* 1996, 77 (18), 3865.
- (97) Grimme, S.; Ehrlich, S.; Goerigk, L. Effect of the Damping Function in Dispersion Corrected Density Functional Theory. *J. Comput. Chem.* 2011, 32 (7), 1456–1465.